WR Muehlberger

NASA Technical Memorandum 88383

Reports of Planetary Geology and Geophysics Program - 1985

January 1986

NASA

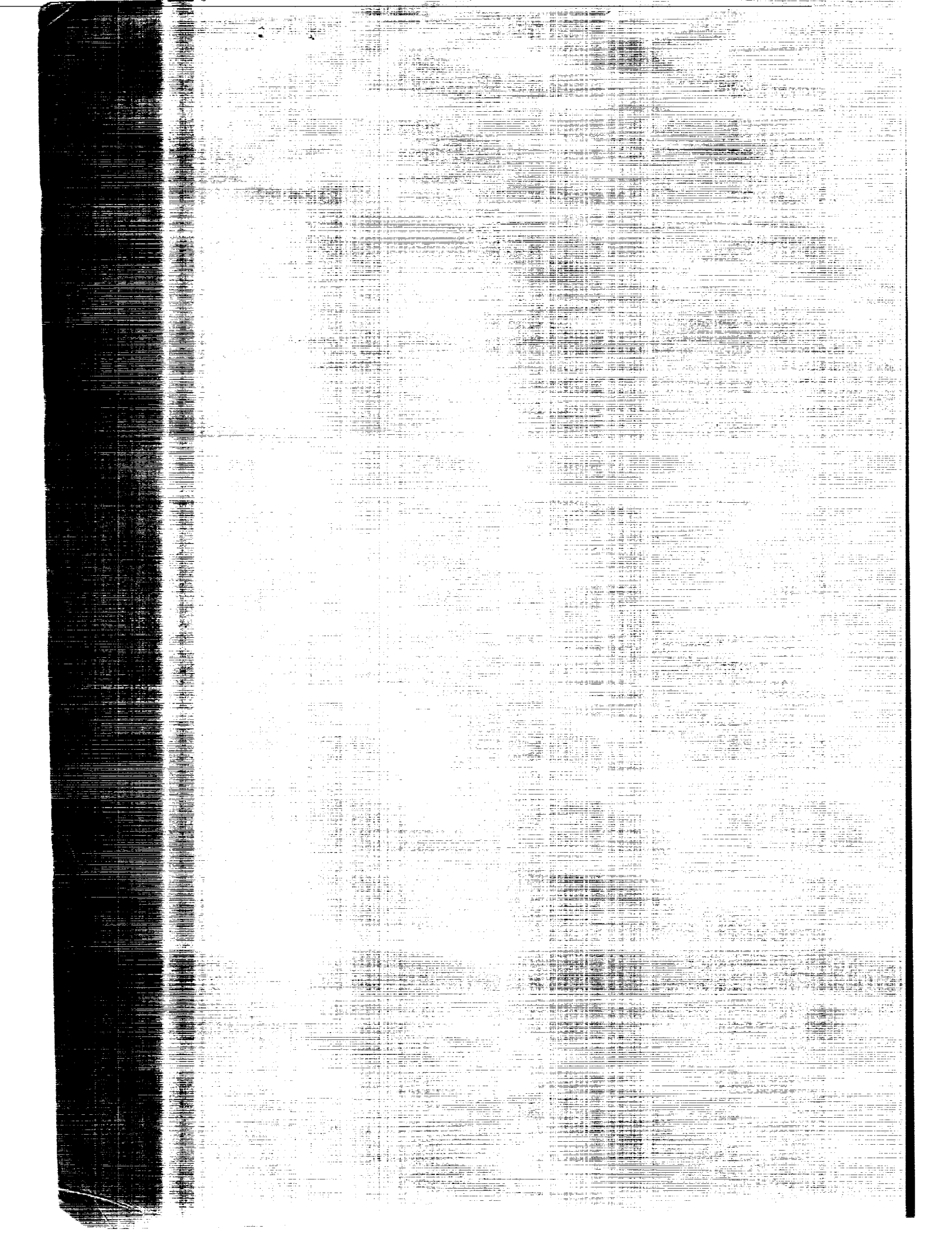

NASA Technical Memorandum 88383

REPORTS OF PLANETARY GEOLOGY AND GEOPHYSICS PROGRAM — 1985

Compiled by
S. J. Bougan
Center for Earth and Planetary Studies
Washington, D.C.

National Aeronautics
and Space Administration

Scientific and Technical Information Branch

1986

FOREWORD

This is a compilation of abstracts of reports from Principal Investigators of NASA's Office of Space Science and Applications, Solar System Exploration Division, Planetary Geology and Geophysics Program.

The purpose is to provide a document which succinctly summarizes work conducted in this program over the past year (1985). Each report reflects significant accomplishments within the area of the author's funded grant or contract.

No attempt has been made to introduce editorial or stylistic uniformity; on the contrary, the style of each report is that of the Principal Investigator and may best portray his research.

Joseph M. Boyce
Discipline Scientist
Planetary Geosciences Program

TABLE OF CONTENTS

Page

Foreword..... iii

CHAPTER 1 - COMETS AND ASTEROIDS

Asteroid 29 Amphitrite: Surface Characteristics and Prospects for the Galileo Flyby..... 3
J. F. Bell, M. J. Gaffey, J. C. Gradie, B. R. Hawke, and T. B. McCord

On the Brightness Variations of Comet Halley at Large Heliocentric Distances..... 4
K. R. Flammer, B. Jackson, and D. A. Mendis

Meteorite Spectroscopy and Characterization of Asteroid Surface Materials..... 5
M. J. Gaffey

The Effects of Electrostatic Charging on the Dust Distribution at Halley's Comet..... 8
M. Horanyi and D. A. Mendis

The Dynamics of Charged Dust in the Tail of Comet Giacobini-Zinner..... 9
M. Horanyi and D. A. Mendis

Trajectories of Charged Dust Grains in the Cometary Environment..... 10
M. Horanyi and D. A. Mendis

The Chemical Differentiation of the Cometary Nucleus: The Process and its Consequences..... 11
H. L. F. Houpis, W. H. Ip, and D. A. Mendis

Surface Morphology of Cometary Nuclei..... 12
M. C. Malin and J. Zimbleman

Asteroid Composition and Meteorite Origins..... 14
L. McFadden and M. F. A'Hearn

Convex-Profile Inversion of Asteroid Lightcurves..... 15
S. J. Ostro

Proper Elements and Mars-Crossing Depths of Planet-Crossing UCAS Asteroids..... 18
E. M. Shoemaker, R. F. Wolfe, S. J. Bus, and J. G. Williams

Brightness Curves and Porosities of Cometary Nuclei..... 22
R. Smoluchowski

How to Make a Comet..... 25
J. Stephens, R. S. Saunders, and F. Fanale

Are Comets Responsible for the Period of Heavy Bombardment?..... 28
R. G. Strom

Dynamics of Long-Period Comets..... 31
P. R. Weissman

Comet Thermal Modeling..... 33
P. R. Weissman and H. H. Kieffer

The Duplicity of P/Holmes..... 35
F. L. Whipple

Small Solar System Bodies..... 38
J. G. Williams and J. Gibson

Small Bodies Databases..... 41
C. A. Wood

CHAPTER 2 - OUTER PLANETS AND SATELLITES

Voyager Saturnian Ring Measurements and the Early History of the Solar System..... 47
H. Alfvén

Coefficient of Restitution of Ice Particles at Very Low Velocities..... 48
F. Bridges and D. Lin

Silicate Volcanism on Io..... 51
M. H. Carr

The Trailing Side of Europa: Possible Detection of Heavy Water Ice..... 54
R. N. Clark and R. H. Brown

Ganymede and Callisto: Toward a New Synthesis..... 57
S. K. Croft

Planetary Ring Dynamics and Morphology..... 60
J. Cuzzi, F. Shu, and R. Durisen

Dynamics of Satellites, Asteroids and Rings..... 63
S. F. Dermott

The Shape and Topography of Io..... 66
R. W. Gaskell, J. E. Riedel, and S. P. Synnott

Extensional Tectonic Features as Indications of Lithospheric Strength and Early Thermal Profiles on Ganymede..... 68
M. P. Golombek and W. B. Banerdt

Geologic Implications of Spectrophotometric Measurements on Europa..... 71
M. P. Golombek and B. Buratti

Observational Evidence for Red Polar Caps on Io..... 73
F. Graham and B. Hapke

Dynamical Evolution of the Galilean Satellites: Orbital Evolution Paths..... 74
R. Greenberg

Dust-Magnetosphere Interactions..... 76
E. Grun, G. E. Morfill, and D. A. Mendis

The Ices of Io: Sulfur Dioxide, Disulfur Monoxide and Polysulfur Oxide..... 77
B. Hapke

On the Sputter Alteration of Regoliths of Outer Solar System Bodies..... 78
B. Hapke

The Dynamical Evolution of Saturn's E-Ring..... 79
J. R. Hill and D. A. Mendis

Charged Particle Induced Charges in Icy Objects in the Outer Solar System..... 80
R. E. Johnson

A Shepherding Model for Neptune's Arc Ring..... 83
J. Lissauer

Aspects of Icy (and Non-Icy) Satellite Structure, Evolution, and Bombardment History..... 84
W. B. McKinnon

Entry of Dust Particles into Planetary Magnetospheres.... 87
D. A. Mendis

Electrodynamic Processes in the Ring System of Saturn.... 88
D. A. Mendis, J. R. Hill, W. H. Ip, C. K. Goertz, and E. Grün

A Note on Jupiter's "Grossamer" Ring..... 89
D. A. Mendis, J. R. Hill, W. Fillius, and T. G. Northrop

Extensional Tectonics of the Saturnian Satellites..... 90
J. M. Moore and R. Greeley

Global Tectonic Mapping of Ganymede: A Preliminary Report..... 92
S. L. Murchie and J. W. Head

Global Reorientation of Ganymede by the Basin Gilgamesh: Models and Evidence from Tectonic Patterns..... 94
S. L. Murchie and J. W. Head

Proton Sputtering of Sulfur and Applications to Io..... 96
D. Nash

Sulfur-Oxygen Processes on Io..... 99
R. M. Nelson and W. D. Smythe

Dynamical Studies of Saturn's Rings..... 101
P. D. Nicholson and C. C. Porco

Orbital Resonances, Unusual Configurations and Exotic Rotation States among the Natural Satellites..... 104
S. J. Peale

Tectonics and Cratering on Icy Satellites..... 105
P. M. Schenk and W. B. McKinnon

Texture Variations on Io: Evidence from Opposition Surges..... 108
D. P. Simonelli and J. Veverka

Distinctive Circular Structure, Central Galileo Regio Quadrangle (JG-3), Ganymede..... 111
J. R. Underwood, A. Woronow, R. Casacchia, and M. J. Teeling

Enceladus: Refined Search for Color and Reflectance Variations among Geologic Units..... 114
J. Veverka and P. Thomas

Subcentimeter-Size Particle Distribution Functions in Saturn's Rings from Voyager Radio and Photopolarimeter Occultation Data..... 117
H. A. Zebker, G. L. Tyler, and E. A. Marouf

CHAPTER 3 - LUNAR ORIGIN AND SOLAR SYSTEM DYNAMICS

Cosmogony as an Extrapolation of Magnetospheric Research..... 123
H. Alfvén

Magnetospheric Research and the History of the Solar System..... 124
H. Alfvén

Dynamical Constraints on the Origin of the Moon..... 125
A. P. Boss and S. J. Peale

Protostellar Angular Momentum Transport by Spiral Density Waves..... 126
P. Cassen and C. Yuan

Moon Origin: The Impact-Trigger Hypothesis..... 129
W. K. Hartmann

Giant Impactors: Plausible Sizes and Populations..... 130
W. K. Hartmann

Equatorial Clustering of Craters and Multi-Ring Basins: Possible Indications of Lunar Polar Displacement..... 131
D. M. Hooper and T. A. Maxwell

Planetesimal Dissolution in the Envelopes of the Forming, Giant Planets..... 134
J. B. Pollack, M. Podolak, P. Bodenheimer, and B. Cristofferson

Orbital Resonances in the Solar Nebula..... 136
S. J. Weidenschilling and D. R. Davis

Accumulation of the Planets..... 139
G. W. Wetherill

Solar System Dynamics..... 142
J. Wisdom

CHAPTER 4 - PLANETARY INTERIORS, PETROLOGY AND GEOCHEMISTRY

Lithospheric Strengths of the Terrestrial Planets..... 147
W. B. Banerdt and M. P. Golombek

Analysis of Harmonic Spline Gravity Models for Venus and Mars..... 150
C. Bowin

The Surface Rocks of Mars: Terrestrial Equivalents..... 153
R. G. Burns

The Theoretical Determination and Experimental Effects of Cooling History on Silicate Glasses..... 156
M. D. Dyar, D. P. Birnie, M. T. Naney, S. E. Swanson

Investigations of Weathering Processes in Cold, Dry Environments - Dry Valleys of Antarctica..... 158
E. K. Gibson

Martian Weathering Products in a Shergottite Meteorite... 161
J. L. Gooding and D. W. Muenow

Lunar Mantle Composition and Density Models Consistent with Seismic Velocity Limits and Other Geophysical Constraints..... 164
L. L. Hood and J. Jones

High-Pressure Experimental Studies Bearing on Oxygen in Planetary Cores..... 167
R. Jeanloz and E. Knittle

Properties of Planetary Material at High Pressures and Temperatures..... 170
W. J. Nellis, H. B. Radousky, M. Ross, and A. C. Mitchell

High Pressure Cosmochemistry of Major Planetary Interiors: Laboratory Studies of the Water-Rich Region of the System Ammonia-Water..... 173
M. Nicol, M. Johnson, and S. Boone

Geophysical Investigations of Venus..... 176
R. J. Phillips

Longevity of a Dense Carbon Dioxide Atmosphere on Mars... 179
J. B. Pollack

Geophysical Interpretation of Venus Gravity Data..... 181
R. D. Reasenberg

Two-Layer Convection Model for the Earth's Mantle..... 184
G. Schubert and K. Ellsworth

Tidal Dissipation in Io and the Moon..... 186
G. Schubert and M. N. Ross

The Martian Atmosphere Before and After the Argyre Impact..... 188
P. H. Schultz

Gravity Data Analysis..... 190
W. L. Sjogren

Valles Marineris as Karst: Feasibility and Implications for Martian Atmospheric Evolution..... 193
J. R. Spencer and S. K. Croft

How Much Anorthosite in the Lunar Crust?: Implications for Lunar Crustal Origin..... 196
P. D. Spudis and P. A. Davis

The Apennine Bench Formation Revisited..... 199
P. D. Spudis and B. R. Hawke

The Proposed Lunar and Procellarum Basin: Some Geochemical Inconsistencies..... 203
P. D. Spudis and P. H. Schultz

Investigation of Lunar Crustal Structure and Isostacy.... 206
C. H. Thurber

Implications of Convection in the Moon and the Terrestrial Planets..... 207
D. L. Turcotte

CHAPTER 5 - CRATERING PROCESSES

Relative Ages of Martian Terrain Units..... 211
N. G. Barlow and R. G. Strom

Impact and Cratering Processes on Asteroids, Satellites and Planets..... 214
C. R. Chapman, D. R. Davis, R. Greenberg, and S. J. Weidenschilling

Impact Experiments..... 217
W. K. Hartmann

Impact Crater Scaling Laws..... 218
K. A. Holsapple

The Nature of Crater Rays: The Copernicus Example..... 221
C. M. Pieters, J. B. Adams, P. J. Mouginis-Mark, S. H. Zisk, M. O. Smith, J. W. Head, and T. B. McCord

Impact-Induced Vaporization: Effect of Impact Angle and Atmospheric Pressure..... 222
P. H. Schultz and D. E. Gault

Experimental Investigation of Crater Growth Dynamics..... 224
R. M. Schmidt, K. R. Housen, M. D. Bjorkman and K. A. Holsapple

The Effect of Projectile Shape on Cratering Efficiency and Crater Profile in Granular Targets..... 227
P. H. Schultz and D. E. Gault

Research Activities in Grant Period '84-'85--NASA Grant: NAGW-439 229
A. Woronow

CHAPTER 6 - AEOLIAN PROCESSES AND LANDFORMS

On the Rate of Formation of Sedimentary Debris on Mars... 233
R. E. Arvidson

The Relative Rates of Aeolian and Tectonic Processes on Venus and Mars..... 234
R. E. Arvidson and R. Kahn

Regional Dust Deposits on Mars: Origin, Age, and Geologic History..... 237
P. R. Christensen

Martian Dust Particles as Condensation Nuclei..... 239
J. L. Gooding

Dust Storms on Mars: Mechanisms for Dust-Raising..... 242
R. Greeley

Distribution of Sedimentary Debris in the South Polar Region of Mars..... 245
E. Guinness, R. Arvidson, R. Kahn, and J. Plaut

Influence of Atmospheric Dust Loading and Water Vapor Content on Settling Velocities of Martian Dust/Ice Grains..... 248
S. W. Lee

Dust Transport at High Altitudes and Low Pressures on Mars: Aeolian Activity on the Tharsis Montes..... 251
S. W. Lee

Sand-Grain Response in Planetary Atmospheres..... 254
D. J. MacKinnon

Transverse Bedforms in High-Density Fluids: Venus and Earth..... 257
J. R. Marshall, R. Greeley, D. Fox, S. Bougan, and M. Sheridan

Distribution of Possible Sources of Dune-Like Material at the Martian Poles..... 260
R. S. Saunders and T. J. Parker

Mars: Color Patterns of Eolian Sediments..... 263
P. Thomas

Particle Speed and Concentration in a Saltation Cloud: Preliminary Wind Tunnel Results..... 265
S. H. Williams and R. Greeley

CHAPTER 7 - FLUVIAL PROCESSES

Evolution of Small Valley Networks in the Heavily Cratered Terrains of Mars..... 271
V. R. Baker

Flow Modeling of Cataclysmic Flood Discharges..... 274
V. R. Baker and J. E. O'Conner

Groundwater Sapping and Morphemetry of Hawaiian Valleys.. 277
R. C. Kochel

Multi-Layered Sediments and Groundwater Sapping Experiments..... 280
R. C. Kochel and D. W. Simmons

Harmonic Shape Analyses of Streamlined Landforms with Ramifications to the Origin of the Martian Outflow Channels..... 283
P. D. Komar and N. G. Pisias

The Effect of Slope on Experimental Drainage Networks: Possible Application to Mars..... 286
L. F. Phillips and S. A. Schumm

CHAPTER 8 - VOLCANIC PROCESSES

The Validity of the Jeffreys' Equation for the Lava Flows at Alba Patera, Mars..... 291
S. Baloga, D. Pieri, D. Schneeberger, and R. S. Saunders

The Geology of Round Mountain, a Bimodal Volcanic Field in Northwest Arizona..... 294
M. M. Bush and J. S. King

Lava-Flow Rheology in the Tharsis Region of Mars..... 297
A. Fox and E. C. Morris

Hadley Rille, Lava Tubes and Mare Volcanism at the Apollo 15 Site..... 302
R. Greeley and P. D. Spudis

Martian Lava Flows: Morphology and Modes of Emplacement..... 306
R. Greeley and E. Theilig

The Role of Lava Tubes in Hawaiian Volcanoes..... 309
R. Greeley

Recent (?) Volcanism in the Valles Marineris, Mars..... 311
B. K. Lucchitta

Lava Flow Profiles: Time Dependent Solutions of the Jeffreys' Equation..... 315
D. Pieri and S. Baloga

Dimensions of Lava Flows at Alba Patera, Mars..... 318
D. Pieri, D. Schneeberger, S. Baloga, and
R. S. Saunders

Graphic Models of Clast Transport During Explosive
Volcanism..... 321
M. F. Sheridan and J. Dehn

Volcanic Collapse Crater at Mount Hope, Arizona and
Extraterrestrial Analogs..... 322
A. M. Simmons and J. S. King

The Study of Long Lava Flows on Mauna Loa..... 325
G. P. L. Walker and S. K. Rowland

Near-Vent Pressure in Planetary Volcanic Eruptions..... 328
L. Wilson and P. J. Mouginis-Mark

Venus Volcanism: Theory and Predictions of Volcanic
Deposits and Landforms..... 331
L. Wilson and J. W. Head

Ashflow Caldera Fields..... 333
C. A. Wood and C. D. Duncan

Estimates of Yield Strength, Effusion Rate, and
Viscosity for Six Lava Flows on the Martian Volcano
Ascraeus Mons..... 336
J. R. Zimbelman and J. H. Fink

CHAPTER 9 - VIKING LANDER SITES

Spectral Mixture Modeling: A New Analysis of Rock and
Soil Types at the Viking Lander 1 Site..... 341
J. B. Adams and M. O. Smith

Viking Lander Multispectral Observations: I. Radio-
metric Calibrations and Photometry of Blocks..... 344
E. Guinness, R. Arvidson, M. Dale-Bannister,
R. Singer, and E. Bruckenthal

Viking Lander Multispectral Observations: II. Compari-
sons to Viking Orbiter Color Data..... 347
E. Guinness, R. Arvidson, M. Dale-Bannister,
R. Singer, and E. Bruckenthal

Are the Viking Lander Sites Representative of the
Surface of Mars?..... 350
B. M. Jakosky and P. R. Christensen

Loss of Fine-Scale Surface Texture in Viking Orbiter Images and Implications for the Inferred Distribution of Debris Mantles..... 353
R. Kahn, E. Guinness, and R. Arvidson

Martian Miniature Slope Failures..... 355
H. J. Moore

Multispectral Interpretation of Geologic Materials Exposed at the Viking Lander Sites..... 358
R. B. Singer, E. A. Bruckenthal, E. A. Guinness, and R. E. Arvidson

CHAPTER 10 - STRUCTURE, TECTONICS AND STRATIGRAPHY

Rifting and Lithospheric Structure on Venus..... 363
W. B. Banerdt and M. P. Golombek

Subsurface Heating During Impact Basin Formation: Constraints from Thermal Contraction and Thermal Stress.. 366
S. R. Bratt, S. C. Solomon, and J. W. Head

Evidence for Major Cross-Strike Structural Discontinuities: Maxwell Montes, Venus..... 369
R. M. V. Bruegge, J. W. Head, and D. B. Campbell

Evidence for Large-Scale Horizontal Motions in Northwest Ishtar Terra, Venus..... 372
L. S. Crumpler, J. W. Head, and D. B. Campbell

Ancient Fractures in the Tharsis Region..... 375
R. A. Francis

Tectonic Tests of Proposed Polar Wander Paths for Mars and the Moon..... 378
R. E. Grimm and S. C. Solomon

Olympus Mons Aureole: Evidence for Extensional and Compressional Deformation Associated with Emplacement.... 381
J. W. Head and N. G. Carras

Creep of Ice: Further Studies..... 383
H. C. Heard, W. B. Durham, and S. H. Kirby

Pedimentation and Origin of the Basin Beds in Candor Chasma..... 385
P. C. Patton

Tectonics of the Elysium Region, Mars..... 387
J. B. Plescia

Framework of Tharsis Tectonics..... 390
J. T. Raitala and R. S. Saunders

Procellarum Basin: A Major Impact or the Effect of Imbrium?..... 393
P. H. Schultz and P. D. Spudis

Global Topographic and Structural Fabric of Venus..... 395
V. L. Sharpton and J. W. Head

The Elastic Lithosphere: Some Relationships among Flexure, Depth of Faulting, Lithospheric Thickness, and Thermal Gradient..... 397
S. C. Solomon

Lava-Flows: Application of Plate Theory to Pressure Ridge Formation..... 400
E. Theilig and R. Greeley

Channels of Mars' Elysium Region: Extent, Sources, and Stratigraphy..... 403
K. L. Tanaka and D. H. Scott

The Tharsis Plateau Ridge System: Inferred and Predicted Compressive Stresses..... 406
T. R. Watters and T. A. Maxwell

CHAPTER 11 - GEOMORPHOLOGY

Granicus Valles in Elysium..... 411
D. M. Anderson and G. Brandstrom

Evolution of Valleys Dissecting Volcanoes on Mars and Earth..... 414
V. R. Baker

Fluvial Drainage Systems and Sedimentary Basins: Margaritifer Sinus, Mars..... 417
J. C. Boothroyd and J. A. Grant

Ring Furrows on Martian Highlands: Guides to Surface Processes and Stratification..... 421
R. A. De Hon and E. E. McDaniel

Extraction of Quantitative Morphology for Irregular Surface Features on Mars..... 424
P. A. Davis and L. A. Soderblom

Morphology and Rheology of the Royal Gardens Basalt Flows, Kilauea Volcano..... 427
J. Fink and J. Zimbelman

Characteristic Structures of the Highland Boundary on Mars and Comparison with Topography..... 430
H. Frey and A. Semeniuk

Regional Variation in Morphometric Properties of Large Symmetric Knobs on Mars..... 433
H. Frey, J. Middleton, and A. Semeniuk

Crater Counts in the Highland Boundary Transition Zone in Eastern Mars..... 436
H. Frey, A. Semeniuk, J. Semeniuk and S. Tokarcik

The Geomorphic Evolution of Eastern Margaritifer Sinus, Mars..... 439
J. A. Grant and J. C. Boothroyd

Drainage Basin Areas and Densities: Samara and Parana/Loire Valles, Southeastern Margartifer Sinus, Mars..... 442
J. A. Grant and J. C. Boothroyd

Effects of Elevation and Plains Thicknesses on Martian Crater Ejecta Morphologies on the Ridged Plains..... 446
V. M. Horner and R. Greeley

Planetary Geomorphology Field Studies at Mount St. Helens..... 449
D. R. Janke and M. C. Malin

An Ancient Ocean on Mars?..... 450
B. K. Lucchitta, H. M. Ferguson, and C. Summers

Planetary Geomorphology Field Studies in Iceland and Antarctica..... 456
M. C. Malin

Photogeological Studies of Mars: Polar Deposits and Small Dunes..... 458
M. C. Malin

Episodic Channeling Punctuated by Volcanic Flows in Mangala Valles Region, Mars..... 459
H. Masursky, M. G. Chapman, A. L. Dial, and M. E. Strobell

Stratigraphic Relationships in the Utopia Region, Mars.. 462
G. E. McGill

Longitudinal Depth Profile for Nirgal Vallis..... 465
T. J. Parker and D. M. Schneeberger

Morphology and Distribution of Sinuous Ridges in Central and Southern Argyre..... 468
T. J. Parker, D. C. Pieri, and R. S. Saunders

Volcano/Ground Ice Interactions and the Origin of Fractured Terrain on Mars..... 471
S. Postawko and P. Mouginis-Mark

Experimental Fracture Patterns: Application to Martian Channels..... 474
H. Pranger

Ejecta from the Glover Bluff Crater, or Other Craters of the Same Age..... 476
W. F. Read

Size and Randomness of Ground Patterns for Earth and Mars: Implications for Origin and Modification..... 477
L. A. Rossbacher

Hierarchical Patterned Ground on Earth and Mars..... 480
L. A. Rossbacher

Impact Structures of Western Australia..... 482
E. M. Shoemaker and C. S. Shoemaker

Morphology of Martian Central-Feature Craters with Some Implications for Genesis Models..... 485
S. J. Steenstrup

Polygonal Ground in the Northern Hemisphere of Mars..... 488
C. A. Summers and B. K. Lucchitta

Lava-Ice Interactions on Mars..... 491
D. E. Wilhelms

Relation Between Thickness and Degradation of Martian Upland Deposits..... 494
D. E. Wilhelms, R. J. Baldwin, and C. J. Hayden

CHAPTER 12 - REMOTE SENSING AND REGOLITH STUDIES

Vega Landing Sites: Venera 15/16 Geologic Unit Analogs from Pioneer/Venus Reflectivity and RMS Slope..... 499
D. L. Bindschadler, J. W. Head, and J. B. Garvin

Identification of Geological Units Representing the Spectra Obtained by the Shuttle Multispectral Infrared Radiometer for a Portion of the Trans Pecos, Texas..... 502
H. G. Blount and J. L. Whitford-Stark

Reflectance Measurements of Planetary Surface Materials at Small Phase Angles..... 505
B. J. Buratti, W. D. Smythe, R. M. Nelson, V. Gharakhani, and B. Hapke

Crystal Chemistry and Origin of Blue Color in Meteoritic Hibonites: Evidence from Mossbauer Spectra of Iron-57 Doped Analogues..... 507
R. G. Burns, M. D. Dyar, V. L. Ryan, and T. C. Solberg

The Composition of the Martian Surface: Determination by Thermal Infrared Spectral Observations..... 509
P. R. Christensen

Mars Water-Ice Clouds..... 512
P. R. Christensen, R. W. Zurek, and R. Greeley

Martian Duricrusts: Interpretation of Thermal, Radio, and Radar Data..... 515
P. R. Christensen and B. Jakosky

Petrologic Province Maps of the Lunar Highlands Derived from Orbital Geochemical Data..... 518
P. A. Davis and P. D. Spudis

Sulfur Deposition of Silicates: Effects on Band Strengths..... 521
J. Gradie

Spectral Reflectance Study of the Hadley-Appenine (Apollo 15) Region..... 523
B. R. Hawke and P. G. Lucey

Remote Sensing Studies of the Nectaris Highlands..... 526
B. R. Hawke, C. R. Coombs, P. G. Lucey, J. F. Bell, P. D. Owensby, P. D. Spudis, and P. A. Davis

Mars: Implications of Detected Igenous Phases..... 528
R. L. Huguenin, R. Carter, and S. Anderson

IRTM Observations of Syrtis Major: An Active Aeolian Environment..... 532
S. W. Lee

The Reflectance Properties of the Surface of Venus from Venera Lander Color Panoramas..... 535
C. M. Pieters

Remote Sensing Information Applied to Geological Studies of Planets..... 536
C. M. Pieters

The Mid-Infrared (2.3-5.4 micron) Spectral Reflectance of Mafic and Phyllosilicates..... 538
T. L. Roush and R. B. Singer

Contrast Reversal in Reflectance Spectroscopy..... 540
A. Williams and B. Hapke

Lunar Science from Lunar Laser Ranging..... 541
J. G. Williams, X. X. Newhall, J. O. Dickey, and C. F. Yoder

CHAPTER 13 - RADAR APPLICATIONS

The Surface of Mercury: Geological Analysis and Interpretation of Radar Observations..... 545
P. E. Clark, R. F. Jurgens, and M. Kobrick

Mercury Radar Altimetry: New Results..... 548
J. K. Harmon, D. B. Campbell, D. L. Bindschadler, J. W. Head, and I. I. Shapiro

Lunar Radar Images - Landform Identification..... 550
H. J. Moore and T. W. Thompson

Venus Surface Composition from Radio/Radar Measurements.. 553
G. H. Pettengill, P. G. Ford, and B. D. Chapman

Viking Radio Science Data Analysis and Synthesis..... 555
R. D. Reasenberg

Mars: Seasonally Variable Radar Reflectivity..... 558
L. E. Roth and R. S. Saunders

Radar Signal Attenuation, "Skin Depth," and "Radar Imaging Depth"..... 560
G. G. Schaber

Radar Backscatter from a Subsurface Interface Following Penetration of a Low-Loss Medium..... 562
G. G. Schaber and R. C. Kozak

Southern Ishtar Terra and Guinevere/Sedna Planitia: New Observations from Earth-Based Radar..... 565
E. R. Stofan, D. B. Campbell, J. W. Head, and A. A. Hine

Multiple Ring Features in Themis Regio: Evidence for Endogenic Origin..... 567
E. R. Stofan, J. W. Head, and D. B. Campbell

Application of Numerical Methods to Planetary Radar Scattering..... 569
G. L. Tyler and R. A. Simpson

Radargrammetry for the Venus Radar Mapper Mission..... 570
S. S. C. Wu, F. J. Schafer, and A. E. Howington

CHAPTER 14 - GEOLOGIC MAPPING, CARTOGRAPHY AND GEODESY

A Digital Image Model of Mars..... 577
R. M. Batson

Mars Planimetric Mapping..... 580
R. M. Batson, P. M. Bridges, and J. L. Inge

Voyager Cartography..... 581
R. M. Batson, P. M. Bridges, and K. F. Mullins

Planimetric Mapping with Radar Images..... 584
R. M. Batson, S. L. Davis, and H. F. Morgan

Cartography of Nonspherical Satellites and Asteroids..... 586
R. M. Batson, K. Edwards, and C. E. Isbell

Geology of the Amenthes (MC-14) Northeast Quadrangle, Mars, and the Fluvial Development of Hebrus Valles and Hephaestus Fossae..... 587
E. H. Christiansen and J. Hopler

The Control Networks of the Satellites of Jupiter and Saturn..... 590
M. E. Davies

The Control Network of Mars: October 1985..... 591
M. E. Davies

A Unified Lunar Control Network..... 592
M. E. Davies and T. R. Colvin

The Galilean Satellite Geological Mapping Program, 1985.. 595
B. K. Lucchitta

Geology of the Ruwa Patera Quadrangle of Io..... 598
G. G. Schaber, D. H. Scott, and R. Greeley

New Geologic Map of Mars..... 601
K. L. Tanaka, R. Greeley, D. H. Scott, and J. E. Guest

Gravity-Profile Analysis Over Central Valles Marineris, Mars..... 603
K. L. Tanaka, N. E. Witbeck, and D. H. Scott

Planetary Radarclinometry in 1985..... 605
R. L. Wildey

A Mars Digital Terrain Model and Sample Correlation with a Mars Digital Image Model..... 608
S. S. C. Wu and A. E. Howington

On-Line Distortion Corrections for Viking Orbiter Images..... 612
S. S. C. Wu, A. E. Howington, and F. J. Schafer

Mars Global Topographic Map: 1:15,000,000 Scale..... 614
S. S. C. Wu, R. Jordan, and F. J. Schafer

Status of Compilation of the Mars 1:2,000,000-Scale Topographic Map Series..... 618
S. S. C. Wu, R. Jordan, and F. J. Schafer

CHAPTER 15 - SPECIAL PROGRAMS

Planetary Geology Speakers Bureau and Short Course..... 623
R. Greeley

Planetology Experiments on Space Station: Workshop Results..... 624
R. Greeley

Space Station Planning in the Solar System Exploration Division..... 626
J. Nuth

Reflectance Experiment Laboratory (RELAB)..... 627
C. M. Pieters

Debris-Cloud Collisions: Accretion Studies in the Space Station..... 628
P. H. Schultz and D. E. Gault

Impacts of Free-Floating Objects: Unique Space Station Experiments..... 630
P. H. Schultz and D. E. Gault

Planetary Nomenclature..... 632
M. E. Strobell, H. Masursky, and C. D. Nordquist

Regional Planetary Image Facilities' Data Directory..... 634
B. Weiss, T. Stein, and R. Arvidson

AUTHOR INDEX..... 637

CHAPTER 1

COMETS AND ASTEROIDS

ASTEROID 29 AMPHITRITE: SURFACE CHARACTERISTICS AND PROSPECTS FOR THE GALILEO FLYBY. J. F. Bell (1,3), M. J. Gaffey (2), J. C. Gradie (1), B. R. Hawke (1,3), and T. B. McCord (1). (1) Planetary Geosciences Div., Hawaii Inst. of Geophysics, Univ. of Hawaii, Honolulu, HI 96822; (2) Geology Dept., Rensselaer Polytechnic Inst., Troy NY 12181; (3) Visiting Astronomers at the NASA Infrared Telescope Facility.

NASA has recently changed the mission plan of the Galileo Jupiter mission to allow a close flyby of the main-belt asteroid 29 Amphitrite. Although the decision to conduct a close encounter will not be made until after launch in 1986 and will be dependent on the condition of the spacecraft, the asteroid and meteorite science communities must confront the possibility of dealing with high-resolution spacecraft data in less than two years.

Amphitrite is one of the larger members of spectral class "S" with a diameter of about 200km, a rotation period of 5.4 hours, and a highly irregular shape inferred from brightness variations. The S class (medium albedo, curved red spectra, olivine/pyroxene absorption bands) have been the focus of the biggest and longest-running controversey in asteroid spectral interpretation. One faction (including many prominent meteorite researchers) holds that these common asteroids are the parent bodies of the similarly common ordinary chondrites, and that the spectral differences can be reconciled by unknown regolith formation processes which exaggerate the apparent abundance of NiFe in the spectra. Another faction (including a large but variable proportion of asteroid observers) holds that the S-class spectra represent rare differentiated stony-iron meteorite classes. Several recent discoveries appear to strongly support this interpretation. A) Gaffey (Icarus 60, 83-114) has shown that the silicate chemistry of 8 Flora is inconsistent with chondritic assemblages, and that the artificial enhancement of metal abundance in simulated regoliths does not produce the characteristic S-type curved red continuum. B) A newly defined spectral class "Q" is spectrally identical to ordinary chondrites and occurs only in the Earth-crossing population(!) C) Another new class "A" appears to be of pallasitic composition and to grade smoothly into the S class. However, many remain unconvinced and discussion between the two factions continues to enliven scientific meetings.

We have explored the role Galileo might play in resolving this controversy by reexamining existing spectral data and obtaining new infrared spectra (similar to those to be returned by Galileo) at Mauna Kea Observatory. The IR reflectivity curve of Amphitrite is typical of observed S asteroids with curved red continuum and silicate absorption bands. Analysis of the bands indicates the silicate mineralogy is 40% olivine, 60% low-Ca (5%) medium-Fe (40%) pyroxene. This pyroxene chemistry could be consistent with an LL chondrite, but the pyx/ol ratio is typical of H chondrites. As with Flora, the detailed mineralogy is inconsistent with any ordinary chondrite. The curved continuum is also characteristic of differentiated metal-rich assemblages. We conclude that Amphitrite is most probably the surviving core of a body which largely melted but in which segregation of silicates and metal was incomplete. Of known meteorite types the lodranites are the closest mineralogical analog; however the large number of other S asteroids makes it statistically unlikely that the lodranites are from Amphitrite. We postulate the existence of a large variety of stony-iron meteorite classes covering the range from pallasites to lodranites to Steinbach (possibly including irons with silicate inclusions) corresponding to class S and A asteroids, most of which are not currently delivered to Earth. Two Galileo experiments may provide evidence to prove or refute the view presented above. The IR spectral mapper will provide spectra similar to that interpreted above for numerous small regions. If non-chondritic variations are found as with Flora, the stratigraphy of a differentiated meteorite parent body will be revealed. A more decisive test will be made by spacecraft tracking data which should provide the first accurate asteroid mass. Combined with a volume derived from imaging, we may hope for a density sufficiently accurate to distinguish between the chondritic and stony-iron interpretations.

ON THE BRIGHTNESS VARIATIONS OF COMET HALLEY AT LARGE HELIOCENTRIC DISTANCES

K. R. Flammer, B. Jackson and D. A. Mendis,
University of California, San Diego

Sporadic variations of its intrinsic brightness of up to 500%, with time scales as short as a few hours, have been exhibited by Halley's comet at large heliocentric distances (11 AU-8 AU). It is shown that many of these brightness enhancements are closely correlated to the encounter of high-speed solar wind streams by the comet. It is proposed that during such periods the night side of the comet gets charged to numerically large negative electrostatic potentials, with consequent electrostatic levitation and blow-off of fine charged dust grains lying on it. This gives rise to the observed brightness variations.

Meteorite Spectroscopy and Characterization of Asteroid Surface Materials

Michael J. Gaffey, Geology Department, Rensselaer Polytechnic Institute.

The purpose of this research program is to characterize the mineralogy and petrology of asteroid surface materials in order to improve our understanding of the nature and history of these minor planets, of their relationships to the meteorites, and of the earliest history of the solar system. The asteroids represent the surviving fragments of the building blocks which accreted to form the Earth and other terrestrial planets. The conditions and processes active in the inner solar system during the first few million years were quite different than those today. A short period of intense heating melted most small bodies, allowing them to differentiate. This coincided with or was followed by a very intense period of collisional breakup of some bodies while collisional aggregation (planet growth) proceeded in certain regions. The inner asteroid belt appears to have suffered from the same early intense bombardment as the region of Mars, which has been suggested as a mechanism to prevent the growth of Mars to an Earth-size object.

Only in asteroids is material preserved in an unaltered form from the formation epoch of the inner solar system. The investigation of the asteroids (which preserve a spatial record of these early conditions) and their samples, the meteorites (which provide a good temporal record of the sequence of events) provides the sole empirical means of investigating this period, of testing the various models of solar system and planetary formation, and of constraining the earliest conditions on the Earth.

The program involves visible and near-infrared (VNIR) laboratory spectral studies of meteorites (which are the best natural analogues to the surface materials of asteroids) and of terrestrial minerals and mixtures in order to identify and to define their mineralogically diagnostic spectral characteristics. These laboratory spectra are used to establish quantitative interpretive calibrations for determination of mineralogy, mineral chemistry, and mineral abundance from remotely obtained telescopic or spacecraft spectra of asteroids. Recent work has lead to the development of a calibration for the determination of phase abundance and composition for olivine-pyroxene mixtures, which are among the most abundant meteoritic and asteroidal silicate assemblages [Cloutis et al., 1985], and to a detailed definition of the spectral and physical properties of nickel-iron metal and of the implications of these properties for the nature and abundance of metal on asteroid surfaces (Gaffey, 1985a). Current projects include: (a) the development of a calibration relating the series of weak (10%) absorption features in the 0.5-1.1um region of carbonaceous chondrite spectra to the abundance and oxidation state of iron in their clay minerals, and to the alteration of the original assemblage by asteroidal sub-surface aqueous processes [Gaffey, 1980]; (b) the establishment of diagnostic spectral criteria for the identification of primitive, undifferentiated silicate assemblages [Gaffey, 1981]; and (c) an investigation of the spectral signatures and detection limits of the white inclusions, which are an important component of C3 meteorites, in asteroid surface materials [Rajan and Gaffey, 1984]. Future work includes an investigation of the spectral effects of thermal metamorphism of

carbonaceous chondritic materials, such as would have occurred in the moderately heated planetesimals. The results of this laboratory meteorite spectroscopy has also been utilized in the interpretation of the dark side of Saturn's satellite, Iapetus [Bell et al., 1984].

The program also involves the acquisition of high photometric precision VNIR telescopic spectra of asteroids. A large existing data base of selected targets already exits, and as needed additional observation are carried out in order to address specific issues concerning the nature, origin and evolution of of these minor planets. For example, the observations of (29) Amphitrite, a possible Galileo-flyby target, are continuing in order to provide the best attainable characterization of this asteroid prior to the December, 1986 encounter [Bell et al., 1985]. In a similar manner, observations of members of the Flora family are being made to test whether these are indeed the fragments of a disrupted body, and to constrain the internal structure of that parent body [Gaffey et al., 1984].

A centerpiece of this research program is the analysis of the asteroid spectra using the best available interpretive calibrations. The goal is to derive the most sophisticated achievable mineralogic and petrologic characterizations of the surface assemblages on each target asteroid, and of any material variations across their surfaces. This has produced detailed characterizations of the surface mineralogy and heterogeneity of asteroids (4) Vesta [Gaffey, 1983] and (8) Flora [Gaffey, 1984], and of the Earth-approaching asteroids [McFadden et al., 1984, 1985]. Current efforts are centered on analysis of the observational data for the asteroids (1) Ceres, (15) Eunomia, and (29) Amphitrite.

These mineralogic and petrologic interpretations, although a valuable result, are not an end in themselves. They are employed to constrain the nature and evolutionary history of each asteroid, and to determine possible meteoritic affinities. Thus the rotational variations of (8) Flora were utilized to establish that this object was indeed a differentiated body, that it was collisionally disrupted, and that its present surface is probably the exposed core-mantle boundary region of the parent body [Gaffey, 1984]. In a similar, manner the surface assemblage of (4) Vesta indicates a differentiated, but intact body, and supports this asteroid as a viable source for the suite of basaltic achondritic meteorites [Gaffey, 1983].

The overall goal of this work is the synthesis of these asteroidal data and models with theoretical cosmological models (nebular processes, late accretionary processes, collisional evolution, post-accretionary heating mechanisms) and meteoritic data sets (genetic relationships, evolutionary chronology, physical properties) in order to provide a better understanding of the early inner solar system and of the processes which produced and modified the terrestrial planets and planetesimals. Based on studies of meteoritic metal [Gaffey, 1985a] and on the S-type asteroids, including (8) Flora [Gaffey, 1984], we have concluded that a strong spectral signature of metal in an asteroid spectrum is persuasive evidence for a physically abundant metal phase at the surface of the body. This indicates that most of the large S-type asteroids, which dominate the inner belt, have been intensely heated, magmatically differentiated, and collisionally disrupted to expose their strong metal-rich cores [Gaffey, 1985b]. The inner belt, and presumably much of the inner solar system, underwent a very rapid and

early thermal, and then, collisional evolution driven by processes which shut off very early in solar system history. Present and future work is concentrating exploring these implications in much more detail.

References

Bell, J.F., D.P. Cruikshank, and M.J. Gaffey (1985) The composition and origin of the Iapetus dark material. Icarus 61, 192-207.

Bell, J.F., M.J. Gaffey, J.C. Gradie, S.L. Gilbert, B.R. Hawke, and T.B. McCord. (1985) Surface composition and heterogeneity of Asteroid (29) Amphitrite. Icarus. submitted.

Cloutis, E.A., M.J. Gaffey, T.L. Jackowski, and K.L. Reed. (1985) Calibrations of phase abundance, composition, and particle size distribution for olivine-orthopyroxene mixtures from reflectance spectra. J. Geophys. Res., submitted.

Gaffey, M.J. (1980) Mineralogically diagnostic features in the visible and near-infrared reflectance spectra of carbonaceous chondritic assemblages. Lunar. Sci. XI, 312-313.

Gaffey, M.J. (1981) Diagnostic spectral properties of ordinary chondrite assemblages: Implications for the S-asteroids. Bull. A.A.S. 13, 717.

Gaffey, M.J. (1983) The asteroid (4) Vesta: Rotational spectral variations, surface material heterogeneity, and implications for the origin of the basaltic achondrites. Lunar Planet. Sci. XIV, 231-232.

Gaffey, M.J. (1984) Rotational spectral variations of asteroid (8)Flora: Implications for the nature of the S-type asteroids and for the parent bodies of the ordinary chondrites. Icarus 60, 83-114.

Gaffey, M.J. (1985a) The spectral and physical properties of metal in meteorite assemblages: Implications for asteroid surface materials. Icarus. submitted.

Gaffey, M.J. (1985b) A paradigm for the S-type asteroids: Implications for the evolutionary history of the inner belt and the search for the ordinary chondrite parent bodies. Lunar Planet. Sci. XVI, 258-259.

Gaffey, M.J., J.F. Bell, and B.R. Hawke (1984) Observational tests of the differentiated nature of the Flora parent body. Bull. A.A.S. 16, 698.

McFadden, L.A., M.J. Gaffey, and T.B. McCord (1984) Mineralogical petrological characterizations of near-Earth asteroids. Icarus 59, 25.

McFadden, L.A., M.J. Gaffey, and T.B. McCord (1985) Near-Earth Asteroids: Possible sources based on reflectance spectroscopy. Science 229, 160.

Rajan, S. and M.J. Gaffey (1984) Spectral reflectance characteristics of Allende white inclusions. Lunar Planet. Sci. XV, 659-660.

THE EFFECTS OF ELECTROSTATIC CHARGING ON THE DUST DISTRIBUTION AT HALLEY'S COMET

M. Horanyi, Supercomputer Computational Research Institute, Florida State University, and D. A. Mendis, University of California, San Diego

Recognizing that the dust grains emitted from a comet get electrically charged in its plasma and radiative environment and are thus subject to electromagnetic forces (besides the ones due to solar radiation pressure and gravitation), we have simulated the fine dust distributions near Halley's comet during both its 1910 and its 1986 apparitions.

The effects of electromagnetic forces on the lower end of the dust mass spectrum are mainly manifested in the projection of the distribution normal to the orbital plane. The projections of the dust morphology as seen from the earth in 1910 largely obscure the effect of the electrical forces. Consequently the values derived by Sekanina and Larson (1984) for the nuclear spin period and orbital obliquity, from the analysis of the near-nuclear "spiral" features seen in 1910 (which are presumably a result of diurnally modulated continuous emission of dust from active spots on the nucleus), are not invalidated when electrical charging is included.

Assuming these values for the spin period and the orbital obliquity, we have simulated the dust distribution that is expected to be encountered by the spacecraft during the March 1986 fly-bys, taking into consideration the effects of electrical forces. We have simulated both the "background" distribution that results from uniform emission of dust from the sunward hemisphere and the "spiral" features that would result from an active equatorial spot similar to the one in 1910. It is seen that the distribution of the lower end of the dust mass spectrum is largely determined by the direction of the interplanetary magnetic field, particularly the component in the orbital plane of the comet. Since the interplanetary magnetic field switches sign with a periodicity of 5-10 days, the spacecraft (which follow each other 3 to 4 days apart) are likely to encounter entirely different dust distributions.

Finally, it is stressed that the larger velocities of the smaller grains that result from their electrical acceleration would result in a significant increase of the impact energies, over the case when they are uncharged, despite the large velocity of the spacecraft relative to the nucleus. This needs to be taken into account in deducing the lower end of the dust mass spectrum from the measured kinetic energy distribution of dust impacts.

THE DYNAMICS OF CHARGED DUST IN THE TAIL OF COMET GIACOBINI-ZINNER

M. Horanyi, Supercomputer Computational Research Institute, Florida State University, and D. A. Mendis, University of California, San Diego

A numerical simulation has been performed to calculate the distributions of dust particles of various sizes down the tail of Comet P/Giacobini-Zinner. When the electrostatic charging of the grains in the plasma and radiative environment of the comet is taken into account, it is found that the distribution of the grains (particularly at the lowest end of the mass spectrum) in a plane normal to the orbital plane is entirely different from what is expected had the grains been uncharged. Although the NASA-ICE spacecraft, which will fly through the tail of this comet almost normal to its orbital plane on 11 September 1985, has no dedicated dust experiments, it is expected that the plasma wave instrument will serve as an indirect detector, even of the smallest grains, via the plasma clouds created by the high-velocity dust impacts. Knowledge of the spatial variation of the grain sizes encountered along the flight path of the spacecraft will provide us with the information necessary to calculate the electrostatic potential of the grains, which in turn will lead to an estimation of the role of the electromagnetic forces on the dynamics of such grains.

TRAJECTORIES OF CHARGED DUST GRAINS IN THE COMETARY ENVIRONMENT

M. Horanyi, Supercomputer Computational Research Institute, Florida State University, and D. A. Mendis, University of California, San Diego

Using a simple model of the particles and fields environment of a comet, we have calculated the trajectories of the smallest (micron- and submicron-sized) dust grains that are expected to be released from the cometary nucleus. It is shown that electromagnetic forces play a crucial role in the dynamics of these particles. The present calculations indicate not only the asymmetry of the sunward dust envelopes that have been suggested earlier by other authors, but they also indicate the possible existence of wavy dust features far down the tail, reminiscent of the peculiar wavy dust feature observed in the dust tail of Comet Ikeya-Seki 1965f. The importance of these findings in studying the lower end of the cometary dust mass spectrum during the forthcoming fly-by missions to Comet Halley is underscored.

THE CHEMICAL DIFFERENTIATION OF THE COMETARY NUCLEUS: THE PROCESS AND ITS CONSEQUENCES

Harry L. F. Houpis, University of California, San Diego
W.-H. Ip, Max-Planck-Institut fur Aeronomie
D. A. Mendis, University of California, San Diego

Many comets, and perhaps a majority of them, behave as if they are H_2O-dominated, with the more volatile species trapped within the H_2O ice lattice to form clathrate hydrates. There are, however, some comets which indicate a production rate of these volatiles that is larger than is consistent with the clathrate hydrate model. Here we develop a model which explains both of these apparently contradictory observations in a natural way. The basis for our model is the gradual chemical differentiation of the outer layers of an initially homogeneous cometary nucleus as it orbits the Sun. The formation and evolution of an outer layer of dust and an inner layer that is depleted of the volatile species control the sublimation of the volatiles from the inner core. This model, in addition to providing a number of other observational tests for its validity, explains the high activity of "new" comets at large heliocentric distance and predicts that all evolved comets will eventually behave as if they were H_2O-dominated, independent of the initial chemical composition. The importance of recognizing this fact in attempting to draw cosmogonic inferences from present and future cometary observations is emphasized.

Surface Morphology of Cometary Nuclei

Michael C. Malin, Department of Geology, Arizona State University, Tempe, AZ 85287
James Zimbleman, Lunar and Planetary Institute, 3303 NASA Road 1, Houston, TX 77058

Differential ablation of volatile ices on comets, resulting from inhomogenieties in the distribution and thickness of mantling dust accumulations, may produce characteristic surface landforms. Numerical modelling suggests that the development of these landforms is extremely sensitive to such factors as mantle thickness, mantle accumulation as a function of time and cometary position, and pre-existing relief. Two types of features might be expected: ice-cored, dust-mantled **cones** created by inversion of relief resulting from partial insulation by thicker mantles, and irregularly shaped **pit and mesa topography**, resulting from spatial variability of mantle thickness and percent cover. Both of these landforms are seen in terrestrial environments where ablation landforms develop. The vertical extent of these forms is proportional to the maximum depth of ablation, while the lateral extent depends on the areal distribution of the dust mantle. Models of comet P/Halley suggest such landforms may be resolvable in images to be acquired by the ESA/Giotto Multicolour Camera.

Dust mantles have a profound effect on the thermal history of cometary nuclei and therefore on the rate of volatile release by comets. Brin and Mendis (1979) found that dust mantles depress the surface temperature sufficiently to inhibit the release of volatiles, which in turn contributes to a change in the observed brightness of the comet. Fanale and Salvail (1984) obtained similar results, and in addition found that a global mantle of 1 to 3 cm thickness can cause irreversible evolution to a non-cometary (i.e., asteroidal) body.

Experimental results of snow ablation beneath an ash layer provide insight into the relationship between the abundance of silicates and the ice sublimation. Driedger (1980) measured the rate of ablation for snow (density $\approx$ 0.5 gm/cm^3) covered by different thicknesses of Mount St. Helens ash. Her measurements showed that an ash layer 0.3 cm thick resulted in the most snow ablation, at a rate nearly double that on an adjacent, ash-free area. The insulating effects of the ash became important for thicknesses greater than 2.5 cm, producing less ablation than on an ash-free area. Ablation differences resulting from the presence of fine, dark silicate materials should be expected to greatly influence the extent and relative rate of activity on a comet nucleus.

The results of Driedger (1980) were used to make some quantitative estimates of the effects of a dust mantle on nucleus ablation and topographic variations caused by the mantle. The ablation results are strictly applicable at a distance of 1 AU from the sun but the gas production rates predicted for comet P/Halley by Weissman and Kieffer (1984) allow the ablation values to be scaled for the 80 days that the comet is within 1 AU of the sun. The mantle here represents that portion of the silicate materials not removed from the nucleus by the escaping volatiles. The total amount of ablation is significant, varying from 10 to 20 m, depending on the dust mantle thickness.

Values computed for a case without a mantle are consistent with the 6.9 m of ablation obtained by Weissman and Kieffer (1984) for an assumed density of 1 gm/cm^3. The results for a constant mantle thickness are symmetric with respect to perihelion while an increasing mantle thickness results in considerably more ablation on the incoming path.

The strong dependence of ablation rate on mantle thickness may be expected to contribute to topographic variability on the nucleus. If the initial mantle thickness is greatest within hollows on the surface, the variable mantle thickness could cause the topography of the

hollow to invert, providing the mantle is not sufficiently thick to act solely as an insulating blanket. The resulting form is likely to be a conical mound with the basic perimeter shape of the original depression. The mantle would be slightly thicker at the top of the mound. These conical mounds would be protected from further modification in shape unless the mantle is removed. Such removal could result from mantle blow-off, or by subtle downslope movements as noted on the martian moon, Diemos (Thomas, 1980). In either case, the scale of landform development would mimic the depth of ablation.

On completely smooth and homogeneous surfaces, little evolution can occur. However, surface undulations and/or mantle thickness variations can evolve over time to features of unusual aspect, as is often seen on ablating snowfields and glaciers (Hall, 1978; Nakawo and Young; 1981). In the case of initial pockets (or hollows or depressions) or thicker mantles surrounded by zones of thinner mantle, topographic inversion occurs. For example, small (10 to 40 cm high) ice–cored mounds on snow and ice form at the toe of one of the Knife Creek glaciers in the Valley of 10,000 Smokes, Katmai, Alaska (Muller and Coulter, 1957). The mantle on these cones consists of re–worked airfall tephra associated with the catastrophic eruptions in the area that occurred in June, 1912. The mantle, approximately 1-2 cm thick, is slightly thicker at the apex and at the base of each cone. Similar ice–cored mounds, up to 6 m in height and 12 m in diameter, have been seen in Antarctica and Iceland. These larger cones usually have thicker mantles, formed over ice or snow by wind–drifted eolian sand or by glacio–fluvial processes (e.g., associated with kame formation).

Ice–cored mounds are end–members of a continuous series of forms that can develop from non–uniform sublimation of snow and ice. In the case of disseminated grains and/or mantles in which grains are not in contact, the microscopic response of the volatile matrix to the enhanced heating of the grains creates a castellated structure of microscopic pits, floored by single grains, and ice spires. As these pits and spires intersect by continued loss of volatile ice, and as a result of movement of grains down the geopotential gradient (i.e., under the action of gravity), the pits enlarge to form macroscopic depressions, often with interior mesas or table–like forms with tops level with the original surface. Such "etch" pits were seen in Antarctica, formed by differential sublimation of seasonal snow containing a dispersed load of windblown basaltic tephra (see abstract in this volume by Malin) This sediment/volatile interaction created irregularly pitted topography with a relief of one to two meters and a horizontal scale of several ten's of meters. Similar ablation and concentration of materials is common on glaciers and ice sheets...the result is a labyrinthine complex of irregular depressions with protected, mantled spires or mesas rising from their floors as noted above. Such features can be many meters high, and the depressions many tens of meters across. In these cases, the mantling is usually complex: the floors of the depressions are often mantled by material residually concentrated during the sublimation process, while the spires are covered and protected by mantle derived during an earlier period of devolatilization.

References

Brin, G. D. and D. A. Mendis (1979) *Astrophys. J.* **229**, 402-408.

Driedger, C. L. (1980) **U. S. Geological Survey Professional Paper 1250**, (U. S. Government Printing Office, Washington, D. C.), 757-760.

Fanale, F. P. and J. R. Salvail (1984) *Icarus* **60**, 476-511.

Hall, K. (1978) *Norsk geogr. Tidsskr.* **32**, 143-151.

Muller, E. H. and H. W. Coulter (1957) *J. Glaciology* **3**, 116-122.

Nakawo, M. and G. J. Young (1981) *Annals of Glaciology* **2**, 85-91.

Thomas, P. (1980) *Icarus* **42**, 234-250.

Weissman, P. R. and H. H. Kieffer (1984) *J. Geophys. Res.* **89**, C358-C364.

ASTEROID COMPOSITION AND METEORITE ORIGINS

Lucy-Ann McFadden and Michael F. A'Hearn
Astronomy Program, University of Maryland, College Park, MD

A.) Existing knowledge about the size of meteorite parent bodies indicates that most of them formed in asteroid-sized bodies. We therefore use the meteorite reflectance spectra as control samples for interpretation of the spectral reflectance of asteroids from which their surface composition is inferred. One of the major issues in asteroid and meteorite studies is the relationship of the composition of the near-Earth and inner belt S-type asteroids to that of the most frequent meteorite type, the ordinary chondrites. The most likely interpretation is that the S-type asteroids are stony-iron meteoritic analogues (1). Recent dynamical models indicate that the predominant source of ordinary chondrite meteorites is the 3:1 Kirkwood gap with a minor contribution from the Flora family region (2). Among some of the petrographically unusual meteorites found in Antarctica are some glass-rich ordinary chondrites with spectral properties similar to those of the S-type asteroids. It is possible that these impact-melted meteorites came from the surface of S-type asteroids and that the less shock-metamorphosed ordinary chondrites originated from beneath the surface layer and escaped shock alteration.

B.) In recent years meteorites have been found which are of lunar origin. We measured the reflectance spectrum of Y791197 to constrain possible source regions on the lunar surface. The clinopyroxene and olivine assemblage which comprises the major mafic mineralogy of this lunar meteorite is not the dominant assemblage found in fresh lunar highland craters on the front side of the moon (3). There is only one crater which is located near the eastern limb with major mineralogy approaching that of the lunar meteorites (4), this crater is named Eimmart A. We don't propose necessarily that this is the source of these meteorites, however the difference in major mafic mineralogy of the meteorite compared to the front side of the lunar highlands is significant, any supports independent geochemical arguments pointing to an origin on the limb or backside of the moon by default.

C.) Dynamical evidence suggests that some of the planet-crossing asteroids might be the devolatilized remnants of comets. What has hindered the testing of this hypothesis is our ignorance of the physical properties of the solid portion of comets (nuclei). In collaboration with H. Campins of the Planetary Science Institute, Tucson, we learned that the visible and near-infrared reflectance characteristics of the nucleus of comet Nuejmin 1 is lower and redder than any of the known asteroid types. Its albedo is 0.02 and its ultraviolet slope is as red as S-type asteroids. We are thus beginning to learn about the solid component of comets to compare them with asteroids.

(1) Gaffey, M.J. (1984) Icarus 60, 83-114.
(2) Wetherill, G.W. (1985) Meteoritics 20, 1-22.
(3) Pieters, C.M. (1985) Reviews of Geophysics, in press.
(4) McFadden et al. (1985) Mem. Nat'l Inst. of Polar Research spec. issue on Y791197, Tokyo, in press.

CONVEX-PROFILE INVERSION OF ASTEROID LIGHTCURVES

Steven J. Ostro, Jet Propulsion Laboratory
California Institute of Technology, Pasadena, CA 91109

Asteroids appear as unresolved point sources when viewed through even the largest Earth-based optical telescopes, and most of our current knowledge of asteroid sizes and shapes has been inferred indirectly from disk-integrated, VIS/IR measurements. Under special circumstances, the modern techniques of occultation timing, delay/Doppler radar, and speckle interferometry can yield direct estimates of dimensions, but the primary observational constraints on shapes per se are optical lightcurves.

The lightcurve of a rotating asteroid is completely determined by the asteroid's shape, its light-scattering behavior, and the viewing geometry. As Russell (1906) noted, even if lightcurves were available for an asteroid at all physically possible Sun-Earth-asteroid configurations, it would be "quite impossible to determine the shape of the asteroid" because of the difficulty of separating albedo variations from curvature variations. Fortunately, the bulk of available photometric and polarimetric data indicate that the forms of most broadband optical lightcurves seem less sensitive to surface heterogeneity than to gross asteroidal shape. Within this framework, many researchers have examined the dependence of lightcurve shape on viewing geometry, asteroid shape, and scattering law. Most of these studies have invoked a mathematically simple figure, such as a triaxial ellipsoid, whose shape is completely parameterized by the two ratios b/a and c/a, where $a \geq b \geq c$ are the semiaxis lengths. However, analyses based on such simplified shapes ignore much of the interesting information that distinguishes individual lightcurves (e.g., all odd Fourier harmonics).

Ostro and Connelly (1984) have developed a new approach, called convex-profile inversion (CPI), to lightcurve analysis. CPI obtains a convex profile, $\underline{P}$, from an asteroid's lightcurve. The number of parameters that characterize the profile is limited only by the number of Fourier harmonics used to represent the parent lightcurve, so CPI can preserve much (if not all) of the salient information contained in the parent lightcurve. Whenever certain ideal conditions are satisfied, $\underline{P}$ is an estimator for the asteroid's "mean cross section" $\underline{C}$, a convex set defined as the average of all cross sections $\underline{C}(z)$ cut by planes a distance z above the asteroid's equatorial plane. $\underline{C}$ is therefore a 2-D average of the asteroid's 3-D shape. The ideal conditions are that (A) all intersections of the asteroid's surface with planes perpendicular to the spin axis are convex; (B) the asteroid's scattering law is geometric, i.e., brightness is proportional to projected, visible, illuminated area; (C) the astrocentric declinations δ_E, δ_S of the Earth and Sun are zero; and (D) the solar phase angle ϕ is known and nonzero. CPI's geometrical conventions (Fig. 1) are such that for any given Sun-Earth-asteroid configuration, the sign of ϕ will correspond to either retrograde or direct rotation.

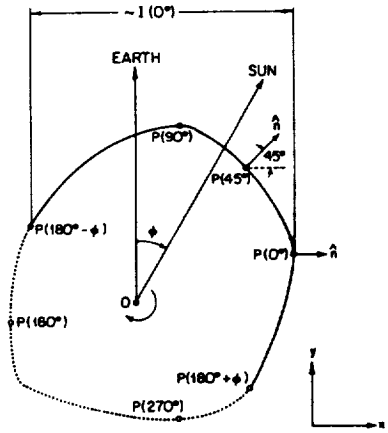

Fig. 1. Geometry for 2-D asteroid lightcurve inversion. The asteroid is a convex profile rotating clockwise, and is shown at rotational phase $\theta = 0°$. The solar phase angle ϕ is indicated, as are the asteroid's illuminated (solid) and unilluminated (dotted) portions. The asteroid's brightness is proportional to the orthogonal projection, in the direction of the Earth, of the visible, illuminated portion of the profile.

To obtain a profile from a lightcurve, we first find the lightcurve's Fourier series: $I(\theta) = \Sigma\, \underline{c}_n e^{in\theta}$ and define the radius of curvature function: $r(\theta) = \Sigma\, \underline{d}_n e^{in\theta}$, where $\underline{d}_n = \underline{c}_n/\underline{v}_n$ and $\underline{v}_n$ is a known function of ϕ and n. The profile is determined by $r(\theta)$ and will be closed and convex only if the N linear constraints, $r(2\pi k/N) \geq 0$ for $1 \leq k \leq N$, are satisfied. In practice, CPI finds that profile $\underline{P}$ which provides the least-squares estimator for $\underline{C}$ by finding that vector of Fourier coefficients which satisfies the constraints and is closest to the vector of unconstrained Fourier coefficients.

We have tested CPI by inverting lightcurves generated analytically for geometrically scattering ellipsoids (GSE's). When $\delta_E = \delta_S = 0$, the inversion yields an ellipse with axis ratio b/a independently of ϕ. When $\delta_E \neq 0$ and/or $\delta_S \neq 0$, the resulting profile is not necessarily an ellipse and has breadth extrema not necessarily in the ratio b/a; the degree to which $\underline{P} \neq \underline{C}$ depends on each of the five free parameters. We have calibrated the deviation of $\underline{P}$ from $\underline{C}$ for GSE's as a function of b/a, c/a, lightcurve noise level, rotation-phase sampling interval $\Delta\theta$, and departure from ideal conditions. The coupling between these factors is considerable. If the rms noise due to all sources is ~ 3% of the lightcurve's peak-to-valley amplitude, then $\underline{P} \approx \underline{C}$ if $\Delta\theta < 5°$. If $|\delta_E|, |\delta_S| > |\phi|$, then distortion of $\underline{P}$ is minimal when δ_E is between 0 and $-\delta_S$ but severe when δ_S is between 0 and δ_E.

To permit quantitative comparison of profiles, we use a scale-invariant, rotation-invariant, Euclidean distance Ω between two profiles $\underline{P}$ and $\underline{P}'$. We also define the "noncircularity" Ω_C as the distance between a given profile and a circle, and β as the ratio of a profile's maximum breadth to its minimum breadth. The lightcurve amplitude Δm is often taken as a measure of an asteroid's noncircularity and elongation. This approach would be justified if every asteroid were a GSE and every lightcurve were obtained at $\phi = \delta_E = \delta_S = 0$. For the purpose of using actual lightcurves to compare the shapes of real asteroids, the statistics Ω_C and β incorporate all the information in a parent lightcurve, and as such are *a priori* preferable to Δm. They also permit a distinction between noncircularity and elongation.

Figure 2 shows results of convex-profile inversion of two lightcurves of 15 Eunomia, obtained at ϕ = -12° and ϕ = -21° by Groeneveld and Kuiper (1954) and van Houten-Groeneveld and van Houten (1958). These authors argue that Eunomia's pole is nearly normal to the ecliptic. If this is the case, then, since Eunomia's orbital inclination is only 12°, Condition C might have been close to being satisfied during the photometric observations. The negative signs for ϕ correspond to retrograde rotation, as deduced by the cited authors. Although the two Eunomia lightcurves were taken at very different solar phase angles, the profiles do seem similar. Under the ideal conditions, $\underline{P}$ should not depend on ϕ, so the profiles in Fig. 2 might be valid approximations to Eunomia's mean cross section despite possible departures from our ideal conditions.

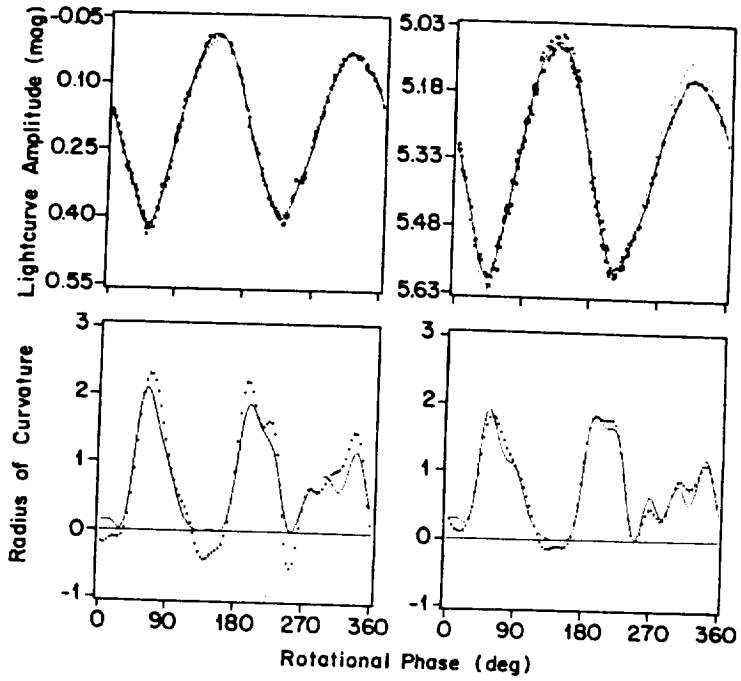

Fig. 2. Convex profiles for asteroid 15 Eunomia. In the top figures, the large symbols are the lightcurve data, the solid curve represents the lightcurve derived from the unconstrained fit, and the tiny dots represent the lightcurve derived from the constrained fit, i.e., from the convex-profile inversion. In the middle figures, the unconstrained and constrained radius-of-curvature functions are represented by symbols and solid curves, respectively. The profiles are shown at rotational phase θ = 0° as in Fig. 1.

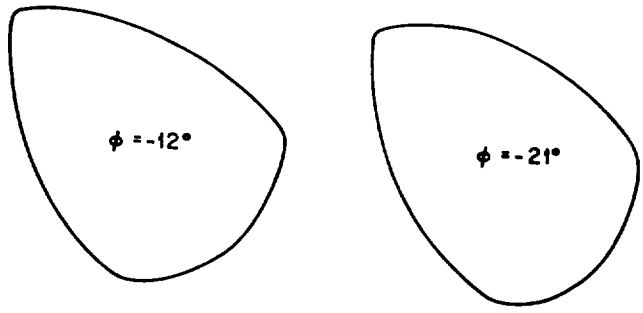

REFERENCES:

Groeneveld, I., and G. P. Kuiper (1954). Astrophys. J. 120, 200-220.
Ostro, S. J., and R. Connelly (1984). Icarus 57, 443-463.
Russell, H. N. (1906). Astrophys. J. 24, 1-18.

PROPER ELEMENTS AND MARS-CROSSING DEPTHS OF PLANET-CROSSING UCAS ASTEROIDS

E. M. Shoemaker and R. F. Wolfe, U.S. Geological Survey, Flagstaff, Ariz., S. J. Bus, Lowell Observatory, Flagstaff, Ariz., and J. G. Williams, Jet Propulsion Laboratory, Pasadena, Calif.

Completion in 1985 of the astrometric phase of UCAS--the United Kingdom-Caltech Asteroid Survey (Bus et al., 1982)--has yielded positional observations adequate for computation of orbits of 1262 newly discovered, mostly faint asteroids. Preliminary orbits calculated by B. G. Marsden at the Minor Planet Center were utilized by us to investigate the proper elements and closest approach to Mars of these new asteroids. Our goal has been to make a preliminary assessment of family membership of the UCAS objects and to complete the identification of Mars crossers. Most orbits investigated were based on about 2-month arcs of observation, but eight of the identified Mars crossers were observed over only 8 to 13 days (Table 1). Ten Mars crossers, however, have been observed at multiple oppositions, and three are now numbered (Table 1).

At the present stage of investigation, 56 Mars crossers have been identified among the UCAS asteroids by means of Williams' (1969) methods of calculation. This represents an increase of 29 objects over 27 Mars crossers previously reported from a much more limited study (Shoemaker et al., 1984). In addition to Mars crossers for which well-defined proper elements were obtained and which can be identified by negative values of Williams' Δ_4 (the closest approach to Mars' orbit at the node), there may be a few Mars crossers whose orbits are too close to secular resonances for proper elements to be calulated. One known new Mars-crossing asteroid not shown in Table 1, but observed by UCAS, 1981 FD, has a mean motion too close to the 2:1 commensurability with the mean motion of Jupiter for proper elements to be calculated.

As future refinements of the orbits of the UCAS objects are obtained, it is anticipated that the final tally of Mars crossers probably will not exceed the number in Table 1 by more than a few objects. None of the orbits yielding Mars-crossing depths shallower than -0.030 AU are based on arcs of less than a month, and most observed arcs for shallow crossers are substantially longer than a month. Previous calculation of Mars-crossing depths shows that the results from orbits based on 1-month arcs generally are accurate to within about ±0.002 AU for shallow crossers. Only one of the 56 recognized UCAS Mars crossers has a crossing depth shallower than -0.006 AU (Table 1); hence all but one object listed are thought to be definite crossers, with the exception of a few for which observations span less than 13 days.

The Mars crossers with well-defined proper elements (exclusive of one Amor asteroid) represent 4.4 percent of the discovered UCAS asteroids, whereas 3.6 percent of the asteroids numbered up to 3259 (exclusive of Amors and Apollos) and 3.4 percent of 1227 relatively faint asteroids with moderately well determined orbits that were discovered in the Palomar-Leiden survey (PLS) are recognized as Mars crossers by Williams' methods of calculation. The differences in the proportion of recognized Mars crossers between UCAS, the numbered asteroids, and PLS is not significant at the 95% level of confidence.

However, observational selection effects should have led to discovery of a slightly higher proportion of Mars crossers among the UCAS asteroids than among numbered or PLS asteroids.

Discovery of faint asteroids is more biased toward objects closest to the Sun and Earth than is the discovery of the numbered asteroids. As Mars crossers are among the closest approaching objects, they should be found with the highest frequency among faint asteroids, other factors being equal. Further selection effects arise, however, from the limited ranges of ecliptic latitude and longitude covered by the faint-asteroid surveys. These effects tend to reduce the proportion of Mars crossers found by PLS; the proportion found by UCAS is reduced to a much lesser extent or possibly not at all. PLS was conducted close to the ecliptic and was strongly biased against discovery of high-inclination asteroids, including Mars crossers, most of which have inclinations above 5°. UCAS covered a much broader range of ecliptic latitude than PLS; the maximum in the distribution of inclination of UCAS Mars crossers is close to the principal maximum in the distribution for numbered Mars crossers. Moreover, PLS covered a range of ecliptic longitude where the perihelia of ordinary main-belt asteroids are fairly concentrated but where the perihelia of Mars crossers appear to be slightly less concentrated. This tends to reduce further the proportion of Mars crossers found by PLS, because asteroids are most commonly discovered when they are fairly close to perihelion. UCAS, on the other hand, surveyed a region about 180° away from that covered by PLS. In the region surveyed by UCAS, the ratio of Mars crossers near perihelion to ordinary main-belt asteroids near perihelion appears to be slightly higher than average. This tends to enhance the proportion of Mars crossers found by UCAS.

Seventy-nine percent of the UCAS Mars crossers have crossing depths shallower than -0.10 AU; the present osculating orbits of these shallow crossers generally do not overlap the present orbit of Mars. Nevertheless, overlap at one of the nodes occurs occasionally, up to the maximum distance given by Δ_4, as a result of secular variation of the orbital eccentricities and advance of the apsides of the asteroids and of Mars. The probability of collision of these shallow crossers with Mars is finite but very small. Dynamical lifetimes of the shallow crossers are thought to be comparable with the age of the Solar System, although detailed statistical estimates of these lifetimes have yet to be made. As we found from their proper elements, all but a few UCAS Mars crossers have orbits fairly remote from commensurabilities and secular resonances. This indicates that few of these objects have been recently injected into Mars-crossing orbits from the resonant regions. The proper elements of most Mars crossers lie in a rather stable part of orbital element phase space with semimajor axes about midway between 2.0 and 2.5 AU and proper inclinations less than 8°. It appears likely that most of the Mars-crossing objects in this stable region either have been crossers from the time of late heavy bombardment on the terrestrial planets or are fragments of old Mars crossers.

REFERENCES

Bus, S. J., Helin, E. F., Dunbar, R. S., Shoemaker, E. M., Dawe, J., Barrow, J., Hartley, M., Morgan, D., Russell, K., and Savage, A., 1982, The United Kingdom-Caltech Asteroid Survey [ext. abs.]: Reports of Planetary Geology Program, 1982, National Aeronautics and Space Administration Technical Memorandum 85127, p. 53-56.

Shoemaker, E. M., Bus, S. J., Dunbar, R. S., Helin, E. F., Dawe, J., Barrow, J., Hartley, M., Morgan, D., Russell, K., and Savage, A., 1984, Mars-crossing asteroids discovered in the UK-Caltech Asteroid Survey [abs.]: Bulletin American Astronomical Society, v. 16, p. 691.

Williams, J. G., 1969, Secular perturbations in the solar system: Ph.D. dissertation, University of California at Los Angeles.

Table 1 Mars-crossing asteroids discovered in the United Kingdom - Caltech Asteroid Survey (UCAS) showing Mars-crossing depths (Δ_4) and proper elements

	Short arc	Δ_4(AU)	a(AU)	e	sin i
1981ET3 = 3122		-0.691	1.768	0.394	0.369
1981EJ30		-0.638	2.022	0.327	0.092
1981EN11		-0.503	2.301	0.405	0.131
1981EG42	13 days	-0.212	2.350	0.306	0.111
1981EF46	9 days	-0.174	2.510	0.336	0.106
1981EL33		-0.168	2.278	0.259	0.120
1981EU27		-0.134	2.263	0.240	0.118
1981EG32		-0.134	2.745	0.305	0.375
1981EK39	9 days	-0.125	2.376	0.287	0.039
1981EH6		-0.124	2.855	0.388	0.123
1981EE17		-0.114	1.933	0.159	0.434
1981EW42	13 days	-0.100	2.302	0.243	0.117
1981ET13		-0.099	2.282	0.238	0.098
1981EU6		-0.080	2.316	0.229	0.168
1981EJ17		-0.078	2.197	0.174	0.124
1981ET37		-0.077	2.260	0.222	0.077
1981EH16 = 3030		-0.076	2.269	0.225	0.080
1981EH42	13 days	-0.067	2.247	0.216	0.034
1981ES27		-0.066	2.235	0.194	0.125
1981EY38		-0.066	2.319	0.222	0.181
1981EU13		-0.065	2.311	0.222	0.168
1981ED4		-0.064	2.738	0.336	0.160
1981ED21		-0.063	2.738	0.334	0.216
1981EQ45	11 days	-0.062	2.558	0.301	0.183
1981EO27		-0.057	2.145	0.087	0.130
1981EJ5		-0.055	2.198	0.177	0.095
1981EN47		-0.053	2.180	0.148	0.123
1981EN20		-0.046	2.253	0.209	0.044
1981EZ6		-0.038	2.397	0.250	0.124
1981ES34	10 days	-0.036	2.565	0.294	0.144
1981DK1 = 3287		-0.035	2.366	0.197	0.243
1981EH35		-0.034	2.326	0.230	0.071
1981EN33		-0.031	2.240	0.193	0.079
1981EB45	8 days	-0.030	2.570	0.292	0.163
1981D01		-0.030	2.346	0.227	0.135
1981ED10		-0.029	2.285	0.214	0.056
1981EC3		-0.029	2.358	0.230	0.151
1981EQ40		-0.028	2.154	0.147	0.038
1981EE7		-0.026	2.254	0.188	0.125
1981EF22		-0.025	2.349	0.236	0.059
1981EJ48		-0.023	2.324	0.242	0.430
1981EJ27		-0.023	2.278	0.210	0.030
1981EH9		-0.021	2.339	0.228	0.084
1981EX19		-0.018	2.154	0.144	0.030
1981EZ42		-0.017	2.288	0.212	0.026
1981EL11		-0.017	2.171	0.142	0.090
1981DK2		-0.016	2.635	0.301	0.147
1981EC8		-0.016	2.200	0.162	0.089
1981EW32		-0.016	2.542	0.280	0.178
1981EN45		-0.014	2.244	0.188	0.071
1981EG15		-0.010	2.113	0.097	0.042
1981EG25		-0.009	2.773	0.323	0.235
1981EU36		-0.009	2.300	0.208	0.090
1981EB19		-0.006	2.249	0.191	0.034
1981DN		-0.006	2.449	0.252	0.148
1981EH8		-0.001	2.280	0.187	0.139

BRIGHTNESS CURVES AND POROSITIES OF COMETARY NUCLEI

R. Smoluchowski, University of Texas, Austin, TX 78712

It is the purpose of this note to discuss the influence of various factors on the brightness curve a comets and to estimate the thermal conductivity and the porosity of their nuclei.

1. Pore migration. Recent studies of sulfur in comets (1) suggest that cometary nuclei formed by accretion of icy or ice-covered micron size grains which were irradiated for a long time before the accretion took place. This irradiation facilitated inter-grain cohesion in analogy to processes taking place in the lunar dust (2). Thus, on the smallest scale, cometary nuclei should have pores of the order of microns while larger pores should be produced during subsequent aggregation of ices into larger conglomerates. Pores tend to migrate up the thermal gradients, sweeping up the smaller ones (3) and thus leaving denser layers behind. Those which reach open surfaces of nuclei disappear leading to densification of the surface layers, this process competing with the evaporation of these layers. Similarly, motion of closed pores in the interior of the nucleus leads to a gradual transfer of more volatile ices, such as CO_2, towards its deeper colder parts. If the motion of pores in H_2O takes place below 150K, they leave behind a trail of amorphous ice whether the original ice was crystalline or not. Because of the difference in vapor pressure, pores containing CO_2 migrate 10^6 to 10^7 times faster than those with H_2O-vapor (3).

2. Phase changes. Apart from sublimation and condensation of ices, the most important phase changes which occur in cometary nuclei are crystallization of amorphous H_2O-ice and the formation and decomposition of the CO_2-clathrate. Inasmuch as H_2O-ice in nuclei of new comets should be mostly amorphous, its exothermic crystallization near 150 K leads to rapid heat release and a flare-up at heliocentric distances about 70 percent larger than if the ice were all crystalline (3). The presence of amorphous ice in nuclei is very important because it has a 10 to 10^3 times lower thermal conductivity than its crystalline form (4). Furthermore, as a result of high brittleness of the underlying amorphous ice, the crystallized surface layer may fall off exposing deeper amorphous layers to solar heat and producing outbursts.

3. Thermal conductivity. Heat transport into or out of the nuclei, which plays a major role in the phenomena here discussed, is influenced by their composition and porosity. The difference between the behavior of amorphous and crystalline H_2O and SiO_2 is particularly striking. The thermal conductivity of pores of various sizes filled with CO_2- or H_2O-vapor in the viscous as well as in the Knudsen range of diffusion can be calculated. At low temperatures the presence of pores lowers the thermal conductivity of ice; with increasing temperature, however, the heat transfer through the pores increases and becomes much higher than that of ice. An example of a realistic temperature dependence of the effective thermal conductivity of a cometary nucleus is given in Fig. 1 for crystalline ice with porosity 0.3 (1 mm pores with CO_2) and 30 percent silicate dust. The fact that in the interesting range of temperatures, the effective conductivity first falls by an order of magnitude and then increases by a comparable, if not greater, factor is crucial for the brightness curve. The dependence of conductivity on porosity is shown in Fig. 2. In these estimates, it is assumed that there is a characteristic pore size which represents the actual, topologically very complicated, heat flow.

4. Thermal history of cometary nuclei. In order to calculate the heat flow into and out of a nucleus it is assumed that the nucleus is spherical, that its radius is big enough so that the use of linear heat flow equation is justified, that the radial temperature gradient is

the same in all directions and that the nucleus is homogeneous without particularly active or inactive patches on the surface. The calculations were made for q = 1.5 AU and parabolic orbits as approximations to orbits of new comets. Near perihelion the nucleus instead of being a sink, becomes a source of heat so that from then on the surface temperature of the nucleus is higher than what it was at the same heliocentric distance before perihelion. The higher surface temperature leads to a higher evaporation rate and higher brightness after perihelion. Figure 3 shows the evaporation rate of various kinds of cometary nuclei in all of which, except for K = O, the maximum of the temperature curve occurs after the perihelion.

Probably in a real nucleus there are layers and pockets rich in CO_2 or other highly volatile ices which on being heated to progressively higher temperatures can produce local pressures exceeding the cohesive strength of the nucleus. If this happens near the surface, the comet shows an outburst; if it happens deeper in the interior, the comet may split. In periodic comets such outbursts and splittings may occur also before perihelion if the nucleus is mechanically weak in a particular area. The higher temperatures of nuclei after perihelion show up in the probability of outbursts and splittings of comets (5).

5. Estimate of thermal conductivity and porosity of cometary nuclei. In order to estimate the thermal conductivity of a nucleus a set of brightness curves was calculated for various compositions and porosities of the nuclei and from these a relationship between the thermal conductivity and the assymetry of the brightness curve or the delay of its maximum after perihelion obtained (Figs. 4 and 5). Once the effective thermal conductivity K(W cm^{-1} deg^{-1}) of the nucleus has been evaluated, its relative porosity P(1 mm pores) can be estimated using Fig. 2 and assuming an average pore size and the nature of volatiles. The results shown in Table 1 were obtained assuming 1 mm pores and CO_2-vapor. It should be noted that the presence of CO_2-vapor covers up completely the role played by the H_2O-vapor. Comet P/Kopff shows a progressive shift of the delay of the maximum of its brightness towards the perihelion during the last 6 apparitions. This shift could be the result of densification, that is loss of pores at open surfaces or of change in their size distribution (3). The low porosity of Comet P/Encke, which is undoubtedly an old comet, seems reasonable while the high porosity of comet P/Giacobini-Zinner agrees with the suggested apparent brittleness of its dust. If there were only H_2O-vapor in 5 mm pores then the porosities would be comparable to that of freshly fallen snow. This result indicates that in contrast to the value of the thermal conductivity the porosities here obtained have primarily a relative value suitable for inter-comparison of cometary nuclei (5).

References.

1. A'Hearn, M.F., and P.D. Feldman, in "Ices in the Solar System" (1985), ed. J. Klinger, D. Benest, A. Dollfus, and R. Smoluchowski (Reidel Publ. Co., Dordrecht) p. 463.
2. Smoluchowski, R., J. Geoph. Res., 71, 1569 (1966).
3. Smoluchowski, R. M. Marie and A. McWilliam, Earth, Moon and Planets, 30, 281 (1984).
4. Klinger, J., Icarus, 47, 320 (1981).
5. R. Smoluchowski, in "Asteroids, Comets, Meteors II", Uppsala, Sweden, June 1985 (in print).

	K	P		K	P
P/Giacobini-Zinner	1.7×10^{-1}	0.5	P/Halley	5×10^{-2}	0.2
P/d'Arrest	1.2×10^{-1}	0.4	P/Tempel 2	5×10^{-2}	0.2
P/Kopff	6×10^{-2}	0.25	P/Encke	4×10^{-2}	0.1

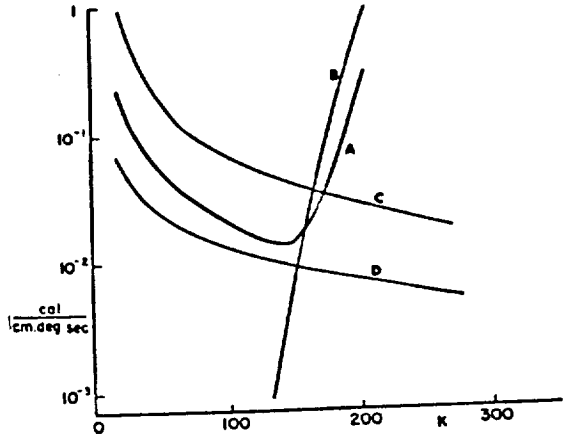

Fig. 1 Thermal conductivity of A) crystalline H_2O ice with 30 percent SiO_2 and 30 percent 1 mm pores with CO_2 vapor; D) H_2O; C) SiO_2; B) pores.

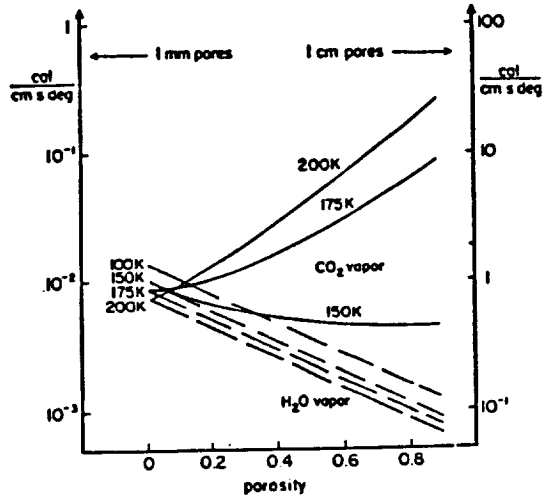

Fig. 2 Thermal conductivity of porous ice.

Figure 3 Brightness curves (evaporation flux Z in $cm^{-2}s^{-1}$) for various cometary nuclei: A) $K=10^{-2}$ cal $cm^{-1}s^{-1}$ deg^{-1} (ε=0.2, 1 mm CO_2); B) K= K(T) (ε=0.3, 1 mm CO_2, 0.3 SiO_2); C) $K=2.5 \times 10^{-3}$ cal cm^{-1} s^{-1} deg^{-1} (ε=0.5, 1 mm H_2O); D) K=0.

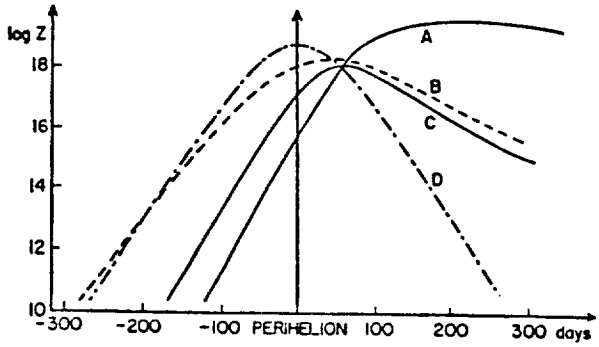

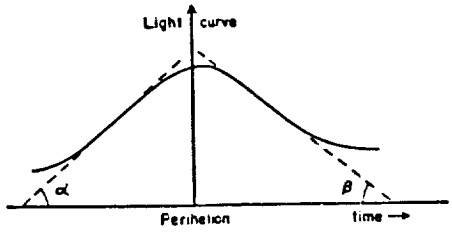

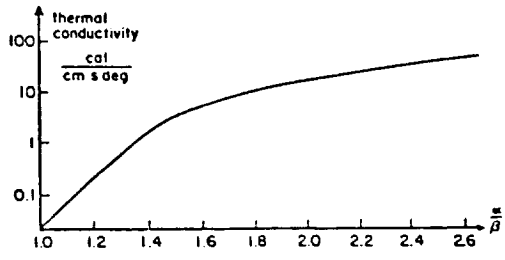

Fig. 5 Relationship between asymmetry of the light curve and the effective thermal conductivity of the nucleus.

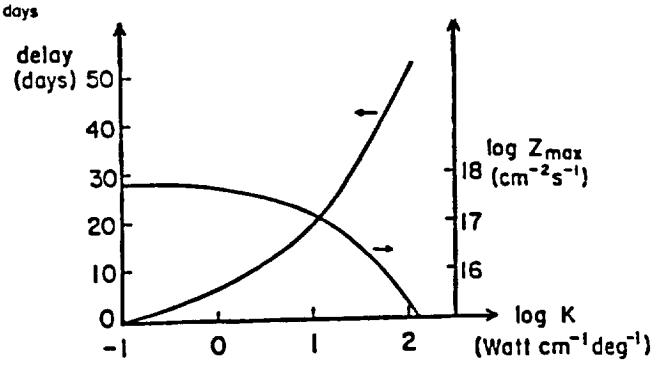

Fig. 4 Relationships between thermal conductivity K, maximum rate of evaporation Z_{max} and the delay of Z_{max} after the perihelion (q=1.5 AU).

HOW TO MAKE A COMET

James Stephens, and R. Steven Saunders, Jet Propulsion Laboratory; and Fraser Fanale, University of Hawaii

The primary mandate of NASA is the study of the nature and origin of the solar system. The study of comets provide us with unique information about conditions and processes at the beginning of the solar system. Short period comets and their relatives, the near Earth asteroids may prove to be second only to the sun in importance to the long term survival of civilization for two reasons. They are a possible candidate as the cause of mass extinctions of life on Earth; and they may provide the material means for the expansion of civilization into the solar system and beyond. They almost certainly represent the most primitive material of the solar system, still tantalizingly unavailable until space craft bring us first-hand information. In the meantime we must study comets by remote means. Laboratory investigations using synthetic cometary materials may add to our knowledge of these interesting objects.

Comets are presumed to be made of ices with noncontacting dispersions of micron and sub-micron sized particles (Whipple, F.L., Ch.1, Comets, page 67 in McDonnell,J.A.M., Cosmic Dust, New York, NY, Wiley & Sons, 1978). The most difficult physical characteristic to simulate is the dispersion of particles in ice in a way that prevents them from touching one another. This requirement is crucial because if the particles touch one another they are unlikely to be separated by the fluid dynamic forces (or electrostatic forces) at the subliming ice surface and the observed free flowing dust plume (comprising the comet's tail) will not be possible. It is possible, however, that even if the particles are not touching in the ice they may not escape the subliming surface and thus may form a mantle under some low rate of solar insolation. It is the study of these two processes, dust and mantle formation, that is the objective of this ongoing laboratory experimental investigation.

If a dispersion of particles in liquid water is frozen by ordinary means the freezing ice crystals push the particles ahead of the freezing solid-liquid interface. The particles are trapped in the ice where the ice crystals collide with one another. In the materials purification industry this phenomenon is referred to as zone refining. This phenomenon must be avoided if particle contact is to be prevented. In synthesizing comet ices we tried several methods of high-speed freezing the liquid dispersions of particles to obtain the requisite noncontacting particle dispersions in ice.

The most reliable means of freezing required that we spray a very dilute dispersion (100:1) of montmorillonite clay in water into liquid nitrogen through a very small nozzle (< 10 microns) at high pressures (500 psi). The nozzle must be within a few milimeters of the surface of the liquid nitrogen so that the droplets hit the liquid at high velocity and are frozen quickly. Because the orifice is nearly as small as the particles, means must be provided for continuously unplugging the nozzle. This was accomplished by using an adjustable coaxial needle valve orifice that could be continuously vibrated to remove any plugs produced by the submicron montmorillonite clay particles.

A slurry of water ice particles was formed in the liquid nitrogen. The liquid nitrogen was decanted and the concentrated slurry was poured into two stainless steel hemispherical salad bowls. A fine wire thermocouple was inserted into a small hole in the center of one hemisphere of the consolidated slurry. The other hemisphere was then joined to the first to form a spherical body of weakly sintered ice particles.

This "snow ball" (0.3 gm/cm3) was then suspended in a fine nylon hair net from a small spring scale. The entire assembly was then hung inside a cryotrapped, diffusion-pumped high-vacuum chamber. The chamber was pumped down to (10 -4 Torr) before all of the absorbed liquid nitrogen evaporated. The thermocouple indicated that some of the liquid nitrogen was in fact frozen during pumpdown.

This miniature "comet" sublimed away its water ice over the next seven days while the vacuum pressure, ice temperature and the weight of the body were recorded periodically. At the end of the experiment the sublimate residue that was left formed a sphere nearly the same size and shape as the original snow ball (.009gm/cm3).

Three slightly different "comet" sublimation experiments were performed in which the dust compositions (graphite was added) and concentrations (500:1) were varied. The sublimate residue spheres formed were similar in most respects (the 50% graphite made a weaker gray residue). They all took 7 to 8 days to sublime completely. The lowest temperature recorded after the solid nitrogen had sublimed was in the range of -60^0 C. The ice probably reached lower temperatures near the end of the experiment but, because the thermocouple lead conducted a significant amount of heat into the ice body the ice probably sublimed away from it early in the experiment. The vacuum chamber pressure continued to drop during the sublimation period (final pressure was 10-7Torr). This indicates that as the sublimate residue became thicker its insulating properties increased and the ice temperature dropped thus reducing the water vapor pressure in the chamber.

During the pumpdown small pieces (< 1 mm) of ice were ejected from the surface of the spherical body. These pieces of "snow" sublimed very quickly once they came in contact with the room temperature floor of the vacuum chamber. No indication of any free dust coming off the ice or from the sublimate residue was observed. The 300K walls of the vacuum chamber apparently did not produce enough radiation load onto the ice to produce a dust plume or the dust plume was so tenuous that we could not observe it. Future experiments using a solar simulator may be able to produce dust plumes. Some form of nephelometry will be used in these subsequent experiments to observe the dust if it is released. The amount of electrostatic charging produced due to the sublimation and the effect of induced electrostatic charge will also be measured.

ARE COMETS RESPONSIBLE FOR THE PERIOD OF HEAVY BOMBARDMENT?

Strom, R.G., Dept. of Planetary Sciences, Lunar and Planetary Laboratory, University of Arizona, Tucson, Arizona 85721

The cratering record in the inner Solar System and at Jupiter and Saturn indicates that at least five different crater populations occur at various locations in the Solar System (1,2). These crater populations are shown in Figure 1. The heavily cratered regions of the terrestrial planets and outer planet satellites represents the period of heavy bombardment early in Solar System history. The crater population superposed on the lightly cratered plains of the moon and Mars (LC Terr., Fig. 1) is very different from that in the heavily cratered regions of these bodies (HC Terr.), and almost surely represents the combined impact of comets and asteroids from the end of plains formation up to the present, i.e., during the last ≈ 4 B.Y. At present, the only objects that cross all planetary orbits are comets. Therefore, it has been proposed that comets were responsible for the period of heavy bombardment throughout the Solar System (3). The different crater populations on the heavily cratered surfaces of the inner planets (HC Terr., Fig. 1), at Jupiter (Jup. Sat.) and at Saturn (Pop. I) have led to the alternative interpretation that the period of heavy bombardment was due to different families of objects originating in those parts of the Solar System in which the different crater populations are found.

The Solar System cratering record in conjunction with an appropriate crater scaling law can be used to test whether comets have been the primary contributors to the period of heavy bombardment. The size/frequency distribution of the objects responsible for the crater populations can be recovered from the cratering record using the Holsapple-Schmidt crater scaling law in the form:

$$d = \left[\frac{D_e \, g^{1/6}}{K(cv)^{1/3}(\sin \Theta)^{1/9}} \right]^{1.2} \qquad (1)$$

where d=projectile diameter, D_e=excavation crater diameter, g=surface gravity, k=coupling factor, c=ratio of projectile to target density, v=impact velocity, and Θ=impact angle from the horizontal. The excavation crater diameter for complex craters is from Croft's (4) empirical relationship: $D_e = D_q^{0.15} D_r^{0.85}$, where D_q is the transition diameter from simple to complex craters and D_r is the observed rim diameter. For simple craters $D_e = D_r$. The impact angle probability is $\sin^2\Theta$. Crater scaling parameters vary greatly for the various planets and satellites on which the different crater populations

occur. It is conceivable that when these differences are taken into account the size/frequency distribution of the projectiles may be similar for two or more crater populations. Thus, one population of impacting objects may account for more than one crater population. For example, if the Callisto crater curve was shifted to the right (larger diameters) by two $\sqrt{2}$ diameter intervals, it would more closely match the inner Solar System highlands curve (see Fig. 1).

The orbital evolution for short-period comets over a period of 821 years has been derived by Carusi et al. (5). These orbital elements can be used to derive the impact velocity distribution for planet-crossing short-period comets. This results in 26 velocities for the moon, 66 for Mars, 101 for Callisto, and 48 for the Saturnian satellites. Figure 2 is an "R" plot showing the projectile (comet nucleus) size distribution derived from the crater size distribution of the heavily cratered regions of the moon, Callisto, and Rhea using equation 1. In this computer simulation, impact velocities and angles were randomly selected and applied to unbinned crater diameters. The projectile diameters were then binned into $\sqrt{2}$ diameter intervals. The curves show that the projectile size distributions closely mimic the crater curves. Furthermore, the Callisto curve has been shifted to the left (smaller diameters) relative to the moon making the disparity between the projectile diameter distributions much greater than for the crater diameter distributions. The difference between the Rhea curve and those of Callisto and the moon is more uncertain. The small dynamic range of Saturnian satellite crater diameters results in only two size bins which lie between the Callisto and lunar curves. This suggests a different size distribution than Callisto and the moon, but the error bars are relatively large. In any event, the large disparity between the derived comet diameter size distributions for the moon and Callisto strongly suggests that comets were not the major contributor to the period of heavy bombardment.

Another way of analyzing the problem is by using the crater scaling equation to solve for the impact velocity of a constant projectile diameter so that the downturn in the lunar highlands and Callisto curves coincide. In this case, a given size projectile must make a 100 km diameter crater on the moon and a 50 km diameter crater on Callisto. The required impact velocities on the moon are 30 times faster than on Callisto for a similar size projectile. This velocity difference is totally unrealistic for either short- or long-period comet orbits. For example, a 100 km diameter crater on the moon requires a comet nucleus 10 km in diameter impacting at 45 km/sec. To produce a 50 km diameter crater on Callisto with the same sized nucleus requires the unrealistic impact velocity of 1.5 km/sec, or 1.6 times less than Callisto's escape velocity. The RMS impact velocity for short-period

comets at the moon and Callisto is 20 and 14 km/sec respectivley; for long-period comets it is 52 and 26 km/sec respectively. Thus, the maximum difference between the RMS impact velocity at the moon and Callisto (long-period comets at the moon and short-period comets at Callisto) is only a factor of 3.7 compared to the factor of 30 required to account for the differences in cratering records of the two satellites.

The differences in the size distribution of projectiles derived from the cratering record and the totally unrealistic comet impact velocities required to make the lunar and Callisto crater curves coincide, strongly indicates that comets were not the major cause of the period of heavy bombardment unless their size distribution in the inner Solar System was radically different from that at Jupiter. This is also unlikely because cometary nuclei would have to be on average about four times larger in the inner Solar System than at Callisto; just the opposite of what would be expected because comets rapidly lose mass in the inner Solar System compared to the outer Solar System.

REFERENCES

1. Strom, R.G., et al. (1981) JGR, 86, A10, 8658.
2. Smith, B., et al. (1981) Science, 212, 4491, 163.
3. Shoemaker, E.M., and Wolfe, R.G. (1983) in Satellites of Jupiter, Univ. of Ariz. Press.
4. Croft, S.K. (1985) Proc. Lunar Planet. Sci. Conf., 15, JGR, 90, C828.
5. Carusi, et al. (1984) IAS Internal Report 12.

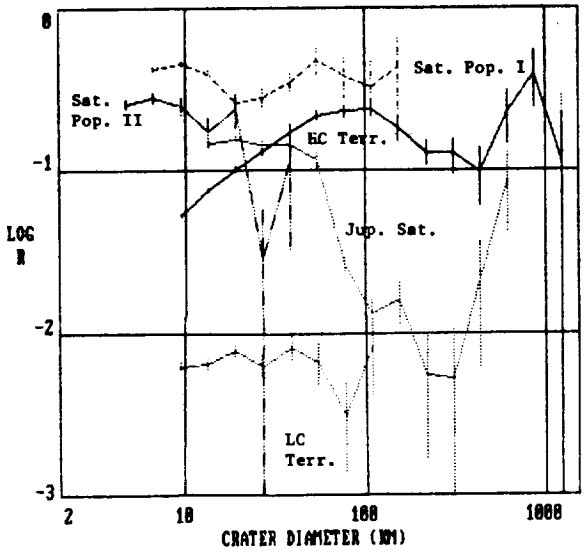

Fig. 1

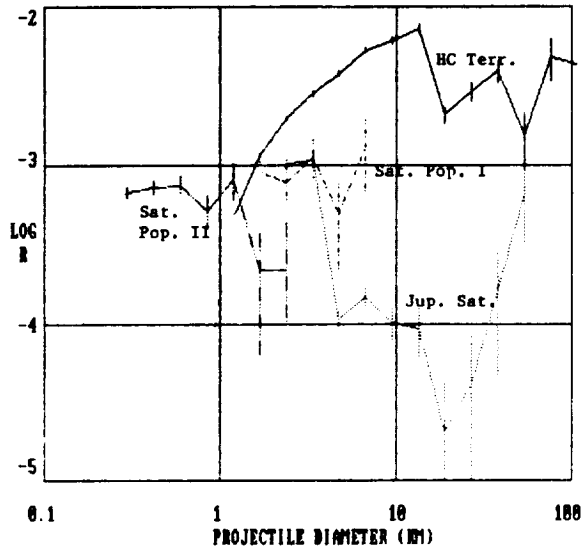

Fig. 2

Dynamics of Long-Period Comets

Paul R. Weissman, Jet Propulsion Laboratory, Pasadena, CA 91109

A considerable part of the effort of this task during the past year has been review of several new hypotheses proposed for explaining periodic cometary showers from the Oort cloud, the possible causes of periodic extinction events on the Earth. For example, it was shown that a hypothetical unseen solar companion star in a distant, 28 Myr orbit was not stable over the history of the solar system and would likely be lost in 10^9 years or less. In addition, the orbital period of the hypothetical companion star would vary about 10% per orbit due to stellar and galactic perturbations, likely resulting in the star random walking away from a fixed 28 Myr period; in only 22% of the cases studied using a Monte Carlo simulation did the star remain within 10% of the initial 28 Myr period.

Other evidence against periodic cometary showers has come from looking for possible direct evidence of the showers. The expected cratering on the terrestrial planets from periodic cometary showers was calculated and shown to result in between 5 and 18 times as many craters on the Earth and Moon as are actually observed. Evidence from impacts melts in six of eight terrestrial craters identified by Alvarez and Muller (1984) as possibly being periodic, indicates that they were likely formed by impacts of asteroids rather than comets. Evidence for clustering of crater ages around the times of major extinctions, or vice versa, is lacking in most instances.

The failure to find adequate mechanisms for creating periodic extinctions has cast considerable doubt on whether the extinctions are indeed periodic. However, this does not negate the possibility of random cometary showers, much rarer in time and caused by random passages of stars very close to the sun, or encounters with giant molecular clouds in the galaxy. The dynamics of such showers is still of considerable interest.

Studies of the dynamics of cometary showers are currently underway with Dr. Pieter Hut at the Institute for Advanced Study. We have shown that the average shower comet from the inner Oort cloud makes 8.5 perihelion passages over an average lifetime of 0.8 Myr. Peak fluxes may reach several thousand comets per year crossing the Earth's orbit. 90% of all cometary returns occur within the first 3.0 Myr, 99% within 4.0 Myr. The flux of comets versus time is largely independent of many of the dynamical model parameters (initial orbit, disruption probability, short-period capture criterion, etc.) with the one exception of the lifetime against sublimation for the comets. Even then, the duration of a typical shower is limited to about 5 Myr. Thus, biological extinction events on the Earth associated with cometary showers should show evidence of multiple impacts (tektites, iridium layers, craters, etc.) and extinctions over a timescale comparable to that described above. Our colleagues studying the paleontological record claim to have found such clusterings, though we believe the evidence is inconclusive. We are currently in the process of extending these studies, in particular looking for distinct temporal signatures caused by different perturbing agents: random passing stars, GMC's, and a hypothetical slow moving solar companion.

Additional dynamical studies have focussed on the question of multiple craters on the Earth and planets. Such crater groups or pairs are typically too far apart to be explained by a single body which split on approach as it passed through the target planet's Roche limit or entered its atmosphere. We propose that they are evidence for asteroids and/or comets with satellites. As a test of this hypothesis we calculate the mass of the impacting bodies for the two objects which caused Clearwater Lakes, a well-known crater pair in northern Canada, formed 290 ± 20 Myr ago. We find the impact energy from the crater energy scaling equation and assume typical impact velocities for long and short-period comets and for Earth crossing asteroids to obtain the impactor masses. We find that in all three cases, the gravitational sphere of influence of the larger body is substantially greater than the observed crater separation. Though this is not an exact comparison because of such unknowns as impact trajectory and satellite orbit orientation, it does show that the idea of a asteroid or comet with a sizeable satellite having caused the crater pair is indeed viable. We are currently investigating other well established cases of crater pairs on the Moon and Mars to develop better statistics of how many craters may be the result of asteroids or comets with substantial satellites.

Comet Thermal Modeling

Paul R. Weissman, Jet Propulsion Laboratory, Pasadena, CA 91109, and Hugh H. Kieffer, U. S. Geological Survey, Flagstaff, AZ 86001

During the past year we have continued to develop our comet thermal model which calculates gas production rates and nongravitational forces on a rotating, icy conglomerate cometary nucleus, including the effects of diurnal heating and cooling, rotation period and pole orientation, surface heat flow and thermal inertia, and coma energy feedback mechanisms from multiple scattering and thermal emission by the dust coma. Improvements to the model during the past year have included the ability to calculate the nongravitational forces on the nucleus, the ability to calculate nucleus models where the nucleus interior acts as a heat reservoir storing energy inbound and releasing it on the outbound leg (as is observed in Halley's Comet), and detailed improvements to the program alogorithms, and input and output routines.

We have continued to emphasize periodic comet Halley in our modeling because of the great interest in that object at this time, and because of the possibility of using the results obtained from ground-based and spacecraft observations of Halley to "calibrate" many of the nucleus parameters in the comet thermal model program, and to "fine tune" the simulated cometary surface processes in the program to give a better representation of reality.

We supplied our predicted gas production rates for P/Halley to Dr. M. Belton of Kitt Peak National Observatory who used them to prepare a predicted brightness curve for the comet. That curve predicted that Halley would begin showing visible coma at in March, 1985 at a heliocentric distance of 5.8 AU. That is exactly what was observed, as is shown in Figure 1 (Wyckoff et al., Nature 316, 241, 1985). The slowly rising dotted curve is the predicted magnitude of the Halley nucleus. The more sharply rising dashed curve at right is the predicted brightness of the nucleus plus coma, based on our model computations. It is seen that the comet followed the predicted behavior quite well.

This is the first time that a short-period comet has been observed to "turn on" at such great heliocentric distance. Previous thought in this area was that comets turned on at about 3 AU where water ice sublimation became significant. That thinking referred to the point at which the cometary water production curve rose very quickly, proportional to r^{-7} or more, and then began to increase more slowly, rising as about $r^{-2.5}$. The new definition of "turn on" used here refers to where visible coma can first be detected. For a relatively young and active comet like Halley it can obviously be quite far from the sun. This new definition results as much from the improved observational techniques and special attention applied to Halley, as it does from our improved understanding of cometary processes through the comet thermal model developed here.

Continued observation of Halley during its inbound leg has tended to confirm the predictions of the comet thermal model within the limits of

observational error. Direct observations of OH, assumed to be the daughter product of water ice sublimation, using the International Ultraviolet Explorer Satellite have generally been a factor of two above the model prediction (Weissman and Kieffer, Adv. Space Res. 4, 221, 1984), while observations of OH at radio wavelengths by the French team at Nancay have generally been a factor of two below the predicted values. Why the radio and UV measurements do not agree is a matter of considerable concern to cometary observers. However, the two sets of measurements bracket the comet thermal model predictions for Halley quite well, and the slope of the increasing gas production is reproduced very well.

During the coming year we will continue to improve the comet thermal model and to run specific cases involving P/Halley. We have just been joined by Dr. Gary Herman from Tel Aviv University who is on a NRC/RRA at JPL, and who will be working on improved modeling of the internal heat flow in comets, temperature at depth, and determination of thermophysical parameters for cometary interiors.

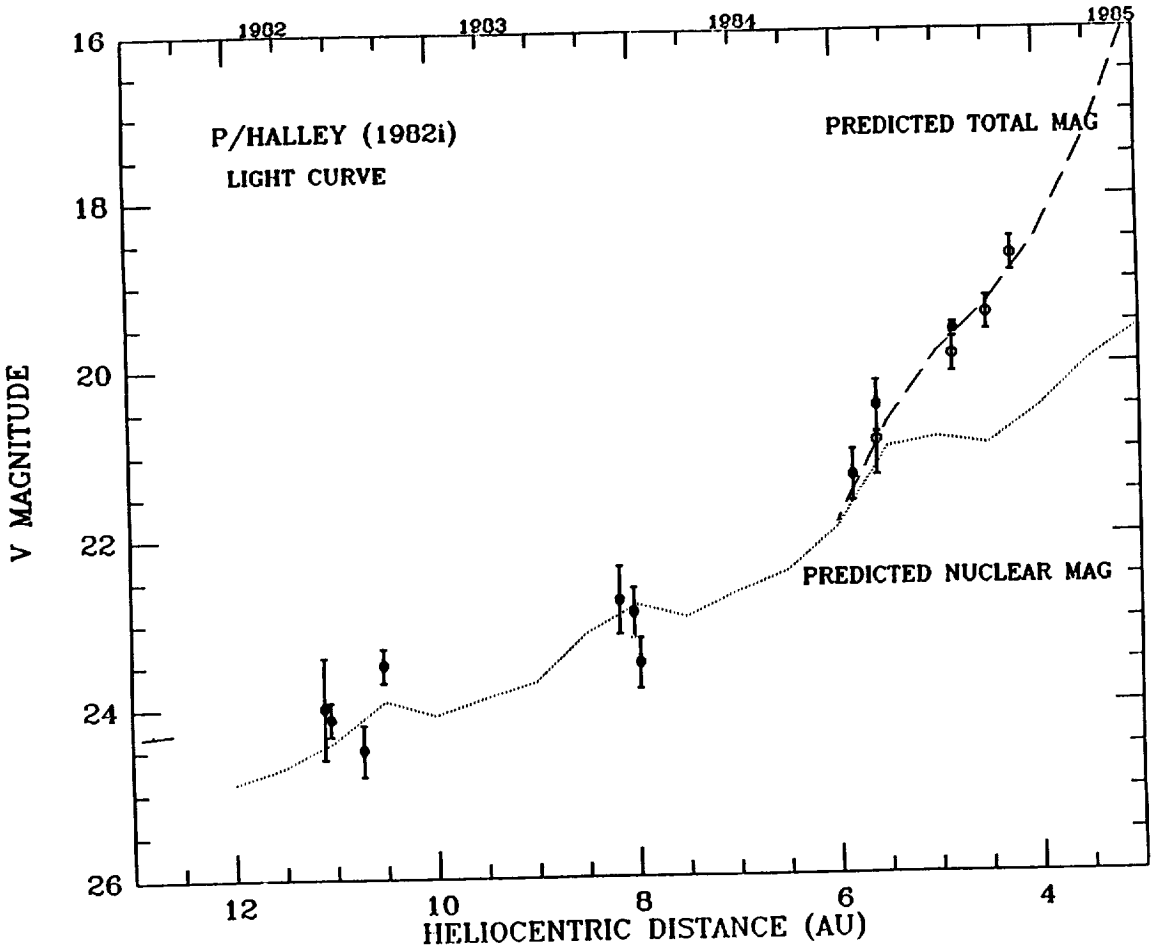

Figure 1. Observations of P/Halley in 1982-85 versus predicted brightness for the bare nucleus (dotted curve), and the nucleus plus coma (dashed curve). The comet "turned on" at 5.8 AU as predicted by the comet thermal model. (from Wyckoff et al. 1985).

The Duplicity of P/Holmes

F.L. Whipple, Smithsonian Astrophysical Observatory
Cambridge, MA 02138

The author's evidence that the double burst of P/Holmes in 1892 was caused by collisions of a small satellite comet with the major nucleus (Whipple, Icarus, 60, 522-531, 1984) requires that the satellite moved in a highly eccentric orbit of semimajor axis in which $2a=131\rho^{1/3}$ R_c km, where ρ is the density of the major nucleus in gm/cm^3 and R_c is its radius in km. The classical special three-body theory when applied to a circular orbit for the comet at perihelion (e.g. T.Y. Huang and K.A. Innanen, Astr. Journ. 88, 1537-1548, 1983) leads to stability against solar perturbations for a maximum value of cometary distance as $228\rho^{1/3}$ R_c km for a direct orbit and $346\rho^{1/3}$ R_c km for a retrograde orbit.

Although this application of the 3-body theory is favorable to the duplicity-theory, the 3-body theory is not directly applicable. Thus numerical intergrations of the motion of a satellite comet moving in various eccentric orbits about P/Holmes were carried out. The intergrations indicate that direct orbits of the satellite would be stable for several hundred revolutions of the comet or a few thousand years if, e.g. $2a=165\rho^{1/3}R_c$km and aphelion distance $Q=165\rho^{1/3}R_c$km.

In retrograde orbits the satellite comet was stable in larger orbits such as e.g. $2a=275\rho^{1/3}R_c$km, and $Q=183\rho^{1/3}R_c$km, as might be expected. The numerical results support the hypothesis that P/Holmes may have been a double comet but also indicate that the conclusions about stability from the special 3-body theory in highly eccentric orbits require more careful consideration.

The Dearth of Faint "New Comets": It has long been superficially apparent that faint relatively "new" comets having small inverse semi-major axis are scarce. Many years ago the writer had expected that more powerful wide-field telescopes such as the 1.2-m Schmidt camera of Palomar would increase rapidly the discovery rate of such comets. In fact, the discoveries have not been unusually frequent and have, in large measure, involved faint periodic comets. Studies of the distribution function of absolute comet magnitude, H_{10}, such as that by E. Everhart (Ast. Journ. 72, 1002-1011, 1967), have shown a rapid fall in brightness below about 6-7 mag. This effect is sometimes called a bimodal distribution. Here the absolute magnitude is given by $H_{10}=m-10\log r-5\log\Delta$, where m=apparent magnitude and r and Δ in AU are, respectively the solar and geocentric distances of the comet.

Accumulation scenarios for comet formation generally lead to a large number of very small comets. Apparently they have largely been eliminated by some physical process or processes that have occurred during accumulation or later.

Very low-density small comets may have been selectively destroyed by encounter with a low-density medium or by tidal destruction at close approaches to planets or proto-planets. More likely, regardless of density, they may have been destroyed because of external heating by the Sun, proto-sun or supernovae, or possibly, after their arrival in the Opik-Oort Cloud, have ejected themselves by jet action induced by a nearby supernova.

Pursuing this problem the writer identified ten very faint relatively "new" comets in Table I by B.G. Marsden and E. Roemer (MR) from Comets (Ed. L.L. Wilkening, U. Ariz. Press, pp707-733, 1982) as having "original" $1/a<10^{-4}(AU)^{-1}$ and H_{10} >8.5 mag. (from various sources). Seven additional "dying comets", relatively "new", were identified by L. Kresak (Bull. Astr. Inst. Czech. 35, 129-150, 1983).

The directions of the lines of apsides (LOA the major axes) of the orbits of these 17 comets were plotted and found to avoid a region of 75° small-circle radius centered on ecliptic longitude, L=4.5° and latitude, B=+3°.0. This region of avoidance covers 0.37 of the total area of the sky. Among 77 remaining brighter comets in the MR catalogue with $1/a< 10^{-4}(AU)^{-1}$, 26 fell within the region of avoidance, near random expectation. Fisher's test applied to the matrix

0	17
26	51

leads to a probability of 1/433 for such a region of avoidance

The LOA of parabolic comets are distributed at random with respect to the region of avoidance shown by the faint "new" comets. For hyberbolic and long-period comets the LOA show a small, not very significant, avoidance for the region while for periodic comets the LOA are somewhat concentrated in the region. For only 4 of 20 split comets do the LOA fall within the region.

Studies are continuing to ascertain other possible correlations with the distributions of the lines of apsides and any possible significance of the correlations in terms of the physical environment and evolution of comets.

References for "The dearth of faint "new" comets"

I E. Everhart, 1967, Astr. J., 72, 1002-1011

II Kresak, L., 1983, Bull. Astr. Inst. Czech., 35, 129-150

III Marsden, B.G., 1982, Catalogue of Cometary Orbits, Smithsonian Astrophysical Observatory

IV Marsden, B.G. and Roemer, E., 1982, Comets, Ed. L.L.Wilkening, Univ. Arizona Press. pp707-733.

SMALL SOLAR SYSTEM BODIES

J. G. Williams
J. Gibson

Jet Propulsion Laboratory
California Institute of Technology

During the past year there has been work on asteroid proper elements and families, and the measurement of comet and asteroid images on plates and CCD frames.

In the category of theoretical and data analysis problems the main tasks during the past year were the generation of proper elements for the PLS II asteroids, their assignment to families, and the hunt for new families. The PLS II material can be divided into two broad catagories according to the accuracies of the orbits. All of the accurate orbits and all but a few of the less accurate orbits have had proper elements generated. Family assignments have been made for all of the accurate orbits. A file of the proper elements and assignments has been made for these 1227 asteroids. The analogous original file of numbered objects, which was deposited as a TRIAD file and published as a table in the book Asteroids (J. G. Williams author, T. Gehrels editor, Univ. of Arizona Press, pp. 1040-1063, 1979), has been updated. The update has 404 new or revised entries and extends sequentially up to asteroid number 2065 plus special entries for 20 higher numbered planet crossers. Secular perturbation theory, which is used to calculate the proper elements, does not accomodate commensurate orbits or Jupiter and Saturn crossing asteroids and comets. At a request from users of the earlier TRIAD file, which did not contain entries for these objects, the new file contains entries noting the special character of the orbit, but gives no proper elements except semimajor axes. The file of numbered objects has been submitted to the collection of IRAS asteroid files, and diskettes or paper copies have been sent to several users. The generation of proper elements for higher numbered objects was terminated due to a reduction of support.

Collisions cause groupings of asteroid proper elements called families. When the new proper element material was compared with the previously discovered asteroid families numerous matches were found. In addition candidates for new families were also found. Of these candidates 13 passed the significance test used. Probably the most interesting of these additions is family number 196 Tinchen which appears to be the second family associated with Vesta. There is a new family, number 200, associated with the large asteroid 423 Diotima. One old family was split into two groupings. A total of 117 families are now recognized. Plots of the more populous families have been prepared for publication and four examples are shown. These are proper e-sin i plots to the same scale for small regions around the families. Family members are open

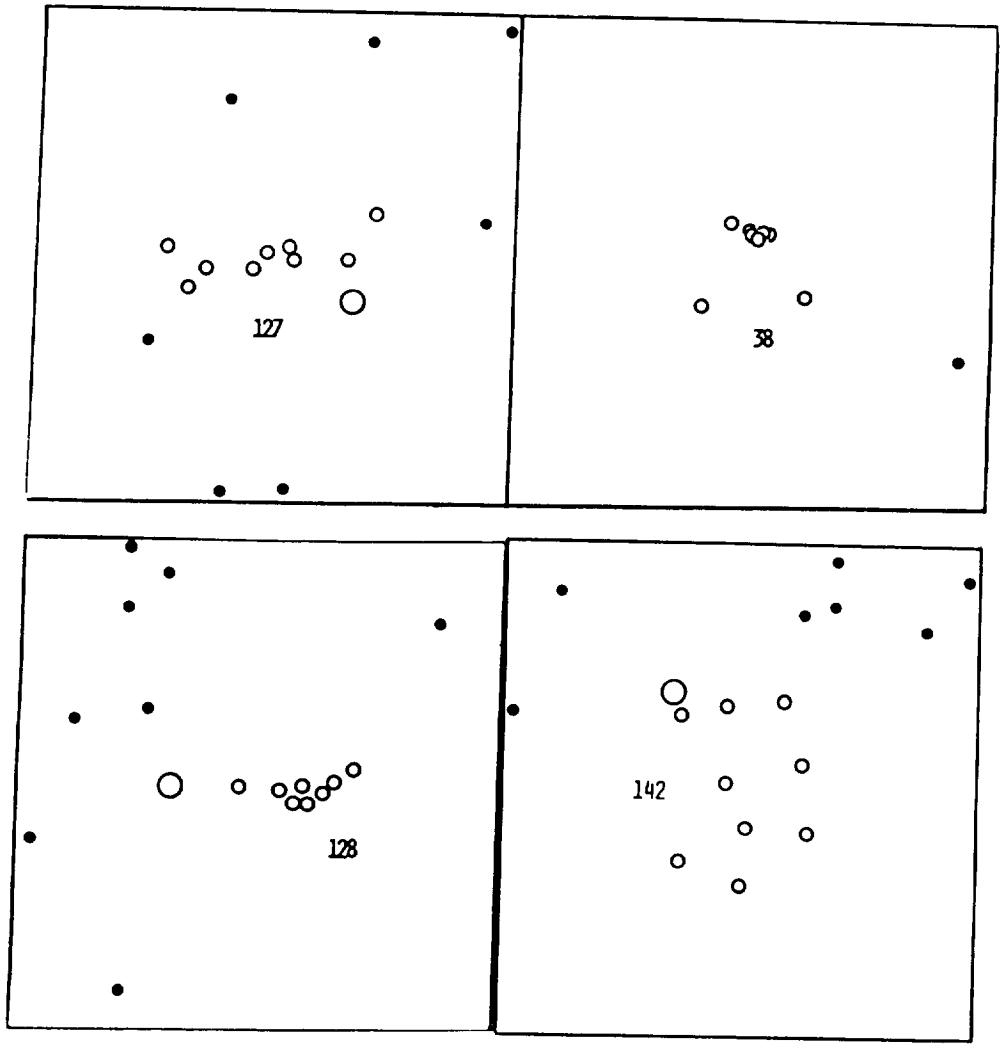

circles and large members use large circles. Family 38 has a very tight core. Many of the families, such as 127, 128, and 142, have a large object at the side and are the remnants of large cratering events. The impacted bodies are 93 Minerva, 351 Yrsa, and 87 Fides respectively. The three large objects in family 138 (not pictured) lie on a straight line in proper a-e-sin i space. It is now apparent that the Eos family (not pictured) has an extension of small objects to the low semimajor axis side. These families form a rich field for future studies. The opportunity to examine the interior of former parent bodies should be pursued.

The astrometry task is directed toward measuring and reducing positions on faint comets and the minor planets with less common orbits. During this year the obsevational material has switched from 1.2m Schmidt camera plates to CCD frames taken by the Palomar 1.5m telescope. Unfortunately the switch does not end the need to measure Schmidt plates because the

CCD is too small to capture an array of reference stars with known positions. It is necessary to use an existing plate to measure the fainter stars on the CCD frame with respect to the less common catalogue stars. During the past year positions of 18 comets and 59 different asteroids have been published on the Minor Planet Circulars. Many of these were first or last observations which particularly strengthen the orbit determination. For example recovery positions were published on the Jupiter crosser 1983 SA and the Geminid stream asteroid 1983 TB. In summary, asteroid positions were given on 7 planet crossers (1981 XA, 1982 DV, 1982 RB, 1983 SA, 1983 TB, 1984 QA, and 1985 JA), 8 high inclination objects, 1 Trojan, 1 Hilda, 1 Hertha, and 41 more ordinary minor planets. These comet and asteroid positions were published on Minor Planet Circulars 8964, 9043, 9125, 9143, 9178, 9256, 9316, 9319, 9330, 9391, 9403, 9449, 9532, 9603, 9604, 9657-9660, 9719-9722, and 9734. Astrometric experience has been distilled into a publication for the International Halley Watch effort. The reference is J. Gibson, "Measuring - the Quantifying Art", in Cometary Astrometry, editors D. K. Yeomans, R. M. West, R. S. Harrington, and B. G. Marsden, pp. 125 - 149, 1984.

MALL BODIES DATABASES.
harles A. Wood, SN-4, Johnson Space Center, Houston, TX 77058

ATIONALE: Implicit to the concept of "comparative planetology" s the comparison of similar objects to learn more about the lass by amalgamating studies of individuals. This has been a ruitful approach for a variety of planetary features, including mpact craters, volcanoes, aeolian landforms, and planets hemselves. Perhaps because the smaller bodies of the solar ystem are nearly unmanagably numerous there have been fewer uses f the comparative planetology methodology. The most significant xception is the consortium-produced TRIAD or Tucson Revised ndex of Asteroid Data (Zellner, 1979a), which has been used for variety of studies including a fundamental classification of steroid types (Zellner, 1979b).

During the last three years, a series of summer interns and have compiled a number of data bases for small bodies in the olar system. This arduous work was undertaken to provide facts or statistical investigations of the origins and interrelations comets, meteorites and asteroids. The labor devoted to ompiling the databases was well spent, for a number of scoveries ensued, including the recognition of (1) discrete amilies of H chondrites with different fall characteristics Wood, 1982a, 1982b), and an inferred origin from comets (Wood nd Mendell, 1982; Wood, 1982b); (2) subtle groupings within the chondrites related to olivine compositions, mass and hour of all (Wood and Silliman, 1983); (3) cometary orbital and physical haracteristics for the majority of Earth-approaching asteroids Wood, 1983); and (4) unexpected relations between cometary tail sconnection events and orbital and physical parameters Bollinger and Wood, 1984).

Whereas these discoveries are intriguing, it is true that he databases on which they depend probably could have many more plications hence this abstract reviews the contents of each of he databases. Note that none of this research was funded hrough the review process - a proposal to compile and analyse hondrite data was not funded although recommended by the review nel - and indeed the catalog of H chondrites was denied blication in a small meteoritics journal because it would be tdated when the next meteorite fell! Thus the compilation of e basic databases into finished products has fallen by the yside...

TEORITES: The Houston Chondrite Register: H Chondrites (Wood d Lee-Berman, 1982 unpublished compilation) contains as much as available of the following information for 577 H chondrites: teorite name, petrologic class, fall location and date and ur, weight, olivine composition, iron weight percent, silica-gnesium ratio, shock class, metal class, helium-4 abundance, Th-He gas retention age, K-Ar age, and exposure age. This talog was distributed to a limited number of active

meteoriticists, who kindly provided corrections and updated information. A similar catalog was also compiled for 576 L chondrites (Wood and Silliman, 1983 unpublished) and a much smaller one for carbonaceous chondrites (Wood, 1983 unpublished).
APOLLO/AMOR/ATEN ASTEROIDS: Earth-approaching asteroids have special significance because they are (1) candidates for sampling missions, and (2) possibly the sources for some meteorites. The following data were compiled for 80 Earth-approaching asteroids: number, name, designation, diameter, q, Q, a, i, e, node, argument of perihelion, orbital period, geocentric velocity, rotation period, shape, associated meteor streams, type, brightness, albedo, and date and minimum distance of closest approach to Earth. This listing has been exchanged with a few active asteroid investigators.
COMETS: Brian Marsdan has continued to update his definitive "Catalogue of Cometary Orbits", but there has been no similar collection of the physical characteristics of comets since Vsekhsvyatskii's 1957 volume of that name. Two successive student interns and I have used these two fundamental sources (plus new data) to compile a massive catalog of the following information for 747 comets: comet name, number, discovery date, current perihelion date, q, e, i, orbital period, argument of perihelion, node, original 1/a, longitude and latitude of perihelion, absolute magnitude (H10 and n), tail type, length and disconnection occurrence, nucleus radius, rotation rate and split, coma size, outburst, and spectral type.
DISCUSSION: It is a remarkable fact that a non-specialist has compiled the various databases described above, each of which is the most comprehensive of its kind. It should be equally obvious that a non-specialist may commit errors due to ignorance and inexperience; to minimize this possibility I have relied as much as possible on previous compilations of individual quantities (e.g. comet rotation periods), and have freely asked for (and received) advice from Brian Marsden, Eleanor Helin, Brian Mason and other experts in each of the fields into which I have transgressed. Except for the Houston Chondrite Registers these databases utilize Lotus 123 as a database management program. As much as possible I will provide data diskettes to serious users, especially those with new data to add!

References:
Bollinger, J.R. and C.A. Wood (1984) The physical and orbital characteristics of comets with plasma tail disconnections. Bull. Am. Ast. Soc. 16, 646.
Gehrels, T. (editor),(1979) Asteroids, Univ. of Arizona Press, Tucson, 1181p.
Wood, C.A. (1982a) Fall statistics of H chondrites: Evidence of cometary origins for ordinary chondrites. Lunar Planet. Sci. 13, 873-4.
Wood, C.A. (1982b) Exposure age as a clue to meteorite streams. Meteoritics 17, 297-8.

Wood, C.A. (1983) Searching for comet cores among Apollo/Amor asteroids. Lunar Planet. Sci. 14, 853-4.
Wood, C.A. and J.R. Bollinger (1984) Changes in comet characteristics with dynamical lifetime. Bull. Am. Ast. Soc. 16, 646.
Wood, C.A. and W.W. Mendell (1982) Comets, asteroids, meteorites, and meteors. Lunar Planet. Sci. 13, 877-8.
Wood, C.A. and C.L. Moore (1984) Comets: A synthesis of physical, chemical, and orbital data. Lunar Planet. Sci. 15
Wood, C.A. and A. Silliman (1983) L chondrites: A photogeologist's search for physical processes. Lunar Planet. Sci. 14, 855-6.
Zellner, B. (1979a) The Tucson Revised Index of Asteroid Data, in Gehrels (1979), p. 1011-1013.
Zellner, B. (1979b) Asteroid taxonomy and the distribution of the compositional types, in Gehrels (1979), p. 783-806.

CHAPTER 2

OUTER PLANETS AND SATELLITES

VOYAGER SATURNIAN RING MEASUREMENTS AND THE EARLY HISTORY OF THE SOLAR SYSTEM

H. Alfvén, University of California, San Diego

The mass distribution in the Saturnian ring system is investigated and compared with predictions from the plasma cosmogony. According to this theory, the matter in the rings was once in the form of a magnetized plasma, in which the gravitation is balanced partly by the centrifugal force and partly by electromagnetic forces. As the plasma is neutralized, the electromagnetic forces disappear and the matter can be shown to fall in to 2/3 of the original saturnocentric distance. This causes the so-called "cosmogonic shadow effect," which has been demonstrated earlier for the asteroidal belt and the large-scale structure of the Saturnian ring system.

The relevance of the cosmogonic shadow effect is investigated for parts of the fine structure of the Saturnian ring system. It is shown that many structures of the present ring system can be understood as shadows and antishadows of cosmogonic origin. These appear in the form of double rings centered around a position a factor 0.64 (slightly less than 2/3) closer to Saturn than the causing feature. Voyager data agree with an accuracy better than 1%.

COEFFICIENT OF RESTITUTION OF ICE PARTICLES AT VERY LOW VELOCITIES

Frank Bridges, Physics Department, and Artie Hatzes and Douglas Lin, Lick Observatory, University of California, Santa Cruz, CA 95064.

Saturn's rings are probably made up of many ice particles with sizes ranging from a small fraction of a centimeter up to a few meters (Tyler et al. 1983). The particles are in nearly circular orbits and collide frequently at very low relative velocities. One of the most important recent theoretical advancements is the realization that such collisions play a very important role in the structure, stability, and evolution of Saturn's rings (Cook and Franklin 1964; Brahic 1977; Goldreich and Tremaine 1978a, 1982; Trulsen 1972; Haimeen-Antilla and Lukkari 1980; Borderies, Goldreich, and Tremaine 1984; Weidenshilling et al. 1984; Shu and Stewart 1985). For example, the thickness of the rings is directly determined by the coefficient of restitution, ε , for particle collisions (Goldreich and Tremaine 1978a). In order to apply these theoretical results to interpret the observational data obtained from the Voyager mission (Lane et al. 1982; Smith et al. 1982), the detailed nature of the collisions must be understood (Borderies, Goldreich, and Tremaine 1984).

The relevant velocities for these experiments occur in the range 10^{-3} cm/s $< V <$ 10 c/s . Our preliminary results using a compound pendulum apparatus to achieve low velocities (Bridges, Hatzes and Lin 1984), indicate that ε depends on the relative particle velocity according to the relation $\varepsilon(V) = AV^{-.24}$. However the apparatus used for these results was not air-tight; consequently the collisions were made in a one atmosphere environment and often a layer of frost formed on the apparatus.

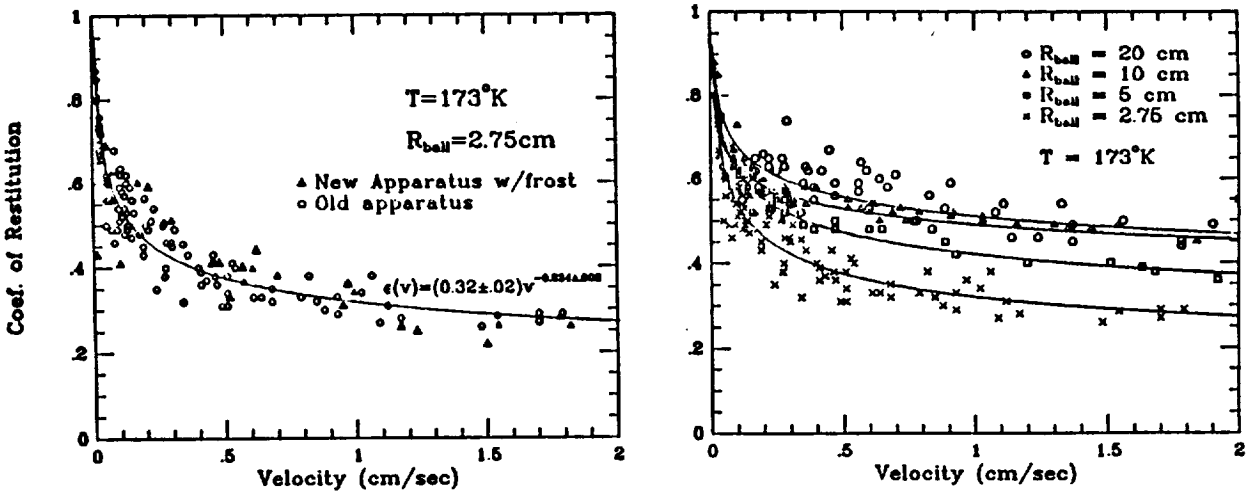

(a) (b)

Fig. 1 (a) A comparison of the coefficient of restitution ε obtained with the old apparatus and the new apparatus with frost on the ice surface. For the frost free surface, $\varepsilon = .6$ at $V = 1$ cm/sec. (b) The dependence of ε on the radius of curvature of the ball at $T = 173$K.

To eliminate these problems we have constructed a new cryostat which enables us to operate down to 80K with pressures (at present) of 20 Torr in the chamber. Recent data indicates that ε is somewhat higher for a clean ice surface but has the $V^{-.24}$ velocity dependence. When a thin layer of frost is formed on the surface, the values of ε are essentially the same as our earlier results (see Fig. 1a).

We have also made preliminary measurements of the dependence of ε on the radius of curvature which indicate that above $r = 20$ cm , ε is essentially independent of r ; for smaller r , ε decreases rapidly with r in the velocity range 0.5-2 cm/sec (Fig. 1b). Additional measurements are in progress to check these results at lower temperatures and with smoother surfaces.

In the last year we have also developed a capacitive displacement device (CDD) which enables us to continuously measure the displacement of the pendulum up to, during, and after the collision. It consists of a series of parallel plates mounted on the pendulum, which sit between three sections of similar plates mounted on the cryostat. As the pendulum oscillates the sets of plates move with respect to each other causing the capacitance of the system of plates to vary. With this device we are able to measure the displacement of the pendulum at a sampling rate of 20 kHz, which enables us to obtain the contact times for collisions, something we were unable to do before. Figure 2a shows the results of rapid sampling at the contact point with our data-taking system. We suspect that the rounded features of the displacement versus time is due to the ice ball compressing.

Another result we have recently obtained with our apparatus is that applying frost to the contact surfaces greatly increases the probability for sticking after a collision. Fig. 2b shows a particularly interesting case in which

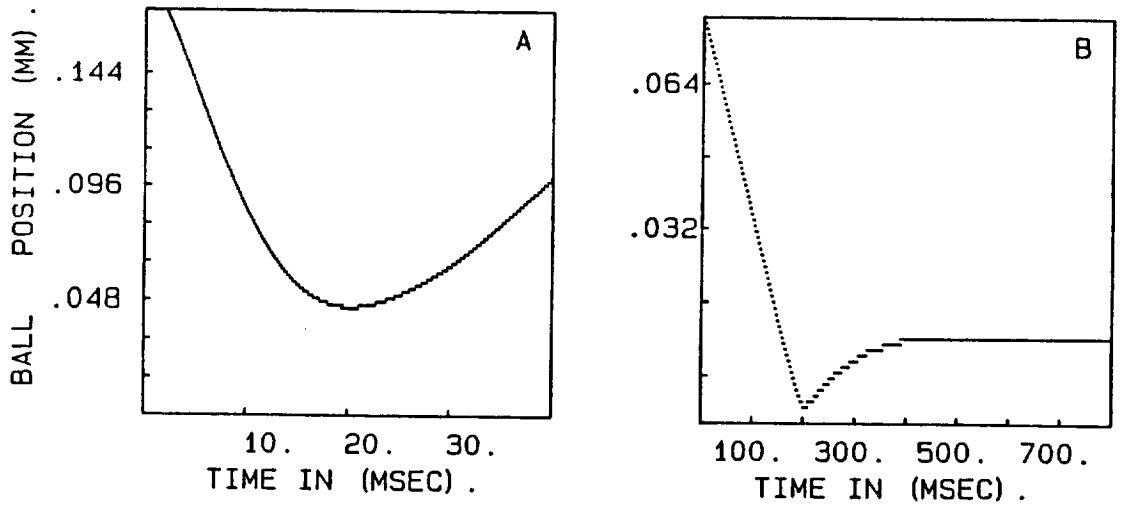

Fig. 2. The pendulum displacement as a function of time during a collision. (a) For an incoming velocity of 1 cm/s. (b) For a sticking collision with an incoming velocity of 0.4 mm/s.

the ice ball started to move away from the point of contact, but the sticking forces due to the frost slowed and eventually stopped the pendulum. An estimate of the sticking force is obtained by lowering the ice block and measuring the deflection angle at which separation occurs. For the collision shown in Fig. 2b, the sticking force was about 10 dynes.

References

Brahic, A., 1977, A. A., 54, 895.

Borderies, N., 1984, in Planetary Rings, ed. R. Greenberg and A. Brahic, (Tucson: University of Arizona Press), 713.

Bridges, F.G., Hatzes, A., and Lin, D.N.C., 1984, Nature, 292, 703.

Cook, A.F., and Franklin, F.A., 1964, A.J., 69, 173.

Goldreich, P. and Tremaine, S., 1978a, Icarus, 34, 227.

Goldreich, P., 1982, Ann. Rev. Astrn. Astrophys., 20, 249.

Lane, A.L., et al., 1982, Science, 215, 537.

Lin, D.N.C., and Bodenheimer, P., 1981, Ap. J. Lett., 248, L83.

Shu, F.H., and Stewart, G.L., 1985, Icarus, in press.

Smith, B.A., et al. 1982, Science 215, 504.

Trulsen, J., 1972, Ap. Space. Sci., 12, 329.

Tyler, G.L., Marouf, E.A., Simpson, R.A., Zebker, H.A., Eschleman, V.R., 1983, Icarus, 54, 130.

Weidenshilling, S.J., Chapman, C.R., Davis, D.R., and Greenberg, R., 1984, in Planetary Rings, ed. R. Greenberg and A. Brahic (Tucson: University of Arizona Press), 367.

SILICATE VOLCANISM ON IO

Michael H. Carr, U. S. Geological Survey, Menlo Park CA 94025

According to the tidal theory of heat generation within Io, as originally proposed by Peale et al.(1979), all the tidal energy is presently dissipated within a thin, rigid lithosphere that overlies a completely molten interior. Estimates of the thickness of the rigid rind range from 8 to 18 km (Peale et al., 1979; Nash et al., in press). If all the tidal energy were dissipated uniformly within a thin, rigid, homogeneous lithosphere, in which the temperature profile had equilibrated with the energy generated, no silicate volcanism would occur since the energy would all be deposited at depths shallower than the zone of melting and conducted upward toward the surface. But a lithosphere thin enough to conduct away all the tidal energy dissipated appears inconsistent with the presence of 10 km high mountains (Smith et al., 1979a) and 2-3 km deep calderas (Clow and Carr, 1980; Schaber, 1982), and with localisation of thermal emission in discrete hot spots. Although the thickness of the lithosphere has not been precisely defined, Nash et al. (in press) estimate that it must be at least 30 km thick in the regions where the 10 km high mountains occur. The lithosphere is probably not the same thickness everywhere. Calderas suggest, however, that the lithosphere is thick even away from the mountains since calderas several tens of kilometers across, and hundreds of meters to kilometers deep are seen in all near-terminator pictures (Schaber, 1982; Clow and Carr, 1980). Unfortunately, no quantitative estimates have been made as to how thick the lithosphere must be to allow formation of the observed calderas, but it appears unlikely that calderas several tens of kilometers across could form if the lithosphere thickness is close to the estimated minimum of 8-18 km. Furthermore, Matson et al. (1981) demonstrate that most of the tidal energy is emitted at hot spots, and that only a fraction of the tidal energy is lost through conduction. If the lithosphere is thicker than the minimum value of 8-18 km, then some of the tidal energy is dissipated by viscous heating below the lithosphere and a significant fraction of such heat generated would be transported toward the surface as magma.

Johnson et al. (1984) estimate that the satellite is currently emitting 1-1.3 W m^{-2}. On the assumption that the thickness of the lithosphere is in equilibrium with the present thermal regime, the rate of generation of silicate magma was estimated by determining the maximum amount of tidal energy that can be dissipated within a lithosphere of a given thickness without causing it to thin. The deficit with respect to 1-1.3 W m^{-2} that is being lost must then be dissipated below the lithosphere and transported toward the surface as silicate magma. Temperature profiles within the lithosphere were calculated numerically so that different thermal conductivities could be assigned to different parts of the profile. For a given lithosphere thickness, heat production rates per unit volume were sought that produced equilibrium temperature profiles satisfying the constraint that solidus temperatures are reached at the base of the lithosphere. Heat production was assumed uniform throughout the profile. After the profile converged, the total energy that could be dissipated in the lithosphere was derived from the heat production per unit volume. Conductivity could be varied within the

profile, for example to account for sulfur rich materials near the surface. The profiles show that the maximum tidal energy that can be dissipated within a 30 km thick lithosphere and conducted to the surface is between 0.28 and 0.36 W m^{-2}. For a 60 km thick lithosphere the figures are 0.14 to 0.18 W m^{-2}. If no tidal energy is dissipated in the lithosphere the figures are 0.18 and 0.09 W m^{-2} respectively for 30 km and 60 km thick lithospheres. The difference between these figures and the 1-1.3 W m^{-2} loss observed gives the amount of heat dissipated below the lithosphere and transported to the surface as silicate magma. The amount of magma generated is equivalent to a resurfacing rate of 0.35-0.45 cm $year^{-1}$ for a 30 km thick lithosphere and 0.45-0.5 cm $year^{-1}$ for a 60 km thick lithosphere.

Given that silicate magma is transported up through the Ionian lithosphere in order to dispose of much of the tidal energy, the question arises as to whether the magma mostly reaches the surface to form volcanic landforms, or whether it is mostly intruded into the lithosphere at relatively shallow depths. Apart from the plumes, the most direct evidence of volcanic activity is the presence of thermal anomalies or hot spots (Hanel et al., 1979; Pearl and Sinton, 1982). Morrison and Telesco (1980) modelled the non-solar part of Io's infrared eclipse spectrum on the basis of three components. They suggested that 9.4×10^{-6} of the surface area is at 600°K, 2.2×10^{-4} at 350°K, and 1.4×10^{-2} at 200°K. Sinton (1981) found a good fit with 2.1×10^{-5} of the area at 615°K and 3.9×10^{-3} of the area at 294°K. Pearl and Sinton (1982) recognized three types of hot spots from the Voyager IRIS data: stable, high temperature (600°K) sources; transient, high temperature (600°K) sources; and stable, low temperature (< 400°K) sources. Most of the anomalies are associated with local dark areas, and in general the darker the area the higher the temperature (McEwan, 1984). Where the resolution is good enough the dark spots are observed to lie mostly within calderas. The favored interpretation of the dark hotspots is that they are lakes of molten sulfur, the result either of eruption of sulfur magma from kilometer depths (Smith et al., 1979a, 1979b; Sagan, 1979), or mobilization of sulfur near the surface by silicate intrusions (Soderblom et al., 1980; McEwan and Soderblom, 1983; Lunine and Stevenson, in press). The sulfur lake interpretation is based on the temperatures which are believed to be too low for silicates, on the similarity in albedo between the dark spots and liquid sulfur, and on the abundant evidence that sulfur is abundant on the Ionian surface.. Implicit in the rejection of a silicate explanation of the anomalies is a belief that many of the dark areas are active lava lakes, so that the observed low temperatures imply low temperature melts.

An alternative explanation of the dark spots is that they are relatively recent flows, and that with time the flows assume the albedo of their surroundings as they become covered with plume debris or condensed volatiles. Terrestrial calderas are rarely, if ever, filled with molten lava. The floors of the summit calderas of the most active volcanoes on Earth, Kilauea and Mauna Loa, are covered mainly by flows. It appears reasonable therefore to consider the possiblity that the floors of the Ionian calderas are dark and warm, not as a result of the presence of lava lakes as has been widely

assumed, but because they are covered by relatively recent and still cooling lava flows. A basic property of silicate eruptions that is fundamental for understanding how a silicate eruption might be detected on Io, is that most of the eruptive energy is initially buried and subsequently lost at low temperatures over several years. For typical conditions on Io only about 15% of the eruptive energy has been lost by the time a flow stops (Carr, in press). The temperatures expected from sustained eruption of silicate flows onto the surface of Io were determined by dividing the flow three components: a lava channel, the active flow, and the inactive flow, then making a variety of assumptions about the viscosity of the flow when its movement stopped, the turnover rate of crust on the surface, the porosity of the newly formed crust, and so forth. The results show that the pattern of thermal emission expected is similar to that observed by the Voyager IRIS experiment provided high eruption rates ($1\text{-}5 \times 10^3$ m^3 s^{-1}) are sustained for several years.

What we know of Io is thus consistent with the following. Its volcanism and hence its surface materials are dominantly silicic. Several percent of volatile materials such as sulfur, but also including sodium and potassium rich materials, may also present. The volatile materials at the surface are continually vaporized and melted as a result of the high rates of silicate volcanism. As the erupted products become buried, as result of ongoing eruption of new material onto the surface, their temperatures rise. Volatile components are melted and volatilized at relatively shallow depths and transported upwards, possibly to be erupted again onto the surface. As a consequence of their mobility the volatile components become progressively depleted with depth. Whether they reach the depths where silicates melt will depend on their rate of diffusion and convection through the overlying lithosphere. Most of the sulfur compounds are likely to be depleted at relatively shallow depths because of their high volatility and so are recycled on a time scale that is short compared with the silicates.

References

Carr, M. H. Submitted to J. Geophys. Res. Clow, G. D., and M. H. Carr, Icarus, 44, 729-733, 1980. Hanel, R., et al., Science, 204, 972-976, 1979. Johnson, T. V., et al., Science, 226. 134-137, 1984. Lunine, J. I., and D. J. Stevenson, Submitted to Icarus. Matson, D. L., et al., J. Geophys. Res., 86, 1662-1672, 1981. McEwan, A. S., Bull. Amer. Astron. Soc., 16, 653, 1984. McEwan, A. S., and L. A. Soderblom, Icarus, 55, 191-217, 1983. Morrison, D., and C. M. Telesco, Icarus, 44, 226-233, 1980. Nash, D. B., et al., In Satellites , U. of Ariz. Press, in press. Peale, S. J., et al., Science, 203, 892-894, 1979. Pearl, J. C., and W. M. Sinton, In Satelltes of Jupiter, U. of Ariz. Press., 1982. Sagan, C., Nature, 280, 750-753, 1979. Schaber, G. G., in Satellites of Jupiter,p. 556-597, U. of Ariz. Press, 1982. Sinton, W. M., J. Geophys. Res., 86, 3122-3128, 1981. Smith, B. A., et al., Science, 204, 951-972, 1979a. Smith, B. A., et al., Nature, 280, 738-743, 1979b. Soderblom, L. A., et al. Geophys. Res. Lett., 7, 963-966, 1980.

The Trailing Side of Europa: Possible Detection of Heavy Water Ice

Roger N. Clark (U.S. Geological Survey, mail stop 964, Box 25046 Federal Center, Denver CO 80225) and Robert H. Brown (JPL, MS 183-501, 4800 Oak Grove Dr., Pasadena CA 91109)

Like Ganymede, Saturn's rings, and many of the satellites of Saturn, infrared spectra of Europa indicates abundant water ice. Ordinary water ice (H_2O) has absorptions at 1.04, 1.25, 1.5 and 2.0μm, and the spectra of all of the objects listed above show the main water bands. The 1.04-μm band is particularly strong on Europa, and because the absorption is normally weak relative to the other ice absorptions, the ice on Europa must be free of absorbing material. Clark (1980) estimated that the trailing side of Europa could have no more than about 2 wt% fine grained dark material. However, there are aspects of Europa's spectrum that cannot be explained by pure H_2O ice. The 1.5- and 2.0-μm bands both appear asymmetric, and the minimum at 1.5 μm has a higher reflectance than the peak at 2.2 μm (Figure 1). Also, the minimum reflectance at 1.5 μm is higher than would be expected for a water ice spectrum having absorptions as strong as those in the spectra of Europa's trailing side. Ordinary water ice can not produce this aspect of Europa's infrared spectrum, regardless of the scattering conditions (e.g. Figure 2). In an effort to explain the absorptions in the spectra of Europa, we examined reflectance spectra of many minerals, and when reflectance spectra did not exist, transmittance spectra. Gaffney and Matson (1980) suggested the possibility of high pressure phases of ice on icy surfaces, but transmission data show that the absorptions are shifted to shorter wavelengths relative to ordinary ice, and have more fine structure; they are not appropriate matches for the spectra of icy satellite surfaces. Also, absorptions due to high pressure phases of ice are not seen in spectra of other icy satellites, and therefore do not explain why the spectrum of the trailing side of Europa is unusual.

The trailing side of Europa is being bombarded by charged particles from Jupiter's magnetosphere, and it is estimated that many meters of ice have been sputtered from the surface (e.g. Haff et al. 1979). If two different species had the same sputtering yield, but different masses, then the heavier species would be sputtered at a lower velocity because the total kinetic energy imparted to each species is the same. In the case of sputtering of water (H_2O, HDO and D_2O), the molecules containing deuterium would have a lower scale height and a lower probability of escape from the satellite. This should result in an enrichment of deuterium over time. Because of this enrichment possibility, we conducted a laboratory study of the spectral properties of heavy water ice.

Triply distilled H_2O, and pure D_2O were mixed in a 50-50 mixture to produce pure HDO at room temperature. These samples were then frozen from the liquid state in liquid nitrogen and ground with a mortar and pestle at 77 K under a dry nitrogen atmosphere. The ground samples were then measured using an environment chamber and the USGS spectroscopy facilities in Denver. The spectral range covered was from 0.85 to 3.25 μm at a resolving power of about 200. The sample temperature during measurement was approximately 180 K.

The results are shown in Figure 3. The spectrum of HDO appears similar to that of H_2O, except that there is an additional feature at 1.73 μm and the 2-μm feature is shifted to 2.08 μm. The spectrum of D_2O has absorptions substantially shifted from those of H_2O. The "1.04-μm H_2O" feature is shifted to 1.40 μm, the "1.25-μm band" is shifted to 1.73 μm and has additional fine structure,

the "1.5-μm band" is shifted to 2.06 μm with a shoulder at 2.16 μm, and the "2.02-μm band" is shifted to 2.71 μm.

Although we also constructed several heavy ice plus ordinary ice mixtures in the laboratory to try and simulate the spectrum of Europa, too many possibilities were necessary, so we derived the absorption coefficients of the heavy ices using the Hapke (1981) scattering theory. Using these newly derived data, spectra of mineral mixtures were computed in an attempt to match the spectrum of the trailing side of Europa. From this study, we determined the spectral properties of the additional material(s) needed to explain the spectrum of Europa.

Because the spectrum of Europa has a minimum at 1.5 μm that is high relative to the spectra ordinary water ice, the spectrum of any additional material on Europa must be relatively transparent in this region, but absorbing in the 2-μm region. Few materials have these spectral properties, one of which is mascagnite, $(NH_4)_2SO_4$. However, the spectral properties of D_2O give a better match. The best match to Europa's spectrum using mixtures of H_2O and D_2O is an intimate mixture with 60% D_2O and 40% H_2O (Figure 1). Because the spectrum of D_2O does not show unique absorption bands when mixed with H_2O in the spectral region covered by the Europa data, we can not uniquely identify the presence of D_2O, but only note that the spectrum of the trailing side of Europa is consistent with the presence of D_2O. The best spectral match, shown in Figure 1, is still poor in the 2.3-μm region, but weak absorptions in this region may result from the presence of small amounts of ammonia hydrate (Brown et al., 1985) and might account for the differences. Further modeling of all three materials is needed, as well as improved measurements of Europa's trailing side spectrum.

REFERENCES

Brown, R.H., and Clark, R.N. (1985). Volatiles on icy satellites: Europa's trailing side. B. A. A. S. in press.

Clark, R.N. (1980). Ganymede, Europa, Callisto, and Saturn's Rings: Compositional analysis from reflectance spectroscopy. Icarus 44, 388-409.

Gaffney, E.S. and Matson, D.L. (1980). Water ice polymorphs and their significance on planetary surfaces. Icarus 44, 511-519.

Haff, P.K., Watson, C.C., and Tombrello, T.A. (1979). Ion erosion on the Galilean satellites of Jupiter. Proc. Lunar Planet. Sci. Conf. 10th 1685-1701.

Hapke, B. (1981). Bidirectional reflectance spectroscopy 1: Theory. J. Geophys. Res. 86, 3039-3054.

FIGURE CAPTIONS

Figure 1. The reflectance spectrum of the trailing side of Europa (line with error bars, scaled to the approximate reflectance level of the surface) is compared to the best fit model (line): bidirectional reflectance of 40% H_2O + 60% D_2O. The model spectrum is at a resolution about 3 times that of the Europa spectrum, so small details in the model spectrum would be lost at the lower resolution.

Figure 2. The absolute bidirectional reflectance spectra of ordinary water frost as a function of grain size. The grain sizes are A: about 50 μm, B: 200 μm, C: 400-2000 μm, and D: an ice block containing microbubbles.

Figure 3. Laboratory reflectance spectra of H_2O, HDO, and D_2O at 180 K.

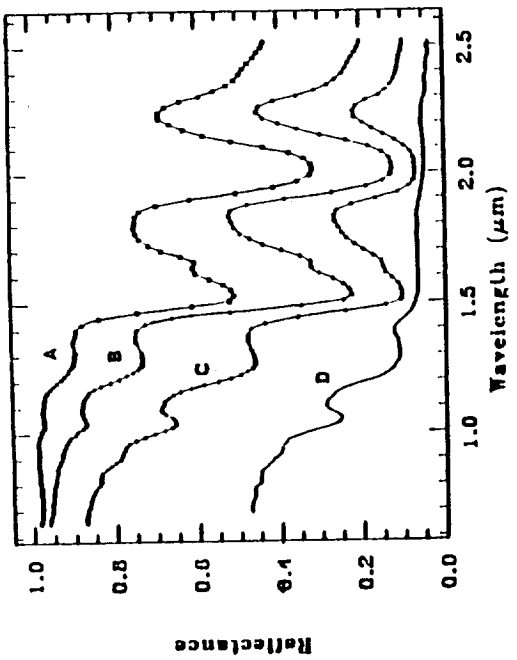

Figure 2.

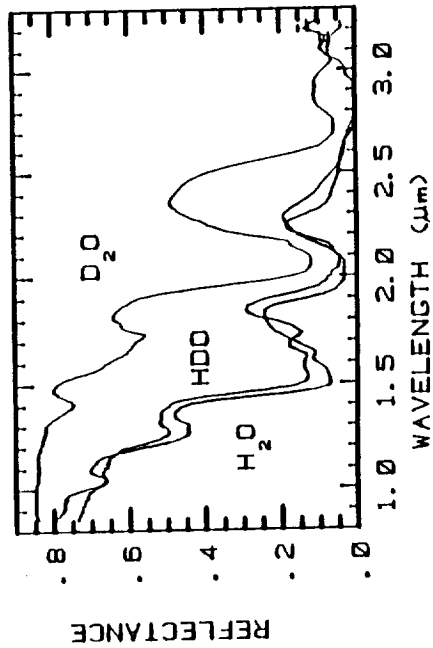

Figure 3.

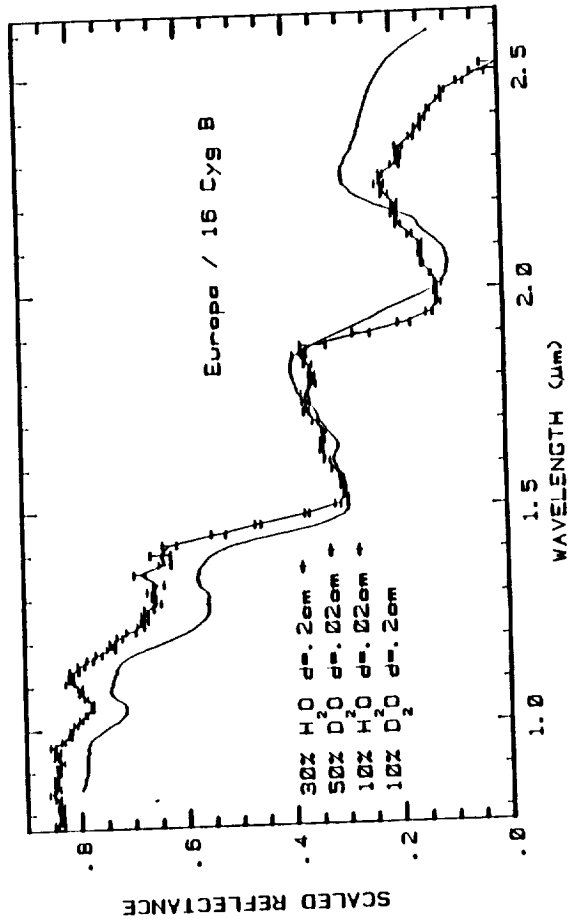

Figure 1.

GANYMEDE AND CALLISTO: TOWARD A NEW SYNTHESIS

Croft, S.K., Lunar and Planetary Laboratory, University of Arizona, Tucson, Arizona 85721

The extraordinary differences in surface structure between Ganymede and Callisto - two satellites of nearly identical size and composition, yet the former exhibiting a heavily endogenically modified surface in contrast to the primitive cratered state of the latter - constitute the primary challenge to our current understanding of solid ice/rock objects in the solar system. Thus, there have been numerous attempts to explain this curious pair of satellites (e.g., 1,2,3,4). Most of these models invoke complete or near complete differentiation of one or both of the satellites. In the last year, a new approach to the problem prompted primarily by geological considerations has been developed (5,6). There are three key aspects to the new model. First, it is assumed that the light terrain on Ganymede was emplaced as a liquid. This assumption is not new (e.g., 7,8), and is made on the basis of the morphology of the light terrain, which is compatible with liquid emplacement, but not with emplacement by solid state diapirism. Second, the hydrogeologic implication of emplacement of the light terrain as a liquid strongly suggests that the outer ice I rock layer of Ganymede retained sufficient rock to drive liquid to the surface and hence never completely melted. Stability considerations then imply that the interior remained unmelted as well. Thus, Ganymede was only marginally melted. Callisto, being slightly smaller and containing slightly less rock per unit mass than Ganymede, remained somewhat cooler in the interior and thus presumably never melted at all. Third, heat transport in both satellites is primarily by vigorous internally heated convection, which produces a global pattern of high and low heat flux (varying typically by a factor of two between warm rising material and descending cool plumes) and tectonic stresses which will affect the distribution of melt zones and tectonism on the satellites. The plausibility and implications of this new model are being tested by a synthesis of thermal history models with geologic and tectonic data.

Thermal History Models. Preliminary thermal histories have been calculated for Ganymede and Callisto using a parameterized convection model assuming an internally heated convecting layer (9,10) coupled to a conducting lid. The adopted ice creep relation was derived from measurements in the antarctic ice cap (11) and correspond well to recent laboratory measurements (12) except at very low temperatures. A slight stiffening of the ice due to silicate inclusions was included (13). The two-dimensional variation of temperature at depth due to convection was approximated by calculating two model histories for each satellite: a "hot" model representing the warm rising plumes with a heat flux of 4/3 chondritic, and a "cold" model representing the cool descending plumes with a heat flux of 2/3 chondritic. The "hot" model for Ganymede was arbitrarily varied by changing the critical Rayleigh number for the onset of convection until melting was obtained. The "cold" Ganymede model was run by changing only the assumed heat flux, and the "hot" and "cold" Callisto models by changing only the satellite mass and rock content to

values appropriate for Callisto. Callisto's interior was found to remain 4° to 6°K cooler than Ganymede's, a difference sufficient to allow eras of melting up to about 400 million years long on Ganymede without generating any melt in the corresponding Callisto models. This result was obtained for a critical Rayleigh number well within the (rather broad) range of theoretical estimates. Thus, this result establishes the possibility of a marginally melted Ganymede and unmelted Callisto within reasonable physical constraints.

Convective stresses in the interior of Ganymede's convection zone were only about 10 KPa, though stresses of about a MPa were obtained in the thermal boundary layer. Convective stresses in Callisto were only about 10% smaller. These stresses are still about an order of magnitude too small to completely fracture a 7-10 km thick ice lithosphere (14). Thus, the interior convective pattern will generate an oriented stress field in the lithosphere, but an additional stress source is apparently needed to generate the observed fractures on Ganymede. One possibility is stress due to expansion caused by partial melting and differentiation (6,15). Another is stress caused by a second, cooler layer of convection in an upper (nearly) pure ice layer in excess of 20-30 km thick. Since both of these mechanisms could be present in a marginally melted Ganymede and absent in an unmelted Callisto, either could account for the tectonism so obvious on Ganymede but absent on Callisto.

Geologic Observations. The morphology of the light terrain on Ganymede was mentioned above as the key factor in assuming liquid emplacement indicative of melting. In addition, it was initially recognized that the light terrain formed over a period of time estimated at several hundred million years (16), implying one extensive melting episode. The dark terrain of Ganymede was also initially recognized to represent a modified surface, though it was assumed that the missing older craters had vanished via viscous relaxation (17). (18) argued, however, that relaxation could not get rid of crater rims completely, thus the uncratered time horizon must represent an endogenic resurfacing. Subsequently, (19) suggested that dark smooth areas within the dark terrain were due to flooding. In the last year, the dark terrain was noted to consist of distinct albedo and tectonic provinces and inferred to have multiple layers, implying a complex vertical and horizontal layered structure indicative of a second earlier extensive era of multiple eruptive episodes (20). The layers, inferred to be hundreds of meters to a few kilometers thick, are sufficient to obliterate the relatively shallow craters on Ganymede. In the thermal model, melting rapidly reaches a maximum and declines slowly over a few hundred million years. The rate of resurfacing is easily capable of burying the old surface rapidly enough to provide a resurfaced "horizon." Melting is confined to the zone of hot rising material, thus as the "heat engine" runs down, the final limited episodes of melting should be found in a pattern reflecting the geometry of the interior convection cells. (5,6) suggested that the pattern of dark and light terrain on Ganymede is similar to an $\ell=2$ convection pattern.

Tectonic Observations. Two sets of observations are relevant here. The first is the set lithospheric thicknesses inferred from furrow widths assuming the furrows to be simple grabens. Furrow widths and spacing are

fairly constant within Galileo Regio. Furrow width and spacing are also fairly constant in nearby Marius Regio, but with dimensions only about half that of Galileo Regio (21), implying that at the time of furrow formation, the lithosphere in Marius Regio was only about half that in Galileo Regio. This pattern is repeated elsewhere on Ganymede (22). Since the dark terrain all formed within a relatively short time period (6,16), and since it is difficult to change the average planetary thermal gradient by a factor of 2 in less than a billion years, the observed variation must represent real spatial variations in lithospheric thickness and heat flow such as is found in convection cells. Further, the areas of thick lithosphere correspond to the areas of cool descending convection plumes inferred from the quasi-ℓ=2 pattern in the light and dark terrain. The unusually thick lithosphere inferred from grabens around Valhalla on Callisto, where the lithosphere should be comparable to Ganymede's, may be due to rate effects and not an anomalously cold interior (22). The second set of observations involve the global trends of groove directions found by (23): great circles inclined $\approx 30°$ to Ganymede's equator. The trends bisect the areas of upwelling warm material inferred from the light/dark terrain pattern and furrow thicknesses, and are perpendicular to the inferred directions of convective stress, consistent with the interpretation of grooves as extensional structures.

Thus, the new model provides a plausible account for an unaltered Callisto and a strongly altered surface of Ganymede. It is also consistent with an extensive period of multiple resurfacing episodes and provides a consistent framework for the pattern of light terrain, furrow geometry, and groove orientations. While there are still many problems, the new model provides a productive paradigm for further research.

REFERENCES

1. Cassen P., S.J. Peale and R.T. Reynolds (1980) Icarus 41, 232-239. 2. Thurber C.H., A.T. Hsui and M.U. Toksöz (1980) PLPSC 11th, 1957-1977. 3. Friedson A.J. and D.J. Stevenson (1983) Icarus 56, 1-14. 4. Kirk R.L. and D.J. Stevenson (1983) LPS XIV, 373-374. 5. Croft S.K. (1985) LPS XVI, 152-153. 6. Croft S.K. (1986) JGR, submitted. 7. Parmentier E.M., S.W. Squyres, J.W. Head and M.L. Allison (1982) Nature 295, 290-293. 8. Allison M.L., J.W. Head, and E.M. Parmentier (1980) Satellites of Jupiter, Abstract 6-7. 9. De la Cruz S. (1973) Master's Thesis, University of Toronto. 10. Turcotte D.L. and G. Schubert (1982) Geodynamics, Wiley, 450pp. 11. Paterson W.S.B. (1977) Rev. Geophys. Space Phys. 15, 47-55. 12. Durham W.B., H.C. Heard, and S.H. Kirby (1983) JGR 88, B377-B392. 13. Hooke R.LeB., R.B. Dahlin, and M.T. Kauper (1972) J. Glaciology 11, 327-336. 14. Golombek M.P. and W.B. Banerdt (1985) in Conf. on Heat and Detachment, 45-49. 15. Squyres S.W. (1980) Geophys. Res. Lett. 7, 593-596. 16. Shoemaker E.M., R.K. Lucchitta, D.E. Wilhelms, J.B. Plescia, and S.W. Squyres (1982) in Satellites of Jupiter, 435-520. 17. Passey Q.R. and E.M. Shoemaker (1982) in Satellites of Jupiter, 379-434. 18. Croft S.K. (1983) LPS XIV, 136-137. 19. Casacchia R. and R.G. Strom (1984) JGR 89, B419-B428. 20. Croft S.K. and R.G. Strom (1985) LPS XVI, 156-157. 21. Zuber M.T. and E.M. Parmentier (1984) Icarus 60, 200-210. 22. Croft S.K. (1985) in Conf. on Heat and Detachment, 34-37. 23. Bianchi R., R. Casacchia, and R.G. Strom (1986) Icarus, submitted.

Planetary Ring Dynamics and Morphology

Jeff Cuzzi, Ames Research Center, Moffett Field, California 94035
Frank Shu, University of California, Berkeley, California 94720
Richard Durisen, Indiana University, Bloomington, Indiana 47405

This activity supports a variety of observational and theoretical projects, primarily dealing with the structure of dense rings in which gravity and collisional effects (pressure, viscosity) dominate. These projects involve a variety of collaborators, those noted above being supported under this activity. A few of our ongoing projects are noted here.

For several years now, the existence of asteroid-sized "moonlets" within the rings of Saturn has been debated. In a series of papers, we have now demonstrated that a 10 km radius moonlet resides in, and is primarily responsible for creating, the Encke gap in Saturn's A ring . The evidence is still inferential, but comes from quite straightforward analysis of several independent observations, and is completely unambiguous. Undulating radial perturbations along the edges of the gap, or edge waves, in the Voyager images (Cuzzi and Scargle 1985, as reported last year) indicated that a single dominant moonlet lay near the gap center within a certain band of longitudes. A simple "wake" model of these perturbations also predicts radial fluctuations of optical depth seen in the Voyager PPS stellar occultation observations. We (Showalter et al. 1986) have now completed a detailed analysis of these fluctuations in light of this model, as well as of similar features seen in the Voyager radio occultation data, and have demonstrated excellent agreement with the moonlet wake hypothesis. Showalter et al. further strengthened the case against more than one dominant moonlet, and obtained a highly accurate determination of the moonlet's longitude and radius at the epoch of observation which placed it right within the band indicated by Cuzzi and Scargle (fig.1). The now well-established existence of such a large object well within Saturn's Roche limit has profound implications for the origin of Saturn's ring system in particular, and of the entire satellite system in general.

Fundamental progress has also been made in theoretical studies of spiral density waves. We reported last year on the development of an inviscid (ie, undamped) theory of the behavior of strongly forced, or nonlinear, density waves (Shu et al. 1985a). Since then, the full damped theory has been developed in a series of two papers. Shu and Stewart (1985) described the application of a "Krook" model to determine pressure and viscous forces in a particle disk from the "kinetic" theory of nearly coherent particle motions.

Essentially, the Krook approximation as modified by Shu and Stewart assumes that inelastic collisions thermalize the particle relative velocities. This technique was used to determine the pressure and viscous forces appropriate for the nonlinear spiral wave problem; the fully damped spiral wave problem was then solved by Shu et al. (1985b), who demonstrated good agreement with wave profiles derived from stellar occultations. We (Shu et al. 1985b) point out that the dependence of the ring particle elasticity on collision velocity is an important, but poorly known, parameter. Fairly elastic particles do seem to be required to produce the moderately strong damping seen in the A ring. The theory predicts a sharp dropoff in damping with increasing optical depth, also consistent with observations (Dones et al. 1985a,b). The theory , while quite successful as far as it goes, will be improved further to self-consistently include transport of mass and angular momentum. It may eventually be necessary to include particle exclusion or "liquid" effects to fully understand the observed ring structure, as noted both by us and by others.

Theoretical studies of transport due to meteoroid erosion have made great progress during this year, as well. We have improved our numerical code so that we can run much longer evolution times, and have included not only mass and angular momentum transport by ballistic transport following meteoroid ejection, but also self-consistently by normal viscous transport. In addition, we have determined the ejecta distribution which results from realistic meteoroid bombardment, which is aberrated and incompletely absorbed. We find that a variety of structure on many radial scales results from the erosion process alone. Also, incoming meteoroids decrease the specific angular momentum of the rings as a whole, but the preferrred prograde ejection expected of realistic impacts may be an important source of matter and angular momentum to the outer ring regions. Some preliminary results are presented by Durisen (1985), and other manuscripts are in preparation.

One other small result of some interest is the solution of the puzzling problem of the anomalous darkness of the Uranian ring particles. Cuzzi (1985) showed that the optical depths inferred for the Uranian rings from stellar occultations (corrected for Fresnel diffraction) measure TWICE the physical particle cross section. This previously neglected factor rests on physics over a century old and subtle properties of this particular application. The lower resultant ring physical cross section, coupled with a more careful radiative transfer analysis of the reflected sunlight, allow the ring particle material, although still dark, to be no darker than other known

material such as the dark side of Iapetus or various meteorites (Table 1). The lower physical cross sections may have implications for collisional processes as well.

References: Cuzzi (1985) ; **Icarus, 63**,312; Cuzzi, J. N. and J. D. Scargle (1985) **Astrophys. J., 292**,276; Dones, H. L. et al. (1985 a), **B.A.A.S. 16**,922; Dones, H. L. et al. (1985b), Baltimore DPS meeting; Durisen, R. H. (1985); **Adv. Sp. Res., 4**,13; Showalter, M. R. et al. (1986), **Icarus**, submitted; Shu, F.H. and G. R. Stewart (1985), **Icarus, 62, 360**; Shu, F.H., et al. (1985a), **Astrophys. J., 291**, 356; Shu, F. H. et al (1985b), **Astrophys. J.**, Dec. 1985.

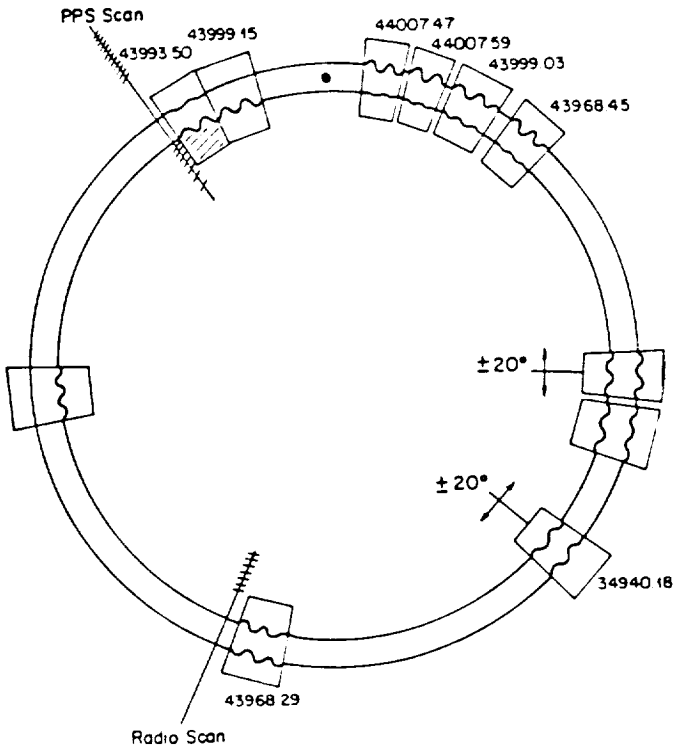

Figure 1: To the right we show a schematic representation of the Encke gap, as seen in a frame rotating with the moonlet, with the moonlet's position denoted by the black dot. The (incompletely observed) angular distribution of the observed edge waves, as produced by the moonlet and determined from analysis of Voyager images, is indicated along with the FDS catalog numbers of the images (Cuzzi and Scargle 1985). The locations of the PPS stellar occultation and the RSS radio occultation, which show systematic radial fluctuations in optical depth also resulting from the moonlet's perturbations, are also shown (Showalter et al. 1986) Direct evidence for these radial fluctuations is also seen in the image FDS 43993.50. These three independent observations all give the same location for the moonlet with very good accuracy, and also rule out additional moonlets of comparable size.

Table 1: PARTICLE SURFACE REFLECTANCES $\mathscr{R}$ (PLANAR FLUX ALBEDOS)

Surface material	At visual wavelengths	At 2-μm wavelength	References
Iapetus dark side	0.04 – 0.05	~0.09	Smith *et al.* (1982) Cruikshank *et al.* (1984)
Black chondrites	0.06 – 0.08	0.08 – 0.10	Gaffey (1976)
Ureilites	0.06 – 0.08	~0.10	Gaffey (1976)
C1 and C2 carbonaceous chondrites	0.03 – 0.04	0.04 – 0.06	Gaffey (1976)
C3V carbonaceous chondrites	0.05 – 0.09	0.07 – 0.11	Gaffey (1976)
Uranus ring particles[a]			
Lambert surface	0.05 ± 0.015	0.11 ± .01	This paper
Lunar-like surface	0.04 ± 0.015	0.09 ± .01	This paper

DYNAMICS OF SATELLITES, ASTEROIDS AND RINGS

S. F. Dermott, CRSR, Cornell University, Ithaca NY 14953

The emphasis in this work is on the dynamical evolution of the solar system. I am particularly concerned with those problems which impact recent or planned space missions and with those problems that have arisen as a result of recent discoveries.

1. **IRAS Solar System Dust Bands** (with P. D. Nicholson and B. Wolven)

IRAS (the Infrared Astronomical Satellite) discovered three narrow bands of far-infrared emission superposed on the broad zodiacal background. The most prominent band lies in or near the ecliptic and is flanked by two other bands ~ 10° above and below it. The distances derived from their color temperatures suggest that the dust bands are approximately at the distance of the main asteroid belt and may be the results of collisions between asteroids. We have Fourier analyzed the data in the IRAS Zodiacal History File in order to separate the smooth, large-scale background from the narrower dust bands. This enables us to determine the latitudes of bands. We have previously shown[1] that the dust bands may be debris produced by the gradual comminution of the asteroids in the prominent Hirayama asteroid families, in particular the Eos and Themis families, and we have predicted (a) that the ecliptic latitudes of the bands should vary with ecliptic longitude[2] (b) that the amplitude and the phase of the latitude variations can be predicted from a low-order secular perturbation theory[2] and (c) that the central dust band should be split. We have now shown that all of these predictions appear to be correct[3,4]. The central dust band is indeed split and the separation in latitude of the two components is consistent with that expected for debris derived from the Themis asteroid family. This is the first evidence that a significant fraction of the dust in the zodiacal cloud derives from known asteroids. The discovery should lead to a major revision of our ideas on the origin and the evolution of the particles in the zodiacal cloud and, perhaps, of the origin of some of the extraterrestrial particles, that is, the "Brownlee particles", that are collected on Earth.

2. **The Shape of Mimas** (with P. Thomas)

Limb profiles from six of the best Voyager images of Mimas have been used to test the hypothesis that the shape of the satellite can be approximated by a triaxial ellipsoid[5]. Correction of image distortions and sub-pixel determinations of limbs allow coordinates on the limbs to be located with an accuracy of one picture element, 1 to 3 km. Ellipses fit to the limbs show that the shape of Mimas is well-represented by a triaxial ellipsoid. It is the smallest satellite in the solar system for which this is possible. We have determined that the radius of the satellite is 200.2 ± 0.9 km and that the difference between the long and the short axes is 16.7 ± 1.5 km, indicating that the satellite is close to hydrostatic equilibrium. This allows a determination of the moment of inertia of the satellite and a discussion of possible interior models. Using the Darwin-Radau relation and the satellite mass of Kozai, and

allowing for a non-linear interaction between the tidal and the rotational deforming potentials, we deduce that the moment of inertia of the satellite, $C = 0.346 \pm 0.024$. If the satellite is differentiated and has a small rocky core, then we deduce that the density of the mantle is 0.96 ± 0.09 g/cm^3. This is entirely consistent with a deep mantle of water-ice. This work represents the first determination of the internal structure of a satellite in the solar system other than the Moon.

3. **The Masses of the Uranian Satellites** (with P. D. Nicholson).

The dynamical theory presently used to obtain the masses of the Uranian satellites from their orbital precession rates contains a fundamental error[6,7]. The theory used by Veillet, and others, assumes that the orbital eccentricities and the pericenter precession rates are constant. However, if the satellite masses are sufficient to increase the pericenter precession rates over and above those rates due to the planetary oblateness, then the mutual secular perturbations also act to vary both the orbital eccentricities and inclinations and the pericenter and nodal precession rates on timescales of decades to centuries. The masses can be derived from the observed precession rates, but only after allowance has been made for the latter secular variations. Since this allowance has not been made, and cannot be made without a complete reappraisal of all the observational data, we consider that the satellite masses should, at present, be regarded as unknown[6,7]. This work highlights the importance of the upcoming Voyager Uranian observations. We have emphasized, in particular, the importance of Voyager obtaining an accurate set of osculating orbital elements at the time of encounter. These accurate observations, when coupled with the extensive set of ground-based observations of the satellite positions, should lead to a determination of the satellite masses.

4. **Resonance overlap in the Asteroid Belt** (with C. D. Murray and R. Malhotra).

There are now a number of circumstances in which chaotic motion has been shown to occur in the solar system. These include the rotation of Hyperion and the motion of asteroids in the 3:1 Jovian orbit-orbit resonance. At the same time that Wisdom published his outstanding paper on chaotic motion in the asteroid belt, we showed[8] that the weak higher-order resonances either side of the 2:1 Jovian resonance overlap for modest values of the orbital eccentricities ($e \sim 0.3$) and thus that large regions of phase space either side of the 2:1 resonance may be regions of chaotic motion. We now intend to prove this using methods similar to those used by Wisdom. R. Malhotra, a graduate student at Cornell has started work on this problem. We hope to show that in regions where resonances overlap, asteroids can diffuse from one part of the asteroid belt to another on a comparatively short timescale.

5. **Dynamics of the Uranian Satellites** (with C. D. Murray).

Work has commenced on the orbital evolution of the Uranian

satellites. We have analyzed the evolution of the orbits due to tidal dissipation and have calculated the change in the orbital elements due to passage through low-order orbit-orbit resonances. We have succeeded in showing that appreciable eccentricites may have been excited by these passages and that tidal damping of these eccentricities may have heated the satellites, as we had previously predicted[9]. More work needs to be done to determine the effects of the heat imput. Our work on the shape of Mimas is also of importance in this respect. If Mimas is differentiated, as our work would appear to indicate, then it follows that even very small icy satellites in the outer solar system may have suffered appreciable heating events.

6. **Orbits of Coorbital Satellites** (with C. D. Murray).

Work on the effects of a wide variety of drag forces on the orbits of coorbital satellites has been completed. The main conclusion is that a certain class of drag forces enhance the stability of the orbits[10].

References

1. Dermott, S.F., 1984. Dynamics of the Uranian Rings. In "Uranus and Neptune" (ed. Bergstralh, J.T.), NASA Con. Pub. 2330, pp. 609-627.
2. Dermott, S.F., Nicholson, P.D., Burns, J.A., and Houck, J.R., 1985. An Analysis of IRAS' Solar System Dust Bands. IAU Colloquium No. 85, "Properties and Interaction of Interplanetary Dust" (ed. Giese, R.H.), (in press).
3. Dermott, S.F., Nicholson, P.D. and Wolven, B., 1985. Preliminary Analysis of the IRAS Solar System Dust Band Data. In "Asteroids, Comets and Meteors, II" (eds. C-I. Lagerkvist and H. Rickman), Uppsala (in press).
4. Wolven, B., Dermott, S.F. and Nicholson, P.D., 1985. Preliminary Analysis of the IRAS Solar System Dust Data. Bull. Am. Astron. Soc. 17, 704.
5. Thomas, P. and Dermott, S.F., 1985. The Shape of Mimas. Bull. Am. Astron. Soc. 17, 738.
6. Dermott, S.F. and Nicholson, P.D., 1985. The Masses of the Uranian Satellites. Nature (in press).
7. Dermott, S.F. and Nicholson, P.D., 1985. The Masses of Uranian Satellites. Bull. Am. Astron Soc. 17, 742.
8. Dermott, S.F., and Murray, C.D., 1983. Nature of the Kirkwood Gaps in the Asteroid Belt. Nature 301, 201-205.
9. Dermott, S.F., 1984. Origin and Evolution of the Uranian and Neptunian Satellites: Some Dynamical Considerations. In "Uranus and Neptune" (ed. Bergstralh, J.T.), pp. 377-404.
10. Dermott, S.F., 1984. Dynamics of Narrow Rings. In "Planetary Rings" (eds. R. Greenberg and A. Brahic), University of Arizona Press, pp. 589-637.

The Shape and Topography of Io

R. W. Gaskell, J. E. Riedel, S. P. Synnott
Jet Propulsion Laboratory
California Institute of Technology

The program in which we are currently engaged began as an attempt to determine the shape of Io by using limb fitting techniques originally developed for spacecraft navigation. The postfit residuals from this fit were large in some viewing situations and small in others. This suggested that the shape of Io was more complex than a simple triaxial ellipsoid, with large scale topography deviating from the geoid by perhaps 10 km.

In order to investigate this question of topography in more detail, we have developed new techniques to determine landmark positions in Voyager images to sub-pixel accuracy. Armed with the line-pixel locations of these landmarks in a number of pictures, we can solve for the camera pointing, the shape of the geoid and the latitudes, longitudes and heights of the landmarks.

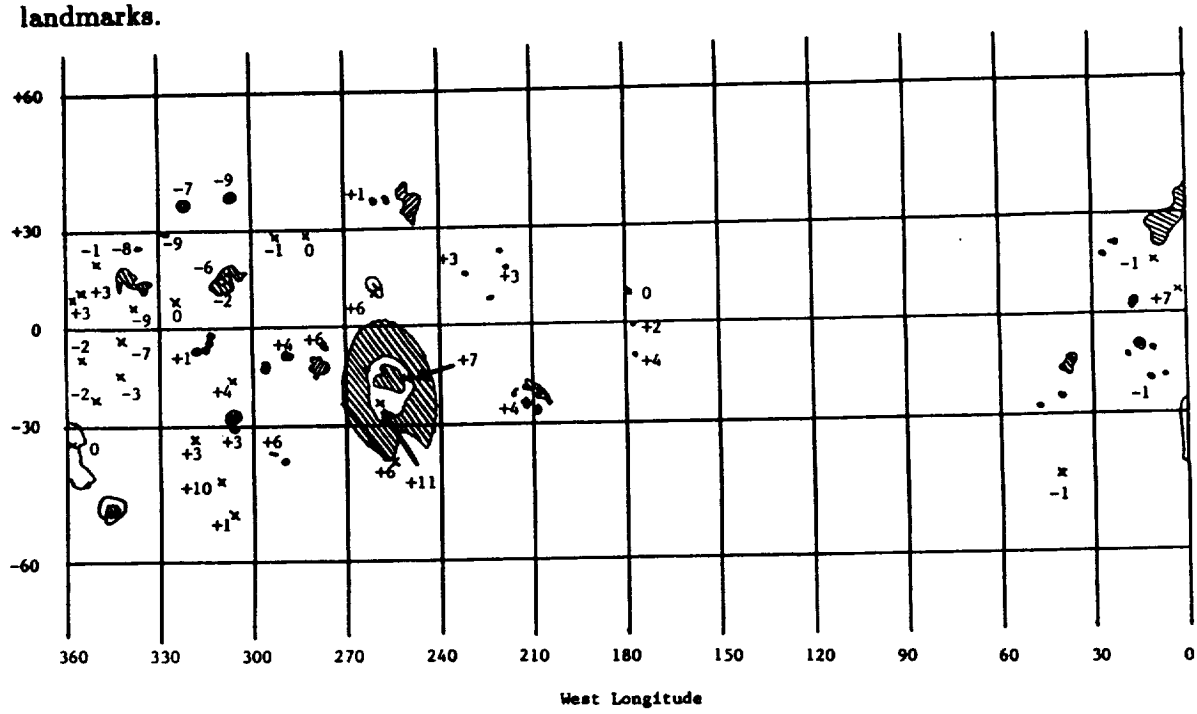

Figure 1. Sketch of portion of Io's surface covered by this study. Some landmarks are indicated with deviations from the geoid given in kilometers.

It is important to define precisely what we mean by a landmark. Instead of using the outline of a feature to define the landmark, we use the brightness data on the interior as well. Thus, for our purposes, a landmark is a circular patch of the surface whose variations in albedo or topography are sufficiently distinct to make identification possible in a variety of viewing situations. At the same time, the variations should be simple enough to allow for modeling with a relatively small number of parameters. This enables us to fit both the model parameters and

the offsets of the landmark positions from their nominal values simultaneously over a number of pictures.

We have recently obtained some preliminary results for landmark heights on Io which suggest some rather spectacular topography. Some of the 90 landmarks used so far and the heights we have found for them are summarized in Figure 1. In particular, it can be seen that the area of Pele is higher than the geoid by about 8 km while Loki is depressed. Curving around Loki, there is a chain of landmarks about 2000 km long and about 8 km below the geoid. One could speculate that this represents a large rift zone or trench. Alternatively, the region bounded by Loki, Amaterasu, Manua, Fuchi, Nyambe and Ra Pateras may be a basin about 10 km lower than the more rugged terrain to the south. We should be able to clarify the topography of this region by increasing the landmark coverage. The geoid itself, obtained from limb fitting and confirmed by the landmark method, had semi axes of 1832.6, 1821.9 and 1819.3 km. The errors in all results are 1 or 2 km.

As mentioned above, these results are preliminary. We have applied our landmark techniques to only nine images and about one third of Io's surface. We are currently completing this work. We are also planning to apply these methods to other satellites for which sufficient Voyager coverage is available. Two promising candidates are Mimas and Enceladus.

EXTENSIONAL TECTONIC FEATURES AS INDICATORS OF LITHOSPHERIC STRENGTH AND EARLY THERMAL PROFILES ON GANYMEDE

M.P. Golombek and W.B. Banerdt, Jet Propulsion Laboratory, California Institute of Technology, Pasadena, CA 91109

Brittle sliding and ductile flow laws allow the quantitative determination of lithospheric strength envelopes, or brittle and ductile yield stress versus depth. Because extensional tectonic features can be used to infer brittle lithosphere thickness, these relations can be used to quantitatively estimate early thermal profiles on Ganymede, thereby constraining its early thermal evolution.

Ganymede is the largest of the four Galilean satellites. Its low density indicates it is roughly half silicates and half water. About half of its surface is covered by low-albedo heavily cratered terrain and the other half by high albedo, less cratered grooved terrain (1). Grooved terrain consists of numerous parallel sets of narrow linear to curvilinear troughs or depressions that separate various sized polygons of cratered terrain. Most photogeologic evidence suggests that the grooves formed by some extensional tectonic and resurfacing process involving shallow flooding of wide grabens with high-albedo water ice and subsequent refracturing of the ice to form grooves (1,2,3,4).

The largest remnant of cratered terrain on Ganymede is Galileo Regio, upon which a well preserved system of arcuate troughs or grabens called rimmed furrows can be found. Initially, these furrows, which mark the first tectonic event preserved on Ganymede, were interpreted as ring structures resulting from a large impact (5). Subsequent analysis, however has substantially weakened this suggestion because they apparently do not describe small circles (6), and a furrow system on the adjacent Marius Regio does not form a continuation of the same arc (7), implying that furrows result from an endogenic process.

A number of attempts have been made to estimate the thickness of the lithosphere from the width or spacing of the grooves and furrows. To first order, the early high heat flow inferred from crater relaxation studies (8) implies a thin lithosphere. The simplest model for determining lithosphere thickness from furrows and grooves assumes that both structures are simple grabens with flat floors and two exactly equal bounding faults that converge downward (5,9). These simple grabens probably form when conjugate normal faults initiate together at the base of a brittle layer and propagate up yielding grabens with similar widths, similar displacements, and similar distances between members of a set. Assuming the bounding faults have the most probable 60° dips suggests a lithospheric thickness of about 10 km for the furrows on Galileo Regio (5,9) and about 4 km average for the grooves. Models that assume the formation of an extensional instability between a brittle plastic surface layer and a ductile substrate derive lithosphere thickness from the spacing between extensional structures(10). These models yield 10 and 2 km brittle layers, respectively, for the 50 km spaced furrows and the 8 km spaced grooves (11). Given the various uncertainties (and the narrower furrows on Marius Regio), the brittle lithosphere thickness was probably 5-10 km at the time of furrow formation and 2-5 km at the time of groove formation. With these geologic constraints on the thickness of the brittle surface layer in mind we now explore possible

lithospheric strength envelopes to quantitatively evaluate temperature profiles for these periods of deformation in Ganymede's history.

To calculate the lithospheric strength on Ganymede we use a combination of Byerlee's law at low temperatures for the brittle yield stress and the ductile flow law for ice I_h at higher temperatures. At low pressures we use the sliding friction as determined by Byerlee, which has been found to hold for a wide variety of geologic materials. At higher confining pressures we have used the friction data for ice (12). We have used the flow law of Durham et al. (13) with modifications (Durham, written communication) for pure ice I_h extrapolated to geologic strain rates of 10^{-15}/sec (~3%/m.y.). It has been shown at high temperatures that the inclusion of small amounts of silicates into ice will greatly increase its creep strength (14). However, quantitatively determining the amount of hardening for our application is not possible because the creep processes that control the deformation of ice are not well known for the temperatures and strain rates of interest on Ganymede. For lack of a better constraint we will assume that the hardening resulting from the addition of less than a few percent of silicates in Ganymede's lithosphere can be bracketed by an order of magnitude increase in creep strength.

Predicting the type of failure from the lithospheric strength envelopes is straightforward. With increasing stress, elastic strain will be built up in the elastic part of the lithosphere until its strength is exceeded (roughly the yield stress at the brittle-ductile transition). At that time major throughgoing faults will initiate near the the brittle-ductile transition depth (e.g, 15). In addition, the extensional instability model directly infers the thickness of the brittle (plastic) lithosphere. Tnus the brittle lithosphere defined by the simple graben and extensional instability models is dependent on the depth to the brittle-ductile transition. This depth is most sensitive to the temperature gradient. As a result we can quantitatively determine the thermal gradient at the times of furrow and groove formation on Ganymede.

The 10 km thick brittle lithosphere on Galileo Regio at the time of furrow formation indicates a thermal gradient of 1.5°/km for clean ice and a little above 2°/km for dirty ice. On Marius Regio the 5 km thick brittle-ductile transition requires respective thermal gradients of 4 and 6°/km. An average 4 km brittle lithosphere at the time of groove formation yields thermal gradients of 6.5 and 8.5°/km for clean and dirty ice. Variations in groove widths and spacings that imply brittle lithospheres of 2-5 km suggest local thermal gradients of 4-15°/km and 6-20°/km for clean and dirty ice, respectively.

Variations in thermal gradient, through its effect on the depth to the brittle-ductile transition, also significantly affects the total strength of the lithosphere (defined as the integral of the yield stress versus depth curve (16)). For example, the lithospheric strength under extension for a brittle lithosphere of 10 km (corresponding to a gradient of 1.5°/km) applicable to Galileo Regio is about 126 in units of 10^3 MPa-m. Marius Regio had a lower strength of 29. Lithospheric strengths at the time of groove formation varied locally from 4 to 29 with an average of about 18. For comparison, lithospheric strength of the continental and oceanic lithosphere under extension on the earth are of order 10^7MPa-m. Note that these strength estimates are insensitive to the assumed strengthening of ice due

to the inclusion of silicates because they are determined almost solely from the inferred thickness of the brittle lithosphere.

Brittle extensional tectonic features on Ganymede indicate a significant lateral and temporal variability in thermal gradient and lithospheric strength. Galileo Regio's long life as a relatively undisturbed remnant of cratered terrain is likely a result of its low temperature gradient and thus increased lithospheric strength. By comparison Marius Regio was fractured and fragmented to its current small size due to its weakness (lithospheric strength 4 times lower than for Galileo Regio at the time of furrow formation) imposed by its higher thermal gradient. The thermal gradient during groove formation could have varied from place to place by as much as a factor of 4 and was up to 5-10 times greater than earlier gradients during furrow formation. This increase in thermal profile is at least partly a result of local heating due to the water ice volcanism that accompanied groove formation and may not indicate a whole-satellite heating event. Nevertheless, the variations in temperature gradient shown by the variations in furrow and groove widths and spacings do indicate that the cooling of Ganymede was highly inhomogeneous with significant lateral thermal anomalies.

In conclusion, brittle lithospheric thicknesses estimated from tectonic features formed during the two periods of extensional tectonism during Ganymede's history allow the quantitative determination of thermal gradients because the depth to the brittle-ductile transition is a function of the thermal gradient. Lithospheric thicknesses of 10 and 5 km inferred from furrow widths and spacings indicate temperature gradients of 1.5-2°/km and 4-6°/km, respectively. An average lithosphere thickness of 4 km for the grooves suggests thermal gradients of 6.5-8.5°/km; local variations in the thickness of 2-5 km implies wide variations in temperature profile, 4-20°/km. This increase in thermal gradient may be a result of local heating during water-ice volcanism accompanying groove formation and may not indicate whole satellite heating. The stability of large remnants of cratered terrain (e.g., Galileo Regio) can be understood in terms of a lower temperature gradient which resulted in an increased lithospheric strength.

References (1) Smith, B.A., and Voyager Imaging Team (1979) Science, 204, 951-972. (2) Golombek, M.P., and Allison, M.L. (1981) Lett., 8, 1129-1142. (3) Lucchitta, B.K. (1980) Icarus, 44, 481-501. (4) Parmentier, E.M., Squyres, S.W., Head, J.W., and Allison, M.L. (1982) Nature, 295, 290-293. (5) McKinnon, W.B., and Melosh, H.J. (1980) Icarus, 44, 454-471. (6) Thomas, P.G., and Masson, P. (1985) Rep. Plan. Geol. Prog., NASA TM 87563, 528-530. (7) Zuber, M.T., and Parmentier, E.M. (1984) Icarus, 60, 200-210. (8) Passey, Q.R., and Shoemaker, E.M. (1982) Lun. Planet. Sci. XII, 277-278. (9) Golombek, M.P. (1982) Proc. 13th Lun. Plan. Sci. Conf., J.G.R., 87, A77-A83. (10) Fink, J.H., and Fletcher, R.C. (1981) Lun. Plan. Sci. XII, 277-278. (11) Grimm, R.E., and Squyres, S.W. (1985) J.G.R., 90, 2013-2021. (12) Beeman, M.L., Durham, W.B., and Kirby, S.H. (1984) EOS Trans. AGU, 65, 1077. (13) Durham, W.B., Heard, H.C., and Kirby, S.H. (1983) Proc. 14th Lunar Planet. Sci, Conf., J. Geophys. Res., 88, B377-B392. (14) Baker, R.W., and Gerberich, W.S. (1979) J. Glaciol., 24, 179-194. (15) Jackson, J., and McKenzie, D. (1983) J. Struct. Geology, 5, 471-482. (16) Vink, G.E., Morgan, W.J., and Zhao, W.-L. (1984) J.G.R., 89, 10072-10076.

GEOLOGIC IMPLICATIONS OF SPECTROPHOTOMETRIC MEASUREMENTS ON EUROPA

Matthew P. Golombek and Bonnie Buratti, Jet Propulsion Laboratory, California Institute of Technology, Pasadena, CA 91109

Detailed photometric measurements are particularly useful for helping to interpret surface features on poorly-imaged planets like Europa because the definition of most surface units is based on color and albedo. Lucchitta and Soderblom (1) used Voyager 2 multispectral images to make a limited number of measurements (3 to 9 per spectrum) of the spectral reflectance of 6 color units on Europa. In this abstract we apply an extensive data set of roughly 500 detailed photometric measurements from Voyager 2 images to the geologic interpretation of 6 mapped geologic units and 3 types of lineations on Europa.

Eight high resolution (~4.5 km/pixel) Voyager images were used to measure camera calibrated I/F in the ultraviolet, violet, blue, and orange filters. Each measurement consists of the average I/F values within a 3x3 pixel box (unless the tectonic lineation was too narrow). Minnaert's photometric function was fitted by a non-linear least squares method to the measurements for each geologic terrain in each filter:

$$I = F B_o \mu_o^k \mu^{k-1}$$

where I is the specific intensity, πF is the incident solar flux, μ_o and μ are the cosines of the incidence and emission angles, k is the limb darkening parameter, and B_o is proportional to the albedo of the surface. For a phase angle of zero degrees and μ_o and μ equal to unity, B_o equals the normal reflectance.

The terrain-averaged measurements fall into two distinct groups: dark, red spectra and light, bluer spectra. The former group, which includes the brown spots, wedge-shaped bands and gray bands, show a shallow increase in reflectance from the ultraviolet to the violet, followed by a uniformly steep increase to the orange wavelength. The light group of spectra which consists of data from mottled gray and brown terrains, bright, dark, and fractured plains, and triple bands all show a steeper increase in the ultraviolet to violet with progressively smaller increases from violet to blue and blue to orange (a convex upward curve). This light group has 3 units (mottled brown terrain, fractured plains, and triple bands) that are slightly darker at all wavelengths.

These observations are consistent with the hypothesis (1) that the plains units (lightest) are fractured and the fractures locally infilled with dark material similar to that constituting the brown spots and wedge-shaped bands. This process of disruption results in slightly darker light terrains (e.g. mottled brown terrain and fractured plains). Triple bands appear lighter than brown spots and wedge-shaped bands due to their central bright stripe.

Histograms of the albedo (Minnaert's B_o) in the orange and violet filters show the variation in albedo for these geologic units and lineations. The lowest albedo features are the brown spots. The albedo range of the wedge shaped bands extends from a region which overlaps with the brown spots into a region which overlaps the generally brighter triple

bands. The mottled gray and brown terrains and fractured plains overlap the albedo range of the triple bands. The dark plains and the fractured plains are the darkest of the plains units.

The overlap in the albedos of the brown spots, wedge-shaped bands, and triple bands is consistent with the latter two features being fractures in-filled with dark silicate-rich ice equivalent in albedo to the dark spots. The albedo distribution of the plains and terrains is similarly consistent with progressive darkening by the addition of fractures filled with this lower-albedo material.

Twelve detailed albedo scans were made across wedge-shaped bands and triple bands. All seven scans across the triple bands show the general decrease in albedo associated with the dark flanking stripes; five of these show a distinct increase in albedo at the central pixel that corresponds with the central bright stripe. This increase is almost to the level of the surrounding plains, which implies they are composed of similar materials. The slightly lower albedo recorded by the middle pixel is due probably only to part of the pixel falling on the adjacent dark band. All five scans across the wedge-shaped bands show the expected darkening within them. Two of these profiles also show an increase in albedo at the center of the structure, similar to that recorded for the triple bands. For approximately half of the triple bands, the orange to violet ratio increases across the dark flanking stripes, then at the central stripe decreases to a value equivalent to that of the surrounding plains material. The other half, however, show only an increase in the ratio within the band. The orange/violet albedo ratio scans across the wedge-shaped bands generally show an increase. In addition, two or three of these show a decrease in the ratio within the center of the structure, similar to some of the triple bands. These profiles indicate that many wedge-shaped bands may, in fact, be triple bands whose bright central stripes are below the resolution of the Voyager images.

The similarity in albedo scans across wedge-shaped and triple bands indicates that both are similar types of structures, perhaps flooded grabens and flooded grabens with uplifted horsts as suggested by Golombek and Bruckenthal (2). The similarity in albedo between the central bright stripe of the triple bands and the surrounding plains implies that the center of the triple band is structurally dislocated plains material, consistent with them being uplifed horsts (2), or high albedo clean ice, consistent with them being subsequent clean ice extrusions (3).

References:

(1) Lucchitta, B. K., and L. A. Soderblom (1982) in Satellites of Jupiter, D. Morrison, ed., U. Ariz. Press, p. 521-555. (2) Golombek, M., and Bruckenthal, E. (1983) Lunar Planet. Sci. XIV, 251-252. (3) Finnerty, A. A., G. A. Ransford, D. C. Pieri, and K. D. Collerson (1980) Nature, 289, 24-27.

Observational Evidence for Red Polar Caps on Io

Graham, Francis and Hapke, Bruce (Dept. of Geology and Planetary Science, University of Pittsburgh, Pittsburgh, PA 15260)

It has long been known that Io has dark polar caps (Murray, 1975), but their color seems to be in dispute. Minton (1973) reported them to be similar in color to the belts of Jupiter when Io was seen in transit across the planet. The so-called "natural color", Voyager-based image (Young, 1985 and McEwan, 1985) shows the poles as a darker shade of the same pale yellow color as the rest of the satellite. However, Voyager did not obtain images at wavelengths longer than about 600 nm and thus would not be able to detect red poles.

Observations made on June 27, 1985 at Allegheny Observatory showed that the poles are indeed red. The differences in brightness when a long, narrow slit was placed across the image of the planet parallel and perpendicular to the equator were measured photoelectrically at red and green wavelengths. In green, the equator was brighter than the poles, but in red the poles were brighter than the equator. Red poles on Io are inconsistent with a pure sulfur-sulfur dioxide surface composition, but are natural consequence of the disulfure monoxide-polysulfure oxide model proposed by Hapke and Graham (1984).

DYNAMICAL EVOLUTION OF THE GALILEAN SATELLITES: ORBITAL EVOLUTION PATHS

Richard Greenberg
Planetary Science Institute, Tucson, Arizona

The Laplace resonance among three Galilean satellites of Jupiter is responsible for maintaining the forced orbital eccentricities of these satellites. As a consequence of this effect, Io and, to a lesser extent, Europa are warmed by tidal energy dissipation (Peale et al. 1979). A key question about the orbital and geophysical histories of the satellites is how the resonance has evolved with time. If the effects on orbit evolution due to dissipation in Io are balanced by tidal dissipation in Jupiter, the resonance might be in equilibrium (Yoder, 1979). However, most estimates of the dissipation rate in Jupiter are two orders of magnitude smaller than the rate needed to balance Io's very high measured heat loss rate (Greenberg, 1982).

If Io's energy loss is not balanced in that way, then the satellite must be losing orbital energy and the system is being driven out of resonance. An important objection to that scenario has been the discovery that the present resonant configuration is unstable in deep resonance (Yoder and Peale, 1981). Thus, going backwards in time, the system would reach an unstable state in only $\sim 10^7$ years. However, it now appears that there is a continuous set of stable orbital configurations, albeit qualitatively different from the present configuration, that form possible evolutionary paths through deep resonance. These paths connect continuously to the present orbital configuration.

In the present state of the resonance, taken by pairs Io (#1)/Europa (#2) and Europa (#2)/Ganymede (#3), the satellites' orbital periods are in ratios near 1/2. Equivalently, the mean motion combinations n_1-2n_2 and n_2-2n_3 are very small and in fact both combinations equal the same small value $\upsilon \approx 0.^{\circ}8$/day, which is much smaller than any of the mean motions ($n_2 \simeq 100^{\circ}$/day, for example). Kinematically, these relations mean that the longitudes of conjunction of the two satellite pairs migrate at the same slow rate υ. Thus the angle between conjunction longitudes ($\phi \equiv \lambda_1-3\lambda_2+2\lambda_3$ where λ is orbital mean longitude) is fixed. The dynamical effect of the commensurability is to maintain ϕ at a constant stable value of 180°, as well as to force the significant eccentricities. Smaller values of υ would mean the system were deeper in resonance with generally larger forced eccentricities. Large positive or negative values of υ would mean the system were out of resonance.

Yoder and Peale (1981) showed that the system is unstable at $\phi = 180^{\circ}$ for $\upsilon \lesssim 0.^{\circ}2$/day, although it is stable at $\phi = 0^{\circ}$ for $\upsilon \lesssim -0.^{\circ}7$/day (the other side of the resonance). A hint that there might be more to the story came from numerical integrations by Wiesel (1981) that showed a system initially in deep resonance (υ near 0) at the unstable $\phi = 180^{\circ}$ state which then evolved into oscillations about $\phi \approx 90^{\circ}$. A formulation of the orbital variation equations that reduces the variations to a set of nine first-order differential equations now shows that there is a stable suite of

configurations at varying values of ϕ. Originally expanded only to lowest order in eccentricity (Greenberg 1981), this approach broke down in deep resonance where eccentricities are large; it did not even show the instability at $\phi = 180^{\circ}$.

Extended to second order in e however, the theory has shown analytically the presence of at least a stable state at $\phi = 90^{\circ}$, and by numerical integration, a path in orbital element space of stable configurations. For any given value of υ, a particular value of ϕ (actually 2 values of ϕ symmetrical about 180°) and of e's, etc., describe a stable state (Greenberg 1984). Now the theory has been extended to third order in orbital eccentricities. Also included are direct Io-Ganymede effects and variation of mean longitude at epoch. This extensive new work qualitatively confirms the stable paths and shows that they reach $\phi = 180^{\circ}$ precisely where Yoder and Peale found the stability limit for that value of ϕ. Although it was not obvious a priori, values of forced eccentricities are large for small υ on these stable paths: At $\phi = 90^{\circ}$, $\upsilon \simeq 0.^{\circ}1$/day and $e_2 \simeq$ 0.1, so for smaller values of υ, even the third-order theory (in e) must break down.

Therefore, the existence of stable paths through $\upsilon = 0$ remains uncertain. Any evolutionary theory that claims evolution from negative υ to the present state must also contend with the problem of the short time scale ($\sim 10^7$ yr.) for evolution from small υ to the present value. Alternatively, an oscillatory history involving a flip-flop of Io's geophysical state coupled with evolution into and out of deep resonance (Greenberg 1982, Ojakangas & Stevenson 1984), appears viable now that stable evolutionary paths seem to exist in deep resonance.

This research is supported by the NASA Planetary Geology and Geophysics Program, contract NASW-3524.

References

Yoder, C.F. (1979). Nature 279, 767-769.

Peale, S.J., Cassen, P. and Reynolds, R.T. (1979). Science 203, 892.

Greenberg, R. (1982). In Satellites of Jupiter (D. Morrison, ed.), University of Arizona Press.

Ojakangas, G.W. and Stevenson, D.J. (1984). Bull. A.A.S. 16, 661.

Greenberg, R. (1984). Bull. A.A.S. 16, 687.

Greenberg, R. (1981). Icarus 46, 415-423.

Yoder, C.F. and Peale, S.J. (1981). Icarus 47, 1-35.

Wiesel, W.E. (1981). A.J. 86, 611-618.

DUST-MAGNETOSPHERE INTERACTIONS

E. Grün, Max-Planck-Institut für Kernphysik,
Gregor E. Morfill, Max-Planck-Institut für Extraterrestrische Physik,
and D. A. Mendis, University of California, San Diego

Micron-sized dust grains were identified by the light scattering characteristics in most rings of the outer planets. A multitude of interactions between the magnetospheric particles, fields and dust grains has been proposed. We review the major effects and indicate the pertinent observations. Energetic particle absorption signatures observed by Pioneer 11 and Voyager 1 and 2 trace the mass concentrations of particulates in the magnetospheres of Jupiter and Saturn. Particulates immersed in the magnetospheric plasma and exposed to solar ultraviolet radiation will charge up to a surface potential which depends on the density and electron energy E_e of the plasma as well as on the concentration n_d of the dust particles. An isolated dust grain ($n_d < \lambda_D^{-3}$; λ_D = Debye length, typically 10^2-10^4cm) becomes negatively charged if the plasma electron flux exceeds the photoelectron flux ($\sim 2.5 \times 10^{10} r^{-2} cm^{-2} s^{-1}$, at distance r in AU from the Sun) from its surface. Its surface potential will reach $V_o \sim E_e/e$ (e = electronic charge). At high dust concentrations ($n_d > \lambda_D^{-3}$) the charge on the dust grains will be significantly reduced. Kinetic effects of charged dust particles arise from the interaction with the planetary magnetic field. Radial drift of dust particles is induced by systematic and stochastic charge variation and by the plasma drag. Sputtering and mutual collisions affect the sizes of grains. Electromagnetic effects are discussed that lead to the halo of Jupiter's ring, the dust distribution in Saturn's E Ring and to levitated dust in the B Ring (spokes) as well as on the Moon.

The Ices of Io: Sulfur Dioxide, Disulfur Monoxide and Polysulfur Oxide

Hapke, Bruce (Dept. of Geology and Planetary Science, University of Pittsburgh, Pittsburgh, PA 15260)

Disulfur monoxide (DSM) and polysulfur oxide (PSO) frosts can be formed from sulfur dioxide (SDO) in a large number of ways on Io. The spectral properties of these frosts have been measured and are found to depend on the maximum temperature reached. These frosts are strong absorbers in the UV and blue. When deposited below about 115K DSM frost is dark red. Over the range from about 115K to 210K DSM polymerizes to different forms of PSO colored red, brown, orange, greenish-yellow and yellow. Above 210K PSO is light yellow and is stable to above 300K.

A mixture of SDO, DSM and PSO frosts on Io accounts for the reflectance spectrum, dark reddish poles and leading-trailing side asymmetries. Hot spots may be dark because the high temperature has driven off the SDO frost, leaving PSO and exposing silicate rocks. There is no evidence for major amounts of elemental S on the surface of Io.

On the Sputter Alteration of Regoliths of Outer Solar System Bodies

Hapke, Bruce (Dept. of Geology and Planetary Science, University of Pittsburgh, Pittsburgh, PA 15260)

This paper discusses several processes that are expected to occur when the porous regoliths on bodies without atmospheres in the outer solar system are subjected to energetic ion bombardment. It is shown theoretically and experimentally that porosity reduces the effective sputtering yield of a soil by an order of magnitude. The other 90% of the sputtered atoms are trapped within the regolith, where they are fractionated by differential desorption, with the more volatile species having higher desorption probabilities. This process is the most important means by which alteration of chemical and optical properties occurs when a regolith is sputtered.

Experiments have shown that when a basic silicate powder is irradiated sputter-deposited films are formed which are enriched in metallic iron, while O, Na and K are preferrentially lost. This process has implications for the Io torus and the Na atmosphere of Mercury (Potter and Morgan, 1985). It is predicted that icy regoliths of sulfur dioxide will be enriched in disulfur monoxide and polysulfur oxide. Bands of these compounds are present in IR spectra of H-sputtered sulfur dioxide reported by Moore (1984). When porous mixtures of water, ammonia and methane frosts are sputtered the loss of H and reactions of C, N and O in the deposits should produce complex hydrocarbons and carbohydrates. Such reactions on the surfaces of small bodies in the early solar nebula surfaces of small bodies in the early solar nebula may have been important in the formation of the matrix material of carbonaceous chondrites.

THE DYNAMICAL EVOLUTION OF SATURN'S E-RING

J. R. Hill and D. A. Mendis, University of California, San Diego

The dynamical evolution of fine dust particles ejected from Enceladus and subsequently electrically charged within the Saturnian magnetosphere is studied. It is shown that the gyro-phase drift, which is radially outwards due to the strong radial temperature and density gradients in the magnetospheric plasma, is, by far, the fastest transport mechanism of these grains. Maintenance of the E-ring in a steady state throughout the age of the solar system would need a mass loss from Enceladus of about 2 parts in 1000.

Charged Particle Induced Charges in Icy Objects in the Outer Solar System

R. E. Johnson Dept. of Nuclear Engineering & Engineering Physics, University of Virginia, Charlottsville, Virginia 22901

An understanding of the effect of charged-particle irradiations of materials is becoming increasingly important for describing the reflectance spectra and surface composition of small bodies in the outer solar system. New developments have been achieved in two important areas. First we have furthered the study of the dramatic changes produced in the reflectance properties of low temperature surfaces having carbon or sulfur containing condensed gases.[1] Whereas we quantitatively evaluated the production of blackened residues when protons or helium ions bombarded condensed CH_4[2] we now have studied such dramatic transformations in the bombardment of CO[3] and CS_2.[4] These are thought to be constituents of cometary ices and CO or CO_2 may be important for other outer solar system bodies. In table 1 we give as an example the relative ejection rates of various molecular and atomic species ejected from CO by keV ions. We note the deficit in C atoms vs O atoms ejected in one form or another. Even though the deficit is small it leads to the formation of the carbon-based residue. Therefore for a dose of ion or electron irradiations $\gtrsim 10^{16}$ particles/cm^2 a strongly sputter resistant, non-volatile surface layer is produced from an initially bright, volatile surface. Therefore surface reflectance spectra may be *misleading* when determining the geology of the objectionless care is taken to understand the irradiation induced changes.

We have used these ideas to propose that the rings of Uranus may be darkened by plasma bombardment and dark materials may be produced on other bodies. We have also used this information to propose that the cometary ejecta collected at earth orbit have been significantly altered from the 'original' state by plasma bombardment. That these particles have received significant doses of ions is evident from the observation of ion tracks by Brownlee and co-workers.[5] We also propose that the ions may be important for producing adhesion in the fairy-castle-like particles collected[6] and for producing the appearance that high temperature processes had occurred by the

production of, for instance, carbides.[7]

Table 1

Relative abundances of dominant species ejected from a low temperature CO sample by keV ions.

Species	Abundance
CO	100
CO_2	4.9
O_2	.4
O	8.3
C_2	.2
$(CO)_2$	.7
Ratio of C/O ejected (~9/10)	

The second area of progress is the measurement of the sputtering yields of sulfur deposits. Linker et al.[8] suggested sputtering of sulfur on the surface of Io could account for a number of important properties of the surface and the plasma environment. These conclusions were based on unrealistic data on sulfur sputtering. We have shown that the sputter yield associated with co-rotating ion bombardment of Io is ~100 sulfur atoms either S or S_2 for temperature <200K. At 200K the yields rise dramatically, but as hot regions comprise a small fraction of the surface (see D. Nash this volume) the yields are, on the average, less than those for SO_2. However, we also showed that the predominant ejected species was S. This was an interesting surprise as the likelihood of ejecting S atoms directly into the plasma region is greater than that for ejecting either SO_2 or S_2. Earlier we evaluate SO_2 as a source of the plasma,[9] we now have obtained energy spectra for S ejection and, therefore, will accurately determine the role of sulfur sputtering in producing the plasma.

(1) R. E. Johnson, L. J. Lanzerotti, W. L. Brown, Adv. Space Res. *4* 41 (1985).

(2) L. J. Lanzerotti, W. L. Brown, R. E. Johnson, "Ices in the Solar System" ed. J. Klinger et al. (D. Reidel Netherlands) (1985).

(3) D. Chrisey, J. W. Boring, R. E. Johnson, W. L. Brown. Nuclear Inst. & Meth. in press (1985).

(4) J. W. Boring, N. Zhao, D. Chrisey, R. E. Johnson "Comets & Meteorites II" ed. C. Lagerkvist and H. Rickman, in press (1985).

(5) J. P. Bradley, D. E. Brownlee, P. Fraundorf. Science *226* 1432 (1984).

(6) R. E. Johnson "Ices in the Solar System" ed. J. Klinger (D. Reidel, Amsterdam) (1985).

(7) J. P. Bradley, D. E. Brownlee, P. Fraundorf, Science *223* 56 (1984).

(8) J. A. Linker, M. G. Kivelson, M. A. Moreno, R. J. Walker. Nature *315* 373 (1985).

(9) E. M. Seiveka, R. E. Johnson, J.G.R. *90* 5327 (1985). R. E. Johnson et al., J.G.R. *89* B711 (1984).

A Shepherding Model for Neptune's Arc Ring

J. Lissauer, University of California at Santa Barbara

ABSTRACT

A model to explain the confinement of Neptune's incomplete arc ring is developed. The ring may be aximuthally confined near a triangular (Trojan) point of an as yet undiscovered satellite of Neptune. Radial diffusion of the ring particles can be prevented by shepherding torques of another moon. Two satellites with diameters of 100-200 km would be sufficient to confine the ring; such moons would be too small to have been photographed from Earth.

ASPECTS OF ICY (AND NON-ICY) SATELLITE STRUCTURE, EVOLUTION, AND BOMBARDMENT HISTORY

W.B. McKinnon, Dept. Earth and Planetary Sciences and McDonnell Center for the Space Sciences, Washington Univ., Saint Louis, MO 63130.

Interplanetary Correlation of Geologic Time

This long-standing and important subject has been recently reviewed (1). Further progress includes an improved geometric model relating initial transient craters to final simple and complex craters. Support for this model comes from a study of ejecta blanket scaling on the moon and Mercury (2), in which it was argued that ejecta blankets on these planets are geometrically similar to the transient crater (which they should be in the gravity regime [3]), and may be geometrically similar to each other. In the model, the final crater diameter is related to the transient diameter raised to the ~1.13 power. The exponent is small enough that complex craters of different sizes (and on different planets and satellites) are more nearly related by "gravity scaling" than the collapse scaling of (1). Comparisons of crater and projectile populations are simplified. An important consequence is that the differential expansion of complex craters on Ganymede and Callisto relative to that of various icy Saturnian satellites is not so important as to reverse the results of simple crater scaling, i.e., craters made by physically similar projectiles on the Saturnian satellites are larger than those made on Ganymede and Callisto.

Armed with this deduction, and based on crater size-frequency and spatial distribution statistics, scaling considerations, and celestial dynamics, C.R. Chapman and I (4) argue the following: (1) The heliocentric projectile population that created the heavily cratered terrains on Ganymede and Callisto ("ancient Jovian") was different (lacking in "large," $\gtrsim$10-km-diameter members) from that responsible for the Late Heavy Bombardment of the terrestrial planets; (2) The timing of the "ancient Jovian" bombardment was either contemporaneous with or earlier than the Late Heavy Bombardment; (3) The heliocentric population that created the ancient Population I craters on the Saturnian satellites ("ancient Saturnian") is poorly characterized at sizes $\gtrsim$10-km-diameter, but may not be statistically distinguishable from the "ancient Jovian" population, especially if a moderate amount of viscous relaxation on Ganymede and Callisto is allowed; (4) Population II craters on the Saturnian satellites are due to Saturnicentric projectiles derived from the debris of very large Population I cratering or catastrophic disruption events; (5) Lower heliocentric projectile velocities at Uranus will result in comparatively smaller craters on the icy Uranian satellites. This should permit a better characterization of large projectiles there provided the external bombardment is not masked by a Uranian "population II;" (6) The lower heliocentric projectile flux at Uranus creates the potential for seeing further back in geologic time on the satellites. Evolution of the heliocentric projectile population may be observable, e.g., the transition from dominance of Uranus-Neptune zone planetesimals to that of newly returning comets.

Very Large Impacts on Intermediate-Sized Icy Satellites

Mimas, Tethys, Dione, Rhea, and Iapetus all possess large craters; the diameter of the largest of each is a substantial fraction of the satellite diameter (~1/3, 2/5, 1/4, 1/4, and 1/4, respectively). For Mimas and Tethys the relative scale implies substantial global seismic effects and ejecta deposition. On Mimas, long, linear, sub-parallel troughs or grooves are interpreted to be manifestations of fractures activated by the formation of Herschel. Limited photoclinometry and morphology support an analogy to Phobos grooves. If the implied deep-seated fracture planes predate the Herschel impact, then Mimas was a brittle conductively-cooling object at that time. Herschel's depth of ~10 km is consistent with that expected for a 130-km-diameter crater on Mimas, based on simple-to-complex crater statistics. On Tethys, the trough system Ithaca Chasma extends at least 270° around the satellite, and is confined to a zone that lies roughly along a great circle concentric to the crater Odysseus. Odysseus appears to have rebounded significantly from the ~10-15 km depth expected for a fresh 390-km-diameter crater on Tethys. Ithaca Chasma is interpreted as a multiple graben formed some time after Odysseus, possibly in response to stresses induced by viscous flow associated with the restoration of Odysseus' floor to match Tethys' geoid (5). In contrast, an unnamed ~450-km-diameter crater on Rhea has an estimated depth of 10±5 km, consistent with an expected depth of ~6-10 km. Rhea may have had a stronger lithosphere or shallower post-impact temperature gradient than Tethys. No large-scale tectonic structures are observed around the unnamed crater, but a fracture pattern similar to that associated with the "wispy" terrain near Amata (~250 km diameter) on Dione could exist.

The Uranian satellites promise to extend these observations. A variety of fracture patterns may be evident, and the possible link between global chasmata and large, rebounded craters may be clarified. In addition, the large, possibly silicate-rich outer satellites may have been active enough ca. 4 GYA to have permitted the formation of multiringed basins.

Origin of the Moon---The Role of Solar Resonance

G.H. Darwin's original version of the fission hypothesis of the origin of the moon invoked not rotational instability, but a resonant excitation of the $_{-2}S_2$ tide by the sun, leading to unstable oscillation and lunar parturition. In fact, if the earth and moon are recombined so as to conserve angular momentum and if the earth were "fluid" (a reasonable accretional state), the resulting protoearth would spin at what would appear to be very nearly the resonant frequency for tidal fission. It is only an appearance of resonance, however, for although the tidal frequency as seen in an inertial frame is the same as the forcing frequency, solar resonance actually means the excitation of a nearly stationary tidal bulge (as seen in an inertial frame). Solar resonance is therefore the excitation and growth of a triaxial Dedekind ellipsoid. (Strictly speaking, a Dedekind ellipsoid is of uniform density and incompressible; all the ellipsoids discussed here are implicitly assumed to be the

equivalent configurations that exist for a moderately compressible fluid.) The point of bifurcation of the Dedekind sequence from the biaxial Maclaurin sequence is the same as the bifurcation of the triaxial Jacobi sequence. The amount of angular momentum required to reach solar resonance is thus significantly in excess of that in the earth-moon system today (by a factor of ~3). Instability on the Dedekind sequence is reached by the addition of still more angular momentum until unstable third-harmonic oscillations set in, presumably leading to mass shedding and formation of an equatorial ring or disk of material from which the moon can form. The angular momentum density at which "pear-shaped" oscillations begin is nearly the same as that for the Jacobi sequence; hence solar resonance does not in any way solve the "angular momentum problem," contrary to original hopes (6,7).

This version of the fission hypothesis was more-or-less abandoned when Jeffreys showed that viscous dissipation was likely to prevent the resonant tidal bulge from growing too large. Tidally induced fission is nearly impossible, however, even if the viscosity of the fluid protoearth approaches the inviscid limit. The resonant Q necessary for fission exceeds $\sim 10^6$, but in this case the solar torque on the bulge is so large that the protoearth most likely moves so quickly through resonance that maximum amplitude is not reached (non-solar torques are assumed to be absent). In order to achieve unstable resonance, two conditions must apply: very high Q (unlikely, ref. 6) and a large continual addition of angular momentum to the protoearth.

Older theories of terrestrial accretion from a heliocentric planetesimal swarm do not naturally account for the angular momentum density of the earth-moon system, so they obviously do not lead to excitation of the solar resonance. New theories of lunar origin involve either an impact-generated hot accretion disk or a circumterrrestrial swarm of planetesimals. Both models feed a substantial amount of mass and solar-orbit-derived angular momentum to the growing protoearth. The megaimpact variant allows the possibility that the moon was created by rotational instability, provided some mechanism causes a subsequent angular momentum loss (see 8). In this context, if collapse of an accretion disk (or diskettes) attempts to feed too much angular momentum to a sufficiently fluid protoearth, then the solar resonance may be able to tap angular momentum out of the system and maintain the protoearth in a near resonant state. Thus rather than act as the savior of the fission hypothesis, solar resonance probably acts as a formidable barrier to rotational instability.

References

(1) Chapman C.R. and McKinnon W.B. (1986) In Satellites, in press; (2) McKinnon W.B. and Schenk P.M. (1985) Lunar Planet. Sci. XVI, 544-545; (3) Housen K.R. et al. (1983) J. Geophys. Res. 88, 2485-2499; McKinnon W.B. and Chapman C.R. (1985) Eos Trans. AGU 66, 946, and in preparation; (5) McKinnon W.B. (1985) Bull. Am. Astron. Soc. 17, in press; (6) McKinnon W.B. and Mueller S.W. (1984) In Conf. Origin of the Moon, 34; (7) McKinnon W.B. (1985) Eos Trans. AGU 66, 295; (8) Durisen R.H. and Gingold R.A. (1986) In Origin of the Moon, in press.

ENTRY OF DUST PARTICLES INTO PLANETARY MAGNETOSPHERES

D. A. Mendis, University of California, San Diego

While interplanetary dust constitutes a primary source of cosmic particulate matter in planetary magnetospheres, the debris produced by its impact with small satellites and ring material provides an important secondary source. Internal processes, such as volcanic activity, particularly in the smaller satellites, could result in a third source. In the case of the terrestrial magnetosphere there are also artifical (internal) sources: 1-10μ sized $A\ell_2O_3$ particles injected by solid rocket mortar burns between near earth and geosynchronous orbit constitute one such source, while the fragments of larger bodies (artificial satellites) due to explosions (e.g., "killer satellites") and collisions constitute another. Finally, if we include the purely induced cometary magnetosphere among planetary magnetospheres, the injection of cometary dust into it due to entrainment by the outflowing gases constitutes another source.

As a result of being immersed in a radiative and plasma environment, these dust grains get electrically charged up to some potential (positive or negative). Particularly in those regions where the magnetospheric plasma is hot and dense and their own spatial density is low, the dust grains could get charged to numerically large negative potentials.

While this charging may have physical consequences for the larger grains, such as electrostatic erosion ("chipping") and disruption, it also can effect the dynamics of the smaller grains. Indeed, the small but finite capacitance of these grains, which leads to a phase lag in the gyrophase oscillation of the grain potential, could even lead to the permanent magneto-gravitational capture of interplanetary grains within planetary magnetospheres in certain situations. Here we will review the sources of dust in planetary magnetospheres and discuss their physics and their dynamics under the combined action of both planetary gravitational and magnetospheric electromagnetic forces.

ELECTRODYNAMIC PROCESSES IN THE RING SYSTEM OF SATURN

D. A. Mendis, J. R. Hill, University of California, San Diego,
W.-H. Ip, Max-Planck-Institut für Aeronomie,
C. K. Goertz, University of Iowa,
and E. Grün, Max-Planck-Institut für Kernphysik

A variety of novel magnetospheric processes are associated with the presence of an extended ring system of particulate matter within the Saturnian ring system. Being immersed in a radiative and plasma environment, the ring material is electrically charged to some potential, which may be positive or negative. While this electrical charging may have only physical effects on the larger bodies, it may also affect the dynamics of the smaller grains. While the rings can also act both as sources and sinks of the magnetospheric plasma, the relative motion between the charged dust and the surrounding plasma constitutes a new type of dust-ring current having interesting consequences for the upper ionosphere, magnetosphere, and the rings themselves. We discuss a number of recently observed ring phenomena including Voyager 1 and 2 observations of the rotating near-radial spokes in the B Ring; waves and braids of the F Ring; and discrete episodic bursts of broadband radio emission, claimed by some authors to originate in the ring. In addition, we discuss several other phenomena, including the origin and evolution of the diffuse E Ring and G Ring (which appear to be composed of fine dust), as well as the existence of a number of sharp discontinuities in the main ring system, within the context of gravito-electrodynamics of charged dust in the magnetosphere.

This is indeed a new and immature field of research. While the single-particle theory of dust particle motion is reasonably well understood, the role of collective dust plasma effects is still under discussion. If electrodynamic processes are responsible for certain phenomena observed in the ring system at the present time, it is possible that they may have also played a role in the past during its formation and early evolution. We conclude by discussing some prevailing ideas about the role of electrodynamic processes in the cosmogony of the ring system.

A NOTE ON JUPITER'S "GOSSAMER" RING

D. A. Mendis, J. R. Hill and W. Fillius, University of California, San Diego, and T. G. Northrop, NASA Goddard Space Flight Center

The newly discovered "gossamer" ring of Jupiter, composed largely of micron-sized grains, exhibits a significant peak very near the synchronous radius. The discoverers believe that this peak may be associated with an unobserved source consisting of large bodies that straddle the synchronous orbit. Here we offer an alternative evolutionary mechanism, namely the "gyro-phase" drift towards the synchronous orbit of fine grains, which necessarily are electrostatically charged within the Jovian magnetosphere.

EXTENSIONAL TECTONICS OF THE SATURNIAN SATELLITES

J.M. Moore and R. Greeley, Department of Geology, Arizona State University, Tempe, Arizona 85287

The saturnian satellites were imaged by the Voyager spacecraft at sufficient resolutions to reveal landforms that indicate histories of extensional tectonics for several of these bodies. The relationships among landforms on various satellites imply that extensional tectonism is a consequence of several different energy sources. Case histories of several satellites will be discussed to illustrate the interaction of various phenomena associated with extensional tectonism.

Mimas

Long, linear, sub-parallel troughs on Mimas (satellite diameter 390 km) are interpreted to be the result of coalesced subsidence above zones of pre-existing weakness that were activated by the impact that formed the 130 km diameter crater Herschel (1). This suggestion is similar to one proposed for the formation of troughs or grooves on the martian satellite Phobos by its crater Stickney (2). It should be noted, however, that the troughs on Mimas do not obviously radiate from Herschel the way grooves do on Phobos from Stickney.

Tethys

A somewhat more complex relationship between impact and extension can be observed on Tethys (1060 km diameter). Ithaca Chasma, an enormous trough system extending at least 270° around Tethys, is narrowly confined to a zone which lies roughly along a great circle that is concentric to the 400-km-diameter Odysseus impact basin (3,4). It was originally suggested that if Tethys was once a sphere of liquid H_2O covered with a thin solid crust, freezing the interior would have produced expansion of the surface comparable to the area of the chasma (3). This hypothesis failed to explain why the chasma occurs only within a narrow zone. Expansion of the satellite's interior should have caused fracturing to occur over the entire surface in order to effectively relieve stresses in a rigid crust (4). It has been recently proposed that the grabens composing the Ithaca Chasma were formed some time after the impact in response to stresses induced by viscous flow associated with the restoration of Odysseus' floor to match Tethys' geoid (1).

Dione and Rhea

Linear troughs and coalescing-pit chains observed on Dione (1120 km diameter) and Rhea (1530 km diameter) have been interpreted as evidence for episodes of extensional tectonics in these satellites' past (3,5,6,7,8). The globally widespread distribution of these features implies that they were formed by surface-layer tensional stresses created by the volumetric expansion of the satellites' interiors. Theoretical models suggest an early but relatively long-lived period of increasing volume resulting from

thermal expansion and/or phase-density changes of H_2O (and hydrates) driven by the rise and fall of output from radionuclide energy sources (9,10).

The location and orientation of some extensional features on Dione may have been controlled by deep-seated fractures established by large impacts and later exploited by endogenic stresses (5,7). The orientation of extensional features on Rhea are not random. However, they do not form a pattern that can be explained by existing models for global lineament trends (8).

Enceladus

The youngest and most tectonically modified surface observed in the saturnian system is that of Enceladus (3). Bands of parallel, alternating troughs and ridges (similar to "grooved" terrain of Ganymede), fissures, and coalescing-pit chains compose a suite of landforms on Enceladus thought to be due to extensional tectonics. Small fissures and troughs probably form initially as tension fractures or graben. Trough-ridge sets may be akin to horst and graben terrains. The morphology of these landforms has probably been significantly modified by the effect of viscous creep and mass wasting thus complicating the identification of the details of their formation. Like similar landforms on Ganymede, the mechanisms by which extensional features are formed on Enceladus is poorly understood (1).

The geological vigor of Enceladus is remarkable in that its diameter is 500 km, only a little larger that Mimas and less than half the diameters of Tethys, Dione, and Rhea. Like the Galilean satellite Io, it is probably heated by the tidal-torque flexing of its interior (11,12). Tidal heating joins large basin-forming impacts and radionuclide decay to form the three identified energy sources for extensional tectonics on the saturnian satellites.

References

(1) McKinnon, W.B. (1985) Geology of icy satellites, submitted to Proc. NATO Conf. Ices in the Solar System, D. Reidel Pub.
(2) Thomas P. and Ververka, J. (1979) Icarus, 40, 394-405.
(3) Smith, B.A. et al. (1982) Science, 215, 504-537.
(4) Moore, J.M. and Ahern, J.L. (1983) Proc. Lunar Planet. Sci. Conf. 13th, in J. Geophys. Res., 88, A577-A584.
(5) Smith, B.A. et al. (1981) Science, 212, 163-191.
(6) Plescia, J.B. (1983) Icarus, 56, 255-277.
(7) Moore, J.M. (1984) Icarus, 59, 205-220.
(8) Moore, J.M. et al. (1985), Proc. Lunar Planet. Sci. Conf. 15th, in J. Geophys. Res., 90, C785-C795.
(9) Ellsworth, K. and Schubert, G. (1983) Icarus, 54, 490-510.
(10) Pollack, J.B. and Consolmagno, G. (1984) in Saturn, T. Gehrels and M.S. Matthews, ed., pp. 811-866.
(11) Squyres, S.W. et al. (1983) Icarus, 53, 319-331.
(12) Lissauer, J.J. et al. (1984) Icarus, 58, 159-168.

GLOBAL TECTONIC MAPPING OF GANYMEDE: A PRELIMINARY REPORT Scott L. Murchie and James W. Head, Dept. of Geological Sciences, Brown University, Providence, RI 02906

Shoemaker et al (1) first mapped the geology of Ganymede on a global basis. This study, together with those of other investigators (2-4), suggested the division of Ganymede's surface into three main material units, crater material, bright terrain, and dark terrain. Both the bright and dark terrains contain systems of parallel linear to curvilinear fracture or graben-like troughs. In the dark terrain most of the troughs, known as *furrows*, belong to two arcuate systems located in the sub-Jovian and anti-Jovian hemispheres respectively (3). Two additional furrow sets have been identified in the largest of the dark cratered regions, Galileo Regio, of which one set is orthogonal to the arcuate furrows (5).

Bright terrain may be divided into three main structural types (3). The most common is *bright grooved terrain*, cut by parallel sets of *grooves*, which are morphologically distinct from furrows. Areas of bright as well as dark terrain contain orthogonal sets of grooves or fractures *(reticulate terrain)* (3,5). In *bright smooth terrain*, grooves are rare and usually divide the smooth terrain into a complex of polygonal regions. Bright smooth material commonly embays craters and the boundaries of dark terrain, suggesting deposition in a fluid mode (1,3,4). The excavation of dark material by craters in the bright terrain (6) and the lack of major lateral offset across regions of bright terrain (4) suggest that dark cratered terrain has been converted to bright terrain *in situ* by emplacement of higher albedo material at most a few km thick. Large regions of bright terrain consist of a complex intersecting pattern of both smooth polygons and grooved structural domains (1) having parallel groove orientations within the domains.

Few studies have been done of regional patterns of groove orientations in the bright terrain. Bianchi et al (7) found two dominant orientations in Uruk Sulcus, a large area of bright terrain south of Galileo Regio. These orientations are parallel and orthogonal to arcuate furrows just to the north. Murchie and Head (8) found dominant orientations of groove sets parallel and perpendicular to furrow sets west of Galileo Regio, and proposed that emplacement of grooved terrain is structurally controlled by furrow sets.

The aim of this study is to identify global distribution of tectonic patterns and structural types. We constructed a global map of regions with uniform structural patterns (dark furrowed terrain, reticulate terrain, grooved terrain, smooth terrain, and crater material). Structural domains were both outlined and the orientations of their groove sets depicted. Structural domains were mapped as two subtypes. One of these, *groove lanes*, is a class of highly elongate domains whose grooves are parallel to the long axes of the domains. As the width of groove lanes decreases, the lanes grade into throughgoing grooves and groove pairs. The other subtype consists of generally polygonal structural domains with a small length to width ratio and groove sets oblique to the long axes of the domains. We call these *grooved polygons*. The dominant relationship between the two structural subtypes of grooved terrain is that intersecting groove lanes or throughgoing grooves define single or multiple grooved polygons. Groove sets in the polygons commonly terminate abruptly at the groove lanes.

Our results indicate that occurrence of groove sets parallel and orthogonal to furrow sets is a global phenomenon. In addition to the previously mentioned regions where groove orientations are consistent with structural control by furrows, we identify two other large areas. One is the region north of 20S and east of 10W. Both groove lanes and throughgoing grooves are dominantly parallel and perpendicular to NE-SW oriented furrows. The other region is between 20S and 60S, and 170W and 210W, where there is a concentration of reticulate terrain of both bright and dark albedo. One of the orthogonal groove sets in the reticulate terrain traces an arcuate pattern that appears to be a continuation of the furrow pattern to the north. In Galileo Regio, the most thoroughly studied region of furrowed terrain, the cross-cutting by the arcuate furrows of the orthogonal furrows led to the interpretation that the arcuate furrows are clearly younger. However, the global nature of apparent zones of weakness parallel and perpendicular to arcuate furrows suggests that orthogonal furrow sets may be related genetically.

Although the largest fraction of smooth terrain is concentrated in the northern part of the sub-Jovian hemisphere, two modes of occurrence of smooth terrain are associated with grooved terrain. These are as flood-type deposits in the central portions of groove domains, and as feather-edged deposits on adjacent dark cratered terrain. Considering the evidence for emplacement of smooth material in a fluid mode, this suggests that the areas of grooved terrain and especially their central portions were topographic lows at the time of smooth terrain emplacement.

In summary, the grooved terrain of Ganymede consists of long groove lanes which outline polygonal blocks containing one or multiple groove domains. Regional distribution of groove orientations suggests structural control of groove emplacement by zones of weakness parallel and orthogonal to furrow sets. The distribution of smooth terrain, believed to have been deposited in a fluid mode, indicates regional slope toward the central portions of grooved regions. Current research involves measurement of global trends in groove orientation, and the synthesis of a model of the sequence of events during the emplacement of grooved terrain.

References: (1) Shoemaker, E.M. et al (1982) in *The Satellites of Jupiter*, Univ. of Arizona Press, p.435-520. (2) Smith, B.A. et al (1979a) *Nature* 204, p.951-972. (3) Smith, B.A. et al (1979b) *Nature* 206, p.927-950. (4) Lucchitta, B.K. (1980) *Icarus* 44, p.481-501. (5) Casacchia, R. and R.G. Strom (1984) *Proc. Lunar Planet. Sci. Conf. 14th*, p. B419-B428. (6) Schenk, P.M. and W.B. McKinnon (1984) *Lunar Planet. Sci. XV*, p. 720-721. (7) Bianchi, R. et al (1984) *Lunar Planet. Sci. XV*, p. 54-55. (8) Murchie, S. and J.W. Head (1985) *Lunar Planet. Sci. XVI*, this issue.

S. Murchie and J. Head

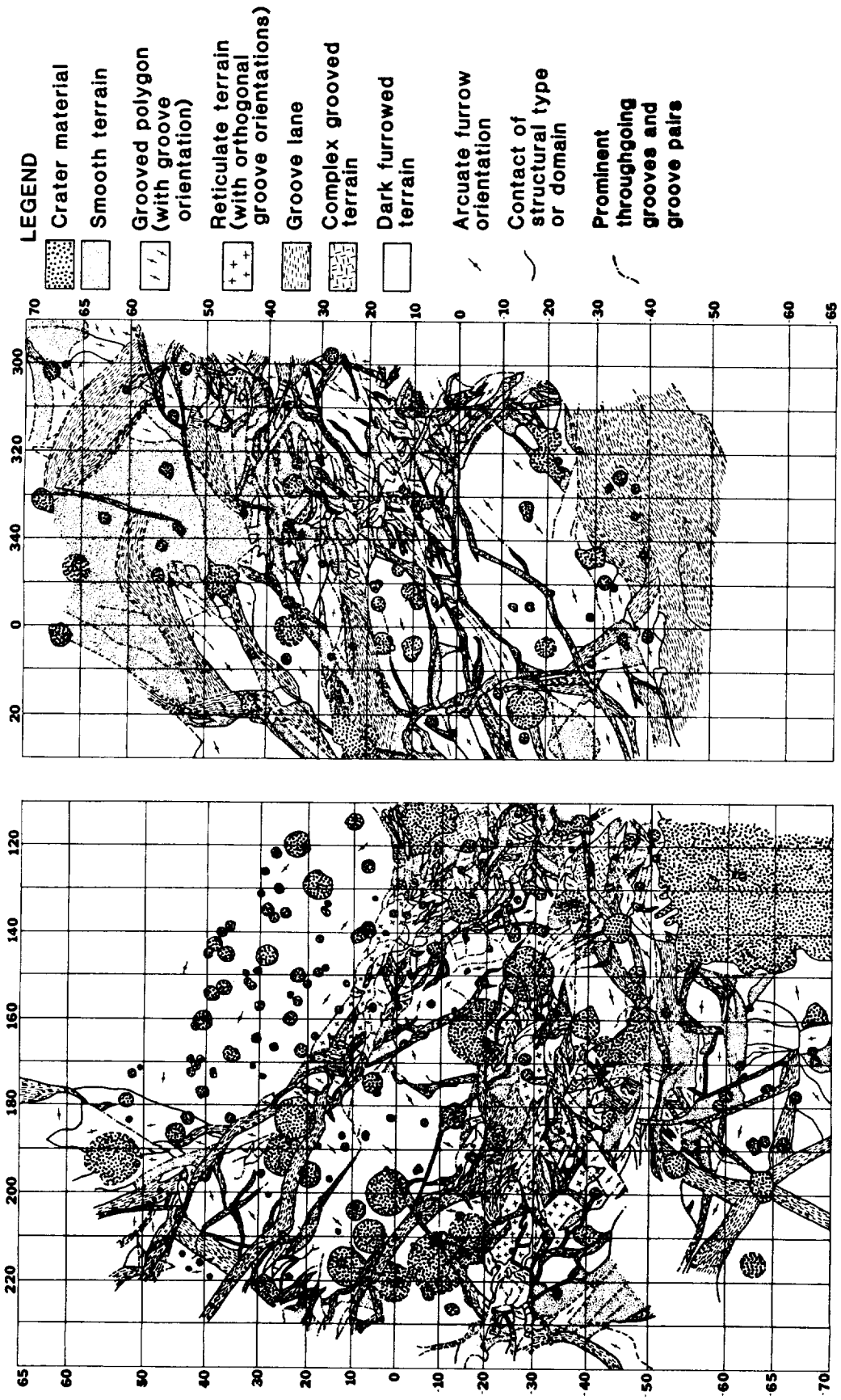

Fig. 1. Preliminary global tectonic map of Ganymede.

GLOBAL REORIENTATION OF GANYMEDE BY THE BASIN GILGAMESH: MODELS AND EVIDENCE FROM TECTONIC PATTERNS. *Scott L. Murchie and James W. Head III, Department of Geological Sciences, Brown University, Providence, RI, 02912.*

One of the important global forces that may affect icy satellites is global reorientation due to perturbations of their momental figures by young impact basins (1). As a negative mass anomaly, a young large impact basin will reorient a satellite so that the basin migrates toward the body's pole. Ganymede in particular may exhibit the effects of this global process, because it both possesses impact basins and has an abundance of tectonic features that may record stresses caused by global reorientation. It is the aim of this study to identify particular basins on Ganymede that may have significantly reoriented the satellite and to determine if there is geologic evidence that such reorientation occured.

The surface of Ganymede is dominated by two types of tectonic features, grooves and furrows (2,3). The grooves are believed to be extensional features, probably degraded grabens or tension cracks (4), and occur in sets of three major types (5,6): narrow elongate parallel bands of grooves (groove lanes), grooved polygons, and reticulate polygons. Groove orientations are structurally controlled on a regional scale by zones of weakness parallel and perpendicular to the furrow systems. However, on a global scale the orientations of major groove lanes follow a pattern not related to a single furrow set. The groove lanes in the anti-Jovian hemisphere are dominantly oriented NW-SE and those in the sub-Jovian hemisphere are dominantly oriented SW-NE. Bianchi et al. (7,8) found that the majority of grooves define two systems of small circles centered about poles at approximately 55^{o}N,73^{o}W and 70^{o}N,180^{o}W.

Ganymede was modelled as a differentiated ice-silicate spheroid (9) with a silicate core (radius 1826 km) and an ice mantle and lithosphere consisting of shells of ice VI, ice V, ice III, and ice I. The principal axes of the satellite's ellipsoid were calculated (10) and transformed to the principal moments of inertia. An impact basin on the planet was modelled as a cylindrical depression whose depth was taken from the empirical depth-diameter relationship for fresh lunar craters (11). The basin's moment of inertia was calculated as by Melosh (12). Global reorientation was modelled numerically by treating cumulative global reorientation as a series of incremental reorientations followed by adjustments of the tidal bulge and relaxation of the basin. The decaying inertial tensor of the basin and the satellite's tensor were added iteratively, and the new figure and principal axes were calculated from the eigenvectors of the summed tensors. For the simple case where reorientation occurred by a rotation about one of the principal axes of the ellipsoid, the maximum deviatoric stress was calculated (13). The damping time of Ganymede's librations about its new orientation was calculated (12) and is less than 2 yrs. The e-folding times (14) for relaxation of the tidal bulge and for isostatic adjustment of the crater by viscous relaxation (15) were determined. If the time for relaxation of the tidal bulge is much shorter than the lifetime of the basin, the satellite will undergo continuous reorientation whose cumulative effect would be analogous to a single reorientation by a much larger basin. Variables relevant to our calculations include viscosity (10^{14}P) (15,16,17) and shear modulus (3×10^{10} dyne cm^{-2}) (18) of Ganymede's icy mantle.

Gilgamesh (62^{o}S, 123^{o}W), which formed during later stages of grooved terrain emplacement (19), was found to be the only basin large enough possibly to have caused global reorientation. In a small basin model, a 9-km topographic depression was modelled to occur only within the middle 600-km ring, while in the large basin model the depression was modelled as occurring across the entire 900-km basin. The time range for relaxation of the bulge, bracketed by the times calculated for the large and small basin models, is 20-200 yrs; the time range for isostatic adjustment of the basin is 30,000-100,000 yrs. In the case of the small basin model, cumulative reorientation would equal about 15^{o}. In the case of the large basin model, reorientation would have the cumulative effect of causing the migration of the basin nearly to the pole, which clearly did not occur. Global reorientation would have been nearly equivalent to rotation of Ganymede about the major axis of its ellipsoid, and the trace of the paleonorth pole would have passed between the two poles of groove concentricity calculated by Bianchi et al. (7,8). The separation between these two poles of 40^{o}-50^{o} suggests that the grooves in fact define a global system of conjugate fractures. The pole defining the system would be at 70^{o}N,110^{o}W, within 4^{o} of the trace of the paleonorth pole and with an offset consistent with a small basin model. Such a global fracture system centered on the paleopole is consistent with fractures created by tidal despinning early in Ganymede's history (20).

We hypothesize that groove sets on Ganymede developed along ancient zones of weakness in the lithosphere, where fractures due to tidal despinning were parallel to one of the orthogonal zones associated with the furrows. During the later stages of grooved terrain formation, Gilgamesh was formed and reoriented the satellite. Three predictions about global geologic features follow from this hypothesis: a thickening of the lithosphere due to the low surface temperature around the paleopoles (19), areal patterns of groove orientation consistent with relict fractures due to tidal despinning, and a preferred orientation of younger groove sets consistent with stresses caused by global reorientation. By extrapolation of the hypothesis of a thicker polar lithosphere, we would expect less tectonic deformation of the thicker lithosphere in the areas of the paleopoles. Lucchitta (21) noted that the greatest concentrations of continuous dark terrain are Galileo Regio and a large antipodal dark area, both areas defining large parts of the paleopolar region. Tidal despining of a body with a constant volume would result in conjugate fractures bisected by lines of latitude equatorward of 48^{o} paleolatitude and fractures parallel to lines of paleolatitude poleward of 48^{o} (20). Groove lanes are dominantly at low oblique angles to paleolatitude lines in the area where conjugate fracture zones would be expected, and in the paleosouth polar region grooves are dominantly parallel to the paleolatitude lines (Fig. 1).

Stresses due to reorientation may have directed uniform tension due to global expansion and affected the orientations of younger grooves. We determined expected stress trajectories using the results of Helfenstein and Parmentier (13), and calculated that the greatest deviatoric stress would have been about 4.6 bars. This compares to a tensile strength of the icy lithosphere of a few to 20 bars (10,13,22). In Fig. 1 the area with deviatoric stress >3 bars is outlined and the trajectories of least compressive stress are shown. The youngest groove lanes are almost entirely at high angles to the trajectories, and are concentrated in the area of greatest deviatoric stress.

In summary, we propose a general tectonic history for Ganymede based on the results of this study and earlier work (4,5,6,7,8,19,20,21,23). The earliest tectonic event which has been recognized was tidal despinning (stage 1). Subsequently to despinning, the furrows were formed (stage 2); the despinning fractures either were resurfaced earlier or their surface expressions were obliterated by furrow formation. Later, groove formation began in older reactivated zones of weakness, preferentially where fracture zones from despinning and one of the orthogonal zones related to furrows were at low angles (stage 3). During the later stages of grooved terrain development the impact basin Gilgamesh was formed (stage 4), and global reorientation of about 20^0 occurred. Associated stresses caused reactivation of older fracture zones and formation of the youngest groove lanes with a preferred orientation (stage 5).

References

(1) Smith, B.A. and the Voyager imaging team, A new look at the Saturn system: the Voyager 2 images, Science, 215, 504-537, 1982. (2) Smith, B.A. and the Voyager imaging team, The Jupiter system through the eyes of Voyager 1, Science, 204, 951-972, 1979a. (3) Smith, B.A. and the Voyager imaging team, The Galilean satellites and Jupiter: Voyager 2 imaging science results, Science, 206, 927-950, 1979b. (4) Parmentier, E.M., Squyres, S.W., Head, J.W., and Allison, M.L., The tectonics of Ganymede, Nature, 295, 290-293, 1982. (5) Murchie, S.L. and Head, J.W., Global tectonic mapping of Ganymede: a preliminary report, Lunar and Planetary Science, 16, 599-600, 1985a. (6) Murchie, S.L. and Head, J.W., Tectonic features in the JG-4 quadrangle of Ganymede, Lunar and Planetary Science, 16, 601-602, 1985b. (7) Bianchi, R., Casacchia, R., Lanciano, P., and Pozio, S., Azimuthal distribution of the grooves on Ganymede, Lunar and Planetary Science, 16, 53-54, 1985. (8) Bianchi, R., Casacchia, R., Lanciano, P., and Pozio, S., Azimuthal distribution of the grooves on Ganymede, oral presentation at Lunar and Planetary Conference 16, March 16-20, 1985. (9) Kirk, R.L. and Stevenson, D.J., Thermal evolution of a differentiated Ganymede and implications for surface features, Lunar and Planetary Science, 13, 373-374, 1982. (10) Helfenstein, P. and Parmentier, E.M., Patterns of fracture and tidal stresses on Europa, Icarus, 53, 415-430, 1983. (11) Pike, R.J., Size-dependence in the shape of fresh impact craters on the moon, in Roddy, D. J., R.O. Pepin, R.B. Merrill, eds., Impact and Explosion Cratering, Pergamon, pp.489-509, 1977. (12) Melosh, H.J., Large impacts and the moon's orientation, Earth and Planetary Science Letters, 26, 353-360, 1975. (13) Helfenstein, P. and Parmentier, E.M., Patterns of fracture and tidal stresses due to nonsynchronous rotation: implications for fracturing on Europa, Icarus, 61, 175-184, 1985. (14) Greenberg, R. and Weidenschilling, S.J., How fast do Galilean satellites spin?, Icarus, 58, 186-196, 1984. (15) Parmentier, E.M. and Head, J.W., Viscous relaxation of impact craters on icy planetary surfaces: determination of viscosity variation with depth, Icarus, 47, 100-111, 1981. (16) Poirier, J.P., Sotin, C., and Peyronneau, J., Viscosity of high-pressure ice VI and evolution and dynamics of Ganymede, Nature, 292, 225-227, 1981. (17) Zuber, M.T., and Parmentier, E.M., Lithospheric stresses due to radiogenic heating of an ice-silicate planetary body: implications for Ganymede's tectonic evolution, Journal of Geophysical Research, 89, B429-B437, 1984. (18) Gold, L.W., Engineering properties of freshwater ice, Journal of Glaciology, 19, 197-212, 1977. (19) Shoemaker, E.M., Lucchitta, B.K., Wilhelms, D.E., Plescia, J.B., and Squyres, S.W., The geology of Ganymede,in Morrison, D., ed., The Satellites of Jupiter, Univ. of Arizona Press, pp.435-520, 1982. (20) Melosh, H.J., Global tectonics of a despun planet, Icarus, 31, 221-243, 1977. (21) Lucchitta, B.K., Grooved terrain on Ganymede, Icarus, 44, 481-501, 1980. (22) Hawkes, I., and Mellor, M., Deformation and fracture of ice under uniaxial stress, Journal of Glaciology, 11, 103-131, 1972. (23) Murchie, S.L., and Head, J.W., Global reorientation and its effect on tectonic patterns on Ganymede, submitted to Geophysical Research Letters.

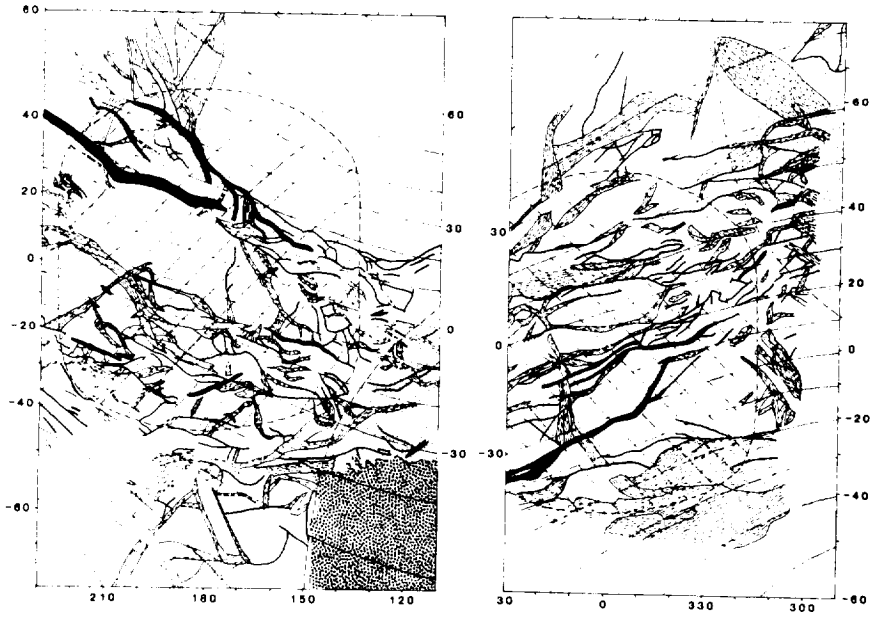

Fig. 1. Mercator projection of major groove lanes on Ganymede. The solid black lanes are youngest and cross-cut other groove sets. Other groove lanes are hatched, and throughgoing grooves are mapped using a heavier-weight line. The curved east-west lines are of paleolatitude, labelled in the center of the figure. The areas outlined by the dashed line experienced deviatoric stresses >3 bars due to reorientation; trajectories of the least compressive stress are shown in these regions. The lightly stippled areas experienced compressive stresses due to reorientation. Gilgamesh is shown in heavy stippling.

PROTON SPUTTERING OF SULFUR AND APPLICATIONS TO IO

Doug Nash, Jet Propulsion Laboratory, Pasadena, CA 91109

I've begun lab experiments on the effects of proton bombardment on the optical and physical properties of sulfur with the intent of trying to understand the effects on Jovian magnetospheric protons on Io's surface. I simulated Io's surface using melted sulfur, heated to several different temperatures and allowed to freeze at room temperature simulating lava flows that erupted at different temperatures. I put the samples in a proton gun system (Nash, 1966; 1967) in which I simulate the low-Kev Jovian proton component, which is the most abundant Jovian proton component in the magnetosphere at Io's orbital position (Divine and Garrett, 1983).

The specific objectives were twofold: (1) to measure sputtering yields (S/H^+) experimentally. Earlier estimates of yield ranged from a low of 0.04 (Haff and Watson, 1981) to high of 10^6 (Fink and Biersack, 1982). I also wanted to determine the effects on yields of the condition of the sample as well as the character of the incident protons. The second objective (2) was to learn the effects of irradiation on surface texture, particularly micro texture and spectral reflectance, and whether or not hydrogen sulfide gas is produced by the irradiation.

First results are as follows: proton irradiation of various solid samples at room temperature (Fig. 1) showed yields of ~1000 and that the prefreeze melt temperature effects the yield, at least by a factor of two: the higher temperature melts which are richer in polymeric sulfur give lower yields than the lower temperature melt freezes which are rich in S_8 ring structure sulfur. This behavior can be attributed to stronger bonding and higher surface binding energy in the polymeric sulfur.

The effects of proton beam characteristics, for energies in the 2.5-16.5 Kev ranges, are summarized in figure 2. Basically there are two dominant controlling factors. One is the total power in the beam. For a given dose when the beam power exceeds the power which is equivalent to the ambient surface temperature, the sample begins to warm and the yields go up due to increased evaporation. The second factor is dose. Increasing dose, to the extent I could carry it, produces higher yields. I explain this behavior tentatively as follows: The surface skin on the melt freeze is rich in polymeric sulfur due to a quicker quench. This polymeric sulfur erodes at a lower rate. The subsurface material is richer in ring structure sulfur which erodes more readily. As the beam erodes a fresh surface, the apparent yield goes up. The erosion rates here for samples at ~310K are equivalent to ~0.1 μm per year on Io's surface.

The effects on texture are shown in Fig. 3 where the scale bar is 20 μm. The scanning electron microscope picture Fig. 3(a) shows the condition of the sample after solidification but prior to irradiation. The condition of the sample after irradiation (Fig. 3b) shows roughening of the surface on a microscale, production of very fine pits and other erosion features, and a residual scaly material -- probably polymeric rich -- that irregularly covers the surface and has very tiny topographic features and high porosity

The effect on spectral reflectance is shown in Fig. 4. The spectra are not effected at wavelengths above 0.5 μm. Between 0.4 and 0.5 μm

however, there is a brightening, and below 0.4 μm there is a darkening. These effects can be attributed to roughening and reduction of the size of the topographic scattering elements on the surface; qualitative, this is very similar to the effects observed when grinding sulfur to finer and finer particle size.

Gas production was examined with a Quadrapole Mass Spectrometer. The results (Fig. 5) are not totally unambiguous. On the far left is shown the mass spectrum with the proton beam off, showing residual gas in the chamber (at 10^{-7} torr) and a tiny H_2S peak. On the right shows the gas phases present when protons impinge on the sample, with a substantial H_2S production. Unfortunately with the beam on but blocked I also observed a H_2S signal; but I attribute this to sulfur that had been deposited on the beam blocker during the preceeding sputtering run.

Conclusions: the sulfur sputtering yields I find experimentally for low energy protons are ~1000, much higher than earlier estimates for protons and lower than values published for He^+ ions; both by a factor of ~1000. Surface Microstructure changes are produced that occur in fairly short proton exposure doses equivalent to ~6 years on Io. Likewise, the spectral reflectance is effected particularly in the blue and the ultraviolet wavelengths. And there is production of some H_2S. Further experiments need to be conducted.

Applications to IO: These results suggest that Jovian protons, if they impact Io's surface, could supply substantial amounts of sulfur to a coronal atmosphere, and thence to the Io torus. My calculations indicate that proton sputtering alone would come to within a factor of 2 to 5 of supplying the required sulfur flux (~2 x 10^{28} sec^{-1}). Spectral aging of Io's surface should occur in areas where volcanic resurfacing rates are low and where protons are impacting the sulfur surface. There may also be some production of an H_2S component to the atmosphere.

REFERENCES

Divine, N. and Garrett, H. (1983). Charged Particle Distribution in Jupiter's Magnetosphere. J. Geophys. Res. 88, 6889-6903.

Fink, D. and J.P. Biersack (1982). Catastrophic Sputtering of Sulfur by Helium. Radiation Effects 64, 89-95.

Haff, P. and C. Watson (1981). Sputter Ejection of Matter from Io. J. Geophys. Res. 86, 6933-6938.

Nash, D.B. (1966). Proton-Excited Luminescence of Silicates: Experimental Results and Lunar Implications. J. Geophys. Res. 71, 2517-2534.

Nash, D.B. (1967). Proton-Irradiation Darkening of Rock Powders: Contamination and Temperature Effects, and Applications to Solar-Wind Darkening of the Moon. J. Geophys. Res. 72, 3089-3104.

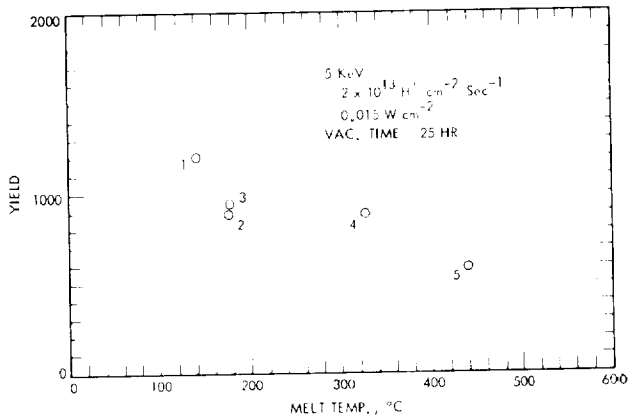

Figure 1.

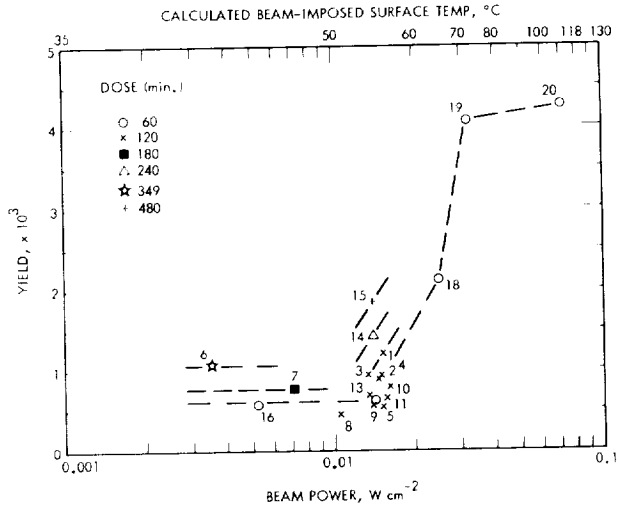

Figure 2.

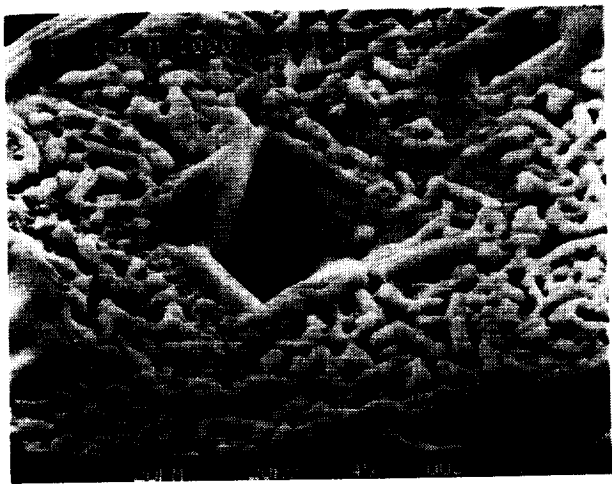

Figure 3(a).

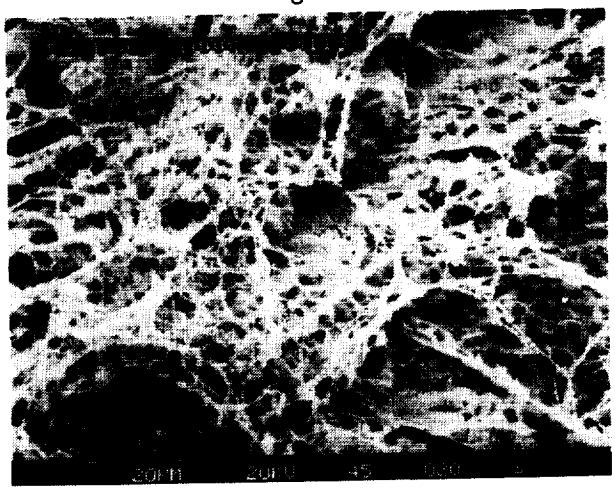

Figure 3(b).

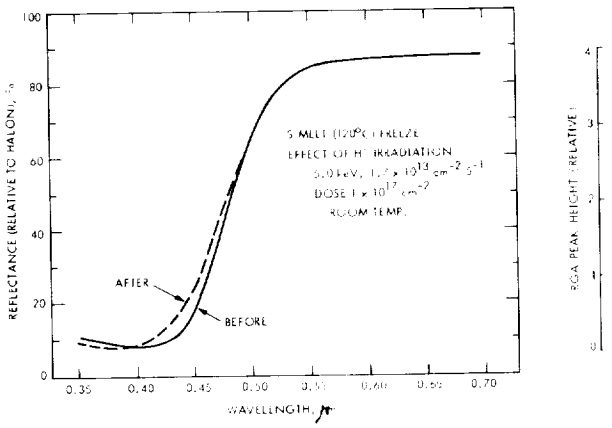

Figure 4.

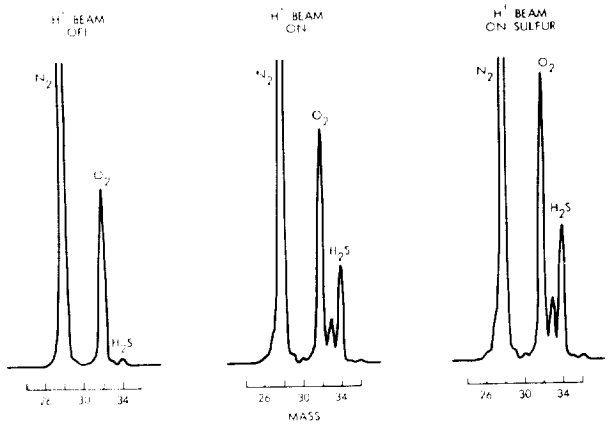

Figure 5.

SULFUR-OXYGEN PROCESSES ON IO

Robert M. Nelson, William D. Smythe

The presence of selected sulfur-oxygen compounds on the surface of Jupiter's satellite Io is now widely accepted, however there remains considerable controversy regarding the presence of elemental sulfur as a major surface phase. At the present, sulfur dioxide is the only compoundwhich is generally agreed to be a major solid state component of Io's surface based on spectroscopic analysis (Smythe et al., 1979). This research is intended to explore problems relating to the presence of sulfur and sulfur-oxygen compounds in the Io environment using laboratory spectral reflectance measurements as a primary tool and comparing these results with Io's spectral geometric albedo. Sulfur dioxide, sulfur trioxide and mixtures of sulfur allotropes derived from USP and ultrapure sulfur have been the principal species under investigation.

We have begun measuring the spectral reflectance of other sulfur oxygen compounds that might also be present on Io's surface. We have measured the spectral reflectance of sulfur trioxide and we have found that SO_3 has strong absorption features at 3.37 and 3.70 μm, Figure 1. These features are not present in Io's spectral geometric albedo. We therefore conclude that SO_3 can only be a minor constituent (<~1%) of Io's surface. Nevertheless, studies by other workers involving irradiation of SO_2 under Io like conditions produce SO_3 as a product. We believe that SO_3 may remain undetectable from groundbased observations; however, it should be detected by instruments such as the Near Infrared Mapping Spectrometer (NIMS) on the Galileo spacecraft which can examine selected areas on the surface. (Nelson and Smythe, 1985).

Elemental sulfur has been proposed as a major surface component of Io based on similarities between the laboratory spectral reflectance of sulfur and its allotropes and Io's spectral geometric albedo. However, it has been argued that the production of these allotropes may not be compatible with Io's environment because the proposed production mechanism (quenching from a liquid melt) may not allow for the retention of particular red colored allotropes which have been suggested. We have produced mixtures of sulfur allotropes in the laboratory by quenching molten sulfur and we find that the colors indicating the presence of particular red colored allotropes are preserved upon quenching. We find that the color of the sulfur glass produced is redder when the temperature of the original melt is higher (Figure 2). This indicates in a qualitative sense that mixtures of sulfur allotropes are reasonable candidate materials to explain Io's surface coloration (Smythe and Nelson, 1985).

Nelson, R. M. and W. D. Smythe (1985). The spectral reflectance of solid sulfur trioxide (0.25-5.2 μm): Implications for Jupiter's satellite Io. Submitted to ICARUS.

Smythe, W. D., R. M. Nelson and D. B. Nash (1979). Spectral evidence for SO_2 frost or adsorbate on Io's surface. Nature 280, 766.

Smythe, W. D. and R. M. Nelson (1985). Spectral reflectance of quenched sulfur glasses: Implications for Io. Bull. Am. Ast. Soc., DPS.

Figure 1. Spectral reflectance of sulfur trioxide normalized relative to Halon. The 3.38, 3.70 and 4.08 μm features are attributable to $\nu_1 + \nu_2 + \nu_3$, $2\nu_3$, and $\nu_1 + \nu_3$ respectively.

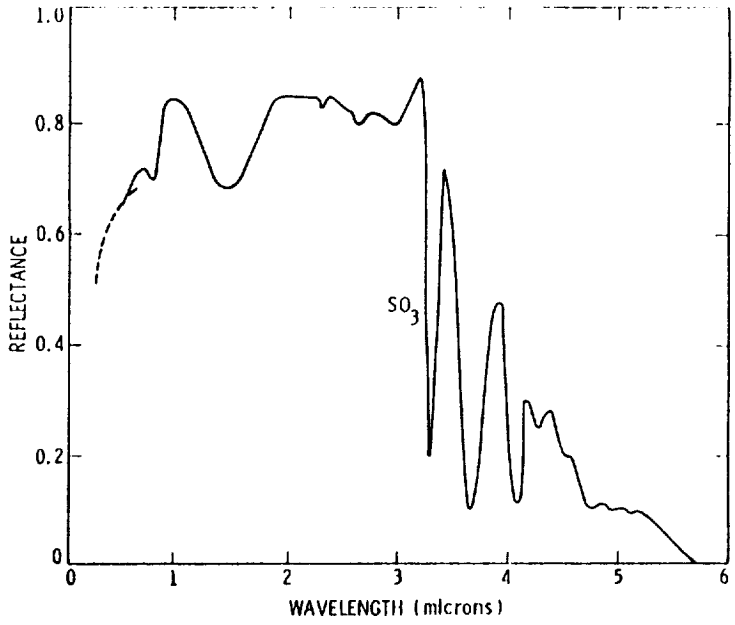

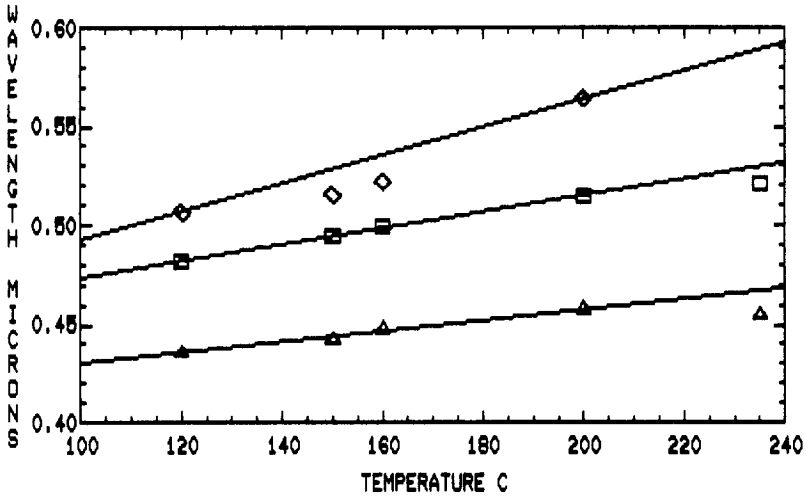

Figure 2. Bandshift versus melt temperature at several reflectance levels for USP sulfur. This plot shows the wavelength shift with melt temperature for three values of reflectance - the lower curve (Reflectance (R) = 0.1) has a displacement of 0.00028 microns per degree C, the middle curve (R = 0.5) a slope of 0.00041, and the upper curve (R = 0.7) a slope of 0.00073. These curves show that the edge of the sulfur absorption moves to the red with increasing melt temperature, and that the shape of the absorption curve changes (the shift at higher reflectance is greater).

DYNAMICAL STUDIES OF SATURN'S RINGS.

Philip D. Nicholson,
Department of Astronomy, Cornell University
Carolyn C. Porco,
Lunar and Planetary Laboratory, University of Arizona.

A detailed dynamical and photometric investigation of Saturn's C Ring is currently in progress, involving data from the Voyager imaging (ISS), radio science (RSS), and photo-polarimeter (PPS) experiments. The ultimate goals of this study are to characterize (i) the dynamical processes responsible for the various structures seen in this region of the rings, and (ii) the variations, if any, in the particle size distribution and photometric behavior between the narrow, relatively opaque ringlets and the low- optical-depth background regions. With the exception of the Cassini Division, the structure seen in the C Ring is unlike that seen elsewhere in Saturn's ring system, and may possibly be more analogous to the Uranian system of narrow, sharp-edged rings separated by broad regions of low (zero?) optical depth.

NON-CIRCULAR FEATURES IN THE C RING:

Our investigations to date have focussed on establishing the shapes of individual sharp-edged features in the C Ring, with the aim of identifying any further non-circular or inclined ringlets similar to the Maxwell (1.45 Rs) and Titan (1.29 Rs) ringlets studied previously (Porco et al. 1984a). In particular, we have searched for direct evidence of radial or vertical perturbations in the rings which might be due to the influence of resonances with Mimas or the F Ring shepherd satellites, 1980S26 and 1980S27. At the present time, we have completed the analysis of the outer half of the C Ring. Of the 35 features examined, only four showed rms deviations in radius greater than 2.5 km, the mean rms deviation for the remaining features being only 1.25 km, or about one-quarter of a pixel in a typical narrow-angle image.

Significantly, these four apparently non-circular features correspond to the inner and outer edges of two relatively narrow and opaque ringlets, one of which is is located within a 29 km wide gap at 1.4704 Rs (1 Rs = 60330 km), and the other forms the inner boundary of a 26 km wide gap at 1.4953 Rs. In addition, the inner edge of the 1.47 Rs ringlet lies ~3 km interior to the Mimas 3:1 inner vertical resonance, while the outer edge of the 1.495 Rs ringlet is ~3 km interior to the Mimas 3:1 inner Lindblad resonance (Cuzzi et al. 1984). Calculations of the strengths of these resonances lead to predicted vertical (1.47 Rs) and radial (1.495 Rs) distortions of the ringlet edges of ~0.2 km and ~2.5 km, respectively.

Attempts to fit the observed radius variations to models of the predicted resonantly-forced distortions, such as those demonstrated to affect the outer edges of the A and B rings (Porco et al. 1984b), were not, however, successful. We therefore find no direct evidence for

resonant control of these two gap edges, contrary to both our own expectations and those of other workers (Holberg et al. 1982, Cuzzi et al. 1984). Further experiments showed that the centerline of the 1.495 Rs ringlet can be satisfactorily modelled as a simple, precessing, eccentric ringlet, similar to the Maxwell ringlet at 1.45 Rs and most of the Uranian rings (Elliot and Nicholson, 1984). The ringlet's eccentricity is (4.0 ± 1.0) E-5, which may be compared with the Maxwell Ringlet's 3.4 E-4 and the Epsilon Ring's 7.94 E-3. The best-fitting model is shown in the Figure, along with the observations precessed to a common epoch. Similarly, it was found possible to model the 1.47 Rs ringlet as a precessing eccentric ringlet, although the very small eccentricity of (2.2 ± 1.0) E-5 is only marginally significant, and at least one other model (involving perturbations by the nearby 1980S27 2:1 Lindblad resonance) was found to yield an equally good fit (Porco and Nicholson, 1985).

These results, together with previous work on the Maxwell ringlet (Esposito et al. 1983, Porco et al. 1984a), suggest a common pattern:

(1) each of the three gaps in the outer C Ring contains, or is bordered by, a narrow, opaque, eccentric ringlet which precesses under the influence of Saturn's oblate figure; (2) there is no direct evidence for resonantly-forced distortions of either the ringlets themselves, or of the gap edges, despite close co-incidences of relatively strong resonances with ringlet edges in two out of three cases; (3) no evidence has been found for the presence of unseen moonlets in any of the three gaps, such as the object recently identified in the A Ring's Encke Division (Cuzzi and Scargle, 1985; Showalter et al., 1985). Finally, we note that no other non-circular features exist in the outer C Ring, down to a limiting eccentricity of ~3 E-5, corresponding to radial variations of ± 2.5 km.

These observations, taken together with the fact that at least six of the nine known narrow Uranian rings are eccentric, appear to support the 'fluid instability' model of Borderies et al. (1985), which predicts that essentially all narrow, isolated ringlets of sufficiently high surface mass density will develop eccentricities, even in the absence of shepherding moonlets.

PARTICLE SIZE DISTRIBUTIONS:

Recently, as a by-product of studies of the Encke Division being carried out by M. Showalter, a potential new method for constraining the upper end of the particle size distribution (1 - 10 meters) using the PPS data has been identified (Showalter and Nicholson, in preparation). The method depends on an analysis of the additional noise (beyond that due to photon statistics) introduced into the occultation data by the 'graininess' of the rings on the scale of the largest particles. Following encouraging results for a small region in the A Ring, we intend to apply this technique to other parts of the rings. If it proves successful, the method should nicely complement the more precise, but spatially limited, determinations of size distributions obtained from the RSS data by Marouf et al. (1983).

REFERENCES:

Borderies, N., Goldreich, P., and Tremaine, S. (1985). **ICARUS 63,** 406-420.

Cuzzi, J. N., Lissauer, J. J., Esposito, L. W., Holberg J. B., Marouf, E. A., Tyler, G. L., and Boischot, A. (1984). In **'Planetary Rings'**, Eds. R. Greenberg and A. Brahic, Univ. of Arizona Press.

Cuzzi, J. N., and Scargle, J. D. (1985). **ASTROPHYSICAL JOURNAL 292,** 276-290.

Elliot, J. L. and Nicholson, P. D. (1984). **In 'Planetary Rings'**, Eds. R. Greenberg and A. Brahic, Univ. of Arizona Press.

Esposito, L. W., et al. (1983). **SCIENCE 222,** 57-60.

Holberg, J. B., Forester, W., and Lissauer, J. J. (1982). **NATURE 297,** 115-120.

Marouf, E. A., Tyler, G. L., Zebker, H. A., and Eshleman, V. R. (1983). **ICARUS 54,** 189-211.

Porco, C., Nicholson, P. D., Borderies, N., Danielson, G. E., Goldreich, P., Holberg, J. B., and Lane, A. L. (1984a). **ICARUS 60,** 1-27.

Porco, C., Danielson, G. E., Goldreich, P., Holberg, J. B., and Lane, A. L. (1984b). **ICARUS 60,** 17-28.

Porco, C. C., and Nicholson, P. D. (1985). **B.A.A.S. 17,** 716.

Showalter, M. R., Cuzzi, J. N., Marouf, E. A., and Esposito, L. W. (1985). **B.A.A.S. 17,** 716.

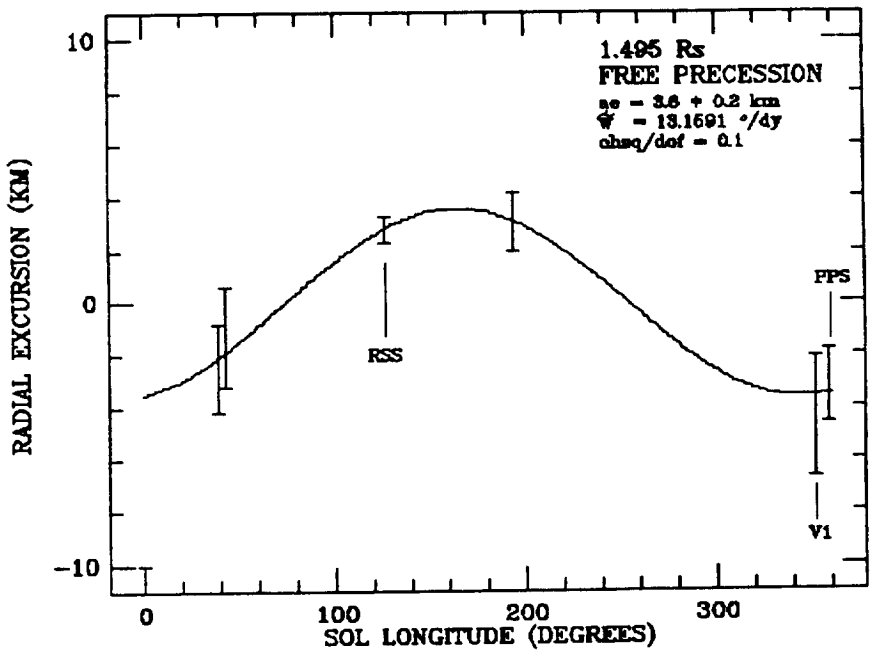

Measurements of centerline radius as a function of longitude, corrected for precession, for the 61 km wide ringlet at 1.495 Rs. The curve is the best fitting model ellipse, with a = 90163.5 km, e = 4.0 E-5, and $\dot{\tilde{\omega}}$ = 13.1591 deg/day.

Orbital Resonances, Unusual Configurations and Exotic Rotation States among the Natural Satellites

S. J. Peale, University of California at Santa Barbara

ABSTRACT

Several examples of satellite dynamics are presented where significant progress has been made in easing the understanding of a complex problem, where a long-standing problem has finally been solved, where newly discovered configurations have motivated novel descriptions and where an entirely new phenomenon has been revealed. The origin of orbital resonances is shown in the demonstration of the evolution of a pair of natural satellites through a commensurability of the mean motions by a sequence of diagrams of constant energy curves in a two dimensional phase space, where the closed curve corresponding to the motion in each successive diagram is identified by its adiabatically conserved area. All of the major features of orbital resonance capture and evolution can be thus understood with a few simple ideas. Qualifications on the application of the theory to real resonances in the solar system are presented. The two body resonances form a basis for the solution of the problem of origin and evolution of the three-body Laplace resonance among the Galilean satellites of Jupiter. Dissipation in Io is crucial to the damping of the amplitude of the Laplace libration to its observed small value. The balance of the effects of tidal dissipation in Io to that in Jupiter leads to rather tight bounds on the rate of dissipation of tidal energy in Jupiter. Motion in the relative horseshoe orbits of Saturn's coorbital satellites is described very well by a simple expansion about circular reference orbits. The coorbitals are currently very stable, and the relative motions can be used for the determination of the masses of both satellites. Pluto and its relatively large satellite Charon form an unusual system where the relative size and proximity of Charon leads to a most probable state where both Pluto and Charon are rotating synchronously with their orbital motion. The normal tidal evolution of a satellite spin toward synchronous rotation is frustrated in the case of Saturn's satellite Hyperion where gravitational torques on the large permanent asymmetry cause it to tumble chaotically. Observations of Hyperion's light curve are consistent with the chaotic rotation but do not verify it with certainty.

TECTONICS AND CRATERING ON ICY SATELLITES

Paul M. Schenk and W.B. McKinnon, Dept. Earth and Planetary Sciences
and McDonnell Center for the Space Sciences, Washington Univ.,
Saint Louis, MO 63130

Impacts both large and small can have profound effects on the structural and chemical evolution of icy "crusts". Trace amounts of non-icy material delivered by projectiles may alter the optical appearance of an icy surface, and the structural response of an icy crust to a cratering event or its subsequent modification can reveal much about crustal configuration or mechanical state. This report summarizes our research into these questions.

GALILEAN SATELLITES

Dark Ray Craters on Ganymede and Callisto: Evidence for the Impact of D-type Asteroids and Cometary Dust

A major question regarding Ganymede and Callisto concerns the origin of the observed surface darkening (1). Is the darker, older crust primordial, or did it darken as a result of meteoritic contamination? The correlation of albedo and age supports the latter interpretation; if so, the identification of the darkening agent could place powerful constraints on the sources of both present and possibly ancient impact projectiles. Current spectral and spatial resolution and coverage are too poor to make the identification directly, but the rare dark-ray class of craters on Ganymede provides an indication of the answer. Their distribution and occurrence are inconsistent with the hypothesis that the dark material is excavated from the target body (2), but are consistent with a projectile origin (3,4). A search is underway for Callistoan dark rays. Voyager three-color data on several Ganymedean dark-rays indicate they are significantly redder in the visible than adjacent terrains (5). Of the possible source classes in the outer solar system (C- and D-type asteroids, outer Jovian moons, and comets), only the D-type asteroids and possibly comets, although they may be too icy, are red in the visible. D-type asteroids, which are most abundant in and dominate the outer asteroid belt and the Trojan group, are, considering the quantity and quality of the data, the projectile type considered most likely to have formed dark-ray craters. Many comets ostensibly have D-type dust incorporated within them, and thus the impact of comets over time may have led to the progressive darkening and reddening of the surface. Ultimately this is a hypothesis that can best be tested by the Galileo NIMS experiment.

Ring Geometry of the Valhalla Impact Structure, Callisto, and the Origin of Furrows on Galileo Regio, Ganymede

The impact origin of the Galileo Regio furrow system on Ganymede has been debated recently (6,7), mainly because the supposed center of the system has not been preserved. Zuber and Parmentier (7) determined that the furrows are not circular or concentric, but that they could be impact related if multiringed structures do not always form concentrically in icy lithospheres. For comparison, we have characterized the geometry of the largest preserved

multiringed impact structure on an icy body, Valhalla. A mercator mosaic of the structure has been processed to produce a Valhalla centered orthographic view from which the geometry can be determined. The central rings are generally concentric although all the rings tend to be meander locally much more than the Galileo furrows. The outer rings of the Valhalla structure do show significant regional deviations from concentricity, in some cases up to 30° (similar to that observed for Galileo Regio by [7]). The conclusion is that regional or global lithospheric variations or the formation mechanism itself can cause significant deviations from circularity and concentricity, and that at least on this basis there is no need to invoke a non-impact origin for the Galileo Regio system.

SATURNIAN SATELLITES

Geometry and Origin of Mimas Grooves

The surface of the intermediate-sized Saturnian satellite Mimas is crossed by at least 40 grooves, or furrows. These grooves could have resulted from the impact that formed the large crater Herschel (KE ~1/3 Mimas' gravitational binding energy). If so, the non-trivial lengths of many of the grooves support arguments based on Herschel's pristine state that Mimas was essentially isothermal early in its history. An alternative explanation is tidal distortion. Stresses due to orbital recession could be large enough to potentially fracture the icy crust. Groove orientations have been mapped using the Davies and Katayama control net (Fig. 1). The orientations have been compared with those of grooves on Phobos (ostensibly due to impact fracturing) and those predicted for tidal distortion. Much of the groove pattern appears to be random. Many of the grooves near Herschel (H), however, have similar orientations and are consistent with strike-slip in response to orbital recession. The crossing of Herschel by many of the grooves points to post-impact formation or continued activity.

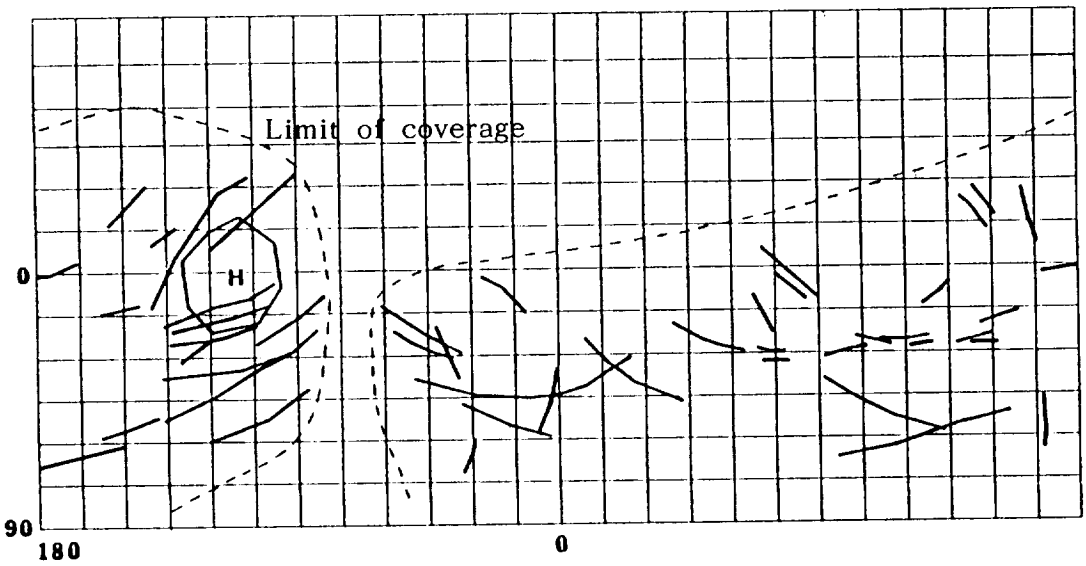

Fig. 1 Simple cylindrical map of Mimas grooves

Ithaca Chasma, Tethys: Geometry and Topography

It has been hypothesized that Ithaca Chasma, a large nearly circumferential trench on Tethys, formed when the large crater Odysseus, the axis of which nearly forms the pole for the plane through Ithaca Chasma, viscously relaxed, inducing extensional stress which caused fracturing along a zone 90° from the crater center (8). The chasma is being mapped in detail, using the Davies and Katayama control net, and the shape and depth of the trench are being examined photometrically to determine the style and sequence of formation. The chasma extends a minimum of 270° around Tethys, in that elements are observable to the limits of the imaging coverage, and it is somewhat tilted with respect to a great circle about Odysseus (Fig. 2). Where the chasma is nearest the crater, it breaks up into a complex set of branches. The morphology of the chasma is complex and varies to a large degree over its length. The present geometrical results support some relation to Odysseus.

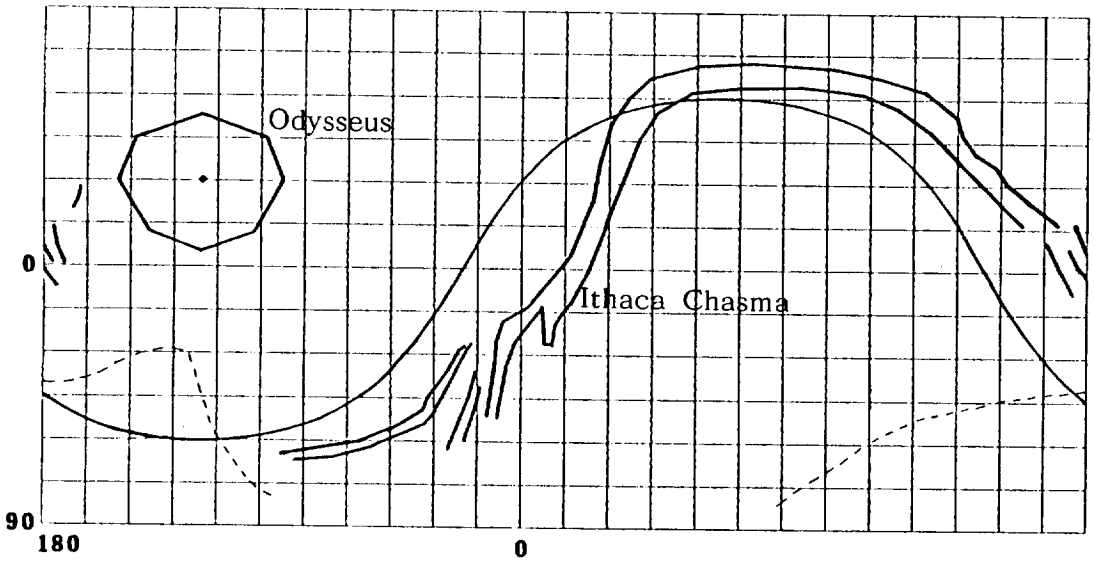

Fig. 2 Simple cylindrical map of Ithaca Chasma, Tethys

REFERENCES

(1) McKinnon, W. B. and Parmentier, E. M. (1986) In Natural Satellites, in press; (2) Hartmann, W. (1980) Icarus, 44, 441-453; (3) Conca, J. (1980) Proc. Lunar Planet. Sci. Conf. 12th, 1599-1606; (4) Schenk, P. and McKinnon, W. (1985) J. Geophys. Res., 90, C775-C783; (5) Schenk, P. and McKinnon, W. (1984) Bull. Am. Astron. Soc., 16, 683; (6) Casacchia, R. and Strom, R. (1984) J. Geophys. Res., 89, B419-B428; (7) Zuber, M. and Parmentier, E. (1984) Icarus, 60, 200-210; (8) McKinnon, W. (1985) In Ices in the Solar System, 829-856.

TEXTURE VARIATIONS ON IO: EVIDENCE FROM OPPOSITION SURGES

Damon P. Simonelli and Joseph Veverka, Center for Radiophysics and Space Research, Cornell University

Simonelli and Veverka (1985) derived near-opposition (α = 2-8°) phase curves for individual regions on the sub-Jupiter face of Io from Voyager observations. Regions were divided into three distinct photometric classes: Bright (white-appearing material), Average (typical Io equatorial material), and Polar (darker material at high latitudes). Significant differences between the near-opposition phase curves of the different classes were found: for example, in the zone where an opposition surge can occur ($\alpha \lesssim 6°$), the slope of the phase curve is significantly higher for Average and Polar material than for Bright material (Fig. 4 in Simonelli and Veverka, 1985). This difference in phase curves can be interpreted using the photometric model for a particulate surface developed by Hapke (1981, 1984) to show that texture/porosity differences exist among these various types of regions.

Close to opposition, where effects of macroscopic roughness are small, one can adopt the simple version of Hapke's function given in Hapke (1981). Using the single particle phase function $P(\alpha,g)$ developed by Henyey and Greenstein (1941), there are three free parameters in the problem: $\tilde{\omega}_0$, the single scattering albedo of an individual particle; h, Hapke's compaction parameter (higher h implies an increasingly compact surface); and g, the Henyey-Greenstein asymmetry factor (positive g represents a forward scattering particle; negative g implies a backscattering one). Theoretical phase curves for a model surface having various values of $\tilde{\omega}_0$, h and g (Fig. 1) show that the amount of opposition surge rises sharply with decreasing $\tilde{\omega}_0$, h, and g, i.e., the surge is larger for darker, more porous, and more strongly backscattering surfaces.

The phase curve data for each class of regions and the corresponding Hapke fits are shown in Fig. 2. As expected, $\tilde{\omega}_0$ is highest for the brightest class. The asymmetry factor g tends to be more toward backscattering for brighter classes. Most importantly, the compaction parameter h is lower for the Average and Polar classes (h = 0.25 and 0.10 respectively) and significantly higher for the Bright class (h > 0.4), suggesting that surface material in the former classes is significantly more porous than that in the latter.

Two of the three color classes have values of h significantly below that of lunar soil (h = 0.4; e.g., Hapke, 1966), and hence porosities in excess of the lunar value (~60% for the top of the regolith according to data in Lindsay, 1976). Our result is consistent with the suggestion by Matson and Nash (1983), based on analysis of eclipse heating/cooling data, that the surface of Io has a very high average porosity ($\approx$ 90%). Note, however, that Pang et al. (1981) deduced an average porosity for the Ionian surface of only ~60% based on their analysis of a disk-integrated phase curve for the satellite.

This work was supported by NASA Grant NSG 7156.

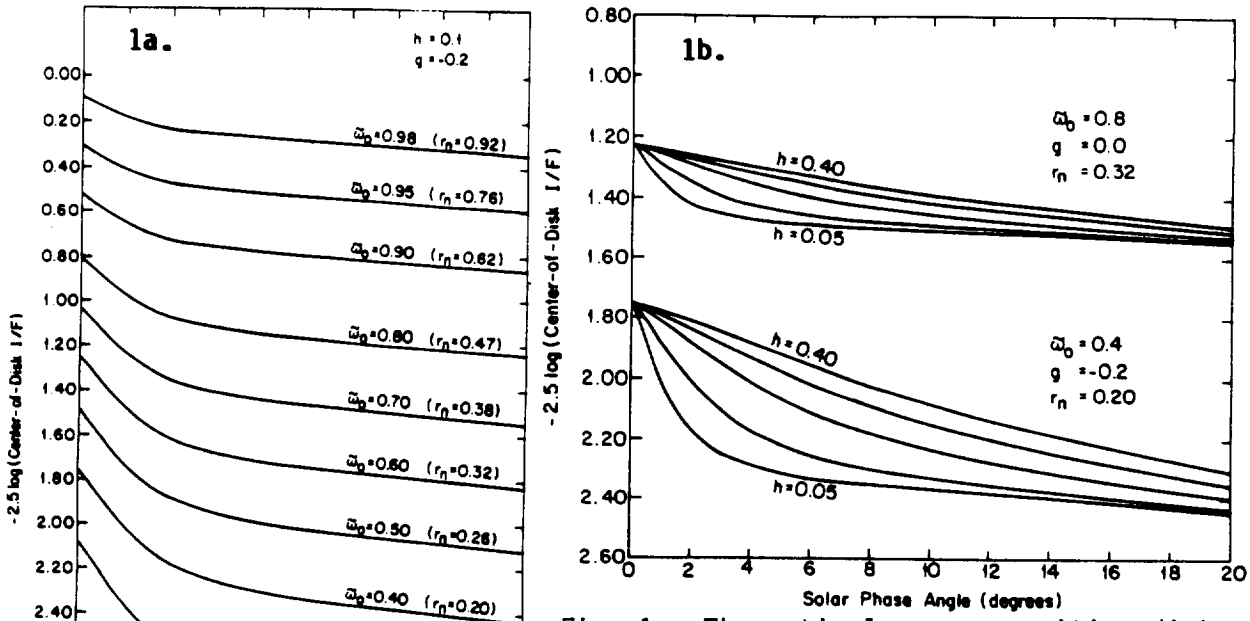

Fig. 1. Theoretical near-opposition disk-resolved phase curves for a Hapke function material having various values of $\tilde{\omega}_0$, h, and g. Fig. 1a emphasizes the changes seen in the phase curve upon varying $\tilde{\omega}_0$, while Fig. 1b explores the effect of variations in h.

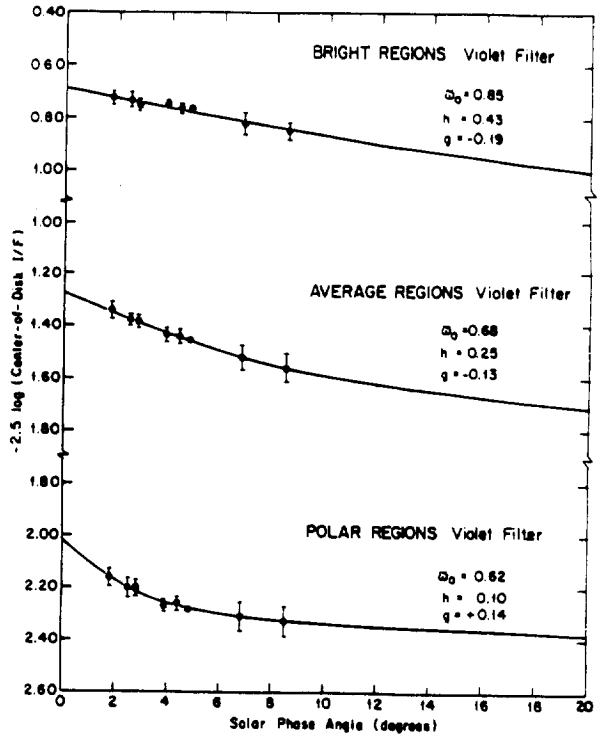

Fig. 2. Average near-opposition phase curves for each of the three classes (points) compared with the best-fit Hapke functions with parameters $\tilde{\omega}_0$, h, and g indicated (solid curves). The data were obtained from Voyager Violet Filter (420 nm) images.

REFERENCES:

Hapke, B. (1966). An improved theoretical lunar photometric function. Astron. J. 71, 333-339.

Hapke, B. (1981). Bidirectional reflectance spectroscopy. 1. Theory. J. Geophys. Res. 86, 3039-3054.

Hapke, B. (1984). Bidirectional reflectance spectroscopy. 3. Correction for macroscopic roughness. Icarus 59, 41-59.

Henyey, L. G., and T. L. Greenstein (1941). Diffuse radiation in the Galaxy. Astrophys. J. 93, 70-83.

Lindsay, J. G. (1976). Lunar Stratigraphy and Sedimentology. Elsevier.

Matson, D. L., and D. B. Nash (1983). Io's atmosphere: Pressure control by regolith cold trapping and surface venting. J. Geophys. Res. 88, 4771-4783.

Pang, K. D., K. Lumme, and E. Bowell (1981). Microstructure and particulate properties of the surfaces of Io and Ganymede: Comparison with other solar system bodies. Proc. Lunar Planet. Sci. 12B, 1543-1553.

Simonelli, D. P., and J. Veverka (1984). Voyager disk-integrated photometry of Io. Icarus 59, 406-425.

Simonelli, D. P., and J. Veverka (1985). Disk-resolved photometry of Io. II. Opposition surges and normal reflectances. Submitted to Icarus.

DISTINCTIVE CIRCULAR STRUCTURE, CENTRAL GALILEO REGIO QUADRANGLE (JG-3), GANYMEDE

Underwood, James R., Jr., Alex Woronow*, Ruggero Casacchia**, and Michael J. Teeling, Department of Geology, Kansas State University, Manhattan, KS 66506; * Geosciences Department, University of Houston, Houston, TX 77004; **Instituto di Astrofisica Spaziale, Reparto Planetologia, Viale dell'Universita 11, 00185, Roma, Italia

A distinctive circular structure (Fig. 1) near the center of the Galileo Regio quadrangle (Jg-3) of Ganymede is unlike any other circular feature observed on this planetary body. The structure is unique in being almost perfectly centered at the intersection of northeast- and northwest-trending furrows, creating a pattern reminiscent of "cross hairs" in optical instruments. The structure may represent a very old palimpsest, or the structure may be the site of early deep-mantle upwelling.

Location and Description: The circular structure, centered at lat 41° and long 143°, has a diameter of 250-275 km; the outer limits of the feature are not well defined but are represented by arcuate ridges and grooves, some of which have distinctly higher albedo than surrounding material.

The structure does not have the relatively high-albedo signature of palimpsests, nor does it have the ring spacing characteristic of multi-ring basins. Although the structure is vaguely concentric, no one arcuate ridge or groove can be traced completely around it. Indeed, few of the arcuate features can be traced through more than a quadrant of the structure. Although it appears to be older than the furrow systems superposed on it, arcuate ridges-grooves of the structure seem to cut the northwest- and northeast-trending furrows at the northwest and northeast margins, respectively, of the structure.

A semicircular ridge, 50 km in diameter and lying in the south half of the structure, is almost at its center. A northwest-trending fracture extends across part of the east quadrant; the south quadrant is cut by an arcuate fracture that trends generally north. Two radial, staight-line fractures diverge slightly as they extend southwestward from the center of the structure, forming a part of the northeast-southwest furrow.

The area of intersection of the northwest- and northeast-trending furrows appears, on some images, to be smooth. That part of the northeast-southwest furrow northeast of the structure is not aligned with that part of the furrow to the southwest but is offset some 50 km northwestward. The indistinct concentric pattern created by arcuate ridges and grooves extends unbroken farther eastward than in any other direction, but 375 km to the northwest, isolated segments of grooves and ridges concentric about the center of the structure can be identified (Fig. 1).

Although no quantitative topographic data are available, the structure does not appear, on the several images on which it has been studied (Voyager 2 PICNO's 0106J2-001, 0437J2-001, 0440J2-001, 0452J2-001), to be significantly higher or lower than the surrounding area. Two 25-km diameter craters lie southeast of the structure's center; two relatively fresh 10-km diameter craters lie southwest of the center; another such

crater lies north-northwest of the center. Based on visual examination and when compared with crater densities determined by Shoemaker and others (1982, p. 440), the area of the circular structure within 125 km radius of the center is deficient in 10-km diameter craters compared to the average for most areas of Galileo Regio.

Discussion: The large circular structure with the "cross-hair" pattern in central Galileo Regio does not have the high albedo nor the generally smooth texture of most palimpsests. Its indistinct, closely spaced, incomplete arcuate ridges and grooves do not resemble the more widely spaced rings of multiring basins. Almost certainly, its location at the intersection of two furrow systems is related to its origin.

Although within the size range of the "coronae" or "ovoids" identified on radar images of Venus returned by the Soviet Venera 15 and 16 spacecraft, and possessing a surface texture similar to the coronae, the structure is not elliptical as are the coronae of Venus reported by Barsukov and others (1985). The structure in Galileo Regio also does not have identifiable flow features associated with it as do the coronae on Venus, interpreted by the Russians as volcano-tectoic features.

Squyres (1981, p. 656-661) identified two domes on Ganymede, both approximately 260 km in diameter; one lies in grooved terrain, the other in uncertain terrain. One of the domes is associated with a field of 5-km diameter craters, interpreted to be secondary craters; the resolution of the image on which the other dome was identified is so low that secondary craters could not be recognized even if they occur there. Squyres (1981) suggested two possible origins for the domes: (1) "ice volcanism triggered by impact," and (2) "isostatic upwarping of an impact crater formed in a thin crust." The Galileo Regio structure, however, does not appear to be domal.

Conclusions: The distinctive circular structure in Galileo Regio may have originated by:

1. Impact and subsequent relaxation of the crust at a sufficiently early time for the albedo to have been lowered to that of the surrounding region, i.e. the structure may be a very old palimpsest.
2. Doming of the type described by Squyres but followed by relaxation of the uplift, thus creating a compressional stress field that produced the arcuate ridges and grooves and, perhaps, associated faults.
3. Tidal stresses acting on a weak, thin area of the crust and generating upwelling of subcrustal material.

The intriguing possibility exists that the structure may represent the locus of early upwelling of mantle material, creating a system of arcuate ridges and grooves as the crustal and mantle material moved radially outward from the center of the upwelling plume. The furrow systems were superposed on the structure later, although renewed movement along some of the arcuate features, including possibly faults, may have resulted in the cross-cutting of the northwest- and northeast-trending furrows. The point of upwelling, as a zone of weakness, may have in-

fluenced the location of the furrows and of their intersection.

References:

1. Barsukov, V. L. and associates, 1985, The geology and geomorphology of the Venus surface as revealed by the radar images obtained by Veneras 15 and 16: Paper presented at Venus symposium, Vernadsky Institute of Geochemistry and Analytical Chemistry, Moscow, August, 1985.
2. Shoemaker, E. M., Joe Boyce, B. K. Lucchitta, Q. R. Passey, S. W. Squyres, and D. E. Wilhelms, 1981, The geology of Ganymede, in Morrison, D. and N. Morrison, eds., Satellites of Jupiter, University of Arizona Press, Tucson, p. 435-520.
3. Squyres, S. W., 1981, the morphology and evolution of Ganymede and Callisto: Ph.D. Thesis, Cornell University (1980), in Advances in Planetary Geology, 1980: NASA TM-84412, p. 365-718.

Figure 1. Circular structure, 250-275 km in diameter and located at lat 41° and long 143°, lies immediately above two relatively large craters (45 km and 75 km diameters), lower right. Prominent furrows oriented N 60° W. Upper left, arcuate ridges whose centers of arc appear to coincide with center of circular structure, 375 km to southeast (Voyager 2 PICNO 0437J2-001).

ENCELADUS: REFINED SEARCH FOR COLOR AND REFLECTANCE VARIATIONS AMONG GEOLOGIC UNITS

J. Veverka and P. Thomas, Center for Radiophysics and Space Research, Cornell University

Arguments that Enceladus may be coated with a layer of relatively fresh frost are based in part on photometric observations including the satellite's very high albedo and the lack of color differences among geologically distinct terrains (e.g., Buratti et al., 1982; Morrison et al., 1984).

Estimates of the Bond albedo (fraction of total incident solar energy reflected by the satellite) can be obtained by two independent methods from Voyager data. From IRIS measurements J. Pearl derived 0.89 ± 0.02 (see Cruikshank et al., 1983), while Buratti and Veverka (1984) obtained 0.90 ± 0.1 from imaging observations. Not only does the satellite reflect 90% of incident sunlight, but the scattering pattern is unusually back-scattering (i.e., the geometric albedo is very high). Three independent methods of determining the average geometric albedo all give values in excess of unity, the most likely value being 1.15. Voyager images suggest that the average geometric albedo of the leading hemisphere is probably 20% lower than that of the trailing hemisphere (Buratti and Veverka, 1984).

We have used Hapke's function to remove first-order photometric effects from Voyager 2 images of the trailing face of Enceladus to better determine the degree to which reflectance and color variations exist among the distinct geologic units. Relative crater counts (Fig. 1) suggest that some of these units must differ significantly in age, although the absolute chronology is uncertain (Smith et al., 1982).

To test for color variations we determined average values of the ORANGE/VIOLET ratio for the different units defined by Smith et al. (Fig. 2). There are two important conclusions: (1) color variations are not detectable within a given unit; and (2) the color of all units on this face of the satellite is essentially uniform. The minute differences seen in Fig. 2 fall within the uncertainties involved in the measurements, and are not correlated with relative "age" of a unit.

Figure 3 shows the variation of reflectance with geologic terrain; the average value of the reflectance for the trailing hemisphere has been set to unity. Note that photometric function effects (i.e., allowing for differences in lighting and viewing conditions) cannot be removed as accurately for topographically rugged terrains (ct and rp) as they can for smoother regions, leading to some of the slight relative differences seen in Fig. 3. All in all, the general variations in reflectance are confined to less than ± 10% of the mean value. The error bars shown in Fig. 3 represent the scatter in reflectance values found among different 5 × 5 km sampling areas within a terrain.

This work was supported by NASA Grant NSG-7156.

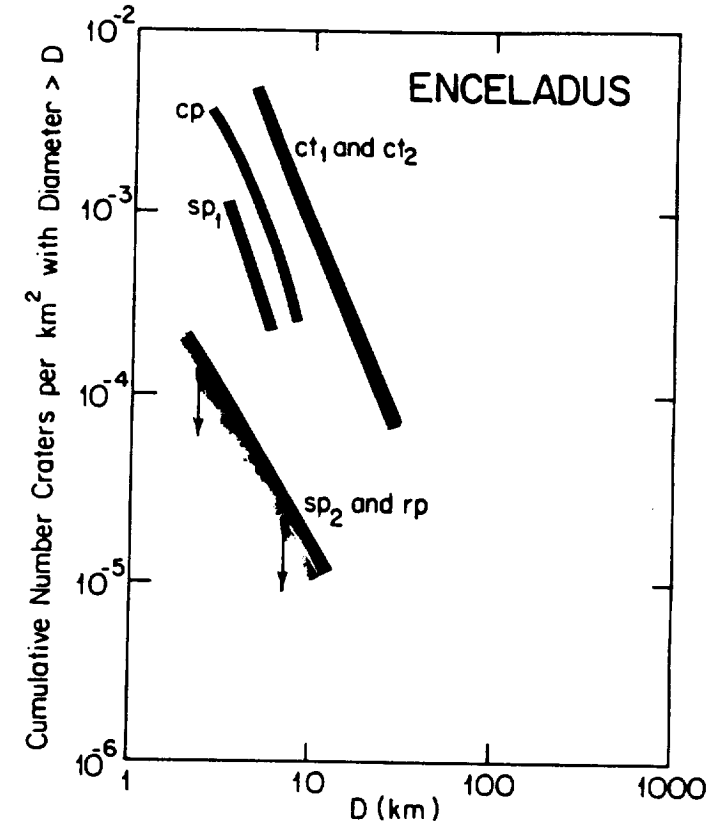

Fig. 1. Cumulative size-frequency distribution of impact craters on Enceladus from Smith et al. (1982). Cratered terrain = ct_1 and ct_2; cratered plains = cp; smooth plains = sp_1 and sp_2; and ridged plains = rp.

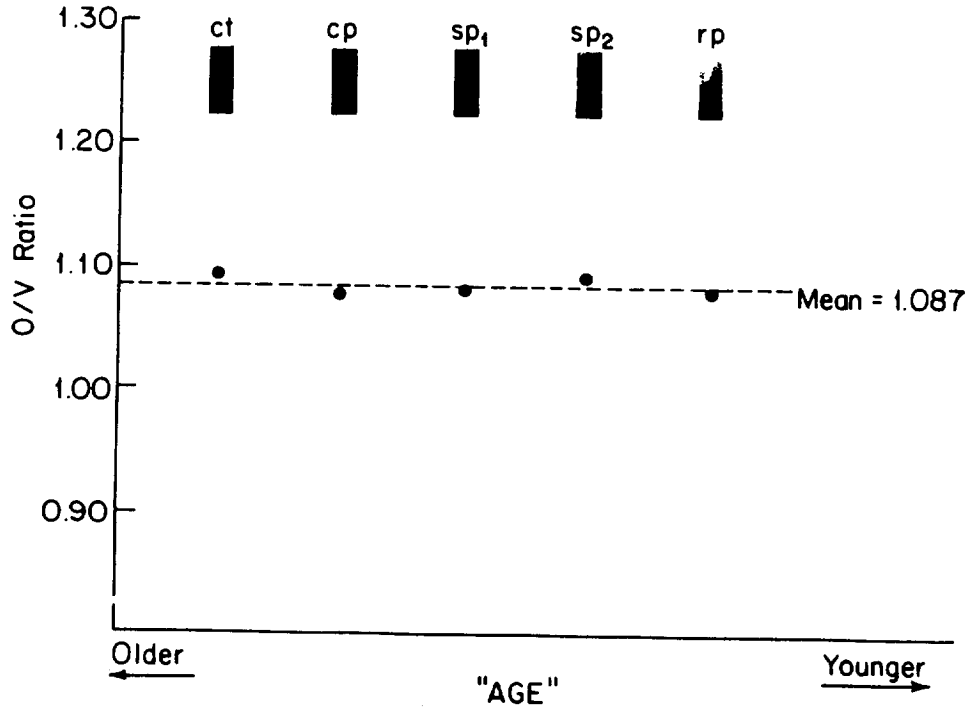

Fig. 2. Average values of the ORANGE/VIOLET color ratio for terrains on Enceladus determined from Voyager 2 images. Approximate effective center passbands are 0.41 μm for VIOLET and 0.59 μm for ORANGE.

REFERENCES:

Buratti, B., and J. Veverka (1984). Voyager photometry of Rhea, Dione, Tethys, Enceladus and Mimas. Icarus 58, 254-264.

Buratti, B., J. Veverka, and P. Thomas (1982). Voyager photometry of Saturn's satellites. Rept. Planetary Geology Program (H. E. Holt, ed.), NASA TM 84127.

Cruikshank, D. P., L. A. Lebofsky, and J. Veverka (1983). Satellites of Saturn: Optical properties. In Saturn (T. Gehrels and M. Matthews, eds.), Univ. of Arizona Press, Tucson.

Morrison, D., T. V. Johnson, E. M. Shoemaker, L. A. Soderblom, P. Thomas, J. Veverka, and B. A. Smith (1984). Satellites of Saturn: Geological Perspective. In Saturn (T. Gehrels and M. Matthews, eds.), Univ. of Arizona Press, Tucson.

Smith, B. A., et al. (1982). A new look at the Saturn system: The Voyager 2 images. Science 215, 504-537.

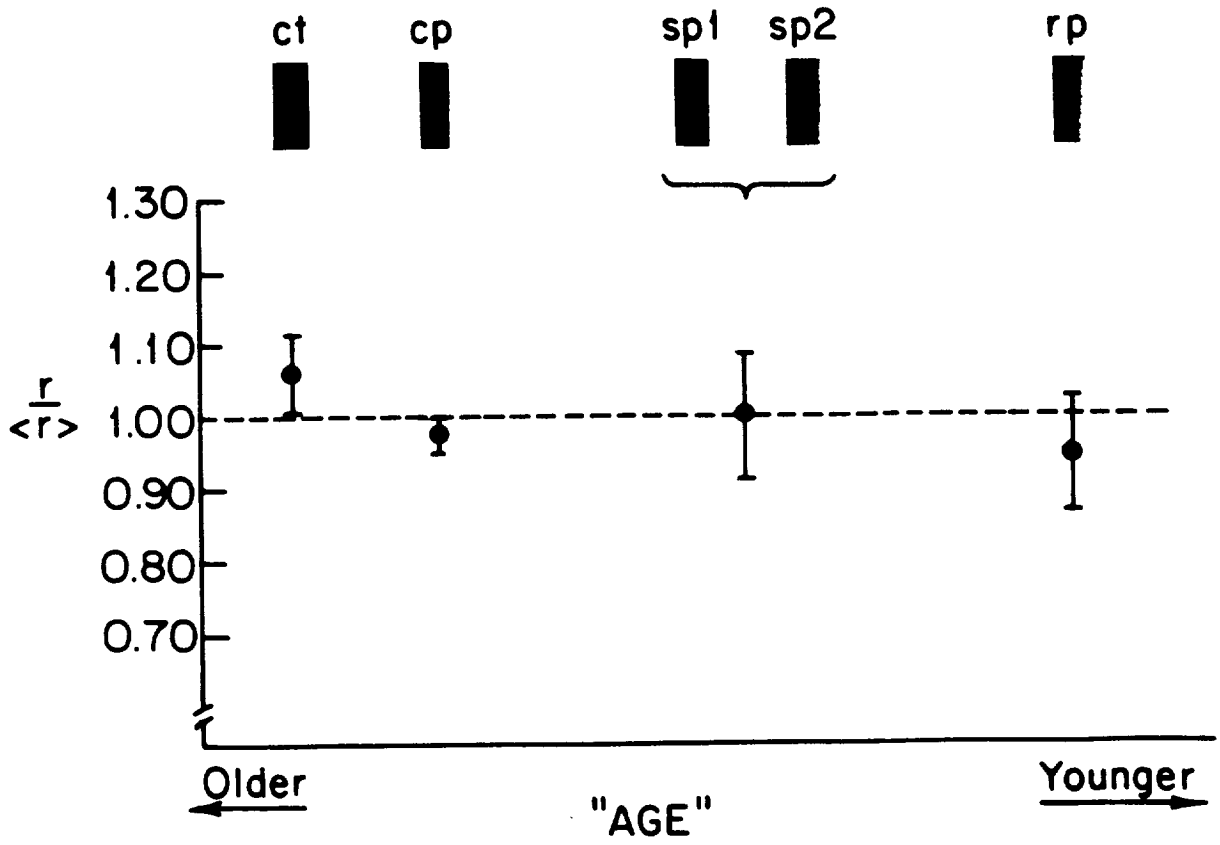

Fig. 3. Average relative reflectances for terrains on Enceladus determined from Voyager 2 VIOLET images. The average value of the reflectance for the trailing hemisphere (<r>) has been set to unity.

Subcentimeter-size particle distribution functions in Saturn's rings from Voyager radio and photopolarimeter occultation data

Howard A. Zebker, Jet Propulsion Laboratory, G. Leonard Tyler and Essam A. Marouf, Stanford University.

Analysis of measurements of the scattered and direct components of Voyager 1 radio occultation signals at 3.6- and 13-cm wavelengths yields estimates of the distribution functions of supracentimeter-size particles and thickness of relatively broad (>1000 km wide) regions in Saturn's rings (Tyler et al., 1983; Zebker et al., 1985; Zebker and Tyler, 1984). The amplitude of these signals is relatively unaffected by particles smaller than a wavelength in size, thus the distribution of subcentimeter-size particles in the rings cannot be inferred from these data alone. If, however, measurements of the signal amplitude at a shorter wavelength are combined with the previously analyzed radio data, we can determine the distribution functions characterizing the smaller particles. In particular, the additional measurement of signal amplitude at 0.26 μm wavelength from Voyager photopolarimeter occultation data (Esposito et al., 1983) allows inference of subcentimeter-size distribution functions for a number of relatively narrow (30-100 km wide) embedded ringlets in ring C and Cassini's division. These narrow features appear to be analogs of the Uranian rings, therefore the same technique can be applied to future Uranus ring occultation observations.

If we consider size distribution functions of arbitrary form, many solutions are found that are consistent with the three available observations of signal amplitude. In order to limit the formal solution set to functions that are likely on a geophysical basis, we constrain the solutions to be of the power-law form with sharp lower- and upper-size cutoffs. We calculate the best-fit power-law (in the least square error sense) to the three observations of signal strength at 0.26 μm, 3.6 cm, and 13 cm, for several of the embedded features in Saturn's rings. Results of this process are given in Table 1. We note that in each case but two the inferred power law index is approximately 3, which is similar to the power-law index that describes the distribution of supracentimeter-size particles in the broad ring features. Thus, it seems likely that the accumulations of particles in the embedded ringlets are distributed similarly to the particles in the ring system as a whole, and that the forces responsible for creation and maintenance of the embedded features are not highly size-selective in nature.

Knowledge of the full particle size distribution functions permits us to reconstruct a picture of how the ring system would actually appear to a nearby observer. Such a computer-generated image is shown in Figure 1, which illustrates a typical 3 m by 3 m region in ring A.

Mie scattering theory predicts that the measured phase of the radio occultation signals is highly sensitive to particles ranging from 0.1 to 1.0 wavelengths in size, thus additional constraints on the subcentimeter-

size particle distribution can in principle be determined from these phase measurements. We illustrate sample amplitude and phase measurements at both radio frequencies in Figure 2, where we plot the phase and the opacity (the logarithm of normalized signal intensity) at both radio frequencies. We note that a shift in phase is coincident in location with the observed signal attenuation. However, the numerical values of the phase shifts (-0.4 radians at 3.6 cm, -2.3 radians at 13 cm) are inconsistent with the values predicted by Mie theory. Thus, it is possible that the theory is incomplete and inapplicable to the present analysis, or that there is an additional physical factor, such as a plasma in the ring system, that is corrupting the measurements. We are continuing to study this.

References:

Tyler, G.L., E.A. Marouf, R.A. Simpson, H.A. Zebker, and V.R. Eshleman, The microwave opacity of Saturn's rings at wavelengths of 3.6 and 13 cm from Voyager 1 radio occultation, ICARUS 54, 160-188, 1983.

Esposito, L.W., D.L. Coffeen, C.W. Hord, A.L. Lane, M. O'Callaghan, R.B. Pomphrey, M. Sato, K.E. Simmons, and R.A. West, Voyager photopolarimeter stellar occultation of Saturn's rings, J. GEOPHYS. RES. 88, 8643-49, 1983.

Zebker, H.A., and G.L. Tyler, Thickness of Saturn's rings inferred from Voyager 1 observation of microwave scatter, SCIENCE 223, 396-98, 1984.

Zebker, H.A., E.A. Marouf, and G.L. Tyler, Saturn's rings: particle size distributions for thin-layer models, in press, ICARUS, 1985.

Table 1

Ringlet Location, km from Saturn Center		Power Law Index	Lower Size Cutoff, M	Upper Size Cutoff, M
Start	Stop			
79230	79260	3.7	0.003162	0.316
84780	84930	2.7	0.000056	0.100
85670	85695	3.6	0.003162	0.178
85930	85970	2.8	0.000316	0.100
86400	86580	2.8	0.000178	0.100
87185	87210	3.0	0.000032	0.178
87300	87325	3.2	0.001778	0.178
87500	87580	3.2	0.000018	3.162
88380	88590	3.0	0.001000	0.178
88707	88723	3.1	0.000032	10.000
89800	89930	3.3	0.001778	0.316
90420	90600	2.9	0.000056	10.000

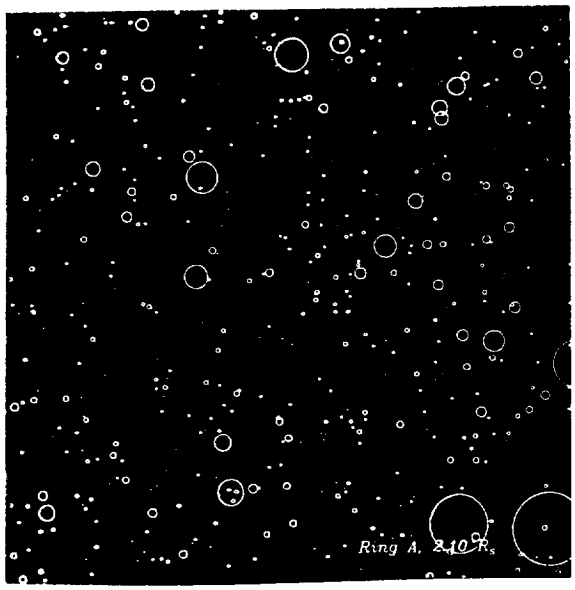

Figure 1. Computer-generated "image" of a 3m by 3m portion of Saturn's ring A.

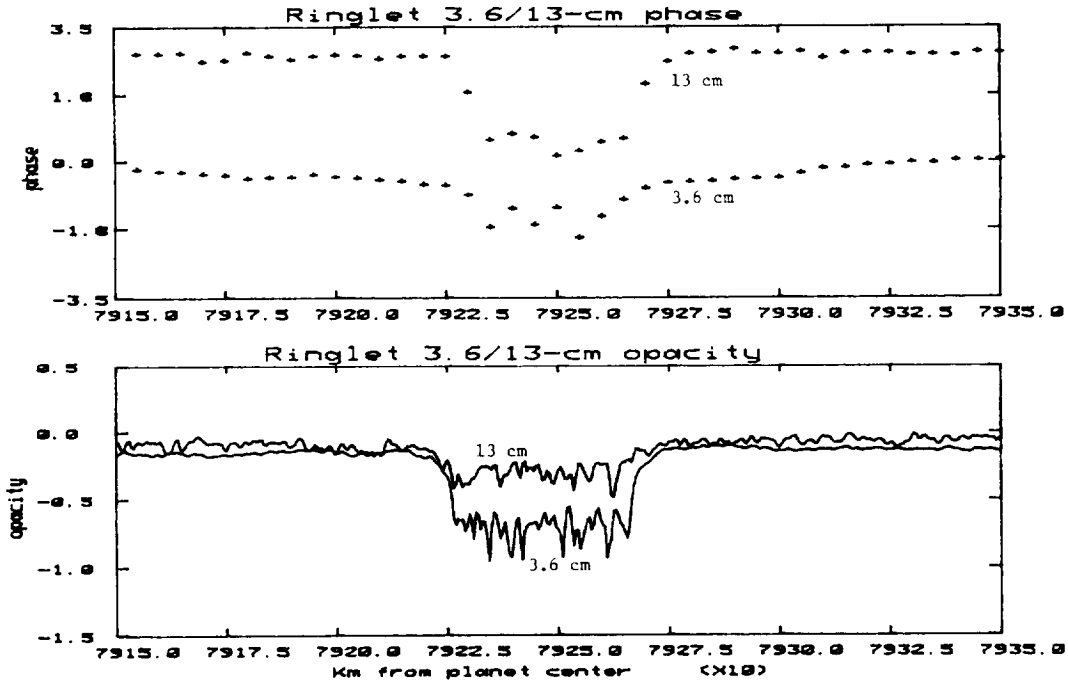

Figure 2. Sample phase and opacity measurements.

CHAPTER 3

LUNAR ORIGIN AND SOLAR SYSTEM DYNAMICS

COSMOGONY AS AN EXTRAPOLATION OF MAGNETOSPHERIC RESEARCH

H. Alfvén, University of California, San Diego

A theory of the origin and evolution of the Solar System which considered electromagnetic forces and plasma effects is revised in the light of new information supplied by space research. In situ measurements in the magnetospheres and solar wind have changed our views of basic properties of cosmic plasmas. These results can be extrapolated both outwards in space, to interstellar clouds, and backwards in time, to the formation of the solar system. The first extrapolation leads to a revision of some cloud properties which are essential for the early phases in the formation of stars and solar nebulae. The latter extrapolation makes it possible to approach the cosmogonic processes by extrapolation of rather well-known magnetospheric phenomena.

Pioneer-Voyager observations of the Saturnian rings indicate that essential parts of their structure are "fossils" from cosmogonic times. By using detailed information from these space missions, it seems possible to reconstruct certain events 4-5 billion years ago with an accuracy of a few percent. This will cause a change in our views of the evolution of the solar system.

MAGNETOSPHERIC RESEARCH AND THE HISTORY OF THE SOLAR SYSTEM

H. Alfvén, University of California, San Diego

Instruments in space make it now possible to observe our cosmic environment not only in the visual and radio wavelengths but also in the infrared, ultraviolet X ray and γ ray parts of the electromagnetic spectrum. This reveals that quite a few of the generally accepted astrophysical concepts can no longer be valid. But in order to understand what we see, it is essential to clarify what laws of physics govern the cosmic phenomena. As (at least by volume) more than 99.99% of the universe consists of plasma, plasma physics is essential. Another and at least as important a change in our basic astrophysical concepts is due to the in situ measurements in the magnetospheres of the planets. These have demonstrated that cosmic plasmas have properties drastically different from those that were rather generally accepted as late as 5 or 10 years ago. These latter were based on the classical theory of plasmas (by Chapman and Cowling and others) which was admirable from a mathematical point of view but unfortunately did not agree very well with experiments and observations. Measurements in the laboratory and in situ measurements by spacecraft have shown that plasma physics must be considered more as an empirical than a purely mathematical science.

Dynamical Constraints on the Origin of the Moon

A. P. Boss, Carnegie Inst. of Washington
S. J. Peale, University of California at Santa Barbara

ABSTRACT

Dynamical studies dealing with the origin of the Moon are described and used to try to eliminate dynamically impossible or implusible theories of lunar origin. The origin of the Moon is discussedd within the context of the general theory of terrestrial planet formation by accumulation of planestesimals. The past evolution of the lunar orbit is of little use in differentiating between the theories, primarily because of the inherent uncertainty in a number of model parameters and assumptions. The various theories that have been proposed are divided into six categories. Rotational fission and disintegrative capture appear to be dynamically impossible for viscous protoplanets, while precipitation fission (precipitation of Moon-forming material from a hot, extended primordial atmosphere of volatilized silicates), intact capture, and binary accretion appear to be dynamically implausible. Precipitation fission and binary accretion suffer chiefly from having insufficient angular momentum to form the Moon, while intact capture requires forming the Moon very close to the Earth without encountering any perturbations prior to capture. The only mechanism so far proposed which is apparently not ruled out by dynamical constraints and which also seems the the most plausible involves formation of the Moon following a giant impact which ejects portions of the differentiated Earth's mantle and parts of the impacting body into circumterrestrial orbit. The moon must have accreted subsequently from this circumterrestrial disk. The giant impact model contains elements of several of the other models, and appears to be dynamically consistent with the absence of major satellites for the other terrestrial planets. While the giant impact mechanism for forming the Moon thus emerges as the theory with the least number of obvious flaws, it should be emphasized that the model is relatively new and has not been extensively developed nor thoroughly criticized. Much further work must be done to learn whether the giant impact mechamnism for lunar formation can be made into a rigorous theory.

Protostellar angular momentum transport by spiral density waves

P. Cassen, Institute for Theoretical Physics, Santa Barbara and Ames Research Center;
C. Yuan, City College of New York

The gravitational collapse of molecular clouds or cloud cores is expected to lead to the formation of stars that begin their lives in a state of rapid rotation. It is known that, in at least some specific cases, rapidly rotating, self-gravitating bodies are subject to instabilities that cause them to assume ellipsoidal shapes. The application of rotational stability criteria to a specific model of star formation (Terebey *et al.* 1984) leads to the conclusion that the growth of stellar angular momentum is limited by its transfer to a disk. Excess accreted angular momentum can be transferred by torques associated with spiral density waves (Goldreich and Tremaine, 1979) induced by even a slight protostellar triaxiality. Furthermore, viscous damping of the density waves is likely to cause the excess angular momentum to be deposited within a small region close to the protostar. Thus, it is appropriate to treat that part of the growing protostellar disk beyond the outer Lindblad resonance as an accretion disk with a torque applied to its inner edge.

This situation is directly relevant to some models of the evolution of the protosun and solar nebula. Hoyle (1960) noted that a protosolar cloud possessing the angular momentum of the planets, augmented to include that of the hydrogen and helium of a solar abundance nebula, would attain centrifugal balance with solar gravity at a radius much smaller than the size of the present solar system. For instance, a disk formed by the collapse of a rotating, singular isothermal sphere would have a radius of only 10^{12} cm under these conditions, assuming strict conservation of angular momentum (Cassen and Moosman, 1981). Hoyle proposed that angular momentum was transferred from the protosun to the planetary material by magnetic coupling, although he did not attempt to calculate the evolution of the disk, and therefore did not demonstrate that a solar nebula, in the usual sense, would be produced. The mechanism discussed here represents another way in which angular momentum can be transferred between star and disk.

Cassen and Summers (1983) calculated the evolution of a viscous disk under similar conditions. They considered the case in which a disk acquired *all* of the angular momentum of a collapsing cloud through the action of an unspecified torque exerted at an inner boundary, r_*. Material falling onto the disk outside of r_* was ignored. The acquired angular momentum was distributed throughout the spreading disk by viscosity. As in that case, a disk receiving angular momentum by gravitational torques would spread to solar system dimensions by viscosity as long as $(\nu M_\odot/\dot{M})^{\frac{1}{2}}$ was large enough, *i.e.*, $\simeq 10^{15}$ cm. Its total angular momentum would be $< M_*(GM_*r_*)^{\frac{1}{2}}/6$, (the excess angular momentum accreted by the star and transferred to the disk), plus that accreted by the disk directly. It is estimated that the angular momentum of the primitive solar nebula was at least 5×10^{51} gm–cm^2/sec (*e.g.*, Cassen and Moosman, 1981). From the above formula, about half of this amount (assuming $r_* = 3 \times 10^{11}$ cm) could have been supplied by gravitational torques as described here. The remainder would have to have been accreted directly onto the disk, or transferred form the star by other means. Unlike the situation considered by Hoyle, in which the sun ends up rotating slowly, the result here would be a solar nebula surrounding a *rapidly* rotating sun, each containing comparable amounts of angular momentum. Presumably the sun

would be subsequently slowed by the action of a magnetic wind (Weber and Davis, 1967).

Variations in the thermal, density, or rotational structure of the cloud could lead to different sequences of events. It is conceivable, for instance, that the star never attains enough angular momentum to become triaxial. This might occur if there was a greater amount of low angular momentum material concentrated toward the center of the protostellar cold than assumed in the model employed here. However, it is likely that the opposite would be more common; that is, toward the center of the could the density would be *less* than that given by the r^{-2} prescription for a singular isothermal sphere. Moreover, the material near the center might have a higher rotation rate than the rest of the cloud if the outward transfer of angular momentum ws not completely effective during the formation of the cloud core. Under these circumstances, the star would be expected to become triaxial before a disk (or an outer Lindblad resonance) existed.

Yet another possibility is that the disk and protostar grow simultaneously, at comparable rates, leading to gravitational instabilities in the disk (Cameron; 1978, 1985). Numerical experiments designed to illuminate theories of galactic structure, in which disks containing as much or more material than is contained in a central condensation are simulated, often develop bar-like or oval structures. Such configurations, which are wave-like themselves, are expected to generate strong density waves and associated torques, thereby delivering angular momentum to material in the outer portions of the disk. In this way, the entire inner region of a massive disk could act as the protostar does in the example previously discussed.

Yet another possibility is suggested by the recent calculations of Boss (1985), in which something similar to that described above happens, although for apparently different reasons. Boss treats the collapse of a cloud with initially uniform density and angular velocity, with imposed nonaxisymmetric density perturbations at the 5% level. After one free-fall time, a bar-like structure occupying the inner 100 AU of the cloud has formed. As Boss demonstrates, the effect of such a configuration is the efficient transfer of angular momentum outwards.

To further define the rotational history of protostars, it will be necessary to construct more detailed models of their internal structures (*i.e.*, their density and angular momentum distributions) on the one hand, and to continue the exploration of the consequences of rotational instability, on the other. Of particular importance will be the determination of the timing of such events as the onset of nuclear burning and the associated redistribution of angular momentum, the growth of secular instabilities, the initiation of mass loss, and the generation of magnetic fields. All of these events are associated with phenomena that are potentially important for the coupling of protostellar rotation and disk evolution.

Boss, A.P. (1985). Three dimensional calculations of the formation of the presolar nebula from a slowly rotating cloud, *Icarus*, **61**, 3-9.

Cameron, A.G.W. (1978). Physics of the primitive sola accretion disk. *Moon and Planets*, **18**, 5-40.

Cameron, A.G.W. (1985). Formation and evolution of the primitive solar nebula, in *Protostar and Planets II*. University of Arizona Press, Tucson.

Cassen, P. and Moosman, A. (1981). On the formation and evolution of protostellar disks, *Icarus,* **48**, 353-376.

Cassen, P. and Summers, A.L. (1983). Models of the solar nebula, *Icarus*, **53**, 26-40.

Goldreich, P. and Tremain, S. (1979). The excitation of density waves at the Lindblad and corotation resonances by an external potential, *Astrophys. J.,* **233**, 857-971.

Hoyle, F. (1960). On the origin of the solar nebula, *Quart. J. Roy. Astr. Soc.*, **1**, 28-55.

Terebey, S., Shu, F.C., and Cassen, P.M. (1984). The collapse of the cores of slowly rotating isothermal clouds, *Astrophys. J.,* **286**, 529-551.

Weber, E.J. and Davis, L. (1967). The angular momentum of the solar wind, *Astrophys. J.,* **148**, 217-227.

MOON ORIGIN: THE IMPACT-TRIGGER HYPOTHESIS

William K. Hartmann
Planetary Science Institute

The concept of large impactors striking the planets late in their formation has been widely developed and supports the impact-trigger hypothesis of lunar origin. One line of evidence comes from the distribution of spin and orbital properties, especially obliquities. These properties are too varied to have resulted if all accreting mass were in very small planetesimals. We have constructed solar system models with different sources of large impactors, to study stochastic variation in resulting obliquities and periods. The models suggest that largest impactor masses often lay in the range of 0.3 to 20% of target planetary masses. Some may have been even larger. Stochastic variations of impact outcomes are considerable, even if impactor size is fixed; a large impactor could thus trigger formation of a relatively large satellite for at least one, but not all, planets.

GIANT IMPACTORS: PLAUSIBLE SIZES AND POPULATIONS

William K. Hartmann and Sheila Vail
Planetary Science Institute

The impact trigger hypothesis proposes that an unusally large planetesimal impact on the early Earth initiated lunar formation. Such an impact would dislodge hot, volatile-poor, iron-poor material to form the moon. Several lunar properties favor this hypothesis: lunar iron and volatile deficiency; angular momentum of the Earth-moon system; similar O isotopes, bulk iron contents, and densities of Earth's mantle and the moon. A common objection, that the impact is ad hoc, is refuted: stochastic large impacts are an acceptable, if not essential, part of planet formation. The intense early bombardment, averaged during Earth's formation, was several 10^9 times the present peteoritic mass flux, consistent with a giant impact. The effects of forward launch of debris as a result of planetesimal shearing or jetting of ejecta in a near-tangential impact, rotational spinup, and ordinary cratering ejection combine in different ways to create different impact-trigger sub-models. An impactor mass of a few M_{moon} to $\sim M_{Mars}$ has been estimated from three independent lines of evidence. A quantitative estimate of ejecta velocities indicates that a few lunar masses of could have been ejected material at speeds between circular and escape velocities; "second burn" gas expansion effects may increase this value and help the material achieve orbit.

EQUATORIAL CLUSTERING OF CRATERS AND MULTI-RING BASINS: POSSIBLE INDICATIONS OF LUNAR POLAR DISPLACEMENT

Donald M. Hooper and Ted A. Maxwell, Center for Earth and Planetary Studies, National Air and Space Museum, Smithsonian Institution, Washington, D.C. 20560

Runcorn (1982, 1983) and Melosh (1975a, 1975b) present the hypothesis that large impacts have reoriented the lunar axis of rotation during multi-ring basin formation. Such a reorientation may be recorded in the remanent lunar magnetism as each period of polar displacement has a corresponding paleo-equator and paleo-pole. Runcorn (1982, 1983) further suggests that the multi-ring basins were formed at low latitudes; the impactors were not in heliocentric orbit but were satellites in the Earth-Moon system, which would settle into orbits exactly coplanar with the Moon's equator. One of the supporting lines of evidence for lunar polar wondering used by Runcorn is the distribution of impact basins about the proposed paleo-equators. This argument was based on qualitative observations of multi-ring basins compared to prior equators, but was not tested rigorously. In order to compare the frequency of basins with the proposed equators, as well as test for other preferential distribution, we have analyzed the locations of both basins and post-mare craters to determine validity of the "great circle" alignments.

The ages of paleo-pole positions based on lunar magnetic data differ from the time-stratigraphic age assignments used in lunar mapping, which results in a somewhat artificial age sequence for pre-Nectarian, lower Nectarian, and upper Nectarian-Imbrian age basins. As summarized in Figure 1, each group of multi-ring basins with a corresponding paleo-pole and paleo-equator position was plotted on overlays of the lunar 1:5,000,000 geologic maps. Distances from each basin to the respective equator were calculated and the number of basins was normalized with respect to the area in each 10° band from the equator in order to determine basin density. The density is plotted against the distance to the corresponding paleo-equator in Figure 2. For both lower Nectarian and upper Nectarian-Imbrian age basins, there is a slight positive correlation between density and decreasing distance from the equator, although this tendency alone does not seem to be sufficient support for the polar wandering hypothesis. Pre-Nectarian basins, in fact, show a negative correlation with the proposed paleo-equator, which is due to the Smythii and Marginis basins, located near the postulated paleo-poles of that time period.

Another test for alignment of lunar multi-ring basins about proposed paleo-equators involved plotting each basin and paleo-equator on an overlay of a Schmidt stereonet. This method produced the same results: Imbrian-Upper Nectarian basins being the most aligned along the paleoequator and pre-Nectarian basins being more scattered. To search for possible alternative alignments of greater basin density, the stereonet was rotated, but no such zones were found.

Assuming that smaller bodies would also impact preferentially in the equatorial zone, a similar analysis was done using the mapped craters greater than 20 km in diameter. The craters were grouped into pre-Nectarian, Nectarian, Imbrian, Eratosthenian, and Copernican Periods,

but the pre-Nectarian and Nectarian craters were dropped from the study due to their susceptibility to later disturbance and obscuration. Imbrian craters were normalized for both obstructions in the Imbrian record and area, and when plotted the data demonstrated an increase in density with distance from the paleo-equator--not indicative of equatorial clustering. Craters of the Eratosthenian and Copernican Periods, however, showed different results. When plotted against the present lunar equator, the graph of these craters, as shown with the 1σ error bars, displayed a significant increase in crater density with decreasing distance from the equator (Fig. 3).

The results of this study do not disprove Runcorn's proposals for lunar polar wandering, but they do indicate the need for alternative supportive evidence, since the results of the basin distribution are inconclusive. If such a hypothesis of equatorial clustering of craters and basins is found to be valid for the planets, as suggested by the distribution of young lunar craters, this technique would serve as an indication of polar displacement. The Moon has probably not always had its present orientation; nevertheless, it is apparent that basin distribution alone cannot be used to support the positions of past lunar axes of rotation.

References

Melosh, H. J., Mascons and the Moon's Orientation. Earth Planet. Sci. Lett., 25, 322-326, 1975a.

Melosh, H. J., Large Impact Craters and the Moon's Orientation. Earth Planet. Sci. Lett., 26, 353-360, 1975b.

Runcorn, S. K., Primeval Displacements of the Lunar Pole. Phys. Earth Planet. Inter., 29, 135-147, 1982.

Runcorn, S. K., Lunar Magnetism, Polar Displacements and Primeval Satellites in the Earth-Moon System. Nature 304, 589-596, 1983.

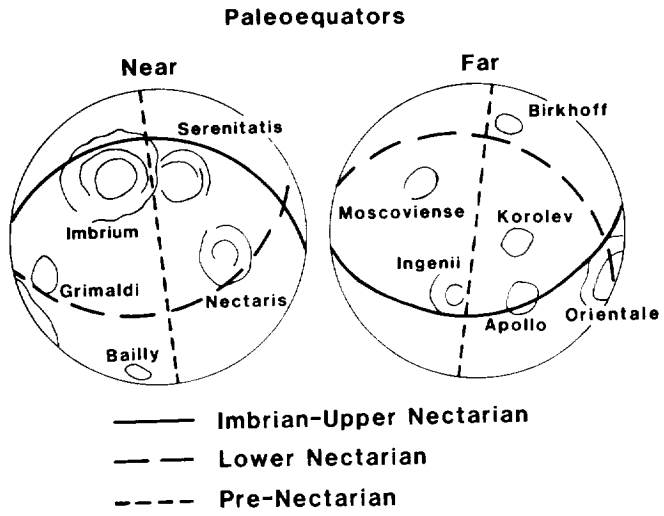

Figure 1. Location of suspected lunar paleo-equators.

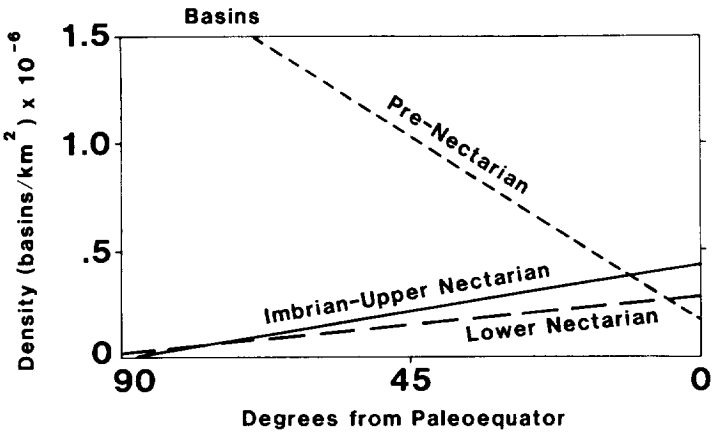

Figure 2. Multi-ring basin density as a function of distance from paleo-equator.

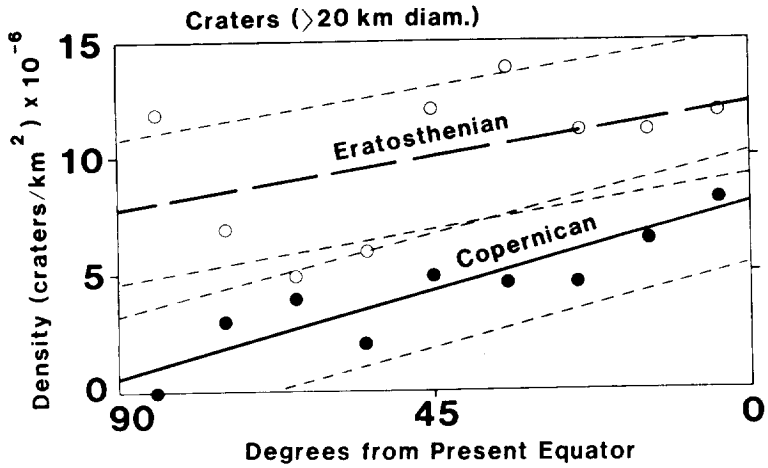

Figure 3. Crater density as a function of distance from present lunar equator.

Planetesimal Dissolution in the Envelopes of the Forming, Giant Planets

James B. Pollack, Space Science Division, NASA Ames Research Center, Moffett Field, CA, Morris Podolak, Tel-Aviv University, Tel-Aviv, Israel, Peter Bodenheimer, University of California, Santa Cruz, CA., Bruce Cristofferson, IMI, Inc., San Jose, CA

We have assessed the ability of planetesimals to penetrate through the envelopes of growing giant planets that form by a "core-instability" mechanism. According to this mechanism, a core grows by the accretion of solid bodies in the solar nebula and the growing core becomes progressively more effective in gravitationally concentrating gas from the surrounding solar nebula in an envelope until a "runaway" accretion of gas occurs. In performing this assessment, we have considered the ability of gas drag to slow down a planetesimal; the effectiveness of gas dynamical pressure in fracturing and ultimately finely fragmenting it; the ability of its strength and self-gravity to resist such fractioning; and the degree to which it is evaporated due to heating by the surrounding envelope, including shock heating that developes during the supersonic portion of its trajectory. We also consider what happens if the planetesimal is able to reach the core at free fall velocity and the ability of the envelope to convectively mix dissolved materials to different radial distances. These calculations were performed for various epochs in the growth of a giant planet with the model envelopes obtained by Bodenheimer and Pollack. As might have been anticipated, our results vary significantly with the size of the planetesimal, its composition, and the stage of growth of the giant planet and hence the mass of its envelope. Over much of the growth phase of the core, prior to its reaching its critical mass for runaway gas accretion, icy planetesimals less than about 1 cm in size dissolve in the outer region of the envelope, ones larger than about 1 cm and smaller than about 1 km dissolve in the middle region of the envelope, and ones larger than 1 km either reach the core interface or dissolve in the deeper regions of the envelope. Similarly rocky planetesimals smaller than about a kilometer dissolve in the middle portion of the envelope, while larger ones can penetrate more deeply. Furthermore, the convection zones of the envelopes during this stage are confined to localized regions and hence dissolved material experiences little radial mixing then. Thus, if much of the accreted mass is contained in planetesimals larger than about a kilometer, the critical core mass for runaway accretion is not expected to change signficantly when planetesimals dissolution is taken into account.

After accretion is terminated and the planet contracts towards its present size, the convection zone in the envelope grows until it encompasses the entire envelope. Therefore, dissolved material should eventually become well mixed through the envelope. We propose that the envelopes of the giant planets should contain significant enhancements above solar proportions in the abundances of virtually all elements except H, He, and some of the other rare gases, with the magnitude of the enhancement increasing in rough proportion to the ratio of high Z mass to H, He mass for the bulk of the planet. This prediction is in accord with the systematic increase in the atmospheric C/H ratio from Jupiter to

Saturn to Uranus and Neptune and with the results of recent interior models of the giant planets. It is not clear whether it is consistent with the abundances of H_2O and NH_3 in the atmospheres of some of the outer planets. In the atmospheres of Uranus and Neptune, even the He/H ratio may be supra-solar due to the hydrogenation of some of the dissolved high Z material.

ORBITAL RESONANCES IN THE SOLAR NEBULA

Stuart J. Weidenschilling and Donald R. Davis
Planetary Science Institute, Tucson, Arizona 85719

The presence of gas in the nebular stage of the early solar system influenced the formation of planetesimals and the growth of planets in ways that are still poorly understood. It is commonly stated that the drag of the gaseous nebula must have damped the eccentricities and inclinations of planetesimal orbits, keeping their relative velocities low. While low relative velocity promotes accretion of small planetesimals, it can prevent the growth of larger bodies by keeping their orbits from crossing. That effect could yield too many small planets in closely spaced orbits, suggesting to some investigators that the gaseous nebula must have dissipated before the terrestrial planets accreted. However, that scenario appears incompatible with the origin of the jovian planets, which probably formed massive solid cores before accreting most of their mass from the surrounding gas.

It has been recognized for about the past decade that the solar nebula was not in strictly Keplerian rotation; a radial pressure gradient caused the gas to rotate more slowly than the orbital speed of a solid body at any given location. Thus, planetesimals experienced a constant "headwind" that caused their orbits to decay (Adachi et al., 1976; Weidenschilling, 1977). The rate of this decay depends on a body's area/mass ratio, and therefore is size-dependent. In principle, differential decay of orbits could promote accretion by bringing together planetesimals of different sizes, originally in non-crossing orbits. In practice, this effect is much too slow to be effective for large ($\gtrsim$ 1 km) planetesimals.

We have recently discovered another phenomenon that can promote planetary accretion in the presence of the gaseous nebula, with the seemingly paradoxical effect that the gas causes orbital eccentricities to increase. Once a large planetary embryo has begun to form, its orbit can be considered fixed. As a smaller planetesimal, originally in a larger orbit, moves inward by drag-induced decay, it must encounter commensurability resonances with the embryo, i.e., their orbital periods have the ratio $j/(j+1)$, where j is an integer. The gravitational perturbations by the embryo tend to increase the eccentricity of the planetesimal. The damping of e by gas drag causes a phase shift in the perturbations, allowing an exchange of orbital energy between embryo and planetesimal (cf. Greenberg, 1978). For exterior resonances, this effect opposes the secular decay of the planetesimal's orbit, allowing it to reach an equilibrium state at which orbital decay ceases. Trapped at the resonance, the planetesimal has its eccentricity pumped up to a steady state value, which can be fairly large. The close spacing of the resonances allows this to happen in a short time.

We have recently published a description of the resonant trapping phenomenon and some of its cosmogonical implications (Weidenschilling and Davis, 1985). We showed by analytic and numerical methods that these

resonances are stable for a wide range of conditions, e.g. the mass of the perturbing embryo and the planetesimal's drag parameter (proportional to gas density and inversely proportional to size). In a swarm of planetesimals, bodies trapped in different resonances have crossing orbits, and eccentricities are large enough for collisions to occur at $\gtrsim$ 1 km/sec. Such velocities, much greater than those induced by non-resonant perturbations, result in comminution of large planetesimals. The embryo is able to accrete the resulting fragments, which are too small to be trapped into resonances themselves. Thus, an early-formed embryo can prevent the growth of potential rivals. This effect works in the direction of producing fewer, larger planets with wider orbital spacing; if completely effective, it would yield roughly the actual number and spacings in the solar system.

The actual outcome of accretion depends on various parameters, such as the early size distribution of planetesimals, their growth rate relative to the rate of eccentricity pumping, collisional strength, and the structure of the solar nebula. We are working toward construction of more realistic quantitative modeling of accretion in the presence of gas. We are using numerical integrations of drag-perturbed orbits to determine how de/dt depends on the perturber mass, the drag parameter, and resonance order. These results will be incorporated into a numerical model of accretion (cf. Greenberg et al., 1978). Thus far, we find that, all other parameters being equal, de/dt is greater for lower-order resonances (smaller j). However, the higher-order resonances are more closely spaced, allowing the e-pumping to begin sooner, so the increase in planetesimal velocities propagates outward from the vicinity of the embryo's orbit.

We are also examining interior resonances (planetesimal's orbit smaller than the embryo's). These have secular decay of semimajor axis due to drag in the same sense as the resonant perturbations, so no equilibrium state exists. Planetesimals are not trapped at resonances, but we find that they reach high $\underline{e}$ while passing through them, nearly twice the equilibrium value for exterior resonances of the same order. Therefore, high velocities are attained interior to the embryo's orbit, and comminution will occur there, although the fragments are driven inward and not accreted by that embryo. This effect could have helped to depopulate the asteroid belt outside of 3.3 AU (the 2/1 interior resonance with Jupiter). To date, we have studied only the planar problem, with evolution of eccentricities. There is the possibility that resonant perturbations could also pump up inclinations of trapped planetesimals. Such stirring of inclinations would affect collision rates and the timescale for evolution of the planetesimal swarm. This possibility will be investigated in the near future.

This research is supported by the NASA Planetary Geophysics and Geochemistry Program, Contract NASW-3214.

Adachi, I., C. Hayashi, K. Nakazawa (1976). Prog. Theor. Phys. 56, 1756-1771.

Greenberg, R. (1978). Icarus 33, 62-73.

Greenberg, R., J. Wacker, W. Hartmann, C. Chapman (1978). Icarus 35, 1-26.

Weidenschilling, S. (1977). Mon. Not. R. Astron. Soc. 180, 57-70.

Weidenschilling, S., D. R. Davis (1985). Icarus 62, 16-29.

Accumulation of the Planets

G.W. Wetherill, DTM, Carnegie Institution of Washington

Earlier simulations of gas-free planetary accumulation (Wetherill, 1980 a,b) have been extended from 100 bodies to 500 bodies, thus permitting exploration of a wider range of initial states for the final stages of accumulation (Wetherill, 1985a,b). These show that for a wide (but not complete) range of initial states accumulation is accompanied by very large (up to 3 times Mars' mass) impacts on the growing Earth and Venus. This work is closely related to that of Mizuno and Boss (1985) who showed that tidal disruption of planetesimals is unlikely to be of great importance during close encounters with Earth and Venus. Their result greatly reduces the likelihood that there is a realistic mechanism that permits larger planets to remove the giant impactors from the swarm prior to planetary impact. If these giant impacts occur, as seems likely, they should have had a major influence on the origin of the moon (Hartmann and Davis, 1975; Cameron and Ward, 1976), the removal of planetary atmospheres (Cameron, 1983) and the iron-rich composition of Mercury (Wetherill, 1985a,b).

Present work is directed toward further exploration of the universality and the limits of terrestrial planet accumulation histories characterized by giant impacts. This involves consideration of natural processes whereby the size of potential giant impactors may be significantly reduced during accumulation. These processes include tidal disruption of impact-melted planetesimals during close encounters, mutual collisional destruction, and fragmentation resulting from rotational instability following off-center collisions between large planetesimals. Preliminary calculations support the inference that occurrence of giant impacts is not sensitive to these phenomena when "best estimates" of the relevant parameters are used.

A study is also being made of the sensitivity of the assumed initial state of the final stage of accumulation to the primordial distribution of $\sim$1 km radius planetesimals. Particular attention is being given to the circumstances under which early runaway accretion (Greenberg et al., 1978) may or may not be expected to occur, including the effects of fragmentation and gas drag. This is also related to the problem of the formation of the cores of the giant planets.

In order to accomplish this, a new numerical approach is being developed to shed light on the causes of the alternative accumulation histories. This consists of dividing an assumed continuous primordial distribution of $\sim 10^{16}$ to 10^{20}g bodies into a discrete number of "batches" of the same mass (including some largest-mass batches containing as few as one member). The growth of the bodies is calculated by sweep-up calculations (as done by previous authors) using the velocity dependence of the gravitational cross-section found by Wetherill and Cox (1985).

The perturbations in velocity and changes in mass of each batch during successive time steps is calculated. In collaboration with Glen Stewart (Univ. of Va.) new expressions, based on transport theory, are being used to calculate these perturbations. These include terms, such as "dynamic friction" that have been ignored by previous workers. Preliminary results show that early runaway is not a true instability, but

requires "seeds", i.e. significant discontinuities in the initial mass distribution.

A second area of emphasis is that of identifying the primitive bodies in the solar system from whence meteorites are derived. This is necessary in order to refer the information concerning the early solar system recorded in meteorites to a planetological context.

The evidence for ordinary chondrites being fragments of S-asteroids in the near vicinity of the 3:1 Kirkwood gap (2.50 A.U.) is now strong (Wetherill, 1985c; Wisdom, 1985) even though questions remain regarding the quantitative identification of S-asteroids with chondritic mineralogy (Gaffey, 1984). By relating the meteorite production rate to the observed and theoretical distribution of asteroidal material it proved possible to calculate the terrestrial flux of meteorites from this region on an absolute basis with minimal use of uncertain parameters such as those associated with cratering mechanics.

This approach is now being extended to calculate the orbits and mass yield of meteorites from the entire asteroid belt within 2.60 A.U. relative to that of the 3:1 gap, and hence, by normalization, the absolute flux as a function of semimajor axis (Wetherill, 1985d). It appears that the predicted absolute flux and P.M. vs. A.M. fall distribution from asteroids at the innermost edge of the belt (2.17 to 2.25 A.U.) will turn out to be in very good agreement with that found for igneous meteorites, excluding SNC (probably martian) and lunar meteorites.

Cameron, A.G.W. (1983) Origin of the atmospheres of the terrestrial planets. Icarus 56, 195-201.

Cameron, A.G.W., and Ward, W.R. (1976) The origin of the moon. In Lunar Science 7, 120-122, Lunar Science Institute, Houston.

Gaffey, M.J. (1984) Rotational spectra variations of asteroid (8) Flora: Implications for the nature of the S-type asteroids and for the parent bodies of the ordinary chondrites. Icarus 60, 83-114.

Greenberg, R., Wacker, J., Chapman, C.R., and Hartmann, W.K. (1978) Planetesimals to planets: a simulation of collisional evolution. Icarus 35, 1-26.

Hartmann, W.K. and Davis, D.R. (1975) Satellite-sized planetesimals and lunar origin. Icarus 24, 504-515.

Mizuno, H., and Boss, A.P. (1985) Tidal disruption of viscous planetesimals. Icarus 63, 109-133.

Wetherill, G.W. (1985a) Occurrence of giant impacts during the growth of the terrestrial planets. Science 228, 877-879.

Wetherill, G.W. (1985b) Accumulation of the terrestrial planets and implications concerning lunar origin. Proc. Conference on Origin of the Moon, Kona, Hawaii, in press.

Wetherill, G.W. (1985c) Asteroidal source of ordinary chondrites. Meteoritics 20, 1-22.

Wetherill, G.W. (1985d) Quantitative calculation of meteorite flux from various regions of the inner asteroid belt. (abstract) Presented at the 48th meeting of the Meteoritical Society, Bordeaux, July 1985. Meteoritics, in press.

Wetherill, G.W. (1980a) Formation of the terrestrial planets. Ann. Rev. Astron. Astrophys. 18, 77-113.

Wetherill, G.W. (1980b) Numerical calculations relevant to the accumulation of the terrestrial planets. In The Continental Crust and its Mineral Deposits, ed. D.W. Strangway, Geol. Asso. of Canada Special Paper 20, pp. 3-24.

Wetherill, G.W., and Cox, L.P. (1985) The range of validity of the two-body approximation in models of terrestrial planet accumulation. II. Gravitational cross-sections and runaway accretion. Icarus 63, 290-303.

Wisdom, J. (1985) Meteorites may follow a chaotic route to Earth. Nature 315, 731-733.

SOLAR SYSTEM DYNAMICS

Jack Wisdom, Department of Earth, Atmospheric and Planetary Sciences, Massachusetts Institute of Technology, Cambridge, Massachusetts 02139

I. Transport of Meteoritic Material to Earth

I have demonstrated that the chaotic zone which accompanies the 3/1 mean motion commensurability with Jupiter is capable of directly transporting meteoritic material from the asteroid belt to Earth (Wisdom 1985a). It has been a long standing embarrassment that the origin of the meteorites is not known. Monte carlo calculations of Wetherill (1968) showed that the more obvious possible sources of meteorites such as the comets, Apollo asteroids or the moon could not reproduce the distribution of radiants, time of fall and exposure ages of the ordinary chondrites. He concluded that there must be an "unobserved source" of material with perihelia near 1 AU and aphelia near Jupiter.

In my mapping studies of the long-term evolution of trajectories near the 3/1 commensurability I found that larger eccentricities were obtained than were previously thought possible and that often the large eccentricities developed after a long period of low eccentricity behavior (Wisdom 1982). I showed that the large eccentricities were characteristic of trajectories in a large chaotic zone accompanying the 3/1 commensurability and that the boundary of the chaotic zone corresponded to the boundary of the 3/1 Kirkwood gap within the errors of asteroid orbital elements (Wisdom 1983). In the mapping studies where the inclinations of the orbits were included higher eccentricities were obtained than in the planar problem. Computed with the three-dimensional map, the eccentricities of chaotic trajectories became large enough for them to cross Earth's orbit. The large eccentricities were outside the range of validity of the derivation of the map, but because of the success of the map at lower eccentricity I felt that these large eccentricities should be taken seriously. I proposed that the 3/1 chaotic zone could provide a mechanism for transporting the ordinary chondrites from the asteroid belt to Earth (Wisdom 1984). The 3/1 resonance had previously been suggested to be the source of the ordinary chondrites, but only with the assist of Mars. Meteorites assisted by Mars will not satisfy the observational data.

There is only one convincing way of verifying the hypothesis that three dimensional chaotic trajectories have the required properties, direct numerical integration. I attempted to guess appropriate initial conditions based on my experience with the map. These numerical integrations are quite time consuming and my first attempts failed. However, the fifth try was successful; in the field of the Jovian planets asteroidal fragments in the 3/1 chaotic zone can reach such large eccentricities as to be directly transported from the asteroid belt to Earth. Wetherill (1985) has shown that this new source is consistent with the ordinary chondrite data.

II. The Qualitative Behavior of Chaotic Trajectories Near Commensurabilities

The unusual behavior of trajectories in the 3/1 chaotic zone has now been abundantly verified (Wisdom 1983, 1985a, Murray and Fox 1984). However, it is unsatisfying to simply report the phenomenon, and have no understanding of the mechanism behind it. Without an understanding of why a phenomenon occurs each new situation requires a new, essentially blind, numerical exploration. The dynamics of the 2/1 and 3/2 commensurabilities are much more complicated than the already very complicated 3/1 resonance; before attempting to map these resonances I felt it was approprite to get a better understanding of the 3/1 commensurability (Wisdom 1985b).

The derivation of the mapping depends on the averaging principle; the success of the mapping is merely a reflection of the fact that the motion near commensurabilities is well represented by disturbing functions which are averaged over the mean longitudes to iso-

late the long period variations. In the planar elliptic problem there are however typically three timescales: the orbital timescale (a few years), the libration timescale (a few hundred years) and the precession timescale (a few thousand years). When these timescales are distinct a second averaging is suggested. In appropriate variables the motion on the libration timescale can be reduced to that of a pendulum and can be solved analytically. Equations of motion for the longest timescale can be derived by averaging over the motion on the libration timescale, and assuming that the action of the pendulum is adiabatically conserved. As long as the action is conserved, the resulting trajectories belong to a one degree of freedom problem (with one external parameter which depends on initial conditions) and can be easily visualized.

The interesting behavior at the 3/1 resonance occurs because the libration timescale and the precession timescale are not always distinct. For long times (of order ten thousand years) trajectories follow closely the trajectories predicted by the doubly averaged equations of motion, but when they enter those regions of the plane where the timescales are not distinct the double averaging breaks down and the trajectories are no longer predictable. After some time the trajectory reemerges from this zone with a new value of the adiabatically conserved action and the process repeats itself. Fortunately the zones in which the timescales are indistinct are small. Thus the behavior of a chaotic trajectory is, for the most part, predictable! The jumps to large eccentricity are among those predictable portions of the trajectory. What is unpredictable is the time at which they occur, and which of the many paths to high eccentricity will actually be taken.

Chaotic trajectories may now be identified with those trajectories which enter those zones where the timescales are not distinct. It turns out that the predicted chaotic zones match very closely the observed chaotic zones, and the precise size of the chaotic zones are relatively independent of the (undetermined) parameter which quantifies when two timescales are "indistinct." It is also interesting to note that this crossing into the "indistinct" zone is not a necessary consequence of the overlap of the three resonances which determine the dynamics near the 3/1 commensurability; integrable counter examples are given in the paper. Thus the resonance overlap criterion, which correctly predicts the onset of chaos when two different mean motion resonances overlap (Wisdom 1980), is not useful in understanding the origin of the 3/1 chaotic zone.

This new semi-analytic perturbation theory is quite successful, and powerful. Given an *adequate* disturbing function, the perturbation theory can predict the location and extent of the chaotic zones.

III. The Outer Solar System For 220 Million Years

The building of the Digital Orrery is an extremely important advance for the whole of planetary dynamics. The Orrery is a highly parallel, special purpose computer for integrating the equations of motion of celestial mechanics. The Orrery is no larger than a cubic foot, yet is 60 times as fast a VAX 11/780 with a floating point accelerator, roughly 1/3 the speed of a Cray.

The outer planets form the backbone of the solar system. Their long term evolution is intrinsically interesting, but a good model for the evolution of the Jovian planets is also useful for the study of other dynamical problems in the solar system, such as the evolution of the asteroids or Pluto. To flex the muscles of the Orrery we have studied the outer planets over a period of 220 million years (Applegate, et al. 1985). We have made a number of runs covering this 220 Myr period, each run taking approximately 20 days. By comparison, the longest published integrations of the outer solar system cover only 500,000 years forward and backward from the present (Cohen et al 1973). There is also an unpublished integration by Kinoshita and Nakai covering 5 million years.

We have made a spectral analysis of the motion of each of the planets in order to

compare our integrations to theory. The most complete analytic theory of the long term evolution of the planets is that of Bretagnon (1974). Bretagnon solves the long period problem including all terms up to second order in the masses and third order in the eccentricities and inclinations. His paper lists over 200 corrections to the Lagrange solution for the secular variations of the planets. It is the standard upon which a number of other investigations rest. Unfortunately, we have found serious discrepancies between our results and the predictions of theory. The fundamental solar system frequency ν_6 as determined by Bretagnon is in error by more than 7 percent. The value of this frequency is particularly important as it determines the location of the most important secular resonance in the inner asteroid belt. We note also a number of strong contributions which do not appear in Bretagnon's solution, one of which is larger than all but 7 of Bretagnon's 200 terms! We have been able to identify this contribution as arising from terms of higher order than those Bretagnon considered. This illustrates a fundamental difficulty in analytic solutions of problems in celestial mechanics.

We also note a number of other interesting features in our numerical solutions. The 20,000 year libration of the resonance argument of Pluto turns out to be a complex set of peaks with a pattern which is characteristic of frequency modulation. Evidently the libration frequency is modulated by the 3.7 Myr circulation of the longitude of the ascending node. Also, the amplitude of the 3.8 Myr period libration of Pluto is modulated with a period of 35 Myr. Very long period variations in the orbital elements of Pluto, on the order of 136 Myr, are seen. This period corresponds to a combination of the frequency of the circulation of the node and the fundamental solar system frequency with a period of 1.87 Myr. The near commensurability between these frequencies is quite striking and could have important consequences for the long term stability of Pluto. However, there is no indication of instability in the orbit of Pluto for the duration of our integrations; the maximum Lyapunov exponent is less than $10^{-6.8}\mathrm{yr}^{-1}$.

Applegate, J.F., Douglas, M.R., Gürsel, Y., Sussman, G.J., and Wisdom, J. 1985. submitted.

Bretagnon, P. 1974. *Astron. Astrophys.* **30**, 141.

Brouwer, D. and van Woerkom, A.J.J. 1950. *Astron. Pap. Am. Eph.* **XII**, II.

Cohen, C.J., Hubbard, E.C., and Oesterwinter, C. 1973. *Astron. Pap. Am. Eph.* **XXII**, I.

Murray, C., and Fox, K. 1984. *Icarus* **59**, 221.

Wetherill, G.W. 1968. *Science* **159**,79.

Wetherill, G.W. 1985. *Meteoritics* **15**, 1.

Wisdom, J. 1980. *Astron. J.* **85**, 1122.

Wisdom, J. 1981. *Astron. J.* **87**, 557.

Wisdom, J. 1983. *Icarus* **56**, 51.

Wisdom, J. 1984. *Meteoritics* **18**, 422.

Wisdom, J. 1985a. *Nature* **315**, 731.

Wisdom, J. 1985b. *Icarus* **63**, 272

CHAPTER 4

PLANETARY INTERIORS, PETROLOGY AND GEOCHEMISTRY

LITHOSPHERIC STRENGTHS OF THE TERRESTRIAL PLANETS

W. B. Banerdt and M. P. Golombek, Jet Propulsion Laboratory,
California Institute of Technology, Pasadena, CA 91109

Knowing the strength of a planet's lithosphere is a prerequisite to both placing limits on the stresses possible within a lithosphere and providing an accurate failure criterion. Unfortunately, efforts to determine the strengths of planetary lithospheres have been hampered by the lack of an accepted criterion for the earth. Recently, however, a relation has been identified [1] that accurately predicts the maximum stress levels found in the brittle portion of the earth's crust [2]. In this abstract, we briefly describe this relation, and apply it to the terrestrial planets. Even given the large uncertainties in determining the important parameters for geophysically poorly understood planets, our application places strong constraints on limiting stress levels and reasonable failure criteria for the lithospheres of the terrestrial planets.

The maximum stress levels found in the earth's upper crust are accurately predicted by Byerlee's law [1,2]. This relation is based on laboratory measurements of the frictional resistance to sliding on pre-existing fractures, which occurs at stresses less than those required to break intact rock. Byerlee's law is of the form $\sigma_1 = K\sigma_3 + b$, where σ_1 and σ_3 are, respectively, the maximum and minimum principal effective stresses (stress minus pore pressure), $K = [(\mu^2+1)^{1/2}+\mu]^2$, μ is the coefficient of friction, and b is a constant. Laboratory friction measurements show that μ and b are virtually independent of stress (except for a slight change at 135 MPa), rock type, displacement, surface conditions, and temperature. Because the vertical stress is generally a principal stress and quite close to the lithostatic load, this relation predicts a linear increase in yield stress with depth.

With increasing temperature, rock deformation occurs predominantly by ductile flow. Flow laws for many rocks and minerals have been experimentally determined for stresses up to 1-2 GPa and strain rates down to 10^{-8}/sec. These results can be extrapolated to geological strain rates via creep equations, which generally are of the form $\dot{\varepsilon} = A(\sigma_1 - \sigma_3)^n \exp(-Q/RT)$, where $\dot{\varepsilon}$ is the strain rate, R is the gas constant, T is absolute temperature, and A, Q (the activation energy), and n are experimentally determined constants. As a result, the ductile strength is negligible at depths where T is high and increases exponentially with decreasing depth. Flow laws are also highly dependent on rock composition, with a silicic crust much weaker than a mafic mantle.

The failure criterion for a given depth in the lithosphere is determined by the weaker of the frictional or ductile strength at that depth. The yield stress increases with depth according to Byerlee's law until it intersects the crustal flow law. It then decreases exponentially until it reaches the crust-mantle boundary, where the greater mantle strength causes an abrupt increase to the frictional yield stress followed by another exponential decrease. In actuality, semibrittle and low temperature ductile processes tend to round off the intersection points between the brittle and ductile curves.

The total yield strength of the lithosphere can be defined as the integral of the yield stress vs depth curve [4]. The parameters to which strength calculations are most sensitive are crustal thickness (c) and composition, and internal temperature. In these calculations we use a crustal density of 2.8 Mg/m^3, a mantle density of 3.3 Mg/m^3, a geologic strain rate of $\dot{\epsilon}=10^{-15}$/sec, and flow laws from [5-7].

Earth: Strength analyses for the earth have been done by several investigators (e.g. [2,4,8,9]) assuming a quartzite flow law within the continental crust and olivine below. For a crustal thickness of 35 km and a thermal gradient of 15°/km this model yields a compressive strength (S_c) of 13 (in units of 10^{12} nt/m) and a tensile strength (S_t) of 7.5, assuming hydrostatic pore pressure. Using a diabase flow law appropriate for an average 10 km thick crust of the oceanic lithosphere results in strengths of S_c=36 and S_t=16. For comparison, a 100 km lithosphere with a uniform yield stress of 100 MPa (1 kbar) would have a strength of 10^{13} nt/m.

Moon: The moon is the only other planet for which we have direct measurements of the parameters needed for strength calculations. We use a thermal gradient of 3.9°/km at the surface decreasing to 1.5°/km at 300 km derived from theoretical thermal models and Apollo heat flow measurements [10]. A crustal thickness of 60 km has been determined seismically. Assuming an anorthositic composition for the entire lunar crust, we calculate strengths of S_c=203 and S_t=103.

Mercury: A thermal gradient of 5°/km is assumed for Mercury, based on thermal history models [11]. We derive the crustal parameters by assuming that the silicate portion of Mercury generated the same relative fraction of crustal material by volume as the moon, resulting in a 35 km thick anorthosite crust. These parameters yield S_c=139 and S_t=78. The strength does not change appreciably unless $c>50$ km.

Mars: A thermal gradient of 9°/km is used for Mars, again from thermal history models [9]. Study of volcanic features [12] and SNC meteorites [13] suggests a predominantly basaltic crust, and 100 km seems a likely upper limit for its thickness, based on gravity constraints [14]. S_c varies from 65 for $c\leq 40$ km, to 26 for c=100 km. S_t ranges from 28 to 9.3 over the same interval. If the pore space of the lithosphere is filled with liquid water, these strengths are lowered by about 20%.

Venus: Venus is the most poorly constrained of the planets. While the assumption of a basaltic crust is well supported by surface analyses [15], its thickness is unknown and the thermal gradient is a matter of debate [16]. If we adopt a gradient of 12°/km [17], the strengths decrease from S_c=12, S_t=5.9 for c=0 to S_c=7.0, S_t=5.8 for $c>35$ km.

Discussion: The compressive lithospheric strengths of the terrestrial planets are plotted as a function of crustal thickness in figure 1, using the thermal gradients assumed above. It can be seen that the moon has by far the strongest lithosphere, over 5 times stronger than terrestrial oceanic lithosphere. It is followed in order of decreasing strength by Mercury, Mars, oceanic and continental lithosphere on the earth, and Venus. Tensional strengths tend to be roughly half the corresponding compressional strengths. Crustal thickness has no effect on strength for

reasonable values of c on the moon and Mercury, but can cause variations of a factor of two on Mars, a factor of three on the earth, and over an order of magnitude on Venus. Strength also depends strongly on thermal gradient, with a factor of 2 or 3 change in gradient causing an order of magnitude change in strength.

It should be noted that these calculations were done assuming parameters corresponding to current conditions. Thus the strengths presented here will not be relevant to deformational events which occurred early in a planet's history, when thermal conditions were much different.

References: [1] Byerlee (1978) Pageoph 116, 615; [2] Brace & Kohlstedt (1980) JGR 85, 6248; [3] Kirby (1980) JGR 85, 6353; [4] Vink et.al. (1984) JGR 89, 10072; [5] Sheldon & Tullis (1981) EOS 62, 396; [6] Christie et.al. (1979) EOS 60, 948; [7] Goetze (1978) Phil Trans RSL 288A, 99; [8] Smith & Bruhn (1984) JGR 89, 5733; [9] Morgan & Golombek (1984) N Mex Geol Soc Guide 35, 13; [10] Toksöz et.al. (1978) Moon & Planets 18, 281; [11] Solomon (1977) PEPI 15, 135; [12] Francis & Wood (1982) JGR 87, 9881; [13] Wood & Ashwal (1981) Proc LPSC 12B, 1359; [14] Phillips & Saunders (1975) JGR 80, 2893; [15] Surkov et.al. (1983) Proc 13 LPSC, A481; [16] Solomon & Head (1982) JGR 87, 9236; [17] Morgan & Phillips (1983) JGR 88, 8305.

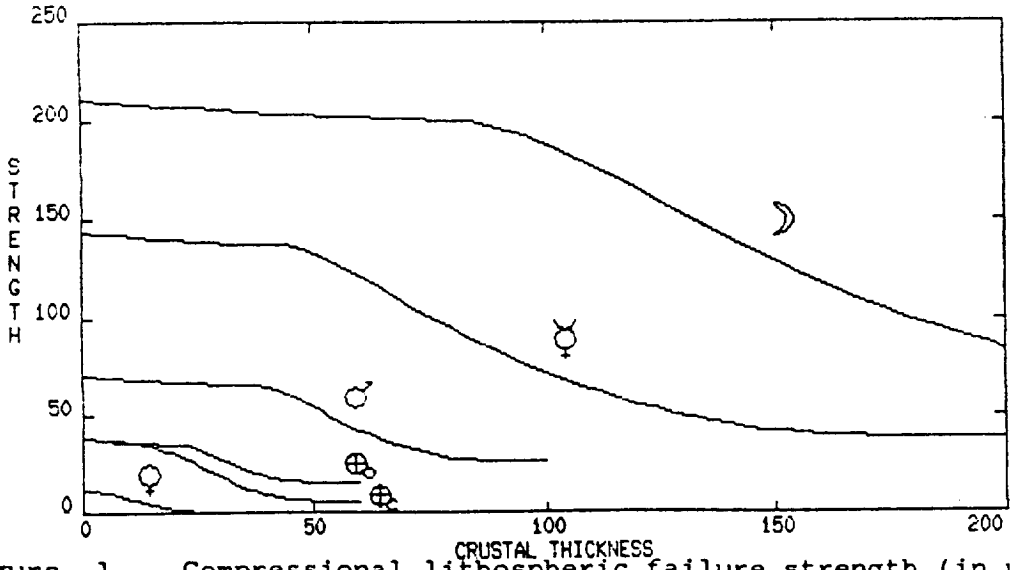

Figure 1. Compressional lithospheric failure strength (in units of 10^{12} Pa-m) as a function of crustal thickness (in km) for the moon, Mercury, Mars, the earth's continents, the earth's oceans, and Venus. Assumed thermal gradients and crustal compositions are given in the text. For thin crusts the strength is dominated by the strong ultramafic mantle, while for crusts sufficiently thick, the strength is that of the crustal material alone. The slow decrease in strength at small values of crustal thickness is due to the decrease in overburden due to the increasing thickness of less dense crustal rocks.

ANALYSIS OF HARMONIC SPLINE GRAVITY MODELS FOR VENUS AND MARS

Carl Bowin, Woods Hole Oceanographic Institution, Woods Hole, MA

The use of harmonic spline methodology to resolve planetary gravity fields from the randomly oriented residual line-of-sight (LOS) vectors that result from processing Doppler tracking data was first demonstrated in our work published earlier this year (Bowin et al., 1985). The LOS vectors are components of the planetary gravity field along that direction that happened to point toward the earth at the time of measurement. The LOS acceleration vectors are computed by differentiating the residual Doppler signal that remains after the Doppler contribution from the central body attraction, along the computed orbit trajectory is subtracted from the observed Doppler data. Least-squares filtering procedures, applied to the Doppler data to obtain the LOS results reduce the true absolute amplitudes of the acceleration vectors (Gottlieb, 1970), perhaps by as much as 40 percent. Apparently that reduction of a maximum of a positive anomaly is accompanied by the pumping of energy into lows that flank a gravity high.

I view the reduction of the positive amplitude as most likely, indicating an uncertain location of the zero reference level. For example, imagine a volcano or ridge upon a planet with a very strong crust. In this case the topographic load would be completely uncompensated, and the free-air gravity anomalies across the structure would be entirely positive, as shown by the solid curve, in reference to the dotted zero line in Figure 1. An integral of the gravity acceleration curve would yield anomalous Doppler frequency variations. Upon a least-squares fitting of a smooth curve through such Doppler data, and its subsequent differentiation, an anomalous gravity curve shown by deviations from the dashed line (which represents an inferred erroneous zero reference level) might result. The resulting gravity profile might then have a reduced positive anomaly with flanking lows. In such a situation, the integral of the positive and negative gravity anomalies along the orbit path would tend to approach closer to zero than in the true condition.

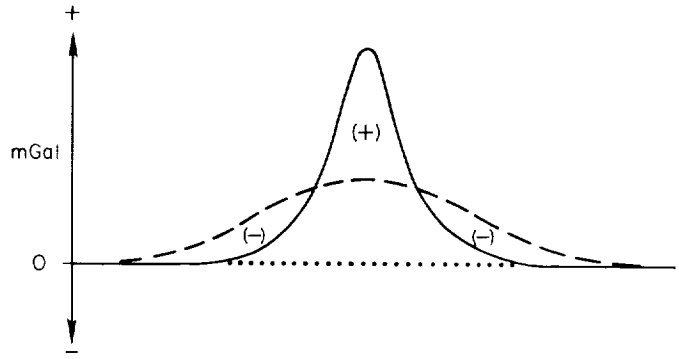

Figure 1. Hypothetical gravity anomaly. See text for discussion.

The above hypothesis is supported by the occurrence of gravity lows flanking positive gravity anomalies associated with topographic highs on Venus and Mars. Where the topographic high is a nearly circular feature, the lows symetrically straddle the positive along the orbit tracks. This is true even though the spacecraft altitude at the two symmetric lows may be quite different. See Figure 2 for the example of this relationship in the orbit passing above the Crest of Beta Regio on Venus. This observation is seen also to be true in maps of LOS accelerations at spacecraft altitude for Venus published by Sjogren et al. (1980,1981), Bowin (1983) and Bowin et al. (1985) for example. In fact it was these relations that led to the above hypothesis.

Tracking data and spacecraft ephermeris have been used to compute the coefficients for spherical harmonic expansions of the potential field of planets. For example, see Bills (1982) and Mottinger et al. (1983) for Venus. These global solutions only have low resolution, however. Point masses and disk models over a grid have been used to compute Doppler residuals along orbit trajectories by the program ORBSIM and results compared with the observed LOS residual accelerations. This process has allowed the construction of radial gravity anomaly maps from the point mass or disk models. Depending on where or how the zero reference errors arise during processing, they may remain in the point and disk mass models since they match to the LOS data.

That the lows flanking the gravity highs are in large part artifacts from the LOS processing is clearly documented by the harmonic spline results (Bowin et al., 1985). The power of the harmonic spline methodology is that it objectively solves for the smoothest field that will match the observed data, and that the data may be of random components of the field, and at random altitudes. Then from the harmonic spline coefficients at the basis points used for the computation, any component of the gravity

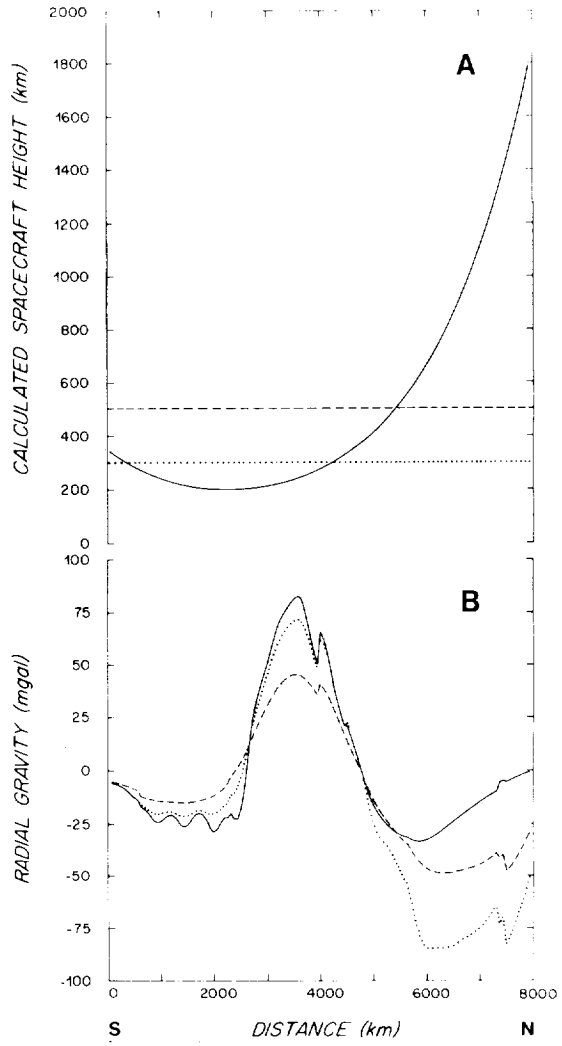

Fig. 6. Comparison of profiles of radial gravity anomaly at spacecraft, 500 km, & 300km altitudes across Beta Regio in a direction parallel to the orbit paths. The line types in the height plot (A) provide identifications for the lines describing the gravity profiles (B) (Bowin et al, 1985, Fig. 6).

field at any location and altitude may be determined. In addition to the gravity profile at spacecraft altitude in Fig. 2, we show the curves at constant altitudes of 300 and 500 km. Note how the low north of Beta Regio becomes greatly exaggerated upon increasing downward continuation. In the 300 km map (Bowin et al., 1985, Fig. 5) that low is seen to greatly exceed the absolute magnitude of all other anomalies on Venus, and thus it is obviously in error. Because downward continuation is a rigorous procedure, that error signifies that its value at spacecraft altitude is too negative. Note, also, that the low south of Beta Regio is upward continued to 300 and 500 km and thus is attenuated at those constant altitudes. Through the use of harmonic spline models, in an iterative manner, we are now attempting a procedure by which a harmonic spline model can be obtained that when appropriately filtered will match the observed LOS data along the spacecraft trajectories, and when unfiltered, will represent the true anomalous gravity field of the planet. At that stage, we can construct grids of gravity values at constant altitudes over the planet surface. Such grids are vital for admittance studies of planetary structures by gravity/topography transfer function methods, and offer the strongest means by which to examine the internal structure of another planet.

For this computer intensive study, as well as for other computing needs, we have acquired a Ridge personal mainframe computer with RISC architecture. This system provides us with an essentially unlimited computer resource. The 'noise' in the harmonic spline results of Fig. 2 along the spacecraft trajectory result from differences in solutions at boundaries of latitude and longitude cells previously used to divide the large LOS data set into manageable sizes. For the present study we have created on the Ridge system a library of Pioneer Venus LOS vectors organized by revolution number (rev) and by time within each rev. Harmonic spline models will be computed for entire revs, thus eliminating the noise described above.

References

Bowin, C.O., 1983. Gravity, topography and crustal evolution of Venus. ICARUS, v. 56, 345-371.

Bowin, Carl, G.A. Abers, and Loren Shure, 1985. Gravity field of Venus at constant altitude and comparison with earth. J. Geophys. Res., v. 70, supplement, p. C757-C770.

Bills, D.B., 1982. Venus: topography, gravity and resonant rotation. EOS, v. 63, No. 45, 1021.

Gottlieb, Peter, 1970. Estimation of local lunar gravity features. Radio. Sci., v. 5, no. 2, 301-312.

Mottinger, N.A, W.L. Sjogren, G.B. Trager and B.G. Bills, 1983. Venus: 10th degree and order global gravity field (abst.). EOS Transactions AGU, v. 64, No. 45.

Sjogren, W.L., R.J. Phillips, P.W. Birkeland and R.N. Winberly, 1980. Gravity anomalies on Venus. J. Geophys. Res., v. 85, No. A13, 8295-8302.

Sjogren, W.L., P.W. Birkeland, P.B. Esposito, R.N. Winberly and S.J. Ritke, 1981. Venus gravity field: Local. Trans. Amer. Geophys. Union, v. 61, No. 17, 386.

THE SURFACE ROCKS OF MARS: TERRESTRIAL EQUIVALENTS

Roger G. Burns, Department of Earth, Atmospheric and Planetary Sciences, Massachusetts Institute of Technology, Cambridge, Massachusetts 02139.

The red color of the surface of Mars has long been attributed to ferric iron-bearing minerals in the regolith, implying that oxidizing conditions have prevailed on Mars. However, the unweathered parent rocks and constituents of Mars' regolith remain ill-defined. Hisingerite, iddingsite and a number of Fe^{3+}-sulfate minerals derived from deuteric alteration of iron-rich basaltic rocks on Earth may provide clues to the evolutionary history of the surface of Mars.

The pathways of chemical weathering processes on Earth, or virtual absence of them on the Moon, are well characterized because we have direct access to samples of primary igneous rocks, their upper mantle sources, and derivative sedimentary rocks forming the regolith. Without having direct access yet to samples of Mars, the compositions of parent magma and upper mantle source rocks must be deduced[1,2] from a variety of evidence, including earth-based and remote-sensed observations and *in situ* Viking Lander measurements of the martian regolith.[3] Results from these experiments match properties of novel terrestrial materials not previously considered to be constituents of Mars' surface. They include hisingerite and iddingsite derived from iron-rich basaltic rocks, such as those occurring in the Duluth complex at Beaver Bay, Minnesota, and several ferric-bearing sulfate and related secondary minerals associated with oxidized sulfide ores and ultramafic rocks. Evidence that these readily accessible rocks and minerals may be analogous to deposits on Mars is described here.

The composition of the mantle of Mars is believed to be considerably more iron rich than the Earth's mantle[1,2] with estimated Mg/(Mg+Fe) ratios ranging from 0.67 to 0.77, compared to 0.85 for the Earth. It was also suggested[2] that the high FeO content of the martian mantle and oxidizing effect of late accreting, volatile rich material allows significant amounts of NiO and Fe_2O_3 to exist in the interior of Mars. Partial melting of the proposed martian mantle would lead to an iron-rich basaltic magma[1] which could be olivine-rich and/or pyroxene-rich. The normative mineralogy of such mafic or ultramafic rocks indicate the presence of fayalitic olivines and Fe-rich pyroxenes,[1,4] which are highly vulnerable to chemical weathering[5] on the surface of Mars. Pyrrhotite was suggested to be a sulfide accessory mineral.[1]

The Viking XRF measurements[6,7] indicated that the regolith of Mars is significantly enriched in Fe, S and Cl, and depleted in Al compared to chemically weathered basalts on Earth. The bulk composition of the surface fines was suggested to match a mixture of Fe^{3+}-rich smectite clay, Mg sulfate, and iron(III) oxide phases apparently present in a caliche-like duricrust, the nature of which indicates the intervention of brine during surface weathering of Mars. The identity and origin of the clay silicate phases has been discussed extensively,[9] and iron montmorillonite (smectite, nontronite) identified in subaqueous palagonite, soils above weathered basalt, and altered impact or volcanic glasses on Earth is generally accepted to be the most probable phyllosilicate mineral in martial regolith.[10-12]

Compositional similarities of the rare SNG meteorites (*shergottites, nakhlites, chassignites*) to martian fines have been noted.[5,13] Indeed,

their textures and mineralogy, consisting of volatile-rich mafic cumulates containing fayalitic olivines, iron-rich pyroxenes, and accessory pyrrhotite or troilite,[14] contribute to the common belief that SNG meteorites are derived from Mars.[15] The question arises whether other primary igneous rock-types and secondary minerals found on Earth might serve as analogues of martian materials and aid in a better understanding of geochemical processes on Mars.

The iron-rich basaltic magmas suggested to have flowed onto the surface of Mars may have terrestrial analogues in the iron-rich gabbros and diabases occurring in the Skaergaard (Greenland) intrusion, Beaver Bay (Minnesota) complex, and New Almalfi (South Africa) intrusive sheet.[16] Of particular interest is the Beaver Bay diabase which is intrusive into the Precambrian Keeweenaw volcanic series above the Duluth gabbro.[16,17] Fayalitic olivines and iron-rich pyroxenes contribute to the mineralogy of the Beaver Bay diabase, bearing remarkable similarities to the 20% partial melt composition of the martian mantle proposed by McGetchin and Smyth.[1]

A common alteration product of Beaver Bay iron-rich gabbroic rocks is hisingerite, a very poorly crystalline hydrous iron silicate formed by deuteric and late-state hydrothermal alteration of pyroxenes and olivine.[18] In massive form, hisingerite has a pitchy luster, conchoidal fracture and pulverizes to an orange-brown powder[19] resembling the color of martian regolith. Some broad, diffuse lines in x-ray diffraction patterns of hisingerite resemble those of nontronite,[20] the phyllosilicate commonly believed to occur on Mars. Moreover, chemical analysis of the Beaver Bay hisingerite[18] bears a remarkable resemblance to the Viking XRF analyses of the martian regolith[7] further supporting the belief that Beaver Bay-type iron-rich basaltic rocks and derivative hisingerite alteration products are martian analogue materials.

A precursor to whole-rock alteration of iron-rich basalts is iddingsite, which is specific to olivine and frequently occurs as reddish-brown pseudomorph after olivine in basic lavas.[21] X-ray diffraction measurements indicate that iddingsite consists of a mixture of more crystalline phases, including phyllosilicates (montmorillonite and chlorite), and iron oxide assumed to be goethite, commonly quartz and calcite, and rarely talc and mica.[22] It was suggested from textural evidence[23] that iddingsite formed from olivine phenocrysts in volatile-rich fluids before magma had consolidated, but a more recent interpretation[24] is that alteration of olivine occurred at lower temperatures (<140°C) producing an orientated intergrowth of goethite and phyllosilicates. The process of iddingsitization is not a simple process of oxidation and hydration, but results from leaching of Mg, addition of ferric iron and water, and constancy of Si content.[25] These element fractionations are comparable to those proposed during the formation of martian regolith,[4,6,7] and again the average chemical composition of iddingsite[21,22] bears resemblances to the Viking XRF analyses of martian fines,[7] as well as that of the "unknown" alteration products occurring in nakhlite meteorites[26] believed to have originated from Mars.[13]

The susceptibility of olivine to iddingsitization may obscure its detection in remote-sensed reflectance spectral profiles of Mars' surface.[27,28] Unaltered Fe^{2+}-bearing olivines produce a distinctive crystal field transition near 1.05 μm.[29] However, earth-based infrared spectra of

dark areas of Mars,[27] which are probably interfered least by wind-blown oxidized duricrust, show absorption bands at 0.99 μm (Fe-rich augite) and 0.88 μm (Fe-rich orthopyroxene and/or Fe^{3+}-bearing phase). The spectrum was interpretted as originating from a pyroxene-rich mafic rock (c.f. shergottite or nakhlite) stained by ferric oxide.[4,13,27] However, oxidization of Fe^{2+} to Fe^{3+} when olivine alters to iddingsite would be manifested by the absorption band at 0.88 μm. Whole-rock alteration to hisingerite would further eliminate Fe^{2+}-pyroxene bands, which are absent in remote-sensed spectra of martian bight areas.[28,30]

In summary, the strong compositional and paragenetic similarities between martian regolith materials and terrestrial hisingerite and iddingsite are consistent with a mineral assemblage on Mars surface consisting of ferric-bearing phyllosilicate, sulfate and oxyhydroxide phases. These were derived from post-magmatic deuteric alteration of volatile-rich iron-rich basaltic rocks containing fayalitic olivine, Fe pyroxenes, and accessory pyrrhotite.[31]

[1] McGetchin, T.R. and Smyth, J.R., Icarus, 34, 512 (1978). [2] Morgan, J.W. and Anders, E., Geochim. Cosmochim. Acta, 43, 1601 (1979). [3] Arvidson, R.E., Goettel, K.A. and Hohenberg, C.M., Rev. Geophys. Space Phys., 18, 565 (1980). [4] Baird, A.K. and Clark, B.C., Icarus, 45, 113 (1981). [5] Siever, R. and Woodford, N., Geochim. Cosmochim. Acta, 43, 717 (1979). [6] Toulmin III, P., Baird, A.K., Clark, B.C., Keil, K., Rose, H.J., Christian, R.P. and Evans, P.H., Journ. Geophys. Res., 82, 4625 (1977). [7] Clark, B.C., Baird, A.K., Weldon, R.J., Tsusaki, D.M., Schnabel, L. and Candelaria, M.P. Journ. Geophys. Res., 87 (B), 10059 (1982). [8] Clark, B.C. and van Hart, D.C., Icarus, 45, 370 (1981). [9] Banin, A., Margulies, L. and Chen, Y., Journ. Geophys. Res., 90 (C), 771 (1985). [10] Gooding, J.L. and Keil, K., Geophys. Res. Lett., 5, 727 (1978). [11] Berkley, J.L. and Drake, M.J., Icarus, 45, 231 (1981). [12] Allen, C.C., Gooding, J.L. and Keil, K., Journ. Geophys. Res., 87 (B), 10083 (1982). [13] Wood, C.A. and Ashwal, L.D., Proc. Lunar Planet. Sci., 12th, 1359 (1981). [14] Smith, J.V., Steele, I.M. and Leitch, C.A., Journ. Geophys. Res., 88 (B), 229 (1983). [15] McSween Jr., H.Y. and Stolper, E., Sci. Amer., 242, no. 6, 54 (1980). [16] Muir, I.D., Mineral. Mag., 30, 376 (1954). [17] Grout, F.F. and Schwartz, G.M., Minnesota Geol. Surv. Bull., 28, 119 pp. (1939). [18] Whelan, J.A. and Goldich, S.S., Amer. Min., 46, 1412 (1961). [19] Inglis, O.G. and Willoughby, D.R., Soil Sci., 104, 383 (1967). [20] Mackenzie, K.J.D. and Berezowski, R.M., Thermochim. Acta, 41, 335 (1980). [21] Deer, W.A., Howie, R.A. and Zussman, J., Rock-Forming Minerals, Vol 1A: Orthosilicates, 170 (Longmans, 1982). [22] Wilshire, H.G., Amer. Min., 43, 120 (1958). [23] Edwards, A.B., Amer. Min. 23, 277 (1938). [24] Baker, I. and Haggerty, S.E., Contrib. Mineral. Petrol., 16, 258 (1967). [25] Gay, P. and LeMaitre, R.W., Amer. Min., 46, 92 (1961). [26] Bunch, T.E. and Reid, A.M., Meteoritics, 10, 303 (1975). [27] Singer, R.B., Journ. Geophys. Res., 86, 7967 (1981). [28] Singer, R.B., Journ. Geophys. Res., 87 (B), 3031 (1982). [29] Burns, R.G., Amer. Min., 55, 1608 (1970). [30] Sherman, D.M., Burns, R.G. and Burns, V.M., Journ. Geophys. Res., 87 (B), 10169 (1982). [31] Research supported by NASA grant NSG-7604.

THE THEORETICAL DETERMINATION AND EXPERIMENTAL EFFECTS OF COOLING HISTORY ON SILICATE GLASSES

M. D. Dyar, Department of Earth, Atmospheric, and Planetary Sciences, Massachusetts Institute of Technology, Cambridge, Massachusetts 02139; D. P. Birnie, III, Department of Materials Science and Engineering, Massachusetts Institute of Technology, Cambridge, Massachusetts 02139; M. T. Naney, Chemistry Division, Oak Ridge National Laboratory, Oak Ridge, Tennessee 37831; and S. E. Swanson, Geophysical Institute and Geology/Geophysics Program, University of Alaska, Fairbanks, Alaska 99701

Cooling history studies of glasses are critical to our understanding of lunar magmatic processes and to the interpretation of remote-sensed reflectance spectra of the Moon's surface. The key issues in such studies are: (1) how can we conveniently determine the cooling history of a given glass, and (2) what features of glass structure are affected by changes in cooling rates. These questions can be best addressed through use of both theoretical calculations and experimental work:

Theoretical cooling rates for any glass quenched in any medium may be calculated if the thermal properties of the sample and its quenching medium both are known. Expressions developed by Birnie and Kingery (1) were applied to typical lunar samples with ρ = 2.5 g/cc, h = 0.3 cal/g·°C, and k = 0.005 cal/cm·sec·°C. To date, cooling rate ($\dot{T}$) calculations for samples quenched in air and water have been made; pending completion of experiments to determine heat transfer coefficients, calculations will be extended to liquid nitrogen and vacuum environments. Preliminary results are tabulated below:

half-thickness, cm:	0.05	0.1	0.2	0.3	0.5	1	5	10	100
$\dot{T}$ (air), °C/sec:	50	25	13	8	5	2.5	0.15	0.04	0.0004
$\dot{T}$ (water), °C/sec:	1100	550	95	42	15	4	0.15	0.04	0.0004

These results for air quenches compare favorably with measurements performed on actual lunar samples (2,3). Development of cooling rate expressions based on sample size may be an easy way to relate known glass size distributions with thermal history scenarios on the lunar surface.

Knowledge of cooling rates is important because previous work (4) has suggested that cooling history can have profound effects on iron site partitioning and redox kinetics in synthetic silicate glasses. To test these effects in natural samples, 100 mg aliquots of representative basalt, andesite, and rhyolite compositions were melted in a CO/CO_2 atmosphere at 1343±2°C, log fO_2 = -7.85±0.5 for 24-48 hrs. Melts were quenched in an air jet, an H_2-Ar gas jet, and an NaCl brine/ice bath (-21°C). Compositions were as follows: (5)

Sample:	SiO_2	Al_2O_3	FeO	MgO	CaO	Na_2O	K_2O	TiO_2	P_2O_5	MnO	Total
Rhyolite:	73.43	13.76	1.74	0.29	1.16	4.19	4.34	0.26	0.05	0.04	99.26
Andesite:	62.91	15.63	5.87	2.70	5.80	3.45	1.83	0.62	0.12	0.11	99.04
Basalt:	54.50	13.61	12.48	3.46	6.92	3.27	1.70	2.20	0.36	0.18	99.68

Mossbauer spectra were taken of each sample using standard procedures (6); spectra were fit to a sum of Lorentzian/Gaussian combined line shapes (7). Sample sizes with minimum projected cooling rates of ~8-13°C/sec were used. In contrast with previously-studied lunar green and brown glasses (which showed Fe^{2+}/Fe^{3+} variations with quenching) (4,8), compositions studied

here show no Fe^{3+} peaks. In these 100 mg samples there are no significant variations of isomer shift and quadrupole splitting parameters. However, for the basalt glass in particular (the sample closest to observed lunar compositions) there is a systematic change in the ratio of $Fe_{oct}^{2+}/Fe_{tet}^{2+}$, which increases as the quench medium changes from brine/ice to H_2-Ar to air. Since heat transfer coefficients of the media probably increase in that order (8), there appears to be a link between preference for octahedral coordination and slow quenches. This can be explained by the known relationship between molar volume and cooling rate: rapid quenches yield high molar volumes, and slow quenches result in denser glasses (9). Therefore the glasses behave predictably when quenched into the three media: more octahedral iron is observed in slowest quenches (densest glasses).

This work on cooling rates has several implications for lunar glass research:

(a) knowledge of size distribution (as it relates to cooling rate) may contribute to our understanding of fire-fountaining processes on the Moon;

(b) the correspondence between Fe site occupancy and cooling rate places constraints on earth-based attempts to synthesize lunar analogues;

(c) changes in Fe partitioning as related to cooling rate may affect interpretations of remote-sensed spectra of areas with high glass contents in the lunar soil (10).

References

(1) Birnie, D. P. and Kingery, W. D. (1985) J. Mat. Sci. in press.
(2) Arndt, J. and Rombach, N. (1976) Proc. Lunar Sci. Conf. 7th, p. 1123-1141.
(3) Uhlmann, D. R., Yinnon, H., and Fang, C.-Y. (1981) Proc. Lunar Planet. Sci. Conf. 12th, p. 281-288.
(4) Dyar, M. D. (1984) Proc. Lunar Planet. Sci. Conf. 15th, in J. Geophys. Res. 89, p. C233-C239.
(5) Naney, M. T. and Swanson, S. E. (1985) Contrib. Mineral. Petrol., in press.
(6) Dyar, M. D. (1984) Am. Min., 69, 1127-1144.
(7) Stone, A. J., Parkin, K. M. and Dyar, M. D. (1984) DEC User's Society Program no. 11-720, Marlboro, MA.
(8) Dyar, M. D. and Birnie, D. P., III (1984), J. Non-Cryst. Solids, 67, 397-412.
(9) Kingery, W. D., Bowen, H. K., and Uhlmann, D. R. (1976) Introduction to Ceramics (Wiley: New York, 1976), p. 92.
(10) Research sponsored by NASA grant no. NSG-7604 (to R. G. Burns) and U.S. DOE, contract DE-AC05-840R21400 with Martin Marietta Energy Systems, Inc.

INVESTIGATIONS OF WEATHERING PROCESSES IN COLD, DRY ENVIRONMENTS - DRY VALLEYS OF ANTARCTICA.

Everett K. Gibson, Jr., SN4/Experimental Planetology Branch, NASA Johnson Space Center, Houston, TX 77058.

As part of our ongoing study of weathering processes in cold, dry environments, which are analogous to those operating on the surface of Mars, we have been studying the weathering processes as recorded in a suite of cores and soils from the Dry Valleys of Antarctica. Previously, Gibson et al. (1983) and Gibson et al. (1982) reported mineralogical and chemical data from the detailed study of a soil trench along with the study of the water soluble cations and anions associated with soils collected at various evaporite sites throughout the Dry Valleys of south Victoria Land, Antarctica. The results of those studies showed that considerable chemical and physical weathering was occurring sub-surface.

The Dry Valleys are located on the eastern flank of the Transantarctic Mountains, a north-south trending chain that borders the Precambrian shield of East Antarctica. The geology of the Dry Valleys is typical of the Transantarctic Mountains, which are dominated by late Precambrian to early Paleozoic fold belts overlain by flat-lying Paleozoic and early Mesozoic sediments (McKelvey and Webb, 1961). The basement complex in the Dry Valley region is made up of late Precambrian to early Cambrian medium- to high-grade metamorphic rocks (metasedimentary hornfelses, schists, and marbles) and mainly felsic igneous intrusives. The youngest basement rocks are dense swarms of granitic and lamprophyre dikes which crosscut all other basement rocks. Sedimentary rocks of the Beacon Supergroup, ranging in age from Devonian to Triassic, rest uncomformably on peneplained basement rocks (Webb, 1963). Beacon sediments were mainly deposited in fluvial, lacustrine, and aeolian environments; arkoses, subgreywackes, and orthoquartzites are the dominant rock type. The source rocks for the sediments were the hornfelses, schists, and acidic to intermediate igneous rocks of the underlying basement complex.

During Jurassic time, the basement complex and Beacon sediments were intruded by thick dolerite sills and sheets (Ferrar Group) on a massive scale. After the emplacement of the Ferrar dolerites in the Jurassic, the Dry Valley region entered a period of volcanic and tectonic quiescence, marked only by erosion (Harris, 1981). This continued until approximately 4 million years ago, when volcanic activity began in the Dry Valleys, lasting until a few hundred thousand years ago. Within the Dry Valleys, volcanism was minor, resulting in a few small basaltic cinder cones and scoria patches. In other parts of the region (i.e., Ross Island), volcanism was more extensive and continues to be active. By mid-Miocene time (10 m.y. B.P.), continental glaciation was fully developed. Glacial erosion by ice from the polar plateau is thought to be responsible for the creation of the Dry Valleys (Bockheim, 1979). The valleys are on the order of 10 m.y. old (Harris, 1981). throughout the valleys are numerous moraines, composed of silty tills and gravels along with deposits associated with previous marine incursions (Vucetich and Topping, 1972). Additional glacial episodes occurred after the retreat of marine waters.

As part of a long-term study of physical and chemical weathering mechanisms in the ice-free valleys of south Victoria Land, Antarctica, Mike Malin of Arizona State University has established test sites in different micrometeorological, topographic, and sedimentological environ-

ments within Victoria, Wright, and Taylor Valleys (Malin, 1984). We have supplied core tubes in which soil samples have been taken at various sites. The soils collected with the cores consist of a variety of types developed from different weathering regimes. The cores have been returned from Antarctica and are presently at NASA-JSC where they are in the early stages of documentation and processing. The soils within the nine cores will be extruded and photographed prior to dissection.

Sampling sites for the cores retured during the 1984-85 Field Season include the following:

Core Number	Location
7	Wright Valley, Middle Moraine, Bartley
11	Wright Valley, Inner Moraine, Bartley
35	Wright Valley, Dias Plateau, Top, Ripple Site
72	Wright Valley, 6th Cirque from Upper Moraine in Asgard Range
33	Bull Pass Upper Moraine
41	Bull Pass Middle Moraine
20	Victoria Valley, Lake Vida, Lower South Side
50	Victoria Valley, Lade Vida, Lower Vida
52	Victoria Valley, Lake Vida, Upper Eastern

Within the soil samples from the Dry Valleys it has previously been shown that the weathering processes have produced a variety of secondary minerals including: halite, mirabilite, bloedite, gypsum, calcite, aragonite, monohydrocalcite, soda niter, thenardite, antarcticite, bishovite, sylvite, trona, and limonite (Gibson et al., 1983). Studies of the water soluble cations and anions in soils from the Dry Valleys has shown that previously developed models of regolith development within the cold, dry environments of Antarctica should be applicable to studies of Martian regolith (Gibson et al. 1982). Because of the previously identified "wet" period of Martian geologic history, it is very likely that conditions on Mars are similar to those found in the Antarctic deserts. The abundance of salts and related phases should be quite high within the Martian regolith. Our study of the soils from the cores collected at different sites within the Dry Valleys should produce additional supporting evidence which can be used to refine soil development models for the Martian regolith.

References

Bockheim, J. G. (1979) Soil Sci. 128, 142-152.

Gibson, E. K. Jr. et al. (1982) Repts. of Planetary Geology Program - 1982, 333-335. NASA TM-85127.

Gibson, E. K. Jr. et al. (1983) Proc. 13th Lunar & Planet. Sci. Conf., Part 2, J. Geophys. Res. 88, A912-A928.

Harris, H. J. H. (1981) Ph.D. Dissertation, U. of Illinois. 341 pgs.

Malin, M. C. (1984) Antarctic J., 19, 14-16.

McKelvey, B. C. and Webb, P. N. (1961) Nature, 189, 545-547.

Vucetich, C. G. and Topping, W. W. (1972) N.Z. J. Geol. Geophys., 15, 660-673.

Webb, P. M. (1963) N.Z. J. Geophys., 6, 361-387.

MARTIAN WEATHERING PRODUCTS IN A SHERGOTTITE METEORITE. J. L. Gooding (1) and D. W. Muenow (2). (1) Planetary Materials Branch, NASA/Johnson Space Center, Houston, TX 77058 USA. (2) Dept. of Chemistry and Hawaii Institute of Geophysics, University of Hawaii at Manoa, Honolulu, HI 96822 USA.

Introduction. Although considerable circumstantial evidence exists for the derivation of shergottite meteorites from Mars [1], the first direct evidence for their Martian origin came from the discovery, in the shergottite Elephant Moraine, Antarctica A79001 (EETA79001), of trapped gases that resembled the Martian atmosphere both in elemental and isotopic composition [2,3].

If, in fact, EETA79001 and other shergottites are samples of the surface or near-surface materials of Mars, other physical evidence might occur in the meteorites that would indicate the nature and extent of interactions between the source rocks and the chemically reactive Martian atmosphere. In other words, traces of Martian weathering products might exist in the meteorites. The discovery and identification of Martian weathering products might provide important new insights into the possible role of the regolith as a reservoir for water and other volatiles on Mars.

Search Strategy for EETA79001. Previous measurements of trapped gases in EETA79001 indicated that the "Martian" atmospheric component was not homogeneously distributed but was concentrated in peculiar glass-rich pockets that occur as millimeter- to centimeter-sized, ovoid to irregular inclusions within the meteorite. Therefore, the present work was focussed on characterizing mineralogical differences between the gas-poor, pyroxene-maskelynite host rock (Lithology A) and the gas-rich, glassy inclusions (Lithology C). Because pre-terrestrial weathering products were the objects being sought, appropriate control samples were included so that Antarctic weathering products would not be mistaken for Martian weathering products. Therefore, adjacent interior (2-cm depth) chips of Lith-A and Lith-C were studied along with weathered exterior chips of Lith-A. Weathered exterior chips of eucrite EETA79004, which was found in Antarctica in the general vicinity of EETA79001, were included as additional control samples. Eucrite EETA79004 is not considered to be a Martian meteorite but probably experienced a "terrestrialization" history that was very similar to that of EETA79001.

Details of the analytical procedures can be found elsewhere [4]. Each chip was examined by scanning electron microscopy (SEM) and quantitative energy-dispersive x-ray spectrometry (EDS) to determine the morphologies and elemental compositions of selected phases. After SEM/EDS, each sample was individually pyrolyzed in a Knudsen cell under high vacuum and evolved volatiles were quantitatively analyzed by quadrupole mass spectrometry.

Sulfur-rich Secondary Aluminosilicates. SEM/EDS revealed that the Lith-C sample of EETA79001 (but not the Lith-A sample) contained traces (< 1 volume percent) of small grains (mostly < 10-μm size) that were substantially different from the primary igneous phases that comprise the bulk of the meteorite. In general, the trace phases possessed micabole-type aluminosilicate compositions (Fig. 1) but with surprisingly high concentrations of sulfur. In addition, one variety of aluminosilicate contained a high concentration of chlorine. Texturally, the aluminosilicates appeared to be either trapped in glass or related to glass as reaction products. The secondary aluminosilicates were texturally and compositionally different from Antarctic weathering products that were abundant in the control samples. Indeed, no weathering products of

demonstrably Antarctic origin were found in the Lith-C sample.

Oxidized Sulfur. During pyrolysis, the Lith-C sample released a surprising amount of oxidized sulfur (SO_2) whereas the Lith-A sample released sulfur mostly as reduced species (H_2S and S_2). Evolution of reduced sulfur gases would be expected if igneous pyrrhotite, the dominant sink for sulfur in EETA79001, was the sole carrier of sulfur in the sample. In fact, the bulk sulfur in Lith-C was twice as oxidized as that in Lith-A and, considering only the sulfur released at high temperature (> 950 C, where Mars-like noble gases and nitrogen are also released), the Lith-C sample was 8 times more oxidized than the Lith-A sample (Fig. 2). Only the weathered control samples, which included gypsum of Antarctic origin, evolved similar proportions of oxidized and reduced sulfur species. However, no gypsum occurred in the Lith-C sample and the pyrolytic release profile of the oxidized sulfur in Lith-C was completely different from that of gypsum. Therefore, a refractory "sulfate" of pre-terrestrial origin must have been the carrier of oxidized sulfur in Lith-C.

Relict Weathering Products. Apparently, the glassy inclusions of Lith-C in EETA79001 formed in an atmosphere that was sufficiently oxidizing to form sulfate from sulfide (which would be achievable by the Martian atmosphere [7]) and at least a small portion of the sulfate was preserved as discrete, sulfur-rich, aluminosilicates. The additional enrichment of chlorine in one variety of aluminosilicate marked a possible petrogenetic link with the sulfur- and chlorine-rich, fine-grained materials that cover much of the Martian surface at the two Viking landing sites [5,6]. In fact, a simple arithmetic mixture of two varieties of the secondary aluminosilcates produced an elemental composition that agreed remarkably well with that of surface fines at the Viking landing sites (Table 1). Unfortunately, the water contents of the tiny grains of pre-terrestrial weathering products in EETA79001 could not be measured although additional analyses are planned for new samples.

If it is hypothesized that the "sulfate" component pre-dated the melting that produced Lith-C, then the glassy pockets in EETA79001 might be understood as areas which were originally enriched in Martian weathering products (or deuteuric alteration products, as in amygdaloidal terrestrial basalts) that preferentially melted, because of their high intrinsic volatile contents, during the (shock-induced?) heating event that formed Lith-C. In that case, aluminosilicates in Lith-C might represent relict grains of Martian alteration products that escaped melting and further evidence for such an origin should exist as relics that can be documented in other samples. The same scenario would suggest that other trapped atmospheric components might also have been inherited from gas-rich alteration products that were melted but incompletely degassed during the event that formed Lith-C. Initial absence or rarity of similar areas of alteration or weathering might explain the absence of large glass pockets, and the concomitant lower concentrations of trapped Martian gases, in other shergottites. As a test of that interpretation, an intensified search for Martian alteration products will be made in EETA79001 and in other shergottites. Positive identification of the phases in question and measurement of their volatile contents should provide important new information about the role of the Martian regolith as a sink for volatiles.

References: [1] Wood C. A. and Ashwal L. D. (1981) Proc. Lunar Planet. Sci. 12B, 1359. [2] Bogard D. D. and Johnson P. (1983) Science, 221, 651. [3] Becker R. H. and Pepin R. O. (1984) Earth Planet. Sci. Lett., 69, 225.

[4] Gooding J. L. and Muenow D. W. (1985) Geochim. Cosmochim. Acta, in press. [5] Clark B. C., Baird A. K., Weldon R. J., Tsusaki D. M., Schnabel L., and Candelaria M. P. (1982) J. Geophys. Res., 87, 10,059. [6] Toulmin P. III, Baird A. K., Clark B. C., Keil K., Rose H. J. Jr., Christian R. P., Evans P. H., and Kelliher W. C. (1977) J. Geophys. Res., 82, 4625. [7] Gooding J. L. (1978) Icarus, 33, 483.

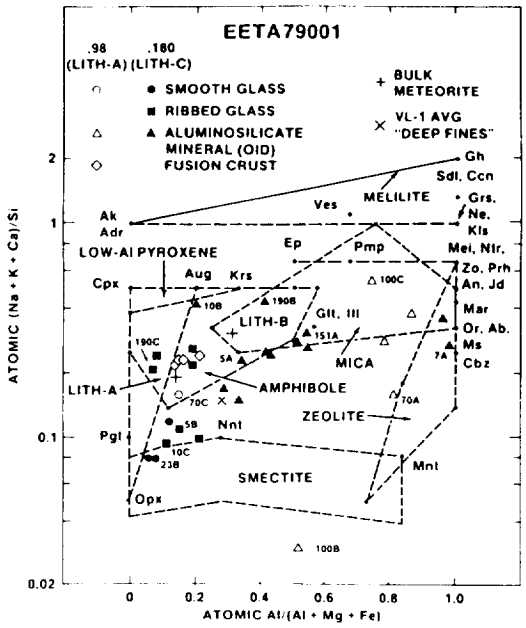

Figure 1. Representative compositions of "glass" and aluminosilicate phases in EETA79001,98 (weathered Lith-A) and EETA79001,180 (Lith-C) compared with those of major groups of aluminosilicate minerals and with other reference materials. The VL-1 "deep fines" composition is from Clark et al. [5]. Note that aluminosilicates in Lith-C are different from Antarctic weathering products in Lith-A.

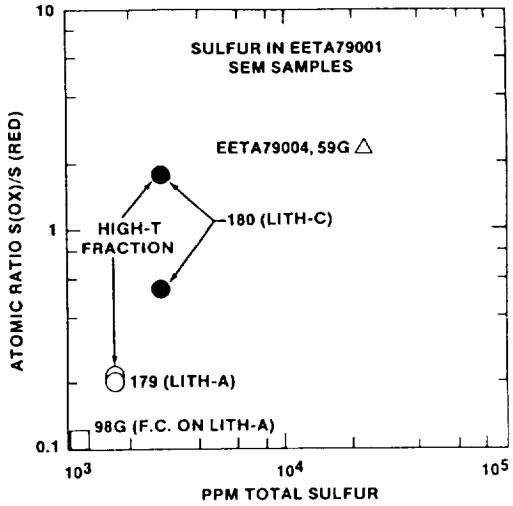

Figure 2. Abundances and relative oxidation states of sulfur in host-rock (Lith-A) and glass-inclusion (Lith-C) samples of shergottite EETA79001. Sulfur pyrolyzed from Lith-A occurred mostly as H_2S and S_2 whereas much of the sulfur pyrolyzed from Lith-C was SO_2. The high oxidation state of sulfur in eucrite EETA79004 is due to gypsum of Antarctic origin. However, the Lith-C sample was verified by electron microscopy to be free of gypsum and other recognizable products of Antarctic weathering. Therefore, the oxidized sulfur in Lith-C must be pre-terrestrial in origin.

Table 1. Weight Percent Composition of Martian Surface Fines Compared with Those of "Martian" Weathering Products in Lithology-C of Shergottite EETA79001[1]

	Chryse Planitia, Mars				EETA79001,180		
	A	B[4]	C[4]	D[4]	E[4]	F[4]	G[4]
SiO_2	44	48	54	55	50.3	41.5	49.4
TiO_2	0.62	0.68	0.76	0.78	0.53	0.45	0.51
Al_2O_3	7.3	8.0	9.0	9.2	11.0	11.9	11.3
Cr_2O_3	nd	nd	nd	nd	0.20	<0.1	<0.1
Fe_2O_3[2]	17.5	19.2	21.6	22.0	14.0	22.3	15.6
MnO	nd	nd	nd	nd	0.76	0.51	0.71
MgO	6	6	3	8	9.9	2.4	8.4
CaO	5.7	6.2	7.0	1.2	7.3	8.4	7.5
Na_2O	nd	2.2	2.5	2.5	1.9	3.2	2.1
K_2O	0.5[3]	0.5	0.6	0.6	0.12	2.3	0.55
P_2O_5	nd	nd	nd	nd	1.3	1.4	1.3
SO_3	6.7	7.4	0	0	2.8	3.0	2.9
Cl	0.8	0.9	1	1	<0.1	2.8	0.55

A: VL-1 avg. "deep fines" [5].
B: A + 2% Na_2O (Na not analyzable by Viking).
C: B minus $MgSO_4$.
D: B minus $CaSO_4$.
E: analysis 5A.
F: analysis 190B.
G: 80% E + 20% F.

[1] nd = not determined.
[2] all iron as Fe_2O_3.
[3] reported upper limit.
[4] normalized to 100%.

LUNAR MANTLE COMPOSITION AND DENSITY MODELS CONSISTENT WITH SEISMIC VELOCITY LIMITS AND OTHER GEOPHYSICAL CONSTRAINTS

L. L. Hood and J. Jones, Lunar and Planetary Laboratory, The University of Arizona, Tucson, AZ 85721.

The moon is the only body in the solar system other than the earth for which seismic data are available and for which the moment of inertia has been observationally determined. At present, however, there is little agreement as to the extent to which these data as well as other lunar geophysical measurements may be applied to constrain the bulk composition and structure of the mantle and (via the moment-of-inertia constraint) the existence and mass of a possible metallic core. A previous investigation with this objective was reported by Buck and Toksoz (1) using a mantle seismic velocity model derived by Goins (2) from a subset of the final Apollo seismic data set (Fig. 1a). However, a significantly different velocity model has more recently been derived by Nakamura (3) based on the complete five-year data set acquired when the four Apollo seismometers were simultaneously operative. Signals were analyzed from 41 independent deep moonquake sources as compared to 24 sources used by Goins and 11 sources used in an earlier study by Nakamura and others. It was concluded that no more than a three-layer mantle velocity model is justified by data resolution (Fig. 1b). Although the Nakamura velocity model is subject to significant uncertainties (only one-standard-deviation error limits could be estimated), the uniqueness of the lunar seismic data set and the probable length of time before a more accurate model will be available (a decade or more) requires that this model be carefully analyzed.

A preliminary investigation of lunar mantle composition and density models consistent with both Nakamura's (3) and Goins' (2) S-wave velocity limits was reported by Hood (4; see also ref. 5). In the upper mantle (< 500 km depth), only olivine-pyroxene mixtures with arbitrary Mg/(Mg+Fe) ratios were considered while in the middle and lower mantle the addition of garnet was considered in amounts up to 20 wt%. The latter limit was imposed to be consistent with recent bulk composition models that are characterized by Al_2O_3 abundances of < 6 wt%. In the case of the Goins model, it was found that the velocity decrease below 400-480 km depth (Fig. 1a) could be explained in terms of an increase in FeO content of mafic silicates. The resulting density increase (Fig. 2a) was either small or large depending on the assumed garnet fraction. The presence of metallic iron cores with radii as large as 400 km and as small as 0 km were needed to match the mean density and moment of inertia constraints. These results generally agree with those of Buck and Toksoz (1) although they chose to consider the presence of free Fe-FeS metal below 480 km in order to lower the seismic velocities. In the case of the Nakamura model, it was found that the velocity increase below 500 km depth could be explained in terms of the presence of garnet alone only if inordinately large Al_2O_3 abundances were allowed (> 7 - 10 wt%). Because this requirement was inconsistent with recent bulk composition models, the alternative possibility of an increased Mg/(Mg+Fe) ratio in the middle and lower mantle was considered as well as the presence of garnet in amounts up to 20 wt%. However, the

corresponding density models (Fig. 2b) were characterized by density decreases below 500 km depth that would have been unstable to convective overturn during early lunar history. Consequently, it was concluded that errors existed either in the Nakamura velocity limits or in the simplified modeling of those limits as reported in Hood (4), or both.

In work that is currently in progress, an effort is being made to more accurately model the Nakamura mantle velocity limits in order to allow final conclusions to be drawn about both the probable validity of these limits and their possible implications for lunar composition and density models. A more self-consistent approach is employed in which a bulk composition model is initially assumed by specifying the total lunar abundances of the oxides, FeO, MgO, SiO_2, Al_2O_3, CaO, TiO_2, Na_2O, and K_2O. It is then assumed that the moon accreted homogeneously and differentiated to some depth d greater than 200 km. Observational limits on mean composition and thickness of the crust are next applied to estimate the incompatible oxide abundances that must be removed from the differentiated portion of the mantle. Finally, the mantle is assumed to have been homogenized after differentiation by subsolidus convection during early lunar history. The final mantle composition is then converted to normative mineral assemblages using procedures similar to but improved in comparison to those employed by Buck and Toksoz. Substitution of aluminum into the pyroxene structure is accounted for in estimating spinel and garnet abundances. Next, seismic velocities are computed as a function of depth in the mantle using available laboratory measurements of velocities and their temperature and pressure derivatives (for a partial compilation, see Table 1 of ref. 5). The calculated velocities are compared to the one-standard-deviation limits of Nakamura (1983) and the assumed bulk composition model is accepted or rejected if agreement is or is not obtained, respectively. For bulk composition models that satisfy the seismic velocity limits, density profiles are calculated by iteratively solving the Murnaghan-Birch equation of state; pressure is determined by integrating the hydrostatic equation and temperature is estimated using the thermal history modeling result of Toksoz et al. (6) which is in reasonable agreement with available observational constraints. Sensitivity of the resulting models to the selected temperature profile is tested, however. All density models are required to match experimental limits on lunar mean density and moment of inertia. When necessary, metallic cores with an assumed iron composition are added to achieve this agreement. Results will be reported at the 17th Lunar and Planetary Science Conference.

References - (1) Buck, W.R. and Toksoz, M.N. (1980) Proc. Lunar Planet. Sci. Conf. 11th, 2043. See also Binder, A.B. (1980) J. Geophys. Res., 85, 4872. (2) Goins, N.R. (1978) Ph.D. Thesis, M.I.T., Boston, 666p; see also Dainty, A.M. et al. (1976) Proc. Lunar Sci. Conf. 7th, 3057. (3) Nakamura, Y. (1983) J. Geophys. Res., 88, 667. (4) Hood, L. L. (1986) in The Origin of the Moon, W.K. Hartmann, R.J. Phillips, and W.J. Taylor, eds., LPI, Houston, in press. (5) Hood, L.L. and J. Jones (1985) in Lunar and Planetary Sci. XVI, p. 360, LPI, Houston. (6) Toksoz, M.N. et al. (1978) Moon and Planets, 18, 281.

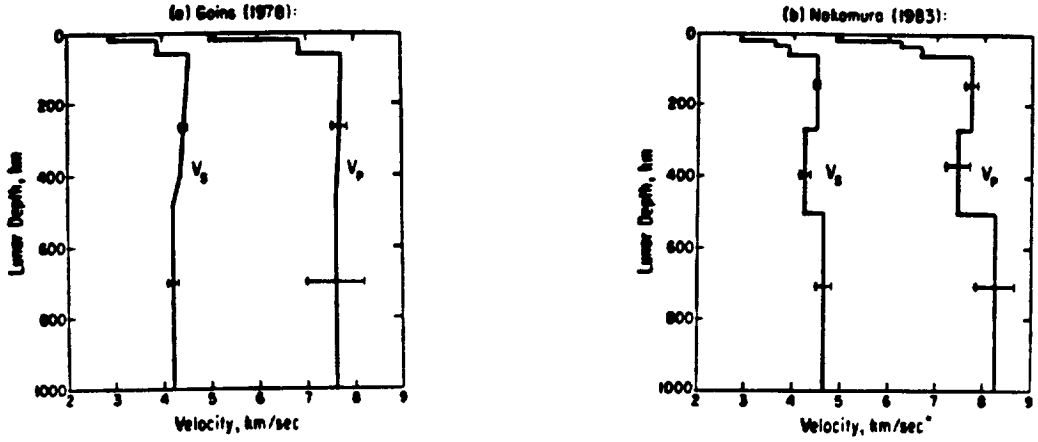

Fig. 1 (a) Lunar mantle P- and S-wave velocity model derived by Goins (1978) from a subset of the final Apollo seismic network arrival time data set. Brackets are taken from Buck and Toksoz (1980).
(b) P- and S-wave model derived by Nakamura (1983) using a nearly complete arrival time data set, including significantly more deep moonquake signals than were available in earlier analyses.

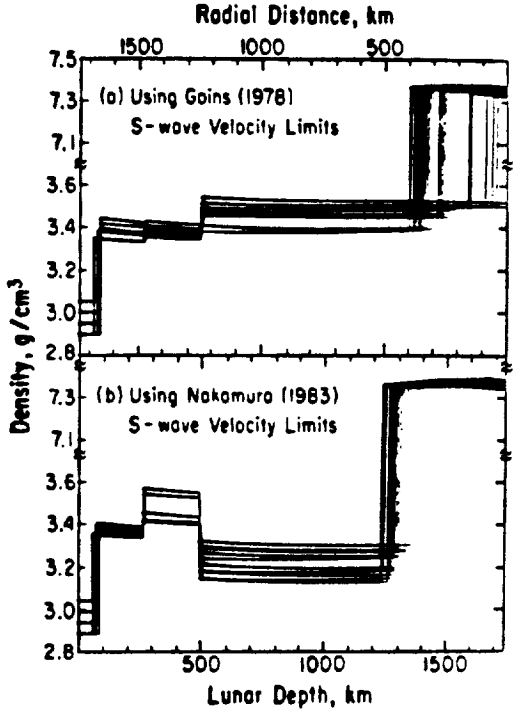

Fig. 2 (a) Density models for simplified mantle compositions consistent with the mantle S-wave velocity model of Fig. 1a. Note that metallic cores with an assumed iron composition were added when necessary to match mean density and moment of inertia constraints.
(b) Same format as (a) using the S-wave velocity model of Fig. 1b.

HIGH-PRESSURE EXPERIMENTAL STUDIES BEARING ON OXYGEN IN PLANETARY CORES

Raymond Jeanloz and Elise Knittle, Department of Geology and Geophysics,
University of California, Berkeley, CA 94720

On the basis of cosmochemical arguments, Ringwood has proposed that oxygen is the primary alloying component of iron in the Earth's core *(1,2)*. This proposal rests on the idea that the chemical bonding character of iron oxide changes radically under pressure, with the oxide becoming metallic at conditions of the deep mantle and hence becoming soluble in core-forming iron. If verifiable, such an oxygen-rich model of core composition would be even more applicable to Venus, which appears to be more oxidized than Earth. Consequently, the classical distinction in composition between oxide mantles (~60 atomic percent oxygen) and metallic cores of the large terrestrial planets is significantly diminished in such models, oxygen making up to 30 percent (atomic) of the core alloy.

High-pressure measurements of electrical resistivity have been performed on iron oxides in order to verify that the proposed metallization occurs. Data have been collected both by static (diamond-cell) and dynamic (shock-wave) techniques, the former being at room temperature and the latter being at temperatures up to about 3600 K. The reliability of the two high-pressure techniques is corroborated by measurements on Fe_2O_3 (Figure 1). A sharp decrease in resistivity observed at 50 GPa in a previous shock-wave study (3) is quantitatively reproduced by our new diamond-cell measurements (4). The resistivity of the high-pressure phase, which had not been determined but was bounded in the previous work, is 3 orders of magnitude less than that of the low-pressure phase. The resistivity change proves that metallization does *not* occur in Fe_2O_3 at 50 GPa. Rather, the new data in combination with published Mössbauer and x-ray diffraction measurements (5,6) indicate that this electronic transition probably involves a valence change.

Wustite ($Fe_{0.94}O$) exhibits a phase transition at 70 GPa under shock-wave loading, but no transition has been observed by x-ray diffraction at room temperature to a static pressure of 120 GPa (7,8). This apparently contradictory set of results is corroborated by our new shock-wave and diamond-cell electrical resistivity measurements (9,10). As shown in Figure 2, wüstite exhibits metallic conductivity at shock pressures exceeding 70 GPa, but no significant change in resistivity is observed to static pressures of 85-90 GPa. That FeO is metallic under the high-temperature shock conditions is confirmed by the absolute magnitude of the observed resistivity, comparable to that of Fe. Also, the increase in resistivity with pressure is characteristic of metals, due to the rapid increase of Hugoniot temperature. The phase diagram implied by the existing high-pressure data for wüstite, Figure 3, is in excellent agreement with a theoretically predicted phase diagram in which the three phase boundaries intersect at a tricritical point (11).

The new resistivity measurements provide strong experimental support for Ringwood's hypothesis that oxygen is an important component of cores in large terrestrial planets. Specifically, his prediction that iron oxide metallizes under pressure is confirmed. In addition, the data suggest that metallization only occurs at elevated temperatures because of competing magnetic interactions; no evidence of metallization is found for a composition with O/Fe as large as 1.5 (i.e., hematite). To the extent that the compositions of the cores of Earth and Venus have equilibrated at pressures exceeding 70 GPa (depths exceeding

1670 - 1800 km for the present internal configurations of the planets), oxygen can apparently become the dominant alloying constituent of the core-forming metal.

REFERENCES

(1) Ringwood, A. E. (1977) *Geochem. J., 11,* 111-1336.

(2) Ringwood, A. E. (1979) *Origin of the Earth and Moon,* Springer-Verlag, New York, 295 pp.

(3) Kondo, K., T. Mashimo and A. Sawaoka (1980) *J. Geophys. Res., 85,* 977-982.

(4) Knittle, E. and R. Jeanloz (1985) *EOS, 66,* in press; submitted to *Solid State Commun.*

(5) Syono, Y., A. Ito, S. Morimoto, T. Suzuki, T. Yagi and S. Akimoto (1984) *Solid State Commun.,* 50, 97-100.

(6) Suzuki, T., T. Yagi, S. Akimoto, A. Ito, S. Morimoto, and Y. Syono (1985) in: *Solid State Physics Under Pressure,* (S. Minomura, ed.), Terra Scientific, Tokyo, pp. 149-154.

(7) Jeanloz, R., and T. J. Ahrens (1980) *Geophys. J. R. Astron. Soc., 62,* 505-508.

(8) Yagi, T., T. Suzuki and S. Akimoto (1985) *J. Geophys. Res., 90,* 8789-8788.

(9) Knittle, E. and R. Jeanloz (1985) *EOS, 66,* 367.

(10) Knittle, E., R. Jeanloz, A. C. Mitchell and W. J. Nellis (1985) submitted to *Solid State Commun.*

(11) Falicov, L. M., C. E. T. Gonçalves da Silva and B. A. Huberman (1972) *Solid State Commun., 10,* 455-458.

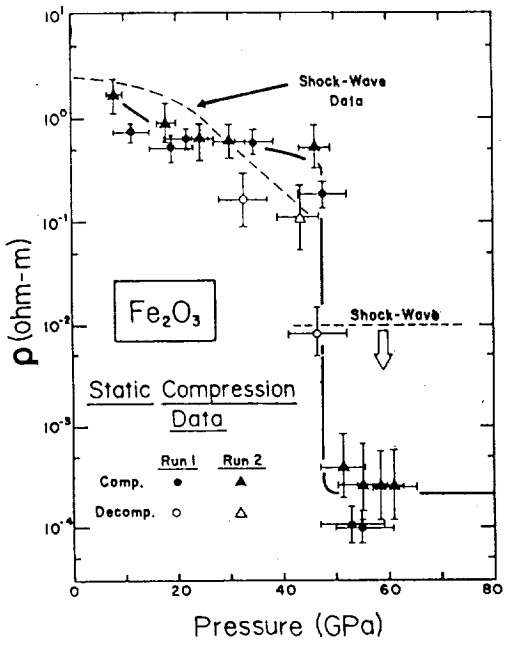

Figure 1. Electrical resistivity of Fe_2O_3 (ρ in $ohm \cdot m$) as a function of pressure: static-compression data are compared with the shock-wave results of *(8)* summarized by the dashed curve. Measurements upon compression and decompression in the diamond cell exhibit little hysteresis.

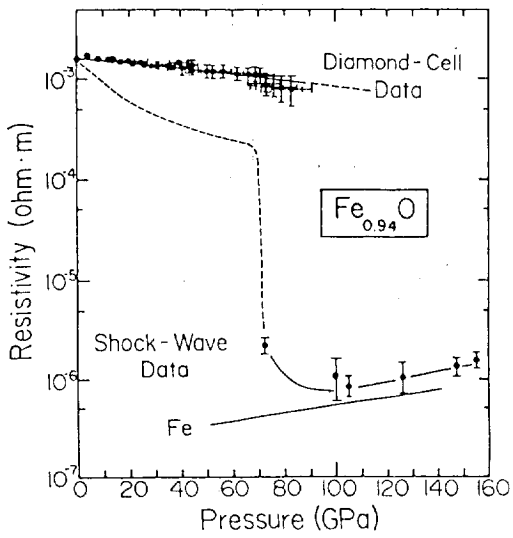

Figure 2. Electrical resistivity of $Fe_{0.94}O$ wüstite obtained in high-pressure diamond-cell and shock-wave experiments is compared with shock-wave measurements for Fe, summarized by solid line without data. The zero-pressure resistivities of wüstite samples used in static and dynamic experiments are identical.

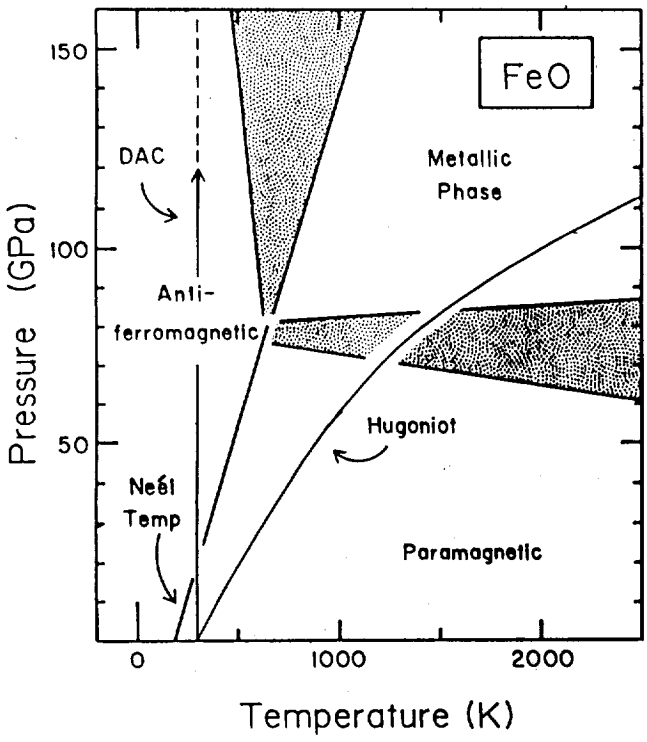

Figure 3. Phase diagram proposed for FeO on the basis of the existing structural and electrical-resistivity data obtained in diamond-cell (DAC) experiments and shock-wave experiments along the indicated paths. The intersection of the boundaries between artiferromagnetic (nonmetallic), paramagnetic (nonmetallic) and metallic phases is not quantitatively constrained: shading illustrates uncertainties.

PROPERTIES OF PLANETARY MATERIALS AT HIGH PRESSURES AND TEMPERATURES

W. J. Nellis, H. B. Radousky, M. Ross, and A. C. Mitchell
Lawrence Livermore National Laboratory, University of California
Livermore, CA 94550

The outer planets Uranus and Neptune are thought to consist of the "ices" H_2O, NH_3, and CH_4, and possibly CO, CO_2, and N_2.[1] In order to understand the nature of these molecules at conditions in these planetary interiors, we have been studying the equation-of-state and the electrical conductivity at high dynamic pressure. The condensed gases in these planets were compressed isentropically starting from very low density and temperature. By virtue of their large masses, however, interior temperatures and pressures are quite large. The conditions in the "ice" layer range between 20-600 GPa (0.2-6 Mbar) and 2000-7000K.[2] Shock compression of liquids achieves virtually the same states.

During the past year we have developed a new, fast optical pyrometer and a cryogenic specimen holder to measure the shock temperature of NH_3 and N_2. Liquid N_2 was used as the coolant for the nitrogen experiments and a cold N_2-gas flow system was used to cool the liquid ammonia holders. High shock pressures were generated by impacting these cryogenic target specimens with planar projectiles accelerated by a two-stage light-gas gun. The experiment is illustrated in Fig. 1 for a Ta impactor. The pyrometer, illustrated in Fig. 2, consists of six photomultiplier detectors which measure the light intensity emitted from the shock-heated specimen at six wavelengths from 254-830 nm. Including the ultraviolet portion of the spectrum allows measurements up to 30,000K which is important for dense He, for example. The time-resolved output of the detectors is recorded on fast oscilloscopes and film. The data are converted to light intensity through calibration data and fit to black body spectra to obtain temperature.

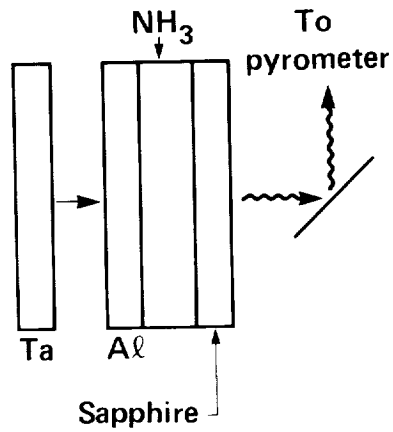

Fig. 1. Experiment. Light from shock front in specimen escapes through unshocked portion of specimen and sapphire window.

Oscillograms are shown in Fig. 3 for NH_3 and N_2 experiments. The signals are initially flat as the steady shock wave traverses the sample. The subsequent increase in voltage magnitude for the NH_3 experiment (left) is caused by the double shock off the sapphire window. This process takes the material to higher pressure, density, and temperature. An increase in double-shock temperature was seen in all our previous experiments except nitrogen. In Fig. 3 (right) we see that the double-shock voltage magnitude and thus the temperature is lower than the first-shock temperature. This is the first known observation of shock cooling. The shock temperature data for NH_3 are shown in Fig. 4.

The solid line in Fig. 4 is the result of a calculation using fluid perturbation theory and an intermolecular potential derived from a fit to the Hugoniot data.[3,4] Energies in molecular rotation and vibration are included. Experiment and theory

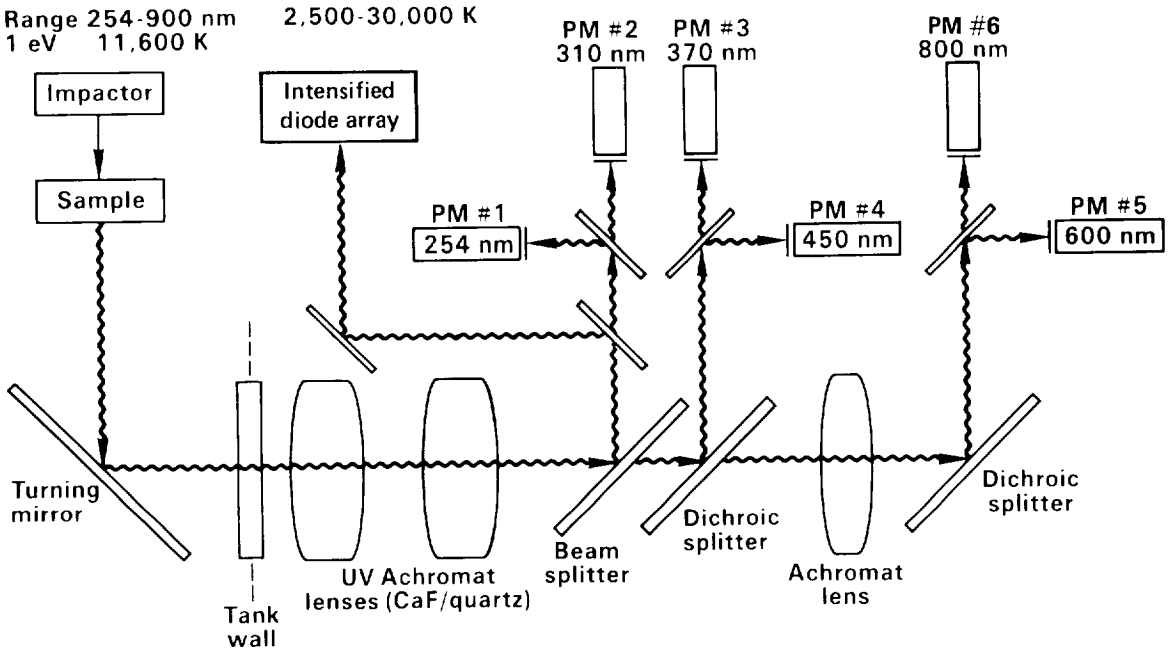

Fig. 2. Optical–ultraviolet pyrometer.

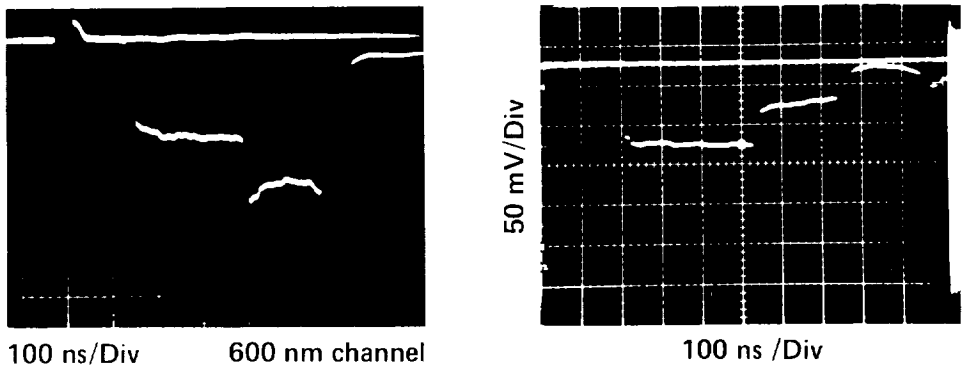

Fig. 3. Oscillograms for NH_3 (left) and N_2 (right) experiments discussed in text. Voltage and temeprature increase downward.

are in good agreement. The 10% deviation at highest pressure may be caused by an additional energy absorption mechanism, dissociation–ionization, as suggested by electrical conductivity data.[5] The relatively small difference between experiment and theory suggest that dissociation is not sufficient to affect the equation of state in a dramatic way.

A theory was also developed for nitrogen which includes a volume–dependent dissociation energy derived from a fit to the Hugoniot data in the phase transition region.[6] Agreement between the first–shock temperatures and theory is excellent. The theory is in qualitative agreement with the double–shock temperatures as well.

Monatomic N can exist in the outer planets by virtue of the decompositon of NH_3 at temperatures and densities above those of our experiments. The fact that nitrogen can be double–shocked to 100 GPa pressures while remaining relatively cool

means that these results are relevant to conditions in Uranus and Neptune. Our work on the dissociation of nitrogen and band theory[7] say that N is a very dense, stiff, diamond-like substance at planetary conditions.

This work was performed under the auspices of the U.S. Department of Energy by Lawrence Livermore National Laboratory under contract number W-7405-ENG-48 with partial support from the U.S. National Aeronautics and Space Administration.

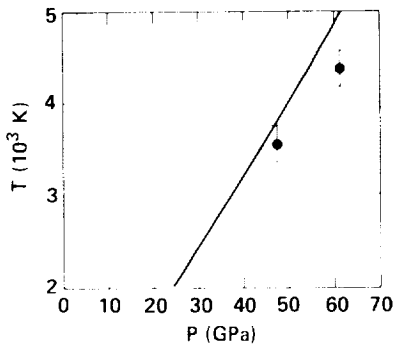

Fig. 4. NH_3 shock temperature vs pressure. Solid line is theory.

REFERENCES

1. D. J. Stevenson, Annu. Rev. Earth Planet Sci. 10, 257 (1982).
2. W. B. Hubbard and J. J. MacFarlane, J. Geophys. Res. 85, 225 (1980).
3. A. C. Mitchell and W. J. Nellis, J. Chem. Phys. 76, 6273 (1982).
4. R. D. Dick, J. Chem. Phys. 74, 4053 (1984).
5. A. C. Mitchell, M. I. Kovel, W. J. Nellis, and R. N. Keeler, High Pressure Science and Technology, edited by B. Vodar and Ph. Marteau (Pergamon Press, Oxford, 1980), Vol II, p. 1048.
6. W. J. Nellis, N. C. Holmes, A. C. Mitchell, and M. van Thiel, Phys. Rev. Lett. 53, 1661 (1984).
7. M. Ross and A. K. McMahan, Physics of Solids under High Pressure, edited by J. S. Schilling and R. N. Shelton (North-Holland, Amsterdam, 1981), p. 161.

HIGH PRESSURE COSMOCHEMISTRY OF MAJOR PLANETARY INTERIORS: LABORATORY STUDIES OF THE WATER-RICH REGION OF THE SYSTEM AMMONIA-WATER

Malcolm Nicol, Mary Johnson, and Steven Boone
Department of Chemistry and Biochemistry
University of California, Los Angeles, CA 90024

Existing models of the major planets and their satellites make simple, rather arbitrary assumptions concerning the deep interiors. "Rock" cores or "ice" (water-ammonia-methane) layers are often invoked without considering whether these are thermodynamically consistent. Furthermore, the behavior of "gas-ice" mixtures at very high pressures is very poorly understood. When this project began, virtually no measurements had been made on binary or multicomponent gas-ice systems at pressures of the order of tens of thousands of atmospheres. We set out, therefore, to determine some relevant pressure-temperature-composition (P-T-X) regions of the hydrogen (H_2)-helium (He)-water (H_2O)-ammonia (NH_3)-methane (CH_4) phase diagram. Such experimental studies, and theoretical modeling of the relevant phases, are needed to interpret the compositions of ice-gas systems of planetary interest.

This project is the first attempt to characterize compositions and structures of a multi-phase, multi-component system at very high pressures. At room temperature, this challanges technology; yet, our goal is to characterize a system over a wide range of temperatures. Thus, our initial task was to demonstrate that the necessary measurements reasonable precision. We began to work with NH_3-H_2O compositions that are relevant to planetary problems yet are easy to prepare.

This system also was chosen because a few parts of the P-T-X space had already been determined. The P-T surface of water had been examined by several groups, most recently by Mishima and Endo [1]; and Mills et al. [2] have determined the corresponding surface for NH_3. Rollet and Vuillard [3] studied the T-X diagram of ammonia-water at atmospheric pressure and found two water-rich phases, ammonia dihydrate ($NH_3 \cdot 2H_2O$), which melts incongruently, and the nonstoichiometric ammonia monohydrate ($NH_3 \cdot H_2O$), which melts at a higher temperature than the dihydrate. These results suggested that we should first study (1) a P-T surface at approximately the monohydrate composition and (2) P-X surfaces at lower ammonia compositions near room temperature. The latter conditions also were studied by our associate, Dr. Boehler, with a large-volume pressure apparatus in order to identify problems of metastability and sample size.

(1) Near the monohydrate composition, we studied melting to 5 GPa and 400 K, despite complications caused by the need to grow samples at low temperatures. We interpreted these observations in terms of congruent melting of the monohydrate melts. Lunine [4] has suggested an alternative interpretation in terms of incongruent melting to dihydrate plus liquid at room temperature. Thus, we are working to identify the phases present near the melting line by visual methods with polarized optics, spectroscopy, or x-ray diffraction.

Our first major step in this direction was to improve the sample preparation techniques. Mr. Boone developed a device to load diamond-anvil cells at room temperature reliably within 0.5 mole percent of any desired ammonia-water composition. The composition of the resulting solution can be determined with better than 0.1% precision. This system has been used to load samples with compositions up to 34-mole percent ammonia for P-T-X work being done by Dr. Johnson, and Mr. Boone will continue the studies near 50-mole percent ammonia.

(2) Near room temperature, Dr. Johnson extended the phase diagram of $(NH_3)_x(H_2O)_{1-x}$ at compositions in the range $0 \leq x \leq 0.5$, pressures up to 4 GPa, and temperatures from 100 to 400 K. She has examined in detail the compositions 5%, 20%, 25%, and 34% in an effort to resolve questions about the diamond-cell work and Dr. Reinhart Boehler's thermophysical studies. We discovered that the melting at 20% NH_3 and higher compositions is more complex than we had expected; the composition of the high-temperature solid phase varies with both temperature and time. At low temperatures (25°C and lower), five well characterized and well behaved phases were observed, including: liquid; ice VI; ice VII; an ammonia monohydrate, M; and an ammonia dihydrate, D. Above 3.3 GPa, D reconstituted into myrmekitic intergrowths of Ice VII with a higher-relief phase which appeared to be isotropic. From calculation of the area of the cell occupied by the various phases, the high-pressure phase was shown to have a composition near $NH_3 \cdot H_2O$. Whether the low-temperature and high-pressure hydrates are equivalent must still be examined.

Ammonia dihydrate (D) is the ammonia-bearing phase most likely to occur near the surfaces of icy planets. Our present understanding of the stability regions of D is shown, superimposed on the H_2O phase diagram, in Fig. 1. Freezing curves for D are shown for bulk compositions of 10, 15, 20 and 25% NH_3. At 25°C, the Ice VI-D eutectic is at 1.5 GPa and 19% NH_3; as temperature decreases, the eutectic shifts to higher NH_3 concentrations and lower pressures. There may be a second Ice VII-D eutectic at 100°C and 2.5 GPa.

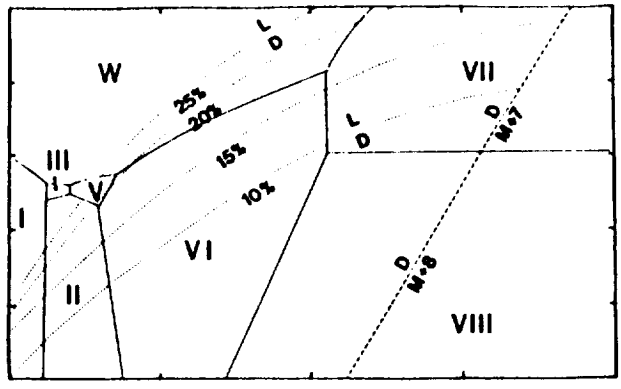

Fig. 1. Melting lines for ammonia-water mixtures at several compositions and the stability region of D superposed on the phase diagram of water.

At planetary surfaces, the expected assemblage is Ice I plus liquid or D. At higher pressures, D converts to M and Ice VII or Ice VIII, in a reaction with a positive Clapeyron slope. Thus, at depth, the stable assemblage is Ice plus M; local heating could cause the less dense D phase to form, creating pressure instabilities. These studies and recent thermophysical measurements made by Dr. Boehler's assistant, Shao Shuhui, will be described in an invited talk to be presented at the Fall meeting of the American Geophysical Union.

During the past year, Drs. Johnson and Nicol have participated in two other projects of planetary interest: a shockwave study of the equations of state of simple C-H-N-O molecules and resistively heating iron wires in diamond-anvil cells in order to obtain structural data relevant to the interior of the Earth by x-ray diffraction. Many "gases" of planetary interest undergo chemical reactions at pressures between 12 and 100 GPa. We are trying to characterize the products by detecting molecular emission spectra during passage of the shock front and have used benzene samples to demonstrate the feasibility of the method.

Experiments have been performed at pressures between 20 and 65 GPa and temperatures between 2000 and 5000 K. Emission spectra were obtained while the shock front passed the collection optics, and many bands of C_2 and other small molecules have been detected. These results were described at several high pressure symposia during the summer. New experiments are planned that will examine methane, carbon monoxide, and other light molecules of planetary interest and determine whether other molecular products can be detected by laser excitation of the shocked material.

During the spring, Professor Nicol and Dr. Reinhart Boehler developed techniques for resistively heating iron and other metals to their melting points in a gasketed diamond-anvil cell. During the summer, they and collaborators from UCLA, Universite Pierre et Marie Curie, Riso, and HASYLAB demonstrated that these techniques could be used to obtain high-pressure, high-temperature x-ray diffraction data for alpha, gamma, and epsilon iron that are needed to understand the nature of the Earth's core. At high temperatures, the temperature of the hot wires are measured with optical techniques which Dr. Johnson developed.

REFERENCES

1. O. Mishima and S.J. Endo (1980), **J. Chem. Phys. 73**, 2454.
2. R.L. Mills, D.H. Liebenberg, and Ph. Pruzan, Ph. (1982), **J. Phys. Chem. 86**, 5219.
3. A.-P. Rollet and G. Vuillard (1956), **Comptes. rendus Acad. Sci. Paris 243**, 383.
4. J. Lunine (1984) [personalcommunication].

GEOPHYSICAL INVESTIGATIONS OF VENUS

R.J. Phillips, Dept. of Geological Sciences, SMU, Dallas, TX 75275

From both Earth-based and Venera radar images it is clear that the surface of Venus has undergone significant tectonic deformation. If plate tectonics is not operating, then there is a clear need to understand mechanisms that will transform the energy of convection in the venusian interior into large horizontal stresses in the lithosphere.

The problem of convective coupling to an elastic lithosphere can be approached using the philosophy of *Richards and Hager* [1984], who showed that for a viscous fluid, boundary deformation is rapid compared to the changes in the convective flow pattern. In their formulation, boundary deformation is governed by the viscous relaxation time, a period in which convective motion in the Earth's mantle is only a few kilometers. The response with an elastic layer overlying a viscous fluid is even more rapid. Thus it is appropriate to consider a convecting system in which density perturbations in a fluid are fixed in position. The problem is solved for a thick elastic plate overlying a constant viscosity fluid. A thick plate is used to study the behavior of the stresses σxz and σzz as well as the usual bending stress encountered in thin-plate theory, σxx. Both no-slip (rigid) and free-slip (free) boundary conditions are used at the elastic-fluid interface. As a check, a thin-plate solution is also generated, using σzz of the fluid and $\sigma xz = 0$ as the lower boundary conditions [see *Jian and Parmentier*, 1985]. Some of the results obtained are (elastic layer thickness, t = 10 km; depth of density disturbance in fluid, d = 100 km; wavelength of disturbance, λ = multiples of 10 of t):

1) Free-slip solutions are in agreement with thin-plate results when $\lambda \geq$ ~100 t. At smaller values of λ, σxz is significant and affects σxx via the horizontal component of the equations of equilibrium.

2) For $\lambda \geq$ ~10 t, there are large (kilobar level) horizontal bending stresses (σxx) in the elastic lithosphere for the rigid case. This is because shear stress is directly coupled from the fluid into the elastic layer and, because shear stress vanishes on the upper boundary, there is a large vertical shear stress gradient in the layer. Large bending stresses are then required at long wavelengths to satisfy the horizontal component of the equations of equilibrium.

The results of these calculations, particularly for the rigid case, suggest that large stresses can be generated in an elastic layer overlaying a region of convective flow. The solution described above is for a density perturbation at a single depth and, because of the linearity of the equations involved, can be treated as a Green's function and integrated over a vertical distribution of density in the fluid. This in turn can be related to a convective temperature distribution [*Parsons and Daly*, 1983]. The first step in improving this solution is to introduce vertical viscosity variation in the fluid. For an exponential dependence with depth, solutions to the flow equations are straightforward [*Parmentier and Head*, 1981]. Other considerations are to treat the lithosphere as viscous

or plastic.

The ultimate application of this work is to calculate theoretical spectral admittance functions to compare with estimates, $Z(\lambda)$, of the same quantity derived from topography and line-of-sight (LOS) gravity data. Attempts to obtain good spectral estimates of the power and cross spectra [needed to estimate $Z(\lambda)$] by averaging raw spectral estimates across a finite wavenumber band were frustrated by the dominance of spectral energy in only one or two wavenumbers. An alternate and successful approach involved averaging spectral estimates for a given wavenumber for a number of neighboring orbits. This is a well-known technique in time series analysis for stationary stochastic processes. Application of this technique to a number of orbital track samplings requires that the statistics of the gross density structure of the subsurface be invariant beneath these tracks. A second requirement is that the orbital geometry be approximately the same for the orbits being averaged.

My initial investigation is of the wavelength region $\lambda < 2000$ km. For 1000 km $< \lambda <$ 2000 km, the gravity and topography are highly correlated, as expected. However, for $\lambda <$ 1000 km at least some of the gravity signal is *not* correlated with the topography. On the one hand, the admittance approach assumes that the gravity and topography *are* correlated, so the uncorrelated signals are a nuisance; on the other hand, they represent a new class of gravity signals for Venus and bear investigation in their own right. Admittance estimates have been calculated for three harmonics in the 1000 km $< \lambda <$ 2000 km range by averaging across 5 Pioneer Venus orbits west of Aphrodite Terra. There is a clear trend of increasing Z with increasing harmonic number that is significant with respect to the 1-σ error bars.

A series of computer experiments indicated that at least to first order the LOS admittance estimates are independent of orbital geometry and dynamics. That is, the estimated $Z(\lambda)$ can be compared directly to their theoretical counterparts. Under what conditions might this be true? The main requirement appears to be that the *differences* between orbital dynamics effects on observed LOS gravity and on topographically-derived LOS gravity must be at most second-order. This is a reasonable supposition when considering that a large part of the observed gravity is correlated with topography in the first place. The transformation from gravitational potential to LOS gravity is a multiplicative operation in the Fourier transform domain. Thus the LOS admittance estimate $Z(\lambda)$ is in essence the ratio of two potential functions and seems to be approximately independent of dynamical effects. The implication of deriving LOS admittance estimates that can be inverted directly for model parameters is important and places planetary density modeling on some of the same footing as terrestrial studies.

The admittance estimates derived above have been compared to theoretical models [*Phillips and Morgan*, 1984, *Morgan et al.*, 1985], specifically, convective flow [*Richards and Hager*, 1984], Airy isostatic and flexural solutions. For the limited wavelength range studied, the convective and isostatic solutions are not separable and fall within the 1-

σ error bars of the data for a depth to density disturbance of approximately 150 km. Flexural solutions can be eliminated, however, by imposing the additional requirement that the compensating density distribution be located within the elastic lithosphere.

Extension of these admittance estimates both spatially and spectrally as well as improvements in the theoretical modeling should result in significant constraints on the tectonics of Venus.

REFERENCES

Jian, L., and E.M. Parmentier, Surface viscosity due to convection in a variable viscosity fluid: Application to short wavelength gravity anomalies in the Central Pacific Ocean, *Geophys. Res. Lett.*, *12*, 357-360, 1985.

Morgan, P., R.J. Phillips, L.V. Block, and M.T. Reagan, Venus topography and gravity models: Preliminary results, *Lunar and Planetary Science XVI*, Lunar and Planetary Institute, Houston, 577-578, 1985.

Parmentier, E.M., and J.W. Head, Viscous relaxation of impact craters on icy planetary surfaces: Determination of viscosity variation with depth, *Icarus*, *47*, 100-111, 1981.

Parsons, B., and S. Daly, The relationship between surface topography, gravity anomalies, and temperature structure of convection, *J. Geophys. Res.*, 88, 1129-1144, 1983.

Phillips, R.J., and P. Morgan, Line-of-sight admittance estimates for Venus, *EOS*, 65, 982, 1984.

Richards M.A., and B.H. Hager, Geoid anomalies in a dynamic earth, *J. Geophys. Res.*, 89, 5987-6002, 1984.

Longevity of a Dense Carbon Dioxide Atmosphere on Mars

James B. Pollack, Space Science Division, NASA Ames Research Center, Moffett Field, CA 94035

There are several pieces of evidence that suggest Mars may have had a warmer and wetter climate during its early history. This evidence includes the ubiquitous occurrence of dendritic gullies in the heavily cratered uplands of the southern hemisphere and the morphological characteristics of impact basins.

Large amounts of carbon dioxide in the early Martian atmosphere represent the most likely way of achieving the necessary greenhouse warming to raise the surface temperature on early Mars above the freezing point of water (1). Surface pressures on the order of 1 bar are required in this case, i.e., a two-orders of magnitude increase in the amount of atmospheric CO_2 over the current content.

A 1-bar CO_2 atmosphere is not inconsistent with estimates of Mars' volatile inventory. However, the occurrence of liquid water on the surface of early Mars would promote the formation of carbonate rocks at the expense of the atmospheric CO_2. Could a large CO_2 atmosphere last a geologically interesting period of time (10^9 years) to account for the formation of the older gullies and the characteristics of the Martian basins?

I have used characteristics of the CO_2 geochemical cycle on Earth to answer the above question. In particular, I have scaled the chemical weathering rates on Earth of carbonate rock formation to allow for the effects of atmospheric pressure, temperature, rock cation content, solar radiation, and the surface area covered by liquid water. These calculations suggest that a 1 bar atmosphere on early Mars would be eliminated in about 10^7 - 10^8 years by carbonate rock formation, in the absence of recycling these rocks back to CO_2. While such time scales are quite large, they are probably not large enough to account for the geological data of interest.

I have therefore investigated the possibility of recycling carbonate rocks on early Mars. Global scale volcanism offers an attractive way to accomplish this. Carbonate rocks could be decomposed either by coming into contact with hot lava or by being buried by colder lava to depths where the temperatures are high enough for decomposition ($\sim$ 750 K). Using surface heat flux as a constraint on the rate of volcanism, I find that the recycling time scales are comparable to the weathering time scales on early Mars. Thus, a dense CO_2 atmosphere could be sustained on early Mars for time scales of 10^9 years by the recycling of carbonate rocks engendered by global volcanism. At later times in Martian history, the rate of volcanism is expected to decline and to become more regional in scale. Both these changes would make recycling much less effective and hence the dense CO_2 atmosphere would be lost.

This hypothesis may be tested by searching for the presence of carbonate rocks on Mars. R. Kahn has independently advocated searching for carbonate rocks on Mars to help verify his hypothesis that carbonate rock formation on Mars is the key determinant of the present atmospheric pressure at the surface (2).

References: 1. Pollack, J. B. (1979) Icarus, 37, 479-553.
2. Kahn, R. (1985) Icarus, 62, 175-190.

GEOPHYSICAL INTERPRETATION OF VENUS GRAVITY DATA

Robert D. Reasenberg, Smithsonian Astrophysical Observatory

SUMMARY OF RESULTS. Our principal scientific objective remains the investigation of the subsurface mass distribution of Venus through the analysis of the data from Pioneer Venus Orbiter (PVO). In particular, we use the Doppler tracking data to map the gravitational potential, which we compare to the topographic data from the PVO radar (ORAD). In order to obtain an unbiased comparison, we filter the topography obtained from the PVO-ORAD to introduce distortions which are the same as those of our gravity models. A discussion of our analysis technique is given in Goldberg and Reasenberg [1985b] and references therein. The work performed with NASA funding during the past year yielded the following results which are discussed further below:

- The extension of the mapped portion of the Venus gravity field from 6 to 9 "inversion regions," thus completing the mapping of the planet.
- The re-mapping of one region using an entirely new set of Doppler data.
- The discovery of a dichotomy in the planet-wide distribution of the relationships between gravity and topography.
- The development of software and procedures for producing color contour maps of gravity and filtered topography.
- The performance of a series of tests to quantify and document the accuracy of the analysis procedure.

COMPLETION OF MAPPED AREA. As of a year ago, we had completed the mapping of six "inversion regions" in two separate spans: one includes the eastern third of Aphrodite Terra (130°E) and extends through Beta Regio to the eastern edge of Guinevere Planitia (≈350°E); the other, just west of Aphrodite Terra, contains the eastern portion of Eisila Regio. These together cover 270 degrees in longitude and are based on Kalman filter residuals taken from 184 spacecraft orbits.

Since then, we have completed the mapping of three additional regions, which has brought the total extent of our coverage to 360 degrees in longitude. This new coverage made use of residuals from 79 newly processed orbits, along with 24 previously used orbits. In order to demonstrate the consistency of our results, we (processed some additional orbits and) remapped one of the inversion regions with an entirely new set of (redundant) data. These 22 orbits, together with 5 as yet unused orbits, brings to 300 the number of orbits for which Kalman filter residuals had been obtained by the end of the reporting period.

We wished to combine maps that were based on a uniform process. For this it was also necessary to remap one of the original regions using the most recent refinements in our inversion technique. Upon completion of the mapping of the last inversion region, we produced a single merged data set containing a uniform gravity model for the entire (360°) longitude range, along with a corresponding data set containing our filtered topography.

GEOPHYSICAL IMPLICATIONS. The first region of Venus analyzed with our current technique (a 4000 km square region west of Beta Regio) exhibited a spectral admittance consistent with the Airy model of isostatic compensation and a depth of compensation of about 50 km (Goldberg and Reasenberg, 1985b). When we extended our analysis to the remainder of the planet, however, we could find no other region that even came close to fitting such a straightforward model.

Instead, we found that if we calculated the depth of compensation separately for each wavelength (i.e., lateral topographic extent) in a given region, to a surprising degree of accuracy the results obeyed a simple power law of the form $d = k \cdot \lambda^{\alpha}$, where d is the depth of compensation, k and α are parameters estimated from the data, and λ is the wavelength. Moreover, although the power-law parameters changed from one region to another, they all tended to pivot around a point (in the d-λ plane) corresponding to a depth of $\approx$70 km and a wavelength of $\approx$1100 km. While we have yet to understand the geophysical significance of the power law, it appears that we have identified an important measure of the near-surface structure of Venus. These results were presented in preliminary form to the DPS (Reasenberg and Goldberg, 1984). With the completion of our gravity mapping, an enhanced version of these results is being prepared for journal submission.

We have used our recently completed gravity and topography models to produce a scatter plot of gravity against topography for the full range of Venus longitude. The plot (Figure 1) shows a clear bifurcation of the data into portions showing distinct linear trends (i.e., ratios of gravity to topography). The bifurcation was confirmed in a series of scatter plots of data in different subsets of the longitude range (Goldberg and Reasenberg, 1985a). The significance of this phenomenon is unclear, but it may indicate that there have been at least two distinct epochs of surface-building on Venus.

DEVELOPMENT OF COLOR GRAPHICS CAPABILITY. With the increase over the past year in the extent of the mapped region of Venus, we found a need to produce maps that contain more information than can be displayed with our customary black-and-white contour maps. We have used the CfA image processing system to produce color contour maps. These make it much easier to discern patterns, such as the similarities and differences between gravity and topography, that may be relevant to geophysical interpretation.

ACCURACY TESTS. Various complexities in our analysis procedure make calculation of formal errors for our estimated gravity parameters difficult and their interpretation even more difficult. In order to provide the community with some measure of the reliability of our results, we performed a series of numerical experiments with both the orbit determination and geophysical inversion stages of the analysis. These tests, together with earlier tests of the inversion stage, confirmed our more preliminary indications that the gravity maps are accurate to about 10%, with the worst errors occurring at the lowest and highest spatial frequencies that can be discerned.

RECENT PUBLICATIONS

R. D. Reasenberg and Z. M. Goldberg, "Spectral Admittance of Venus," BAAS, 16, 693, 1984. Presented at the AAS/DPS Meeting #16, Kona, Hawaii, 8-12 October 1984.

Z. M. Goldberg and R. D. Reasenberg, "Venus: High-Resolution Gravity Maps and Their Comparison to Topography," BAAS, 17, 721, 1985. Presented at the AAS/DPS Meeting #17, Baltimore, MD, 28 October-1 November 1985a.

Z. M. Goldberg and R. D. Reasenberg, "Venus Gravity West of Beta Regio," Icarus, 62, 129-142, 1985b. (A computer tape containing digital representations of the gravity and topography maps published in this paper was deposited with the National Space Sciences Data Center in July of this year.)

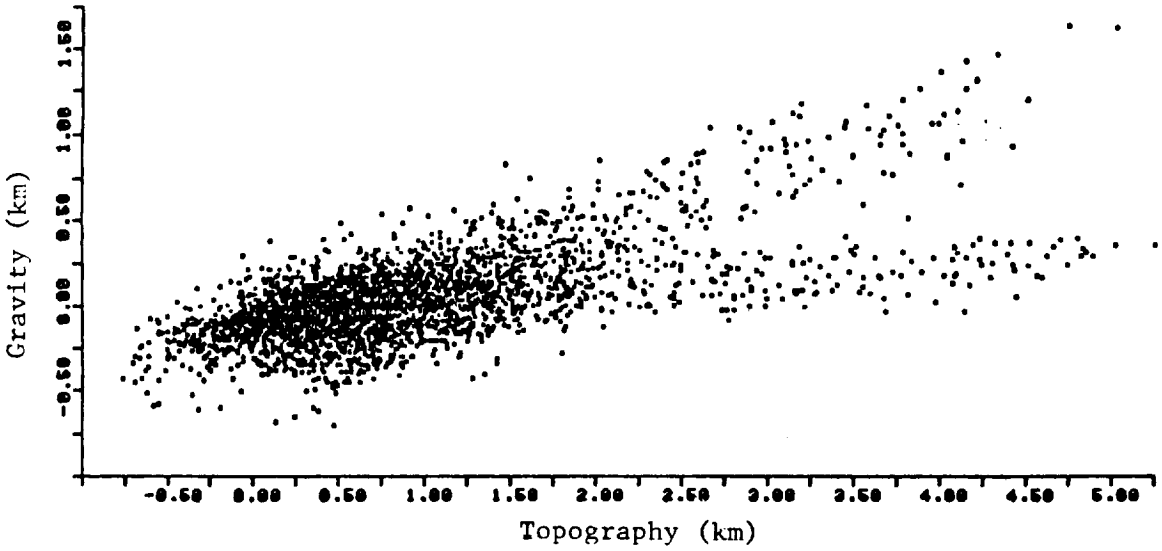

Figure 1. Scatter plot showing gravity (y axis) and topography (x axis), both in units of kilometers with arbitrary additive constants, for a region covering -5 to +35 deg latitude and 360 deg of longitude. (The gravity is shown as the equivalent height of the uncompensated topography of half the mean density of Venus required to produce the observed external potential.) The two distinct trends seen here persist when the data are divided into 40 deg longitude segments.

Two-Layer Convection Model for the Earth's Mantle

G. Schubert and K. Ellsworth, (University of California, Los Angeles, CA 90024)

Linear stability analyses and finite amplitude calculations have been carried out for two-layer convection with free-slip outer boundaries, fixed interface (zero vertical velocity), an isothermal upper surface, and the layer depths in the ratio of the upper and lower mantle thicknesses. Several heating configurations, including an isothermal lower boundary, a prescribed bottom heat flux, and an insulated bottom boundary with heat sources concentrated in either the upper or the lower layer, as well as different material property distributions are considered.

At the onset of convection, when the material properties are the same in both layers, the lower layer thickness determines the horizontal wavelength even if the heat sources are concentrated in the upper layer by a factor of 10 more than in the lower layer. Two-dimensional, steady-state, finite-amplitude solutions, when the material properties are the same in both layers, have been obtained for Rayleigh numbers Ra up to 2000 times the critical Rayleigh number Ra_{cr} with an isothermal bottom boundary, $5000Ra_{cr}$ for a prescribed heat flux bottom, and $100Ra_{cr}$ for an insulated bottom with internal heat sources in the lower layer only.

At $25Ra_{cr}$ or below, flow in the upper layer for all three finite amplitude cases is indirect, with upwelling over regions of low heat flux and downwelling over regions of high heat flux, as well as mechanically coupled with the flow in the lower layer. By $100Ra_{cr}$ for both the isothermal bottom boundary and the internally heated case, the upper layer has two full convection cells, both flowing in the same directions along the interface as the lower layer cell, with a partial counter-cell between them. By $200Ra_{cr}$ for the isothermal bottom boundary, the small wavelength upper layer convection cells are replaced by a single convection cell mechanically coupled with the lower layer cell that remains up to at least $2000Ra_{cr}$. For the prescribed heat flux case, the two full convection cells with a partial cell in between do not appear until $500Ra_{cr}$, and by $5000Ra_{cr}$ the short partial cell extends down to the interface and is thermally coupled with the lower layer cell, with upwelling over upwelling and an intense shear zone at the interface; the one long convection cell is mechanically coupled with the lower layer.

Finite-amplitude, steady-state solutions have also been obtained for the isothermal bottom boundary with a variety of different material property distributions. The first case has the lower layer sufficiently more viscous and heat conducting (a factor of 50 and 7, respectively) that the horizontal lengthscale is determined by the upper layer thickness (short wavelength) at the onset of convection. The lower layer convection cells are viscously coupled with the four short wavelength cells in the upper layer at $5Ra_{cr}$, but by $25Ra_{cr}$ the lower layer has a single, long wavelength convection cell while the upper layer has the three short wavelength convection cells, with the two outer ones thermally coupled with the upwelling and downwelling plumes of the lower layer. Similar solutions were found at $50Ra_{cr}$, and no

steady-state solutions were found at $100Ra_{cr}$ or above.

In the next case, with the same material property values as the previous case except the lower layer is only three times more heat conducting than the upper layer, no steady-state solutions at $15Ra_{cr}$ or higher were found, even when using a refined grid. For the final case examined, the lower layer thermal conductivity and viscosity are only 2.57 and 10 times, respectively, larger than the upper layer values, and are chosen so that the Rayleigh numbers of each layer are the same. There are two minima for this case at the onset of convection involving different critical horizontal wavelengths for each layer. When the flow is initialized to have four short cells at only $2Ra_{cr}$, the lower layer begins convecting with a single, long wavelength convection cell while the upper layer convects with five short wavelength convection cells. By $5Ra_{cr}$, however, there are only three upper layer convection cells, and by $15Ra_{cr}$ there are only two cells that do not disappear up to $100Ra_{cr}$, when no steady-state solutions are found.

Tidal Dissipation in Io and the Moon

G. Schubert and M. N. Ross, (University of California, Los Angeles, CA 90024)

We investigate tidal dissipative heating in several different models of Io and the Moon. The partially molten asthenosphere Io model consists of a rigid inner core and a thin (less than 400 km thick) partially molten ('decoupling') layer (asthenosphere) surrounded by an elastic lithosphere. In the partially molten interior model of Io the interior beneath the lithosphere is partially molten throughout. The partially molten layer in each case is assumed to possess negligible shear strength and to be characterized by a Newtonian viscosity. Tidal deformation and dissipation in the core are assumed negligible. The fluid in the viscous layer is forced to circulate by the tidal distortion of the outer shell, modeled here as a sinusoidal variation with time of the distortion amplitude. As a result, heat is generated in the fluid by viscous dissipation.

There are two heating mechanisms in our Io models: 'elastic' dissipation in the lithosphere $\propto 1/Q$ and viscous dissipation in the partially molten region. Numerical calculations are carried out for a 90 km thick lithosphere with $Q = 100$. This thickness maximizes dissipation in a decoupled lithosphere; other reasonable values of lithosphere thickness do not alter our conclusions. Under the constraint that total dissipation equals the observed radiated heat loss we derive the viscosity of the partially molten region in each model. We a posteriori evaluate the assumption that the lithosphere is decoupled from the interior. We find that if the interior viscosity is such that the total dissipation is equal to the observed heat flux from Io, viscous stresses produce negligible distortion of a 90 km thick shell. This validates the assumption of a decoupled shell.

The derived viscosity for both Io models is characteristic of partially molten rock. In the thin asthenosphere Io model the derived viscosity is so low that a very high degree of partial melt is necessary, about 40% crystal fraction in a 400 km asthenosphere and about 0% in a 1 km asthenosphere. For the partially molten interior Io model the derived viscosity corresponds to a magma with about 60% crystals. Considerations of convective efficiencies demonstrate the plausibility of a stable thermal steady state for both models. A significant portion (75% for $Q = 100$) of Io's tidal heating can be the result of viscous dissipation in a partially molten region that decouples the outer shell from the interior. The partially molten thin asthenosphere can be considered a 'global magma ocean'.

Tidal heating rates in Kelvin-Voigt, Maxwell, and standard linear solid (SLS) viscoelastic Moon models are calculated for a hypothetical past lunar orbit with semimajor axis 34.2 Earth radii and obliquity = 49°. Viscosities of 10^{14} and 10^{18} Pa s for the Kelvin-Voigt and Maxwell rheologies, respectively, are needed to match the dissipation rate calculated using the ad hoc Q approach with a quality factor $Q = 100$. The SLS model requires a short time viscosity of 3×10^{17} Pa s to match the $Q = 100$ dissipation rate independent of the model's relaxation strength. Since $Q = 100$ is considered a representative value for the

interiors of terrestrial planets, the derived viscosities should characterize planetary materials. Neither the Kelvin-Voigt nor SLS models simulate the behavior of real planetary materials on long timescales. Therefore, the significance of the viscosities inferred for these models is unclear. The Maxwell model behaves realistically on both long and short timescales. The inferred Maxwell viscosity, corresponding to a timescale of days, is several orders of magnitude smaller than the longer timescale ($\geq 10^{14}$ years) viscosity of the Earth's mantle. Io's present heat loss can be accounted for in a Maxwell Io model with viscosity about 10^{15} Pa s.

THE MARTIAN ATMOSPHERE BEFORE AND AFTER THE ARGYRE IMPACT.

P.H. Schultz, Dept. of Geological Sciences, Brown University, Box 1846, Providence, RI 02912.

The early history of the martian atmosphere is recorded in the ancient cratered terrain. Ancient narrow valley networks indicate fluid flow but debate remains concerning their precise mode of origin: rainfall drainage under atmospheric conditions different from today (1,2); melting beneath a global snowfall (3); or subsurface release of water and ground sapping (4,5). Martian narrow valley networks appear to represent immature drainage systems more analogous to sapping processes on the Earth (4,5), thereby weakening the need for an early stage of high atmospheric temperatures and pressures conducive for rainfall. It is reproposed here, however, that different climatic conditions did exist during the first 0.5 by and that the inferred sapping by melting of buried ices reflects a relatively late-stage process which followed up to about 3 by. The basis for this proposal principally centers on: (a) the gradation of ancient impact basins and other early landforms; (b) the change in drainage density and style following the Argyre impact; and (c) the change in basin ejecta emplacement style after the Argyre impact. Ancient Impact Basins: Early studies concluded that large impact structures (diameter > 200 km) were deficient relative to the Moon and Mercury (6,7). Recent studies, however, document a much larger inventory of subtle but unmistakable impact basions (8,9). The identification of such structures is based on recognition of not only the familiar primary landforms used for the Moon (concentric massifs, scarps, and ridges) but also secondary landforms including topographic and structural diversion of drainage patterns, concentration of plain units, and diversion of prominent structural patterns. In certain regions of the ancient cratered highlands, the number density of impact basins exceeds the Moon. Consequently the deficiency in other regions is not believed to reflect a low impact flux but a much higher gradation rate early in martian history. The furrowing and channeling of ancient basin massifs and ejecta facies indicate that the high gradation rate is at least in part related to the formation of narrow valley networks.

A second clue to different atmospheric conditions in the past comes from the absence of basin secondaries. On the Moon and Mercury, numerous large secondary craters surround large craters and basins with the largest approaching 5-7% the diameter of the parent crater. On Mars, only basins smaller than 200 km in diameter have identifiable secondaries beyond the continuous ejecta deposits. The 1900 km-diameter Argyre basin (measured to the outer ring scarp) is the only exception with a few 20-30 km secondaries. The condition of these very few secondaries indicates that this basin is relatively well preserved, yet the extensive radial lineations and vast secondary crater fields similar to those around Imbrium and Orientale on the Moon (see 10) are missing. If Mars had the same atmospheric pressure as it does today, then such an atmosphere would not have prevented the radial facies and secondaries from forming -- just as secondary craters were produced around numerous other more recent martian impact craters smaller than 200 km in diameter. A possible explanation invokes a much higher atmospheric pressure that either prevented secondaries from forming due to high aerodynamic pressures during ejecta re-entry or violent post-impact winds that quickly modified the ejecta emplacement process. Both processes have been documented experimentally and predicted theoretically (11).

It remains equivocal whether or not pre-Argyre impact basins once had the characteristic secondary crater fields. However, if narrow valley networks represent an immature drainage system -- thereby indicating a limited erosional capacity, then it is paradoxical that these valleys 1-2 km in width could be preserved today while secondary craters 10-30 km in diameter have been destroyed. A more reasonable scenario invokes a

higher erosional capacity early in martian history with a change in conditions leading to the formation of presently preserved narrow valley networks. Such a scenario is supported by a documented change in the style and density of narrow valley networks soon after the formation of the Argyre impact (12).

Conclusions: The impact basin record on Mars suggests that atmospheric conditions during and prior to the formation of the Argyre impact were dramatically different than today. This conclusion is based on: (a) the heavily eroded state of pre-Argyre basins; (b) an incomplete basin population probably not related to a deficit of impactors; (c) an inverse relation between the existence of crater/basin secondaries and density of narrow valleys; (d) the absence of typical basin ejecta facies around Argyre that should have been produced and preserved; and (e) the dramatic decrease in drainage density and change in drainage style after the Argyre impact. It is further proposed that the present record of narrow valley networks is dominated by immature drainage patterns that are only the last stages of a more extensive period of gradation contemporary with the formation of pre-Argyre impact basins.

References:

1. Sagan C., Toon, O.B., and Gierasch, P.J. (1973) *Science, 181,* 1045-1049. 2. Masursky, H., Boyce, J.M., Dial, A.L., Schaber, C.G., and Strobell, M.E. (1977) *J. Geophys. Res., 82,* 4016-4038. 3. Carr, M.H. (1984) *Lunar and Planetary Science XV,* 131-132. 4. Sharp, R.P. (1973) *J. Geophys. Res., 78,* 4063-4072. 5. Pieri, D.C. (1980) *Science, 210,* 895-897. 6. Wood, C.A. and Head, J.W. (1976) *Proc. Lunar Sci. Conf. 7th,* 7. Malin, M.C. (1976) *Proc. Lunar Sci. Conf. 7th,* 8. Schultz, P.H., Schultz, R.A., and Rogers, J. (1982) *J. Geophys. Res., 87,* 9803-9820. 9. Stam, M., Schultz, P.H., and McGill, G. (1984) *Lunar and Planetary Science XV,* 818-819. 10. Schultz, P.H. (1976) Moon Morphology, *Moon Morphology,* p. 246. 11. Schultz, P.H. and Gault, D.E. (1982) in *Geol. Sco. Amer. Spec. Paper 190,* 153-174. 12. Schultz, P.H., Rogers, J., and Haber, S. (1984) *MECA Workshop on Water on Mars,* 74-75, Lunar and Planetary Institute, Houston.

Gravity Data Analysis

William L. Sjogren, Jet Propulsion Laboratory, Pasadena, CA

Our research this past year has concentrated on the analysis of Venus gravity data as derived from Doppler radio tracking of the Pioneer Venus Orbiter. There are three aspects to the analysis. The first deals with a phenomenon that was discovered when we derived a global 10th degree and order field model last year (Ref. 1). A problem in long data arc fits versus short data arc fits was clearly evident, so we have been investigating why this occurred. The second aspect is the isostatic depth of compensation modeling for the Niobe-Aphrodite region. The third aspect is the study of the Sedna-Isthar region where Russian SAR imaging will be available soon.

The analysis of the unknown phenomenon that produced disastrous results for the long data arc reduction has monopolized a major portion of our time and computer usage. New data reductions for some forty data arcs (covering 260 days) with approximately a thousand data points per arc have been analysed. There were many other reductions made prior to this that tested various suggestions which we thought might be contributing to the poor data fits. This included such parameters as drag effects, gravity anomalies, radiation pressure, gas leaks from the spacecraft, gravity waves, non-Newtonian mechanics, large relativity effects, and planetary perturbations from Mercury or a Planet X. The parameters that seemed to do the best in reducing the Doppler residual signatures were solar pressure forces, however some systematic effects still remained in the residuals. Thus based on this result we proceeded with the forty new reductions in which we estimated solar pressure parameters over three day arcs. Although three days is not a very long arc there were significant unexplained signatures in these arcs.

Figure 1 is a summary plot of the solar pressure results. The ordinate is the RMS difference of the three estimated solar pressure force parameters and the standard apriori solar pressure model. For example, the December and January results indicate greater than a 50% change from the standard model, for the standard amplitude is approximately 1.2. In May there is a 100% change. Beyond July the geometry is such that solar conjunction places significant noise on the data and the results are dubious. We are not convinced that this is a dynamical phenomenon where a force must be integrated with the equations of motion or whether this is a media bias that distorts the Doppler data. If it is dynamical, the acceleration amplitude is approximately 10^{-8} m/sec^2. This is relatively small, but well above the data resolution.

Assuming that the effect is non-dynamical we have extracted a smooth function over six days that allows the data to be fit to its inherent noise level without any systematic signature. This smooth function is shown in figure 2. The peak deviations occur where the line-of-sight velocities are greatest. The peaks become larger and then decrease, as though there is an acceleration and then a deceleration, or there is a

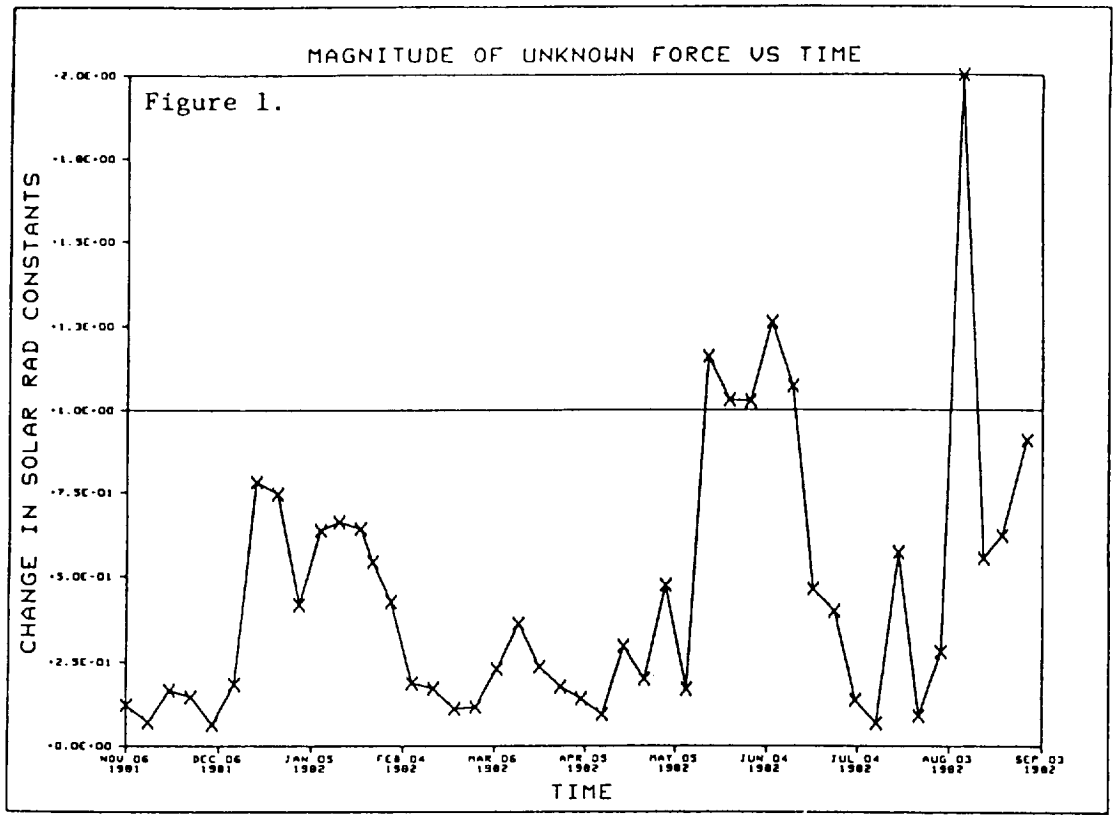
MAGNITUDE OF UNKNOWN FORCE VS TIME
Figure 1.
CHANGE IN SOLAR RAD CONSTANTS
TIME

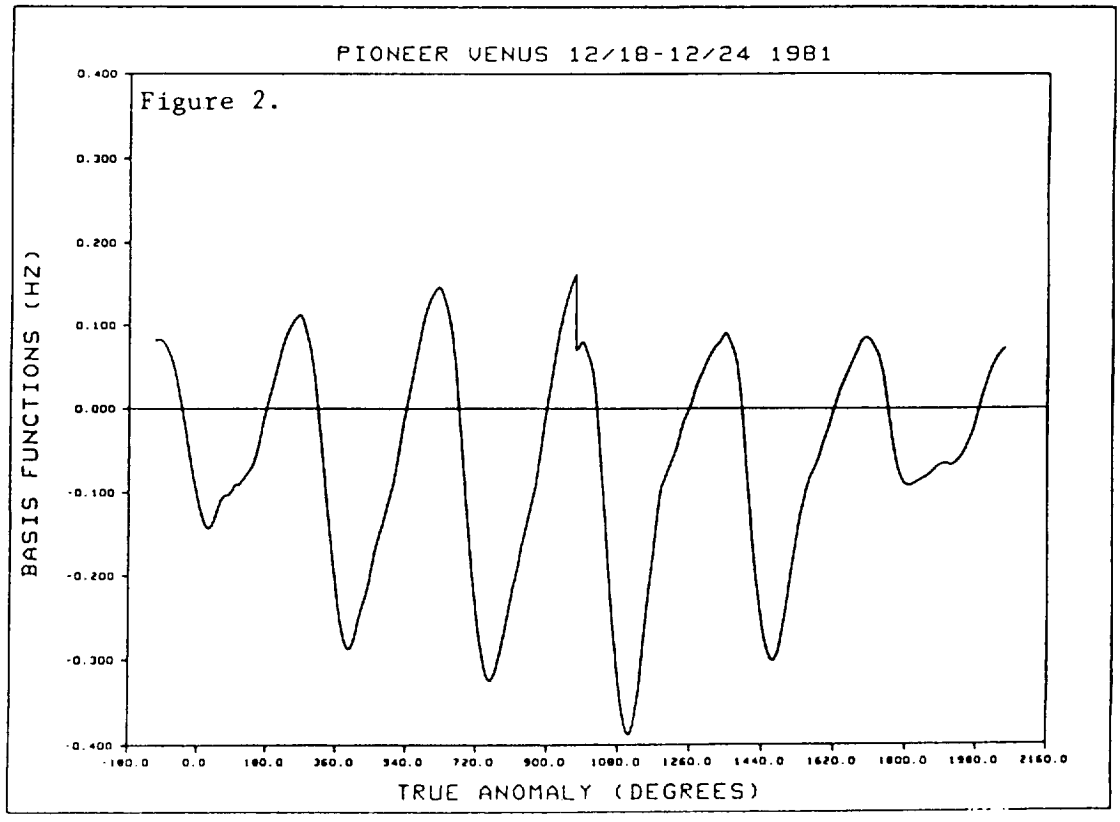
PIONEER VENUS 12/18-12/24 1981
Figure 2.
BASIS FUNCTIONS (HZ)
TRUE ANOMALY (DEGREES)

bias that grows and then shrinks over these six days. Removal of this function may not be unique and tests are continuing on this and other data to determine stability of the results.

If some specific characteristics of these systematic signatures can be determined such as period of occurance, amplitude, shape, etc. there may be a possibility of removing it so that these and future data (VRM) can be processed successfully. There may even be some new physics or science that can be extracted.

The second effort that has been completed this past year and reported at the Lunar and Planetary Science Conference is the isostatic modeling of the Niobe-Aphrodite region of Venus (Ref. 2). It was found that the depth of compensation for Aphrodite was about 75 Km which was in contrast with 200 km for Niobe. A consistent anomaly (on 6 profiles) over the transition zone of the lowland to highland was revealed that could be indicative of uncompensated subsurface material. The large depth of compensation for Niobe seems unrealistic, suggesting that isostatic modelling is not correct and elastic, plastic, and or dynamic support parameters should be included (see figure 3).

The third effort which is just underway is the analysis of the Sedna-Ishtar region. Now that SAR imaging from the Russian spacecraft are available, a detailed study of this transition zone could shed some light on the Niobe-Aphrodite anomalies mentioned above. This effort will also tie into our previous Ishtar analysis (ref. 3).

Ref. 1. Venus Gravity: A Harmonic Analysis and Geophysical Implications, N. A. Mottinger, W. L. Sjogren and B. G. Bills, J. of Geophy. Res., Vol 90, C739-C756, 1985.

Ref. 2. Venus Gravity: Niobe-Aphrodite, W. L. Sjogren, R. N. Wimberly, R. S. Saunders and W. B. Banerdt, LPSC XVI, 791, 1985.

Ref. 3. Venus: Ishtar Gravity Anomaly, W. L. Sjogren, B. G. Bills and N. A. Mottinger, GRL, 11, 489-491, 1984.

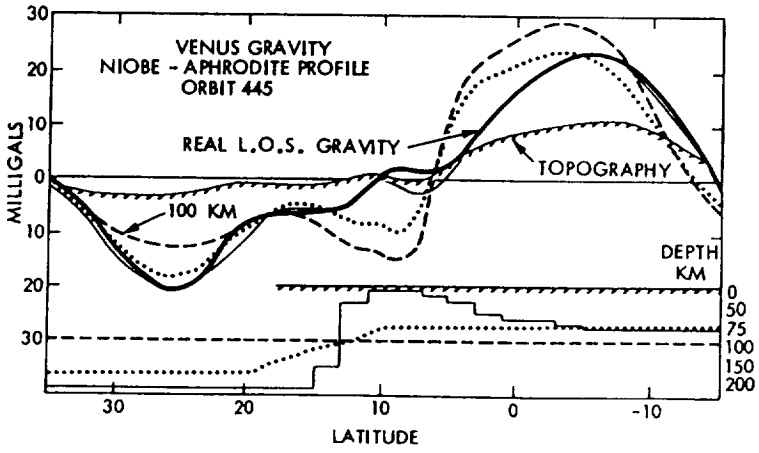

Figure 3.

VALLES MARINERIS AS KARST: FEASIBILITY AND IMPLICATIONS FOR MARTIAN ATMOSPHERIC EVOLUTION.

J.R. Spencer and S.K. Croft, Lunar and Planetary Laboratory, University of Arizona, Tucson, AZ, 85721

The origin of the vast Martian equatorial canyon system, Valles Marineris, is still a mystery. There is much evidence for tectonic control (1), but the blunt, irregular or closed shape of many of the troughs, and the abundant collapse features, indicate that the loss of material cannot be due mostly to simple downdropping of the crust along faults (2).

The collapse features (chains of pits developed along small graben, apparently coalescing to form linear depressions which then enlarge into full size canyons) have led many authors to suggest the removal of subsurface material as a major contributor to canyon formation. Sharp (3) suggested that ground ice removal led to collapse and canyon formation or enlargement. A serious problem, however, may be the difficulty of maintaining such extreme topography in an ice-rich crust.

Hebes Chasma, for example, has a depth of 7 km, and as it is closed, material cannot have been moved out of it laterally except by wind, which is considered unlikely (3,2). Assuming none of the non-ice has left, if the crust is more than 50% ice by volume, the ice must have been removed to a depth of more than 14 km, or 7 km below the present floor. This is geologically very hard to justify. We thus assume a lower limit of 50% ice in the upper crust, if ice removal is significant in canyon formation.

The melting point of ice near the Martian equator is probably achieved at a depth of only 1 km (4), which in itself makes a very ice-rich crust unlikely as the canyons are much deeper than this. However, we assume that the canyon walls contain ice close to, but below, the melting temperature. The viscosity of pure ice at 270K is between 10^{15} and 10^{16} poise (5), and the viscosity of a 50/50 (by volume) ice-silicate mixture is less than 100 times greater than pure ice (6,7), so on the ice-removal hypothesis, the viscosity of the canyon wall material is likely to be no more than 10^{18} poise. The timescale for collapse of 10 km - amplitude Martian topography in material with this viscosity is of the order of 50 years! The viscosity argument does not rule out models in which the ice is a minor component which acts as a binder, whose loss causes the material to loose cohesion so that it can be removed by wind. Such models face the problem of reducing all the canyon wall rock to dust size prior to wind removal, however.

We propose an alternative method of canyon excavation, in which much of the subsurface rock is carbonate, and is dissolved by groundwater in a manner analagous to terrestrial karst. Subsurface dissolution of carbonate and subsequent collapse of cavities thus formed, followed by continued enlargment of the depressions by further solution, would explain the canyon morphology just as well as collapse due to ground ice removal, without the problem of maintaining the topography against viscous flow.

Some models of Martian evolution (e.g. 8) propose an atmospheric history in which H_2O and CO_2 are largely retained, allowing for the possibility of abundant CO_2-saturated water on the early surface. Formation of large amounts of carbonate by silicate weathering is then very

likely (9,10). Large local deposits of carbonate rock could be built up by migration of water to low regions. If this "wet" phase of Martian evolution ended before the termination of heavy bombardment, which probably occured around 3.9 b.y., all morphological traces would have been removed. If the entire Valles Marineris region contained a 10 km thickness of limestone, the stored CO_2 would be equivalent to roughly 5 bars atmospheric pressure over the whole planet, and the uniqueness of the canyon region suggests that it might contain the bulk of the present subsurface carbonate.

The dissolution and transport of the supposed carbonates requires an active groundwater system. Transport of materials in suspension in groundwater, possibly connected with a system of lakes within the major canyons (11), has been invoked by Carr (2) to explain the collapse features and the layered deposits in the canyons. Transport of carbonates in solution is equally feasible.

The ultimate fate of the vast quantities of material that must be removed to excavate the canyons is a difficult question, though no more difficult for this theory than for competing ones. The dissolved carbonate could be removed slowly by downhill percolation of carbonate-saturated groundwater towards the channelled terrain to the east of the canyons, and deposited either in mega-regolith pore spaces or near the surface. Because of the limited solubility of carbonate in water ($\sim 4\times10^{-5}$ by volume for pure water at 0°C in equilibrium with the Martian atmosphere) very active atmospheric recycling of water is required to circulate enough through the canyons to dissolve them. A more attractive possibility is that convection of deep groundwater might dissolve carbonate in the upper crust and redeposit it at depth in mega-regolith pore spaces in a continuous cycle, without the water ever appearing at the surface. The increase in solubility of carbonate with decreasing water temperature would facilitate downward carbonate transport as part of the convective process.

The spectral features of carbonates have not been seen in either the near-IR reflectance spectrum of Mars (12) or the thermal emission spectrum of dust clouds (13). An approximate upper limit of 5% carbonates in the surface material is indicated (14). It might be expected that carbonates removed from the Valles Marineris area and subsequently re-deposited near the surface would be detectable in the apparently globally-homogenized surface dust layer. However, it may be that the carbonates are diluted below the 5% detection threshold, or are broken down by SO_2 (14). MGCO observations will be invaluable in helping to resolve this question by providing high resolution maps of surface mineralogy.

In conclusion, the possibility that the Valles Marineris system indicates the storage of several bar's worth of CO_2 in the form of carbonates beneath one portion of the Martian surface is offered for consideration by geologists, geochemists, and atmospheric scientists concerned with Martian evolution. Much of the idea's strength lies in the difficulty of explaining Valles Marineris by other models, but more detailed work on the likely chemistry and circulation of deep Martian groundwater, and mineralogical and topographic data obtained by MGCO, may allow refinment or rejection of the hypothesis on its own merits.

References
(1) Blasius et al., 1977, J.G.R. 82, 4067-4091. (2) Carr, 1981, The Surface of Mars, Yale Univ. Press. (3) Sharp, 1973, J.G.R. 78, 4063-4072. (4) Fanale, 1976, Icarus 28, 179-202. (5) Durham et al., 1983, J.G.R. 88, B377-B392 (6) Hooke et al., 1972, J. Glaciol. 11, 327-336. (7) Friedson and Stevenson, (1983), Icarus 56, 1-14. (8) Lewis and Prinn, 1984, Planets and Their Atmospheres, Origin and Evolution, Academic Press. (9) Kahn, 1985, Icarus 62, 175-190. (10) Pollack, 1985, MECA Workshop on the Evolution of the Martian Atmosphere, LPI Technical Report. (11) McCauley, 1978, Geological Map of the Coprates Quadrangle of Mars, U.S.G.S. (12) Singer et al., 1984, Water on Mars Workshop Abstracts, 77-79, L.P.I. (13) Hunt et al., 1973, Icarus 18, 459-469. (14) Clark and Van Hart, 1981, Icarus 45, 370-378

HOW MUCH ANORTHOSITE IN THE LUNAR CRUST?: IMPLICATIONS FOR LUNAR CRUSTAL ORIGIN. P.D. SPUDIS[1,2] and P.A. Davis[1], 1. U.S. Geological Survey, Flagstaff, AZ 86001; 2. Dept. of Geology, ASU, Tempe, AZ 85287.

Introduction. Sixteen years after return of the first sample, the composition and origin of the lunar crust is still debated. The initial concept, that the lunar crust was formed by a large global magma system, originated after the Apollo 11 mission when it was postulated that anorthositic fragments within the soil represent highland material [1]. On the basis of analysis of gravity data and isostatic considerations, Wood [2] suggested the presence of a 20- to 30-km-thick layer of pure plagioclase within the lunar crust; from this postulate he inferred a global magma ocean. Walker [3] recently challenged the long-standing concept of the magma ocean, and suggested instead that the lunar crust is made up of a series of flows and plutons (serial magmatism model) and that the bulk composition of the lunar crust is noritic. Longhi [4] used orbital geochemical data and highland topographic relief to argue that the minimum amount of anorthosite in the crust is equivalent to a layer 5-6 km thick. In order to provide some clues as to which of these hypotheses is most likely, we have attempted to estimate the amount of anorthosite within the lunar crust, also using orbital geochemical data but incorporating the additional effects of multi-ring basins that have excavated many kilometers of the crust.

Method. Several advances toward understanding the mechanics of basin excavation have been made in recent years. Geologic studies of lunar basins [5,6], analytic descriptions of cratering flow fields [7], studies of terrestrial impact craters [8], and numerical code calculations [9] have all converged on a basin-forming model whereby the excavation cavity is significantly smaller than the presently observed basin diameter and effective excavation of material is from shallow levels of the target. These relations are here quantified by two equations (footnote 2, Table 1) that describe diameter and depth of the excavation cavity and encompass the relations given in [5,7,8]. Lunar orbital geochemical data for basin ejecta blankets have been analyzed by previous mixing-model studies [6,10-12]. From the mixing-model results, we have extracted, summed, and converted the proportions of anorthositic components into an equivalent volume of pure plagioclase. By applying the relations of size and depth of a basin-excavation cavity to a spherical Moon [5], the volume of plagioclase observed in basin ejecta may be converted into a hypothetical equivalent thickness of plagioclase (pure anorthosite) in the basin crustal target.

Results. Selected data for nine lunar multi-ring basins covered by Apollo geochemical data are presented in Table 1. These basins are distributed throughout most of the lunar equatorial region (lat $\pm$ 30°). Results suggest a substantial quantity of anorthosite at all basin target sites except Serenitatis and Imbrium (Table 1). Several workers [5,11,13] have suggested that the dominantly noritic compositions of ejecta from these two basins are the result of impact into a distinct geochemical province of the Moon that may never have had a significant amount of anorthosite. When these quantities of anorthosite in basin targets (Table 1) are expressed as a hypothetical layer within the crust, the mean equivalent layer thickness in all the basin targets studied is 16.7 $\pm$ 2.6 km; when values from the Serenitatis

and Imbrium Basins are excluded, the mean layer thickness is 21 ± 3 km. When this higher value is expressed as a fraction of the total average crustal thickness of the Moon (about 70 km) [14], an equivalent layer of anorthosite is found to make up about 30% of the crust.

Discussion. The average lunar highlands crust is about 70 km thick; approximately one-third consists of pure anorthosite. The widespread occurrence of highly aluminous soils in the highlands [15] suggests that the bulk of anorthositic rocks is concentrated in the upper part of the crust. If so, what rocks make up the lower two-thirds of the crust? One possibility is a sequence of Mg-suite rocks, dominantly norite. This composition is suggested by several lines of evidence that include: the dominantly noritic clast populations of basin impact melts; an apparent positive correlation between increasing fractions of norite in ejecta and increasing basin size [6]; and the distinctive noritic composition of the mixed rock type low-K Fra Mauro, which appears to be basin-related impact melt [16]. Such a crustal composition (upper 1/3, anorthositic; lower 2/3, noritic) is consistent with some previous suggestions [17,18]. Moreover, the bulk composition of a lunar crust consisting of 1/3 anorthosite and 2/3 norite would be chemically equivalent to anorthositic norite [Al_2O_3 25%], which is close to geochemical estimates of bulk crustal composition [19].

If we assume that lunar anorthosites were formed at the same time [19], a simple analogy to the Stillwater Complex [20] suggests that a 140-km-thick magma body could produce a 21-km-thick anorthosite layer. Furthermore, no mafic cumulates complementary to ferroan anorthosites have been found in the lunar samples, despite collection from at least three ejecta blankets of lunar basins. Therefore, we suggest that the serial magmatism model of [3] cannot be dominantly responsible for the formation of the lunar crust. This is not to say that serial magmatism does not occur: the dominantly noritic targets of the Imbrium and Serenitatis Basins imply significant intrusive activity in the early lunar crust. Our results do suggest, however, that early Moon-wide plagioclase fractionation is responsible for lunar anorthosites, a result consistent with a large magma body such as a magma ocean.

REFERENCES: [1] Wood J. et al. (1970) PLSC 1, 965. [2] Wood J. (1983) Workshop Pristine Rocks, LPI Tech. Rept. 83-02, 87. [3] Walker D. (1983) PLPSC 14, B17. [4] Longhi J. (1983) Workshop Pristine Rocks, LPI Tech. Rept. 83-02, 58. [5] Spudis P. (1983) LPS XIV, 735. [6] Spudis P. et al. (1984) PLPSC 15, JGR 89, C197. [7] Croft S. (1981) PLPSC 12A, 207; (1984) LPS XV, 188. [8] Grieve R. et al. (1981) PLPSC 12A, 37. [9] Schultz P. et al. (1981) PLPSC 12A, 181. [10] Hawke B. and Spudis P. (1979) Conf. Lunar Highlands Crust, 53. [11] Spudis P. and Hawke B. (1981) PLPS 12B, 781. [12] Spudis P. et al. (1984) LPS XV, 812. [13] Ryder G. (1981) LPS XII, 918. [14] Bills B. and Ferrari A. (1976) PLSC 7, frontispiece. [15] Davis P. and Spudis P. (1985) LPS XVI (this vol.). [16] Spudis P. (1984) PLPSC 15, JGR 89, C95. [17] Ryder G. and Wood J. (1977) PLSC 8, 655. [18] Warren P. and Wasson J. (1977) PLSC 8, 2215. [19] Taylor S. R. (1982) Planetary Science, LPI press, 481 p. [20] Longhi J. (1982) Workshop Magmatic Processes, LPI Tech. Rept. 82-01, 17.

Table 1. Estimated amounts of anorthosite within the lunar crust at basin target sites.

Basin[1]	Dia.(km)	Dtc (km)[2]	AN(%)[3]	Equiv.T (km)[4]	Crust T (km)[5]	% of AN in crust
Orientale	940	582±77	90	40±5	90	44±6
Hertzsprung	570	408±59	75	20±3	90	22±3
Korolev	440	347±52	81	20±4	100	20±4
Freundlich-Sharonov	600	422±60	56	14±2	70	20±3
Smythii	740	488±67	60	18±3	60	30±5
Crisium	540	394±57	62	15±3	60	25±5
Nectaris	860	544±73	62	21±3	70	30±4
Serenitatis	920	572±76	2	0.5±0.2	60	0.8±0.3
Imbrium	1160	685±88	6	1.5±0.3	50	3.0±0.6
Average[6]	-	-	-	21±3	70	30±4

1 Multi-ring basins overflown by Apollo geochemical experiments.
2 Transient cavity (Dtc) = 0.47±0.05 D+(140±30), where D = basin diameter; excavation depth (d_x) = 0.1±0.02 Dtc (see text)
3 Sum of all anorthositic components in ejecta [5, 10-12] converted to equivalent volume percent of pure anorthosite.
4 Thickness of hypothetical layer of pure anorthosite in basin target.
5 Thickness of crust, estimated by gravity data [14].
6 Excluding Serenitatis and Imbrium (see text).

THE APENNINE BENCH FORMATION REVISITED P. D. Spudis, U.S. Geological Survey, Flagstaff, AZ 86001 and B. R. Hawke, HIG, University of Hawaii, Honolulu, HI 96822

Introduction. The Apennine Bench Formation consists of pre-mare light plains materials that crop out south of the crater Archimedes, inside the Imbrium Basin [1]. This material has been ascribed either impact [2,3] or volcanic origins [1,4,5]. Several workers [4,5,6] have argued that the Apennine Bench Formation is represented in the lunar-sample collection by Apollo 15 KREEP basalts, which have been interpreted as endogenically generated volcanic rocks [e.g., 7,8]. More recently, Taylor [9] has challenged the concept that the Apennine Bench Formation consists of volcanic KREEP basalt flows on two grounds: the Apollo 15 KREEP basalts are not volcanic, and the Apennine Bench Formation morphologically resembles an expected "melt sheet" produced by the Imbrium impact. The purpose of this note is (1) to review briefly the characteristics of both Apollo 15 KREEP basalts and the Apennine Bench Formation and (2) to demonstrate that all of these characteristics are compatible with a volcanic origin. The solutions of both problems are important cornerstones in the deciphering of the geology and history of the Apollo 15 site.

Apollo 15 KREEP Basalts. Among its other attributes, the Apollo 15 site is remarkable as a source of numerous, small basaltic fragments with KREEP trace-element patterns. The petrology of these basalts is described in [7,8,10,11]; they consist of glassy, intersertal to subophitic-textured basalts that completely lack clastic inclusions and have no detectable meteoritic siderophile element contamination. Modally, they consist of 40%-50% plagioclase, 30%-40% pyroxene (most commonly orthopyroxene rimmed with pigeonite or augite), and minor phases including cristobalite, ilmenite, apatite, and brown, Si- and K-rich glass [7,10]. In bulk chemistry, they are equivalent to high-Al basalt (Al_2O_3 ~15%-18%), with trace-element concentrations at about the same level as Apollo 14 soils (="medium-K Fra Mauro basalt"). The Apollo 15 KREEP basalts have been dated by the following techniques: Rb-Sr (internal isochron age 3.85 ± 0.02 b.y., [12]), ^{40}Ar-^{39}Ar (internal isochron age 3.85 ± 0.05 b.y., [13]), and Sm-Nd (internal isochron age 3.85 ± 0.08 b.y., [14]). The isotopic data are consistent with a crystallization age of these basalts of 3.85 b.y., which is at present indistinguishable from the age of the Imbrium Basin impact [15].

Apollo 15 returned several unequivocal impact-melt rocks, none of which resemble the Apollo 15 KREEP basalts in any way. Moreover, clast-poor impact-melt rocks from elsewhere on the Moon (e.g., 14310; 68415) also differ from the Apollo 15 KREEP basalts in that: (1) they invariably contain xenocrystic debris, consisting of undigested (refractory) clasts; and (2) they have high contents of siderophile elements, indicating meteoritic contamination. Taylor [9, p. 215] argued that lack of siderophile contamination does not prove an endogenic origin. Although this point is valid, we contend that both the lack of clastic debris and the low siderophile concentrations are strongly suggestive of an endogenic origin; such data certainly would be conclusive in the case of a mare basalt. Taylor [9] further stated that "model ages for KREEP point back to the initial differentiation of the Moon, not to more recent volcanic events" [9, p. 216]. But model ages

for mare basalts also point back to initial lunar differentiation [16], yet no one doubts their volcanic origin. We conclude that all petrologic, chemical, and chronologic data are consistent with Apollo 15 KREEP basalts being true, endogenically generated volcanic rocks, extruded onto the lunar surface at the time of or shortly after the Imbrium Basin impact.

The Apennine Bench Formation. Orbital geochemical data [6] indicate an area southwest of Apollo 15 landing site that is strongly enriched in radioactive elements (indicative of KREEP). The dominant geologic unit in this area is the Apennine Bench Formation, a light-plains unit originally interpreted to be of volcanic origin [1]. Intensive study of impact-melt deposits in lunar craters and basins has resulted in a fuller appreciation of their importance in lunar history and some workers have assigned such an origin to the Apennine Bench Formation [e.g., 2,3,9]. However, comparison of its occurrence, distribution, surface texture, morphology, and stratigraphic relations recognized melt deposits in the Orientale Basin [e.g., 4,5] suggests that the Apennine Bench Formation does not represent an Imbrium Basin impact-melt sheet.

The Apennine Bench Formation occurs within the Imbrium Basin in the vicinity of the Archimedes ring (790-km diameter), the ring just inside the main basin ring (Apennine ring; 1160-km diameter). At the Orientale Basin, the analogous geologic setting (i.e., Outer Rook/Cordillera rings) contains a knobby-textured unit, the Montes Rook Formation [3,17]. This unit is not similar to the Apennine Bench Formation [cf. 9; p. 38]. An Orientale unit that does bear superficial resemblance to the Apennine Bench material is the Maunder Formation [3], but this unit is confined within the Outer Rook ring [3,17,18] and does not extend outward to the main basin ring. Moreover, the Apennine Bench Formation has a relatively flat, smooth surface in contrast to the rough, pitted, and cracked texture of the Maunder Formation. The Apennine Bench Formation does not drape pre-existing topography, as does the Maunder Formation, but rather terra islands, as do the mare basalts [4,5].

A more important line of evidence for the origin of the Apennine Bench Formation comes from its chemical composition as determined from remote-sensing data (Table 1). Early workers [4,5,21] noted a rough chemical correspondence between the Apennine Bench Formation and Apollo 15 KREEP, based on early reductions of the orbital chemical data. In recent years, these data have been refined [6,18,19] and the resemblance of the Apennine Bench Formation to Apollo 15 KREEP now seen to be is remarkable (Table 1). Composition of the Apennine Bench Formation does not correspond to the composition of probable Imbrium impact melt (15445 and 15455 black matrix; [22]), but it does closely resemble Apollo 15 volcanic KREEP basalt (Table 1). Taylor's argument that portions of the Apennines (Imbrium ejecta) possess the same Th concentrations as the Apennine Bench Formation [9, p. 215] is incorrect; the highest Th concentration in Apennine material is 7.6 ppm [6]. Thus, the orbital data strongly support the contention that Apollo 15 volcanic KREEP basalt and the Apennine Bench Formation have identical compositions.

Finally, we note that the KREEP-basalt composition of the Apennine Bench Formation (Table 1) precludes an Imbrium impact-melt origin. If the Imbrium basin target had a pure Apollo 15 KREEP-basalt composition, much higher heat-flow values would be found at the Apollo 15 landing site than are recorded [4, 23]. In fact, the crust would have been so

enriched in radiogenic elements that it would be part molten. We conclude that considerations of the probable chemical nature of the Imbrium Basin crustal target suggest that the presently exposed portion of the Apennine Bench Formation cannot represent an Imbrium Basin-impact melt sheet.

Conclusions. We contend that a variety of data support previous interpretations [1,4,5,21] that the Apennine Bench Formation consists of post-Imbrium, volcanic KREEP-basalt lava flows. The observations leading to this conclusion are: (1) petrologic, chemical, and isotopic data suggest that Apollo 15 KREEP basalts are of volcanic origin; (2) the morphology of the Apennine Bench Formation is more consistent with a volcanic origin than with an impact-melt origin; and (3) the Apennine Bench Formation and Apollo 15 KREEP are chemically identical. Additionally, Swann (24) has recently found that the Apennine Bench Formation may be in the shallow subsurface within 10 km of the Apollo 15 site, supporting the likelihood that this material was probably sampled during the mission.

As it provides a major preserved exposure of post-Imbrium volcanic KREEP flows, the Apennine Bench Formation is an important target for future lunar exploration. At the Apollo 15 site the geology and processes of lunar KREEP volcanism will continue to be studied and may eventually be deciphered.

References

[1] Hackman, R.J. (1966) USGS Map I-463. [2] Wilhelms, D.E. (1980) USGS Prof. Paper 1080A. [3] McCauley, J.F. et al. (1981) Icarus 47, 184. [4] Spudis, P.D. (1978) PLPSC 9, 3379. [5] Hawke, B.R. and Head, J.W. (1978) PLPSC 9, 3285. [6] Metzger, A.E. et al. (1979) PLPSC 10, 1701. [7] Irving, A.J. (1977) PLSC 8, 2433. [8] Dowty, E. et al. (1976) PLSC 7, 1833. [9] Taylor, S.R. (1982) Planetary Science, LPI, 481 p. [10] Meyer, C. (1977) Phys. Chem. Earth 10, 239. [11] Basu, A. and Bower, J.F. (1976) PLSC 7, 659. [12] Papanastassiou, D.A. and Wasserburg, G.J. (1976) PLSC 7, 2035. [13] Stettler, A. et al. (1973) PLSC 4, 1865. [14] Carlson, R.W. and Lugmair, G.W. (1979) EPSL 45, 123. [15] Wilhelms, D.E. (1984) Moon in NASA SP-469. [16] Basaltic Volcanism Study Project (1981), p. 699. [17] Head, J.W. (1974) Moon 11, 327. [18] Clark, P. and Hawke, B.R. (1981) PLPSC 12B, 727. [19] Davis, P. (1980) JGR 85, 3209. [20] Ryder, G. (1985) Catalog of Apollo 15 rocks, NASA-JSC. [21] Schonfeld, E. and Meyer, C. (1973) PLSC 4, 125. [22] Ryder, G. and Bower, J.F. (1977) PLSC 8, 1895. [23] Ryder G. and Wood J. (1977) PLSC 8, 655. [23] Swann, G. (1985), this volume.

Table 1. Comparison of the compositions of the Apennine Bench Formation, Apollo 15 volcanic KREEP, and Imbrium Basin impact melt.

	Apennine Bench Fm[1]	Apollo 15 KREEP[2]	Probable Imbri Impact Melt[3]
TiO_2	1.7%-2.3%	1.8%-2.3%	1.35%-1.70%
Al_2O_3	16.0%	14.8%-17.8%	16.2%-17.5%
FeO	9.5%-12.4%	8.6%-11.1%	7.9%-10.2%
MgO	5.7%	6.3%-8.2%	13.4%-16.0%
Th	10.7-12.0 ppm	10.5-12.0 ppm	2.4-2.9 ppm

1. Values from [18] (Al, Mg), [19] (Fe, Ti), and [6] (Th).

2. Values from [8,10].

3. Values for black matrix of 15445 and 15455, compiled in [20].

THE PROPOSED LUNAR PROCELLARUM BASIN: SOME GEOCHEMICAL INCONSISTENCIES.
P.D. Spudis[1] and P.H. Schultz[2] 1. U.S. Geological Survey, Flagstaff, AZ 86001 and Dept. Geology, ASU, Tempe, AZ 85287. 2. Dept. Geol. Sci., Brown Univ., Providence, RI 02912

Introduction. Over a decade ago, Cadogan [1] proposed that a giant impact basin (Gargantuan), encompassing Oceanus Procellarum and Mare Imbrium, was responsible for the asymmetric distribution of KREEP-rich rocks in the lunar crust. Whitaker [2] outlined specific morphological and structural evidence as proof of the existence of the giant basin, which he named Procellarum. Wilhelms [3,4] suggested that many apparently perplexing relations of lunar geochemistry could be adequately explained by the presence of this proposed basin. Subsequently, several investigators (e.g., [5-7]) have used this concept as a working hypothesis to explain various lunar geologic relations. The purpose of this paper is to suggest that the geochemical evidence for the existence of the Procellarum Basin is not conclusive and is subject to alternative interpretations; a companion paper [8] describes the ambiguous nature of morphologic and structural evidence for the basin. We do not attempt to "prove" the nonexistence of Procellarum; we merely assert that the principle of multiple working hypotheses should not be abandoned.

Geochemical relations cited as evidence for Procellarum Basin. The following are summaries of several lines of geochemical evidence that are cited by proponents of the Procellarum Basin as consequences of a giant basin impact: (A) The concentration of KREEP in the Procellarum region [1-5]. Cadogan [1] proposed that crustal unloading produced by the Gargantuan Basin impact induced partial melting of near-surface mantle materials. Volcanic KREEP basalt resurfaced the basin interior, thereby accounting for the high levels of KREEP in the Procellarum region. (B) The Al "gradient" [3,4]. Wilhelms has suggested that the abundance of ferroan anorthosite at Apollo 16 and its paucity at Apollos 14, 15, and 17 reflects the location of these landing sites outside and inside the Procellarum excavation basin, respectively. In this model the Procellarum impact removed ferroan anorthosite crust. (C) Similarity of geochemical relations at Procellarum with those around the South Pole- Aitken (Big Backside) Basin [2-4]. The major KREEP-rich anomaly of the lunar farside (Van de Graaf region) occurs within a large, 2000-kilometers-diameter basin whose existence is well established. This relation is cited as having been produced by a process analogous to the proposed Procellarum impact. (D) Crustal overplating of circum-Procellarum regions by basin ejecta [3,4]. Wilhelms suggested that highly aluminous zones of thick crust surround Procellarum as a result of both removal of crust at the basin target site and addition of several kilometers of ejecta from the Procellarum impact. (E) Most young maria occur within Procellarum Basin [3,4]. Oceanus Procellarum has a remarkable diversity of volcanic complexes and young flows, which Wilhelms suggested is a consequence of an anomalously thin lithosphere induced by the Procellarum impact. (F) Al-rich mare basalt flows [3,5]. Al-rich mare basalts supposedly occur in Maria Smythii and Fecunditatis [9]. Wilhelms suggested that these occurrences are a consequence of emplacement through an anomalously thick highland crust outside Procellarum Basin (see D above).

Another look at the geochemical evidence for Procellarum Basin. The six points listed above would seem to support the Procellarum Basin hypothesis. On close examination, however, they are equivocal or invalid. All are discussed as follows: (A) KREEP is distributed Moonwide and is not confined to Procellarum; moreover, its presence correlates inversely with crustal thickness [10,11]. The crust is thinnest and hence has the highest KREEP concentration in the Imbrium/Procellarum region. The existence of KREEP basalts in the Balmer and Marginis Basins [11,12] negates the theory that KREEP extrusion was limited to Procellarum [1]. On the basis of petrology [13], Cadogan's model for KREEP petrogenesis [1], whereby KREEP magmas were generated in the lunar mantle, is unlikely. (B) Although it is true that there is a paucity of ferroan anorthosite at landing sites within the Procellarum Basin [3,4], this is also true for several farside regions unrelated to either Procellarum or South Pole-Aitken Basins. Plutonic Mg-suite provinces occur near but outside the Balmer [14], Mendeleev [15], and Korolev [16] Basins and do not appear to be consistently related to basin interiors. Mg-suite intrusive activity was probably Moonwide, dependent on a number of factors that are not presently well understood. Moreover, ferroan anorthosite is present at Apollo 15, although it is a minor component (5%). It is difficult to explain the fact that it is present here, close to the center of the Procellarum Basin, but virtually absent at the Apollo 17 site, on the rim of Procellarum [17,18]. (C) The anomalous chemistry near 25° S, 170° E is directly related to the Van de Graaf-Ingenii region, not to the South Pole-Aitken Basin; specifically, no clear petrologic anomaly occurs where the eastern part of the basin ring is crossed at 24° S, 149° W. Its absence here suggests that the zone of anomalous chemistry is localized and is not necessarily related to the South Pole-Aiken Basin. (D) The concept that the crust is anomalously thick surrounding Procellarum is not supported by a crustal-thickness map derived from gravity data [19]. The results of this map are sometimes rejected because it is based on an extreme Airy compensation model. Its rejection on this basis, however, implies a Pratt crustal model, i.e., a laterally heterogeneous region where anorthositic crust is surrounded by Mg-rich crust, a model exactly the reverse of that implied by Procellarum Basin plutonism [3,4]. Moreover, studies of basin ejecta composition [15] demonstrate that the Smythii Basin, outside Procellarum Basin, displays ejecta compositions comparable to other lunar basins. Thus, evidence is not compelling for an anomalously thick crust surrounding the Procellarum Basin. (E) Although numerous young mare units occur within Procellarum Basin, they also occur outside the basin; specifically, maria in Smythii Basin are as young as all but the very latest flows in Procellarum [20]. Additional young maria occur in Mare Marginis and southeastern Mare Tranquillitatis, both of which are outside the Procellarum Basin. (F) The Al-rich mare flows proposed by [9] are probably the result of mixing of anorthositic highland rock with mare basalt. Such composition can be clearly seen in the high-Al signature of eastern Mare Tranquillitatis, where vertical mixing of highland debris into the mare regolith provides a simple explanation. The main objection to point F comes from the landing site (Apollo 14) where high-Al mare basalt was first identified. These basalts must have been extruded into the Procellarum Basin regardless of the origin of the Fra Mauro Formation--whether it is primary Imbrium ejecta or of local

origin. As such, the existence of these basalts is not predicted directly by the Procellarum Basin hypothesis.

Conclusions. We find that most of the geochemical arguments advanced in favor of the proposed Procellarum Basin are, at best, inconclusive. The Procellarum Basin hypothesis, although attractive as a paradigm, suffers from numerous inconsistencies that most likely reflect the complexities of the geologic processes and history of the Moon.

REFERENCES: [1] Cadogan P. (1974) Nature 250, 315. [2] Whitaker E. (1981) PLPSC 12A, 105. [3] Wilhelms D. (1982) PGPI NASA TM 85127, 111. [4] Wilhelms D. (1983) LPS XIV, 845. [5] Hubbard N. and Andre C. (1983) Moon and Planets 29, 15. [6] Pieters C. et al. (1984) LPS XV, 643. [7] Shervais J. et al. (1984) PLPSC 15, JGR 89, 25. [8] Schultz P. and Spudis P. (1985) LPS XVI (this vol.) [9] Hubbard N. (1979) PLPSC 10, 1753. [10] Schonfeld E. (1977) PLSC 8, 1149. [11] Spudis P. (1979) Conf. Lunar Highlands Crust, 157. [12] Haines E. et al. (1978) PLPSC 9, 2985. [13] Taylor S.R. (1982) Planetary Science, LPI Press, 481 p. [14] Spudis P. and Davis P. (1983) Workshop Pristine Rocks, LPI Tech. Rpt. 83-02, 69. [15] Spudis P. et al. (1984) LPS XV, 812. [16] Davis P. and Spudis P. (1985) LPS XVI (this vol.). [17] Ryder G. (1981) LPS XII, 918. [18] Spudis P. and Hawke B.R. (1981) PLPSC 12B, 781. [19] Bills B. and Ferrari A. (1976) PLSC 7, frontispiece. [20] Schultz P. and Spudis P. (1983) Nature 302, 233.

Investigation of Lunar Crustal Structure and Isostasy

C. H. Thurber, State University of New York at Stony Brook

Regional variations in lunar gravity can be considered to arise from two principle sources: an isostatic component due primarily to crustal thickness variations and a flexural component due primarily to the elastic support of mascons. Values for the thickness of the elastic lithosphere underlying major mare basins have been derived from the analysis of concentric rilles, presumably due to tensional failure [1,2]. Thickness estimates of mare basin fill have been derived from gravity and photogeologic studies [3-7]. Taken together, these should constitute the flexural component of the moon's gravitational field.

A simple global model of the lunar gravity field is being developed. Starting with the major mascon loads emplaced on lithosphere of the locally appropriate elasitc thickness, the flexural deformation is calculated, and isostatic variations are superimposed to match the observed topography. The mascon loads will be modeled as thin disks both for the flexure calculation [8] and the subsequent gravity calculation; the gravity anomaly due to flexure of the lithosphere will be treated as a set of concentric rings of anomalous density. The complete model gravity field (flexural and isostatic parts) will be compared to the observed field to test the self-consistency of the elastic lithosphere and mare basalt thickness estimates. If successful on the lunar near side, this formalism could be extended to the lunar limb and far side to produce a predictive model for the global lunar gravity field.

REFERENCES: [1] R. P. Comer, S. C. Solomon and J. W. Head, PLPSC 10, 2441, 1979; [2] S. C. Solomon and J. W. Head, RGSP 18, 107, 1980; [3] C. H. Thurber and S. C. Solomon, PLPSC 9th, 3481, 1978; [4] S. R. Bratt et al., JGR, 90, 3049, 1985; [5] J. W. Head, Moon Planet, 26, 61, 1982; [6] R. A. De Hon and J. D. Waskom, PLPSC, 7th, 2729, 1976; [7] R. S. Phillips et al, JGR, 77, 7106, 1972; [8] Brotchie and Silvester, JGR, 74 5240, 1969.

Implications of Convection in the Moon and the Terrestrial Planets

Donald L. Turcotte, Department of Geological Sciences, Cornell University, Ithaca, NY 14853-1504

During the past year we have worked on two principle lines of research:

1) The early thermal and chemical evolution of the moon. The work on the early thermal evolution of the moon was completed and published (1). This work determined the time evolution of magma oceans on the earth and moon. Calculations showed that the magma oceans were relatively shallow but would provide total fractionation of the earth to form the core and the atmosphere and partial fractionation on the moon. Work was also carried out on the evolution of isotopic systems on the moon. The rubidium-strontium, neodymium-samarium, and uranium-theorium-lead systems were studied. The relation of source region heterogeneity to the mixing associated with mantle convection was considered. This work was presented at the Conference on the Origin of the Moon, October 13-16, 1984. Subsequently this work was written up and is now in press (2).

2) Fractals and fragmentation. The concept of fractals and the renormalization group approach are having a major impact on a variety of scientific disciplines. We have applied the fractal concept to fragmentation with applications to the frequency-size distribution of meteorites and asteroids. This work was presented at the XV Lunar and Planetary Science Conference (3) and was subsequently written up for publication (4).

(1) D.L. Turcotte and J.C. Pflugrath, Thermal structure of the accreting earth, J. Geophys. Res., 90, C541-C544 (1985).

(2) D.L. Turcotte and L.H. Kellogg, Implications of isotope data for the origin of the moon, Prof. Conf. Origin Moon, in press (1985).

(3) D.L. Turcotte, Fractals, fragmentation and a renormalization group determination of the frequency-mass distribution of meteorites and asteroids, Lunar Planet. Sci. XV, 872-873 (1985).

(4) D.L. Turcotte, Fractals and fragmentation, J. Geophys. Res., in press (1985).

CHAPTER 5

CRATERING PROCESSES

RELATIVE AGES OF MARTIAN TERRAIN UNITS

Barlow, N.G., and Strom, R.G., Dept. of Planetary Sciences, Lunar and Planetary Laboratory, University of Arizona, Tucson, Arizona 85721

The cratering record within the inner solar system over the past ≈ 4.5BY has been retained by the surfaces of Mercury, Mars, and the Moon. The crater size/frequency distributions for the heavily cratered highlands of these three bodies all show a highly structured curve of approximately the same shape and crater density. These multi-sloped curves have an approximately -2 slope in the diameter range ≈ 8 to 70 km and represent the period of heavy bombardment. The end of heavy bombardment has been dated ≈ 3.8BY on the Moon, and most plausible origins for the impacting objects have orbital dynamics which suggest that this event occurred essentially contemporaneously within the inner solar system, although the end of heavy bombardment on Mars may be model dependent (1,2). A younger crater population is seen on the plains regions of the Moon and Mars which shows a ≈ -3 slope over the diameter range ≈ 8 to 70 km. A Chi-square statistical test indicates that the highlands population is different from the plains populations at the 99% confidence interval. Thus, at ≈ 3.8BY ago, at least in the Earth-Moon vicinity, the family of objects responsible for the period of heavy bombardment became extinct, and the subsequent cratering record was caused by a second family of objects (probably asteroids and comets) which has impacted up to the present time.

Mars exhibits a number of terrain units with various crater densities (Figure 1). These units can be dated relative to the end of heavy bombardment depending on whether they show a highlands crater size/frequency distribution or a plains distribution. Furthermore, the relative ages of the units within these two time divisions can be determined by crater densities.

The Viking 1:2M photomosaic series has recently been completed for the entire Martian surface, providing for the first time high quality, medium resolution pictures of all terrain units. We have divided the surface into ≈ 25 terrain units based on published Mariner 9 geologic maps and extensive remapping using the Viking photomosaics. All craters larger than 8 km in diameter have been mapped and classified by terrain type, ejecta and interior structure, relationship to tectonic features, and whether the crater pre- or post-dates the surrounding surface. This information has been entered into a computer data base management system which allows ease of access to the data by crater location, diameter, or other characteristics.

The craters have been binned by diameter, and the resulting binned data are also accessible through a data base management system. All regions of a particular terrain have

been combined, and crater size/frequency distributions have been determined using "R" plots (3,4). Average ages relative to the end of heavy bombardment have thus been obtained from the shape of the crater distribution, and average ages among different terrains have been obtained by crater densities.

In general, about 60% of the Martian surface dates from the period of heavy bombardment and is located primarily in the southern hemisphere. The heavily cratered regions with intercrater plains are slightly younger than those regions of "pure" uplands, which are the oldest units on the planet. The ridged plains regions of Lunae Planum, Syrtis Major, and Chryse Planitia, the large volcanic region near the Hellas Basin, the large Hellas and Argyre Basins, and almost all small volcanic constructs, including those with channeled flanks date from near the end of heavy bombardment (Figure 2).

The remaining 40% of Mars has formed since the end of heavy bombardment, and is situated primarily in the northern hemisphere. About 30% of this area is covered by plains with a crater density similar to that of the lunar maria. The volcanic plains in the Elysium region are approximately the same age as the average northern plains. The remaining 10% consists of young volcanic constructs (Elysium Mons and the large Tharsis volcanoes), the plains surrounding Tharsis, the canyon deposits, and the polar and equatorial layered deposits (Figure 3).

The general terrain results are based on the use of the large crater population (≥ 8 km diameter) and therefore large areas have been utilized to obtain statistically significant results. These dates should thus be considered as average ages, since individual geologic units may contain smaller areas that are either older or younger than the average age of the unit. Some local units of geologic interest have been studied in greater detail, such as Lunae Planum, Syrtis Major, Chryse Planitia, the Hellas and Argyre Basins, and the volcanic regions. Continuing analysis of local regions will allow construction of a more detailed chronology for the Martian surface units.

REFERENCES

1. Wetherill, G.W. (1975) Proc. Lunar Planet. Sci. Conf. 6, 1539-1561.
2. Wetherill, G.W. (1977) Proc. Lunar Planet. Sci. Conf. 8, 1-15.
3. Barlow, N.G., and Strom, R.G. (1984) Reports of the Planetary Geology Program--1983, NASA TM86246, 85-86.
4. Strom, R.G., and Barlow, N.G. (1985) Reports of the Planetary Geology and Geophysics Program--1984, NASA TM87563, 177-179.

POST-SURFACE CRATERS

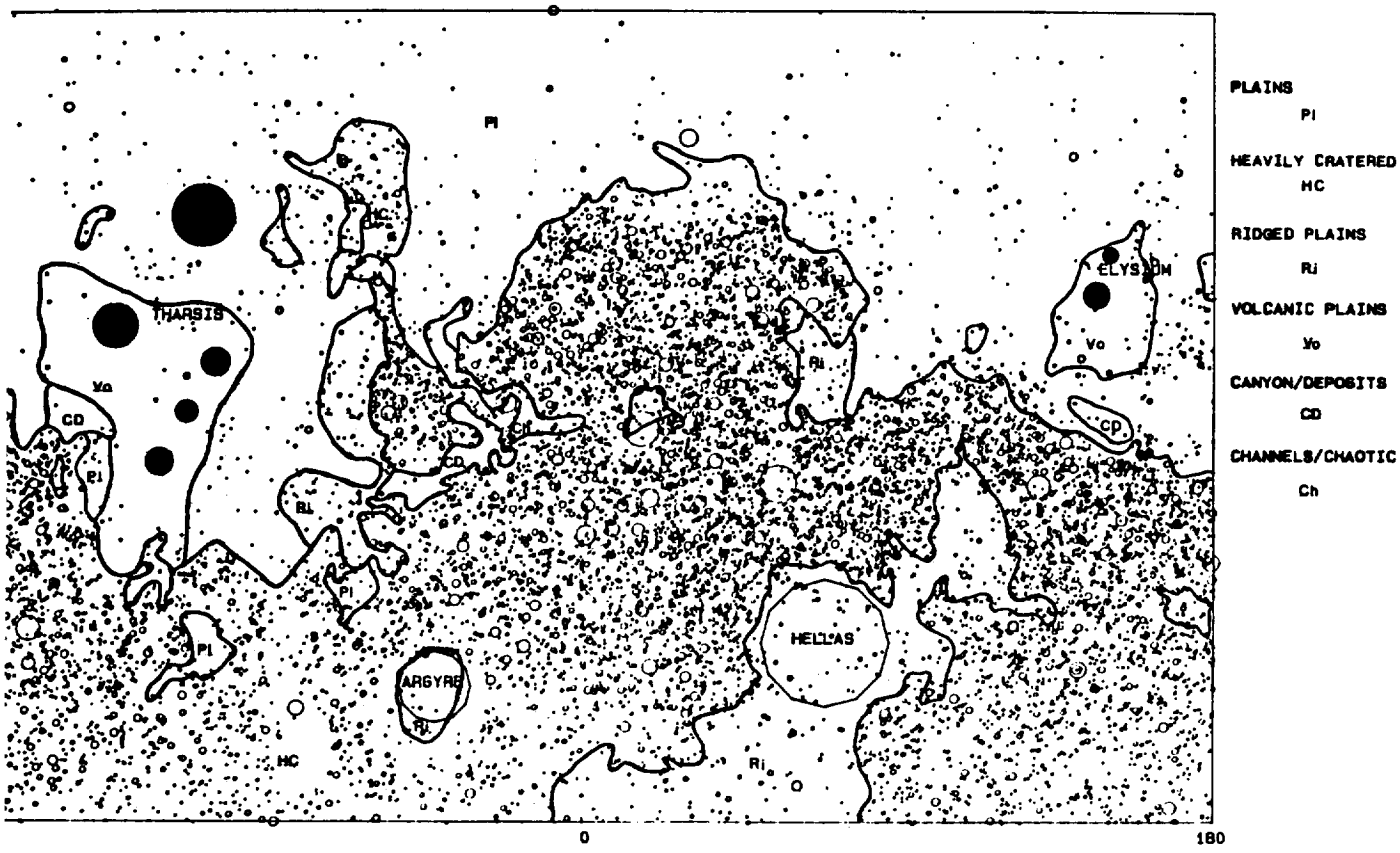

Fig. 1

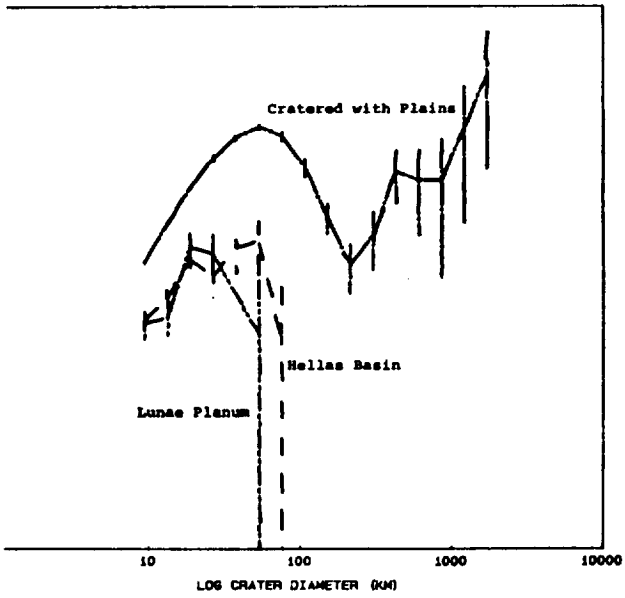

Fig. 2

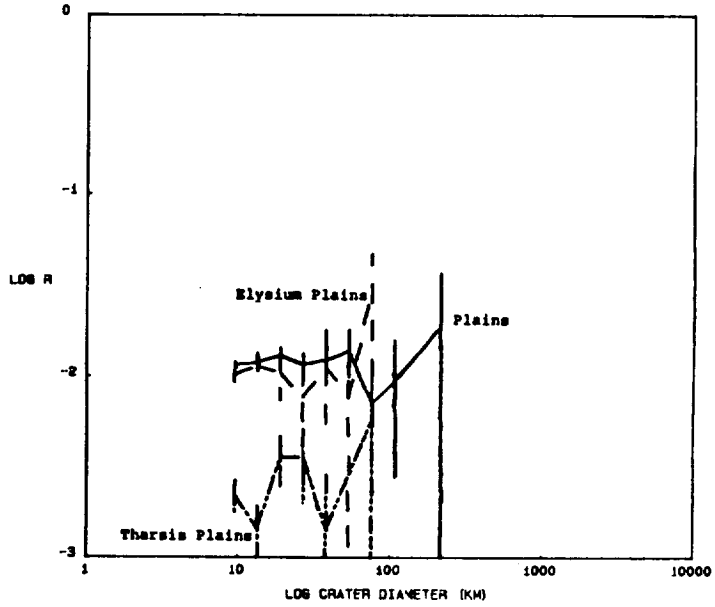

Fig. 3

Impact and Cratering Processes on Asteroids, Satellites and Planets

Clark R. Chapman, Donald R. Davis,
Richard Greenberg and Stuart J. Weidenschilling
Planetary Science Institute, Tucson, Arizona

We are studying impact processes, particularly large-scale catastrophic collisions, relevant to asteroids, planetary satellites, and planets. Our primary emphasis has been toward understanding the sizes, structures and rotation of asteroids as they are affected by the continuing collisional evolution. We combine laboratory experimental data (obtained from the literature and from our collaterally funded projects) with theoretical collisional models in numerical simulations in order to study the evolution of the asteroid belt, formation of Hirayama families, etc. Our past work has suggested that many asteroids are gravitationally bound rubble-piles, which have been thoroughly fractured in (at least) their outer layers. More recent analysis has set constraints on the fraction of asteroids that are expected to have such structure and on the extent of collisional evolution of the main-belt population. Large, oblique impacts may spin-up asteroids to the point that objects with rubble-pile internal structures might adopt figures approximating hydrostatic equilibrium (i.e. near biaxial or triaxial ellipsoids). Still more energetic collisions may impart so much angular momentum that a binary object would result. Our studies of the extent of collisional evolution, and on the evolving size-distribution since primordial epochs, may help determine planetesimal size distributions during accretionary epochs.

More recently we have applied some of the same theoretical analysis to the smaller satellites of Saturn and other planets. Some aspects of satellite break-up are analogous to the asteroidal processes we have been studying, whereas some other aspects that are different (reaccumulation in circumplanetary orbit). We have also been investigating the sweep-up of planetesimal, asteroidal, cometary, and circumplanetary projectile populations and the expected crater distributions for comparison with observed size-frequency distributions on planetary satellites and the terrestrial planets (emphasizing the icy outer-planet satellites planet Mercury).

We have developed and published (Davis et al. 1985) a new model for calculating the size distribution of resulting fragments, together with the collisional energy required to collisionally disrupt large asteroids. This model enables us to better match the observed size distributions of Hirayama families (particularly the Themis family), which presumably resulted from the collisional disruption of larger parent bodies. This new algorithm includes a pressure-dependent impact strength which predicts that large asteroids behave as intrinsically strong objects due to compressive loading of overburden throughout their interiors. For small bodies ($\lesssim$ few kilometers diameter), where the gravitational loading is negligible, this model assumes that the impact strength is independent of size.

There was considerable discussion of scaling laws for disruption at the 1985 Workshop on Catastrophic Disruption of Asteroids and Satellites held in Pisa, Italy, and attended by Drs. Chapman and Davis. The pressure strengthening impact strength model was viewed as physically quite plausible; however, it was argued that the impact strength should <u>decrease</u> with size in the size range where gravitational compression is negligible. The

physical basis for this decrease is ultimately found in the Griffith crack theory for the size distribution of fractures in natural materials. While this alteration to our scaling model does not affect the major results in Davis et al. it could affect the calculated small size distribution of asteroids.

Numerical simulations of asteroid collisional evolution, which investigate possible initial asteroid mass distributions at the time their collisional speeds were pumped up to ~5 km/s, have been carried out using the above described collsional outcome model. Successful candidate initial populations must satisfy three constraints: (a) they must evolve to the present observed size distribution, (b) Vesta must not be shattered in order to preserve its observed nearly-homogeneous basaltic crust, and (c) there must be enough collisional evolution to produce at least the observed number of Hirayama families. We considered various hypothetical initial population distributions, and found that a very steep size distribution, containing very few large bodies but numerous small bodies totalling only several times the current belt mass best satisfied all constraints. This result implies that the asteroid region already was depleted in mass relative to the terrestrial planet region by the time velocities were stirred up to ~5 km/s.

We also calculate the number of asteroids that are formed by different mechanisms, e.g. unshattered original survivors, gravitationally bound rubble piles, fragments from the collisional disruption of larger bodies, etc. We then relate these distributions to statistical properties of the observed asteroid population that may be influenced by asteroid physical states. For example, intermediate size asteroids (~100-200 km diameter) are the sizes at which gravitationally bound rubble piles should be most abundant. This is also the size range at which Zappala et al. 1984 found observational evidence for large amplitude lightcurves among rapidly rotating asteroids. One interpretation is that the gravitationally bound rubble piles relax to quasi-equilibrium rotating asteroids. Other relationships between observable properties and the calculated physical state are being investigated.

The idea that rotational properties of asteroids constrain their physical nature and collisional history has been stimulated by demonstrations that the mean spin period varies with size and taxonomic class (Farinella et al., 1981; Dermott et al., 1984). These studies show that intermediate-sized asteroids ($20 < D < 200$ km) rotate more slowly, on average, than do smaller and larger ones. Dobrovolskis and Burns (1984) interpret this as due to "angular momentum drain" (i.e., braking by preferential escape of impact ejecta in the direction of rotation). They make the explicit assumption that small impacts alter an asteroid's spin, but that disruption has no effect on the rotation rate of the largest fragment, which seems implausible. Thus, it may be premature to draw quantitative conclusions as to asteroid properties and collisional history based on this model. Still, we note that Farinella, et al. (1982) conclude that the observed angular momenta of large asteroids is compatible with only a moderate depletion, about a factor of five, of the original mass of the belt, in substantial agreement with our own results based on the observed size distribution.

Chapman and McKinnon completed their lengthy chapter on cratering of planetary satellites for the Natural Satellites book. The chapter contains a thorough review of cratering physics, with particular application to icy satellites, together with a critical review of cratering statistics on planetary satellites and the terrestrial bodies. The authors, using numerical models and crater-scaling relationships, conclude that there are 4 (possibly 5) distinct projectile populations implied by the observed crater distributions. Saturn Population II is due to cratering by saturnicentric projectiles. If comets are responsible for the remaining populations, substantial physical evolution of different groups of comets is required, because the two production functions observed in the inner solar system (late heavy bombardment, and the more recent cratering) and the Ganymede/Callisto population are all different from each other. The analysis demonstrates that there is no good link between cratering of the moon and terrestrial planets and the cratering of outer-planet satellites. In the inner solar system, there is an unknown contribution by asteroids; also the comet size distributions (both shape and absolute numbers) are very uncertain, rendering the present relative cratering rates very uncertain. Any link involving earlier heavy bombardments is even more speculative; several scenarios for the late heavy bombardment in the inner solar system would not impact on the outer planet satellites. With no physical or temporal connection between the inner and outer solar system, there is no basis for estimating -- even crudely -- the cratering chronologies for the satellites of Jupiter and Saturn.

We, in collaboration with Mr. Jeffrey Cargill and Robert Strom of the University of Arizona, have studied the hypothesis that the breaking up of a proto-Hyperion could be one source of projectiles that cratered the Saturnian satellites. A multi-body scattering program based on the Öpik-Wetherill theory is used to calculate the probability that projectiles from the catastrophic disruption of a proto-Hyperion would impact the inner Saturnian satellites. Our calculations show that only a tiny fraction of such fragments would reach Mimas or Enceladus. In fact, only Rhea receives enough impacts so that Population II craters might be explained by this mechanism. Hence another source must be sought for the saturnicentric flux of projectiles inferred from widespread Population II cratering. Perhaps breakup and reaccumulation is the mechanism for the inner satellites while scattered fragments from a hypothesized proto-Hyperion breakup could have cratered the more distant satellites.

References

Davis, D.R., C.R. Chapman, S.J. Weidenschilling, and R. Greenberg (1985). Icarus **62**, 30-53.

Dermott, S.F., A.W. Harris, and C.D. Murray (1984). Icarus **57**, 14-34.

Dobrovolskis, A.R. and J.A. Burns (1984). Icarus **57**, 464-476.

Farinella, P., P. Paolicchi, and V. Zappala (1981b). Astron. Astrophys. **104**, 159-165.

Farinella, P., P. Paolicchi, and V. Zappala (1982). Icarus **52**, 409-433.

Zappala, V., P. Farinella, Z. Knezevic, and P. Paolicchi (1984). Icarus **59**, 261-285.

IMPACT EXPERIMENTS

William K. Hartmann
Planetary Science Institute

Velocity distributions are determined for ejecta from 14 experimental impacts into regolithlike powders in near-vacuum conditions at velocities from 5 to 2321 m/sec. Of the two powders, the finer produces slower ejecta. Ejecta include conical sheets with ray-producing jets and (in the fastest impacts at $V_{imp} \gtrsim 700$ m/sec) high-speed vertical plumes of uncertain nature. Velocities in the conical sheets and jets increase with impact velocity. Ejecta velocities also increase as impact energy and crater size increase; a suggested method of estimating ejecta velocity distributions in large-scale impacts involves homologous scaling according to R/R_{crater}, where R is radial distance from the crater. The data are consistent with Holsapple-Schmidt scaling relationships. The fraction of initial total impact energy partitioned into ejecta kinetic energy increases from around 0.1% for the slow impacts to around 10% for the fast impacts, with the main increase probably at the onset of the hypervelocity impact regime. Crater shapes are discussed, including an example of a possible "frozen" transient cavity. Ejecta blanket thickness distributions (as a function of R) vary with target material and impact speed, but the results measured for hypervelocity impacts agree with published experimental and theoretical values. The low ejecta velocities for powder targets relative to rock targets, together with the paucity of powder ejecta in low-speed impacts (<1 projectile mass for $V_{imp} \sim 10$ m/sec) enhance early planetary accretion efficiency beyond that in some earlier theoretical models; 100% efficient accretion is found for certain primordial conditions.

IMPACT CRATER SCALING LAWS

K.A.Holsapple, University of Washington
Seattle, WA 98195
November, 1985

Impact craters of interest in planetary geophysics occur in a variety of conditions of size and velocity not amenable to experimentation. Consequently, the development of the correct scaling rules becomes an issue of utmost importance. This research is to develop and apply such scaling laws.

The fundamental basis for the research is the observation that many power-law forms are obtained experimentally, and that those forms are precisely the form that would be obtained when there exists a single scalar measure of the impactor size and velocity. Such a single scalar measure has been called a coupling parameter by the author. A recent exposition of the coupling parameter concept has been given [1]. An important result of that paper is that this particular measure is the type of measure that arises in 'point-source' solutions: solutions that govern the deposition of energy and motion in a target at ranges sufficiently far removed from the region of the deposition of that energy so that the details of that source no longer matter. This simple physical idea is presented in a precise way in [1].

There has been progress in three distinct areas. First, a recent application of the concept to develop scaling relations for icy materials has been given [2,3]. That application was inherently more difficult than previous applications, and remains more uncertain, for the following reasons. First, the experimental data-base is rather sparse, particularly for the higher velocities that characterize 'hyper-velocity' impacts, and for the colder temperatures that are of primary interest for the planetary applications. Secondly, the final form of the scaling laws depends not only on the introduction and the form of the coupling parameter, but also on the choice of the measure of the strength of the target material. For a material such as ice, there appear to be significant strain-rate effects in measurements of its strength. Further, it is uncertain whether measures of the fracture strength or of a yield strength are dominant for cratering. Several combinations of possibilities are worked out in [3], and compared to the existing data. Important summary results of general interest are final prediction curves for impact cratering in icy targets: such a curve is shown in fig. 1.

A second new application of this theory was recently presented [4]. This application, while closely related to cratering, is somewhat different: the catastrophic breakup of asteroids and small satellites by impacts. This problem shares much of the same physics as does the ice cratering problem: the form of the resulting scaling laws depends in a crucial way on both the

coupling parameter measure and also on the form of the strength measure of the impacted body. Concepts from the theory of the dynamic fracture of brittle materials were used and further developed for this application. A measure of the distribution of micro-cracks in a body was introduced, and the measure of the critical stress under which a crack of a given size will propagate was included. These concepts were shown to determine a macroscopioc strength measure of the rate-dependent type that matches measured strengths of brittle, rock-like materials. More importantly, the theory was shown to predict definite results that could be compared to measurements. Such a comparison is shown in Fig. 2, a plot of measured largest remaining fragment size in a catastrophic impact versus the kinetic energy of the impactor, divided by the mass of the target body. The theory predicts the curve labeled "m=9" on that plot, which is seen to match the measurments very well. No other theory exists that predicts this result. A summary plot of the conditions that are predicted for the onset of catastrophic impact is shown in Fig.3. Comparisons to other existing theories are also shown on this figure.

The final progress that can be reported on this research are further numerical calculations. The purpose of this aspect of the research is to determine how the material properties of the materials involved determine the coupling parameter, which then determines the form of the final scaling laws. This is a task that is ideally suited to numerical calculation, where parametric studies are possible, using physical models that are thought to be appropriate. Previous results have been reported that showed that a code calculation could be obtained that reproduced certain idealized results in porous and non-porous mateials.

In the current year, it was realized that there is a significant body of data existant that is very closely related to the cratering theories, but is in one sense simpler, and is also for large events with determinate input conditions (in contrast to cratering results). This is the body of data that exists for the cavity formation of underground nuclear explosives. Since this problem has, to first order, spherical symmetry, it is significantly easier to study and to model using a code than is the cratering problem which is strongly two-dimensional.

Significant results on this calculational effort can be reported. Calculated results have been compared to analytical solutions, see fig. 4 attached. The results are now being compared to the unclassified actual field results. Preliminary results show that there are significant differences in scaling due to the material properties of the site, and that the coupling theory scaling does correctly predict those dependences.

REFERENCES:

1. Holsapple, K.A. and R.M.Schmidt,"Point-source solutions and coupling parameters in cratering mechanics", submitted to J. Geophys. Res., April, 1985.
2. Holsapple, K.A., and K.R.Housen, "Cratering estimates for ice", To be published in Proc. Lunar Planet. Sci. Conf XVI, July, 1985.
3. Holsapple, K.A., and K.R.Housen, "Ice Cratering Scaling Laws", Poster presentation, 16th LPSC, Houston, March, 1985.
4. Holsapple, K.A., and K.R.Housen,"The scaling of catastrophic impacts", Presented at the workshop on "Catastrophic Disruption of Asteroids and Small Satellites" Pisa, Italy, July, 1985.

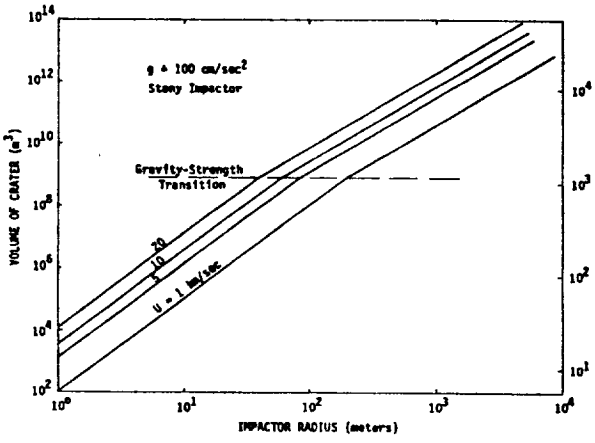

Fig.1. Cratering estimates for ice.

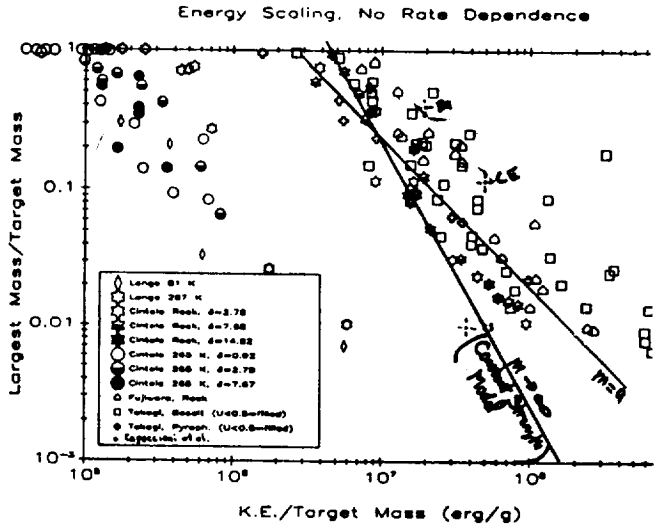

Fig.2. Largest fragment in catastrophic impacts.

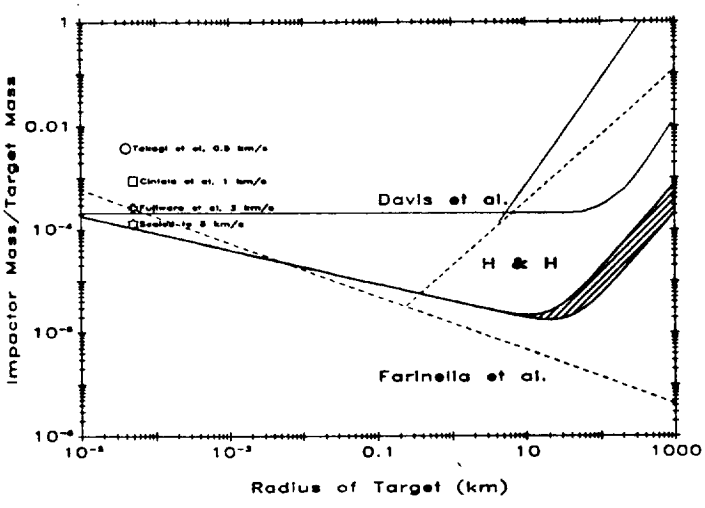

Fig. 3. Radius for catastrophic breakup.

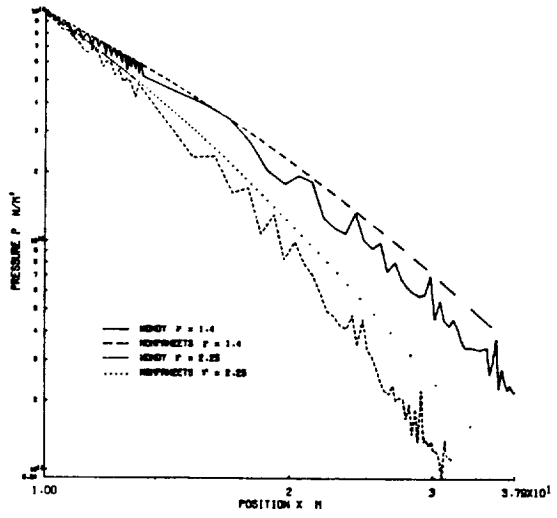

SPHERICAL CAVITY GROWTH

Fig.4. Pressure decay for cavity growth.

THE NATURE OF CRATER RAYS: THE COPERNICUS EXAMPLE

Carle M. Pieters (Department of Gelolgical Sciences, Brown University, Providence, RI 02912)
John B. Adams, Peter J. Mouginis-Mark, Stanley H. Zisk, Milton O. Smith, James W. Head, and Thomas B. McCord

Crater rays are formed during a cratering event as target material is ballistically ejected to distances of many crater radii forming narrow, generally high albedo, approximately linear features extending outward from the crater. The nature of crater rays was examined for the lunar crater Copernicus using new information on the composition of surface material (from near-IR reflectance measurements), surface roughness (from radar backscatter measurements), and photogeologic data (from available images). Part of data analysis included use of mixing models to quantify the mixing systematics observed between primary ejecta and local substrate of the ray based on compositional parameters from reflectance spectra. Primary material from Copernicus can be detected in the surface material of rays in decreasing amounts with increasing radial distance (e.g. 20-25% primary ejecta at six crater radii). For distances greater than three crater radii, the proportion of local material to primary ejecta observed from these compositional reflectance data is approximately equal to that predicted by previous laboratory and ballistic studies of craters. Within three crater radii the compositional data indicate a higher proportion of primary ejecta than predicted. For extended areas along the ray that do not contain large secondary craters, the primary ejecta is intimately mixed on the granular scale with local material throughout the regolith. The relatively high albedo of the rays of Copernicus is due to the feldspathic composition (highland) of the primary ejecta in rays emplaced on a mare substrate. Immature local substrate is only observed in Copernicus' ray at large unmantled secondary craters or other areas with sufficient topographic slope to prevent the accumulation of mature soils. (Copernicus, crater rays, lunar spectroscopy)

IMPACT-INDUCED VAPORIZATION: EFFECT OF IMPACT ANGLE AND ATMOSPHERIC PRESSURE.

P. H. Schultz, Dept. of Geological Sciences, Brown University, Providence, RI 02912 and D. E. Gault, Murphys Center of Planetology, Box 833, Murphys, CA 95247

BACKGROUND: Most impacts on the three inner planets and the Moon occur at velocities high enough for vaporization: velocities higher than what is presently attained in the laboratory. Several timely issues required not only numerical estimates of impact vaporization but also general phenomenology in order to constrain present models. Of particular importance are the effects on the following problems: impact-generated vaporization on early-time dispersal of a meteorite signature (1); modification of ejecta dynamics from a volatile-rich substrate (2); acceleration of material from the martian and lunar gravity fields (2,4); and the accretion of the Moon from impact vaporization of a primordial terrestrial crust (5). Although extremely high impact velocities are not yet possible, the effects of impact vaporization can be simulated by the use of easily volatilized target materials. A series of exploratory experiments at the NASA-Ames Vertical Gun Range used dry-ice targets and a high frame-rate camera. Simplified calculations following (6) from the Hugoniot for dry ice indicate that 35 projectile masses may be vaporized from a 5 km/s aluminum impactor 0.635 cm in diameter. This gives an overestimate but serves to demonstrate that significant quantities of CO_2 vapor products will be produced. Both vertical and oblique (15^{o} from the horizontal) impacts were produced by 0.635 cm aluminum spheres with/without dry-ice targets, and with/without an atmospheric envirnoment. The events were recorded on color film at 35,000 fps with a shutter speed of 3 μs using the illumination generated by the impact-generated ionized gas. For the oblique impacts, downrange witness plates documented the ricochet components as in previous work (7).

RESULTS: *VERTICAL IMPACT (NO DRY ICE):* Both vacuum and non-vacuum experiments used compacted pumice targets for comparison with previous studies recorded at lower frame rates (8,9). Under vacuum conditions (< 1 mb) a 6.24 km/s impact generated an intense but short-lived glow visible only in the first frame (within 28 μs). A very faint ionized gas cloud inside and above the ejecta curtain expanded at a velocity of about 2.5 km/s. Under near-ambient atmospheric conditions (0.9b, argon) a 5.56 km/s impact produced an intensely bright but short-lived (< 28 μs) disc at the surface believed to be a toroid of ionized gases from high-speed jetting material interacting with the atmosphere. A glowing basal ejecta lobe remained visible after about 30 μs but was consumed by the enlarging ejecta plume within 60 μs. Inside the vertical ionized gas created by the projectile, a small (2 cm) bright ball rose above the growing ejecta curtain after 90 μs with a constant velocity of about 0.6 km/s. After 460 μs it was indistinguishable from the fading ionized projectile wake. *VERTICAL IMPACT (DRY-ICE TARGET):* Two types of dry-ice targets were used: A solid dry-ice block (about 5 cm thick) embedded in a sand target; and dry-ice powder sprinkled on top of the sand to a depth of about 5 cm. The impact chamber was evacuated to only 33 mb in order to avoid violent boiling of the dry ice. Impact velocities of 6.04 and 5.08 km/s into both dry-ice powder and block, respectively, produced no significant difference from the 6.24 km/s impact compacted pumice at < 1 mb of air. At 0.9b (argon), however, significant differences from the vacuum experiments and the argonatmosphere without a dry-ice target were observed. A 4.72 km/s impact into a dry-ice block produced a 2-component ejecta plume within the first 28 μs: a basal toroid and high-angle cone. Subsequently a bluish ionized jet inside the ejecta curtain traveled upward initially at 1.5 km/s slowing to 1.1 km/s after 100 μs. This jet was much more intense than the fading ionized projectile wake. After 120 μs, an opaque column rose vertically at 0.5 km/s. This may represent sand/dust being drawn upwards by the rising ionized jet. In contrast, the 5.62 km/s

impact into dry-ice powder generated an intense but small ball of ionized gas that initially moved up through the jet at 1.8 km/s with a diameter of 1 cm. This fast moving ball was not produced by the 4.72 km/s impact into the dry-ice block (perhaps due to the lower velocity). Luminescence for both impacts into dry ice was much more intense than impacts into pumice. Most of this inferred ionized gas was contained within or above the silhouetted ejecta ejecta curtain. *OBLIQUE IMPACTS (NO DRY ICE):* Under near-vacuum conditions (< 1 mb), a bright ionized region occurred only at impact (6.07 km/s). The witness plates indicated ricocheted fractions impacting at -7^{o} above the horizontal. Under atmospheric conditions (0.9b, argon), a 5.55 km/s impact produced a small intense cloud (2-3 cm) of high-speed ionized material traveling downrange at about 5.3 km/s. Most of this material was concentrated at 7^{o} from the horizontal with several spikes at higher trajectory (15^{o}) and lower velocity. A trail of less luminescent debris trailed behind the low angle downrange component. No vertically expanding gas or ejecta cloud occurred directly above the impact. *OBLIQUE IMPACTS (DRY ICE TARGET):* In dramatic contrast with vertical impacts into dry ice under low atmospheric pressures, oblique impacts at 5.86 km/s and 5.44 km/s into dry-ice powder and block, respectively, produced an intense expanding gas cloud. In both cases, the luminescent cloud rapidly expanded (2 km/s) as it traveled downrange at about 5.0 km/s. Impacts into both powder and block produced intensely bright low-angle (7^{o}) spikes that preceded the expanding cloud downrange at a velocity close to the initial impact velocity. The expanding cloud clearly interacted with the surface and only a few pits were observed on the witness plates in both cases. Under atmospheric conditions (0.9b, argon), the results were remarkably similar to the experiment without dry ice. A 5.14 km/s impact into a dry-ice block at 15^{o} produced a very contained event with a high velocity (5 km/s) downrange ionized ball. In contrast with the non-dry-ice experiment, however, a small ionized ball moved back up the projectile wake at low velocity (0.07 km/s).

PRELIMINARY CONCLUSIONS: These experiments indicate that impact vaporization strongly depends on impact angle: oblique impact (15^{o}) vaporized significantly more material than did vertical impacts. The presence of an atmosphere appears to enhance vaporization of dry ice in vertical impact (perhaps due to the ionized air cap in front of the projectile) but appears to suppress or contain vaporization for oblique angles. Impact-generated gas forms a vertically directed jet that is contained within the ejecta curtain for vertical impacts. Low-angle impacts under low atmospheric pressure, however, generate a rapidly expanding cloud that travels downrange at a velocity nearly 60% of the original impact velocity. The effects of these impact-generated gases are restricted to the earliest times of crater formation and do not appear to affect the later stage cratering process. Future experiments will explore the effects of impacts at more probable impact angles (45^{o}), examine the dynamics of non-luminescent ejecta, and consider the effects on cratering efficiency.

References: (1) O'Keefe, J.D. and Ahrens, T.J. (1982) in *Geol. Soc. Sp. Paper 190,* 103-120; (2) Wohletz, K.H. and Sheridan, M. (1983) *Icarus 56,* 15.37; (3) Nyquist, L.E. (1983) *Proc. Lunar Planet. Sci. Conf. 13th, J. Geophys. Res. 88,* A785-A798; (4) Wood, C.A. and Ashwal, L.D. (1981) *Proc. Lunar Planet. Sci. 12B,* 1359-1375; (5) Conference on the Origin of the Moon (1984), Hawaii, Lunar and Planetary Institute, Houston; (6) Gault, D.E. and Heitowit, E.D. (1963) in *Proc. 6th Hypervelocity Impact Symp.,* 413-456; (7) Gault, D.E. and Wedekind, J. (1978) *Proc. Lunar Planet. Sci. Conf. 9th,* 3843-3875; (8) Schultz, P.H. and Gault, D.E. (1982) in *Geol. Soc. Amer. Sp. Paper 190,* 153-174; (9) Schultz, P.H. and Gault, D.E. (1984) *Lunar and Planetary Science XV,* 730-731.

Experimental Investigation of Crater Growth Dynamics

Robert M. Schmidt, Kevin R. Housen, Michael D. Bjorkman and Keith A. Holsapple
Boeing Aerospace Co., M/S 1F-72, P. O. Box 3999, Seattle WA 98124.

This work is a continuation of an ongoing program whose objective is to perform experiments and to develop scaling relationships for large-body impacts onto planetary surfaces. The centrifuge technique is used to provide experimental data for actual target materials of interest. With both powder and gas guns mounted on the rotor arm, it is possible to match various dimensionless similarity parameters, which have been shown to govern the behavior of large-scale impacts. The development of the centrifuge technique has been pioneered by the present investigators and is documented by numerous publications, the most recent of which are listed below.

Understanding the dependence of crater size upon gravity has been shown to be key to the complete determination of the dynamic and kinematic behavior of crater formation as well as ejecta phenomena. (See Table 1 in ref. 7). We have identified three unique time regimes in the formation of an impact crater.[2,5] The "early" time regime represents the initial contact during which the target material is overdriven by the impactor. The particle velocity in the target, initially one dimensional, is determined by the high pressure material properties of the impactor and the target.

As the process continues into the "intermediate" time regime, the flow becomes two dimensional and a length scale based upon impactor size evolves. The specific characteristics of the impactor such as size, velocity, and density can no longer be identified in the flow field. In their place an overall size scale evolves which then holds out to much later times. The properties of the flow field depend only upon a particular product of powers of the impactor size a, and impactor velocity U. This quantity aU^{μ} is referred to as a coupling parameter.[5] In particular cases the flow field in the intermediate regime has very special motions. For example, if subsequent to the early-time regime, crater growth is independent of gravity, material strength and wave speed, then crater dimensions should grow as a simple power-law in time with exponent equal to $\mu/1+\mu$.

"Late" time refers to the final stage when retarding forces due to gravity or material strength arrest the decaying flow field to form the final crater or maximum transient crater. For this stage, we have shown that the final crater should depend only upon the coupling parameter product aU^{μ}, gravity and/or strength.[6,10]

The existence of a coupling parameter for water was previously demonstrated by showing that the time of formation could be simply related to the maximum transient crater volume and gravity.[9,11,15] Data for rate of crater growth spanning over two orders of magnitude, were also presented. Those data are now supplemented with microsecond resolution results which show that the power-law growth regime extends over a range of 5 orders of magnitude from a size scale on the order of source dimensions to approximatly 70% of the maximum transient crater volume.[18] This was true for all the different test conditions, which covered a range of gravities from 1 to 500G and produced final formation times on the order of 100 msec for the largest of the 1G tests and less than 4msec for the 500G tests.

An ultra high speed framing camera has now been used to obtain very early time explosion crater growth in water. Framing rates up to 1.4 million pictures/sec provided interframe times on the order of source relaxation times. However, no definitive observation of early-time growth has been observed for the types of sources tested to date. Higher-velocity impacts should extend the duration of the early time regime and will be pursued next. The complete growth curve for crater volume is shown below. Comparable curves for crater depth and radius also show power-law growth. Both are in good agreement with the expected value of the exponent equal to $\mu/3(1+\mu)$.

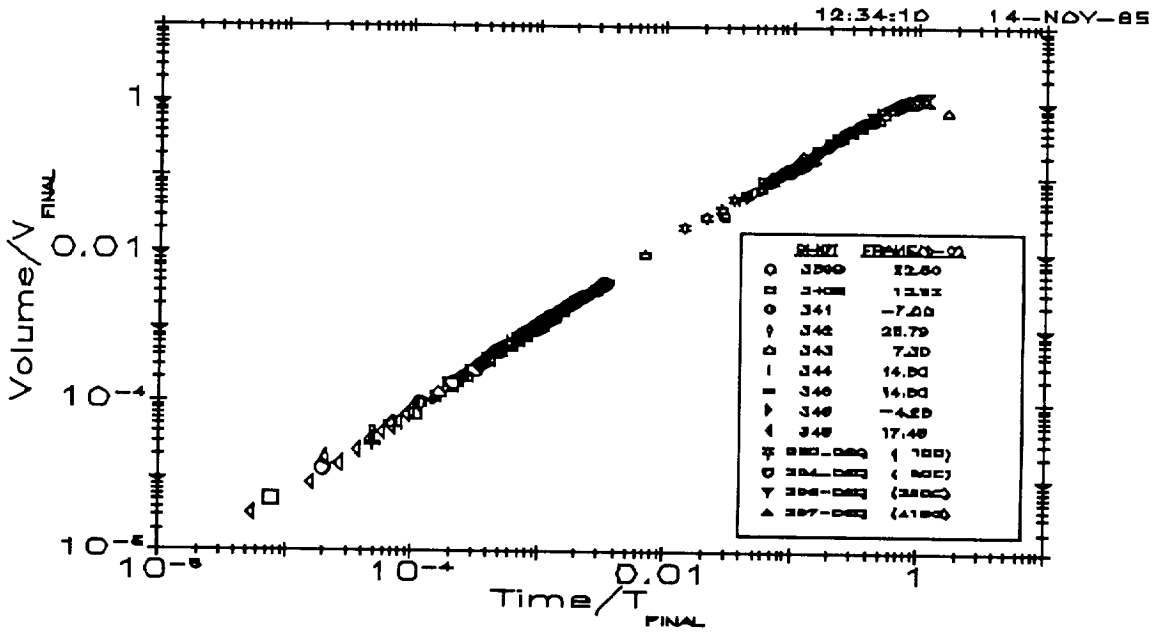

Other ongoing data analysis of high-G experiments in saturated sand also are in good agreement with the appropriate power-law growth behavior as was seen for the water experiments above.[12,14] Detailed examination[16,17] of previous data for explosions in dry sand obtained by Piekutowski[8] and more recent impact data in both dry and wet sand obtained at Ames by Schmidt and Piekutowski[13] indicates that these data have many of the same growth features also. While there are still individual details that are not completly understood, it appears that the radius follows the expected growth rule in most of the shots. However, especially for the dry Flintshot sand, the depth has already "flattened out" by the earliest times observed (200-600μsec). We suspect that the effects of gravity occur earlier in time for depth than for radius, since the latter is at zero depth. The volume, which depends more strongly on the radius tends to be in resonable agreement with the expected power-law behavior. Another explanation now being examined is that the effective origin of the flow field does not coincide with the center of the explosive charge, but seems to be at the bottom of the charge as observed by Piekutowski.[8] For the impact experiments, it very clearly depends upon the impact conditions and for the lower velocities into water the effective origin was on the order of 10 diameters below the surface.

These experiments to record dynamic data for crater growth provide a very detailed and critical test of a complete and unified scaling theory for impact cratering. They provide very important information that is required to apply and extend the scaling to planetary problems currently under investigation by the technical community.

1) Bjorkman, M. D. (1984) Feasibility of determing impact conditions from total melt volume (abstract). In *Lunar Planteary Science XV*, 64-65.

2) Holsapple, K. A. (1984) On crater dynamics: Comparisons of results for different target and impactor conditions (abstract). In *Lunar Planetary Science XV*, 367-368.

3) Holsapple, K. A. and K. R. Housen (1985) Cratering estimates for rock and ice (abstract). *Lunar Plant. Sci. XVI*, Houston.

4) Holsapple, K. A. and K. R. Housen (1985) Scaling of catastrophic impacts. *Memoirs of Italian Astronomical Society* (in press).

5) Holsapple, K. A. and R. M. Schmidt (1985) Point-source solutions and coupling parameters in cratering mechanics. Submitted for publication to *J. Geophys. Res.*

6) Housen, K. R. (1984) Cratering flow fields: A general form and the Z-model (abstract). In *Lunar Plantary Science XV*, 377-378.

7) Housen, K. R., R. M. Schmidt, and K. A. Holsapple (1983) Crater ejecta scaling laws: Fundamental forms based upon dimensional analysis. *J. Geophys. Res.* **88**(B3), 2485-2499.

8) Piekutowski,A. J.(1980) Formation of bowl-shaped craters. *Proc. Lunar Sci. Conf. 11th*, 2129-2144.

9) Schmidt, R. M. (1981) Scaling crater time of formation (abstract). *EOS (Trans. Amer. Geophys. Union)*, **62**, 944.

10) Schmidt, R. M. (1983) Strength-gravity transition for impact craters in wet sand(abstract). In *Lunar Planetary Science XIV*, 666-667.

11) Schmidt, R. M. (1983) Centrifuge quarter-space cratering results: A gravity criterion for kinematic similarity (abstract). *EOS (Trans. Amer. Geophys. Union)*, **64**,747.

12) Schmidt, R. M. (1984) Transient crater motions: Saturated sand centrifuge experiments (abstract). In *Lunar Planetary Science XV*, 722-723.

13) Schmidt, R. M. and A. J. Piekutowski (1982) Quarter-space impact experiments: Particle-motion and crater-growth measurements (abstract). *EOS (Trans. Amer. Geophys. Union)*, **63**, 1020.

14) Schmidt, R. M. and A. J. Piekutowski (1983) Development of the quarter-space technique for cratering experiments on a centrifuge (abstract). In *Lunar Plantary Science XIV*, 668-669.

15) Schmidt, R. M. and K. A. Holsapple (1984) Explosively generated water waves (abstract). *EOS (Trans. Amer. Geophys. Union)* **65**, 221.

16) Schmidt, R. M., K. R. Housen, M. Luke, and A. J. Piekutowski (1984) Scaling consistency tests for cratering experiments (abstract). *EOS (Trans. Amer. Geophys. Union)* **65**, 983.

17) Schmidt, R. M., K. R. Housen, and A. J. Piekutowski (1985) Experimental observations on crater growth regimes (abstract). *EOS (Trans. Amer. Geophys. Union)* **66**, 296.

18) Schmidt, R. M., K. R. Housen, and V. T. Webbeking (1985) Growth of water cavities over a range of 10^6 in time (abstract). *EOS (Trans. Amer. Geophys. U.)* **66**.

THE EFFECT OF PROJECTILE SHAPE ON CRATERING EFFICIENCY AND CRATER PROFILE IN GRANULAR TARGETS.

P.H. Schultz, Dept. of Geological Sciences, Brown University, Providence, RI 02912 and D.E. Gault, Murphys Center of Planetology, Box 833, Murphys, CA 95247.

INTRODUCTION: Recent studies (1,2) have shown that projectile deformation significantly modifies both cratering efficienty and crater profile for impacts into granular targets. In order to better understand the variables controlling these observed changes, we performed a series of impact experiments using 0.635 cm-diameter aluminum cylinders with 4:1, 2:1, and 1:2 aspect ratios (diameter:length). Both No. 24 sand and compacted pumice targets were used under low atmospheric pressures (< 0.1 mb) with impact velocities ranging form 0.4 km/s to 2.1 km/s. The experiments were performed at the NASA-Ames Vertical Gun Range, a national facility operated through the Planetary Geology and Geophysics Program.

RESULTS: Figure 1 shows the effect of projectile shape on the displaced-mass ratio as a function of kinetic energy (KE). The PI_2 dimensionless scaling parameter described in (3) is not used here in order to examine potential physical processes potentially hidden in dimensionless scaling relations. Aluminum cylinders with large aspect ratios displace more relative mass than cylinders with small aspect ratios for the same KE. Wafer-shaped projectiles (aspect ratios of 4:1 and 2:1) form similar slopes in this representation but are vertically displaced according to the aspect ratio. Rod-shaped projectiles (aspect ratios of 1:2) produce a slightly lower slope but insufficient data exist to draw meaningful conclusions. If these data are compared with data for 0.3175 cm aluminum spheres (0.2 km/s to 7 km/s), the relation between KE and displaced mass ratio is matched only for impacts at velocities >1.7 km/s. Thus, previously observed changes in the scaling relations (1,2) can be understood if the spheres had deformed during impact to larger aspect ratios. Such deformation is observed in recovered projectiles for impact velocities greater than about 1.7 km/s.

The effect of projectile shape and deformation on crater shape is shown in Figure 2. Figure 2a illustrates the change in crater diameter and Figure 2b, the change in crater depth. For aluminum spheres, crater diameter has a break-in-slope at a KE corresponding to a velocity of ~1.7 km/s where projectile deformation becomes significant. Figure 2b shows that crater depth is relatively unaffected over this transition, although there is marginal evidence for a slight decrease in depth for velocities above 1.7 km/s. As a result, the crater aspect ratio changes with kinetic energy (velocity since mass is constant). Crater depth for relatively undeformed projectiles is remarkably similar for all aspect ratios although large aspect ratios systematically result in slightly shallower depths. Crater depth for relatively undeformed aluminum wafers with a 2:1 aspect ratio increases with a slope steeper than the average slope of aluminum spheres over the entire velocity range from 0.2 to 7 km/s (log-log plot). However, wafers exhibiting significant deformation resulted in a pronounced decrease in depth. In summary, these experiments further document the importance of projectile deformation on crater scaling relations. The primary effects of deformation are increase in crater diameter, decrease in crater depth, and increase in cratering efficiency. Future experiments will separate additional variables such as projectile/target strengths and projectile size in order to evaluate further the implications for planetary-scale events.

References: (1) Schultz, P.H. and Gault, D.E. (1984) *Lunar and Planetary Science XV*, 730-731; (2) Schultz, P.H. and Gault, D.E. (1985) *J. Geophys. Res.* (in press); (3) Schmidt, R.M. and Holsapple, K.A. (1980) *J. Geophys. Res. 85*, 235-252.

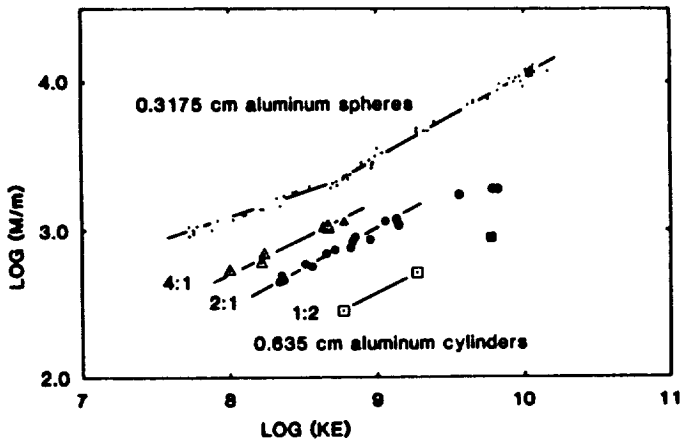

Figure 1. Relation between displaced target mass (M) relative to projectile mass (m) and kinetic energy for aluminum spheres and cylinders with different aspect ratios (diameter:length). Change in scaling relation for aluminum spheres coincides with projectile deformation. Aluminum cylinders exhibit slopes similar to deformed aluminum projectiles. Filled symbols indicate impacts with velocities $\geq$ 1 km/s.

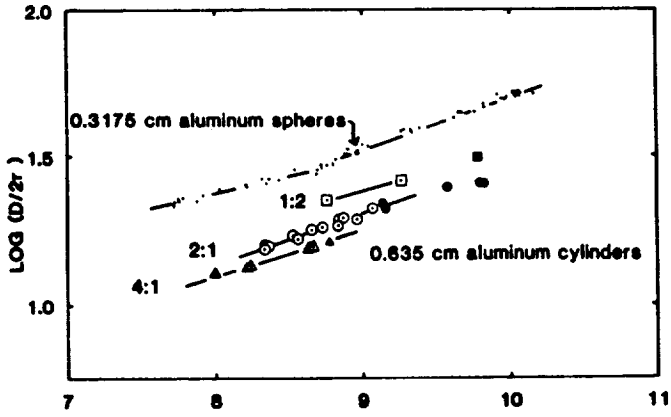

Figure 2a. Change in crater diameter (D) relative projectile diameter (2r) with kinetic energy. Crate diameter increases for velocities sufficiently high to deform projectiles. Aluminum wafers appear to simulate this trend.

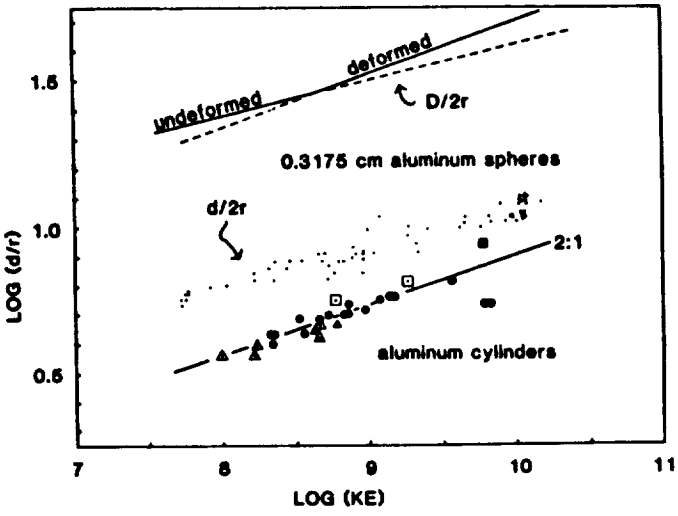

Figure 2b. Change in crater depth (d) relative to projectile diameter (2r) with kinetic energy. Alum spheres exhibit no significant change within limits data. Aluminum cylinders increase in depth mor rapidly until deformation occurs (filled symbols).

Research activities in grant period '84-'85:
NASA GRANT: NAGW-439
Alex Woronow, University of Houston
Houston, TX 77004

Among the basic tools available to students of planetary geology and the evolution of planetary surfaces, "crater statistics" comprises one of the the most powerful. Because meteorite impacts occur on the surfaces at more or less random locations and with statistically defined (but largely unknown) size distributions called the "production functions," they potentially represent a landform with known properties that can be altered by its environment. Craters may be destroyed by geologic processes such as filling by lava or dust, thereby recording geologic conditions and events, or, unfortunately, be obliterated by subsequent impacts. The modification of the production function by subsequent impacts greatly complicates interpretative models of geologic histories. If the production functions were well established, then the effects of subsequent overlaps could be removed to leave the signatures of the other geologic processes open for evaluation. Unfortunately, in some cases the crater densities have become so high that more craters have been obliterated by crater-crater overlap than are currently visible on the surface.

Several means have been proposed, and applied, to recover the production function so that the geologic history can be deconvolved from the statistical evolution of the crater population. We have modeled and evaluated the reliability of two of these means: the use of crater degradation classes to peel back layers of time, and the use of partial-crater statistics to statistically reconstruct the production function. The former technique is founded on the premise that subsequently older craters are proportionally more degraded in appearance. We have shown that, unfortunately, a size bias enters in to such a degree that all such studies must fail. Because this method has been repeatedly used, one must now re-assess the concepts derived by those means. A prime example is the widely accepted period of aeolian obliteration of landforms on Mars, which was deduced fully from crater-class analyses.

The latter technique is potentially useful. However, we

found that it requires accuracy and completeness in crater measurements that are undoubtedly beyond feasibility. We therefore conclude that simulations of crater production and obliteration that target the observed statistics offer the only currently well known means of evaluating the evolution of cratered surfaces.

However, we have also been evaluating the use of the areal distribution of craters to constrain the general form of the crater production function for Callisto, and to establish the plausibility of crater relaxation as a major geologic process there. This is a new technique, that has unexplored potential, but provides a totally independent approach that may serve well to verify the straight-out simulation approach.

Another direction of study involves simulating the lunar mega-regolith. A new Monte Carlo model for this is producing results significantly different from earlier, less complete and complex, models. The improvements appear to come from the encorporation of an evolving topography into the model. Our model is now matching what is known about the lunar subsurface stratigraphy quite nicely to layers of varying comminution. The conclusions drawn by the seismologist about the subsurface state seem more in concert with reality than those conclusions implied by earlier impact-based models.

Finally, we are examining the difficulties in evaluating "closed data." Data are termed "closed" when they are constrained to sum to a constant. A prime example of the use of closed data in planetary geology is in the evaluation of crater classes--either degradation classes or classes tagging the presence/absence or degree of development of some feature (e.g. no central peak, central peak, central ring, multiple central rings). For these type of data, an increase in the abundance of one class necessitates the decrease in at least one other, and the evaluation of correlations and trends is no longer possible by standard techniques although that is the approach normally taken. Through techniques recently developed in theoretical statistics, we have constructed computer codes to do the statistical evaluations correctly. Those programs will be applied to problems of crater classifications.

CHAPTER 6

AEOLIAN PROCESSES AND LANDFORMS

ON THE RATE OF FORMATION OF SEDIMENTARY DEBRIS ON MARS

Raymond E. Arvidson, McDonnell for the Space Sciences, Department of Earth and Planetary Sciences, Washington University, St. Louis, MO 63130

We now have enough information to place rather meaningful constraints on the current rates of aeolian redistribution of fine grained debris on Mars. For example, from the three years of Viking Lander 1 observations, typical values of sediment redistribution are micrometers per year, although centimeters of loose, disturbed material were removed during a brief interval in the third year (1). Rates of erosion of rocks were too small to be observed, either by tracking changes in morphologies or by tracking changes in rock photometric properties. Consideration of the large number of pristine-looking, small bowl-shaped craters at the Lander 1 site suggests a rate of rock breakdown and removal of only meters over the lifetime of the surface. Thus, averaged over the lifetime of the Chryse Plains, rock breakdown and removal has been meters per billions of years, orders of magnitude lower than the micrometers per year for soils (2). Most of the equatorial regions of Mars likewise preserves ancient surfaces, with craters even at small sizes seemingly in production. Thus, rock breakdown and removal over the equatorial terrains has been quite small for much of geological time. Even the fretted terrains have probably been inactive for a long while, considering that the crater abundances in much of fretted terrain are second in abundance only to the cratered terrains (3). The younger fretted areas seem to be embayed by younger deposits (4) or to be in areas of relatively recent tectonic activity, such as the chaotic terrains. By areal extent, most of the equatorial terrains of Mars have been subjected to very low erosion rates, significantly less than the debris redistribution rates witnessed by Viking Lander 1. Thus, as noted by (2), differential aeolian erosion on Mars is a major geological process, with debris deposits accumulating and eroding to depths of hundreds of meters over geological time, while rock breakdown has been occurring in most regions at vanishingly small rates. Given the low rates of production of new debris, one is forced to conclude that Mars has had a decidedly non-linear history of debris production. In particular, most sedimentary debris must have been produced relatively early, perhaps in the first billion years of geological time. Impact cratering, production of volcanic ash, and chemical corrosion may all have been important debris-forming processes. Given that the mineralogy of martian debris has apparently not come into equilibrium with the present ambient conditions (5), we may have some chance of deciphering the relative importance of various debris forming processes. For example, if analyses of Mars Observer Imaging Spectrometer data show a dominance of palagonitic materials, then early volcanism would be indicated.

REFERENCES

1. Arvidson, R. and others, 1983, Science, v.222, p.463-468.
2. Arvidson, R. and others, 1979, Nature, v.278, p.533-535.
3. Coradini, M. and R. Arvidson, 1976, Proceed., Int. Colloq. Planetary Geology, Geol. Romana, v.15, p.377-381.
4. Frey, H. and A. Seneniuk, 1985, Geol. Soc. Am., Abstracts, p.586.
5. Gooding, J., 1978, Icarus, v.33, p.483-513.

THE RELATIVE RATES OF AEOLIAN AND TECTONIC PROCESSES ON VENUS AND MARS

Raymond E. Arvidson and Ralph Kahn, McDonnell Center for the Space Sciences, Department of Earth and Planetary Sciences, Washington University, St. Louis, MO 63130

INTRODUCTION: Our growing knowledge of Venus surface conditions permits an assessment of the relative importance of aeolian and tectonic processes for shaping landforms. In this paper we consider Earth-based, Pioneer Venus, and Venera radar data, Venera Lander observations, and comparisons with Mars, to place constraints on the relative efficacy of these mechanisms on Venus. We also discuss results in light of the higher spatial resolution radar images to be returned by the Venus Radar Mapper in 1988.

GLOBAL-SCALE CONSTRAINTS ON CONSTRUCTION AND EROSION: Pioneer Venus and Arecibo data covering the Beta Regio area show relatively pristine landforms associated with rifting and volcanism. The region is part of a broad topographic swell, with rift valleys at the swell crest, and conical constructs that are probably volcanoes (1,2). Venera radar observations that reveal much of the northern hemisphere contains a wide variety of landforms, also indicative of active volcanism and tectonism (3). Impact craters are rare, and evidence for other exogenic erosional processes is absent in the images that we have examined. Generally there is a positive correlation between radar roughness and both elevation and slope on Venus (4). This correlation implies that surfaces associated with local volcanic and tectonic processes have not been significantly reworked by aeolian activity or by other exogenic processes that would tend to homogenize surface properties.

By comparison, Mariner 9 and Viking Orbiter images of Mars also show surfaces that appear to be dominantly of volcanic and tectonic origin. However, impact crater densities are quite variable, and indicate that most surface features seen from an orbital perspective have been retained for hundreds of millions to billions of years (5). In many locations, the morphologies of landforms have been modified by surficial processes, including wind erosion, fluvial phenomena, and perhaps periglacial activity (6). Wind is the most widespread exogenic process, forming polar deposits, thin mantles or scoured regions extending downwind of topographic obstacles, dunes, and areas that have been deflated, leaving behind pitted terrains, pedestal craters, and yardangs. Lateral redistribution of material probably also accounts for the general lack of correlation between radar reflectivity, roughness, and landform type on Mars, and can be used to explain the similarity in major element chemistry at the two Viking Lander sites, located on opposite sides of the planet (7). The principal aeolian deposits and deflated areas on Mars can even be identified at several kilometers resolution in Mariner 9 images (8). In contrast, evidence implying that aeolian erosion has played a discernible role in landform evolution on Venus is not found at roughly equivalent length scales in the Venera radar data.

LOCAL OBSERVATIONS: The Venera Landers are located on the eastern flank of Beta Regio, with more than a thousand kilometers between landing sites. Despite the large separation, the sites are quite similar at the decimeter to meter scales seen by the Lander cameras, exhibiting platy, often polygonally fractured rock, with cloddy structures (9,10). Dark soil is observed covering parts of the slabby bedrock, and sometimes filling space between discrete blocks. The areal extent of the soil varies from region to region, but even at the Venera 13 site, where it is most abundant, the fines appear to be much less widespread than those observed by the Viking Landers on Mars. The settling time of dust clouds raised upon impact of the Veneral Landers and the Pioneer-Venus Day Probe indicate soil particle sizes of 20 to 60 micrometers, although particles between a few and a few hundred micrometers may have participated (11). With the higher resolution Venera 13 and 14 data, streaks of dark soil, possible scour zones, and what may be a rippled slab can be seen. In general, the sites do not appear to be pristine depositional surfaces. The uneven, fractured bedrock, and the presence of soils, suggest erosion, transport, and desposition. However, indications of the action of these processes are not as pervasive as they are at the Viking Lander sites on Mars, and unlike Mars, there is no evidence for chemical homogenization of material among the Venera Lander locations.

CONSTRAINTS ON CURRENT AEOLIAN ACTIVITY: Measurements of the near-surface wind speed at the Venera 9 and 10 sites range from 0.4 to 1.3 m/s, while tracking of the Pioneer entry probes yields speeds of less than 2 m/s (12,13). These values are well within the threshold free stream velocity required to set grains of about 100 micrometers in diameter into motion, according to wind tunnel experiments performed under simulated Venusian conditions (14,15). The simulations reproduced the atmospheric density, but at room temperature, with a CO2 pressure of about 30 bars.

Except at impact, when the Venera Landers produced shear stress at the surface estimated to be equivalent to a free stream wind speed of about 8 m/s (16), there is no unequivocal evidence for stress-induced particle motion that occurred during the Lander observations. The apparent clarity of the near-surface atmosphere, as observed in the Venera Lander images, implies that the threshold for lifting particles is not exceeded on a continuing basis in this region, in spite of the presence of fine-grained material. A likely possibility is that particle cohesion, which was a small effect for the wind tunnel simulations, plays a more important role under actual Venus conditions. In summary, the very limited data set currently available contains no indication that aeolian processes are as active on Venus today as might be suspected on theoretical grounds. However, fine material is present, and it seems probable that at least some transport has taken place.

CONCLUSIONS: In contrast to Mars, available data suggest that surficial phenomena alter only decimeter to meter scale landforms on Venus, and probably only on a localized basis. Vigorous aeolian activity, currently found on Mars, is not required on Venus by existing data. This observation implies that, relative to tectonic and volcanic activity,

landform modification by exogenic processes occurs more slowly on Venus than on Mars. The Venus Radar Mapper may provide diagnostic information needed to calibrate the extent to which landforms have been modified by exogenic processes, since the VRM resolution will be a factor of 3 higher than the Venera radar measurements. That increase in resolution may, for example, provide key observations of landforms that have been modified by wind action over length scales of hundreds of meters.

REFERENCES:

1. Masursky et al. (1980) J.G.R., 85, 8232-8260
2. Campbell et al. (1984) LPSC 15th, 123-124
3. Soviet Oral Presentation, LPSC 15th
4. Pettengill et al. (1980) J.G.R., 85, 8261-8270
5. Mutch et al. (1976) The Geology of Mars
6. Carr (1981) The Surface of Mars
7. Baird et al. (1981) Icarus, 45, 113-123
8. McCauley et al. (1973) J.G.R., 78, 4123-4137
9. Selivanov et al. (1983) Cosmic Res., 122-129
10. Garvin et al. (1984) J.G.R., 89, 3381-3399
11. Garvin (1984) LPSC 15th, 286-287
12. McGill et al. (1983) in Venus, Arizona Press, 69-130
13. Kerzhanovich, V., and M. Marov (1983) in Venus, Arizona Press, 766-778
14. Greeley et al. (1984) Icarus 57, 112-124
15. Greeley et al. (1984) Icarus 60, 152-160
16. Garvin (1981) Proc. Lunar Planet. Sci. 12B, 1493-1505.

REGIONAL DUST DEPOSITS ON MARS: ORIGIN, AGE, AND GEOLOGIC HISTORY

P.R. Christensen, Department of Geology, Arizona State University, Tempe, Arizona 85287

Major dust storms on Mars play an important role in the deposition and removal of fine dust material. Thermal, radar, and visual remote sensing observations provide important constraints on the martian regolith which have been used to determine the location and physical properties of regional dust deposits (Christensen, 1985). These deposits are located in three northern equatorial regions, Tharsis (-20°S to 50°N, 60° to 190°W), Arabia (-5°S to 30°N, 300° to 360°W), and Elysium (10° to 30°N, 210° to 225°W). They are covered by fine (~2-40 μm), bright (albedo > 0.27) particles, with fewer exposed rocks and coarse deposits than found elsewhere. Dust is currently deposited uniformly throughout the equatorial region at a rate of ~40 μm/global storm as determined from the total dust loading observed in the 1977 global storm (Pollack et al., 1979). Over geologic time the rate of accumulation may vary from 0 to 250 μm/year due to changes in atmospheric conditions produced by orbital variations (Ward, 1974). These estimates are based on the fact that for very low atmospheric density no dust may be moved, while at high atmospheric density dust storms may be continuously generated. At present, however, there appears to be a decay phase of several months between major storms, so that even at peak dust activity, only 10 storms may be generated each year.

Dust storm fallout is subsequently removed from dark regions following global storms as evidenced by: 1) higher dust content over dark regions during clear periods, 2) post-storm darkening of dark regions, 3) removal of dust at the Viking Lander 1 site, and 4) the historical persistence of classic dark features. Non-removal of dust from low-I, bright regions results in a net accumulation of dust in these areas. The thickness of these current dust deposits is 0.1 to 2 meters. The thermal inertia places a lower limit of ~0.1 m on the thickness of these deposits, while the sparse but ubiquitous presence of exposed rocks and the degree of visible mantling indicate that the thickness is less than 5 meters. Dual-polarization radar observations of a very rough texture in Tharsis (Harmon et al., 1980) are consistent with this model, with a ~2 m thick dust layer burying most of the surface rocks but permitting radar sampling of the rough sub-surface.

Based on their thickness and rate of accumulation, the age of these deposits is 10^5-10^6 years, suggesting a cyclic process of deposition and removal. One possible cause may be cyclic variations in the magnitude and location of maximum wind velocities related to variations in Mars' orbit. At present, perihelion and maximum wind velocities occur in the south whereas regional dust deposits occur in the north, suggesting net transport from south to north. Orbital parameters oscillate with periods ranging from 5×10^4 to 10^6 years. The agreement between these periods and the dust deposit age suggests a possible link. At different stages in orbit evolution, maximum wind velocities will occur in the north, with subsequent erosion and redistribution of the accumulated fines.

Several mechanisms exist for the subsequent erosion of the regional dust deposits. Perhaps the most effective may be "dust-devil" activity. There is some observational evidence for vortices at the Viking Lander sites which produced a factor of 2 to 3 enhancement in wind velocities (Ryan and Lucich, 1983). Because vortices form due to convection in an atmosphere with a superadiabatic lapse rate, they should be more common during periods of maximum solar heating. Thus, this process will be most effective over low inertia regions at times of perihelion summer. This is exactly the time when the regional dust deposits may be eroded.

The presence and history of regional dust deposits on Mars provide some direct evidence for cyclic processes of deposition outside the polar regions. They therefore support models of cyclic variations in martian climate over geologic time. In addition, the occurrence of these deposits and the model for their evolution suggest that the upper few meters over much of the martian surface is young and is being continually reworked.

REFERENCES

1. Christensen, P.R., 1985, Regional dust deposits on Mars: Physical properties, age, and history, submitted to J. Geophys. Res.
2. Harmon, J.K., D.B. Campbell, and S.J. Ostro, 1982, Dual-polarization radar observations of Mars: Tharsis and environs, Icarus, 52, 171-187.
3. Pollack, J.B., D.S. Colburn, F.M. Flasar, R. Kahn, C.E. Carlston, and D. Pidek, 1979, Properties and effects of dust particles suspended in the martian atmosphere, J. Geophys. Res., 84, 2929-2945.
4. Ryan, J.A. and R.D. Lucich, 1983, Possible dust devils, vortices on Mars, J. Geophys, Res., 88, 11,005-11,011.
5. Ward, W.R., 1974, Climatic variations on Mars 1. Astronomical theory of insolation, J. Geophys. Res., 79, 3375-3386.

MARTIAN DUST PARTICLES AS CONDENSATION NUCLEI. J. L. Gooding, Planetary Materials Branch, NASA/Johnson Space Center, Houston, TX 77058 USA.

Introduction. On Earth, the naturally occurring low degrees of atmospheric water-vapor supersaturation cannot support homogeneous nucleation so that condensation of water, either as liquid droplets or as ice crystals, occurs primarily by heterogeneous nucleation on dust [1,2]. Therefore, at a given temperature and degree of supersaturation, prospects for condensation depend to a large extent on the nature of available dust particles.

Condensation of water on Mars should also proceed by heterogeneous nucleation on dust particles although three additional considerations might apply. First, liquid water is, at best, metastable in the surface/atmosphere environment [3] and both the abundances and apparent degrees of saturation of water vapor in the atmosphere are consistent with ice, rather than liquid water, as the long-term, condensed-phase buffer [3,4]. Second, the very low temperatures and the expected dominance of vapor/solid transitions might favor formation of H_2O-Ic on Mars whereas H_2O-Ih is the common polymorph of water ice on Earth [2,5]. Third, the major gas in the Martian atmosphere, CO_2, is also condensible as a frost, as is $CO_2 \cdot 5.75\ H_2O$ and possibly other clathrate hydrates. Identification of minerals among atmospheric and surface dusts and determination of their effects on condensate formation comprises an important interdisciplinary problem for geology and meteorology.

Heterogeneous Nucleation. As summarized elsewhere [1,2], the intrinsic properties that determine the favorability of a given substrate in heterogeneous nucleation of a condensate are (1) degree of misfit, or disregistry, between the crystal structures of the substrate and condensate, (2) similarity or compatibility of the substrate with the condensate in terms of chemical bonds between their respective atoms or ions, and (3) abundance of submicroscopic defects (steps, dislocations, cracks, cavities, or chemical inhomogeneities) in the substrate that would be "active" sites of assembly for clusters of condensate atoms or molecules. A fourth factor, insolubility of the substrate, applies when the condensate is water. With respect to nucleation of ice, the three available modes of condensation are freezing, contact, and deposition. The freezing mode applies to cooling of a wet substrate whereas the contact mode involves freezing upon collision of a foreign nucleus with an undercooled liquid droplet. In the deposition mode, water vapor is adsorbed onto the substrate and freezes as ice upon further cooling.

Cloud-chamber experiments, that probably involved condensation by a combination of the deposition and contact modes, have shown that ice-nucleation abilities vary substantially among minerals [1]. At least for clay minerals, the dependence of ice nucleation on substrate mineralogy has also been demonstrated for freezing-mode conditions by low-temperature differential thermal analysis and scanning calorimetry [6,7] and some of those results have been applied to conceptual studies of ice formation in the Martian regolith [8,9]. However, the overall role of mineral particles in condensate formation on Mars has not been throughly treated.

New Data from Differential Scanning Calorimetry (DSC). Using methods that were described in detail elsewhere [10,11], DSC was used to determine the systematics of freezing and thawing of water in wet geologic substrates, including minerals and mineraloids that were not included in earlier, similar studies. For all other conditions being constant, the variation of ice-nucleation threshold temperature, T_{in}, and other measurable properties

were determined as a function of substrate mineralogy. Systematic correlations among the variables were sought as an aid to ranking candidate Martian minerals according to relative effectiveness as water-ice nucleators and, by analogy, as nucleators of other Martian condensates.

Condensate/Substrate Disregistry Calculations. Among the three principal attributes that control the effectiveness of heterogeneous nucleators, disregistry is the parameter that is most easily quantified through direct calculation. Consequently, disregistry was selected as the main model parameter in physical interpretation of DSC data. For a given substrate plane, disregistry, , between the substrate structure and the condensate structure was defined as

$$\delta = [k_c (d_{s,x} + d_{s,y})/2\, k_s a_c] - 1 \qquad [1]$$

where $d_{s,x}$ and $d_{s,y}$ are the substrate unit-cell dimensions in the arbitrarily assigned x- and y-directions, a_c is the unit-cell dimension of the matching condensate plane, and k_c and k_s are integers that can be used to define "supercells" of the condensate or substrate structures, respectively. Using Eqn. [1], which is patterned after the definition given by Pruppacher and Klett [2], and crystallographic data from the literature, disregistry calculations were made for attempted matches of candidate condensates (hexagonal and isometric H_2O ices, solid CO_2, and CO_2 hydrate) with each other and with selected mineral substrates. For each condensate/substrate pair, computations proceeded by holding either k_c or k_s constant and varying the other until a minimum was found in the absolute value of disregistry, $/\delta/$. Similar calculations were performed for condensates as substrates (e.g., condensation of CO_2 on H_2O-Ic or H_2O-Ih).

Preliminary Conclusions About Mineralogically Controlled Condensation on Mars. New DSC data confirmed previous evidence for systematic variations in ice-nucleation temperatures among geologic materials. Both DSC data and cloud-chamber (literature) data indicate that T_{in} varies inversely with minimum absolute value of disregistry, $/\delta/$ (Fig. 1). Although much scatter exists in the data, more coherent inverse trends emerge when individual structural groups of minerals are considered as separate cases (e.g., tectosilicates vs. phyllosilicates). Therefore, $/\delta/$ values appear to be useful first-order indicators of the relative effectiveness for ice nucleation among geologic substrates (Fig. 2).

Phase H_2O-Ic offers the lowest overall $/\delta/$ values for heterogeneous nucleation of other condensates, including H_2O-Ih, solid CO_2, and CO_2 hydrate, suggesting that the best overall mineral nuclei might be those that most effectively nucleate H_2O-Ic. Based on $/\delta/$ values, good nucleators of H_2O-Ic should include non-expandable clay minerals (e.g., kaolinite, chlorite), certain zeolites (e.g., clinoptilolite), goethite, and bassanite (Fig. 2). Although goethite might preferentially nucleate H_2O-Ic, hematite should preferentially nucleate H_2O-Ih. Cryptocrystalline mineraloids (e.g., palagonite) should be generally poor nucleators and nucleating abilities of expandable clay minerals (e.g., nontronite, montmorillonite) should vary significantly with degree of c-axis expansion, as controlled by degree of interlayer hydration.

More DSC experiments are needed to test these preliminary inferences. In addition, direct determination of the mineralogy of Martian dust units of various ages is needed in order to better assess the role of heterogeneous condensation as a process that might have significantly influenced the migration and storage of volatiles throughout Martian geologic history.

References: [1] Mason B. J. (1971) The Physics of Clouds (second ed.), Clarendon, 671 pp. [2] Pruppacher H. R. and J. D. Klett (1978) Microphysics of Clouds and Precipitation, Reidel, 714 pp. [3] Farmer C. B. (1976) Icarus, 28, 279. [4] Davies D. W. (1979) J. Geophys. Res., 84, 8335-8340. [5] Shumskii P. A. (1964) Principles of Structural Glaciology (D. Kraus, transl.), Dover. [6] Anderson D. M. (1968) Israel J. Chem., 6, 349. [7] Anderson D. M. and Tice A. R. (1971) Soil Sci. Soc. Amer. Proc., 35, 47. [8] Anderson D. M., Gaffney E. F., and Low P. F. (1967) Science, 155, 319. [9] Anderson D. M., Schwarz M. J., and Tice A. R. (1978) Icarus, 34, 638. [10] Gooding J. L. (1985) In Workshop on Water on Mars (S. Clifford, ed.), LPI Tech. Rept. 85-03, Houston, 29. [11] Gooding J. L. (1985) Icarus, submitted.

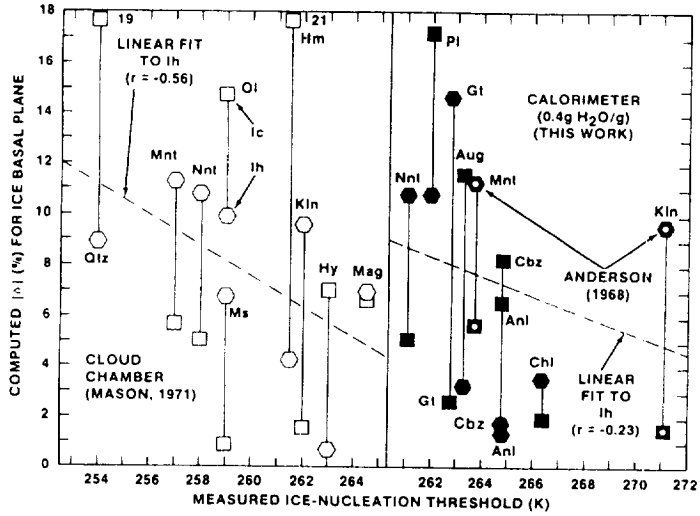

Figure 1.

Variation of computed, minimum absolute values of crystallographic disregistry with measured ice-nucleation temperatures, T_{in}, of various minerals relative to the basal planes of the Ih (hexagon symbol) and Ic (square symbol) polymorphs of water ice. Although the relationship between $/\delta/$ and T_{in} is not necessarily expected to be linear, the inverse covariations revealed by the linear fits agree qualitatively with the intuitive expectation that T_{in} should increase as $/\delta/$ decreases. Note that stronger covariations of $/\delta/$ with T_{in} can be found by dividing the minerals into major groups of common bond type (e.g., phyllosilicates, non-phyllosilicates, Fe-oxides) that more closely isolate the bonding and active-site parameters.

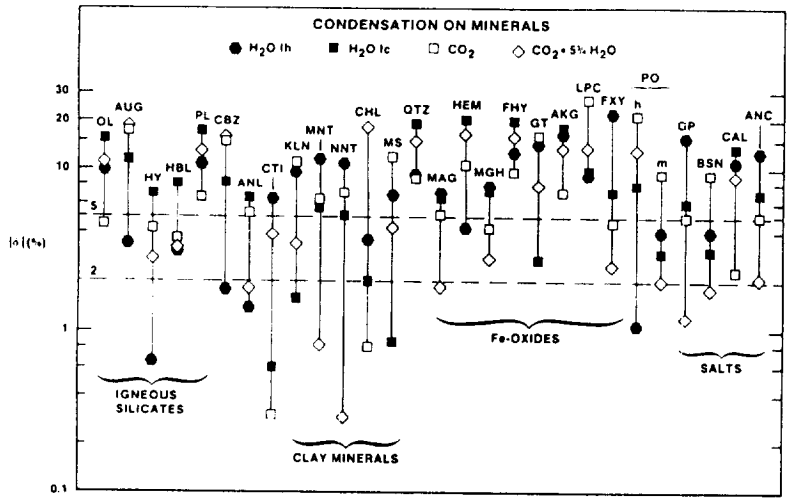

Figure 2.

Minimum absolute values of crystallographic disregistry computed for each of four condensates on individual minerals. Based on the known effectiveness of β-AgI as a water-ice nucleator, and its calculated disregistry values (relative to condensate basal forms) of + 1.8% for H_2O-Ih and of - 4.9% for H_2O-Ic, computed values of $/\delta/ < 2-5\%$ are taken to be indicative of comparably favorable substrates for heterogeneous nucleation of Martian condensates. Values depicted for montmorillonite (Mnt) and nontronite (Nnt) are those that apply to c-axis expansions of 15 Å. (Values of $/\delta/$ vary significantly with the c-axis dimensions of expandable clay minerals).

DUST STORMS ON MARS: MECHANISMS FOR DUST-RAISING

Ronald Greeley, Department of Geology, Arizona State University, Tempe, Arizona, 85287

"Dust" is generally defined as solid particles 60 μm in diameter carried by the wind in suspension (1,2). Estimates for particle sizes in martian dust storms yield values of <0.2 to >30 μm in diameter (3). Thus, dust storms on both Earth and Mars involve principally silt- and clay-size particles. Estimates of fluid "threshold" wind speeds for particles of this size show that markedly higher winds are required for progressively smaller particles, which is attributed both to aerodynamic effects and to various interparticle forces such as cohesion. However, once threshold is attained, very low winds can keep dust aloft. Because threshold scales inversely with atmospheric density, the winds required to move "dust" on Mars are exceedingly high; for example, minimum winds required to move 10 μm grains exceed the speed of sound (4) and are far higher than winds measured (or expected) on Mars. Thus, mechanisms other than simple fluid threshold have been proposed for raising dust on Mars. These include a) dust fountaining by desorbed CO_2 (5) and H_2O (6,7); b) dust devils (8); c) presence of "triggering" particles (9); and d) "clumping" of fine grains to produce particles of larger, more easily moved sizes (aggregates, chunks of duricrust, etc.). These mechanisms are reviewed and experiments are described to assess their potential for dust-raising on Mars.

Dust-fountaining. Johnson et al. (5) conducted experiments involving 1-10 μm silica particles in a CO_2 atmosphere which was cooled until CO_2 was absorbed into the particles; the system was then heated so that desorption occurred. The surface initially formed a crust which acted as a "barrier," causing buildup of subsurface gas pressure until the crust ruptured; the gas jets injected dust above the surface several cm. The authors suggested that similar processes on Mars could inject very fine particles into the atmosphere where they could be carried aloft by relatively gentle winds.

A similar mechanism could occur involving water; Huguenin et al. (6) suggested that some of the "blue clouds" observed on Mars could be water vapor released to the atmosphere. Exploratory experiments were conducted (7) to study the effects of water vaporization on the movement of dust. Experiments were performed in both a bell jar and in a wind tunnel using a range of particle compositions and sizes (10 to 1000 μm). In bell jar tests, as the atmospheric pressure was reduced below 10 mb (temperature ~24°C) absorbed water vaporized and ejected particles by one of two processes: 1) vent holes and fissures developed in the surface, followed by a fountainlike spray of particles as high as 20 cm above the surface, or 2) violent "eruptions" occurred in a boiling fashion; the smaller the grain size, the more violent the eruption. Some activity increased with depth of particle bed, with 20 cm high fountains occurring for beds 10 cm deep; some activity was also observed in beds as shallow as 1 mm. The amount of absorbed water also affected activity, with ejection occurring with water contents as low as 0.75% by weight. Similar effects were observed in tests conducted in the wind tunnel. However, in some experiments the particle

bed remained stable until a low velocity wind passed over the surface at which time injection was "triggered." Although there is no clear explanation for this effect, the triggering could be related to slight differences in pressure resulting from the wind. In some cases, desorption of water did not eject dust, but caused the surface to crack. Erosion began as the wind picked up crust-like sections of the particles; the wind speed of ~25 m/s was substantially lower than threshold for undisturbed particles. Evidently, the fissures sufficiently roughened the surface to lower the threshold speed.

Dust devils. Dust devils are local cyclonic winds that result from atmospheric instabilities. They have been suggested as a dust-raising mechanism on Mars, an idea enhanced by the recent discovery of possible dust devils in Viking Orbiter images (10). Field studies of dust devils on Earth (11,12) show that a wide range of particle size can be raised even when unidirectional winds are very gentle. Laboratory experiments (13) suggest that the entrainment mechanism for raising particles via dust devils is markedly different than for a uniform wind boundary-layer case. In dust devils, the primary factor may be the difference in pressure between the top and bottom of the particle layer; in cyclonic motion, the size and density of the particles seem to have little importance in threshold and even the very small grains are easily raised.

Presence of "Triggering" particles. Numerous authors have suggested that dust could be entrained by saltation impact of larger (e.g., "sand"), more easily moved grains (7,9,14). In order to assess this mechanism, wind tunnel experiments were run (15) involving basaltic particles (<40 μm) that were impacted by saltating sand grains (120 μm diameter). Although some basaltic "dust" was entrained upon impact by the sand, the effect was minimal. Additional experiments are planned in which the test bed will consist of a mixture of particle sizes.

Dust "clumps". Any means that could increase the effective diameter of dust particles could lower the threshold necessary for entrainment. Aggregation of small particles by electrostatic bonding occurs in dust storms (16) and volcanic eruptions (17) on Earth and has been proposed for Mars (18). Wind tunnel experiments (15) show that threshold winds for aggregates of basaltic silt are ~25% lower than the same non-aggregated silt grains. Even though the aggregates are very fragile and do not survive saltation impact, the "soils" are sufficiently rough that clumps are more easily picked up by the wind. Disrupted crusts developed on deposits of fine grains may also produce clumps that are more easily entrained by low winds. Gillette (19) notes significantly lower threshold values for silt and clay on Earth where crusts on the deposits have been disturbed. For application to Mars, duricrust and "cloddy" soils have been described; disturbance by events such as the slumping in drift deposits at "Big Joe" could provide local surface roughness which would lower the effective threshold wind speed for martian dust.

The four mechanisms described above appear viable for raising of fine (<60 μm) particles on Mars. However, additional testing is required, including: 1) determination of the limits for dust-fountaining on Mars via desorption of volatiles, 2) assessment of dust devils at low atmospheric densities for dust entrainment, 3) threshold experiments using mixed particle sizes under martian conditions, and 4) assessment of the physical properties of various aggregates, clumps, and crusts on Mars.

REFERENCES

(1) Pewe, T.L., 1981, Geol. Soc. Amer. Sp. Pub. 186, 1-10.
(2) Jackson, J.A. and R.L. Bates, 1980, Glossary of Geology, Amer. Geol. Inst., Falls Church.
(3) Gierasch, P.J. and R.M. Goody, 1979, J. Atmos. Sci., 30, 169-179.
(4) Greeley, R. et al., 1980, Geophys. Res. Lett., 7, 121-124.
(5) Johnson, W. et al., 1975, Icarus, 26, 441-443.
(6) Hugnenin, R. et al., 1979, NASA Conf. Pub. 2072, 40.
(7) Greeley, R. and R. Leach, 1979, NASA TM 80339, 304-307.
(8) Neubauer, F.M., 1966, J. Geophys. Res., 71, 2419-2426; Sagan, C. and J.B. Pollack, 1969, Nature, 223, 791-794.
(9) Peterfreund, A.R., 1981, Icarus, 45, 447-467.
(10) Thomas, P. (per comm. 1984).
(11) Carrol, J.J. and J.A. Ryan, 1970, J. Geophys. Res., 75, 5179-5184.
(12) Sinclair, P.C., 1966, Ph.D. dissertation, Univ. Arizona.
(13) Greeley et al., 1981, Geol. Soc. Amer. Sp. Pub. 186, 101-121.
(14) Christensen, P.R., Icarus,
(15) Greeley et al., 1985, this issue.
(16) Kamra, A.K., 1972, J. Geophys. Res., 77, 5856-5869.
(17) Sorem, R.K., 1982, J. Volc. Geotherm. Res., 13, 63-71.
(18) Greeley, R., 1979, J. Geophys. Res., 84, 6248-6254.
(19) Gillette, D.A. et al., 1982, J. Geophys. Res., 87, 9003-9015.
(20) Gillette, D.A., 1976, Amer. Soc. Ag. Eng., paper 76-2018.

DISTRIBUTION OF SEDIMENTARY DEBRIS IN THE SOUTH POLAR REGION OF MARS

E. Guinness, R. Arvidson, R. Kahn, and J. Plaut, McDonnell Center for the Space Sciences, Department of Earth and Planetary Sciences, Washington University, St. Louis, MO 63130.

The location, age, and volume of sedimentary debris provide important constraints on the climate history of Mars. In this abstract we report on an inventory of debris deposits in the south polar region we use to infer depositional and erosional histories (including rates) of this climatically sensitive area. Viking Orbiter images with the best available resolution for this region (typically 150-200 m/pixel) were examined. The location of the permanent ice cap, layered terrain, and older debris units were mapped. The atmosphere in the south polar area is relatively clear in the fall and winter. Thus, morphologic studies are not severely hampered by atmospheric obscuration of the fine-scale surface details during those seasons [1].

The major debris unit, other than layered terrain, corresponds in large part to the etched terrain mapped by [2]. The etch pits suggest that this terrain consists of relatively friable materials, easily eroded by wind. The stratigraphic relationships between one location of etched terrain and surrounding units is shown in Figure 1. The sketch map covers a region centered at about -75 deg latitude and about 90 deg west longitude. This area was mapped as a single unit based on Mariner 9 data [2]. There is a clear topographic boundary along the northern edge of etched terrain. To the south of the boundary, the etched terrain overlies an older smooth plains unit. Further to the north (at the bottom edge of Figure 1) the smooth plains unit overlies densely cratered terrain. To the southwest (not shown in Figure 1) layered terrain overlies etched terrain, and partially covers several pits. The area appears to have experienced separate episodes of deposition, erosion, and further deposition. These secular variations in polar sedimentary geology clearly indicate that climates producing layered deposits have varied over geologic time.

We have attempted to estimate a lower bound on the rate of deposition for the etched terrain. The thickness of the debris was determined by measuring the depth of etch pits, which provide lower limits on the thickness of etched terrain because it is not known whether an individual pit has eroded to the base of the unit. Depths were derived from shadow measurements. Over 70 pit depths were measured, with depths that ranged from less than 100 m to about 1 km. Since these estimates are lower limits, we have taken 1 km as an estimate of the etched terrain's overall debris thickness. The age interval for deposition of the etched terrain unit was constrained by crater density data for the smooth plains and etched terrain units. The crater density for etched terrain was determined for two areas. The crater densities were converted to ages by assuming that Lunae Planum was 3.5 billion years old [3] and by scaling the crater density as determined by [4]. The resulting age estimates for

the two areas are 1.5 and 2.9 billion years with a 20% cumulative uncertainty due to counting statistics. The smooth plains unit has such a high crater density that linear scaling from Lunae Planum is not reasonable. Thus, we have assumed that the smooth plains unit is about 4 billion years old. Using these ages and a thickness of 1 km gives a deposition rate of between 0.4 and 0.9 micrometers/year. This rate is of course uncertain to an order of magnitude because of age uncertainties. Even so, the estimated rate is of the same order as the present day rates inferred for the three years of Viking Lander observations [5,6]. Our calculations provide a lower bound on accumulation rates for etched terrain debris since we assume that climate remained constant and that no erosion occurred over the 2 billion years period. We conclude that the deposition rate was at least as high, and was probably higher in the past than the current rate of aeolian deposition.

REFERENCES

1. Kahn, R., et. al., (1985), Icarus, in press.
2. Condit, C., and L. Soderblom, (1978), USGS Misc. Invest. Map I-1076.
3. Carr, M., (1981), The Surface of Mars, Yale Univ. Press.
4. Gregory, T., et. al., (1979), NASA Tech. Memo. 80339, 75-77.
5. Guinness, E., et. al., (1979), J. Geophys. Res., 84, 8355-8364.
6. Guinness, E., et. al., (1982), J. Geophys. Res., 87, 10,051-10,058.

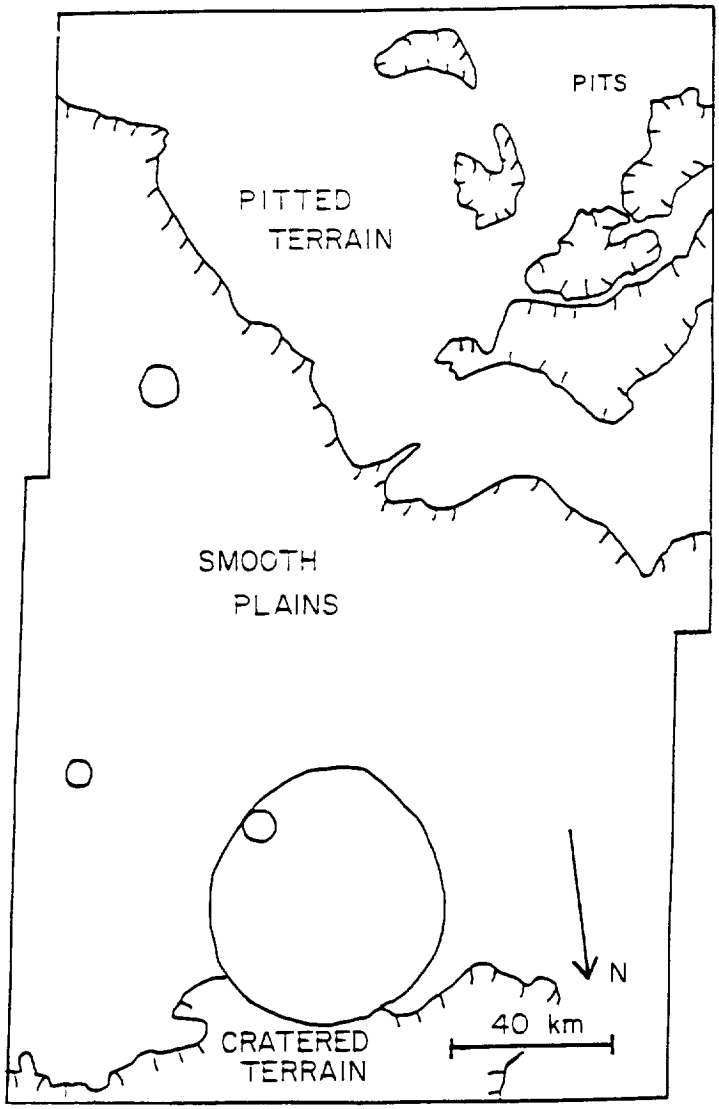

Figure 1. Sketch map derived from mosaic of Viking Orbiter frames 491B67 and 491B69 showing the etched terrain unit at about 75 deg south latitude and 90 deg west longitude.

INFLUENCE OF ATMOSPHERIC DUST LOADING AND WATER VAPOR CONTENT ON SETTLING VELOCITIES OF MARTIAN DUST/ICE GRAINS

S.W. Lee, Department of Geology, Arizona State University, Tempe, Arizona 85287

Previous studies have indicated that condensation of water vapor and/or CO_2 onto suspended dust grains can significantly increase the sedimentation rate of dust/condensate particles on Mars [1,2,3]. This process was assumed to be particularly effective in the polar regions, especially in the northern hemisphere following global dust storms. However, recently reported thermal observations of the north polar region indicate that atmospheric temperatures are above the CO_2 condensation point everywhere except at the surface [4]. In the absence of CO_2 condensation, the principal dust/volatile interaction affecting sedimentation rates on Mars will be the condensation of water ice onto dust grains.

Settling velocities of dust/ice grains have been modelled to investigate the influence of variable atmospheric dust loading and water vapor content on sedimentation rates. The model accounts for differing temperatures and elevations, determines the size and density of dust/ice grains produced assuming various initial dust loads, particle sizes, and water vapor abundances, and predicts the settling velocity of the resulting composite particles. Model results (Fig. 1, Fig. 2) show that a composite particle rapidly increases in size and decreases in average density with condensation of only a few precipitable microns (pr μm) of water; atmospheric drag apparently reduces the settling velocity relative to that expected for a "naked" dust grain. With increasing atmospheric optical depth (and hence, dust loading), this process is effective at higher water vapor abundances. Under conditions prevailing during global dust storms (optical depths $>>1$), the sedimentation rate is significantly reduced, even though each composite particle has grown to several times its initial mass. Under conditions of lower dust loading, increasing vapor content allows continued growth of particles, resulting in an increased settling rate following the initial decline.

This study indicates that under conditions of low dust loading, condensation of only a few pr μm of water vapor onto dust grains will reduce their sedimentation rate; availability of larger quantities of water vapor, however, will enhance the fallout of dust. With high dust loading (such as occurs during global dust storms), the sedimentation rate is reduced by the condensation of any available water vapor. Such behavior implies that scavenging of dust by rapid fallout of dust/ice grains during major dust storms is not an effective process in the polar regions (or elsewhere). Subsequent to dust storm clearing, condensation of more than a few pr μm of water may enhance the dust sedimentation rate anywhere on the planet.

REFERENCES: [1] Cutts, J.A., J. Geophys. Res., 78, 4231-4249, 1973.
[2] Pollack, J.B. et al., J. Geophys. Res., 82, 4479-4496, 1977.
[3] Pollack, J.B. et al., J. Geophys. Res., 84, 2929-2945, 1979.
[4] Jakosky, B.M. Bull. Am. Astron. Soc. 15, 847, 1983.

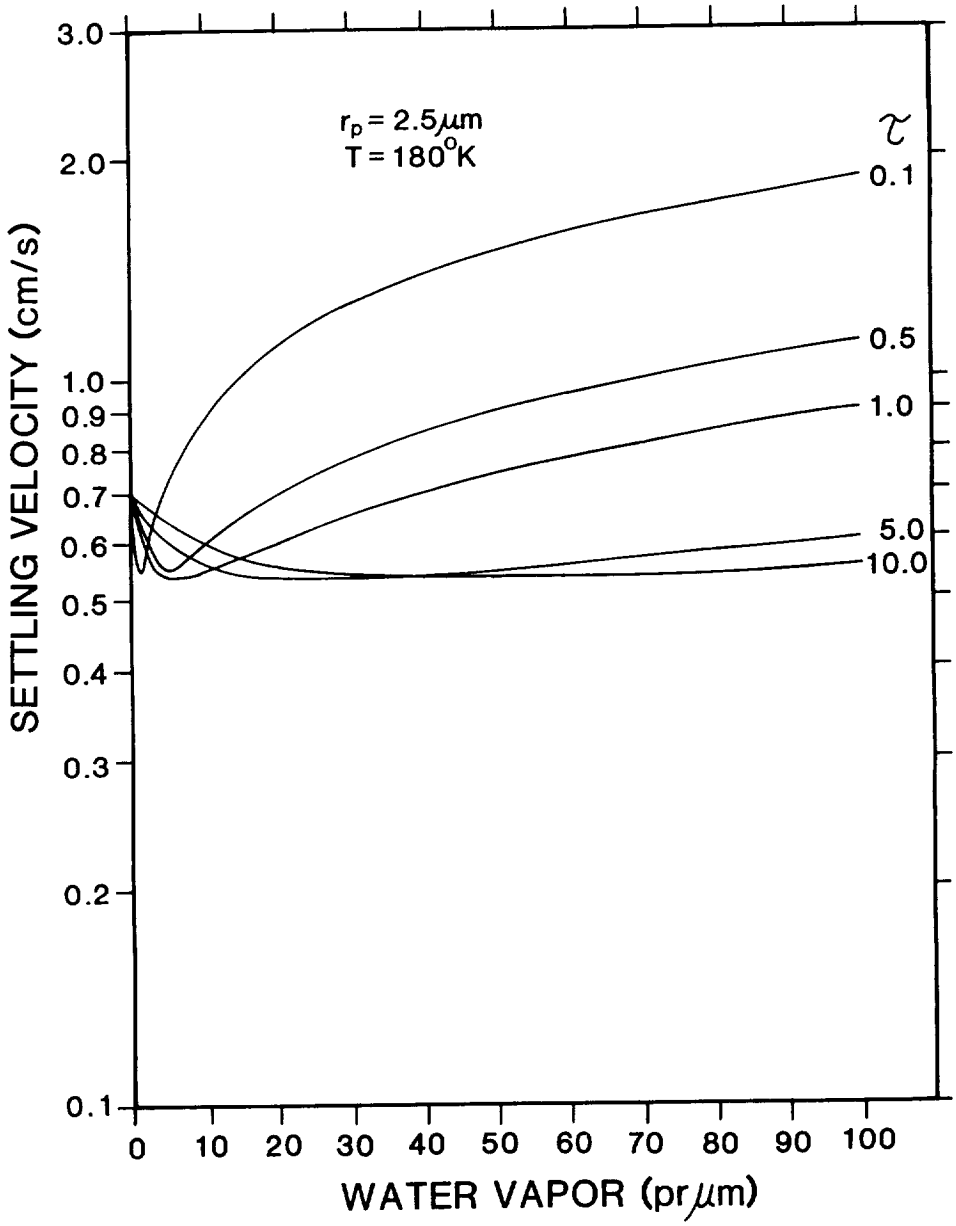

Figure 1: Settling velocity of dust particles as a function of atmospheric water vapor content (complete condensation assumed) and dust loading. A dust grain radius (r_p) of 2.5 μm, temperature of 180°K, and atmospheric pressure of 6.1 mb is assumed. Behavior for several different dust loading conditions (optical depth, τ = 0.1 to 10.0) is shown.

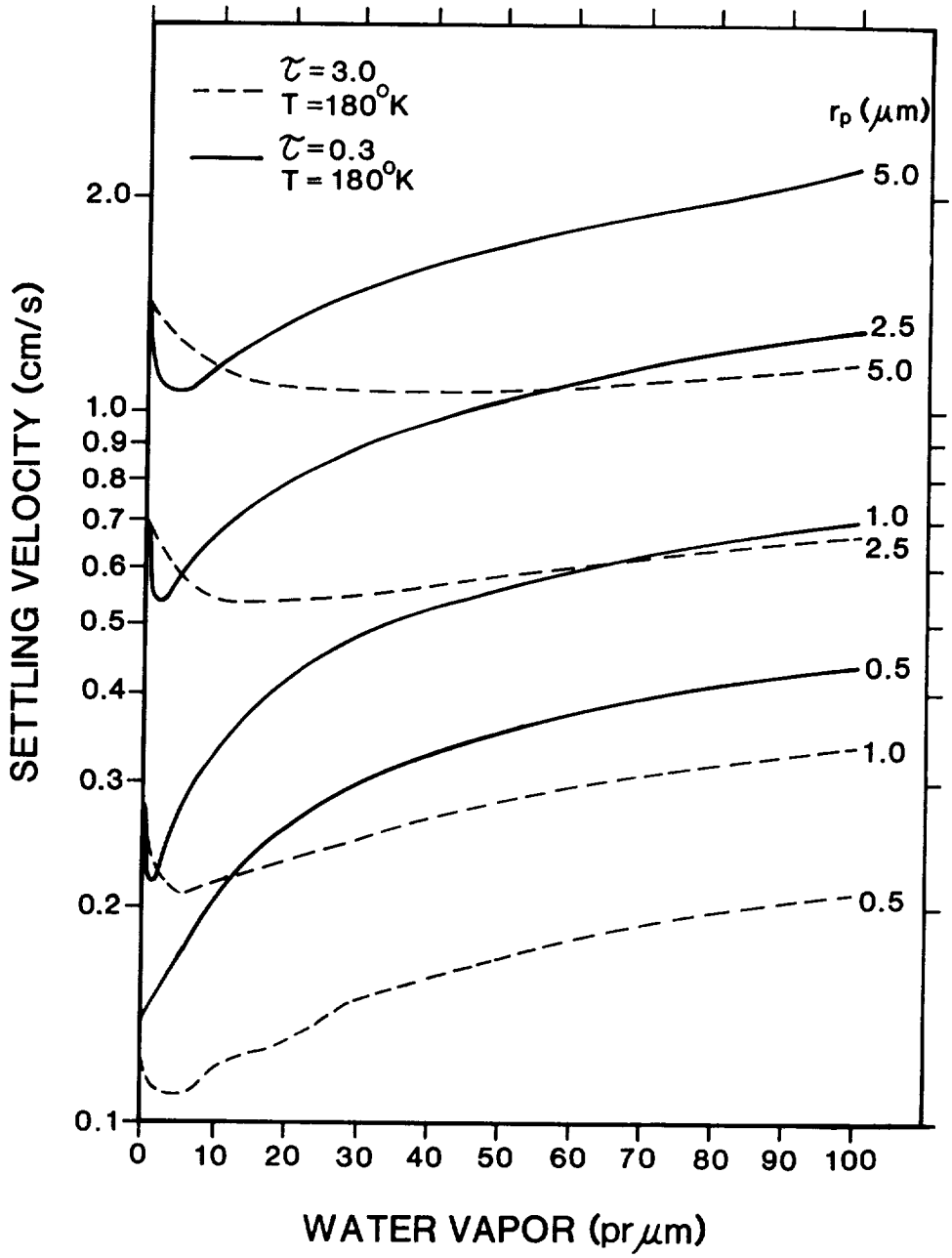

Figure 2: Settling velocity of dust particles as a function of atmospheric water vapor content (complete condensation assumed), dust loading (τ = 0.3 and 3.0), and dust grain size (r_p = 0.5 to 5.0 μm). Temperature and pressure conditions are as in Figure 1.

DUST TRANSPORT AT HIGH ALTITUDES AND LOW PRESSURES ON MARS: AEOLIAN ACTIVITY ON THE THARSIS MONTES

S.W. Lee, Department of Geology, Arizona State University, Tempe, Arizona 85287

Some of the most time-variable albedo features on the surface of Mars are associated with the Tharsis shield volcanoes (Arsia, Pavonis, Ascraeus, and Olympus Mons); these occur at the highest elevations and lowest atmospheric pressures on the planet. Viking Orbiter images have revealed distinct dark collars encircling the flanks of these constructs (Fig.1), reaching the summits (elevations of up to 26 km and pressures below 1 mb) and extending up to 400 km down the flanks. These features exhibit major seasonal variations as well as minor changes over time scales of days, and have been attributed to coalescing dark wind streaks trending downhill [1,2]; as such, they provide dramatic evidence for the efficacy of slope winds as agents of aeolian dust transport.

Modelling of the sedimentation rates at various elevations on the volcanoes [3] indicates the observed short-term changes in the dark collars are consistent with regular deposition from the atmospheric dust load contained in a stably stratified near-surface air mass during early morning. The deposited dust is subsequently redistributed by nightly slope wind activity (produced by the combination of long, steep slopes and large diurnal temperature excursions [4,5] found on the volcanoes). Seasonal variations in the albedo features are explained by large increases in the sedimentation rate due to enhanced dust loading during major dust storm activity, again followed by rapid removal of bright surface dust by slope winds. On a yearly basis, the dark collars are generally repeatable in form and position - they appear to have persisted throughout the span of the available spacecraft and ground-based observations. Given the evidence for rapid redistribution of dust, the residence time of dust on the surface of the Tharsis Montes appears to be much less than one martian year.

While the study presented here indicates that the flanks of the volcanoes are swept relatively clean of dust on short time scales, interpretation of photogeology [6] and IRTM-derived thermal inertia data [7] suggests that these surfaces may be mantled to a depth of several meters. In addition, maps of Lambert albedo (derived from IRTM visual brightness data) show the surfaces of the volcanoes, including the dark collars, to be brighter than ~0.2. Major dark albedo features elsewhere on Mars are considerably darker - for example, the lowest albedo encountered in Syrtis Major is ~0.08 [8]. Production of the dark collars by removal of bright dust from a surface already deeply mantled by dust is very difficult to reconcile with laboratory studies which indicate that deposition or erosion of the tens of μm of dust predicted by the sedimentation models will not alter the albedo of such a mantled surface [9]. Several possible scenarios for producing the variable nature of the dark collars remain: (1) The surface is deeply mantled by dust except for outcrops of darker bedrock protruding through the mantle. If a few tens of percent of the surface consists of such outcrops, deposition and erosion of bright dust

from these non-mantled surfaces will result in variable albedo features [10]. 2) The surface is highly vesicular; dust has accumulated in the vesicles, resulting in a higher albedo and lower thermal inertia than would be the case without such infilling. Other than that trapped in vesicles, the surface dust remains mobile, thus allowing variable albedo features. 3) The surface is mantled with relatively bright but coarse material (perhaps including aggregates of smaller particles [6]), resulting in a 'background' albedo much higher than that found in areas such as Syrtis Major. Deposition and erosion of bright dust from this material could still occur; in fact, removal of dust could be aided by saltation of the coarser particles.

Future research will include analysis of high-resolution IRTM data to determine the emission phase function of the surface of the Tharsis Montes. Such an effort should yield a better understanding of the small-scale surface morphology found on the volcanoes, and allow the viability of the various models outlined above to be evaluated.

REFERENCES: [1] Veverka, J. et al., J. Geophys. Res. 82, 4167-4187, 1977. [2] Lee, S.W. et al., J. Geophys. Res. 87, 10025-10041, 1982. [3] Lee, S.W., submitted to Icarus, 1985. [4] Magalhaes, J. and P. Gierasch, J. Geophys. Res. 87, 9975-9984, 1982. [5] Kahn, R. and P. Gierasch, J. Geophys. Res. 87, 867-880, 1982. [6] Zimbelman, J.R., Ph.D. dissertation, Arizona State Univ., 1984. [7] Christensen, P.R., J. Geophys. Res., in press, 1985. [8] Simpson, R.A. et al., Icarus 49, 258-283, 1982. [9] Wells, E.N. et al., Icarus 58, 331-338, 1984. [10] Thomas, P. et al., Icarus 60, 161-179, 1984.

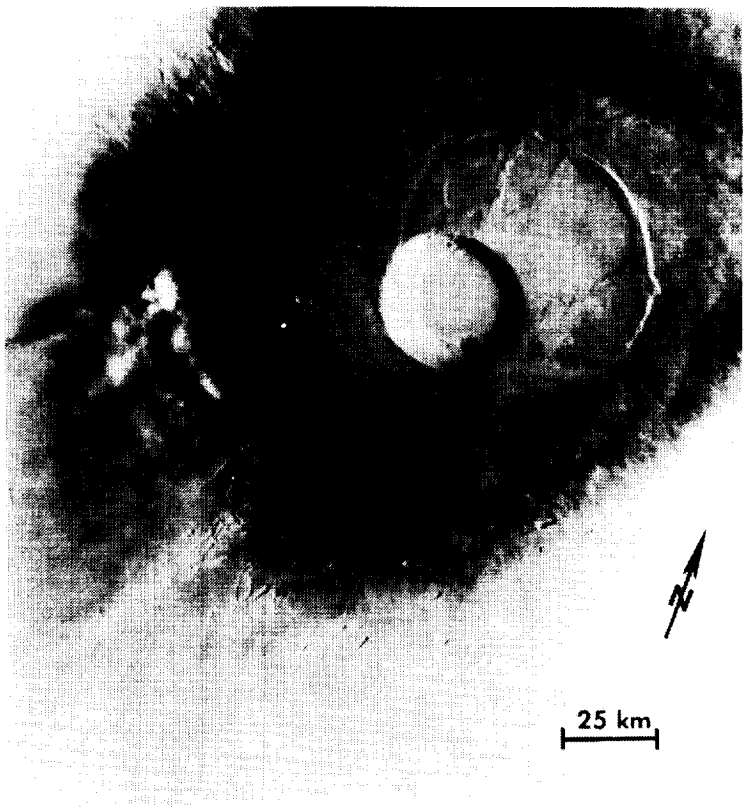

Figure 1: Coalesced dark streak collar encircling the summit of Pavonis Mons. Note the crater-related dark streaks which blend into the collar west of the caldera. Viking Orbiter image 358S59; centered at 0.4°S, 113°W; L_s = 80°; slant range, 8576 km; minus blue filter.

SAND-GRAIN RESPONSE IN PLANETARY ATMOSPHERES

MacKinnon, D. J., U.S. Geological Survey, Flagstaff, AZ

The work presented here is part of a continuing theoretical study to account quantitatively for sediment responses on Mars and Venus and the shapes of their observed eolian landforms. A two-part relation for the response of sand-size sediment to an applied wind field has been derived. The first part is a collision condition at the surface expressing the interaction between two grains during collision. The second part is a computer model to calculate sand-grain trajectories in the complex wind field over eolian landforms. The grain responds by gaining momentum from the airflow and losing it through surface collisions. In order to examine the reliability of the computational analysis, an analytic solution was derived for the sediment response on a flat surface subject to a horizontal wind field whose speed increases logarithmically with height. Some of the most important results of the analytic solution are summarized here.

The relation for the collision condition at the surface has elements similar to expressions by Tsuchiya (1969) and Anders (1970), but more explicitly accounts for the detailed geometry of collisions between two grains and differentiates between normal (e_n) and tangential (e_t) fractions of momentum lost during collision. (These fractions are referred to in the literature as coefficients of restitution.) A colliding spherical grain of diameter D that makes an angle α with respect to the horizontal may strike any of an ensemble of similar-size surface grains within a cross section defined by the shadowing of an immediate upstream grain and a grazing collision with the surface grain in question. The surface grains are separated by a center-to-center distance s to simulate surface roughness. The particular relation presented here selects the grain trajectory that impacts the center of the collision cross section to represent the characteristic collision. The relation expresses grain speed after collision ($v\uparrow$) as a function of grain speed before collision ($v\downarrow$) and a collision parameter (H). The relation also includes an explicit expression for the angle (β) that the colliding grain makes with respect to the horizontal after collision. The relation is:

$$v\uparrow = H\, v\downarrow \tag{1}$$

where

$$H = [(1 - \alpha^2)\, e_t^2 + 2\alpha(e_n^2 - e_t^2)\, Q \approx]^{1/2} \tag{2}$$

$$Q = (\alpha s/D)^{1/2} - \alpha - (s/D)(\alpha^2/2) \tag{3}$$

$$\beta = Q(e_n + e_t)/\, e_t + (e_n/\, e_t)\, \alpha \tag{4}$$

The component speeds are $u\downarrow = v\downarrow \cos \alpha$, $w\downarrow = v\downarrow \sin \alpha$, $u\uparrow = v\uparrow \cos \beta$, $w\uparrow = v\uparrow \sin \beta$, where u and w are the horizontal and vertical grain speeds, respectively, and ($\uparrow$) and ($\downarrow$) refer to the upward and downward portions of the grain trajectory.

The analytic solution for the sand-grain trajectory begins with the two-dimensional equations of motion that are similar to equations by White and others (1975). The upward and downward component speeds for the grain in a

logarithmic horizontal wind field emerge when four assumptions are made: (1) the effect of turbulent wind-speed fluctuations is negligible, (2) the 'lift force' is small in comparison with the drag force for strongly saltating grains, (3) the drag coefficient for a sphere is described by one relation with high and low Reynolds-number sensitivity, and (4) the effect of coupling between the equations of motion, as expressed by the relative speed terms, is small. The results simplify for the physically interesting situation in which the horizontal grain speed never exceeds the horizontal wind speed. The results for the vertical equation are:

$$t_T(\text{time to reach top}) = w_\uparrow/(g + Bw_\uparrow/2) \tag{5}$$

$$z_T(\text{height at top}) = z_B + w_\uparrow t_T/2 \tag{6}$$

$$t_B(\text{time to return}) = \{2(z_T - z_B)/g[1 - B/3\{2(z_T - z_B)/g\}^{1/2}\approx\}^{1/2} \tag{7}$$

$$w_\downarrow(\text{return vertical speed}) = gt_B/(1 + Bt_B/2) \sim w_\uparrow/(1 + Bw_\uparrow/2g) \tag{8}$$

The results for the horizontal equation for the upward and downward portions of the trajectory have been combined to yield:

$$u_\downarrow = u_\uparrow(1 - 2Bt_T) + 2u_B Bt_T + (u_*/\kappa)\, Bt_T \tag{9}$$

$$B = 0.75(\rho_a/\rho_p)[b\nu/(XD^2)\approx \tag{10}$$

In equations (5) through (10), g is gravity, z_B is the saltation roughness height (Bagnold, 1941), u_B is the horizontal threshold speed at z_B, u_* is the saltation friction speed associated with the logarithmic profile, κ is an experimentally determined constant (=0.4), ρ_a is atmospheric density, ρ_p is the mass density of a sand grain of diameter D, ν is the atmospheric viscosity, b is the drag coefficient for a sphere (=24.0) at a low Reynolds number, X is the Cunningham slip factor (=1 for Earth and Venus; on Mars it ranges between 1.33 for a 100μ-diameter grain and 1.04 for a 1000μ-diameter grain; White and others, 1975).

Equations (1) through (10) form a system that uniquely describes the characteristic grain trajectory for any planetary atmosphere in which the grain gains as much momentum from the airstream as it loses to the surface after collision. These equations have been solved to yield relations that describe the characteristic grain trajectory:

$$v_\downarrow = \{g/2B[(H\cos\beta - \cos\alpha)/H\sin\beta\approx + u_B + u_*/2\kappa\}/H\cos\beta \tag{11}$$

$$\alpha = \sin^{-1}[H\sin\beta/(1 + w_\uparrow B/2g)\approx \sim \sin^{-1}(H\sin\beta) \tag{12}$$

Equation (11) shows direct dependence on parameters that vary in the atmospheres of Earth, Mars, and Venus (Iversen, Greeley, and Pollack, 1976). Equation (12) reduces almost exactly to the value given after the approximation sign except for small grains of about 100μ in diameter where B is large for Earth, Mars, and Venus. A large value of B implies that the grain has a very low terminal speed. If a small grain is injected into the atmosphere with high vertical speed after a fortuitous collision, it will return to the surface for the next collision with a vertical speed never greater than its terminal value. If the grain gains a large amount of horizontal momentum on this vigorous initial trajectory, the incident angle before the next collision will be quite small ($z_{\downarrow}$ is low and $u_{\downarrow}$ is high). A small incident angle implies a small upward vertical speed after the next collision. Thus, small grains are limited by the terminal speed to small characteristic values of upward and downward vertical speeds. This limitation makes the approximation of equation (11) true even for the small grains. Equation (11) then has a most striking implication: the shape of the characteristic grain trajectory depends only on the collision condition at the surface -- not on wind speed. The result of relative uniformity in trajectory incident angles over wide wind-speed ranges is supported by experimental observation in the field and laboratory (Bagnold, 1941; Chepil, 1945). Equation (11) suggests that the shapes of grain trajectories are not fundamentally different in the planetary atmospheres of Earth, Mars, and Venus.

References

Anders, R.M., 1970, The mechanics of dust lifting with particular emphasis on the planet Mars: Ph.D. dissertation, St. Louis University, 147 p.

Bagnold, R., 1941, The physics of wind blown sand: London, Chapman and Hall, 265 p.

Chepil, W.S., 1945, Dynamics of wind erosion: I. Nature of movement of soil by wind: Soil Science, v. 60, p. 305-320.

Iversen, J.D., Greeley, R., Pollack, J.B., 1976, Windblown dust on Earth, Mars, and Venus: Journal of Atmospheric Sciences, v. 33, p. 2425-2429.

Tsuchiya, Y., 1969, The mechanics of successive saltation of a sand particle on a granular bed in a turbulent stream: Bulletin of the Disaster Prevention Institute, v. 19, part 1, no. 152, p. 31-44.

White and others, 1975, Particle motion in atmospheric boundary layers of Mars and Earth: NASA TM X62463, 200 p.

TRANSVERSE BEDFORMS IN HIGH-DENSITY FLUIDS: VENUS AND EARTH

J.R. Marshall[1], R. Greeley[1], D. Fox[2], S. Bougan[1], and M. Sheridan[1],
[1] Arizona State University, Department of Geology, Tempe, AZ 85287
[2] Kent State University, Department of Geology, Kent, OH 44242

"High density" fluids are defined here as those with a density greater than that of the Earth's atmosphere at sea level. In the Earth's surface environment, the principal high-density fluid is water (although others exist as in pyroclastic flows), and this generates small (<1m) wavelength, highly asymetrical, transverse bedforms under conditions of unidirectional flow. These bedforms are referred to as "current ripples" and their small size relates to the short trajectories of transported particles which in turn is a function of the low fluid velocities required for the threshold of transport. Current ripples are essentially the high-density (fluid) equivalent of an aeolian dune insofar as their migration occurs by continual transport, burial, and recycling of material within the structure. Simulations of the venusian aeolian environment with the Venus Wind Tunnel (VWT) have shown that high density (0.06 gm/cm^3) (microdunes) unidirectional gas flows also give rise to transverse bedforms which are dune-like in appearance and behavior and are the same size as current ripples.

Present investigations of microdunes in VWT show that the basic dune-like transverse nature of the structures is valid for a variety of conditions, but their precise geometry and behavior is variable in response to: 1) wind speed, 2) particle size distribution, and 3) interparticle cohesive forces (e.g., electrostatic attraction). It is now possible to present a brief "catalogue" of transverse microdune structures which indicates the potential for a wide variety of bedforms on Venus and which may provide some insight into fluid transport phenomena in general. Since interparticle cohesive forces of an electrostatic nature are absent in water, some of the bedform varieties found in the VWT will not have subaqueous analogs amongst current ripples.

A. Bedform varieties in unimodal, well-sorted sands. Figure 1 (upper set) shows a well-developed microdune in unimodal sand. It is characterized by a slip face, a gently-sloping stoss side, and internal cross bedding. Flow separates at the brink of the structure, and wake flow, which is typically reversed, can produce scour hollows between structures. As wind speed increases, the structures "degrade" to ridges and waves. The waves are similar in appearance and size to aeolian ripples but are not of the same origin.

B. Bedform varieties in multimodal sands. Figure 1 (middle set) depicts microdunes formed in bimodal or trimodal sands. Transport results in the concentration of the finer material in the crests and coarser material as a basal layer. This graded bedding is notably the reverse of that found in aeolian ripples. Increasing wind speed again degrades the dunes to ridges and waves but, in some cases, the ridges have a steep stoss-side slope and a flat or reversed-sloping area separating the stoss

slope from the lee slope. The former is always composed of the finer material, the latter of the course.

C. Bedform varieties in multimodal, cohesive materials. Pyroclastic particles were used to generate the bedforms in the lower set of Fig. 1. These are of a lower density and higher angularity than the quartz grains developing other bedforms in Fig. 1 and they appeared to be characterized by greater electrostatic charging. Microdunes in this material were fundamentally different from those in the other sets, but with some similarity in form to the "reversed" ridges described above. Invariably, the structures had a flat top which was terminated at the stoss side by a steep erosional slope. Material from this slope was plucked loose, rolled or saltated across the flat, and deposited on the lee slope. The whole structure was a concentration of the coarsest material in the bed, but the upper surface was coated with a very thin veneer of the finest silt and clay-size material. This appeared to be electrostatically clinging to the top of the dune and provided a smooth armouring that enhanced transport across the structure while inhibiting erosion of underlying particles. At high wind speeds, the structures were also reduced to less well-defined forms with the coarse material forming simple transverse patches of sand only a few grains diameters in thickness.

For this group of bedforms, the effects of particle shape, particle density, and electrostatic cohesion are undifferentiated and it is not possible at the present time to ascribe aspects of bedform behavior to the separate or combined effects of the three parameters. It is surmised, however, that the apparently strong cohesive nature may be, in part, a function of the adherance of fines to irregular pockets in the coarse vesicular grains.

Beforms in all groups, but particularly those in pumice, may provide a useful input to the study of small-scale transverse structures observed in pyroclastic surge deposits and windblown snow where ice-welding cohesion and crystal structures may have similar effects to electrostatic cohesion and vesicularity, respectively. Undoubtedly, the catalogue will require further additions in the future and it seems, therefore, that the surface of venus (where it is affected by aeolain action) has the potential for a wide variety of bedforms. We do not know, however if electrostatic interparticle forces can exist to the same degree on Venus as they do on Earth.

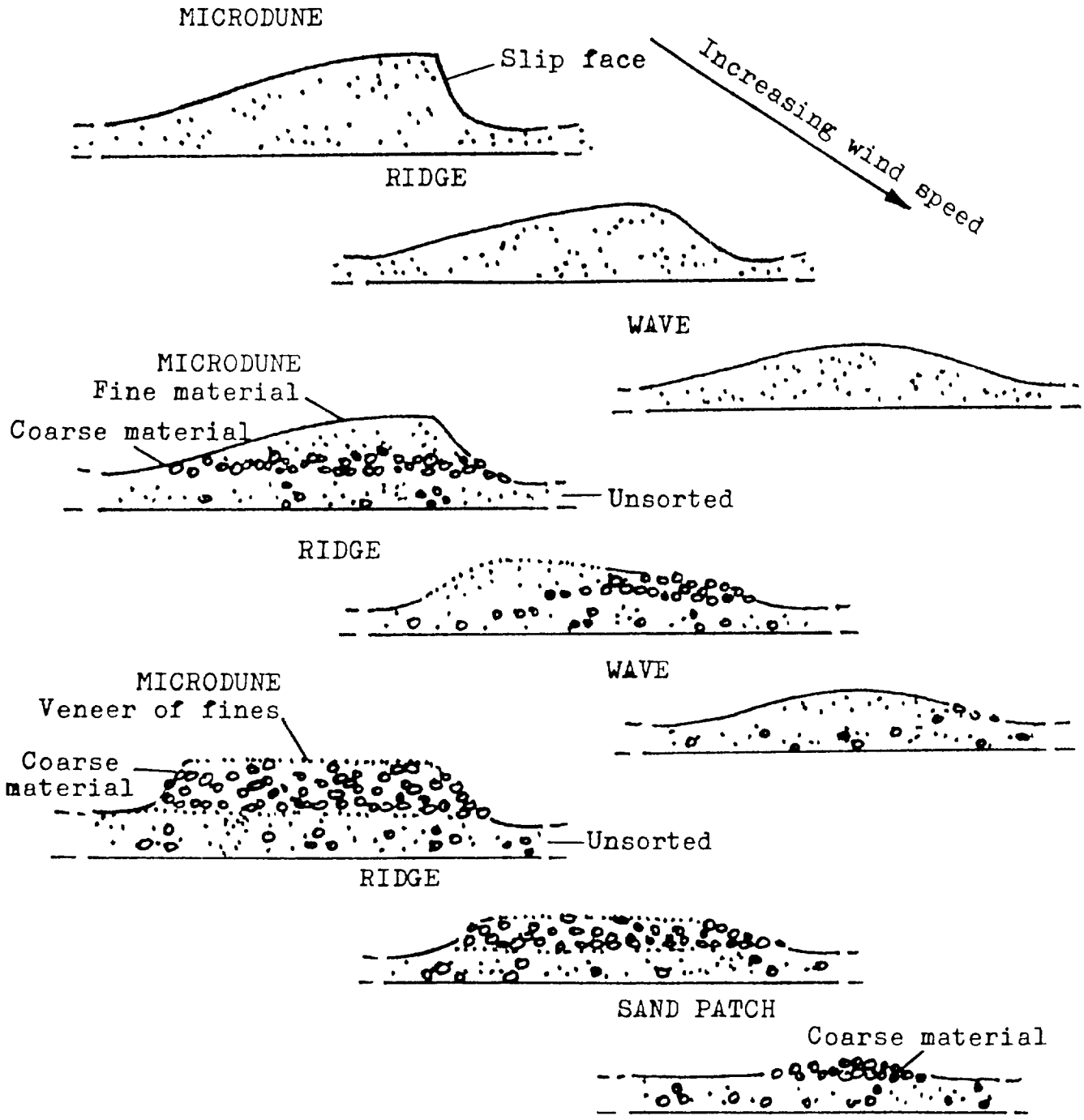

FIGURE 1. TRANSVERSE BEDFORMS IN VWT
Upper group: Unimodal, well-sorted sand (quartz)
Middle group: Bimodal or trimodal sands (quartz)
Lower group: Bimodal pyroclastic materials (pumice)

Wind direction is from the left in all cases. Wind velocities range from approx. 0.8 m/s to 2.0 m/s from left to right.

DISTRIBUTION OF POSSIBLE SOURCES OF DUNE-LIKE MATERIAL AT THE MARTIAN POLES

R. Stephen Saunders and Timothy J. Parker, Jet Propulsion Laboratory, Pasadena, California.

Previous experiments with filamentary sublimate residues derived from micron-size clay particles dispersed in water ice (Saunders et al, 1984; Stephens et al, 1984) have demonstrated the possibility that sand-size aggregates may form from martian polar material. This, in turn, may provide a source for at least some of the material comprising the north circumpolar dune sea. We have begun investigating some of the possible source regions for this material and their distributions within the north polar layered terrain.

Figure 1 is an oblique Viking Orbiter view of the cap looking north from about 10^0 longitude. The two dark patches near the center and to the lower right of center are steep-walled, west facing escarpments about 100 kilometers apart within Chasma Boreale. Figure 2 illustrates a closer view of the eastern escarpment and the dune-like features associated with it. This second escarpment lies at the easternmost end of Chasma Boreale. Other occurrences of similar steep escarpments within the polar layered terrain can be seen at 84^0 latitude, 130^0 longitude, and at 83^0 latitude, 235^0 longitude. All have dune-like deposits nearby. They also tend to occur at the heads of broad, flat-floored troughs similar to, but much shorter than Chasma Boreale. These shorter chasms, like Chasma Boreale, tend to spiral clockwise outward from the pole. The presence of these escarpments at the heads of the chasms might suggest that the chasms grow headward into the polar dust/ice layered terrain by sublimative sapping along these escarpments.

A search of the south polar layered terrain did not reveal any similar steep escarpments, though the south polar cap also possesses several chasms at scales similar to those in the north. Those in the south, however, spiral counterclockwise away from the pole. Additionally, the southern chasms do not display any dune-like deposits on their floors, even though imagery of sufficient resolution to reveal such features certainly exists. Except for the presence of these features in the north and their complete absence in the south, the gross morphology of the deposits at the two poles is very similar (though reversed). These differences may be indicative of a process presently active at the north pole that is not occurring in the south. Perhaps this process alternates from one pole to the other over some period of time so that the gross morphological similarity between the two poles is preserved.

REFERENCES

Saunders, R. S., Parker, T. J., Stephens, J. B., Laue, E. G., and Fanale, F. P., 1984, Transformation of polar ice sublimate residue into martian circumpolar sand, Reports of the Planetary Geology Program, NASA TM 87563, p. 300-302.

Stephens, J. B., Parker, T. J., Saunders, R. S., Laue, E. G., and Fanale, F. P., 1984, Properties of filamentary sublimation residues from dispersions of clay in ice, Reports of the Planetary Geology Program, NASA TM 87563, p. 440-442.

Figure 1: Oblique view of the north polar cap and Chasma Boreale. V.O. #332S48.

Figure 2: Moderate resolution (57m/pixel) image of steep escarpment and associated dune-like deposits at the head of Chasma Boreale. V.O. #66B13.

MARS: COLOR PATTERNS OF EOLIAN SEDIMENTS

P. Thomas, Center for Radiophysics and Space Research, Cornell University

A. Dunes and related materials. The colors and albedos of martian features such as dunes, crater splotches, polar layered deposits and polar frosts are being used to investigate the different materials moved by the wind, their possible sources, and the changes in materials with transport. Isolated features such as intracrater dunes and splotches show consistent local color patterns (number of components on red-violet plots, mixing lines, and relative albedos) with greater variations between splotches in different areas. This pattern is consistent with the intracrater features being the result of considerable transport and sorting. Regionally, the materials available for sorting are different, causing the geographic variation in average colors of splotches and related markings.

Dunes near the north polar deposits show more complex albedo and color changes. Changes in dune color near their apparent source in the layered deposits are more rapid than in dunes considerably removed from the layered deposits. The dune colors on the layered materials are quite distinct from the layered deposits suggesting (as expected) the immediate segregation of sand and dust loads. We are taking data from more areas to make global maps of dune color variations.

B. Dust. Although some areas on Mars appear to have a complete or fractional coverage by a bright, red, fine dust (especially parts of Arabia) this material need not be considered the only martian dust. Areas that have low thermal inertia have a large range in albedos (Zimbelman, 1985) and almost certainly have a substantial eolian dust component. Laboratory studies of Mars analog materials (especially iron oxides) emphasize that material which can be carried in suspension (<60 μm) and which can satisfy the thermal inertia data can have very much lower albedos than the very finest fraction (<5 μm) which is probably typical of some deposits in Arabia and other areas of Mars, and the higher parts of dust clouds. Dark collars on volcanoes and some other low inertia, "dark" eolian features may be deposits from which the very finest particles have been removed or not deposited; this effective sorting of dust is perhaps not surprising at the very low atmospheric densities near the tops of volcanoes.

C. Suspended dust. Dust devils have been found on Mars (Thomas and Gierasch, 1985) and the photometry of clouds and their shadows together offer additional measures of the properties of martian "dust." Our preliminary study of the dust devils indicates loading of $\sim 5 \times 10^{-8}$ g/cm^3 in a dust devil, which may entrain 1-5 tons of dust in a typical cloud. The probable lifetimes of these features of only a few hours and their slow surface speeds still allow entrainment of this amount of dust from a reasonable surface area with patchy dust of $\sim 10^{-3}$ g/cm^2 (on the order of annual dust loading). Vertical velocities of up to a few m/s may be required to life dust to the highest parts of some dust devils. Work is continuing on using clouds and shadows to delineate dust loading in other clouds.

This work is supported by NASA grant NAGW-111.

REFERENCES

Thomas, P., and P. Gierasch, 1985. Dust devils on Mars. Science 230, 175-177.

Zimbelman, J. R., 1985. Surface properties of Ascraeus Mons: Dust deposits on a Tharsis volcano. LPSC 16th, 1934-935.

PARTICLE SPEED AND CONCENTRATION IN A SALTATION CLOUD: PRELIMINARY WIND TUNNEL RESULTS

S.H. Williams and R. Greeley, Department of Geology, Arizona State University, Tempe, Arizona 85287

Movement of surficial material by the wind can be an important part of the planetary geologic cycle. The effectiveness of the wind as a geologic agent is controlled by the speed and quantity of particles moved. Saltation flux, the mass of material moved by the wind, has been studied intensively (Bagnold, 1941; Kawamura, 1951; Zingg, 1953; Williams, 1964; Greeley et al., 1984; and many others), however, particle speeds during saltation are poorly understood. The purpose of this study is to measure particle speeds under a range of saltation conditions and combine the results with saltation flux measurements to determine the particle concentration (particles per unit volume) in the saltation cloud. Previous saltation studies make two assumptions: 1) particles move in smooth trajectories without mid-air collisions and 2) any particle on the surface is free to move and there are sufficient saltation impacts nearby to initiate motion. Particle concentration, n_o, is important in the first assumption, for it is clear that, at some high value of n_o, particles can no longer move freely (Williams and Greeley, 1985). When n_o is sufficiently large, less material is transported by the wind than predicted. Knowledge of the quantity and speed of material in saltation over the entire range of possible wind speeds is required to constrain models of sediment transport and surficial erosion on any planet where aeolian processes are significant.

Particle speed, vp, is determined using a particle velocimeter develop developed from a USDA Forest Service design (Schmitt, 1977; Greeley et al., 1982). Saltation flux, q, is measured using a stack of collectors (Greeley et al., 1982) during different runs under similar conditions. The concentration of mass in the saltation cloud at the point of measurement is q/vp. Particle concentration is the mass concentration divided by mp, the mass of an average particle. The mean free path (MFP) of a particle at this point is $(n_o\ \sigma_c)^{-1}$, where σ_c is the collisional cross-sectional area of the particle, $4\pi r^2$. In the experiment program currently underway, particle size, density, and height above the surface are individually varied to assess their influence on saltation. Some general trends have emerged from the experiments conducted to date: smaller particles accelerate more quickly than large particles, low-density particles accelerate more quickly than dense particles and particle velocity increases with height. The results are consistent with the variation of drag force, particle inertia and flight time in each case considered. Typical results are presented in Figure 1, which shows the relationship between particle speed and wind speed at a height, z, of 4.0 cm above the surface for particles with a diameter, Dp, of 400-500 μm and various densities. In most terrestrial cases, the particle mean free path is very long (Table 1). Few mid-air collisions occur, satisfying the assumption made in predicting saltation flux. However, our results indicate that when

the mean free path of a particle near the surface becomes small relative to the saltation path length, mid-air collisions alter the distribution of saltating material above the surface. Saltation is impaired, or "choked" by the large quantity of material in motion (Williams and Greeley, 1985). Some terrestrial cases, particularly those with low particle size and/or density approach this condition, which many be analogous to changing flow regimes (Table 1). On Venus, this condition could occur more readily, due to the effective compression of the saltation cloud caused by low saltation trajectories and the corresponding increase in particle concentration.

The second saltation flux equation condition that there are a sufficient number of saltation impacts to cause movement of all available particles does not apply at wind speeds just below threshold. In this case, particles move in isolated hops or by rolling (Greeley and Marshall, 1985), not the cascade of fully developed saltation. Hence, some mass is moved at sub-threshold wind speeds. On Mars, fewer particles strike a unit surface area due to longer saltation trajectories and higher particle speeds, making the immature saltation case to be more common than on Earth. Martian saltation might become fully developed only at very large wind speeds, with the actual saltation flux being less than that predicted for typical conditions. This is currently under study, as are the particle velocity experiments. Further work on particle concentration in the saltation cloud should allow determination of where the saltation flux predicitons are valid for all three planets, and quantify the parameters of particles in a saltation cloud to allow prediction of erosive capabilities.

REFERENCES

Bagnold, R.A., 1941, The Physics of Blown Sand and Desert Dunes, London: Meuthen, 265 p.

Greeley, R., et al., 1982, Rate of wind abrasion on Mars, Jour. Geophys. Res., v. 87, n. B12, p. 10009-10024.

Greeley, R., et al., 1984, Abrasion by aeolian particles: Earth and Mars, NASA Contractor Report 3788, 50 p.

Greeley, R. and J. Marshall, 1985, Transport of venusian "stones" by wind? Nature, v. 313, p. 771-773.

Kawamura, R., 1951, Study on sand movement by wind, NASA Techn. Trans. F-14, 215 p.

Schmitt, R.A., 1977, A system that measures blowing snow, USDA For. Serv. Res. Pap. RM-194, 80 p.

Williams, G., 1964, Some aspects of the eolian saltation load, Sedimentology, v. 3, p. 257-287

Williams, S. and R. Greeley, 1985, Aeolian activity on Venus: The effect of atmospheric density on saltation flux (abs.), Lunar Plan. Sci. Conf. XVI, p. 908-909.

Zingg, A.W., 1953, Wind-tunnel studies of the movement of sedimentary material, Proc. 5th Hydraulics Conf., Iowa Univ. Bull. 34, p. 111-135.

Figure 1 Particle speeds as a function of wind speed under terrestrial conditions are shown for three different particle densities. Particle speed is normalized by the freestream wind speed.

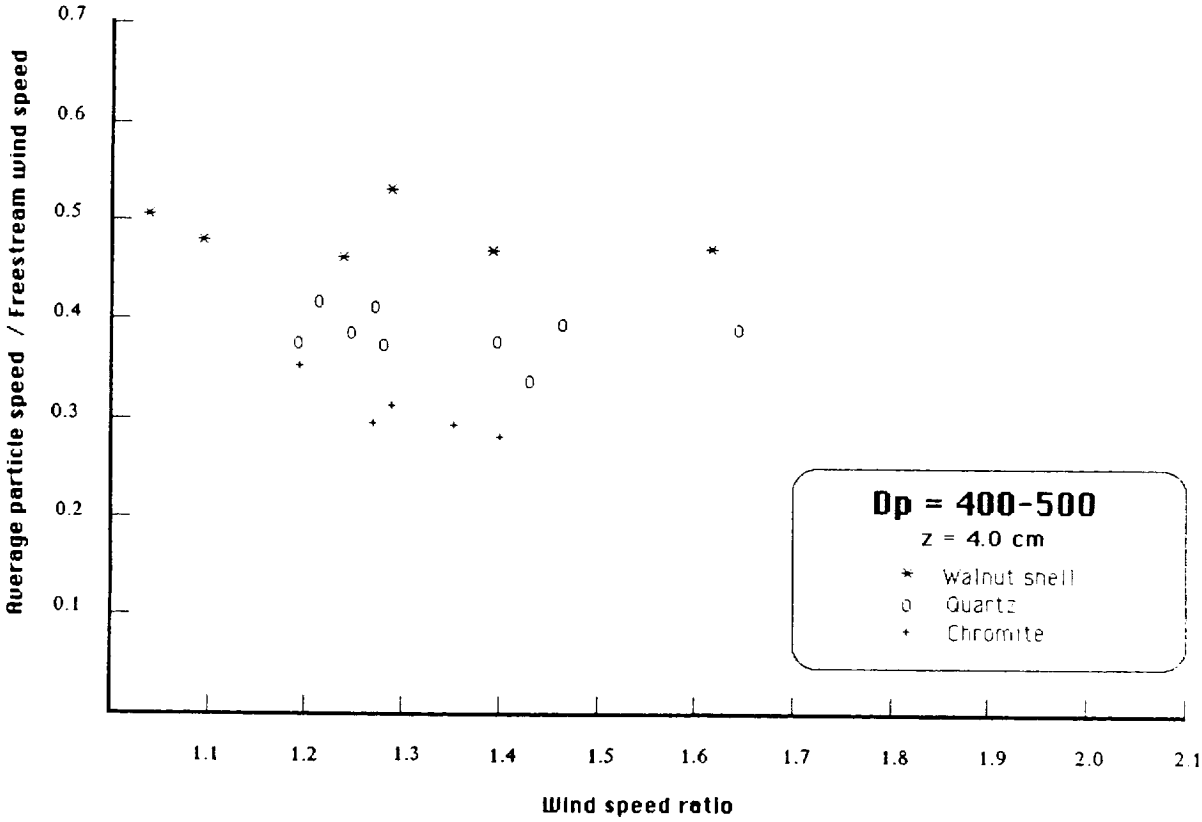

Table 1 Typical saltation parameters are listed for the terrestrial case using particles of different sizes and densities. The density of walnut shell is 1.1, quartz, 2.65 and chromite, 4.5 g/cm^3. Wind speed ratio is the wind tunnel freestream wind speed divided by that at saltation threshold. Scientific notation is used in the q column with the exponent in paraentheses.

Material	Size μm	Height cm	Wind speed ratio	$\bar{v}_p$ cm/sec	q	n_o	MFP cm
WALNUT	170-211	2.0	1.32	250	1.8 (-3)	1.95	480
WALNUT	170-211	2.0	2.69	280	1.4 (-1)	125	7.1
QUARTZ	250-300	4.0	1.33	330	8.0 (-3)	0.83	510
QUARTZ	250-300	4.0	1.64	370	1.9 (-2)	1.7	240
CHROMITE	170-211	2.0	1.32	275	5.8 (-2)	13	68
CHROMITE	170-211	2.0	2.36	300	5.4 (-1)	110	7.9
WALNUT	400-500	2.0	1.21	316	4.7 (-3)	0.38	410
WALNUT	400-500	4.0	1.40	320	1.7 (-3)	0.10	1500
WALNUT	400-500	8.0	1.20	336	8.9 (-5)	5.0(-3)	31000

CHAPTER 7

FLUVIAL PROCESSES

EVOLUTION OF SMALL VALLEY NETWORKS IN THE HEAVILY CRATERED TERRAINS OF MARS

Victor R. Baker, Department of Geosciences and Department of Planetary Sciences, University of Arizona, Tucson, AZ 85721.

The equatorial heavily cratered uplands of Mars are dissected by two classes of small valleys that are intimately associated in compound networks (1). Pristine valleys, exhibiting steep valley walls, preferentially occupy downstream portions of compound basins. Degraded valleys, exhibiting eroded walls, are laterally more extensive and have higher drainage densities than pristine valleys (2). Morphometric and crater-counting studies indicate that relatively dense drainage networks were emplaced on Mars during the heavy bombardment about 4.0 billion years ago. Over a period of approximately 10^8 years, these networks were degraded and subsequently invaded by headwardly extending pristine valleys.

The great lateral extent of degraded networks, as indicated by their high network dissection ratios, certainly indicates a different process for their evolution than for the pristine valleys. Cross grading (3) as opposed to simple headward extension (4) might explain the differences between degraded and pristine network morphology. However, degraded networks are so difficult to map that this distinction may have to await the acquisition of higher quality imagery of Mars.

Pristine network segments possess numerous attributes associated with an origin by sapping (5,6). The pristine valleys probably evolved by headward growth and structurally-controlled bifurcation, as modeled for terrestrial networks by Dunne (7). Paleoenvironmental implications of this process center on the need for an active hydrologic cycle to recharge the high water tables necessary to sustain spring discharge at the valley heads.

Figure 1 shows a hypothetical sequence of valley network evolution on Mars that is consistent with the data generated in this study. In scene A, a relatively dense network of valleys has developed during the heavy bombardment, approximatley 4.0 billion years ago. The valleys formed on slopes dictated by large (> 20 km-diameter) craters that already had been emplaced by this time. Valley formation may have contributed to the obliteration of smaller craters that formed coeval with the large ones.

Scene B shows the formation of intercrater plains (IC), which broke the densely cratered terrain into zones of rugged, cratered plateau (HC) and intervening plains (IC). Plains formation probably buried portions of the older valleys. However, the intercrater plains became sites for the initiation of new headwardly extending pristine valleys. As these grew into the now-relict predecessor network (scene C), relatively small craters were superimposed on the landscape. Unlike the large craters, which are now highly degraded in appearance, the small craters are relatively fresh. Nearly all are less than 10 km in diameter, and this population dominates the final configuration of the compound network (scene D). The high density of these craters indicates that they were part of the heavy bombardment, but probably were emplaced during the rapid decline of cratering rates about 3.8 to 3.9 billion years ago.

The data indicate that in a relatively short period after the emplacement of large craters, perhaps 10^8 years, the extensive networks were formed, degraded by erosional processes, and invaded by headwardly extending pristine valleys. It is tempting to hypothesize that the degradation of the valleys may have been the same degradation interpreted to have affected the large craters (8,9). This period of high erosion rates seems to have been coincident with the rapid decline in cratering rates about 3.8 to 3.9 billion years ago.

The relict compound valleys on Mars are morphometrically distinct from most terrestrial drainage systems. The differences might be caused by a Martian valley formation episode characterized by hyperaridity, by inadequate time for network growth, by very permeable rock types, or by a combination of factors. Clearly the valleys have had a complex history that is intrimately associated with the cratering of the heavy bombardment. Because cratering and other erosive proceses have removed so much of the evidence, it may not be possible to discern an unequivocal origin.

REFERENCES

(1) V.R. Baker and J.B. Partridge, in Lunar and Planetary Science XV (Lunar and Planetary Inst., Houston, 1984), p. 25-26. (2) V.R. Baker and J.B. Partridge, in Lunar and Planetary Science XV (Lunar and Planetary Inst., Houston, 1984), p. 23-24. (3) R.E. Horton, Geol. Soc. America Bull. **56**, 275-370 (1945). (4) A.D. Abrahams, Amer. Jour. Sci. **277**, 626-645 (1977). (5) D. Pieri, Science **210**, 895-897 (1980). (6) V.R. Baker, The Channels of Mars (University of Texas Press, Austin, 1982). (7) T. Dunne, Progress in Physical Geography **4**, 211-239 (1980). (8) W.K. Hartmann, Jour. Geophys. Res. **79**, 3951-3957 (1973). (9) C.R. Chapman and K.L. Jones, An. Rev. Earth and Planet. Sci. **5**, 515-540 (1977).

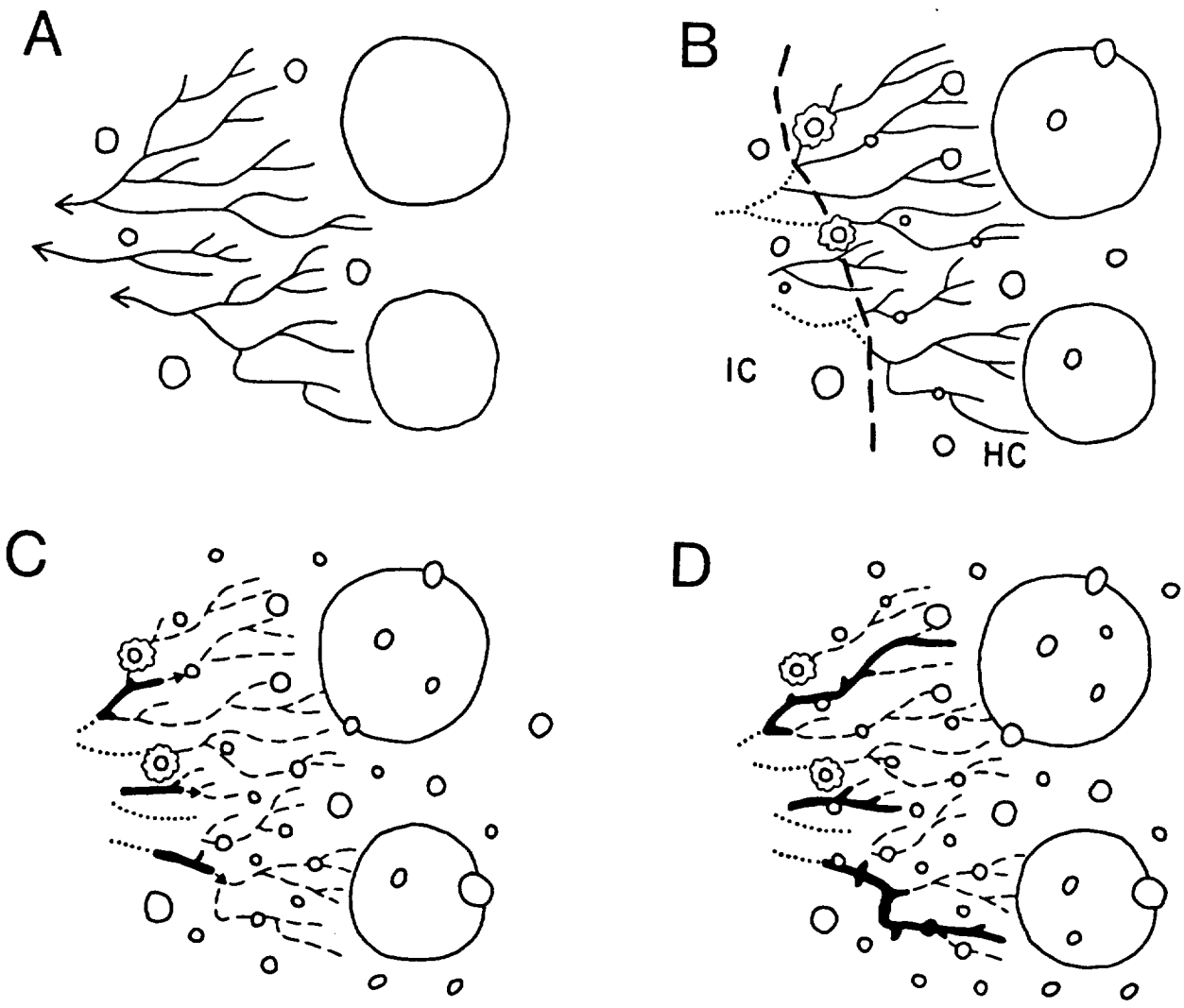

Figure 1. Hypothetical sequence of valley development in the equatorial highlands of Mars. A. Relatively dense network of valleys forms coeval with heavy bombardment approximately 4.0 billion years ago. B. Intercrater plains (IC) begin formation, burying downstream extensions of some valleys (dotted lines). Intercrater plains become distinct from the rugged, densely cratered plateau (HC). C. Pristine valleys (heavy lines) form in intercrater plains and migrate headward (arrows) into areas of now-inactive degraded valleys (dashed lines). D. Pristine valleys cease headward migration about the same time as the termination of the heavy bombardment, approximately 3.8-3.9 billion years ago. Landscape experiences extremely slow degradation up to the present.

FLOW MODELING OF CATACLYSMIC FLOOD DISCHARGES

Victor R. Baker, Department of Geosciences and Department of Planetary Sciences, University of Arizona, Tucson, AZ 85721; and Jim E. O'Connor, Department of Geosciences, University of Arizona, Tucson, AZ 85721.

The indirect calculation of flow hydraulics from paleochannel dimensions is generally accomplished using semi-empirical formulae such as the Manning equation:

$$Q = VA = n^{-1} AR^{2/3} S^{1/2} ,$$

where Q is discharge (m^3/s), V is mean flow velocity in m/s, A is channel cross-sectional area (m^2), n is the Manning roughness coefficient, R is the hydraulic radius (m), and S is the energy slope. This equation also serves as the basis of the slope-area procedure, which accounts for nonuniform flow (1,2). In applications to paleochannels it may be necessary to substitute flow depth (D) for hydraulic radius (R) and to substitute channel-bottom slope or water-surface slope for energy slope (S). An additional source of error derives from the specification of Manning's n.

Slope-area procedures have been applied to paleoflood discharge calculations in the Channeled Scabland (3). Maximum Missoula flood outflow in the Rathdrum Prairie area was found to be approximatley 21 x 10^6 m^3/s. This is the largest known terrestrial fresh-water discharge.

Paleoflood discharge calculations for Martian outflow channels have followed terrestrial experience. The Manning equation, modified for Martian gravity and flow depths,

$$Q = VA = 0.5\ n^{-1} AR^{2/3} S^{1/2} ,$$

can be used to calculate discharges based on outflow channel dimensions (4,5,6). However, because of the complexity of the gravitational influence, Komar (7) proposed an alternative calculation procedure based on frictional drag of the flow boundaries,

$$Q = VA = C_f^{-1/2} A (gDS)^{1/2} ,$$

where C_f is a dimensionless drag coefficient and g is the acceleration of gravity. Although this procedure has interplanetary versatility, it remains highly sensitive to a very uncertain parameter (C_f) and it assumes uniform flow (which would rarely occur in a cataclysmic flood situation).

Because of the above uncertainties, we have investigated a relatively new approach to paleoflood reconstruction employing step-backwater analysis (8). The method employs computer programs (9) to generate energy-balanced water-surface profiles for various discharges in reaches where channel geometry is well specified. The modeled profiles are then matched to geologic evidence of high-water levels to establish the optimum discharge. Advantages of this procedure include the following: (a) it provides a more

accurate accounting of flow-energy losses associated with steady, nonuniform (gradually varied) flow in irregular channels; (b) it allows multiple cross sections to accurately define channel constrictions and expansions; and (c) it is relatively insensitive to uncertainties in specifying various friction-loss coefficients, such as Manning's n (10,11). All these factors make flow modeling the procedure of choice in various paleoflood reconstruction studies (12).

A reach of North Kasei Vallis (Fig. 1) was selected to apply flow modeling to Mars. It was assumed that canyon depths (calculated by shadow measurements on Viking images) corresponded to maximum probable depths of paleoflood water. Channel slope was established from the regional slope indicated by radar data (13). A gradient (S) of 2.5 km/Km was used. Roughness (n) was assumed to be 0.020, or about 1/2 a reasonable terrestrial value. For the six cross sections (Fig. 1) a discharge of 20×10^6 m^3/s results in a modeled water-surface profile that nearly matches the canyon depths. For this modeled discharge the flow was found to be subcritical in all cross sections. In general, channel slopes, discharges, and Froude numbers are remarkably similar to values obtained for the Channeled Scabland employing both slope-area (3) and flow modeling (14) procedures.

Present topographic data for Mars are sufficiently crude that the simpler paleohydraulic equations are adequate. However, proposed radar altimetry measurements by the Mars Observer Mission will greatly enhance our ability to specify outflow channel geometry. The computerized flow modeling procedures reported here will allow accurate paleodischarge calculations to be made from this new data base.

REFERENCES

(1) V.T. Chow, Open Channel Hydraulics (McGraw-Hill, New York, 1959). (2) T. Dalrymple and M.A. Benson, U.S. Geol. Survey Tech. of Water Resources Inv., Bk. **3**, Ch. **A-2**, 1-12 (1967). (3) V.R. Baker, Geol. Soc. America Special Paper **144**, 1-79 (1973). (4) D. Nummedal, J.J. Gonsiewski, and J.C. Boothroyd, Geologica Romana **15**, 407-418 (1976). (5) M.H. Carr, J. Geophys. Res. **84**, 2995-3007 (1979). (6) V.R. Baker, The Channels of Mars (University of Texas Press, Austin, 1982). (7) P.D. Komar, Icarus **37**, 156-181 (1979). (8) A.D. Feldman, in Advances in Hydrosciences (Academic Press, New York, 1981), pp. 297-423. (9) Hydrologic Engineering Center, HEC-2 Water Surface Profiles, Users' Manual (U.S. Army Corps of Engineers, California, 1979). (10) J.E. O'Connor and R.H. Webb, in Flood Geomorphology (in preparation). (11) R.H. Webb, Late Holocene Flooding on the Escalante River, South-Central Utah (Ph.D. Dissertation, Univ. Arizona, Tucson, 1985). (12) J.E. O'Connor, R.H. Webb, and V.R. Baker, Geol. Soc. America Bull. (in press). (13) B.K. Lucchitta and H.M. Ferguson, J. Geophys. Res. **88**, A553-A568 (1983). (14) J.E. O'Connor and V.R. Baker, Quaternary Research (in review).

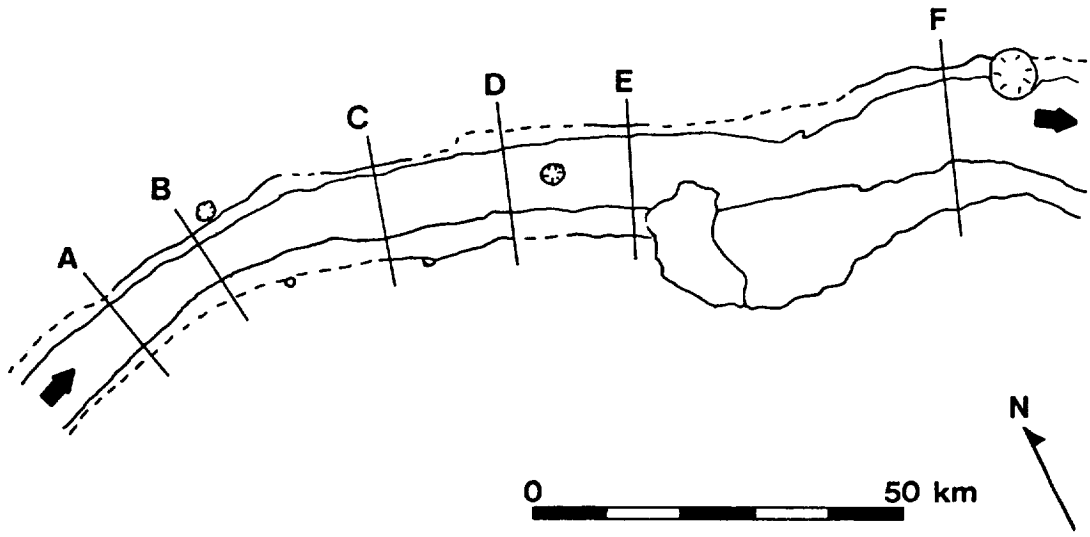

NORTH KASEI CHANNEL

Figure 1. Sketch map of a portion of North Kasei Vallis prepared from Viking Photomosaic 211-5882, rev. 665A. Note locations of cross sections used in flow modeling of this outflow channel reach.

GROUNDWATER SAPPING AND MORPHEMETRY OF HAWAIIAN VALLEYS

R. Craig Kochel, Department of Geology, Southern Illinois University, Carbondale, Illinois 62901

Drainage basins are morphometrically distinct, on windward and leeward slopes of Hawaiian Islands i.e., Hawaii, Maui, and Molokai. Leeward slopes are less dissected with numerous high density channel networks developed in parallel arrangement. Windward slopes are dominated by deeply dissected valleys having broad, U-shaped cross-sections and amphitheater heads. Tremendous differences in mean annual rainfall occur between these slopes. Windward slopes receive up to two orders-of-magnitude greater rainfall than leeward slopes because of orographic effects. However, it is unlikely that the remarkable morphometric and morphologic differences can be explained solely by the assymetry of the rainfall-runoff regime. This seems especially true because undissected valleys also occur between the dissected valleys on the windward slopes.

Groundwater sapping processes are suspected to play a dominant role in producing the observed morphometric differences outlined in Table 1. Evidence favoring the importance of groundwater sapping comes from a combination of studies of imagery, topographic maps, field observations, and laboratory experiments. The contribution of groundwater to the formation of large Hawaiian valleys was suggest by early workers (Stearns 1966, Macdonald et al. 1983). They noted the coincidence of central volcanic dike swarms with the headward terminations of the large valleys and suggested that erosion of these valleys was being augmented by the flow of groundwater from perched aquifers trapped by the dikes. Runoff valleys probably continued to incise until some of them tapped the perched aquifers. Once the aquifer was tapped, valley growth rates were exceedingly rapid. These sapping valleys grow at the expense of neighboring runoff valleys through subsurface piracy.

Morphometric analyses done on topographic maps of 53 basins draining the slopes of Kohala and Molokai indicate strong differences in basin morphometry between valleys presumed to be influenced by sapping and those formed solely by runoff. The differences are statistically quantifiable using multivariate analysis and discriminant analysis techniques.

Field reconnaissance of several large valleys on Hawaii and Molokai verified the influence of groundwater sapping on these valleys. Plunge pool erosion appears to be minor in the large valleys. Few pools were observed and hanging tributary valleys enter main valleys via waterfalls without major recesses in the straight main valley walls. In addition, large springs occur at the base of amphitheater valley heads even if no falls were there. Preliminary chemical analyses of water above and below the valley heads indicates discharges are from groundwater sources.

Runoff valleys between the large sapping valleys on Kohala have been unsuccessful in incising their channels to sea level, hence, they enter the sea as spectacular coastal waterfalls. The lower few km of many of these valleys exhibit morphometries suggestive of sapping processes. These

valleys probably began sapping when their floors intersected perched dike waters, but have developed at retarded rates or may have ceased enlargement by groundwater sapping when their groundwater recharge areas were beheaded by subsurface piracy by the neighboring large sapping valleys.

An evolution of morphometric development of these sapping basins can be suggested based on these studies (Fig. 1). Runoff valleys are elongate and have high drainage density with parallel channels. Once sapping begins, the amphitheater-headed form grows headwardly, gradually consuming the valley. Sapping valleys have lower drainage density, dendritic patterns, and tremendous cross-axial relief (Fig. 1). Eventually, as for several basins on Molokai, no uplands remain. Mature valleys exhibit light-bulb shapes in plan view with increasing basin width toward the head. Runoff and mass wasting processes continue to modify the valleys by widening, reduction of relief, and gradually increasing drainage density. Valley forms on Oahu and older Hawaiian islands are indistinct because of coalescing valleys and continued degradation.

Our flume sapping experiments in unconsolidated sediments have resulted in similar evolutionary scenarios as the one proposed for Hawaii through the use of subsurface aquifers (Kochel et al. 1985). These morphometric relationships may prove useful in developing skills for interpreting the valleys networks on Mars with regard to runoff vs sapping processes.

TABLE 1

PARAMETER	RUNOFF-DOMINATED	SAPPING DOMINATED
BASIN SHAPE	VERY ELONGATE	LIGHT-BULB SHAPED
HEAD TERMINATION	TAPERED, GRADUAL	AMPHITHEATER, ABRUPT
CHANNEL TREND	UNIFORM	VARIABLE
PATTERN	PARALLEL	DENDRITIC
JUNCTION ANGLE	LOW (40-50)	HIGHER (55-65)
DOWNSTREAM TRIBS.	FREQUENT	RARE
RELIEF	LOW	HIGH
DRAINAGE DENSITY	HIGH	LOW
DRAINAGE SYMMETRY	SYMMETRICAL	ASYMMETRICAL low down-dip
A CANYON/A BASIN	VERY LOW	HIGH

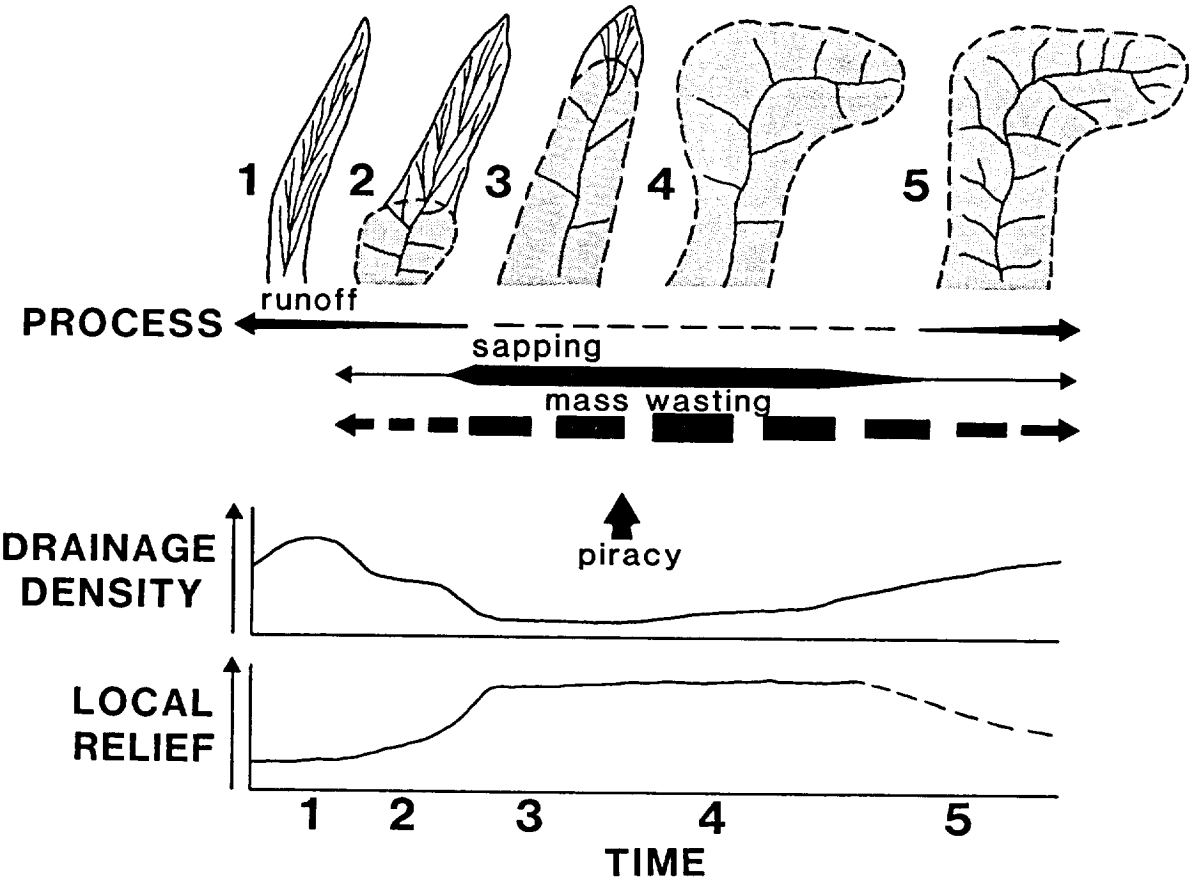

Figure 1. Evolution of sapping valleys on Hawaii. See text for explanation.

References

Kochel, R.C., Howard, A.D., and McLane, C., 1985, Channel networks developed by groundwater sapping in fine-grained sediments: analogs to some Martian valleys: in Woldenberg, M.J., ed., Models in Geomorphology, New York, Allen and Unwin, p. 313-341.

Macdonald, G.A., Abbott, A.T., and Peterson, F.L., 1983, Volcanoes in the sea, the geology of Hawaii, 2nd edition: Honolulu, Univ. Hawaii Press, 517 p.

Stearns, H.T., 1966, Geology of the state of Hawaii: Palo Alto, California, Pacific Books, Pub., 266 p.

MULTI-LAYERED SEDIMENTS AND GROUNDWATER SAPPING EXPERIMENTS

R. Craig Kochel and David W. Simmons, Department of Geology, Southern Illinois University, Carbondale, Illinois 62901

Experimental sapping studies have recently showed promise in providing analogs to help explain the development of amphitheater-headed valleys on Mars and in a variety of terrestrial situations (Kochel et al. 1985, Howard and McLane 1981). At Southern Illinois University, we have been experimenting with valleys developed by groundwater sapping in layered sediments in attempts to mimic the large valleys seen along the slopes of Hawaiian volcanoes where sapping processes are suspected to be important (Kochel 1986, this volume).

A series of sapping runs were done with uniform fine-grained sand from a Mississippi River point bar to trace the history of valley development in uniform materials. In uniform sand, 4 channels formed within the first few hours at equally spaced intervals across the 2.2 m wide flume. After about 6 hours, one of these channels ceased to flow because of subsurface piracy from neighboring channels. The remaining three channels continued to enlarge throughout the 46-hour run. Initially, channel head-cutting, widening, and incision rates were rapid. Growth rates equilibrated after 6 hours as amphitheater-headed valleys became established. Throughout the remaining 46 hours, growth rates remained more or less constant. Final morphology showed linear valleys with gradually tapering heads that terminated in blunt amphitheaters. No tributaries formed.

Experiments using a buried central layer of coarse sand as an aquifer with higher hydraulic conductivity resulted in different channel morphology. In these cases, 4 channels formed initially and grew rapidly for the first few hours like in the previous runs. Subsurface piracy again resulted in the abandonment of one of the central valleys. Constant growth rates occurred until channel incision tapped into the central aquifer at about 17-20 hours into the run (Fig. 1). After the aquifer was tapped, channel growth rates increased substantially (Fig. 1). In particular, the rate of head widening (B) and incision (C) increased. The outer dominant channels widened parallel to the aquifer and virtually joined at their heads, resulting in total piracy of water to central channels. The rate of head cutting virtually ceased after the aquifer was intersected.

When the run was terminted after 42 hours, the valleys exhibited a pronounced light-bulb shape with enlarged head regions. This morphology is strikingly similar to that displayed by the mature sapping valleys on Hawaii and Molokai discussed by Kochel (1986, this volume).

The wide heads of Waipio and Honokane valleys on Hawaii (Kohala Volcano) are suspected to have been formed in a similar manner. The Kohala valleys probably slowed their rate of head-cutting and increased their rate of head widening when perched water tables above dikes were intersected by the channels.

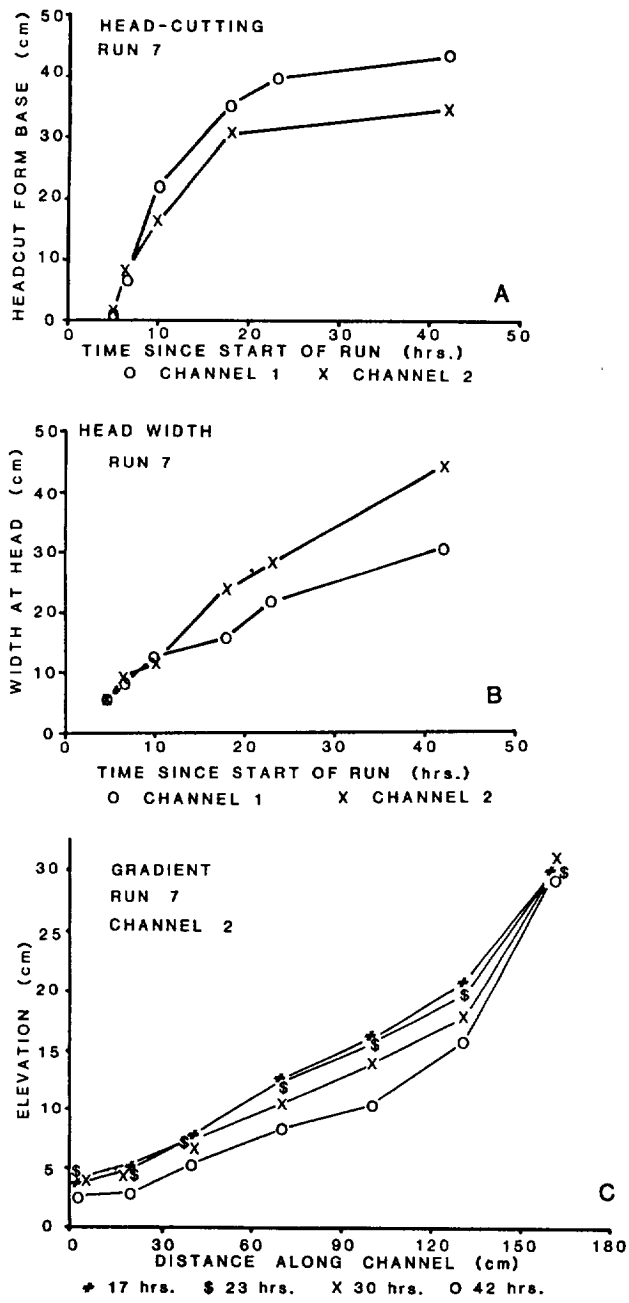

Figure 1. Channel development in flume sapping experiments with buried aquifer.

References

Howard, A.D., and McLane, C., 1981, Groundwater sapping in sediments: theory and experiments: N.A.S.A. Tech. Mem. 84211, p. 2883-285.

Kochel, R.C., 1986, Groundwater sapping and morphometry of Hawaiian valleys: this volume.

Kochel, R.C., Howard, A.D., and McLane, C., 1985, Channel networks developed by groundwater sapping in fine-grained sediments: analogs to some Martian valleys: in Woldenberg, M.A., ed., Models in Geomorphology, Boston, Allen & Unwin, p. 313-341.

HARMONIC SHAPE ANALYSES OF STREAMLINED LANDFORMS WITH RAMIFICATIONS TO THE ORIGIN OF THE MARTIAN OUTFLOW CHANNELS

Paul D. Komar, Karen E. Clemens, and Nicklas G. Pisias
College of Oceanography, Oregon State University, Corvallis, OR 97331.

Harmonic shape analyses have been undertaken on streamlined islands within rivers, on glacial drumlins and on the streamlined landforms found within the outflow channels on Mars. The objective was to determine whether subtleties in shapes of the Martian erosional residuals offer evidence as to their origin and thus to the erosion of the outflow channels.

Past studies have described these various landforms as elliptical to airfoil-shaped (Komar, 1984), so that harmonic analyses were first performed on those ideal end-member shapes, the geometric lemniscate representing the airfoil. The harmonic shape analysis technique was first employed by Schwarcz and Shane (1969) and Ehrlich and Weinberg (1970), and has been applied to investigate the shapes of lunar craters by Eppler et al. (1983). For the most part our analyses follow the same procedures. The shape analyses of the ellipses and lemniscates demonstrated that all harmonics vary systematically with the length-to-width (L/W) elongation. For a given L/W ratio, the even harmonics of the ellipse and lemniscate are almost the same and so offer little potential for distinguishing landforms of different origins. In contrast, the odd harmonics largely reflect shape asymmetry, and are zero for the perfectly symmetrical ellipse while having finite through small values for the lemniscates.

The second (C_2) and third (C_3) harmonics obtained in the shape analyses of the landforms are shown in Figure 1. The drumlins yield odd harmonics that are intermediate between the values for ellipses and lemniscates, but the lack of trends for the odd harmonics and best agreement of the even harmonics with the ellipses indicate that drumlins are more elliptical than airfoil-shaped. The streamlined river islands are seen to have reasonable conformity with the harmonic trends of the lemniscates, both for the even and odd harmonics. The Martian landforms yield still higher odd harmonics than the lemniscates, especially the triangular third harmonic. This is apparently due to their erosion in most cases having been controlled by flow separation around impact craters, producing more length-wise asymmetry than for the ideal lemniscate as well as a more triangular tail.

Discriminant function analysis is a statistical technique that permits simultaneous consideration of all of the harmonics in the landform comparison. A discriminant function was first determined using the ellipses and lemniscates as end members, and then the harmonic representations of the landforms were entered into this function yielding scores according to their similarities to these geometric end members. The scores for the drumlins ranged from ellipses to lemniscates, while the scores for the river islands distributed evenly around the mean score for the lemniscates, none falling into the ellipse range. Many of the Martian islands had scores that placed them in the lemniscate range, but more than half had

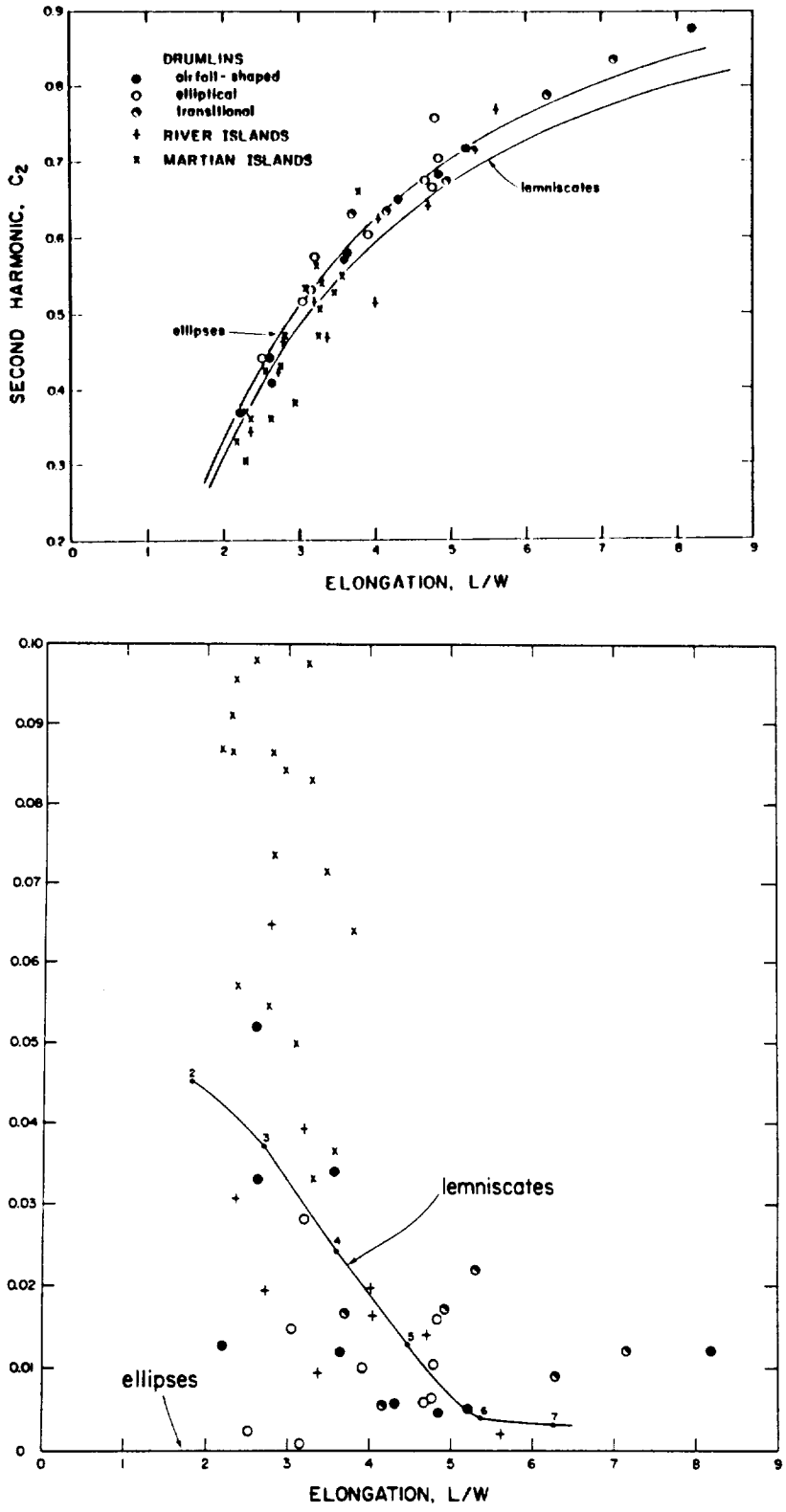
DRUMLINS
airfoil - shaped
elliptical
transitional
RIVER ISLANDS
MARTIAN ISLANDS
lemniscates
ellipses
SECOND HARMONIC, C_2
ELONGATION, L/W
THIRD HARMONIC, C_3
lemniscates
ellipses
ELONGATION, L/W

FIGURE 1:

scores indicating a significant departure. This departure is away from ellipses and drumlins, being in the direction of "super-lemniscates". The results indicate that the Martian islands are not at all drumlin like in shape, whereas they do overlap in shapes with the terrestrial river islands. The extreme scores of many Martian islands indicate, however, that they do have subtle shape differences from the river islands.

Diversion of flowing water by impact craters can be expected to have produced the observed contrasts in harmonic shape analyses between river and Martian islands, but this interplay between flow hydraulics, structural control and the resulting shapes as reflected in harmonic analyses requires further investigation. Flume experiments are now underway with this objective. Although the harmonic shape analyses do not provide a definitive conclusion as to the origin of the streamlined landforms on Mars, the results are consistent with their erosion by channelized water floods.

REFERENCES:

Ehrlich, R., and B. Weinberg (1970) An exact method for characterization of grain shape: Jour. Sedimentary Petrology, v. 40, p. 205-212.

Eppler, D.T., R. Ehrlich, D. Nummedal and P.H. Schultz (1983) Sources of shape variation in lunar impact craters: Fourier shape analysis: Geol. Soc. Amer. Bull., v. 94, p. 274-291.

Komar, P.D. (1984) The lemniscate loop — Comparisons with the shapes of streamlined landforms: Journal of Geology, v. 92, p. 133-145.

Schwarcz, H.P., and K.C. Shane (1969) Measurements of particle shape by Fourier analysis: Sedimentology, v. 13, p. 179-212.

THE EFFECT OF SLOPE ON EXPERIMENTAL DRAINAGE NETWORKS: POSSIBLE APPLICATION TO MARS

Loren F. Phillips and Stanley A. Schumm, Department of Earth Resources, Colorado State University, Fort Collins, Colorado 80523

Drainage patterns have been studied by geologists for over 100 years, and they can be important in yielding information about surface slope. Twenty-three drainage patterns have been identified (Zernitz, 1932; Parvis, 1950; Howard, 1967). Junction angle is a basic morphometric component of all patterns, and pattern classification rests largely on planimetric form and junction angle. However, no quantitative distinction between these patterns has been established, and quantitative relations between surface slope and pattern character have not been developed.

In order to investigate the effect of a systematic increase of slope on the development and evolution of drainage patterns a small 2 by 3 m tilting erosion-runoff flume (TERF) was designed and built. The major features of this flume are: (1) accurate slope control, (2) baselevel control, (3) variable sprinkler system, and (4) ease of operation and data collection.

The experimental material that was used is a homogeneous mixture of sand, silt, and clay with a D_{50} of 0.2mm. A falling head permeameter indicated a hydraulic conductivity of 3.04×10^{-4} cm/sec. Once the experimental material had been placed in the box, and the sprinkler system (set at low intensity) was in place, the slope was set at the desired inclination. This slope remained constant throughout the experiment. Baselevel was lowered 0.75 inches (1.9 cm) and the water was turned on to produce a miniature drainage network. When network growth was so slow that it was imperceptible, baselevel was lowered by 0.75 inches (1.9 cm) to rejuvenate the system. This procedure was repeated until the network filled the available space in the TERF.

Eight experiments were conducted at slopes of 1.06%, 2.13%, 2.93%, 3.72%, 5.05%, 7.45%, 10.1%, and 15.96%. Three conclusions result from these experiments as follows: (1) Glock's (1931) stages of network evolution were noted during all experiments. On steep slopes these stages were obvious, whereas on gentle slopes they were subtle and hard to distinguish, (2) Channel generations (groups of morphologically similar channels that evolve at different times during the development of a drainage network) were identified in all experiments. On moderate to steep slopes ($\geq$ 3%) channel generations are obvious, whereas on gentle slopes, channel generations are subtle. Primary generation of channels correspond to Glock's elongation stage, while secondary generation channels correspond to Glock's elaboration stage, (3) There was a definite pattern change from dendritic at a 1.06% slope, to sub-dendritic at a 2.13% slope, to sub-parallel at 2.93%, to parallel at a 5.05% slope.

Data on junction angles from one area in Wyoming (Walck Ranch and Jack Creek Quadrangles) and four areas on Mars were collected to compare with the experimental data (Table 1). Channel generations were not identified in the martian drainage patterns, perhaps due to resolution limitations of the images or the cessation of runoff in these networks at an early stage of development. Although there is a great disparity of age and scale between the martian and experimental networks, junction angles and patterns are similar for both. Therefore the formation of martian channels by surface runoff cannot be discounted.

References

Glock, W.S., 1931, The development of drainage systems: A synoptic view: Geogr. Rev., v. 21, p. 475-482.

Howard, A.D., 1967. Drainage basin analysis in geologic interpretation: Amer. Assoc. Petroleum Geol., v. 51, p. 2246-2259.

Parvis, M., 1950. Drainage pattern significance in airphoto identification of soils and bedrock: Highway Research Board, Bull. 28, p. 36-62.

Zernitz, E.R., 1932. Drainage patterns and their significance: Jour. Geol., v. 40, p. 498-521.

	EXPERIMENTAL PATTERNS				WYOMING PATTERNS	MARTIAN PATTERNS			
PATTERN	DENDRITIC	SUB-DENDRITIC	SUB-PARALLEL	PARALLEL	PARALLEL	PARALLEL	PARALLEL	PARALLEL	PARALLEL
SLOPE	1.06%	2.13%	2.93% & 3.72% (3.72%)	≥ 5.05% (10.1%)	2.36%	?	?	?	?
PRIMARY GENERATION JUNCTION ANGLES	N=70 X̄=64.4 S=21.2 Range: 32°-109°	N=190 X̄=61.3 S=17.0 Range: 28°-115°	N=273 X̄=41.8 S=20.9 Range: 14°-95°	N=59 X̄=36.8 S=9.4 Range: 17°-56°	N=49 X̄=43.1 S=14.6 Range: 14°-85°	N=19 X̄=40.6 S=10 Range: 21°-60°	N=15 X̄=40.7 S=15.7 Range: 24°-78°	N=37 X̄=40.4 S=13.2 Range: 16°-72°	N=9 X̄=41.2 S=13.8 Range: 21°-64°
SECONDARY GENERATION JUNCTION ANGLES	N=407 X̄ =81.1 S=15.0 Range: 47°-110°	N=432 X̄ =82.2 S=17.1 Range: 53°-102°	(3.72%) N=643 X̄=80.2 S=9.6 Range: 62°-94°	(10.1%) N=275 X̄=83.2 S=8.3 Range: 59°-99°	N=189 X̄=78.1 S=14.0 Range: 30°-104°				
SURFACE CONCAVITY	a=1 1/2"	a=1"	(3.72%) a=1/8"	(10.1%) a=3/4"		V.O.#853A01 LAT. 44.96° LON. 118.17°	V.O.#625A31 LAT. -24.99° LON. 266.88°	V.O.#606A56 LAT.-43.28° LON. 92.88°	V.O.#611A33 LAT. -24.19° LON. 23.71°

TABLE 1

CHAPTER 8

VOLCANIC PROCESSES

THE VALIDITY OF THE JEFFREYS' EQUATION FOR THE LAVA FLOWS AT ALBA PATERA, MARS

Stephen Baloga, David Pieri, Dale Schneeberger, and R. Stephen Saunders
Jet Propulsion Laboratory, Pasadena CA 91109

It is well-known that the Jeffreys' equation provides a mechanism for estimating the effective Newtonian viscosity of solitary lava flows from either dynamic or topographical data (1). Numerous terrestrial applications have attributed flow depth thickening with distance from the source of the extrusion to increases, as much as several orders of magnitude, in the viscosity. It is not widely recognized, however, that the Jeffreys' equation is a special solution of the Navier-Stokes equations and specific fluid dynamic conditions are required for its validity. Here, we discuss one important condition for validity and its relevance to the lava flows observed at Alba Patera.

Jeffreys' equation applications to terrestrial lava flows indicate that the viscosity changes downstream. However, the existence of a spatial viscosity dependence suggests that additional terms of the Navier-Stokes equations may need to be considered. In other works (2,4), the concept of a "viscous scale length", L_ν, has been proposed to characterize this dependence and illuminate the complex physical processes operating within the flowing lava. For a lava flow with an arbitrary spatially dependent viscosity $\nu(x)$ on a plane inclined at an angle θ, it can be shown that the steady-state Navier-Stokes equations simplify to

$$g \sin\theta + \nu^{-1}(x) \frac{\partial}{\partial x}\left[\nu^2 \frac{\partial u}{\partial x}\right] + \nu(x) \frac{\partial^2 u}{\partial y^2} = 0, \qquad (1)$$

where x and y are the downstream and vertical coordinates, respectively, $u = u(x,y)$ is the flow velocity, g denotes the gravitational constant, and $\nu = \nu(x)$ is the spatial viscosity dependence. The middle term in equation (1) represents the extension of the standard Jeffreys' formulation that accommodates a viscosity changing with distance from the source. To estimate the relative contribution of the terms (5), eq. (1) is rewritten with respect to characteristic parameters of the flow, u_o, ν_o, L_ν, and a flow depth scale length h_o. Thus, in dimensionless for

$$\nu(x)\left[\frac{\partial^2 u}{\partial y^2} + \omega^2\left(\frac{\partial^2 u}{\partial x^2} + \frac{\partial u}{\partial x}\frac{\partial}{\partial x}\ln \nu^2(x)\right)\right] + \beta = 0 \qquad (2)$$

where $\omega = h_o/L_\nu$ and $\beta = h_o^2\, g \sin\theta/(\nu_o\, u_o)$.

Eq. (2) indicates that $h(x) = h_o \cdot [\nu(x)/\nu_o]^{1/3}$, the steady-state Jeffreys' solution, is valid when the ratio of the characteristic flow depth to the viscous length scale is negligible. Detailed solutions of equation (2) and their mathematical properties

will appear elsewhere. Conceptually, however, it is clear that rapid changes in downstream viscosity relative to the depth of the flow require consideration of the full form of eq. (2).

We have analyzed the topographic profiles of 12 lava flows at Alba Patera (3), as well as numerous terrestrial flow morphologies. All of the Alba Patera flows and many terrestrial flows produce statistically satisfying results with the assumption that the viscosity increases exponentially downstream. The least squares fitted values of the viscous length scales for martian flows are shown in Table 1 along with flows from the 1951 Mihara eruption in Japan (6), the April 7, 1984 eruption of Mauna Loa, an emplaced Holocene flow on Mt. Shasta, and a flow from the May 1966 eruption on Mt. Etna (7). Two of these results, the Mihara and Mauna Loa values, were obtained from active flows. Because the maxima of the flow depths for the Alba Patera complex range from 75 to 150 meters, these viscous length scales suggest that the additional viscous shear terms in eqs. (1) and (2) were not significant, at least during the latter stages of emplacement. The terrestrial examples shown below support the same conclusion. It should also be noted the topographic profiles associated with flows listed in Table 1 increase exponentially downstream with a length scale $3L_v$ regardless of any theoretical considerations.

As a means of morphologically classifying flows with exponentially increasing topographic profiles, the "form factor",

$$F = \frac{L}{3\,L_v(\exp(L/3L_v)-1)}\,, \qquad (3)$$

has been suggested (2), where L is the length of the flow excluding the nose and $3\,L_v$ is the measured length scale of the flow depth profile. The form factor is a new quantitative morphological index that measures the distribution of lava downstream. Low F values indicate proportionately greater mass accumulation toward the flow terminus, while higher F numbers indicate more gentle flow depth increases downstream. Table 1 shows the form factor computations for the flows studied. Although the form factor may have a physical basis related to the considerations such as effusion rate history, viscous length scale, the validity of the Jeffreys' equations and so forth, the values shown in Table 1 are based completely on flow dimensions and are thus independent of any theoretical interpretations. In view of the difficulties inherent in remote topographical profile measurements, it is remarkable that Alba Patera flows show such consistency in form. Flow F-10 represents the only significant anomaly for which we have no explanation at present.

In future efforts, we plan to use these preliminary results as a starting point for constraining the time-dependent dynamics of Alba Patera flow emplacement, including effusion rate variations, duration of the eruptions, and compositional inferences. The results of this examination suggest that the time-dependent techniques developed in

reference (2) can be applied meaningfully to the topographic measurements of the lava flows at Alba Patera.

TABLE 1.

FLOW NAME	L (km)	L_v (km)	F
Alba Patera F1	383	83	.42
" F2	324	71	.42
" F3	286	66	.45
" F4	227	52	.44
" F5	449	84	.36
" F6	492	86	.33
" F7	71	14	.39
" F8	130	24	.36
" F9	215	42	.38
" F10	275	98	.61
" F11	177	31	.33
" F12	57	11	.38
Mauna Loa 1984	25	3.6	.25
Mihara 1951	0.43	0.1	.44
Etna 1966	0.05	0.08	.89
Shasta Holocene	7.0	4.3	.76

REFERENCES

1. Williams, H. and McBirney, A.R., 1979, Volcanology, Freeman & Cooper, San Francisco, 397 pp.
2. Baloga, S.M. and Pieri, D.C., 1985, "Time dependent lava flow thickness profiles", submitted to Jour. Geophys. Res.
3. Pieri, D.C. et al., 1985, "The dimensions of lava flows at Alba Patera, Mars", this volume.
4. Pieri, D.C. and Baloga, S.M., 1985, "Lava flow thickness profiles: time dependent solutions of the Jeffreys' equation", this volume.
5. Schlichting, H., 1968, Boundary Layer Theory , McGraw-Hill, New York, 747 pp.
6. Minakami, T., 1951, "On the temperature and viscosity of the fresh lava extruded in the 1951 Oo-sima eruption", Bull. Earthquake Res. Inst., 29, p. 487-498.
7. Walker, G.P.L., 1967, "Thickness and viscosity of Etnean lavas", Nature, 213, p. 484-485.

THE GEOLOGY OF ROUND MOUNTAIN, A BIMODAL VOLCANIC FIELD IN NORTHWEST ARIZONA

Mark M. Bush and John S. King, Department of Geological Sciences, State University of New York at Buffalo, 4240 Ridge Lea Road, Amherst, NY 14226

Round Mountain is a distinctive silicic volcanic center lying in the southwestern edge of the Colorado Plateau. It is located approximately 11.8 miles northeast of Seligman, Arizona and 3 miles due north of the Mount Floyd volcanic field. Round Mountain rises to a maximum elevation of 7080 feet above sea level and has a local relief of 880 feet.

Potassium-argon data from the Mount Floyd bimodal volcanic field, bordering the Round Mountain volcanics to the south, yield an age of 2.7 + 0.7 m.y. (Nealey, 1980). No potassium-argon dates are available for the Round Mountain volcanics, but it is considered by the authors to be younger than Mount Floyd, based on the observed volcanic stratigraphy.

Round Mountain has received no previous investigative attention. The purpose of this study is to develop a working hypothesis to describe the volcanic emplacement history of Round Mountain. This history will be used as a comparative tool to determine the relationships, if any, to the nearby Mount Floyd and San Francisco volcanic fields. Data have been collected from intensive geologic field mapping of approximately 8 square miles, whole rock chemical analyses, and petrographic investigations. In combination with the terrestrial volcanic study, an investigation of a planetary analog will take place to correlate possible origins of similar morphologic features of martian terrains to that of Round Mountain.

The volcanic rocks of the Round Mountain volcanic field are strongly bimodal, with basaltic and rhyolitic rocks occuring without the presence of those of intermediate compositions. Round Mountain is a volcanic dome composed predominately of successive rhyolite flows of limited lateral extent. These rhyolites have been classified on the basis of texture and color. Major textures observed were classified as brecciated, flow-banded, vesicular, and massive; the colors range through light gray, tan, dark brown, pink, and gray-black. The southern sector of the volcanic field contains light-gray perlites with elongate lenses of pure black obsidian, both of which are of rhyolitic composition.

The basalts that occur in intimate contact with the rhyolites are confined in the southern half of the volcanic field. These basalts occur as small domes, radiating dikes, flows, bombs, and cinders. Macroscopically, these basalts are very fine grained, usually containing olivine phenocrysts of 2-4 mm in size, with a few basalts containing xenolithic

quartz ranging from 2 to 6 mm in diameter.

Based on major element data, the basaltic rocks fall into two groups, those of olivine tholeiite and alkali compositions. The basalts of olivine tholeiite classification have subalkaline affinities, while the alkali basalts contain normative nepheline and therefore fall into the alkaline field as described by Chayes (1966).

Chemically, all the rhyolites sampled are strongly subalkaline with their alkali content tightly grouped at 9 percent. The rhyolites calc-alkaline based on Miyashiro's (1975) classification. Microscopically, these rhyolites are very glassy, commonly comprising 80 to 90 percent of the matrix, and containing phenocrysts of sanidine, plagioclase, and quartz.

Previous investigations of the southwestern Colorado Plateau by Eastwood and others (1974), and Shoemaker (1974), have shown strong correlations between the locations of volcanic centers relative to the locations of major fault systems on the plateau. Round Mountain lies along the southern projection of the northeastern trending Bright Angel fault system. This regional fault system may have been a controlling factor in the slight northeasterly elongation of Round Mountain. The preferential rhyolite flow direction to the south, could reflect either the local topography at the time of eruption or differential lava effusion from an asymmetrical vent.

The initial stages of eruption in the Round Mountain volcanic field were characterized by rhyolitic breccias. The first known stage of eruption is a pumaceous flow breccia which incorporated inclusionary clasts of perlite, pumice, and a variety of quartz grains and gravels. This was followed by a major breccia eruptive flow which contains mega-breccia clasts of various rhyolitic and perlitic textures, ranging from a few inches to 4 feet in diameter. The cumulo dome of Round Mountain continued development with successive superpositioned rhyolitic flows of varying textures.

The basalts in the southern end of the Round Mountain volcanic field intrude the previously emplaced rhyolite as domes and radiating dikes. The locations of these basaltic constructs are controlled in part by local faulting, which is a subsequent result of the structural adjustments made following the rhyolite eruptions. There is evidence to confirm that these basaltic constructs were formed by synchronogenic basaltic cinder and flow eruption phases.

There is no evidence to support a differentiation sequence from either an olivine tholeiite or alkali basalt to a subalkaline rhyolite. Due to the lack of those rocks of intermediate compositions, only a thermal relationship exists between the basalts and the rhyolites. The basalts are believed to be derived from the mantle by partial melting and then emplaced into a granitic crust as the heat source for the

generation of rhyolites. Further studies are in progress to determine whether any mixing of the basalt and rhyolite took place, and to determine the depths of rhyolite genesis.

REFERENCES

Chayes, F., 1966, Alkaline and subalkaline basalts, American Journal of Science, vol. 264, p. 128-145.

Eastwood, R. L., 1974, Cenozoic volcanism and tectonism of the southern Colorado Plateau, in Geology of northern Arizona, in Pt. 1 - Regional Studies, Geological Society of America Rocky Mountain Section Meetings, p.236-256.

Miyashiro, A., 1975, Volcanic rock series and tectonic setting, Annual Reviews Earth and Planetary Sciences, vol. 3, p. 251-269.

Nealey, David L., 1980, Geology of Mount Floyd and vicintity - Coconino county, Arizona, Northern Arizona University, M.S. thesis, p. 144.

Shoemaker, E. M., Squires, R. L., and Abrams, M. J., 1974, The Bright Angel and Mesa Butte fault systems of northern Arizona, in Geology of northern Arizona, in Pt. 1 - Regional Studies, Geological Society of America Rocky Mountain Section Meetings, p. 355-387.

LAVA-FLOW RHEOLOGY IN THE THARSIS REGION OF MARS

Andrew Fox, Planetary Geology Undergraduate Research Program, and Elliot C. Morris, U.S. Geological Survey, 2255 N. Gemini Dr., Flagstaff, Ariz. 86001

Yield strengths of 35 lava flows on the flanks of Alba Patera and Olympus Mons have been calculated according to the Bingham model (Hulme, 1974). Flows on these volcanoes were examined because (1) Viking high-resolution images are available; (2) the rheology of some flows in these areas has been studied (Hulme, 1976; Moore et al., 1978); and (3) new topographic data (Wu et al., 1981; F. J. Schafer, unpub. data, 1985) permit accurate measurement of flow dimensions.

Hulme (1974) suggested that lava-flow morphology can be related to the rheological properties of the lava and perhaps to its chemical composition. The final form of a flow is determined by the physical properties of the lava, including its temperature and rate of extrusion. Other parameters, such as the volume fraction of solids (Moore and Schaber, 1975), slope, and gravitational field strength, have also been shown to influence flow morphology. The hypothesis that lava behaves primarily as an isothermal Bingham liquid (Bingham, 1922) has been examined (Hulme, 1974; Moore et al., 1978), but the validity of the hypothesis has not been clearly established. It may be applicable for only a limited range of physical conditions, but it was assumed valid for the purposes of this study.

Hulme (1974) predicted the formation of levees in flowing lava. Many of the flows examined in this study display levees and related channels. The levee widths obtained from measurements on the Viking images and the new topographic information were used to calculate yield strengths, employing the Bingham model equations derived by Hulme (1974).

Most of our yield strengths (Table 1) were calculated for flows on Olympus Mons. Alba Patera flows exhibit fewer levees, probably because their gradients are lower: our measurements range from 0.005 to 0.047 on Alba Patera and 0.035 to 0.147 on Olympus Mons. The difference in flow form at the two volcanic centers may also be a result of variation in lava properties, such as viscosity and volatile content, or of different effusion rates (Carr et al., 1977). However, narrower, channeled flows are usually associated with steeper slopes.

The calculated yield strengths were plotted against their associated gradients (Fig. 1). The strong relation between yield strength and gradient is even more evident than that presented by Moore et al. (1978, Figs. 10, 11), and supports their conclusion that yield strengths are not constant for a given composition but vary with changes in slope. In fact, difference in gradient, rather than in composition, may be the only reason for the difference in the plots of the Olympus Mons and the Alba Patera flows. The plots of Moore et al. (1978),

however, show yield strengths clustered in groups according to composition. The yield strengths of andesites, rhyolites, and trachytes vary with gradient, but overall have higher values than basalts. Unlike the plots presented by Moore et al. (1978), the alignments of the yield strengths calculated for this study (Fig. 1) appear to be oriented more like those of terrestrial rhyolites and andesites than those of terrestrial and lunar basalts. This similarity may mean that Tharsis flows are more silicic and viscous than the basaltic lavas of the Hawaiian shield volcanoes (Hulme, 1976) or that the density of the Tharsis flows is less than the 2.8 gm/cm^3 value used in the calculations.

Yield-strength calculations for the Alba Patera flows were based on accurate elevations obtained on an analytical stereoplotter (F. J. Schafer, unpub. data, 1985); they vary by a factor of less than 1.5 for similar gradients. The Olympus Mons yield-strength calculations, however, were based on less accurate topographic information; for similar gradients, they vary by a factor of about 3.5. A factor that may be responsible for this variation in calculated yield strengths for a given gradient is the difference in aspect ratios (height/width) among the flows. Hulme (1974) emphasized the importance of a low aspect ratio when applying the Bingham model to a lava flow.

A general inverse relation exists between gradient and levee or channel widths. Measurement of levee widths, however, is difficult and imprecise because the initial levees are rarely preserved (Sparks et al., 1976). Different effusion rates on similar slopes may also account for variations in their widths. Also, unequal post-flow structural distortions of the surface may account for the problems encountered in comparing the calculated yield strengths of flows in different areas.

Although heights of the flows used to calculate yield strengths in this study were not measured, a comparison of flow heights and gradients reported for lunar, terrestrial, and Martian lava flows (Moore et al., 1978) is shown in Fig. 2. An expected inverse relation exists: the more viscous rhyolite and andesite flows are higher than the basalt flows on a similar gradient. Plots of the lunar flows, of assumed basaltic composition, lie in the same range as the terrestrial rhyolites and andesites, but such would be expected when the difference in gravity of the Moon and Earth is considered. The flows plotted in Figure 2 appear to segregate according to composition and gravitational field strength.

The application of the Bingham model to lava-flow rheology appears to have only relative utility, considering the uncertainties of flow characteristics involved, which include density, silica content, gradient, postflow distortion of the surface, and aspect ratio. When the model is used, comparisons between flows at different locations should be made with caution and only relatively.

REFERENCES

Bingham, E.C., 1922, Fluidity and plasticity: McGraw-Hill, New York, 440 p.

Carr, M.H., Greeley, R., Blasius, K.R., Guest, J.E., and Murray, J.B., 1977, Some martian volcanic features as viewed from the Viking Orbiter: Journal of Geophysical Research, v. 82, p. 3985-4015.

Hulme, G., 1974, The interpretation of lava flow morphology: Geophysical Journal of Royal Astronomical Society, v. 39, p. 361-383.

Hulme, G., 1976, The determination of the rheological properties and effusion rate of an Olympus Mons lava: Icarus, v. 27, p. 207-213.

Moore, H.J., Arthur, D.W.G., and Schaber, G.G., 1978, Yield strengths of flows on the Earth, Moon and Mars: Proceedings of the Lunar and Planetary Science Conference, 9th, p. 3351-3378.

Moore, H.J., and Schaber, G.G., 1975, An estimate of the yield strength of the Imbrium flows: Proceedings of the Lunar and Planetary Science Conference, 6th, p. 101-118.

Sparks, R.S.J., Pinkerton, H., and Hulme, G., 1976, Classification and formation of lava levees on Mount Etna, Sicily: Geology, v. 4, p. 269-271.

Wu, S.S.C., Garcia, P.A., Jordan, Raymond, and Schafer, F.J., 1981, Topographic map of Olympus Mons: 3rd International Colloquium on Mars, NASA, Pasadena, Calif., p. 287-288.

Table 1

Pic No.	Locations (deg.) Lat.	Long.	Gradient (sine θ)	Yield Strength (N/m^2) $p=2500\ kg/m^3$	$p=2900\ kg/m^3$
Olympus Mons					
890A66	20.6	133.2	.0443	$7.94X10^3$	$9.21X10^3$
DAS 05492413	19.814	134.585	.0729	$1.53X10^4$	$1.77X10^4$
47B21	21.80	133.08	.0443	$7.64X10^3$	$8.86X10^3$
222A18	16.45	135.29	.0664	$1.97X10^4$	$2.28X10^4$
694A39	16.16	137.44	.0555	$5.31X10^3$	$6.16X10^3$
222A67	16.54	129.47	.0767	$2.99X10^4$	$3.47X10^4$
222A26	16.46	129.44	.0767	$2.85X10^4$	$3.31X10^4$
47B25	21.99	130.50	.0426	$6.00X10^3$	$6.96X10^3$
694A42	15.50	137.24	.147	$4.55X10^4$	$5.28X10^4$
694A29	17.07	138.68	.109	$2.60X10^4$	$3.02X10^4$
694A32	16.4	138.5	.141	$5.14X10^4$	$5.96X10^4$
694A31	16.9	138.5	.145	$4.60X10^4$	$5.34X10^4$
694A41	16.0	137.2	.0443	$4.22X10^3$	$4.90X10^3$
694A35	16.5	138.0	.0797	$1.10X10^4$	$1.28X10^4$
47B27	22.1	129.2	.0352	$6.45X10^3$	$7.48X10^3$
48B16	23.43	130.87	.0400	$7.85X10^3$	$9.10X10^3$
45B36	13.97	136.79	.0555	$1.04X10^4$	$1.21X10^4$
45B40	14.22	133.92	.0500	$8.44X10^3$	$9.79X10^3$
45B44	14.48	131.04	.0555	$1.05X10^4$	$1.22X10^4$
890A36	20.20	127.66	.0500	$1.60X10^4$	$1.86X10^4$
Alba Patera					
252S23	33.65	117.63	.00526	$1.10X10^2$	$1.27X10^2$
252S69	43.61	110.05	.015		$3.34X10^3$
252S71	42.21	110.19	.016		$4.69X10^3$
252S73	40.75	110.26	.029		$1.07X10^4$
252S74	41.26	112.34	.029		$9.52X10^3$
252S76	39.90	112.48	.047		$2.46X10^4$
7B91	43.09	111.02	.008		$1.13X10^3$
7B92	41.23	111.87	.024		$8.42X10^3$
7B93	42.82	107.76	.011		$1.92X10^3$
7B94	41.21	109.27	.015		$3.39X10^3$
7B15	49.09	126.70	.0426		$2.26X10^4$
252S38	44.22	115.16	.011		$2.011X10^3$

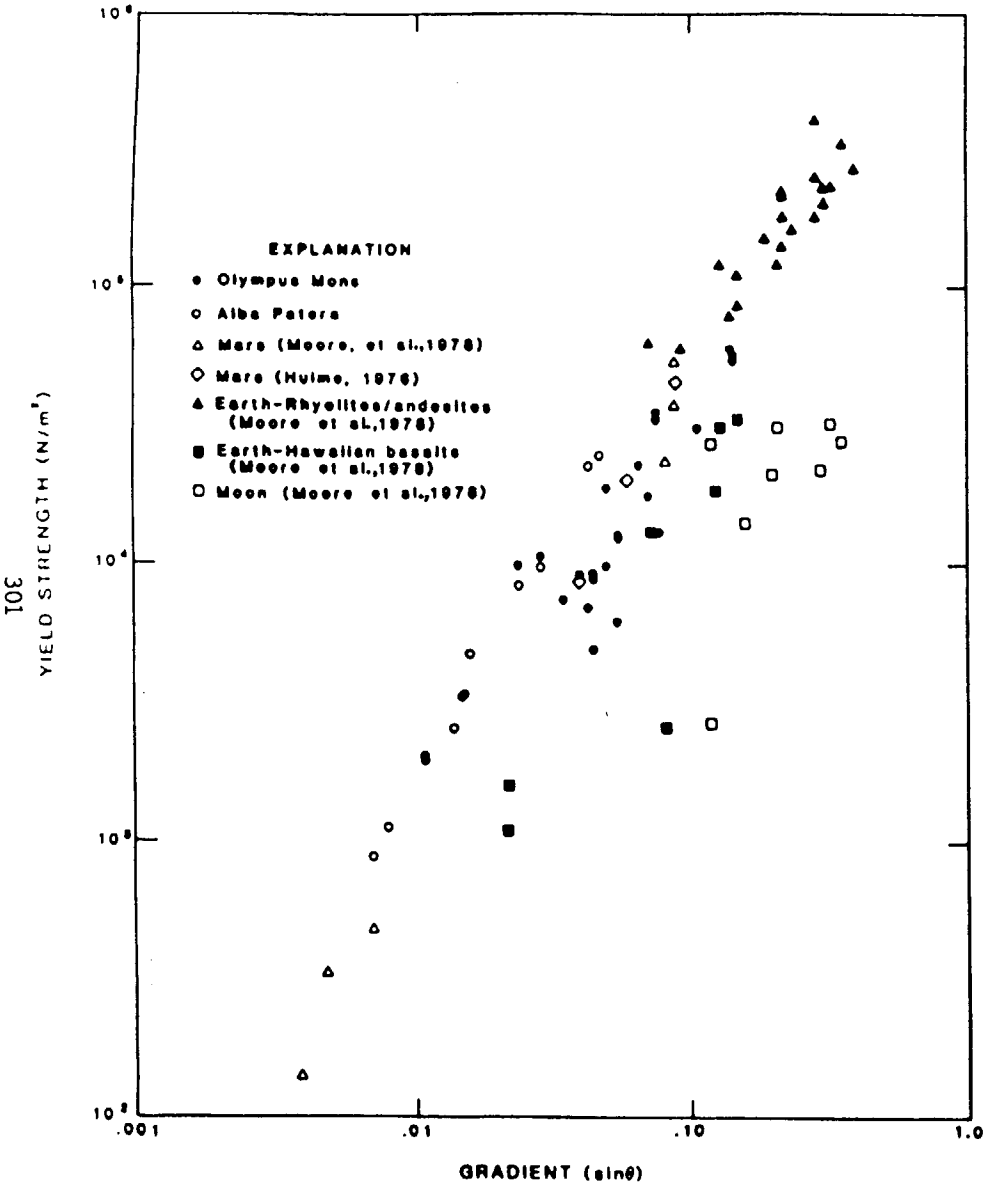

Figure 1. Comparison of yield strength computed by the equation $\tau_y = \rho g \sin^2\theta 2w_b$ (Hulme, 1976) and topographic gradient. Only highest estimates plotted.

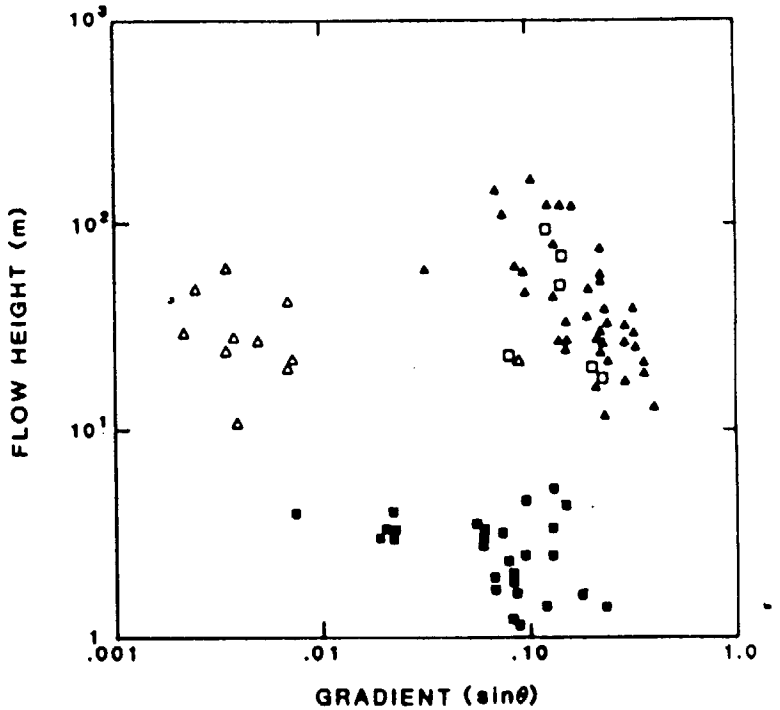

Figure 2. Comparison of flow height and topographic gradient (Moore et al. 1978). Symbols same as in Fig. 1. Note separation of terrestrial basalts and terrestrial rhyolites and andesites.

HADLEY RILLE, LAVA TUBES AND MARE VOLCANISM AT THE APOLLO 15 SITE

Ronald Greeley (1) and Paul D. Spudis (2). 1. Department of Geology, Arizona State University, Tempe, Arizona 85287. 2. U.S. Geological Survey, Flagstaff, Arizona 86001.

INTRODUCTION. Prior to the Apollo missions, the origin of sinuous rilles--including the Hadley Rille--was a contentious topic. Although most workers agreed that a fluid of some sort was involved in rille origin, the nature of the fluid and of the process(es) involved in rille formation were debated. Hypotheses included origins related to volcanic ash flows (1), water, including periglacial and fluvial processes (2), fluidization of regolith resulting from outgassing (3), and to processes associated with basaltic lava flows (4). Based on comparisons with terrestrial analogs, it was proposed that the Hadley Rille (and similar lunar sinuous rilles) was a lava channel, parts of which were roofed to form lava tube segments (5). This interpretation was based on observations that Hadley and other lunar sinuous rilles (6): (a) appear to originate in irregularly-shaped depressions (inferred to be vents), (b) trend generally down slope, (c) have discontinuous channels and cut-off branches, (d) are fairly uniform in width, or narrow toward the terminous, (e) are restricted to mare surfaces and appear to be controlled by pre-mare topography, and (f) may form topographic highs along their axes. Moreover, lava tubes and channels are common in certain types of basaltic lavas; thus with determination of basaltic compositions for the mare lavas, the lack of extensive ash flows, and the lack of evidence for water, the hypothesis for rille origin narrowed to the now-generally-accepted lava channel/tubes origin.

GEOLOGY OF LAVA TUBES AND CHANNELS. Results from the Apollo 15 mission raised several key questions regarding the general geology and volcanic history for the site, and the role of the rille in the emplacement of lavas within the Hadley valley (7). Among these are questions related to: the sequence and style of emplacement of the mare lavas; thickness(es) of the flow unit(s) and total flow accumulation; possible ponding of lavas in the Hadley valley; sources of glasses and other volcanic materials near the landing site; and explanations for the topography along the rille. Consideration of the general geology of terrestrial lava tubes and channels (8) may shed light on some of these questions:

1. Lava tubes/channels typically form in flows of basaltic composition (although they could form in other flows of comparable rheological properties), erupted at moderate rates of effusion (lower than flood eruptions); this style of eruption ("Hawaiian") tends to produce thin ($\leq$ 5m), flows that are produced by long-duration eruptive periods. However, the effusion of lava is sporadic, not continuous, and this results in surges of lava and the formation of multiple flow units.

In general, the longer a given eruption sequence is active, the better established and larger the feeding tube/channel system. Moreover, previous tube-channel systems are frequently reactivated by later flows, even after long periods of quiescence. Thus, one would expect to see multiple, thin flow units in the walls of Hadley Rille. Although the size

of Hadley Rille exceeds the largest of terrestrial tubes/channels by an order of magnitude, one might infer that it was the consequence of a very long-duration eruptive sequence, perhaps more than 100 years.

2. Flows fed through tubes and channels are emplaced by secondary (distributary) tubes and channels, as well as by overflow from open channels. Because lunar lavas are so low in viscosity (9), they would be expected to spread out in thin sheets from the rille as surges and flow units, leaving little in the way of flow fronts. The roofs of lava tubes, including distributary tubes, often rupture and produce local flows and other volcanic material. There is often the appearance of local vents that may, in fact, be "rootless". Thus, samples obtained in the vicinity of the Apollo 15 landing site may resemble near-vent products, but may have been derived from the cleft-shaped source-vent for the rille.

3. The formation of a tube roof, or of a crust on channelized flow, retards heat loss from the active lava, allowing greater flow lengths, and also retards loss of volatiles (in some respects, lava tubes are extensions of the vent conduit). Thus, some flow units emplaced via tubes/channels are vesicular at long distances from their source vents. On the other hand, fountain-fed flows may also collect and be emplaced via previously-formed tubes and channels; during fountaining, degassing often occurs. Thus, some of the flow units may also be nonvesicular.

4. Lava tube flows may erode by thermal (i.e. partial melting) and mechanical processes, as has been documented in terrestrial flows (10, 11, 12); in one case, a tube entrenched into pre-flow materials to a depth 4x the thickness of the flow (13). In addition, numerical models (14,15,16) suggest that extensive thermal erosion may occur in the development of lunar sinuous rilles. Thus, Hadley Rille may be entrenched substantially below the flow contact with valley floor. Thermal erosion (melting) could, in principle, alter lava compositions by assimilation during the lava flow emplacement via the tubes/channels.

5. Lava tubes/channels are primarily constructional features in that they emplace lava flows, both laterally and at the flow front. Accretion of lava along the sides of open channels, and via distributary tubes and channels raise the topography along its axis. However, the position of the tube may shift as it migrates (meanders) during active flow, and the axis does not always coincide with the topographically highest part of the flow. With drainage of the tube/channel and collapse of the roof segments, one side of the structure may be higher than the other side. In addition, the final "trench" may expose flow units of different textures and possibly different compositions, and the trench may cut into pre-flow rocks.

HADLEY RILLE AND APOLLO 15. Hadley Rille trends northwest and then east over 120 km in a valley between the Apennine scarp of the Imbrium basin and large terra slump blocks from the front. The rille is almost completely confined within mare material, although the source crater stradles the

mare-highlands boundary (5,17). At the Apollo 15 site, the east (near) rim of the rille is about 30 to 40 m higher than its corresponding farside. In this locality, the rille is about 300 m deep and 1500 m wide. Apollo 15 photographs and observations show that the rille walls expose at least three different mare units. The lowermost layered unit (8 m thick) is overlain by talus and debris (5 m). This sequence is overlain by a massive, poorly-jointed unit, about 17 m thick. On top of the massive unit is a thin (1-2 m) dark unit, on which regolith is developed (7). These exposures give direct evidence for at least 30 to 40 m thickness of basalt in the landing site area. On the basis of geologic reconstruction of returned mare samples, it appears that Apollo 15 olivine-normative and quartz-normative basalts are representative of the upper dark unit and middle massive units, respectively (18,19).

On one of the traverses, Scott noted a dark band and topographic bench along the base of Mt. Hadley. This bench, clearly seen on orbital pan photographs, has been taken as evidence that the mare lavas in the site vicinity were ponded in this area to a thickness on the order of 90 m (7). If this interpretation is correct, the rille may have served to drain this ponded lava. Of the two Apollo 15 basalt groups, the olivine-normative basalts show an olivine fractionation trend (20). Moreover, "peridotitic" basalts, originally interpreted as from a separate lava flow (21) but in fact, possibly related to the olivine-normative group by olivine crystal accumulation, are found in Spur crater ejecta, 60 m above the current mean mare topographic level. This may be consistent with ponding of the olivine-normative basalts in the site area; if the rille served as a conduit to drain the lavas, the 1-2 m thickness of olivine basalt observed at Sta. 9A is not a simiple flow unit, but a veneer of lava left by the draining lava lake. The present exposure of this unit within the rille wall would then be due to post-draining collapse of the rille walls inward (7).

A question of crucial importance to Apollo 15 site geology is the total thickness of basalt at the site. The actual LM site lies atop a low (5 m), broad ridge; at this location, only one (quartz-normative) mare basalt (15058) was collected. The remaining samples are regolith breccias (that contain comminuted mare basalt debris). Petrography of soils at this site indicate up to 50% non-mare material (22). Although this could be due to post-mare ray material (18), it is also possible that mare basalts in this area are very thin (23). This is not precluded by the observations of basalt in the rille walls; the LM site is 2 km from Sta. 9A and if 60 m of basalt pinched out to zero at the LM site, it would imply an average pre-flow slope of less than 2°.

It is possible the exposed portion of basalt seen in the walls of Hadley Rille represent the entire thickness of basalt at the site. In this case, rille formation must have included downcutting and erosion of some type (14). Both thermal and mechanical erosion during rille formation may have occurred, but it is difficult to say which was dominant. Significant

erosion by complete melting is unlikely because extruded mare lavas would not be superheated, as evidenced by phenocrysts in Apollo 15 mare basalts. However, some assimilation could produce partial melting of sub-mare, brecciated basement and this in turn would exacerbate mechnical erosion, which was probably already occurring during the high volume effusion of low-viscosity mare lavas (9). There is no evidence for a "delta" of eroded basement debris at the rille terminus, but this material could be covered by the late-draining lava pond, described above.

CONCLUSIONS. Hadley Rille appears to be a collapsed lava tube/channel, whose formational history may be more intimately related to the mare units sampled at Apollo 15 than had been previously thought. More work is needed relating samples and observations from Apollo 15 to the rille and its geologic evolution. As the only sinuous rille visited during the Apollo missions, Hadley Rille presents us with a data resource that is directly applicable to the deciphering of processes involved in lunar mare volcanism.

REFERENCES

(1) Cameron, W.S., 1964, J. Geophys. Res., 69, 2433.
(2) Lingenfelter, S., et al., 1968, Science, 161, 266.
(3) Schumm, S.A., 1970, Geol. Soc. Amer. Bull., 81, 2539.
(4) Oberbeck, V.R. et al., 1969, Modern Geology, 1, 75.
(5) Greeley, R., 1971, Science, 172, p. 722-725.
(6) Greeley, R., 1971, Moon 3, 289.
(7) Howard, K.A. et al., 1972, Proc. Lunar Sci. Conf. 3rd, 1-14.
(8) Greeley, R., 1985, U.S. Geol Survey, Prof. Paper, 1350, Hawaiian Volcanism (in press).
(9) Murase, T. and A.R. McBirney, 1970, Science, 167, 1491.
(10) Greeley, R. and J. Hyde, 1972, Geol. Soc. Amer. Bull., 83, 2397-2418.
(11) Peterson, D.W. and D.A. Swanson, 1974, Studies in Speology, 2, 209-222.
(12) Wood, C., 1981, Trans. Brit. Cave Res. Assoc., 8, 111-129.
(13) Greeley, R., and R. Baer, 1971, Geol. Soc. Amer. Abs., 3, 129.
(14) Carr, M.H., 1974, Icarus, 22, 1-23.
(15) Hulme, G., 1973, Modern Geology, 4, 107-117.
(16) Carr, M.H. and F. El-Baz, 1971, map USGS I-723.
(17) Head, J.W. and L. Wilson, 1981, Lunar Planet. Sci. XII, 427-429.
(18) ALGIT, 1972, Science 175, 407.
(19) Lofgren, G. et al., 1975, Proc. Lunar Sci. Conf. 6th, 79.
(20) Spudis P. and G. Ryder, 1985, EOS (in press).
(21) Dowty, E. et al (1973) Univ. New Mexico Spec. Publ.
(22) Heiken, G., 1975, Rev. Geophys. Space Phys., 13, 567.
(23) Horz, F., 1978, Proc. Lunar Planet. Sci. Conf. 9th, 3311-3331.

MARTIAN LAVA FLOWS: MORPHOLOGY AND MODES OF EMPLACEMENT

R. Greeley and E. Theilig, Dept. of Geology, Arizona State University, Tempe, Arizona, 85287

Volcanic terrains cover >50% of Mars and span nearly the entire visible history of the planet (1). Although Olympus Mons and other large volcanoes are impressive, they constitute less than 1% of the volcanic surface, with various volcanic plains being the dominant terrain. The geologic evolution of Tharsis has been described by Scott and Tanaka (2,3) who show that the region was built by a wide variety of lava flow types. The morphologies and flow textures reflect differences in styles of volcanism and modes of flow emplacement (4). The objective of this study is to assess some of the flows in southwest Tharsis and to use differences in morphology to interpret their emplacement and style of eruption.

Of the various flows, four were examined on high-resolution VO images: a) mega-ridged flows at 3°S, 138.2°W and 22°S, 141.1°W, b) ring-ridged flows at 21.6°S, 141.5°W, c) fissure flows at 22.2°S, 120.8°W, and d) tube and channel flows at 22.2°S, 120.8°W. All of these flows are associated with Arsia Mons; however, mega-ridged and ring-ridged flows represent early-to-intermediate activity, whereas the fissure flow and the tube and channel flows were emplaced during a later stage of activity (2,3,5-7).

Mega-ridged flows, described by Schaber (8), are characterized by ridges 40-200 m wide arranged in a festoon pattern transverse to flow direction. These ridges typically exhibit a regular spacing and are similar to ridges modelled by Fink and Fletcher (9) and Fink (10) as forming by compression of a flow in which viscosity decreases with depth. Even though the size (up to 50 m high) and spacing (100-400 m) of these ridges are consistent with dacitic or rhyolitic flows (8), the size and setting of the flows do not support this interpretation. Therefore a factor other than composition probably influenced ridge formation. The Trolladyngja flow, Iceland, may serve as an analog: the early stage eruptions were basaltic fissure-fed and produced some of the longest flows on Iceland; the distal portions were ponded and produced festoon ridges which evidently reflected increasing viscosity of the flow crust which folded with flow surges. Similarly, mega-ridges on the martian flows occur in the distal and marginal parts of the flows and where flow advance was inhibited by ponding against a highland area. Ponding of a flow either behind a halted flow front or from a topographic barrier could enhance large-scale folding by increasing viscosity as the flow cools and/or by allowing greater compressive stress within the flow if more lava is emplaced. By analogy to the Trolladyngja flow and because of the size of these flows and their occurrence >1000 km from Arsia Mons, mega-ridged flows are interpreted as being emplaced as flood basalts which in the late stages were folded in the terminal parts where the flows were ponded.

The ring-ridged flows are characterized by circular to elongate features 40-800 m across ranging from simple ring-ridges to mesas with smooth or knobby surfaces. Similar ring and mesa features 50-500 m across

are associated with terrestrial flood basalts and have been called "sag-flowouts" (11) and "ring structures" (12). These features are best exposed in the Columbia Plateau where Missoula flooding removed the overlying loess; although the extent of erosion is unknown, it appears minimal. On Earth, the ring structures are associated with unusually thick (70-100 m) sections of a flow and formed after a thick (~30 m) crust had developed. Two hypotheses have been proposed for their formation: 1) crustal foundering when density of the crust exceeds that of the molten interior (11) and 2) crustal sagging following phreatic eruption as water interacted with the molten interior (12). In both cases lava is intruded from the interior of the flow into cracks which, in places, intercept the flow surface. Ridges and mesas which form the ring structures are composed of crustal flow material and/or autointrusive dikes. The martian flows occur >1100 km from possible vents and the presence of the ring-ridges may imply thick flows which cooled as static pools of lava. This is consistent with the interpretation that these flows were emplaced as flood basalts.

Fissure flows range from massive--as in the emplacement of flood lava--to minor--as occur on the flanks of shield volcanos and in basaltic "plains" regions (13). The fissure flow examined on Arsia Mons is of the latter form; it issued from a fissure system >22 km long and formed a series of pressure ridges 20-270 m long and 20-90 m wide. These ridges appear analogous to inflational pressure ridges in Idaho and New Mexico in that they: 1) are similar in size (terrestrial ridges are 16-1000 m long and 4-100 m wide), 2) are located across the flow but tend to become larger and more numerous near the flow margin, 3) lack of regular spacing, 4) some ridges grade into low mounds, and 5) where ridges do not form the flow margin, the flow thins outward and no scarp is detected. Inflational pressure ridges are formed by inflation of the surface crust behind a slowly advancing flow front and are associated with long duration, sporadic eruptions with moderate effusion rates (14). By analogy, mapping of the ridges on the martian flow suggests that the flow moved predominantly down the fissure and that the fissure eruption was from point sources along the fissure, similar to some Hawaiian eruptions, and do not represent massive, continuous effusion.

Tube- and channel- flows are associated with the southwest rift zone of Arsia Mons and are characterized by channels 60-100 m wide, lobate flow outlines, and collapsed segments of lava tubes. These flows are indicative of prolonged, sporadic eruptions involving low-to-moderate rates of effusion, typical of shield and "plains"-forming volcanism.

This preliminary assessment of flows in southwest Tharsis suggests that the sequences of flow emplacement and shield growth is similar to basaltic volcanism on Earth: early stage eruptions were of high effusive rates to produce long, thick flows that were ponded in some areas, evidenced by surface features (large scale festoons, possible "sag-flow outs") found only on such flows; later eruptions involved local vents along

fissures and tube-and-channel fed flows, all indicative of prolonged, sporadic effusion, leading to shield-building volcanism.

REFERENCES: 1) Greeley, R., and P.D. Spudis, 1981, Rev. Geophys. Space Phys. 19, 13-41. 2) Scott, D.H., and K.L. Tanaka, 1981, Icarus 45, 304-319. 3) Scott, D.H., and K.L. Tanaka, 1984, unpublished map. 4) Greeley, R., 1976, Proc. Lunar Sci. Conf. 7th, 2747-2759. 5) Scott, D.H., and G.G. Schaber, 1981, U.S. Geol. Surv. Misc. Inv., Map I-1270. 6) Scott, D.H., G.G. Schaber, K.C. Horstman, and A.L. Dial, Jr., 1981, U.S. Geol. Surv. Misc. Inv., Map I-1271. 7) Scott, D.H., G.G. Schaber, and A.L. Dial, Jr., 1981, U.S. Geol. Surv. Misc. Inv., Map 1275. 8) Schaber, G.G., 1980, Icarus 42, 159-184. 9) Fink, J.H., and R.C. Fletcher, 1978, J. Volcanol. Geotherm. Res. 4, 151-170. 10) Fink, J., 1980, Geology 8, 250-254. 11) McKee, B., and D. Stradling, 1970, Geol. Soc. Amer. Bull. 81, 2035-2044. 12) Hodges, C.A., 1978, Geol. Soc. Amer. Bull. 89, 1281-1289. 13) Greeley, R., 1982, J. Geophys. Res. 87, 2705-2712. 14) Theilig, E., 1984, Geol. Soc. Amer. Absts. with Programs 16, 674.

THE ROLE OF LAVA TUBES IN HAWAIIAN VOLCANOES

Ronald Greeley, Department of Geology, Arizona State University, Tempe, AZ 85287.

Studies of terrestrial analogs have shed light on complex planetary features and have enabled a better understanding of planetary surface evolution. At the same time, such studies have also contributed to the solution of geological problems on Earth. This abstract represents a review paper of the geology of lava tubes in Hawaiian eruptions and represents work carried out principally through planetary analog studies. The paper will be part of the U.S. Geological Survey Professional Paper 1350 Hawaiian Volcano, to celebrate the Diamond Jubilee of the Hawaiian Volcano Observatory.

Studies of active and inactive flows show that lava tubes are involved in many aspects of Hawaiian eruptions. Rarely are either tubes or channels produced in the early phase of eruption, regardless of flow-type (aa, pahoehoe, etc.). Thus, short-duration eruptions (i.e., less than a day or two) seldom produce lava tubes (Holcomb, 1980). The often-stated comment that lava tubes form nearly exclusively in pahoehoe flows appears to be correct, although some tubes are documented in aa flows (Wentworth and Macdonald, 1953). Guest and others (1980) note that tubes are often found in aa flows near vents on Mt. Etna formed from long duration eruptions. Not all pahoehoe flows develop lava tubes, however, and factors other than the rheology must be involved. These factors are at least partly related to the style of eruption, especially in regard to the vigor, rate, and duration. Highly vigorous eruption, as reflected by fire fountaining, causes rapid changes in flow regime and lack well-defined channels to evolve to tubes. In addition, fire fountaining may degas the lava rapidly (Swanson and Fabbi, 1973), producing aa flows, most of which are too viscous to form roofs, or producing "degassed" pahoehoe which may not become channelized.

High rates of effusion, exemplified by the 1823 flow of Kilauea, may spread out rapidly as sheets, and fail to become channelized. Moreover, high effusion is often associated with fissure vents in which the zone of eruption shifts along the fissure; as such, there is not a focused flow of sufficient duration for channels and tubes to develop. Thus, the presence of lava tubes (Holcomb, 1980, Chapter 3) reflects a style of volcanism involving moderate rates of effusion and of durations typically greater than a day or two, and eruption of relatively fluid (e.g. pahoehoe) lavas that have not greatly "degassed".

Lava tubes may transport lavas between vents, along rift zones, and directly from vents to flow fronts. They are effective conduits for the emplacement of the longest flows on Hawaii and play a critical role in the sub-marine extension of many flows. Although not well documented in Hawaii, erosion by both thermal (melting) and mechanical ("plucking") means appear to take place by flow within some tubes.

Thus, in summary, lava tubes develop from eruptions that typically involve: 1) moderate rates of effusion, 2) durations greater than a day or two, and 3) effusion of fluid (e.g. pahoehoe) lava that has not been greatly degassed. Although some fountain-fed lavas and aa flows can form lava tubes, such occurrences are rare in Hawaii. Lava tubes feed flows: 1) directly from the vent (acting as extensions of the conduit), 2) from various "holding" reservoirs (e.g. lava ponds, lava lakes, filled pit craters), and 3) from flows on the flanks of volcanoes. Historic flows of greatest length in Hawaii were emplaced primarily via lava tubes, and many subaqueous flows involve lava tubes. Sustained flow of lava in tubes appears capable of erosion into pre-flow terrain. Photogeological analyses suggest that at least 30% of the flows (by area) on Mauna Loa, 58% of the flows on Kilauea, and 18% of the flows on Mount Etna were at least partly emplaced via tubes. Differences in the percentages for the three volcanoes studies may reflect differences in data analysis or may represent differences in evolution or "stage" of development. Nonetheless, their high occurrence in all cases demonstrate that lava tubes emplace many of hte flows in the evolution of basaltic volcanoes.

The identification of lava tubes and channels or extraterrestrial surfaces may allow styles of eruption and modes of flow emplacement to be better interpreted based on analysis of terrestrial analogs.

REFERENCES

Guest, J.E., Underwood, J.R. and Greeley, R., 1980, Role of lava tubes in flows for the Observatory Vent, 1971 Eruption on Mount Etna: Geology Magazine, v. 117, p. 601-606.

Holcomb , R.T., 1980, Kilauea Volcano, Hawaii: Chronology and morphology of the surficial lava flows, unpublished Ph.D. thesis, Department of Geology, Stanford University, 321 p.

Swanson, D.A. and Fabbi, B.P., 1973, Loss of volatiles during fountaining and flowage of basaltic lava at Kilauea Volcano, Hawaii: Journal of Research, U.S. Geological Survey, v. 1, p. 649-658.

Wentworth, C.K., and MacDonald, G.A., 1953, Structures and forms of basaltic rocks in Hawaii: U.S. Geological Survey Bulletin, v. 994, 98 p.

RECENT(?) VOLCANISM IN THE VALLES MARINERIS, MARS

B. K. Lucchitta, U.S. Geological Survey, Flagstaff, AZ 86001

High-resolution stereoimages of the central Valles Marineris troughs show that they contain young deposits that unconformably overlie all other units. The albedo, shape, and association of these deposits suggest that they are of volcanic origin (Lucchitta, 1985).

Conspicuous among these deposits are small (generally less than 5 km in diameter), very dark patches. These characteristically occur along faults (fig. 1) and are here interpreted to be composed of mafic or ultramafic volcanic materials. Dark mantles on the Moon have been recognized as mafic and ultramafic pyroclastic deposits (Heiken et al., 1974), but on Mars the association of dark patches with volcanism has been largely overlooked because many dark patches contain dunes and are obviously accumulated by the wind. The evidence that dark patches in the Valles Marineris are of volcanic origin comes mostly from their association with structures: they are aligned along the basal fault of the north wall of Coprates Chasma, along the basal faults of the wallrock spur separating Ophir and Candor Chasmata, and along a young fault in central Candor Chasma that offsets layered basin beds. Elsewhere, the dark material emanates from dark knobs and forms diffuse patches and short, stubby flows.

The dark patches locally terminate as feathery bands that extend from the center of the patches in two directions or radially. The observation implies explosive jetting of material from the source of the patches rather than eolian reworking of dark outcrops (necks, dikes, sills, or flows); wind tails commonly extend only in one direction. Furthermore, dark patches occur on top of landslide deposits that bury fault scarps; the dark material apparently penetrated the slides and thus postdates them.

Color ratios show that the dark materials in the Valles Marineris are relatively blue by Martian standards. The patches resemble in color and albedo those inside craters and in Kasei Vallis (Thomas, 1984; Singer et al., 1984). They are identical to dark patches in Juventae Chasma in color, albedo and morphology (Thomas, 1984). All of these dark deposits have been interpreted as wind-blown concentrations of slightly weathered mafic or ultramafic materials (Thomas et al., 1984) by analogy with terrestrial volcanic materials of compatible spectra (McCord et al., 1982). The color similarity of the dark patches in the Valles Marineris to other dark patches suggests that those patches in the Valles Marineris are also of mafic or ultramafic composition; their other characteristics suggest that they are the vents that furnished some of the dark materials concentrated by the wind elsewhere on Mars.

Further insights are gained by thermal-inertia measurements. Material of dark patches inside craters is thought to have grain sizes between 1 mm and 1 cm; dune material in these patches probably has grain sizes less than 0.5 mm (Christensen, 1983). Furthermore, the presence of dunes implies sand-size particles (Christensen and Kieffer, 1979; Peterfreund, 1981). Circumstantial evidence indicates that the dark material in the Valles Marineris has similar grain sizes: the materials are blown about and are apparently easily transported by the wind. On

the other hand, the movement appears to have been ground hugging, as dark materials are trapped in depressions and cracks and generally do not rise to the top level of interior deposits. The dark material apparently contains an abundance of saltating particles; it is also reworked into dunes. Both observations indicate particle sizes near 100 microns (Greeley et al., 1980). This size range is compatible with the size range of lunar pyroclastic beads (1 micron to 1 mm; McKay et al., 1978). The apparent prevalence of fine grain sizes in the dark deposits of the Valles Marineris is consistent with an explosive pyroclastic origin; a rarefied atmosphere may have resulted in the formation of pyroclastic beads like those resulting from fire fountains on the Moon (Heiken et al., 1974). On the other hand, materials could be composed of palagonitic glasses (Singer, 1982).

The dark deposits of the Valles Marineris occur only at elevations lower than 6 km above the Martian datum (Wu et al., 1980); the highest deposits are 3 km below the rim of adjacent plateau surfaces. This 6-km elevation appears to be the maximum height reached by extruding magmas. Inferences concerning the densities of magma fluids and surrounding country rock can be made by using this elevation and equating the weight of the liquid of the magma column with the weight of the surrounding solid country rock; the rock has exerted a hydrostatic pressure on the fluid, forcing it upward (Eaton and Murata, 1960; Vogt, 1974). Hypothetical magma of 2.8 g/cm^3 (Carr, 1981, p. 99) apparently was not able to reach the plateau surface surrounding the Valles Marineris; therefore, the column of combined crust and mantle rock must have been lighter than the liquid magma column. Upper crustal rock composed of poorly consolidated breccia mixed with water ice might fulfill such a requirement. Alternatively, the liquid in the magma conduit might have been heavier than solid crust and mantle rock of average densities.

The well-preserved, feathery edges of some of the dark deposits suggest that the deposits are young. Their youth is further indicated by the very low albedo (0.05) of some of the dark patches in the Valles Marineris; even minor additions of dust as a coating or as deposits trapped in cracks and crevices would significantly lighten the albedo of the dark material. Thomas et al. (1984) calculated that a coating that contains only 30%-50% light-colored dust (deposited in checkerboard fashion) will cause maximum contrast between light and dark areas on Mars. Only one quarter of the annual dust fallout (Pollack et al., 1979) is needed to form such a 30%-50% coating. Moreover, albedo of dark materials on Mars becomes visibly lightened if only 4% of a dark area is blanketed in checkerboard fashion by lighter dust (Thomas et al., 1984). Clearly, very minor amounts of dust trapped in crevices would lighten the dark patches significantly. In fact, some of the darkest Martian patches were totally obscured by a mantle of light-colored dust after the second dust storm of 1977 (A. McEwen, oral communication). This storm postdated the acquisition of the images on which albedo measurements were performed. The very low albedo of measured patches implies that little light dust is trapped in spite of frequent dust storms on Mars. It seems unrealistic to invoke removal of all traces of dust between storms. It appears more likely that the dark

patches are so young that they did not build up a dust cover sufficiently thick to lighten the albedo noticeably. If true, these considerations imply that the volcanism that formed the very low albedo patches in the Valles Marineris is of recent age.

References

Carr, M.H., 1981, The surface of Mars: Yale University Press, New Haven, Conn., 232 p.; Christensen, P.R., 1983, Eolian intracrater deposits on Mars: Physical properties and global distribution: Icarus, v. 56, p. 496-518; Christensen, P.R., and Kieffer, H.H., 1979, Moderate resolution thermal mapping of Mars: the channel terrain around the Chryse Basin: Journal Geophysical Research, v. 84, no. B14, p. 8233-8238; Eaton, J.P., and Murata, K.J., 1960, How volcanoes grow: Science, v. 132, no. 3432, p. 925-938; Greeley, R., Leach, R., White, B., Iversen, J., and Pollack, J., 1980, Threshold windspeeds for sand on Mars: wind tunnel simulations: Geophysical Research Letters, v. 7, no. 2, p. 121-124; Heiken, G.H., McKay, D.S., and Brown, R.W., 1974, Lunar deposits of possible pyroclastic origin: Geochimica et Cosmochimica Acta, 1974, v. 38, p. 1703-1718; Lucchitta, B.K., 1985, Young volcanic deposits in the Valles Marineris, Mars (abs.), in Lunar Science 16, The Lunar and Planetary Institute, Houston, Texas, p. 503-504; McCord, T.B., Singer, R.B., Hawke, B.R., Adams, J.B., Evans, D.L., Head, J.W., Mouginis-Mark, P.J., Pieters, C.M., Hugenin, R.L., and Zisk, S.H., 1982, Mars: Definition and characterization of global surface units with emphasis on composition: Journal of Geophysical Research, v. 87, no. B12, p. 10129-10148; McKay, D.S., Heiken, G.H., and Waits, G., 1978, Core 74001/2: grain size and petrology as a key to the rate of in situ reworking and lateral transport on the lunar surface: Proceedings Lunar Planetary Science Conference 9th, p. 1913-1932; Peterfreund, A.R., 1981, Visual and infrared observations of windstreaks on Mars: Icarus, v. 45, p. 447-467; Pollack, J.B., Colburn, D.S., Flasar, M., Kahn, R., Carlston, C.E., and Pidek, D., 1979, Properties and effects of dust particles suspended in the martian atmosphere: Journal Geophysical Research, v. 84, no. B6, p. 2929-2945; Singer, R.B., 1982, Spectral evidence for the mineralogy of high-albedo soils and dust on Mars: Journal Geophysical Research, v. 87, no. B12, p. 10159-10168; Singer, R.B., Cloutis, E., Roush, T.L., Mouginis-Mark, P.J., and Hawke, B.R., 1984, Multispectral analysis of the Kasei Vallis Lunae Planum region of Mars, in Lunar Science 15, The Lunar and Planetary Science Institute, Houston, Texas, p. 794-795; Thomas, P., 1984, Martian intracrater splotches: occurrence, morphology, and colors: Icarus, p. 205-227; Thomas, P., Veverka, J., Gineris, D., and Wong, L., 1984, "Dust" streaks on Mars: Icarus, v. 60, p. 161-179; Vogt, P.R., 1974, Volcano height and plate thickness: Earth and Planetary Science Letters, v. 23, p. 337-348; Wu, S.S.C., Schafer, F.J., and Jordan, R., 1980, Topographic mapping of Mars: 1:2 million contour map series, in Reports of Planetary Geology Program - 1980, U.S. National Aeronautics and Space Administration Technical Memorandum 82385, p. 458-461.

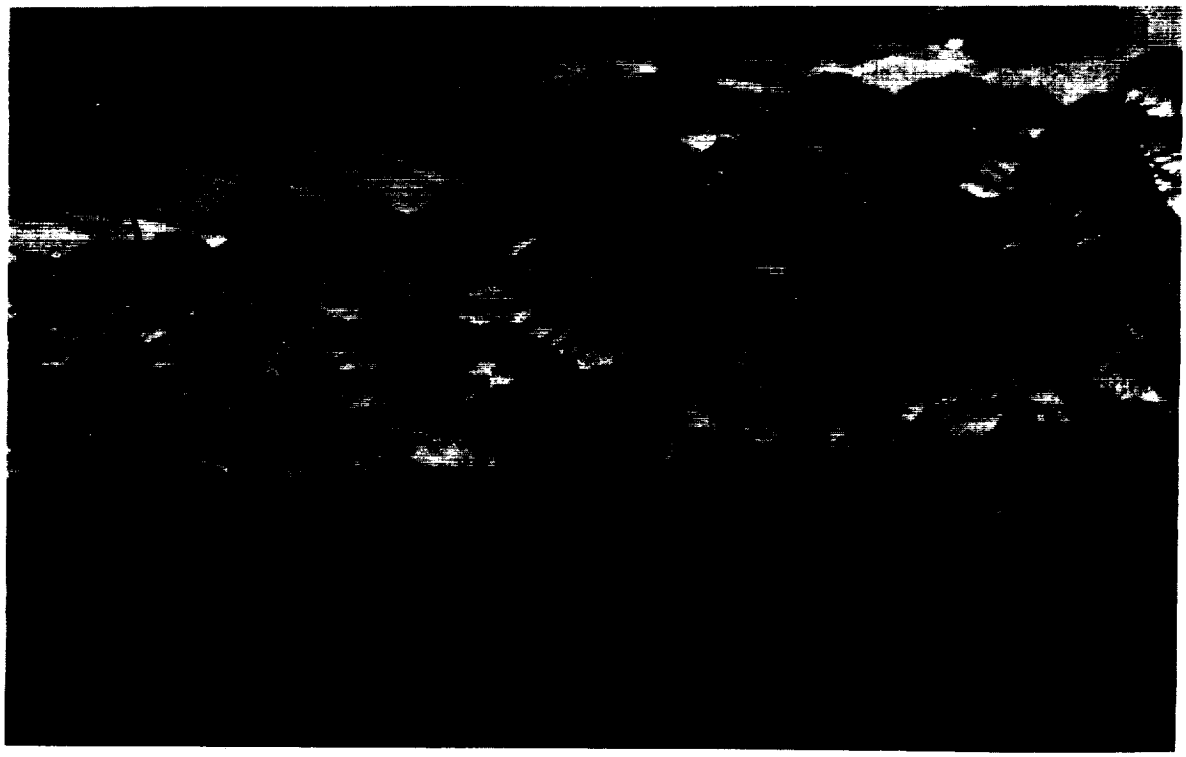

Figure 1

Fault scarp at base of north wall, Coprates Chasma, showing dark patches aligned along fault (Viking Orbiter Image 81A04).

LAVA FLOW PROFILES: TIME DEPENDENT SOLUTIONS OF THE JEFFREYS' EQUATION.

David Pieri and Stephen Baloga
Jet Propulsion Laboratory, Pasadena, CA 91109

As silicate lava flows lose heat, their effective viscosity increases. Field and laboratory studies suggest that monotonic viscosity increases of at least a few orders of magnitude occur in the flowing lava between the vent and the terminus of basaltic flows (e.g., refs. 1,2,3,4). Other physical processes, including radiative cooling, crystallization of the melt, vesiculation, volatile exosolution, and non-Newtonian shearing have received both theoretical and laboratory attention with regard to downstream changes along the flow and consequent effects on the morphology of lava extrusion. Nevertheless, viscosity, viewed either as a primary variable or the secondary result of other physical processes, must still be regarded as a dominating factor on the local character of the flow motion and morphology. A seemingly contrarian view holds that effusion rate is the dominant influence on lava flow morphology (ref. 5), supported by logarithmic correlations of eruption rate with length, although there seems to be significant scatter in the data on Hawaiian volcanoes (refs. 6,7). Effusion rate, however, is generally not a constant, and although morphological correlations with eruption rate have been investigated, there appears to be little data and analysis showing the effect of a time-dependent effusion rate on the morphology of individual flows (refs. 7,8).

Recognizing the interplay between effusion rate and viscosity, we have focused on the combined effects of the time dependence of the source effusion rate and the spatial dependence of the viscosity along the flow path. Holding constant all other variables (e.g., density, slope, flow width), the variable of interest is the lava flow thickness as a function of (1) time since the start of the eruption, and (2) distance downstream. The upper surface of the flow is a free-boundary which allows the longitudinal thickness profile of the flow to reflect the changing effusion rate and the viscosity influence accumulated along the flow. Only the main results of this approach are summarized here. The full theory development in provided in ref. (9). The governing nonlinear equation for the dynamics of the flow profile is taken as,

$$\frac{\partial h}{\partial t} + \frac{g \sin\theta}{3} \frac{\partial}{\partial x} \left[\frac{h^3}{\nu(x)} \right] = 0 \ . \qquad (1)$$

We have investigated the time-dependent lava flow thickness profiles associated with the solutions of eq. (1) for three distinct time-dependent boundary conditions at the source in combination with three models of the viscosity variation downstream. The forms chosen for the spatial viscosity dependence are: (a) a linear increase of viscosity with distance, $\nu(x) = \nu_o \ (1 + x/L_\nu)$; (b) an exponential increase of viscosity with distance, $\nu(x) = \nu_o \exp x/L\nu$; and (c) the so-called Arrhenius model, $\nu(x) = \nu_o \exp k(1 + x/L_\nu)^{1/3}/T_o - k/T_o$; where the variables are as described in Table 1. The third model assumes a Stefan-Boltzmann radiative heat loss for a fully thermally mixed flow. The general solution of equation (1) is given by

$$h(x,t) = (\nu(x)/\nu(0))^{1/3} \cdot H\left[(t/\tau) - \left[\frac{L\nu\ \nu(x)^{2/3} \int_0^{x/L_\nu} \nu(s)^{1/3} ds}{h(x,t)^2\ g\ \tau\ \sin\theta}\right]\right] \quad (2)$$

Here, a time-variable effusion rate is described by the functional dependence of H(t), the depth of the flow at its source. For each viscosity model, we impose three boundary conditions on the effusion rate via the flow depth, namely: (i) $H(t) = h_o$ = constant; (ii) $H(t) = h_o/(1 + t/\tau)$; and (iii) $H(t) = h_o [(t/\tau) e^{-t/\tau}]$. Case (i) is just the steady state, case (ii) is a monotonically decaying effusion rate, and case (iii) represents a rapidly rising, rolling over, then gradually falling effusion rate.

Typical flow thickness profiles resulting from the combinations of these models and boundary conditions are provided in Figure 1. There are two main morphologic end-members of thickness-distance profiles. The first is a **convex upward** profile produced by the linear viscosity-distance dependence for all three effusion-rate conditions. This character is observed in very silicic (e.g., rhyolite) flows erupting with the initial viscosity relatively close to its effective cessation viscosity. These flows attain their average thickness very rapidly and remain relatively flat in distal reaches.

The other profile type is a **concave upward** profile produced for the exponential and Arrhenius viscosity models by all effusion rate conditions. This profile is typical of Hawaiian flows erupting at initial viscosities ($\sim 10^3$ poise much lower than their effective cessation viscosities $\sim 10^{10}$-10^{11} poise at the flow terminal rampart, $\sim 10^7$-10^8 poise in the portion immediately upstream of the terminus--H. Moore, personal communication). These concave upward profiles are similar to thickness profiles measured for flows at Alba Patera (refs. 10,11). Subsequent investigations will explore the implications of time-dependent source conditions for the emplacement of the Alba Patera lava flows.

REFERENCES

1. Shaw, H.R., T. Wright, D.L. Peck, and R. Okamura, 1968, The viscosity of basaltic magma: an analysis of field measurements in Makaopuhi lava lake, Hawaii, Amer. Jour. Sci., 266, p. 255-264.
2. Pinkerton, H. and R.S.J. Sparks, 1978, Field measurements of the rheology of lava, Nature, 276 , p. 383-385.
3. Williams, H. and A.R. McBirney, 1979, Volcanology, Freeman, Cooper, & Co., San Francisco, 394 pp.
4. McBirney, A.R., and T. Murase, 1984, Rheological properties of magmas, Ann. Rev. Earth and Planet Sci., 12 , p. 337-358.
5. Walker, G.P.L., 1973, Lengths of lava flows, Phil. Trans. R. Soc. London, , Ser. A. 274, p. 108-118.
6. Malin, M.C., 1980, Lengths of Hawaiian lava flows, Geology, 8 , p. 306-308.
7. Pieri, D.C., and S.M. Baloga, 1985, Effusion rate, area, and length relationships for some Hawaiian lava flow, submitted to Jour. Volc. Geotherm. Res.

8. Wadge, G., 1981, The variation of magma discharge during basaltic eruptions, Jour. Volc. Geotherm Res., 11, p. 139-168.
9. Baloga, S.M. and D.C. Pieri, 1985, Time dependent lava flow thickness profiles, submitted to Jour. of Geophys. Res..
10. Baloga, S.M., D.C. Pieri, D. Schneeberger, and R.S. Saunders, 1985, The validity of the Jeffreys' equation for the lava flows at Alba Patera, Mars, this volume.
11. Pieri, D.C., D. Schneeberger, S.M. Baloga, and R.S. Saunders, 1985, Dimensions of lava flows at Alba Patera, Mars, this volume.

TABLE 1.

Symbol	Meaning	Symbol	Meaning
x	distance	g	gravity
t	time	h	slope
t	time constant	$\nu=\nu(x)$	viscosity
$h=h(x,t)$	depth	L_ν	scale length
H(t)	source depth	k,T_o	constants
h_o	depth constant	d	days

FIGURE 1. CAPTION

Typical time-dependent lava flow thickness profiles

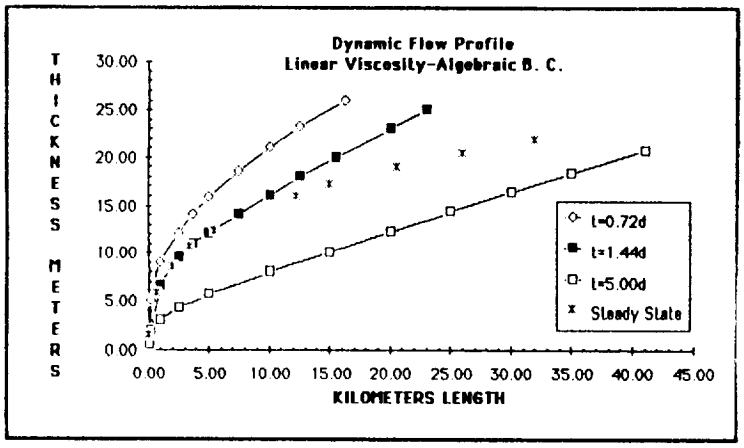

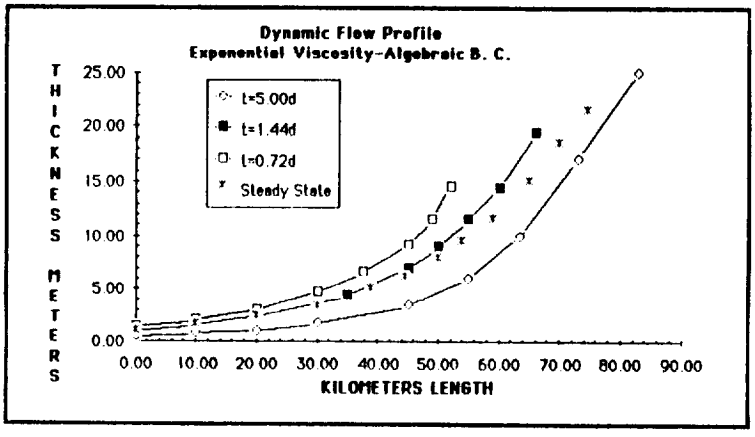

DIMENSIONS OF LAVA FLOWS AT ALBA PATERA, MARS

David Pieri, Dale Schneeberger, Stephen Baloga, and R. Stephen Saunders
Jet Propulsion Laboratory, Pasadena, CA 91109

The topographic thickness profile of a lava flow is perhaps one its most obvious and most useful characteristics (Walker, 1967; Booth and Self, 1973; Williams and Mc Birney, 1979; Moore, 1982 and personal communication, 1985). The thickness profile provides a powerful observational constraint on a number of important parameters, including the viscosity scale length, the initial viscosity, and the effusion rate (Baloga and Pieri, 1985a). Since flow thickness as a function of distance from the vent can be gotten from spacecraft image data by both shadow measurement and photoclinometric techniques, such data are accessible constraints on models for compositional and process parameters.

As a first step in creating a quantitative data base for martian lava flows, we have compiled dimensional data on 12 flows at Alba Patera (Figure 1, Table I). Flows were mapped from Viking Orbiter photomosaics at 1:700,000 scale (Flows F-1 to F-4, northwest flank), and 1:500,000 (Flows F-5 and F-6, southeast flank; Flows F-7 to F-12, intracaldera flows). Estimated lengths, measured widths, and estimated mean thicknesses are shown in Table I. Thickness estimates were recorded as a function of distance from the vent, however, for brevity Table I only includes maximum and minimum values. Despite the availability of clear image data with resolution in the range of 25-75 meters/pixel, several major uncertainties exist, the primary one being an inability to unambiguously identify the vents of individual flows. Most likely, this inability is due to the thinning of flows near the source, producing flow edge shadows shorter than the resolution limit of the pictures. Also, it is patently unclear how accurately the the flow edge thickness represents the average flow depth at a given distance from the source. Additionally, for complicated superjacent flow sequences, such as for flows F-1 to 4, the separation of individual flow units can be difficult. Finally, as with many terrestrial flows, the local pre-flow geometry is unknown, a situation compounded in the case of Mars, by unknown regional slope. Difficulties notwithstanding, to our knowledge, these data represent one of the most comprehensive dimensional data sets for extraterrestrial flows.

Lava flows at Alba Patera are astonishing in their volume and length. Observed flow lengths in the three groups examined range from about 60 km to over 500 km and the largest flow volume is estimated at over 500 km^3 (F-6 flow). By comparison, the 1859 flow on Mauna Loa, the longest subaerial flow on Hawaii, is about 60 km long with a subaerial volume of the order of 1-2 km^3. Even allowing that the 1859 flow may extend for tens of kilometers underwater (P. Mouginins-Mark--personal communication), the total volume is still almost certainly no more than a factor of 2 beyond the observed subaerial volume. The F-6 flow of Alba Patera is probably the longest discrete confined flow yet observed in the solar system. As a suite, the Alba Patera flows suggest tremendously voluminous and sustained eruptions and provide dimensional boundary conditions typically a factor of 100 larger than terrestrial flows (Baloga and Pieri, 1985b). Although such flows clearly

challange our ability to constrain compositional and formational parameters, their dimensions provide a basis for analytical comparisons with terrestrial flows.

REFERENCES

Baloga, S.M. and D.C. Pieri, 1985a, Time dependent lava flow thickness profiles, submitted to Jour. of Geophys. Res.

Baloga, S.M. and D.C. Pieri, 1985b, Estimates of lava eruption rates at Alba Patera, Mars, p. 245-247, Rpts. of Planet. Geol. Prog. 1984, NASA TM-87563, H. Holt & T.R. Watters, eds., 618 pgs.

Booth, B. and S. Self, 1973, Rheological features of the 1971 Mount Etna lavas, Phil. Trans. R. Soc. Lond., p. 99-106.

Moore, H.J., 1982, A geologic evaluation of proposed lava diversion barriers for the NOAA Mauna Loa Observatory, USGS Open-File Report 82-314.

Walker, G.P.L, 1967, Thickness and viscosity of Etnean lavas, Nature, 213 p. 484-485.

Williams, H. and A.R. McBirney, 1979, Volcanology, Freeman, Cooper, & Co., 394 pgs.

TABLE I.
ALBA PATERA FLOW MEASUREMENTS

FLOW NAME	LENGTH (km)	THICKNESS (m)		WIDTH (km)	
		MAX	MIN	MAX	MIN
F-1	401	113	27	119	68
F-2	340	97	26	100	29
F-3	307	86	21	97	39
F-4	249	97	24	50	24
F-5	454	102	32	19	2
F-6	497	126	36	35	8
F-7	72	120	27	3	1.3
F-8	131	80	13	2.6	1.6
F-9	219	125	27	10.3	0.5
F-10	278	104	27	9.2	2.3
F-11	189	175	47	8	1.3
F-12	61	124	45	6	2.5

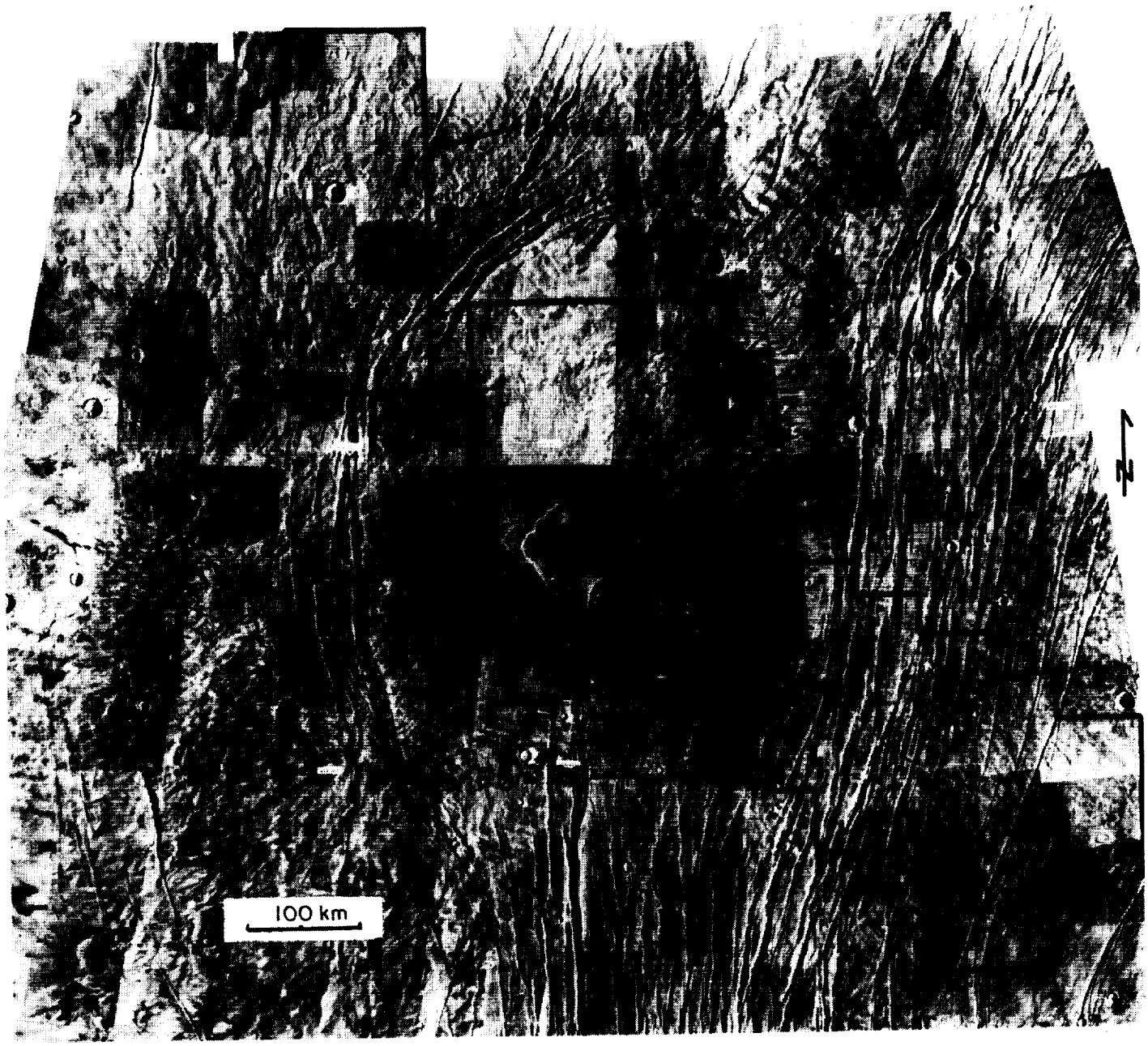

Figure 1: Index map of Alba Patera showing the general locations of lava flows for which dimensional data were collected.

GRAPHIC MODELS OF CLAST TRANSPORT DURING EXPLOSIVE VOLCANISM

Michael F. Sheridan and Jonathan Dehn, Geology Department,
Arizona State University, Tempe, AZ 85287

A series of two-dimensional graphic models were developed and tested as interactive codes on a micromputer as the first step in constructing three-dimensional models of particle transport by volcanic processes under various planetary conditions. A dynamic model of strombolian-type eruption and cinder cone growth was formulated on a microcomputer using the photo-ballistic study and model of McGetchin et al. (1974). The ballistic calculation of particle paths includes consideration of gravity, ejection velocity, atmospheric density, particle density, particle shape, particle size, wind velocity and vent geometry. For the graphic demonstration on the computer monitor a representative number of particles are traced on the screen through their ballistic trajectories and accumulated in an array where they arrive on the surface.

Cinder cone growth is modeled by continuous modification of the accumulation array generated by the strombolian eruption taking into account slope instabilities. Downslope movement by avalanche depends on variables such as the slope angle, the angle of internal friction, particle density, pre-existing topography, and slope stability models. A modified "energy line" algorithm (Malin and Sheridan, 1982) is used to test for the initial instability of the slope, followed by a slip face calculation to determine the size of the resulting avalanche (Terzaghi, 1950). This graphic model can be superimposed on a real topographic data set for comparison with the morphology of terrestrial cinder cones that have been observed to grow. This model reproduces the external form as well as the internal structure of the cinder cone.

A new dynamic model has been developed for pyroclastic surge and flow, also using a modification of the "energy line" algorithm. This model only depicts the movement of the cloud along the ground and does not yet consider deposition of tephra. The energy line model is static and does not yield good predictions for flow paths that are not radial from the source region. The new finite difference model determines the flow path given the initial velocity of the blast out of the vent and a digitial array that represents the surrounding topographic surface. The energy loss due to friction along the flow path is balanced against the sum of the initial energy and the energy loss or gain due to gravity, the positive remainder being expressed as kinetic energy. The change in flow acceleration due to gravity is calculated at sufficiently small increments of distance to allow accurate calculations of new flow velocity and flow path.

REFERENCES:

Malin, M.C. and Sheridan, M.F., 1982. Computer assisted mapping of pyroclastic surges. Science, v. 217, p. 637-639.

McGetchin, T.R., Settle, M., and Chouet, B., 1974. Cinder cone growth modeled after northeast crater, Mount Etna, Sicily. Jour. Geophys. Res., v. 79, p. 3257-3272.

Terzaghi, K., 1950. Mechanism of landslides in Paige, S. (editor) Application of Geology to Engineering Practice. Geol. Soc. America Berkey Volume, p. 83-123.

VOLCANIC COLLAPSE CRATER AT MOUNT HOPE, ARIZONA AND EXTRATERRESTRIAL ANALOGS

Ardyth M. Simmons and John S. King, Department of Geological Sciences, State University of New York at Buffalo, 4240 Ridge Lea Road, Amherst, NY 14226

Mount Hope is a low-silica rhyolite dome located about 70 miles northwest of Prescott, Arizona. Based on a general younging trend eastward across the southern margin of the Colorado Plateau (Arney and others, 1985), Mount Hope is believed to be the youngest in a group of silicic centers in the Mohon Mts. A flow at its summit was K-Ar dated at 8.0 + 0.9 m.y.

Underlying the breccias, tuffs and rhyolite flows whose source was Mount Hope are flows and small cones of andesite, basaltic andesite and basalt. Directly northwest of Mount Hope these flows form walls of a basin believed to be a collapse crater, as defined by Greeley and Schultz (1977). It has a level, sub-circular rim with a diameter of 1.2 miles, a nearly flat floor, wall relief of 500 feet on the west wall and only 150 feet on other sides due to greater erosion and subsidence. Structural control by faults does not appear to have influenced formation of the basin. Its present size can be attributed to enlargement by slumping and fracturing of portions of the western wall.

The flows dip less than 10 degrees westward from the basin, suggesting it was their source, although no evidence of a vent can be seen. Flows which form the western wall extend two miles westward; their original extent in other directions is not known because in other areas they have been eroded.

Eruption of the basin andesites preceded deposition of ash flow tuffs which initiated the first phase of development of Mount Hope. A portion of a magma chamber located at a relatively shallow depth beneath the Mount Hope basin could have caused the basin floor to collapse along fractures as magma withdrew laterally along fissures and located to the southeast beneath the present position of Mount Hope. While eruptive activity at Mount Hope was underway, gradual withdrawal of magma from the Mount Hope basin probably caused shrinkage of its nearly level summit and weakened the floor of overlying units. This process continued until the final stages of dome-building, when no magma existed beneath the basin. At this point isostasy was restored and the basin collapsed probably as a single block along bounding fractures. Later weathering and erosion could have been responsible for producing the present level relief of the crater floor as well as for scalloping the western wall and reducing its slope.

The Mount Hope basin is similar to a pit crater (Macdonald, 1972). The basin is a bit large for a pit crater; however, it formed over what appears to have been a small, shield-type fissure eruption and is associated with subsequent constructional activity at Mount Hope.

Similar collapse craters have been described in the Amboy lava field, California (Greeley and Bunce, 1976); Snake River Plain, Idaho (Spear, 1975); and Columbia Plateau, Washington

(McKee and Stradling, 1970). In these regions nearly circular depressions can be found which formed on the flanks or at the vents of basalt flows either by withdrawal of magma and subsequent loss of support or by sinking due to density differences between the crust and underlying magma.

Volcanic collapse depressions on earth are not limited in occurrence to one type of volcanic terrain, but can be found in provinces exhibiting explosive eruptions as well as those producing more quietly effusive fissure eruptions and shield volcanism. If one assumes that some of the same volcanic processes which operate on earth are also responsible for creating volcanic landforms on extraterrestrial bodies such as the moon and Mars, then the analog problem becomes a search for extraterrestrial terrains which exhibit major characteristics of differing styles of volcanism. Within broad areas of recognized volcanic terrain one must then search for smaller, secondary features which provide clues to the history of formation of the morphologic structures. A volcanic collapse crater will often be located near a constructional landform, as the Mount Hope basin is found adjacent to the dome. This is particularly true if magma withdrawal and eruption in a new location is responsible for loss of support resulting in the crater.

Collapse can occur for reasons not related to volcanic activity. In addition, heavy impact cratering can confuse or obscure recognition of small volcanic craters on Mars and the moon. However, circularity and dimension ratios aid in distinguishing between volcanic and crater-like features of other origins. The disinction is useful because dating schemes based on density of craters in an area break down when the size distribution of small lunar morphology classes does not match those predicted by an erosional model. Many sub-kilometer craters are probably of endogenetic origin, which would complicate dating with their use (Basaltic Volcanism Study Project, 1981).

The volcanic origin of martian landforms is evident from their geologic setting and morphologic similarity to terrestrial volcanoes. The most numerous volcanic structures on the northern plains of Mars are kilometer to sub-kilometer circular, dome-like structures which lack sharply defined rims. Pit diameters range from 0.25-0.45 kilometers and are generally about 40% of the diameter of the dome. Comparisons with crater/cone ratios of terrestrial volcanoes indicate Icelandic pseudocraters may be good analogs of the small martian cones (Frey and Jarosewich, 1982). Pseudocraters on earth are formed when lava flows over water-logged ground, causing a phreatic eruption. If the small martian cones are like Icelandic pseudocraters, they probably formed as a result of contact of lava with ice rather than with water.

Unambiguously volcanic craters on the moon are all less than three kilometers in diameter (Pike, 1980). Cratered volcanic edifices on the moon may be characterized as domes, cones, or dark halo craters. Little effusive activity appears to have occurred and the nearly rimless craters may be largely collapse pits and not true volcanoes (Pike, 1980). Examination of the crater frequency distribution for the Maunder Formation (Greeley, 1976) reveals a high number of craters about one kilometer in

diameter, higher than the number of comparably sized craters in the ejecta, which suggests an endogenetic origin for some of the craters (Schultz, 1972). Drainage through rilles could have caused general collapse of the crust of the Maunder Formation, leading to formation of endogenetic craters (Greeley, 1976). Mutch (1970) documents the presence of collapse craters in the maria; they are sub-circular, rimless depressions probably formed by collapse of a lava crust as lava was evacuated from below. Some may be source craters for lava flows. Even though most lunar craters which have been identified as volcanic are probably impact craters that have been volcanically modified, one cannot rule out the possibility of a volcanic origin for at least a small number of these when they are found within volcanic terrain.

REFERENCES

Arney, B.H., Goff, F.E., Eddy, A.C., 1985, Chemical, petrographic, and K-Ar age data to accompany reconnaissance geologic strip map from Kingman to south of Bill Williams Mountain, Arizona: Los Alamos National Laboratories, , LA-10409-HDR, 26 p.

Basaltic Volcanism Study Project, 1981, Basaltic Volcanism on the Terrestrial Planets: New York, Pergamon Press, 1286 p.

Frey, H., and Jarosewich, M., 1982, Subkilometer martian volcanoes: properties and possible terrestrial analogs: J. Geophys. Res. 87, p. 9867-9879.

Greeley, R., 1976, Modes of emplacement of basalt terrains and an analysis of mare volcanism in the Orientale Basin: Proc. 7th Lunar Sci. Conf., p. 2747-2759.

Greeley, R., and Bunce, T.E., 1976, Basalt models for the Mars penetrator mission: geology of the Amboy lava field, California: NASA Tech. Mem. TMX 73,125, p. 20-33.

Greeley, R., and Schultz, P.H., 1977, Possible planetary analogs to Snake River Plain basaltic features, in Volcanism of the Eastern Snake River Plain, Idaho: a comparative planetary geology guidebook, R. Greeley and J.S. King, eds., NASA.

Macdonald, G.A., 1972, Volcanoes: Englewood Cliffs, New Jersey, Prentice-Hall, Inc., 510 p.

McKee, B., and Stradling, D., The sag flowout: a newly described volcanic structure: Geol. Soc. Am. Bull. 81, p. 2035-2044.

Mutch, T.A., 1970, Geology of the Moon: Princeton, Princeton U. Press, 324 p.

Pike, R.J., 1980, Geometric interpretation of lunar craters: U.S. Geological Survey Prof. Paper 1046-C, p. 23-30.

Schultz, P.H., 1972, Moon Morphology: Austin, U. of Texas Press, 626 p.

Spear, D., 1975, Explosion-collapse hypothesis for the origin of Crater Rings, Elmore County, Idaho: SUNY at Buffalo, unpublished M.A. thesis, 30 p.

THE STUDY OF LONG LAVA FLOWS ON MAUNA LOA

George P.L. Walker and Scott K. Rowland
Hawaii Institute of Geophysics, Honolulu, Hawaii 96822.

We have established a correlation between the various basaltic lava structural types found on Hawaii with the rheological condition of the flowing lava. This correlation was made by measuring the distribution of mafic crystals (olivine, augite) contained in the lava. In a pahoehoe lava which is porphyritic, mafic crystals are typically depleted from the upper part of a flow unit and concentrated in the lower part. The close similarity of many of our measured crystal concentration profiles with theoretical profiles generated by numerical modeling indicates that a simple in-situ settling of crystals has taken place through the lava. The models yield crystal settling rates, which in turn yield lava viscosity values. We find that Hawaiian pahoehoe lavas had a viscosity of $<10^3$ to 10^4 poises, values which are similar to those measured in the field by Wentworth et al (1946), Macdonald (1963), and others.

The close similarity of our measured profiles with the theoretical ones also implies that the Hawaiian pahoehoe lavas were Newtonian or nearly Newtonian in rheology at the time when their crystals settled. This conclusion conforms with the observations by Shaw (1969) on Hawaiian lava, and experimental studies by Scarfe (1973), which show that basaltic lava is Newtonian at or near its liquidus temperature.

Similar studies demonstrate that Hawaiian "toothpaste lava" and "proximal-type" a'a had a distinctly higher viscosity than pahoehoe, namely $>10^4$ poises, but still had an approximately Newtonian rheology; which of these two structural variants formed depended on the flow velocity which in turn depended in part on the ground slope. We recognize another structural variant, namely "distal-type" a'a, and we conclude from the relative uniformity in crystal content and various structural features that this variant was not Newtonian but had a finite yield strength. We have developed a simple theory that correlates the four Hawaiian lava structural types with the flow velocity profiles, and hence shear rates, across them.

The relevance of this work to planetary volcanoes is that we can now examine meso-scale and mega-scale structural features on terrestrial lavas, and by inspection we can assess the rheological condition of the lava at the time when these structures were created. We can hence deduce the origin and significance of these structures.

As an example we can investigate the origin and significance of lava channels which are such common features of Martian and terrestrial lavas. We find that lava channels are common in proximal type a'a and also in some pahoehoe flows. They have upraised levees which on examination are found to have been built up by repeated overflow events, each of which deposited a thin layer of lava having Newtonian characteristics. We find that lava channels are almost invariably present in distal-type a'a and tend to be wider than those in proximal-type a'a. They also have a different structure, and we conclude that they were formed in the manner envisaged by the Binghamian model of Hulme (1974).

Another way in which our work is relevant to planetary volcanoes is that it throws further light on the debated question of what factors determine the lengths of basaltic lava flows (Walker, 1972; Malin, 1980). It is clear that several different factors contribute. For distal-type a'a, which is Binghamian, the distance may prove to be a rather simple function of discharge rate.

For pahoehoe two additional factors complicate the issue because they operate in opposing directions. One factor is the channeling of much of the flowing lava in lava tubes; by efficiently conserving thermal energy (Swanson, 1973), tube-flow enables lava having a low viscosity and Newtonian rheology to extend all the way from the vent to the far-distal end of the flow. The opposing factor is the very strong tendency of the lava to emerge from tubes from a multiplicity of secondary (rootless) vents to produce a great number of thin flow units.

We agree with Pieri and Baloga (1985) that thermal dynamics plays an important role in determining the final morphologic configuration of volcanic flows. The fact however that pahoehoe lava flows show an extreme subdivision into flow units implies that the effective cooling area is a multiple (for a lava flow 10 m thick, typically 15 to 20 times) of the actual plan area of the lava flow. In consequence, despite tube flow the overall rate of heat loss from a pahoehoe flow may be comparable with that from a distal a'a flow covering the same plan area. We are currently seeking ways to quantify these two complicating factors and hence compare the far-travel potential of pahoehoe and distal-a'a flows. Our field studies show that some of the long lava flows of Mauna Loa are channel-fed distal-type a'a along much of their length, while other similarly far-reaching flows are tube-fed and predominantly pahoehoe along their entire length.

References cited

Hulme, G., 1974 The interpretation of lava flow morphology. Geophys. J. Roy. Astron. Soc. 39, 361-383.

Macdonald, G.A., 1963 Physical properties of erupting Hawaiian magmas. Geol. Soc. Am. Bull., 74, 1071-1078.

Malin, M.C., 1980 Lengths of Hawaiian lava flows. Geology, 8, 306-308.

Pieri, D., & Baloga, S., 1985 Effusion rate, area, and length relationships for some Hawaiian lava flows. J. Volcanol. Geotherm. Res. (in press).

Scarfe, C.M., 1973 Viscosity of basic magmas at varying pressure. Nature Phys. Sci., 241, 101-102.

Shaw, H.R., 1969 Rheology of basalt in the melting range. J. Petrol., 10, 510-535.

Swanson, D.A., 1973 Pahoehoe flows from the 1969-1971 Mauna Ulu eruption, Kilauea Volcano, Hawaii. Geol. Soc. Am. Bull., 84, 615-626.

Walker, G.P.L., 1972 Lengths of lava flows. Phil. Trans. Roy. Soc. Lond., A, 274, 105-116.

Wentworth, C.K., Carson, M.H., & Finch, R.H., 1946 Discussion on the viscosity of lava. J. Geol., 54, 94-104.

NEAR-VENT PRESSURE IN PLANETARY VOLCANIC ERUPTIONS

L. Wilson (a, b) and P. J. Mouginis-Mark (b): a) Environmental Science Dept., Lancaster Univ., Lancaster LA1 4YQ; b) Planetary Geosciences Division, Hawaii Institute Geophysics, Univ. Hawaii, Honolulu, HI 96822

The pressure at which magmatic gases emerge through the vent in an explosive eruption is vital in determining the style of volcanic activity and there should be significant differences between the eruption styles of a given magma on different planets (1). In order to predict the morphological form of volcanic materials which might be observed in diverse planetary environments, we have been modelling aspects of volcanic eruptions on planetary surfaces (1). Part of this investigation has involved consideration of the ambient pressures into which volcanic materials have been erupted. Such pressures span a wide range: up to 30 MPa on the Earth's ocean floor, 4-10 MPa on Venus, 100 kPa at sea-level on Earth, about 30 Pa at the summit of Olympus Mons on Mars and probably less than one micro-Pascal on the night-side of Io.

The most obvious influence of planetary atmospheric pressure is in determining the extent to which dissolved volatiles can be released from a magma. Decompression of a rising magma leads to volatile saturation, gas bubble nucleation, and bubble growth; this may cause disruption into magma clots and released gas if bubbles occupy more than about 75% of the total magma volume (2). However, if the atmospheric pressure is high enough, as in the case of Venus (1) and on the terrestrial ocean floor, sufficient gas exsolution to lead to magma disruption may not occur for common magma gas contents, and only very volatile-rich magmas may erupt explosively.

The above only applies to steady explosive activity in which gas bubbles remain relatively uniformly distributed in the magma. If bubbles can rise at a speed comparable to or greater than that of the liquid (this can occur only in low effusion rate eruptions of low viscosity basaltic magmas; ref. 3), there is time for significant overtaking of small bubbles by faster, larger ones and runaway coalescence can occur, with large bubbles emerging intermittently through a lava lake in the vent to generate strombolian explosions. Since gas from a large volume of liquid is concentrated into a small fraction of the total volume, such activity can occur under much higher external pressures than the steady explosive discharge that characterises hawaiian or plinian activity on Earth. Thus, strombolian activity has been shown to be possible in magmas on Venus for carbon dioxide contents between about 3 wt % (below which steady explosive eruptions are not possible) and 0.02 wt % (4).

We have now extended our analysis to conditions on the terrestrial ocean floor and find that the range of volatile contents for which strombolian activity is possible is a strong function of the volatile solubility function and, hence, the depth of gas nucleation and the time available for gas bubble coalescence. If carbon dioxide dominates, then a very similar scenario to that given above for Venus emerges. However, if water dominates, at least 0.3 wt % must be exsolved if strombolian activity is to occur even at the lowest magma discharge rates. On the other hand, if more than 1.3 wt % are released, strombolian activity can occur down to ocean depths of at least 2 km.

These findings emphasise the extent to which the Earth's oceans provide an eruption environment analogous to that of Venus. However, we stress that there will be great differences in the dispersal of pyroclasts in the two cases due to the differences in the way that the magma volatiles interact with the local "atmosphere". On Venus the volatiles will remain gases as the eruption products mix with the atmosphere, whereas on the ocean floor on Earth water vapor will progressively condense on mixing and other gas species will progressively dissolve in the water. The general effect, the details of which are currently being studied, is to reduce the potential for convective dispersal of submarine pyroclastic eruption products.

Recently, Kieffer (5) has drawn attention to the significance of large-scale eruptions on Earth and Io in which the exit pressure in the vent is greater than the local atmospheric pressure. This situation is dictated by the shape of the conduit or fissure system connecting the magma reservoir to the surface. If, as magma accelerates (driven by gas expansion) from regions of higher to lower pressure, the velocity becomes equal to the local speed of sound (of order 100 m/s; ref. 3, 6) no further increase can occur unless the walls of the conduit system form an outward-flaring nozzle with a wall slope greater than a critical value (3). The amount of flaring required to allow supersonic speeds is quite small (generally in the range 0.2 to 1 degree; ref. 3), and it is an easy matter to show that the transition will occur at a pressure close to one half of that at which the magma disrupts into pyroclasts.

Once a supersonic velocity is reached, the gas/pyroclast mixture will continue to accelerate towards the surface as long as the outward flaring of the vent is maintained. However, as the ambient pressure decreases, the wall slope required increases. The consequence is that a vent must be both very wide and widely flaring to permit the exit pressure to be equal to the atmospheric pressure on a planet with a relatively thin atmosphere (3, 5, 7). Wilson *et al.* (8) have argued that, on Earth, the shapes of the vents associated with long-lived plinian or hawaiian eruptions (which are characterised by the relatively steady discharge of gas and pyroclasts) are generally able to evolve (either by the erosion of near-surface rock layers or by the appropriately-distributed deposition of pyroclastic material on top of the original surface) in such a way as to permit the pressure to be everywhere lithostatic at depth and in hydrostatic equilibrium with the atmosphere at the surface. However, in the early stages of an eruption, and throughout an eruption of short duration, it is likely that pressures in excess of that of the atmosphere will occur in the vent. In the case of Io, Kieffer (6) argues that so much change of the vent shape may be needed to allow the exit pressure to be equal to that of the atmosphere that in some cases such evolution does not take place even in long-lived events, and the entire eruption takes place under over-pressured conditions. A similar arguement would apply to eruptions in the lunar environment.

It is important to consider the matter of how commonly eruptions on planets with low or negligible atmospheric pressure have taken place under over-pressured or pressure-equilibrium conditions. The reason is that the dispersal of pyroclasts will be critically dependent on the vent geometry; the outward slope of the vent walls will fix the maximum angular distance from the zenith at which pyroclasts will be projected and this, together with the ejection velocity, determines the maximum range that they can reach. We have used the fluid dynamic equations describing magma eruption given in Wilson and Head (3) to simulate vertically-directed over-pressured eruptions on

Earth, Mars, the Moon and Io in which the pressure in the vent is held at the value corresponding to choked flow, i.e., the magma velocity is limited to the acoustic speed. We solve for the velocity of ejected pyroclasts and the slope of the vent walls and are thus able to calculate the maximum range of the ejecta.

Ejecta distributions calculated in this way are subject to two modifications. First, the excess pressure in the volatiles emerging from the vent is relaxed by the formation of a series of shocks (6). Passage of pyroclasts through these shocks will induce increased vertical and horizontal velocity components. Second, the pyroclastic material falling in the vicinity of the vent will exert a dynamic pressure on the surface. If a lava lake is present around the vent, this pressure will be communicated to the rising magma and may act to limit the amount of gas decompression in the vent.

This process is of potentially fundamental importance on Io and the Moon, where the negligible atmospheric pressure would otherwise lead to extremely thorough disruption of low-viscosity magmas (3). It provides a means of retaining significant amounts of gas in the liquid in a lava lake until such time as cooling of the surface of the liquid leaving the lake to form a flow can occur, thus providing a skin with appreciable mechanical strength. Preliminary calculations show that pressures of 1 to 70 kPa may be reached on Io (and the Moon) in this way, making it is possible to produce crusts rendered buoyant by trapped sulphur dioxide in sulphur lakes on Io and to generate vesicular sulphur flows. Similarly, vesicular basaltic lavas can be produced under lunar or ionian conditions.

Under martian gravity, pressures of 1 kPa to 0.2 MPa are possible (a factor of 10 to 100 times greater than the atmospheric pressure). On Earth, pressures may reach 2 or 3 times atmospheric in basaltic fire fountains and at least 10 times atmospheric in large scale ignimbrite-forming eruptions. The consequences of these conditions for the dispersal of pyroclasts are currently being investigated.

REFERENCES: (1) Wilson, L. & Head, J. W. (1983) *Nature 302*, p. 663. (2) Sparks, R. S. J. (1978) *J. Volcanol. Geotherm. Res. 3*, p. 1. (3) Wilson, L. & Head, J. W. (1981) *J. Geophys. Res. 86*, p. 2971. (4) Garvin, J., Head, J. W. and Wilson, L (1982) *Icarus 52*, p. 365. (5) Kieffer, S. W. (1982) in: *Satellites of Jupiter*, ed. D. Morrison p. 647. (6) Kieffer, S. W. (1977) *J. Geophys. Res. 82*, p. 2895. (7) Wilson, L., Head, J. W. & Mouginis-Mark, P.J. (1982) *ESA SP-185*, p. 107-113. (8) Wilson, L., Sparks, R. S. J. & Walker, G. P. L. (1980) *Geophys. J. R. Astr. Soc. 63*, p. 117.

VENUS VOLCANISM: THEORY AND PREDICTIONS OF VOLCANIC DEPOSITS AND LANDFORMS; L. Wilson[1,2], and J.W. Head[1], [1]Dept. Geological Sciences, Brown Univ., Providence, RI 02912; [2]Dept. Environmental Science, Univ. of Lancaster, Lancaster LA1 4YQ England.

The major mechanisms for lithospheric heat transfer on Venus are not well understood (1), although volcanism is thought to play an important role. On the basis of radar images and Pioneer-Venus mission results, several regions on Venus appear to be influenced by volcanic activity (2) and high-resolution radar images reveal volcanic centers and geologic units interpreted to be flows (3,4). In earlier papers we have modelled the ascent and eruption of magma on Earth and the Moon (5), and on Venus in the current Venus environment, taking into account the influence of the extreme surface temperatures and pressures on these processes (6). We predict the nature of effusive and explosive eruptions on Venus and compare these to similar eruptions under Earth conditions. In this paper, we use the previous work (6,7,8) as a basis to outline a series of predictions on the nature of volcanic deposits and landforms on Venus. On Venus, the large atmospheric mass is responsible for both a high surface pressure (40-100 bars) and a high surface temperature (650-750 K) and so leads to smaller values for both the pressure and temperature gradients in the upper part of the crust relative to those of the Earth. The pressure gradients are significantly different only within about 1 km of the surface, whereas the temperatures in the two planets at a given depth differ over a much greater range of depths. The fact that the temperature is higher at a given depth on Venus than on Earth will, therefore, tend to counteract the effects of possible water depletion of venusian magmas on their depths of origin. A further consequence of the lower venusian temperature gradient is that there will be less cooling of magma in the final stages of its approach to the surface. This means that the minimum fissure width needed to allow magma to reach the surface before significant chilling occurs will be smaller on Venus than on Earth and that the magma emerging through a fissure of a given width will be hotter on Venus. However, the differences between the two cases will not be very great so that the ratio of the heat loss rates is less than a factor of two even at the surface where the contrast is greatest. These minimum fissure widths are very similar to values calculated for basalts on the Earth and Moon (a natural consequence of the dominantly fourth root dependence of the minimum width on the other variables). Although the mass discharge rate in an eruption is controlled mainly by the fissure width and magma rheology in the lithosphere, the details of the eruption style are determined by processes occurring within the region extending from a few hundred m below the surface to a few tens of m above it. The vital subsurface process is exsolution of volatiles; the super-surface process is interaction of the magma with the atmosphere. The latter is particularly important if there is an explosive component to the eruption style as a consequence of volatile release. The main effect on erupting magmas of the high surface pressure and lower subsurface pressure gradient on Venus is the suppression or reduction of exsolution of volatiles (8). Even when explosions do take place in venusian magmas, less gas expansion occurs between the depth at which gas bubble nucleation begins and the level at or above the vent at which ambient pressure is reached than on any other terrestrial planet. On Venus both the temperature and the rheological properties of the lava in a flow leaving the vicinity of its vent are likely to be much closer to the properties of the magma at depth than on Earth.

VENUS VOLCANISM

Wilson, L. and J.W. Head

Following is a summary of the sizes of features and deposits predicted by our analyses as a first step toward the interpretation of volcanic landforms and deposits on Venus. Lava flows: Basaltic flows can travel for several tens of km from the vent if effusion rates are similar to those now on Earth; this can be extended to a few hundred km if lunar-like effusion rates occur. Strombolian (the intermittent discharge of gas and fluid magma): Coarse material (>0.3 m) can be projected ballistically to about 100 m; fine material (<10 mm) can be transported in small eruption clouds for up to 1-2 km. Hawaiian (the relatively steady discharge of magma which disrupts below or at the surface into released gas and pyroclasts with a range of grainsizes sufficiently coarse that little of the pyroclastic material is entrained into a convecting cloud over the vent): Fire fountains will be nearly vertical and hot ejecta will land very close to the vent; pyroclasts carried into eruption clouds can form welded deposits out to 1-2 km from the vent. Unwelded ash cones grade into ash layers several km from the vent and these grade into larger blankets formed in subplinian and then plinian eruptions. Plinian (the relatively steady discharge of magma which has disrupted into pyroclasts havint grainsizes sufficiently small that most of them are able to be entrained into an eruption cloud): Continuous variation of air-fall deposit size up to maximum of about 50 km wide and detectable deposits up to 100 km downwind of vent. Ignimbrites may travel for several tens of km but probably not more than 100 km. Vulcanian (the episodic discharge of magma, volatiles and accidental rock debris where the ejecta are coarse-grained and consist mainly of the accidental debris): Coarse material (>1 m) can be thrown ballistically to about 5 km (perhaps 10 km?) from the vent. Fine material carried in small eruption clouds can also travel to about 5 km. Any pyroclastic flows should be very localized within 1 km of the vent. Pelean (the episodic discharge of magma, volatiles and accidental debris where the pyroclasts consist mainly of fine-grained juvenile material): Air-fall deposits may extend to about 5 km from the vent. Pyroclastic flows may extend for several km (but less than 10 km). On the basis of these predictions, it would seem that lava shields with diameters up to 200 km would be relatively easy to produce from central vents in the Venus environment. Construction of larger (wider) shields would require additional non-central vents or effusion rates higher than those common on Earth. Stratovolcanoes produced from vulcanian or pelean activity could commonly have diameters up to 10 km and some could possibly extend up to 20 km in diameter. Ignimbrites and air-fall mantles could cover zones with long axes or diameters up to 100-200 km.

1. Solomon, S.C. and Head, J.W., J. Geophys. Res., 87, B11, 9236, 1982.
2. Masursky, H. et al., J. Geophys. Res., 87, 8232, 1980.
3. Campbell, D.B. et al., Science, 226, 167, 1984.
4. Barsukov, V.L. et al., Geochimie, 12, 1984.
5. Wilson, L. and Head, J.W., J. Geophys. Res., 86, B4, 2971, 1981.
6. Wilson, L. and Head, J.W., Ascent and eruption of magma on Venus, manuscript, 1985.
7. Garvin, J.B. et al., Icarus, 52, 2, 365, 1982.
8. Wilson, L. et al., Proc. Lunar Planet. Sci. Conf. 15th, 922, 1984 (abstract)

ASHFLOW CALDERA FIELDS

Charles A. Wood, SN-4, Johnson Space Center, Houston, TX 77058 and
Claire D. Duncan, Lunar & Planetary Inst., Houston, TX 77058

Introduction: Isolated volcanoes are rare. Except where volcanoes form along a line (e.g. above a subduction zone or along a rift valley) they typically occur in clusters of similar type volcanoes within a relatively well-defined area. Such a cluster is presumably the surface expression of a zone of melting within the mantle. Clustering is common both for small scoria cones (monogenetic volcanic fields - Wood, 1982) and for large ashflow caldera volcanoes. The best studied ashflow caldera field (ACFs) is the San Juan Volcanic Field of Colorado, which consists of more than a dozen separate calderas, each of which erupted 10^2-10^3 km^3 of ashflows. Individual calderas are often hard to recognize within ACFs because commonly they are very large and have very low relief. Frequently, the only clue that a mammoth caldera exists in an area is an extensive ashflow sheet. Many previous workers have mapped a variety of ashflow calderas, but only rarely is an ACF considered as a single magmatic unit, and rarer still are various ACFs compared. The notable exception being Peter Lipman's (1984) excellent analysis of structural and volcanic patterns among a number of ACFs in the western USA. We have attempted to extend Lipman's work by compiling and synthesizing existing data for 11 ACFs in the USA and Africa (Table 1).

ASHFLOW VOLCANIC FIELD SYSTEMATICS

ACF Name	Area	Volume	Lifetime	# of Calderas	Ave. Cald. Dia.	NND	Cald. Duration
Kane Springs	200	100	2.6	1	16	-	2.6
Long Valley	2000	500	3.0	1	23	-	0.7
Jemez	6200	600	1.3	2	16.5	28	0.3
Marysvale	25000	700	21	5	10.2	15	8.0
McDermitt	20000	1700	2.9	7	19.4	22	1.1
Tibesti	30000	3100	?	9	11.7	45	47.0
Timber Mt.	11000	6000	10.0	6	19.7	15	10.0
Yellowstone	17000	6000	2.2	3	54.3	33	1.4
San Juan	25000	20000	17.5	17	16.4	18	9.0
Nigeria	62000	?	50	44	?	25	?
Mog.-Datil	50000	100000	18.0	31	21.3	34	15.0

Notes: Mog.-Datil refers to the Mogollon-Datil field in southern New Mexico, and Nigeria to the Younger Granite Province of central Nigeria. Area is in km^2, volume in km^3, total field lifetime and caldera duration (the interval between the first and last calderas) in m.y., and NND (nearest neighbor distance) and average caldera diameter are in km. Data from a variety of sources.

Discussion: These 11 ACFs span 3 orders of magnitude in volume (which is a critical control on many aspects of volcanism from individual lava flows to planets), and include volcanic fields which are long dead and other active ones. It is assumed that this selection of fields provides information on changes in activity as a function of both field volume and evolutionary stage.

1) Field Area vs. Field Volume: Not surprisingly, these two measures of the size of a field increase together, although there is a break in the relationship. For areas <10,000 sq. km and volumes <1,000 cu. km. there is a rapid increase in area with volume; at larger sizes the area does not increase significantly whereas the volumes increase by a factor of 100. This roughly maximum area of ACFs (corresponding to circles with diameters of 70 km), may represent the size limit of underlying batholiths or magma source regions. The ACFs defining the rapid areal growth phase are all <3 m.y. old, whereas, the ACFs in the approximately constant area phase have lifetimes of 10-22 m.y. Thus, ACFs appear to reach their final widths (within a factor of two or three) in 3 m.y., and for the next 20 m.y. they simply grow thicker.
2) Field Volume vs. Caldera Number: The smallest ACFs, with volumes <500 cu. km., have only 1 caldera, but caldera number triples with each factor of 10 increase in volume. In other words, field volume increases not by proportionate increases in numbers of calderas, but rather by dramatic increases in the amount of erupted material at each caldera.
3) Field Volume vs. Average Caldera Diameter: For 10 of the sampled ACFs the average caldera diameter is about 15 km, with a range varying only from 10 to 23 km. This suggests that batholith cupolas - the magma chambers that volcanoes collapse into to form calderas - are approximately equal in size. The eleventh ACF - Yellowstone - has an average caldera diameter of 54 km! Two implications arise: Caldera size does not vary with total field volume; field volume increases not because of increased numbers of calderas, nor due to bigger calderas, but simply because each caldera is the vent for larger volumes of magmatic material. The second implication is that Yellowstone is either a unique volcano complex, or perhaps its caldera complexes result from multiple episodes of caldera collapse that have yet to be distinguished in the field.
4) Lifetime vs. Caldera Number: Caldera formation rate is among the most variable relations investigated. Average intervals between caldera formation range from 0.16 to 5.2 m.y., with an average of about 1.3 m.y. These values (which appear to be independent of field volume) may indicate the time required to establish or replenish a high level magma chamber.
5) Field Volume vs. NND: Nearest neighbor distance (NND) - the center to center distance of adjacent calderas - ranges from 15 to 45 km, apparently without correlation to any measured variable in this study. This is somewhat disappointing, but perhaps not surprising, for Mohr and Wood (1976) found that NND correlates with the thickness of the lithosphere for a variety of volcano types in East Africa. We have not yet determined crust/lithosphere thicknesses for all of the ACFs investigated.
6) Field Lifetime vs. Duration of Caldera Formation: Two ages can be distinguished (where fields are well dated) for each ACF: The total time interval between the earliest and latest

activity (e.g. from early cone construction to late stage dome eruption inside a caldera), and the time interval between and first and last formed caldera. The latter quantity is usually much better constrained than the former. For small volume fields caldera activity spans only .2 to .4 of the total field lifetime, but for more mature fields the caldera phase lasts .5 to .8 of the entire lifetime. This statistic obscures the fact that often, but not always, caldera formation occurs as a burst of activity, erupting the majority of total field volume, in just a short interval of total field lifetime.

7) Field Volume vs. Lifetime and Eruption Rate: The total duration of activity or lifetime of ACFs tends to increase with field volume; Marysvale is a pronounced exception with a long lifetime and a small volume. The general relation can be transformed into a more meaningful one by comparing the average eruption rate (volume/lifetime) and volume. There is a clear increase in eruption rate with total field volume, as is true for individual lava flows (Walker, 1973), scoria cones (Wood, 1980), and monogenetic volcano fields (Wood and Shoan, 1981).

Conclusions: The preliminary results recorded here demonstrate that ACFs have statistically predictable properties and general eruption habits. The single most important factor controlling ACFs is the total field volume: Given a field volume it is possible to make order of magnitude (or better) estimates of field area, lifetime, number of calderas, and eruption rate. Caldera size does not vary very much (except for Yellowstone), probably reflecting some limit on the dimensions of batholith cupolas. Near neighbor distances may reflect depths to magma source regions.

REFERENCES:

Lipman, P.W. (1984) The roots of ash flow calderas in Western North America: Windows into the tops of granitic batholiths. JGR 89, 8801-8841.

Mohr, P.A. and C.A. Wood (1976) Volcano spacings and lithospheric attenuation in the Eastern Rift of Africa. EPSL 33, 126-144.

Walker, G.P.L. (1973) Lengths of lava flows. Phil. Trans. R. Soc. Lond. A274, 107-118.

Wood, C.A. (1980) Morphometric evolution of cinder cones. J. Volc. Geothermal Res. 7, 387-413.

Wood, C.A. and W. Shoan (1981) Growth patterns of monogenetic volcano fields (abstract). EOS 62, 1061.

ESTIMATES OF YIELD STRENGTH, EFFUSION RATE, AND VISCOSITY FOR SIX LAVA FLOWS ON THE MARTIAN VOLCANO ASCRAEUS MONS

J.R. Zimbelman (Lunar and Planetary Institute, 3303 NASA Road 1, Houston, Texas, 77058) and J.H. Fink (Department of Geology, Arizona State University, Tempe, Arizona, 85287).

Measurements of the geometric dimensions of six well-defined volcanic flows near the summit of the martian volcano Ascraeus Mons were used to calculate the yield strength, effusion rate, and viscosity of the lavas. High resolution photographs (22 m/pixel) were used to measure flow dimensions at several locations along the six flows (Fig. 1). Relative heights were calculated from shadow lengths and the solar incidence angle and slopes at each location were obtained from a published topographic map (1). Estimates of potential errors due to the measurement procedures are less than a factor of two for yield strengths and less than a factor of three for viscosities (2).

Lava flow morphology has been related to the rheologic properties of lava by treating the flow as a Bingham material with a finite yield strength (3). Yield strength values can be calculated from the flow thickness, flow width, leveed channel width, slope, and density (4). Assuming a density of 2500 kg m^{-3} (4,5), the calculated yield strengths for the six flows range from 3.5 X 10^3 to 8.3 X 10^4 Pa, with an average value of 2.1 X 10^4 Pa (see Table 1). These values are comparable to yield strengths calculated for flows on other martian and terrestrial shield volcanoes (4,6) but they are a factor of 10 less than the values for terrestrial andesite and rhyolite flows (4) and a factor of 100 greater than the values for lunar flood basalts (7,8).

The lava effusion rate can be estimated from the dimensionless Graetz number which relates flow height, width, length, and thermal diffusivity to the cooling of the lava (7,9). The Ascraeus Mons flows are very intermingled so that the traceable flow length is only a lower limit to the total flow length (2,10). Measured flow lengths indicate lower limits for the effusion rate of 18 to 60 m^3 s^{-1}, with an average value of 35 m^3 s^{-1}. These results are consistent with the effusion rates observed for Hawaiian (11) and Icelandic (12) basaltic eruptions.

The effusion rate lower limits and the yield strengths can be used to calculate viscosity upper limits for the martian lavas. Calculated maximum viscosities range from 6.4 X 10^5 to 2.1 X 10^8 Pa-s, with an average value of 2.3 X 10^7 Pa-s (equal to 2.3 X 10^8 poise). These values are considerably larger than most laboratory or field measurements of viscosity for basaltic lavas (13) but they are comparable to field measurements on basaltic andesite lavas of Arenal volcano, where blocky/clinkery flow characteristics contribute to the large effective viscosity (14). The martian flow with the highest yield strength and viscosity (A in Fig. 1 and Table 1) has regularly spaced ridges near its distal end (Fig. 2). The ridge height and spacing allow an independent estimate of lava viscosity to be made using the viscosity model of Fink (15). The martian flow has a viscosity lower limit of 1.1 X 10^8 Pa-s for

a ridge growth time of 1 hour; this value is less than the largest upper limit value obtained at the distal end of the flow. Flows on Mt. Etna ceased their motion when the lava viscosity was 10^8 to 10^{10} Pa-s (16), consistent with the calculated viscosities for the martian flows.

Field measurements of relief on recent Hawaiian basalt flows where pre-flow topography was known indicate that the assumption of a planar pre-flow surface can significantly affect the calculated rheologic properties of the flows, particularly where flow thickness is important (17,18). No down-flow trends were evident in the rheologic properties of the martian flows but the precise cross-sections obtained for the Hawaiian flows do reveal a down-flow increase in yield strength and viscosity (17). The precision available from the Ascraeus Mons photographs is apparently insufficient to reliably detect down-flow variations in rheologic properties. Future work will include continued precise measurement of flow dimensions on recent terrestrial flows and analysis of clearly preserved flow features near the southern base of Olympus Mons (468S31-41).

References: 1) U.S.G.S. (1981) Map M2M 7/101T. 2) J.R. Zimbelman (1985) submitted to Proc. Lunar Planet. Sci. Conf. 16th. 3) G. Hulme (1974) Geophys. J. Roy. Astron. Soc., 39, 361-383. 4) H.J. Moore et al. (1978) Proc. Lunar Planet. Sci. Conf. 9th, 3351-3378. 5) B. Booth and S. Self (1973) Phil. Trans. Roy. Soc. Lond. A, 274, 99-106. 6) G. Hulme (1976) Icarus, 27, 207-213. 7) G. Hulme and G. Fielder (1977) Phil. Trans. Roy. Soc. Lond. A, 285, 227-234. 8) H.J. Moore and G.G. Schaber (1975) Proc. Lunar Planet. Sci. Conf. 6th, 101-118. 9) L. Wilson and J.W. Head (1983) Nature, 302, 663-669. 10) J.R. Zimbelman (1984) Ph.D. dissertation, Arizona St. Univ., Tempe, Arizona. 11) M.C. Malin (1980) Geology, 8, 306-308. 12) H. Williams and A.R. McBirney (1979) Volcanology, Freeman, Cooper, & Co., 101. 13) G.A. Macdonald (1972) Volcanoes, Prentice-Hall, 64. 14) C. Cigolini et al. (1984) J. Vol. Geotherm. Res., 29, 155-176. 15) J. Fink (1980) Lunar Planet. Sci. XI, 285-287. 16) G.P.L. Walker (1967) Nature, 213, 484-485. 17) J.H. Fink and J.R. Zimbelman (1985) submitted to Bull. Volcan. 18) J.H. Fink and J.R. Zimbelman (1985) this volume.

Table 1. Average rheologic properties for six martian lava flows (see Fig. 1).

Flow	Yield strength (Pa)	Minimum effusion rate ($m^3 s^{-1}$)	Maximum viscosity (Pa-s)
A	3.8×10^4	24	6.3×10^7
B	1.6×10^4	--	--
C	1.5×10^4	47	2.5×10^7
D	1.7×10^4	25	4.3×10^6
E	2.3×10^4	46	1.4×10^7
F	1.2×10^4	--	--

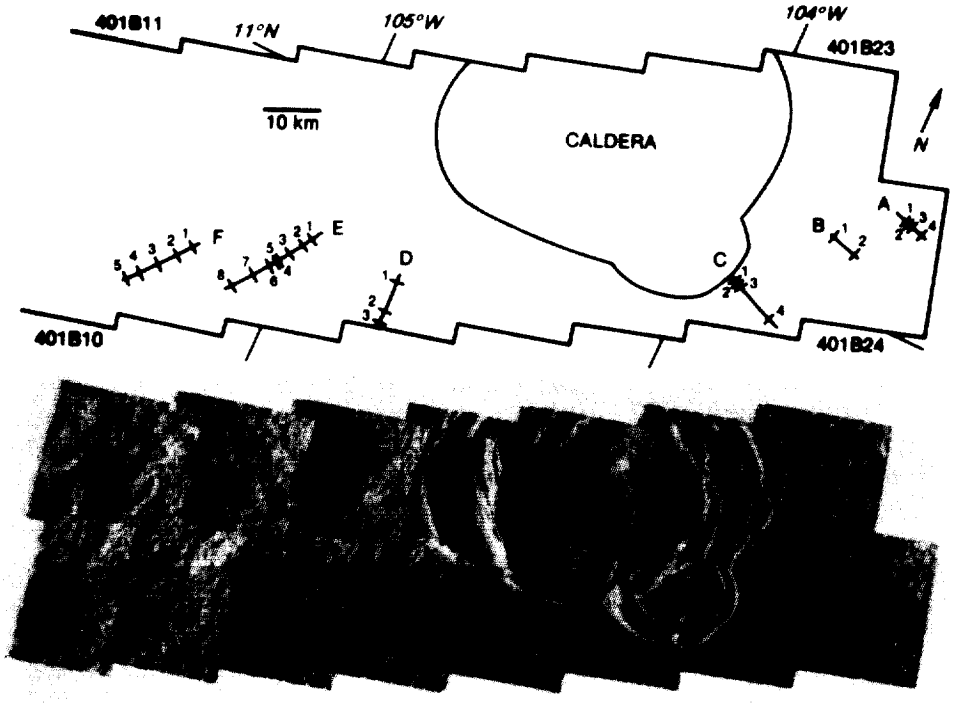

Figure 1. Location of six martian flows measured for rheologic estimates. Letters identify individual flows and numbers indicate positions along each flow where geometric measurements of flow dimensions were made. Photographs: 401B16-24, high-pass filtered.

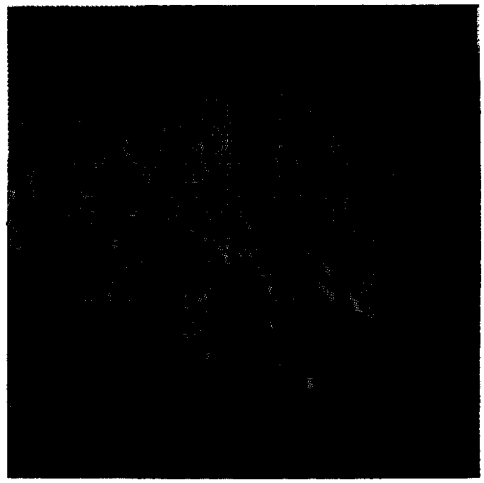

Figure 2. Ridged flow (A in Fig. 1 and Table 1). Viscosity estimates from ridge dimensions agree with viscosity obtained from yield strength and effusion rate estimates. Photograph: portion of 401B24, high-pass filtered. Area shown is 11 km wide.

CHAPTER 9

VIKING LANDING SITES

SPECTRAL MIXTURE MODELING: A NEW ANALYSIS OF ROCK AND SOIL TYPES AT THE VIKING LANDER 1 SITE

John B. Adams and Milton O. Smith
Department of Geological Sciences
University of Washington, Seattle, Wa. 98195

We have analysed a Viking Lander 1 multispectral image using, for the first time, a new method that employs a spectral mixing model. Spectral endmembers in the image were defined that corresponded to soil, rock, shade, and a minor component that was later found to be the effects of secondary illumination. Mixtures of these endmembers explained the observed variance in pixel DN's to the level of the noise of the imaging system. The soil and the rock spectral endmembers (Fig. 1) were found to have close analogs in a library of laboratory spectra (Fig. 2). The best laboratory spectral analogs for soil and rock were used to redefine the mixing space of the image, and, thereby to calibrate the image by calculating the gains for each bandpass. Incorporated in these gains are the combined effects of the response of the imaging system and any atmospheric attenuation. The residual error between the model and the image was found to be randomly distributed across the image, and to be at the noise level of the Viking cameras.

The rocks that can be observed clearly at the Viking 1 site are spectrally homogeneous. The best spectral analog in an extensive library of reference samples is a gray andesite from Arizona. Although a material of this type is geologically reasonable the spectrum does not warrant assignment of a specific rock name, which would require additional information on the mineralogy and rock texture. The rocks appear fresh or with coatings of dust.

Two types of soil were identified in the Viking Lander scene. The most extensive is spectrally analogous to an amorphous yellow-brown palagonite that is the product of weathering of a Hawaiian glassy tephra of basaltic composition. The analog was selected over several hundred other samples which included a wide variety of ferric oxides and oxyhydroxides. This martian soil is inferred to be a finely particulate dust based on its low shade component. The other soil, like the rocks, is spectrally identical to the gray andesite from Arizona. It is inferred to have a coarser particle size than the dust based on its greater shade content.

The dust covers much of the surface of the Viking scene (Fig. 3), and is concluded to be widely distributed wind-transported material that is not directly related to the rocks or the coarser soil. It coats parts or all of many of the rocks, and appears to be mixed and interlayed with the coarser soil. The coarser soil is interpreted to occur as a lag deposit in deflated areas around the larger rocks and on top of a drift. It is inferred to be derived from the rocks by aeolian abrasion and/or spallation.

An important result of this analysis is a method for calibrating a multispectral image by using laboratory or other reference spectra. The Viking image is not fully calibrated, and the use of published and unpublished gains for the spectral bandpasses led to image spectra that had no counterparts in laboratory or telescopic spectra, and were theoretically implausible. After calibrating the image to the closest reference spectra the image became interpretable in terms of the extensive data base of laboratory and telescopic observations. An independent check on this bootstrap calibration method was made by Guinness et al.(1985), and the results are within 10% reflectance for all bandpasses. The mixing model method offers the advantage of simultaneously

treating instrumental and atmospheric gains, and of being readily evaluated in terms of the spatial distribution of residual errors.

By using shade as a spectral endmember which was allowed to mix with the other spectral components, the identity of each surface material was maintained throughout the image, regardless of whether the material was fully illuminated or in partial shade. The soil and the rock compositions, therefore, could be mapped without the ambiguities of shade and shadow. The additional ambiguity of secondary illumination due to bounce lighting and sky lighting also was removed in the same way.

The above approach to shade and secondary illumination has potentially important applications to all multispectral images, including satellite images. Present methods for suppressing the effects of topography on spectral signatures rely on ratioing bands, normalizing with respect to one or more bands, or using digital terrain models. The shade mixing approach does not discard the albedo (absolute DN) values, as occurs in ratioing or normalizing. Albedo often is a key discriminator among spectra, especially when they have indistinct absorption bands or are undersampled, as is the case with the Viking Lander images. Without the albedo component in the Viking spectra it was impossible to narrow the choice of possible reference analogs sufficiently to develop a complete compositional and textural model. Digital terrain models (if available) can be used to make first order corrections for topographic lighting effects if the photometric function of the surface is known or assumed. In comparison the shade mixing model accounts for shade and shadow on all scales from topography to fine particles; therefore, topographic and photometric effects potentially can be removed together.

REFERENCES

Adams, A. B., M. O. Smith, and P. J. Johnson, Spectral Mixture Modeling: A new analysis of rock and soil types at the Viking Lander 1 site. J. Geophys. Res. submitted, 1985.

Guinness, E. A., R. E. Arvidson, M. Dale-Bannister, and R. B. Singer, On the types of rocks exposed at the Viking Lander sites, J. Geophys. Res. submitted, 1985.

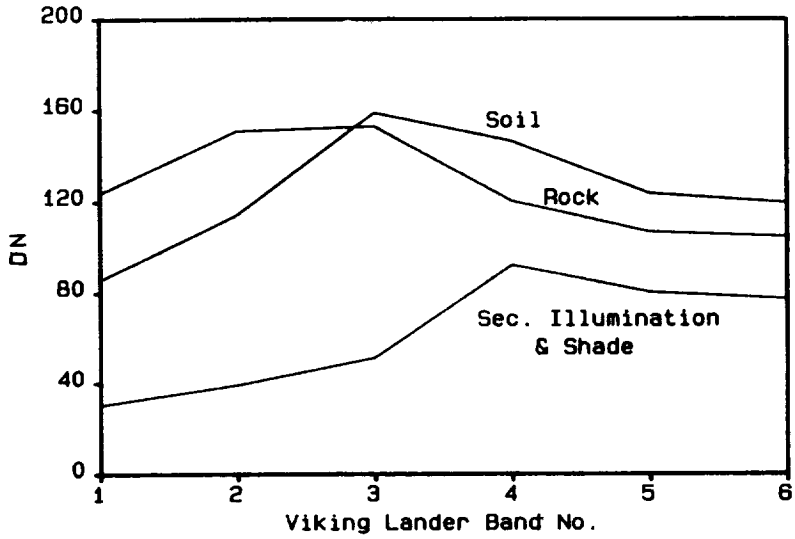

Figure 1. Six-bandpass pseudospectra of endmembers (excluding shade) from the uncalibrated images.

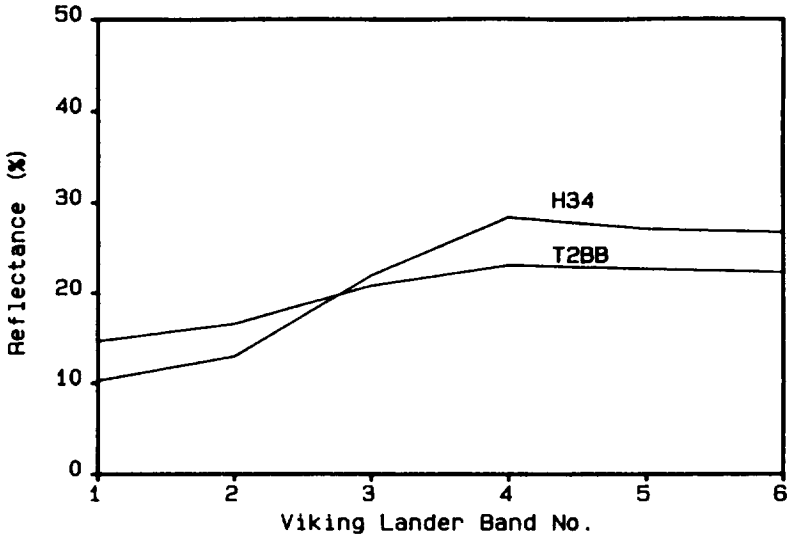

Figure 2. Pseudospectra of laboratory analogs H34 (palagonite soil from Hawaii) and T2BB (andesite from Arizona), derived by convolution with the six Viking Lander 1 bandpasses.

Figure 3. Concentration image of rock. Brighter tones are spectrally more similar to rock; darker tones are either soil or shade.

VIKING LANDER MULTISPECTRAL OBSERVATIONS: I. RADIOMETRIC CALIBRATIONS AND PHOTOMETRY OF BLOCKS

E. Guinness, R. Arvidson, M. Dale-Bannister, McDonnell Center for the Space Sciences, Department of Earth and Planetary Sciences, Washington University, St. Louis, MO 63130, and R. Singer, E. Bruckenthal, Planetary Geosciences Division, Hawaii Institute of Geophysics, University of Hawaii, Honolulu, HI 96822.

Multispectral data were acquired by the Viking Lander cameras in six broad wavelength bands covering the 0.4 to 1.0 micrometer region. A number of research efforts have used the six channel data to constrain the types of soils and blocks exposed at the landing sites [1-5]. Despite the previous efforts, there has yet to be a comprehensive examination of the multispectral data that combines testing of the camera radiometric calibrations, removing the effects of atmospheric attenuation and skylight, correcting soil and block reflectance estimates to values of common lighting and viewing geometries, and quantitatively comparing the corrected data to reflectance estimates from analog materials. This abstract and the two companion abstracts report on such comprehensive efforts.

Crucial to analyses of reflectance estimates from Lander camera data is a rigorous consideration of radiometric calibrations, and thus how well derived reflectance estimates will be known. The components of the imaging system and the integrated system were initially calibrated through a series of preflight experiments where targets of known radiometric properties were illuminated by a calibrated light source [6]. Sterilization of the Landers to meet Mars quarantine requirements, and neutron radiation from radioisotope thermoelectric generators on the Landers, apparently caused changes in calibrations relative to preflight conditions. These effects should be greatest for the three infrared channels [7]. We chose to evaluate the preflight calibrations directly with martian data, using images of a series of gray patches (known as Reference Test Charts [RTC]) mounted on the Landers in an experiment where we explicitly remove shadowing effects and compensate for atmospheric attenuation. The voltage received from a RTC gray patch can be modeled as the contribution from the direct solar beam and a second term from skylight and any light reflected from the Lander. Atmospheric optical depths varied from approximately 0.5 during the beginning of the mission to values in excess of 8.0 during dust storms [8]. Even with an optical depth of 0.5 and an incidence angle as low as 10 deg, the solar irradiance will be about 60% of its extra-atmospheric value. The remaining 40% is absorbed or scattered, with some fraction of the scattered light diffusely illuminating the scene as skylight. Thus, the skylight term must be dealt with in testing calibration of Lander data or in quantitative analyses of the soil or block data.

As a means of directly evaluating skylight we examined a partially shadowed RTC. An RTC contains 11 gray patches, each with a different absolute reflectance that exhibits a Lambertian scattering behavior. Figure 1 is a plot of the red channel preamplifier voltage verses gray patch bi-directional reflectance for sunlit and shadowed RTC patches. The voltage from the shadowed patches should be the diffuse illumination

voltage term for any given patch. Thus, the diffuse illumination term can be removed from the brightness of any given sunlit patch by subtracting the voltage predicted from the linear fit to the shadowed patch data. For our calibration experiments, we corrected observed voltages of sunlit patches by removing the diffuse illumination term as described above. We then computed an expected voltage for the patches assuming preflight calibrations and using a measured optical depth. The computed voltage values were within 10% of observed values for the color channels, except for Lander 1, camera 2. Partially shadowed RTC images acquired with the three infrared channels are only available for Lander 1, camera 1. Computed values of voltages are a factor of 2 to 3 higher than measured values. This suggests that there have been changes in the calibration constants of the infrared channels or major changes in the spectral responsivity functions [7]. We conclude that the infrared channels are poor prospects for extraction of absolute reflectance.

A number of authors [2,5,9] have noted what appear to be variations in color and albedo between different portions of Lander blocks. The variations can be interpreted in terms of a variable extent of staining or coating of blocks by fine-grained ferric-rich weathering materials. On the other hand, the differences might be apparent and due to variations in local incidence angle. To test for homogeneity in spectral properties of given blocks, we considered in detail the local geometry and reflectance properties of two relatively large, angular blocks. Bi-directional reflectance estimates for the blocks as a function of incidence, emission, and phase angle were fit using the Hapke-Irvine photometric function. Stereo ranging from high spatial resolution images was used to measure the orientation of the various faces on the blocks from which the lighting and viewing angles were computed. The reflectance data for the block referred to as VL2 block (from the VL2 site) are shown in Figure 2. If the block had surfaces with homogeneous spectral properties, when seen at similar lighting and viewing geometries, the reflectances for each face would converge to similar values. Scatter exists in the data, but two distinct trends are evident. When the reflectance data for both faces on VL2 block are corrected to the same geometry, face 2 is darker and less red than face 1. The reflectance of both faces was computed for an incidence and phase angle of 20 deg and an emission angle of 0 deg. The blue, green, and red reflectances for face 1 are 0.08, 0.14, and 0.32, respectively. Similarly, reflectance values for face 2 are 0.05, 0.07, and 0.13. Thus, it appears that VL2 block exhibits heterogeneous surfaces with regards to its spectral properties, with face 2 being among the darkest, least red material at the site.

REFERENCES

1) Arvidson, R., and others, (1983), Science, 222, 463-468. 2) Evans, D., and J. Adams, (1979), Proc. Lunar Planet. Sci. Conf. 10th, 1829-1834. 3) Guinness, E., (1981), J. Geophys. Res., 86, 7983-7992. 4) Huck, F., and others, (1977), J. Geophys. Res., 82, 4401-4411. 5) Strickland, E., (1979), Proc. Lunar Planet. Sci. Conf. 10th, 3055-3077. 6) Huck,F., and others, (1975), NASA Tech Memo X-72692. 7) Patterson, W., and others, (1977), J. Geophys Res., 82, 4391-4400. 8) Pollack, J., and others, (1979), J. Geophys. Res., 84, 2929-2945. 9) Sharp, R., and M. Malin, (1984), GSA Bull., 95, 1398-1412.

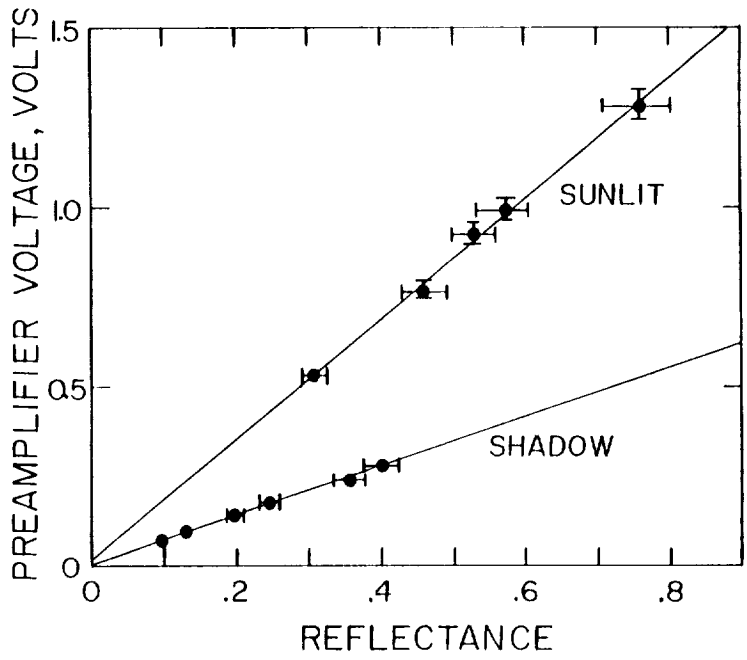

Figure 1. Plot of voltage verses reflectance for sunlit and shadowed RTC patches from an image taken by Lander 2, camera 1. Data for the red channel is shown. The relative error in voltage and patch reflectance is 3% and 6%, respectively.

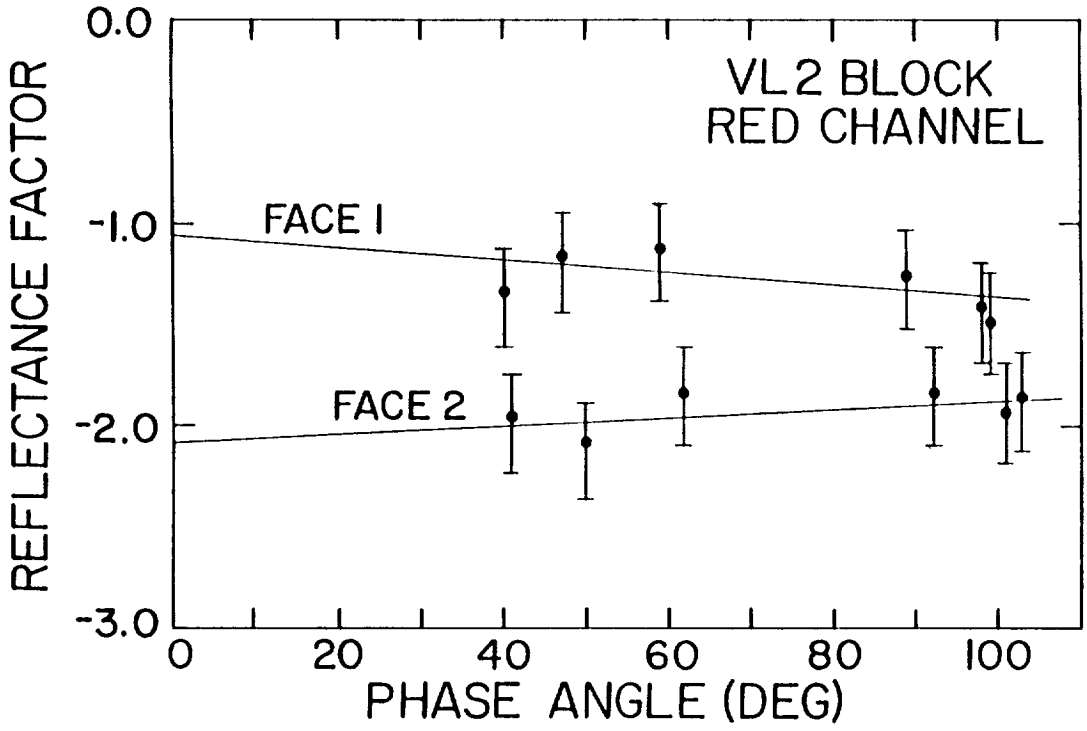

Figure 2. Hapke-Irvine plot for VL2 block. The reflectance factor is a function of reflectance and cosine of incidence and emission angles. The solid line is the least-square fit to the data. The relative error in the data points is 23%. Data for the red channel is shown.

VIKING LANDER MULTISPECTRAL OBSERVATIONS: II. COMPARISONS TO VIKING ORBITER COLOR DATA

E. Guinness, R. Arvidson, M. Dale-Bannister, McDonnell Center for the Space Sciences, Department of Earth and Planetary Sciences, Washington University, St. Louis, MO 63130, and R. Singer, E. Bruckenthal, Planetary Geosciences Division, Hawaii Institute of Geophysics, University of Hawaii, Honolulu, HI 96822.

Lander multispectral observations provide the high spatial resolution needed to resolve various rock and soil components in the lower spatial resolution data obtained from orbit. Thus, the reflectance signatures can be thought of as possible spectral end members that from orbit are integrated in some fashion to produce a composite reflectance. Blue (0.47 +/- 0.05 micrometers), green (0.54 +/- 0.02), and red (0.67 +/- 0.06) bi-directional reflectances were determined for about 30 exposures of soils and blocks seen at both Viking Lander sites. The reflectances were calibrated to within ten percent uncertainties, based on brightness values from images of gray patches mounted on the Landers. Reflectances were corrected for atmospheric attenuation by using optical depth measurements obtained by the Lander cameras, and for skylight illumination by subtracting the brightness values for adjacent shadowed areas. In some cases, the reflectances were also corrected for differences in lighting and viewing geometry using the Hapke-Irvine photometric function and stereophotogrammetric analyses.

As part of the Mars Consortium efforts [1,2] a number of overlapping Viking Orbiter violet (0.45 +/- 0.03 micrometers), green (0.53 +/- 0.05), and orange (0.59 +/- 0.05) images were radiometrically calibrated to have brightness values in proportion to bi-directional reflectance. The set of Viking Orbiter frames 663A22 (violet), 663A26 (green), and 663A28 (orange) were used obtain reflectance estimates of the surface. These frames were acquired over the VL1 site 613 days after VL1 touched down and after two global dust storms deposited layers of bright, red dust over the landing site [3]. Figure 1A shows the Lander reflectance data for soils and blocks plotted on a scatter diagram with blue and red reflectance axes. The reflectance values for a sample of the post-dust storm Lander soil are also plotted. These data were derived from Lander images acquired within three days of the Orbiter image. The post-dust storm soil values are shown corrected to a 20 deg phase angle using the Hapke-Irvine function [4]. The Orbiter reflectance values are also plotted. Orbiter values were corrected to reflectances for Lander passbands using a linear interpolation from violet and orange to blue and red wavelengths.

Note that the distribution of Lander soils and Orbiter values are approximately the same, with a shift to slightly higher values for the blue axis. A higher blue reflectance is probably due to the fact that the Orbiter data have not been corrected for atmospheric skylight. Skylight should be relatively higher for blue verses red wavelengths if skylight were less wavelength dependent than the surface reflectance. In fact, hazes and clouds are much more noticeable on violet as opposed to green or orange frames. Thus, a normalization is in order. We normalized the

Orbiter data by shifting the equivalent blue and red reflectances by amounts that make the values over the VL1 site equivalent to the bright, red soil signature that pertained to the bulk of the site after the two global storms. Results are shown in Figure 1B. Lander soils and Orbiter data now become approximately coincident in range to blue and red reflectances. Some of the Orbiter data for dark areas (low blue and red reflectances) are similar in reflectance to some of the dark blocks seen at the Lander sites. On the other hand, Lander blocks occupy a factor of 4 greater variation than Lander soils and Orbiter data, ranging from the darkest, grayest to the brightest, reddest materials seen by the Landers. Figure 1B demonstrates that the spectral signatures seen from orbit are dominated by soils, an observation consistent with the relatively low rock abundances (about 15% surface, [5]) exposed at the sites, and with the 5 to 10% abundances inferred from Viking IRTM observations [6].

REFERENCES

1. Kieffer, H., et. al., (1982), Proc. Lunar Planet. Sci. Conf. 12th, 1395-1417.
2. Strickland, E., (1982), Lunar and Planet. Sci. XIII, 780-781.
3. Guinness, E., et. al., (1979), J. Geophys. Res., 84, 8355-8364.
4. Guinness, E., (1981), J. Geophys. Res., 86, 7983-7992.
5. Moore, H., et. al., (1979), J. Geophys. Res., 84, 8365-8377.
6. Christensen, P., (1982), J. Geophys. Res., 87, 9985-9998.

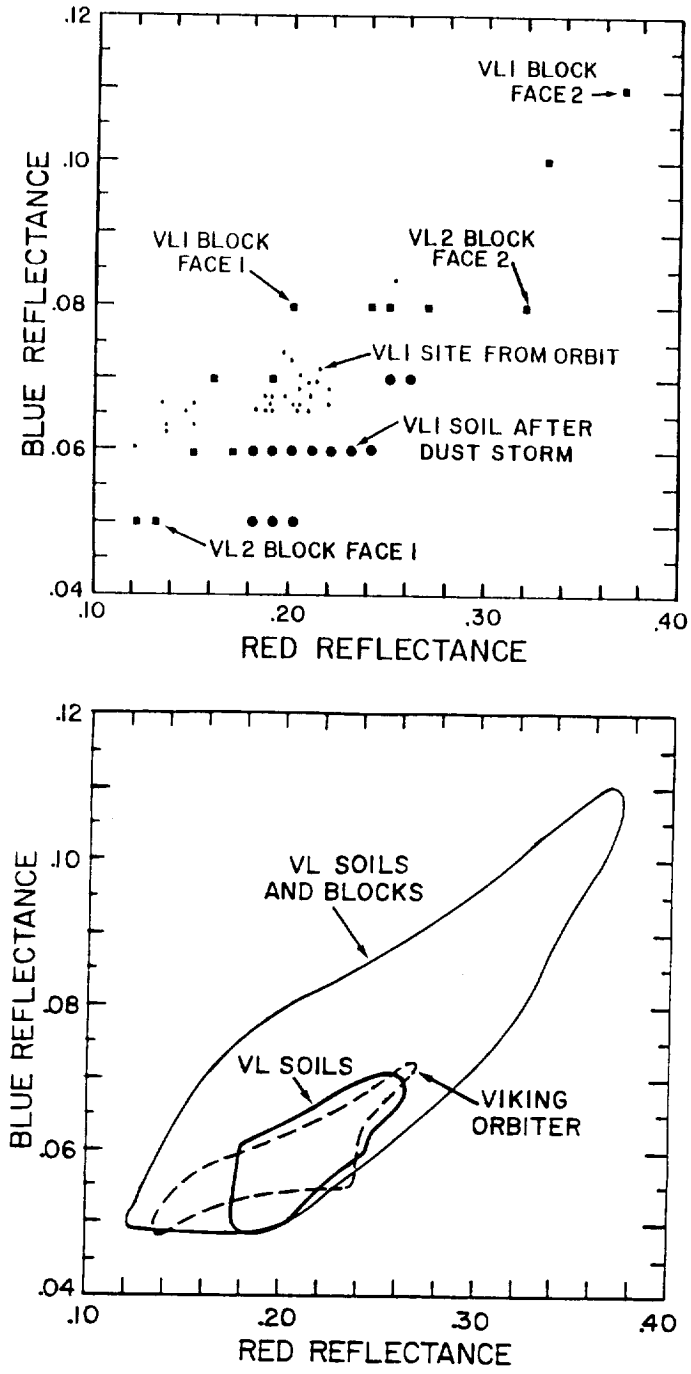

Figure 1. Scatter plot of blue verses red reflectances with Lander values for rock and soils and with Viking Orbiter color data. A) Orbiter data corrected to Lander passbands. B) Orbiter data corrected to Lander passbands and translated to make the Orbiter data over Viking Lander 1 site coincide with the Lander soil after the first year dust storm.

ARE THE VIKING LANDER SITES REPRESENTATIVE OF THE SURFACE OF MARS?

Bruce M. Jakosky (LASP/U. of Colorado) and Philip R. Christensen (Department of Geology, Arizona State University)

We compare the properties of the two Viking lander sites with global surface properties inferred from remote-sensing observations from spacecraft and from Earth. This will allow us to determine whether the observed properties of these locations are representative of the entire surface, and whether the entire range of surface processes extant are represented at the landing sites.

Both lander sites have a boulder-strewn surface with abundant fine material, and they show abundant evidence for the occurrence of aeolian processes. The VL-1 site contains numerous large drifts of fine material. Although it also has abundant fines, the VL-2 site has none of these large drifts. Evidence for active aeolian activity at both sites includes linear ridges or ripples of fine material, sculpting of rocks reminiscent of ventifacts, deposits of fines in the lee and scouring of fines on the windward sides of obstacles, and possible lag deposits left upon removal of fines. Trenching operations show that the fine material beneath the surface at both sites is darker than the surface, suggesting the presence of a thin veneer of bright dust. In addition, deposition of additional dust onto the surface was observed after the global dust storms, in amounts sufficient to change the reflectance properties of the surface. This added dust appears to have been eroded away at VL-1 in a subsequent year by a relatively rare wind event. A duricrust is also present at both lander sites, consisting of a case-hardened bonding of the fine material. Due to the high salt content at both sites (comprising up to 25% of the surface material) and the increased salt concentration in the duricrust, it is likely that the salts act as the cementing agent holding the grains together.

Viking orbiter images suggest that the regions containing both lander site regions are homogeneous at scales up to tens of kilometers; this fact is important if we are to be able to compare non-imaging remote-sensing observations, which have a typical resolution of several kilometers or more, with what is seen in the immediate vicinity from the landers themselves.

Remote-sensing observations of Mars, including the regions containing the lander sites, have been made from the Viking Orbiter using thermal infrared, broadband albedo, and color imaging techniques. Additional observations of global properties from Earth have been obtained using radar and spectral reflectance techniques.

Observations from the Viking orbiters of the diurnal variation of surface temperature have been used to derive the thermal inertia of the upper 10 cm. Thermal inertia is predominantly a measure of thermal conductivity, and, hence, of particle size within the regolith, but the presence of rocks and duricrust will also affect the values. The thermal inertia values at VL-1 and VL-2, about 8×10^{-3} cal/cm^2-s$^{1/2}$-K at both sites, are consistent with the distribution of fines, rocks, and duricrust observed by the landers. Globally, values of the thermal inertia range from about 1 to 15 $\times 10^{-3}$; the distribution is bimodal, with peaks at

about 3 and 7 x 10^{-3}. Using temperature measurements at different wavelengths, the value of the thermal inertia can be separated into the contributions made by the rock and fine components of the surface. Values of 15 ± 5 and 20 ± 10% coverage by rocks are obtained for VL-1 and VL-2, respectively, which are also consistent with the observed surface properties. Unlike the distribution of thermal inertia, the global distribution of rock abundance is unimodal with a peak near 5-10% rock coverage. This low rock abundance, and the fact that it does not vary dramatically from place to place, suggests that the rock abundance does not determine the thermal inertia, but rather that the properties of the fines are the controlling factor.

The broadband albedo of the surface as measured from the orbiters is about 0.26 at both lander sites. Albedo and color are determined predominantly by the composition and particle size of the uppermost tens of microns of the surface due to the efficient scattering and absorption by small particles. There is a correlation between thermal inertia and albedo, with low-inertia regions generally having high albedo. It is significant that the two lander sites, however, do not fit into this global correlation, having both a high inertia and a high albedo.

Radar observations from Earth provide a means of extending our knowledge of the surface properties to include up to a meter depth. Although much mapping has been done at 12.5-cm wavelength using continuous-wave (cw) techniques, reflected energy includes a significant diffuse scattering component that reflects from a large region of the planet. Comparison with the lander site properties is therefore not appropriate. Harmon and Ostro, however, analyzed their cw data to include contributions from both a diffuse and a specular component. Effectively, then, they solved for an r.m.s. slope and reflection coefficient that applies to the non-rock (specular) component of the surface in the region immediately surrounding the sub-radar location. For the Chryse region surrounding the VL-1 site, the reflection coefficient was about 0.12. The reflection coefficient depends primarily on the density of the top wavelength of the regolith; a density in Chryse of about 2.1 g/cm^2 is thus indicated. We can compare this result with the global radar properties as measured by Downs et al., who used a delay-Doppler technique that effectively eliminates the scattered contribution and measures only the specular reflection from the non-rock part of an isolated region of the surface. There is a general trend of low inertias and low reflection coefficients being associated together, and of high values being associated together. The region containing VL-1, with a relatively high reflection coefficient and thermal inertia, falls along this trend. We can also examine the limited set of 70-cm cw observations. Because of the small scattering cross-section of most rocks observed at the lander site (with size much less than 70 cm, the contribution of energy scattered from rocks will be small compared to the specular reflection term. Most of the VL-1 latitude band shows a strong correlation of radar reflection coefficient at 70 cm with thermal inertia. Interestingly, the Chryse region, which contains the VL-1 site, is in the region where the 70-cm reflection coefficient and thermal inertia do not correlate. Radar observations of the VL-2 site are not possible due to its high latitude.

The general correlation between thermal inertia and radar cross-

section at both wavelengths requires the bulk density and the thermal conductivity to be correlated. Although an independent variation of both properties could occur, it is unlikely. Unless rocks are unrealistically small, variations in the surface and subsurface rock abundance are ruled out by the relative contributions of the rocks and fines to the thermal inertia, as discussed above. The presence of a globally-variable, near-surface duricrust could explain these trends, however. Low-thermal-inertia regions would consist of unbonded, recently-deposited fines with a relatively low density (and, hence, low radar reflection coefficient); high-thermal-inertia regions would consist of fines which have been cemented together and which therefore have both a high conductivity and density. Because the trend holds at both radar wavelengths over much of the planet, the duricrust in those high-inertia regions must dominate at least the top meter of regolith. Because the VL-1 region fits the trend at 12.5 but not at 70 cm, the duricrust there is probably typically only several centimeters to several tens of centimeters thick. This inference appears to be consistent with the direct observations at VL-1 which indicate a relatively thin and variable duricrust.

About 75% of those regions of Mars observed with the 70-cm radar show the correlation of reflectivity with thermal inertia. The correlation of albedo with thermal inertia holds for regions comprising 87% of the 2° x 2° latitude-longitude bins between 60° and -60° latitude; regions not correlating are Chryse (including VL-1), Utopia (VL-2), Hellas, Argyre, and Isidis. Thus, regions not fitting the general trends of the remote-sensing data occupy only a small fraction of the planet. Because the lander sites are contained within two of those regions, they appear to be somewhat anomalous with respect to the global surface properties. Also, notice that the regions not fitting the global trends are all low-elevation basins. Because the landers were targeted to low regions, they were therefore destined to land in an anomalous region.

The lander sites appear to be intermediate in properties and processes between classical bright and dark regions of the planet. Deposition of dust onto the surface occurs globally each year. Dark regions remain dark because dust is removed rapidly after the end of the dust storms. Bright, low-inertia regions retain the dust over a longer time, accumulating it to a thickness of at least several centimeters. The VL-1 site retains enough dust to raise the albedo, but the dust is removed before it becomes thick enough to dominate the surface morphology and thermal behavior. Thus, the VL-1 site differs primarily due to the timescale on which dust deposition and removal occurs. It may be a region of incipient formation of a low-thermal-inertia surface.

A paper on these results has been submitted for publication. Copies are available from the authors.

LOSS OF FINE-SCALE SURFACE TEXTURE IN VIKING ORBITER IMAGES AND IMPLICATIONS FOR THE INFERRED DISTRIBUTION OF DEBRIS MANTLES (*)

Ralph Kahn, Edward Guinness, and Raymond Arvidson (**)
McDonnell Center for the Space Sciences, Department of Earth and Planetary Sciences, Washington University, St. Louis, MO 63130

The absence of fine-scale surface features in Viking Orbiter images must be interpreted with caution. A reduction in contrast due to the presence of atmospheric haze will preferentially obscure small features. Two sets of images of the same region, taken near the Viking Lander 1 site with similar viewing geometry, but under different atmospheric conditions, were studied. Combined Orbiter and Lander data allow us to demonstrate that a single scattering model quantitatively accounts for the effects of the atmosphere. Craters five to seven times the size of the camera picture element should be resolved in Viking Orbiter images if the atmosphere is clear. When atmospheric haze effects dominate, larger craters are obscured and crater size frequency distributions appear to be depleted in small sized craters in a predictable way (Figure One).

Twelve crater size-frequency distributions obtained from Viking images in the northern hemisphere behave in the manner predicted for hazy conditions. Their characteristics also follow the pattern of increasing atmospheric opacity with latitude in spring and summer deduced from other measurements of cloudiness. Loss of surface resolution due to the nearly ubiquitous atmospheric obscuration in the northern mid to high latitudes makes it difficult to assess, with existing images, the validity of suggestions that fine-scale surface features have been preferentially degraded by surface processes. Thus, unless fine-scale features can be discerned in images over the mid to high northern latitudes, one should not assume that the lack of detail is due to geomorphic processes. The atmosphere in the southern mid and high latitudes is relatively clear during autumn and winter, and a preliminary review of existing image data suggests that features with sizes down to five to seven picture elements can be detected in these regions. No evidence for a recent circumpolar debris mantle can be found in the southern hemisphere data, based on crater size frequency distributions. Because the smallest craters that can be resolved in Viking images are several tens of meters in diameter, we cannot rule out the occurrence of debris deposits less than a few tens of meters thick, regardless of atmospheric clarity. We explore these findings further in a separate abstract by Guinness, et al.

(*) Icarus, in press, 1985. (**) This work is supported in part by NASA Grants NAGW-6612, under the Planetary Atmospheres Data Analysis Program, and NGG-7545 under the Mars Data Analysis Program.

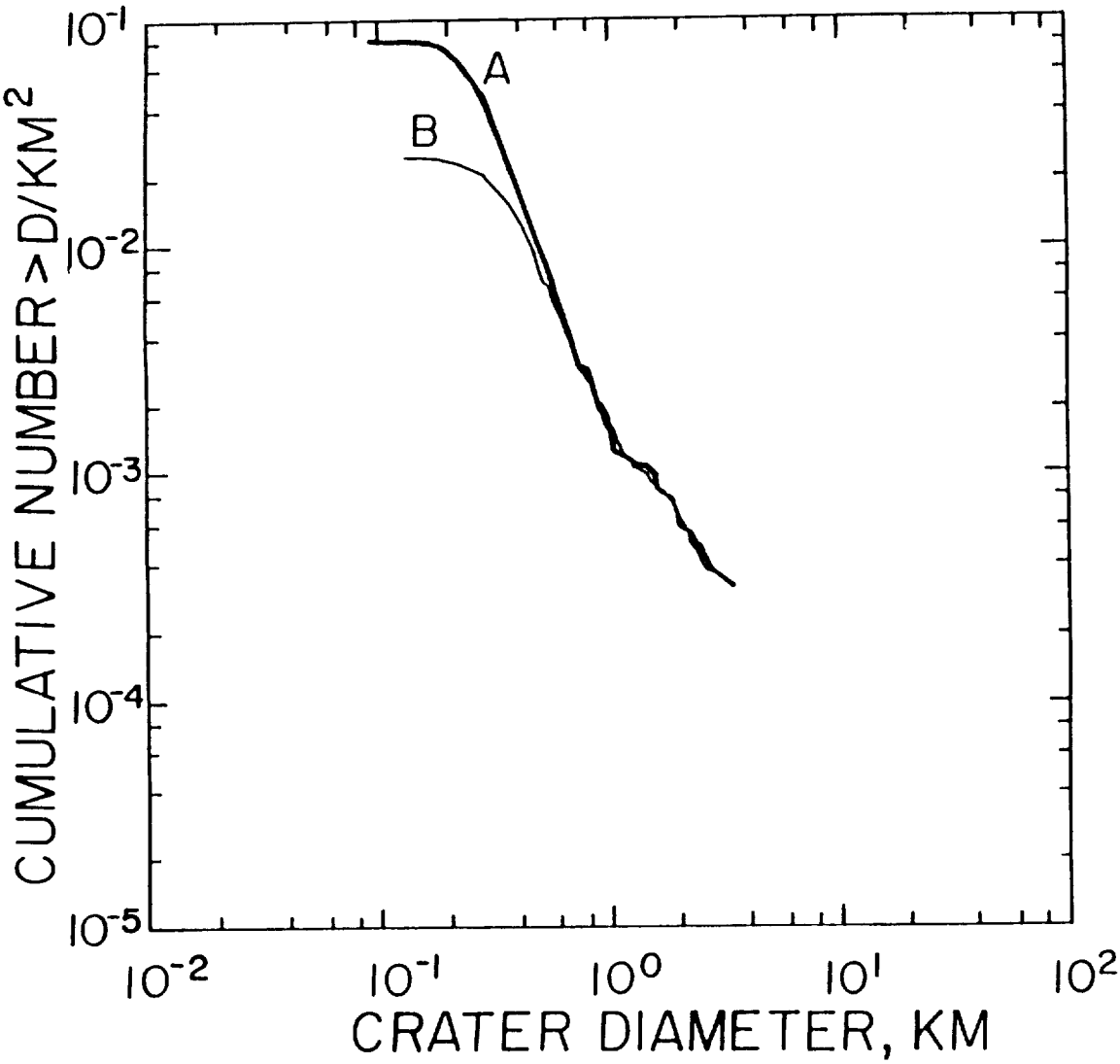

Figure Caption. Cumulative crater density vs. diameter curves for a region of Chryse Planitia about 900 km northeast of the Viking Lander 1 site. A) Images acquired during relatively clear conditions (Ls=74.6). There are 1223 craters counted, down to the limit of detectability. B) Images acquired through a thin haze (Ls=58.5). 389 craters were observed.

MARTIAN MINIATURE SLOPE FAILURES

Henry J. Moore, U.S. Geological Survey, Menlo Park, CA., 94025

Two slope failures occurred at the Mutch Memorial Station (Lander 1) about 8 and 25 m from the lander [1,2,3] on steep slopes of drifts downwind of large rocks. The slope failure 25 m away is too distant for adequate description, much less measurement, and the fact that the slope failure 8 m away was viewed only by camera 1 precludes stereometric measurements. The nearest slope failure produced a miniature landslide (fig. 1) with three units: a scar, a runout tongue, and a runout mound. As viewed, the scar and runout tongue appear to slope 38°; however, this apparent slope is too large. Shadows indicate that local slopes exceed 27.8°. In the absence of better data, the slope is assumed to be about 30°. The failure is estimated to be 0.2 m long, and so the scar and runout tongue are about 0.4 m long. The runout mound, about 0.07 m wide, has a maximum relief of about 0.04 m. Relief of the scarp delineating the scar is about 0.01 m, and that near the toe of runout tongue is about 0.01-0.02 m. The two slope failures occurred in a material that resembles drift material; however, as discussed below, drift material appears to be too strong to permit failure. The failures may have occurred in a layer formed by the accumulation of reworked dust from major and global dust storms on protected lee slopes downwind of the rocks. Elsewhere, dust deposits from major and global dust storms are easily moved by light winds after they settle to the surface, and so the cohesions of such dust deposits are very small.

The drift material sampled by the lander is too strong to permit the slope failures. Drift material has an angle of internal friction of about 20° and a cohesion of about 1-3 kPa [4]. With these properties, the slopes are stable. In the absence of positive pore pressures, the slopes are also stable for angles of internal friction greater than 30° and for cohesions greater than 25-50 Pa, depending on the angle of internal friction, the thickness of the sliding units, and the presence or absence of slope toes with cohesions. Cohesions within the slope failures must be very small. Separation of the body of the slide from its surroundings suggests a tensile strength of about 20 Pa, which should be the same order of magnitude as the cohesion for a homogeneous soillike material. The slide is so thin that normal stresses are about 40 Pa, and positive pore pressures of only 40 Pa are required to reduce the effective internal friction to zero. Thus, slope failure could occur when positive pore pressures reduce the effective coefficient of friction to zero and the cohesion is less than about 20 Pa.

The reasons for the initiation of the slope failures are unclear but may involve factors related to seasonal changes because both slides occurred during the summer. The time of formation of the failure 8 m away is poorly constrained to the summer, but that of the failure 25 m away is well contrained to the late summer. During late summer, peak near-surface "soil" and atmospheric temperatures are maxima, and pressures are minima. Because of their seasonal occurrence, changes in pore pressure by

adsorption-desorption of CO_2 gas in a nontronite-like substrate [5] could initiate failure. The failures also could have been initiated by marsquakes, windstresses, chemical changes within the materials that altered the mechanical properties, an increase in thickness of the layer beyond a critical thickness, and pore pressures generated by the release of gases caused by humidification of the substrate [6]. Geometric relations between the sliding units and the local surface are also important.

To estimate the magnitudes of pore pressures that might develop in a confined unit of "soil," BET equations [7] were derived from the published curves for CO_2 adsorption on nontronite at three temperatures [4]. The unimolecular-layer parameters (Vm) and the parameters related to heats of adsorption (C) were empirically correlated with temperature, using exponential equations. Footpad 2 temperatures were used to represent the temperatures at a depth of 0.01 m because the burial of the temperature sensors is 0.01 m. Pore pressures that could be generated by adsorption and desorption of CO_2 on and from surfaces of a confined nontronite-like material depend on temperature and pressure. Starting with a temperature of 225 K and a CO_2 pressure of 800 Pa (8 mb), CO_2 pressures in a confined unit of nontronite would rise and fall with the diurnal and seasonal temperature changes. If the diurnal temperature changes are 205 to 245 K, pressures in the confined unit would range from 490 to 1150 Pa. In summer, the mean pressure would climb to 990 Pa (T = 235 K) and diurnal temperatures of 211 to 255 K would cause pressures to range from 580 to 1350 Pa. In winter, the mean pressure would drop to 640 Pa (T = 215 K) and diurnal temperatures of 200 to 230 K would cause pressures to range from 420 to 890 Pa. For this confined unit of "soil," pore pressures in excess of the external ambient pressure would range from (+) 700 to (-) 500 Pa and thus exceed the 40 Pa pore pressure required to reduce the effective coefficient of friction to zero. Indeed, these pressures are large enough to produce tensile failure and disruption of a material with cohesions of several hundred Pa.

Desorption of CO_2 by humidification could develope pore pressures as large as 80 kPa (800 mb) [6], if sufficient amounts of water vapor were made available. For such extreme pressures, the slope failures would be characterized by extensive disruption, even if the cohesion was as large as 1-3 kPa. Indeed, the entire area of drift material around the landing site would literally "boil." The introduction of rather modest amounts of water vapor (a few micrograms of H_2O) apparently could displace or desorb enough CO_2 to generate pore pressures of about 1 kPa.

In conclusion, the layers that failed are probably composed of a nearly cohesionless dust that was deposited on protected lee slopes of drift material. Positive pore pressures exerted by gases on the upper centimeter of the martian surface could have initiated the failures. Seasonal and diurnal variations in pressure, temperature, and water-vapor content suggest that the slope failures initiated by positive pore pressures should preferentially occur during the late martian summers at the landing site. Negative pore pressures developed because of adsorption of gas during the winter could conceivably cause contraction of the soil and formation of the open fractures observed in the drifts.

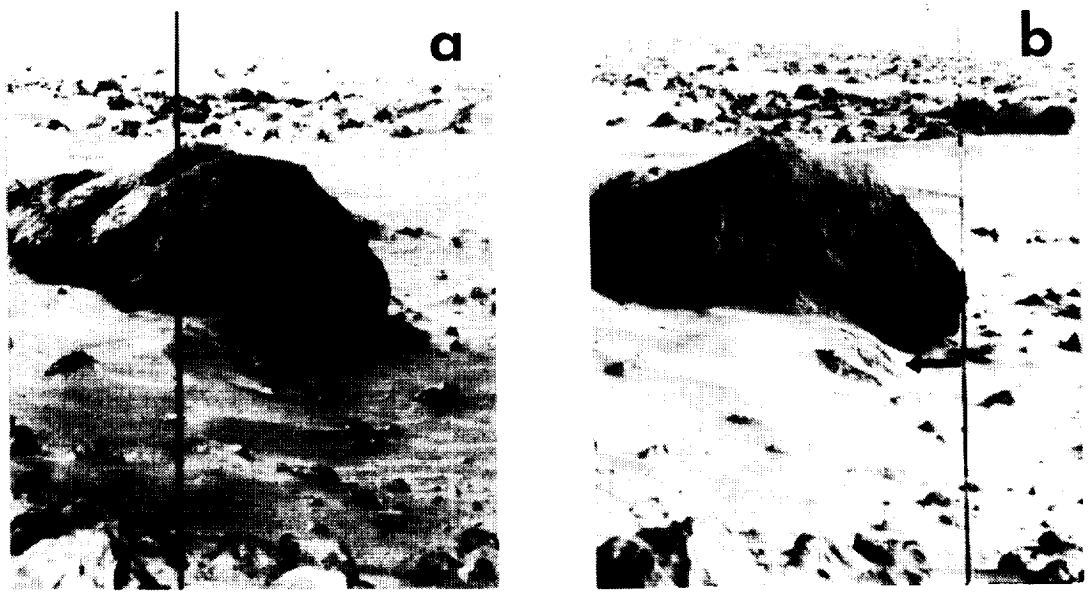

Figure 1. Images showing the surface before (a) and after (b) the miniature landslide 8 m away from the lander near the base of the rock called "Big Joe." Rock is about 2 m wide. Slide in (b) shown by arrow.

REFERENCES CITED

[1] Jones, Kenneth L. and others, 1979, One Mars year: Viking lander imaging observations: Science, v. 204, p. 799-805.

[2] Guinness, Edward A., and others, 1982, Two Mars years of surface changes seen at the Viking landing sites: J. Geophys. Res., v. 87, p. 10,051-10,058.

[3] Arvidson, R.E., and others, Three Mars years: Viking Lander I imaging observations: Science, v. 222, p. 463-468.

[4] Moore, H.J., Clow, G.D., and Hutton, R.E., A summary of Viking sampler trench analyses for angles of internal friction and cohesions: J. Geophys. Res., v. 87, p. 10,043-10,050.

[5] Fanale, F.P., and Cannon, W.A., 1979, Mars: CO_2 adsorption and capillary condensation on clays-significance for volatile storage and atmospheric history: J. Geophy. Res., v. 84, p. 8404-8414.

[6] Huguenin, R., Harris, S., and Carter, R., 1985, Freeze/thaw injection of dust into the martian atmosphere: Lunar and Planetary Science XVI, part 1, p. 376-377.

[7] Brunauer, S., and others, 1938, Adsorption of gases in multimolecular layers: J. Amer. Chem. Soc., v.60, p. 309-319.

MULTISPECTRAL INTERPRETATION OF GEOLOGIC MATERIALS EXPOSED AT THE VIKING LANDER SITES

R.B. Singer, E.A. Bruckenthal Planetary Geosciences Division, Hawaii Institute of Geophysics, 2525 Correa Rd., Honolulu, HI 96822
E.A. Guinness, R.E. Arvidson McDonnell Center for the Space Sciences, Department of Earth and Planetary Sciences, Washington University, St. Louis, MO 63120

INTRODUCTION: Work was performed on Viking Lander data with a newly refined calibration developed by Ed Guinness and coworkers at Washington University in St. Louis (see accompanying abstracts). The calibration provides absolute reflectance values for both Lander scenes, using three channels in the visible wavelength region between 0.4 and 0.75 microns. These data are sensitive to ferric iron absorptions, and can be used to help constrain both composition and mineralogy of landing site materials. Toward this end, the reflectances of a variety of soils and rocks at both sites were derived. Laboratory spectra of martian analog materials and Earth-based telescopic spectra were then convolved to Viking lander bandpasses and compared to the three-channel lander data. The data were separated into three groups on the basis of spectral shape, defined as amount of curvature (see Figure 1). The interpretations which follow combine both spectral shape and overall reflectance.

DISCUSSION: The least curved group contains one soil and three rock units. A martian rock in this category with low absolute reflectance closely matches a laboratory-measured basalt coated by ~30 microns of palagonite (see Figure 2), and therefore, the martian rock is consistent with dark, volcanic, and relatively fresh basalt or dark andesite thinly coated by palagonite. The martian rock data are also consistent with convolved Earth-based telescopic spectra of martian dark regions (Figure 2). A close match was also obtained between the soil in this group and a laboratory-measured palagonite (see Figure 3). However, the fit was obtained by scaling down the palagonite by a factor of 1.6, which suggests that the soil's spectral signature may be dominated by palagonite, but that additional factors are causing a lower overall reflectance for the lander material. A phase effect may be involved, or the soil may contain rock and glass contaminants, in addition to the palagonite. It is also significant to note that this soil is consistent with Earth-based telescopic bright region spectra (Figure 3). One of the two rock units remaining in this spectral category is higher in overall reflectance and in red/violet ratio than the one previously discussed, and is consistent with both laboratory-measured palagonite and telescopic bright region spectra. These units are interpreted as dark volcanic rock similar to the type previously noted, coated by an optically thick layer of palagonite. The most sharply curved spectral group contains a soil unit which is an excellent match to a laboratory-measured red, hematitic cinder (see Figure 4). Previous tests with lander bandpasses has proven them to be sensitive towards determining different ferric oxide phases, thus supporting but not proving mineralogical similarity. The possibility that crystalline hematite may exist on Mars is highly significant, since it implies a different alteration environment than the one in which amorphous palagonite would form. The final spectral category is intermediate in curvature between the two spectral groups just discussed. It contains the overwhelming majority of soils at the landing sites, as well as additional rock units. This category was not consistent with any of the lab or telescopic spectra to which it was compared, and thus its compositional interpretation remains unclear. However, it is possible that this group's mineralogy represents an intermediate degree of crystallinity between amorphous palagonite and crystalline ferric oxide. If this is true, it might represent the maturation or further alteration of initially amorphous palagonitic soil. Alternately, this common soil type may represent a physical mixture of other surface components, although a simple linear mixing model is inadequate to relate this unit to other

although a simple linear mixing model is inadequate to relate this unit to other observed units.

CONCLUSIONS: It is important to stress that our use of only three points to infer composition and mineralogy was done with caution, and in the context of previous interpretation from Earth-based spectra, Viking Lander chemistry results, and terrestrial analog research. Although a possibility of ambiguous interpretations exists, we feel confident in making the following conclusions: 1) Certain soils are spectrally similar to amorphous palagonites, and these soils closely match telescopic spectra of martian bright regions; 2) Many rocks appear to be coated to varying degrees by these palagonites. Thinly coated rocks resemble telescopic spectra of dark regions, while thickly coated ones resemble bright regions; 3) Certain soils may be hematitic and represent a much greater degree of ferric oxide crystallinity than do the palagonites above; 4) Most soils and some coated rocks at both landing sites do not match laboratory or telescopic spectra. These materials may represent a genetically separate unit, matured (further crystallized) palagonitic material, or a complex physical mixture of other compositional units.

ACKNOWLEDGEMENTS: This work was supported by NASA grants NSG 7590 and NSG 7545.

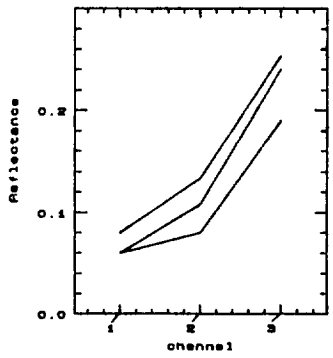

Figure 1. The three spectral categories; least curved at top, intermediate in middle, most sharply curved at bottom.

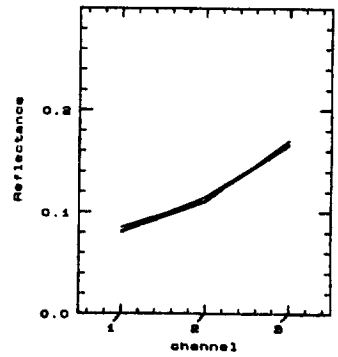

Figure 2. Overlay of data for a thinly-coated basalt, telescopic dark region, and one martian rock unit.

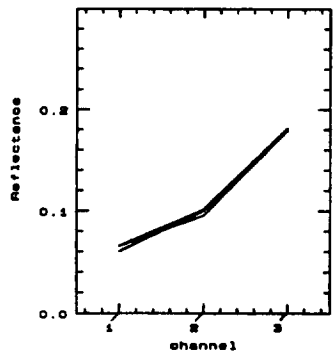

Figure 3. Overlay of amorphous palagonite, telescopic bright region, and one martian soil unit.

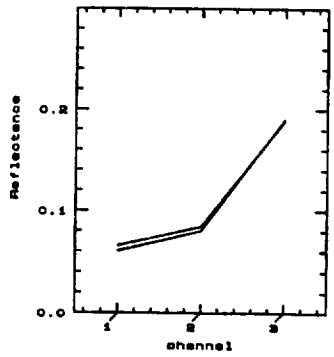

Figure 4. Overlay of red, hematitic cinder with an area of martian soil at VL2.

CHAPTER 10

STRUCTURE, TECTONICS AND STRATIGRAPHY

RIFTING AND LITHOSPHERIC STRUCTURE ON VENUS

W. B. Banerdt and M. P. Golombek, Jet Propulsion Laboratory,
California Institute of Technology, Pasadena, CA 91109

Introduction: Several approaches have been used to estimate the elastic lithosphere thickness (L) on Venus. In particular, Solomon and Head [1] have used a number of compressional (elastic and viscous folding) and tensional (wedge subsidence, imbricate normal faulting, and plastic necking) models to predict L based on the hypothesis that the linear bands of greater and lesser backscatter observed in earth-based radar images of Ishtar Terra are of tectonic origin. All of these models predict very thin lithospheres, on the order of 0.3 to 8 km. These values are in agreement with those obtained from strength calculations based on laboratory measurements of crustal rocks which give negligible yield stresses at shallow depths due to a combination of high surface temperature and a probable earth-like thermal gradient [2].

However, rift-like features which are at least superficially similar in size, morphology, and association with volcanism and doming to continental rifts on the earth [3] also exist on Venus. They typically have widths on the order of 75-100 km and depths of up to 2.5 km. Estimates of L derived from the widths of these features in Aphrodite Terra and Beta Regio using a wedge subsidence model are on the order of 50-70 km [4], which is inconsistent with our knowledge of rock rheology at probable Venus temperatures. This has led most investigators to abandon the graben hypothesis in favor of plastic necking models (e.g. [5]).

In this abstract we explore the implications of lithospheric strength envelopes for the graben model as applied to large scale rifting on Venus. We then use these results to constrain possible crustal thicknesses and thermal gradients.

Lithospheric Strength on Venus: The failure criterion for a given depth in the lithosphere is determined by the weaker of the frictional or ductile strength at that depth [6,7]. The yield stress increases with depth according to Byerlee's frictional law until it exceeds the strength predicted by the flow law relevant to crustal rocks. It then decreases exponentially until it reaches the moho, where the greater strength of ultramafic mantle rocks causes an abrupt increase in yield stress followed by another exponential decrease (see Figure 1). The lithosphere will behave elastically at a given depth for stresses less than the yield stress.

Figure 1 illustrates a typical lithospheric strength curve for Venus with a crustal thickness (c) of 10 km. For these calculations we assume a crustal density (ρ_c) of 2.7 Mg/m^3, a mantle density (ρ_m) of 3.2 Mg/m^3, a surface temperature of 740°C, a thermal gradient of 12°/km, and a strain rate of 10^{-15}/sec (equivalent to about 3% extension per million years). Based on surface geochemical measurements which indicate a basaltic composition, we use a dry diabase flow law [8] for the crustal layer. A dry olivine flow law [9] is assumed for the mantle. In this abstract we are interested in horizontal tensional stresses, which correspond to the left-hand branch of the curves in Figure 1.

Implications for Rift Formation: One consequence of this model is that the mechanical structure of the lithosphere depends strongly on the crustal thickness. For crusts thicker than about 30 km, there is no appreciable strength in the mantle and the brittle extension of the upper crustal layer should be effectively decoupled from the mantle. This was the implicit assumption of Solomon and Head [1]. However if the crust is thin, the lithospheric strength will be dominated by the upper mantle, and it is possible that this layer will control the style of deformation. In this case the effective lithosphere which controls rift width would be much thicker than the few km expected from crustal rock rheology. Instead, the elastic lithosphere thickness would be on the order of 20-30 km, based on an olivine flow law.

Here we consider the implications for the wedge subsidence, or graben model of rift formation [10,11]. This model predicts that the graben width, w will be given by $w=k\pi\alpha/4$, where $1<k<2$, $\alpha=(EL^3/3g\Delta\rho(1-\nu^2))^{1/4}$, E is Young's modulus, g is gravitational acceleration, $\Delta\rho$ is the difference in density between the layers above and below the faulted layer, and ν is Poisson's ratio. For rifting of a crustal layer, $\Delta\rho$ is just ρ_m, while for a layer at depth with an effectively fluid layer above it, $\Delta\rho=\rho_m-\rho_c$. We can define the effective density as $\Delta\rho=\rho_m-\beta\rho_c$, where $0<\beta<1$ is the degree of decoupling between displacements at the moho and the surface due to flow in the ductile lower crustal layer. Assuming $E=1.25\times10^{11}$ Pa, $\nu=.25$, $\beta=0.5$, and L=20 km gives the width for a graben formed in the mantle brittle zone of between 50 and 100 km, in good agreement with observed rift widths on Venus' surface. In addition, it can be shown using energy considerations (e.g. [11]) that graben depths in excess of 2 km are possible using these parameters.

The layered rheology implied by the strength envelope also offers an explanation for the spacing of tectonic structures observed using Earth-based radar [12,13]. Images of Beta Regio show subparallel bands of high radar backscatter, which have been provisionally interpreted as fault scarps. These features are superimposed on the rift zone, and have a characteristic spacing of roughly 20 km. While the mantle layer controls the width of the rift, the thin surface layer will respond to its tensional and flexural deformation by pervasive faulting at a characteristic spacing determined primarily by the thickness of the crustal strong layer. For reasonable assumptions about the rheology of the crust, a variety of models predict spacings of features in agreement with observations (see [1]).

In Ishtar Terra, where no rifts are observed, the banded terrain was probably formed by compressive stresses [1,14]. It is likely that the crust in this region is thicker than in the rifted areas [2,14]. If the crust is thicker than about 30 km, there will be virtually no strength contributed by the mantle, and the crust will deform independently with a characteristic wavelength of again 10-25 km for reasonable assumptions regarding crustal structure [1].

In order for the wedge subsidence model to be applicable to the Venusian rifts, rather tight constraints on allowable crustal thickness and somewhat less severe constraints on the thermal gradient are required. The crust must be less than about 20 km thick to allow the existence of a mantle brittle zone. In addition,

in order for there to be a ductile layer above this zone the crust must be at least about 5 km thick. The requirement that the elastic layer thickness be $\geq$20 km implies a thermal gradient on the order of 15°/km or less. Lower thermal gradients will accommodate somewhat thicker crusts, as the brittle-ductile transition will be deeper and thus the crust can be thicker without eliminating the mantle brittle zone. These constraints are dependent on the detailed deformation mechanisms of olivine at conditions of low strain rate and relatively low temperature which cannot be duplicated in laboratory experiments. For example, semi-brittle and low temperature mechanisms may combine to round off the high stress points of the yield envelope [15], allowing a somewhat higher thermal gradient.

Conclusions: Lithospheric strength envelopes provide a framework with which to explain the formation of both the large (∿75 km wide by 2.5 km deep) rifts and the narrow, closely spaced (∿20 km) banded terrain on Venus. In particular, a simple wedge subsidence model in which a zone of significant mantle strength is separated from a thin brittle surface layer by a ductile lower crust accurately predicts the observed widths and depths for the equatorial rifts, as well as the spacing of associated normal faults. The model requires thermal gradients of on the order of 15°/km, and crustal thicknesses of about 5-20 km. In contrast, the close spacing of the highlands banded terrain is likely due to a thick (>30 km) crust, resulting in a thin mechanically strong layer at the surface and no upper mantle strength.

References: [1] Solomon & Head (1984) JGR 89, 6885; [2] Morgan & Phillips (1983) JGR 88, 8305; [3] McGill et.al. (1981) GRL 8, 737; [4] Schaber (1981) GRL 9, 499; [5] Zuber et.al. (1985) LPSC XVI, 948; [6] Brace & Kohlstedt (1980) JGR 85, 6248; [7] Banerdt & Golombek (1985) LPSC XVI, 23; [8] Shelton & Tullis (1981) EOS 62, 396; [9] Goetze (1978) Phil Trans RSL A288, 99; [10] Vening Meinesz (1950) Bull Inst R Colon Belge 21, 539; [11] Bott (1976) Tectonophys 36, 77; [12] Campbell et.al. (1983) Science 221, 644; [13] Campbell et.al. (1984) Science 226, 167; [14] Banerdt (1985) JGR, in press; [15] Kirby (1980) JGR 85, 6353.

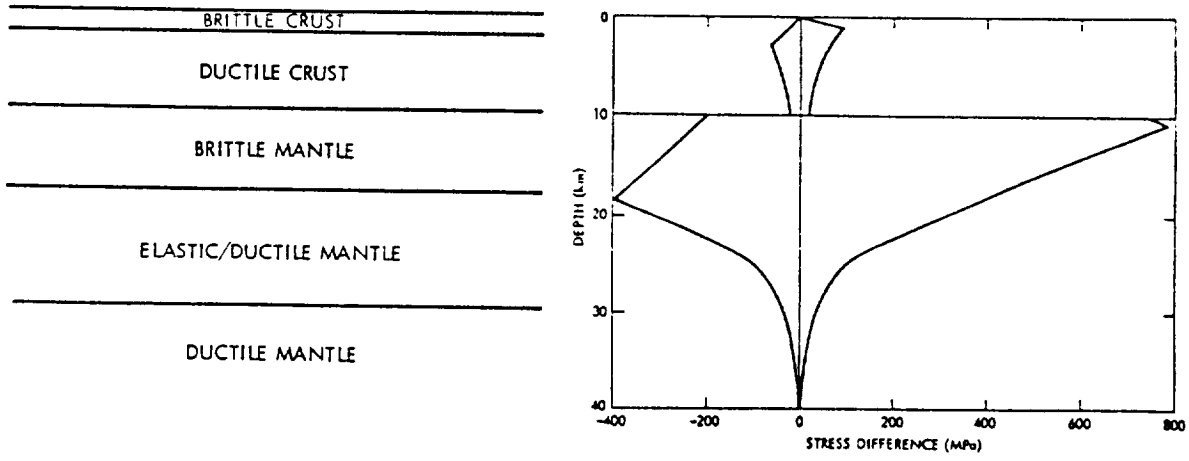

FIGURE 1.

SUBSURFACE HEATING DURING IMPACT BASIN FORMATION: CONSTRAINTS FROM THERMAL CONTRACTION AND THERMAL STRESS

Steven R. Bratt and Sean C. Solomon (Dept. of Earth, Atmospheric, and Planetary Sciences, Massachusetts Institute of Technology, Cambridge, MA 02139) and James W. Head, Dept. of Geological Sciences, Brown University, Providence, RI 02912.

Introduction. Potentially important contributors to the topography and tectonics of multi-ringed basins are the thermal contraction and thermal stress that accompany the loss of heat emplaced during basin formation [1]. In order to assess the significance of thermal stress for the tectonics of impact basins, we develop models for the anomalous temperature structure immediately following basin formation, for the subsequent cooling of the lithosphere, and for the resulting thermal displacements and stresses as functions of time. The displacement and stress fields are compared to topographic profiles and tectonic features for the relatively well-preserved Orientale basin [2-4]. The quantity and distribution of impact kinetic energy retained as buried heat may be constrained by these comparisons.

Geologic observations: The Orientale basin, the youngest and best preserved of all lunar basins [2,5], is an optimum location to look for topographic and tectonic expressions of basin cooling and contraction. The central depression displays 4 km of topographic relief [3]; the depression is filled with mare basalt units less than 1 km thick [2]. We therefore suggest 5 km as an upper bound on the subsidence produced by thermal contraction near the basin center. A number of narrow fissures roughly concentric to the basin are preserved at radial distances between 150 and 230 km from the basin center [4]. The fissures postdate the cooling of the melt-sheet and predate the emplacement of mare units 100-200 m.y. after basin formation, and they may be the product of local thermal stress [4]. These fissures appear to be analogous to extension fractures formed normal to the direction of maximum extensional stress in laboratory samples at low confining pressure [6]. Thus the orientation of the fissures suggests that they were formed in a state of radial extensional stress.

Analysis. We assume that the model for basin thermal evolution obeys cylindrical symmetry. We include two primary sources of initial heating of the basin region: (1) uplift of crustal and mantle isotherms during collapse of the transient cavity, and (2) conversion of impact kinetic energy to heat. Heating contributed by isotherm uplift is estimated from an assumed basin age of 3.8 b.y., a global thermal history model [7], and the extent of mantle uplift indicated by an inversion of gravity and topographic data [8]. The quantity (E_B) and spatial distribution of impact energy converted to buried heat are highly uncertain. Following several investigators [9,10], we assume that E_B varies as $e^{-R/s}$, where R is the slant-range distance $(r^2+z^2)^{1/2}$ from the center of symmetry on the pre-impact surface and s is a spatial decay constant. The quantities E_B and s are free parameters.

The thermal evolution of the basin is calculated from the superposition of solutions for cooling cylinders in a half-space of uniform physical

properties [1]. The thermal displacement and thermal stress fields as functions of time are computed using the method of thermoelastic displacement potentials [11]. We also consider models in which material at temperatures above an elastic "blocking temperature" [12] does not contribute to thermal stress in the elastic portion of the lithosphere.

Orientale model. Gravity and topographic data indicate that the upper mantle beneath the center of Orientale was uplifted by about 55 km [8]. The total anomalous heat generated by isotherm uplift beneath the basin is estimated to be 1.4×10^{32} erg. If this were the only source of initial heat, subsidence of the basin center following complete cooling would be about 0.5 km. Radial thermal stress σ_{rr} is predicted to be compressional (positive) near the basin center and extensional at greater radial distances. However, σ_{rr} reaches the extensional strength of rocks, ~ -0.2 to -0.4 kbar [6], only at distances beyond the region of extensive fissuring in Orientale. If fissuring is a product of thermal stress, then isotherm uplift cannot be the primary source of initial heat. This suggests that the magnitude of impact heating was comparable or greater than 10^{32} erg.

The thermal subsidence and radial thermal stress predicted by an impact heating model ($E_B = 7 \times 10^{32}$ erg, s = 50 km) that produces a good match to the topography and tectonics of Orientale are shown in Figure 1. The final subsidence of 4.5 km at the basin center, when added to the subsidence contributed by the cooling following isotherm uplift, accounts for the entire pre-mare relief of the Orientale central depression. By 100 m.y., accumulation of thermal stress is nearly complete, in agreement with the inferred timing of fissuring. By suitable choice of s, σ_{rr} is most extensional in the radial distance range where fissures are observed. Inclusion of a blocking temperature in a model otherwise similar to that of Figure 1 moves the location of maximum extensional radial stress to greater radial distance, thus requiring a smaller value of s to match the fissure positions and a somewhat smaller value of E_B to be consistent with the upper bound on subsidence.

Conclusions. Exploratory models of the thermoelastic effects of basin cooling indicate that thermal displacement and thermal stress were important contributors to the topography and tectonics of multi-ringed basins. The analysis also leads to new constraints on the quantity and distribution of impact kinetic energy converted to buried heat during an Orientale-size impact. We suggest that the magnitude of buried heat during the Orientale impact was between 1 and 7×10^{32} erg and that most of this heat was localized within the inner basin ring.

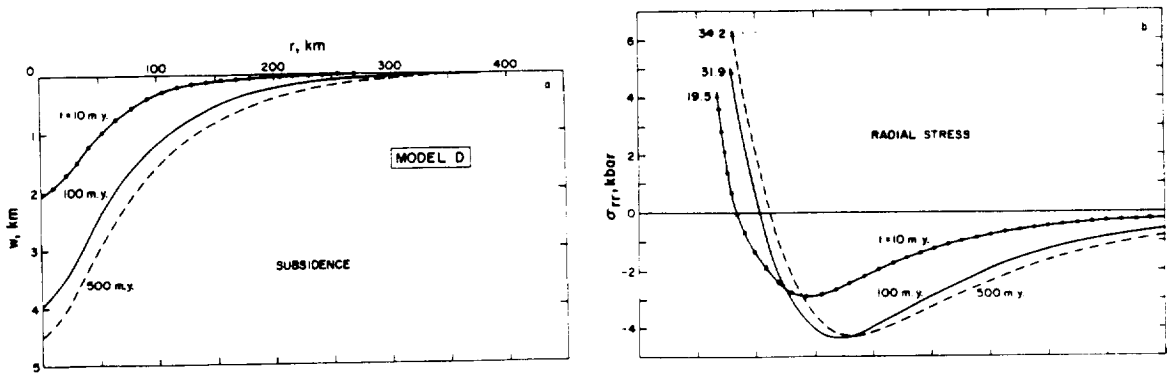

Figure 1. Thermal subsidence and radial thermal stress as functions of time for an impact heating model with $E_B = 7 \times 10^{32}$ erg and s = 50 km.

References: [1] S.R. Bratt et al., LPS, 12, 109, 1981; [2] J.W. Head, Moon, 11, 327, 1974; [3] J.W. Head et al., LPS, 12, 421, 1981; [4] S. Church et al., LPS, 13, 98, 1982; [5] H.J. Moore, PLSC 5th, 71, 1974; [6] W.F. Brace, in State of Stress in the Earth's Crust, ed. W.R. Judd, 110, 1964; [7] S.C. Solomon and J.W. Head, JGR, 84, 1667, 1979; [8] S.R. Bratt et al., JGR, in press, 1985; [9] J.D. O'Keefe and T.J. Ahrens, PLSC 8th, 3357, 1977; [10] W.M. Kaula, JGR, 84, 1994, 1979; [11] R.D. Mindlin and D.H. Cheng, J. Appl. Phys., 21, 931, 1950; [12] D.L. Turcotte, PLPSC 13th, JGR, 88, A585, 1983.

EVIDENCE FOR MAJOR CROSS-STRIKE STRUCTURAL DISCONTINUITIES: MAXWELL MONTES, VENUS

R. W. Vorder Bruegge[1], J. W. Head[1], and D. B. Campbell[2]; 1) Dept. Geo. Sci., Brown Univ., Providence, RI 02912; 2) NAIC Arecibo Observatory, Arecibo, PR 00612.

The nature of tectonic activity on Venus sets important constraints on mechanisms of lithospheric heat transfer (1). Evidence for a variety of extensional and compressional deformation has been found (2-5), but information is still insufficient to characterize the global tectonic style. Ishtar Terra, with its relatively steep bounding and internal slopes (6), and its distinctive mountain ranges (2), shows evidence of major compressional deformation and associated strike-slip faulting (7,8), particularly in the Akna/Freyja mountain region. Here we present an analysis of the most distinctive mountain belt on Venus, Maxwell Montes, and show that in addition to the major compressional deformation, there is a series of lineaments oriented obliquely to the strike of the compressional features that appear to represent a fundamental aspect of the deformation patterns in this region.

Radar images of Maxwell Montes obtained by the Arecibo Observatory show the surface at 1-3 km resolution and 60-70°incidence angles (Figure 1). Early analysis of Arecibo radar images revealed the presence of linear radar bright and dark bands spaced about 10-20 km apart in Maxwell and these were interpreted to be ridges and troughs representing extensive compressional deformation (2). Further analysis suggested that the deforming medium might correspond to the elastic lithosphere (9). In this analysis we have mapped the bands in detail and examined variations in their distribution and characteristics over Maxwell Montes. In the southwest part of Maxwell, bands trend N 35°- 45° W, while in the central region, bands trend N 20°- 25° W; in the east, bands tend to be less continuous, somewhat sinuous, and trend N 15°- 25° W (Figure 1). Although bands tend to show the orientations indicated above, there is some variability within each area. Detailed mapping has revealed the presence of numerous linear features (referred to here as cross-strike structural discontinuities {10}, or CSD's) that trend at angles to the main structural trend of the banded terrain. Of the numerous CSD's that we have mapped we focus here on those that trend generally N 50°- 70° W; the seven main features are shown in Figure 1. These CSD's are defined by a combination of several characteristics: 1) radar dark and bright linear features a few km wide and 50-150 km in length, 2) disruptions in the continuity of the bright and dark linear bands forming the banded terrain either in the form of slight offsets or distinct terminations. These characteristics combine to define numerous CSD's with total lengths ranging from 400-1000 km in this trend direction (N 50°- 70°W), the most prominent of which are shown in Figure 1.

Cross-strike structural discontinuities are seen in at least two structural settings in compressional tectonic environments on Earth: 1) long, continuous linear features that occur at relatively low angles to the strike of compressional features and which represent strike-slip movement (11); 2) shorter linear features that occur at higher angles to the strike (often normal) and that may represent relative deformation between slightly decoupled blocks (10). On the basis of the extreme length and continuity of these features and the fact that bands are seen to terminate or change character at these discontinuities, we are pursuing the hypothesis that they may represent large-scale strike-slip faulting. Present analyses involve comparison of digital profiles

on both sides of the CSD's to establish potential directions and magnitudes of offset, and comparison with images taken under different radar illumination conditions.

References:
1. Solomon, S.C. and J.W. Head, J. Geophys. Res., 87, 9236, 1982.
2. Campbell, D.B. et al., Science, 221, 644, 1983.
3. McGill, G. et al., Geophys. Res. Lett., 8, 737.
4. Phillips, R. and M. Malin, Venus, Univ. AZ Press, 1983.
5. Barsukov, V. et al., The geology and geomorphology of the Venus surface as revealed by the radar images obtained by Veneras 15 and 16, Lunar and Planet. Sci. Conf. XVI, in press, 1985.
6. Sharpton, V.L. and J.W. Head, J. Geophys. Res., 90, 3733, 1985.
7. Crumpler, L.S. et al., Evidence for large-scale horizontal motions in northwest Ishtar Terra, Venus, PGPI abstract, 1985.
8. Basilevsky, A.T. et al., Styles of tectonic deformations on Venus: Analysis of Veneras 15 and 16 data, Lunar and Planet. Sci. Conf. XVI, in press, 1985.
9. Solomon, S.C. and J.W. Head, J. Geophys. Res., 89, 6885, 1984.
10. Wheeler, R., AAPG Bull., 64, 2166, 1980.
11. Taponnier, P. et al., Geology, 10, 611, 1982.

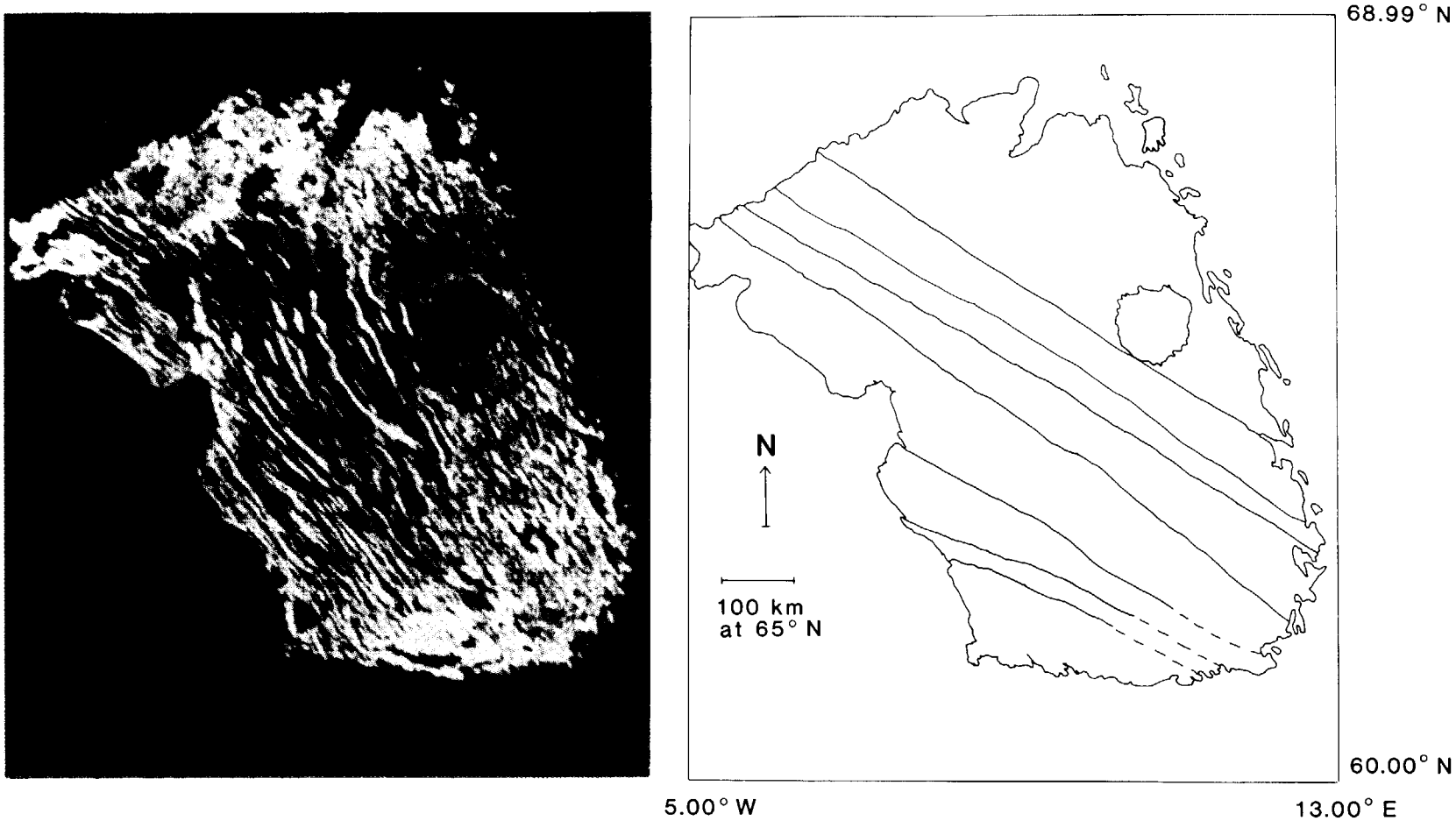

Figure 1. (left) Arecibo radar image of Maxwell Montes region in Ishtar Terra. (right) Sketch map of Maxwell Montes region outlining the area of high reflectivity and showing the location of some major cross-strike structural discontinuities. Dashed lines indicate areas of uncertainty.

EVIDENCE FOR LARGE-SCALE HORIZONTAL MOTIONS IN NORTHWEST ISHTAR TERRA, VENUS; L.S. Crumpler[1], J.W. Head[1], and D.B. Campbell[2]; 1) Dept. Geo. Sci., Brown Univ., Providence, RI 02912; 2) NAIC Arecibo Observatory, Arecibo, PR 00612.

Introduction - The detailed nature of tectonism on Venus is not yet clear, but the lineated and parallel bands seen in radar images of Lakshmi Planum (1,2) are distinctive evidence for a style of deformation unlike that seen elsewhere with the exception of compressive orogenic belts on the Earth (2,3). In this report we discuss the results of new analysis of complex patterns in the northwestern part of Ishtar Terra seen in Arecibo radar imagery (4) between 60° to 77° north and 300° to 340° east which suggests that large-scale strike-slip and thrust faulting types of deformation may be important in the physiographic development of this terrain. We here report on the analysis of Arecibo radar obimages of the Ishtar Terra region (5). Several characteristics of the lineated terrain are visible in Arecibo images (Figure 1). The brightest bands correspond with higher topography of Akna Montes and Freyja Montes identified in Pioneer-Venus altimetry maps. Individual slightly sinuous radar-bright bands generally strike parallel to the margins of the Lakshmi Planum upland forming a distinctive "banded terrain" (2) halo up to 1200 km (600 km typical) from the radar-dark interior of Lakshmi Planum. Near Lakshmi Planum the change in strike of bands is abrupt from nearly north-south in Akna Montes to east-west in Freyja Montes. Farther from Lakshmi Planum, the change in strike occurs in a smoother arc suggesting that the bands at great distance are controlled by the shape of the upland or by the trends of Akna Montes and Freyja Montes. The overall impression is one in which bands parallel the margins of Lakshmi Planum, but distinct departures from this trend are evident west of Akna Montes. Beginning on the north and west of northern Akna Montes, bands curve southwesterly away from Akna Montes forming an arc in band trends in the western quarter of the area of FIgure 1. Although individual bands are continuous for 150 km (50 km typical), large areas of bands tend to have abrupt linear truncation zones striking 60° to 70° with respect to the strike of the bands. These are most notable where the bands terminate against darker areas such as the triangular dark area of 73° N 314° E, or the termination at 76° N/305° E. Similar terminations occur within banded zones in which parallel bands terminate against bands with similar strikes, but which are discordant or non-matching linear offset zones, such as the east-northeast trend through the east-west striking bands of central Freyja Montes. A radar-bright circular feature centered at 74°N/315°E correlates with the slopes of a PV altimetry identified depression. Several smaller circular features, two near 71°N/321°E and 324°E, and one near 71°N/301°E are probably impact craters as suggested by their circularity and central peak-like bright centers.

Analysis - The parallel and continuous form of the bands has been compared with regions of compressional deformation on the Earth (2,3) in which bands may be radar expressions of fold crests. The overall pattern, particularly the band termination zones,are additional support for this interpretation. We interpret these terminations as the result of strike-slip displacements (Figure 2). Although normal faulting can be considered locally, the evidence for lateral offset is suggested in Freyja Montes where the continuous linear trend of individual bands can be restored along discordant zones if 50 to 100 km of right lateral slip is assumed to have occurred. Similarly, several bands and dark zones match along the discordant zones west of Akna Montes when inferred left lateral displacements are reversed. A consequence of this interpretation of displacements is that the relatively dark area containing the circular depression may be viewed as a wedge which has undergone a net northerly displacement analogous to extrusion wedge tectonic features on the Earth. Examples of the latter include the Mojave Block (6) and Caribbean plate (7). If bands are compressional in origin, then these directions of displacement are consistent with the orientation of principal stresses that would be responsible for band formation. The arcuate pattern of bands west of Akna Montes may be bounded to the south by a similar discordant trend-line like that bounding it on the north. Kinematically, the impression is one of compression and lateral southeasterly translation of a thrust sheet-like domain defined by this arcuate group of bands. The wedge containing the depression in this scenario, like the Mojave Block between the San Andreas and Garlock faults, is caught between the southeasterly verging arcuate band zone and the uplands of Lakshmi Planum and Freyja Montes. The through-going shears of Freyja Montes are a consequence of continued clockwise rotation of the principal stress direction resulting from the extrusion wedge style of kinematics.

Comparison with the Himalaya-Tibet Orogenic Belt - The banded terrain of Maxwell Montes has been previously compared with the Himalayas because both areas are the highest terrains on Venus and Earth (8). We consider the Akna/Freyja area to be more analogous on the basis of similarities in deformation patterns. The pattern of deformation in the Himalaya-Tibet-Southeast Asia orogenic belt has been interpreted in a similar manner (9, 10). In terms of counterparts, Lakshmi Planum is similar to India; Akna Montes, the high Himalayas; Freyja Montes, the Indo-Burma range; the through-going shears of northern Freyja Montes, the Red River and Sagaing Faults; the circular depression, the Shansi graben system; and the Akna-Freyja change in band strike is analogous to the Assam Syntaxis. Other similarities can be cited, but there are also conspicuous dissimilarities: the scale of the Himalaya-Tibet orogenic belt is about 2.5 times that of the comparable Akna-Freyja deformation zone; the highest topography is restricted to a zone about 200 km wide in the Akna Montes, whereas high topography extends considerably in excess of 500 km north-south across the Himalaya-Tibetan Plateau; Freyja Montes is comparable in height to Akna Montes, whereas the Indo-Burma range is lower than the Himalayas; Lakshmi Planum is dominated by large volcanic constructs, whereas no corresponding volcanic feature occurs in India. Although there are differences, the tectonic patterns and inferred kinematics are remarkably similar. It is not clear whether the scale of horizontal deformation is also analogous to the scale (hundreds of km) of convergence of the Asia-India collision (11). If the scale of strike-slip movement is as large as that implied by the most extreme interpretation applicable to the inferred shears in Akna Montes and Freyja Montes, then comparable convergence is implied.

Conclusions - The Akna-Freyja orogenic belt is strikingly similar in many fundamental ways to the tectonic and morphologic character of the Tibetan Plateau and the general Indian-Asian convergence zone, although the horizontal extent of the zone of deformation on Earth is about 2.5 times that on Venus. The nature of the Akna/Freyja orogenic belt argues strongly for large areal-scale horizontal compressional deformation in this part of Ishtar Terra. Although the Akna/Freyja zone may represent convergent plate processes and the production of a collisional zone, additional analyses of the rest of Ishtar Terra must be completed, and explanations must be sought for the numerous differences between Akna/Freyja and the Indian/Asian zone, before lithospheric plate recycling can be confidently identified as the fundamental formational process.

References - 1) D.B. Campbell et al. (1983) Venus: Identification of banded terrain in the mountains of Ishtar Terra: Science, 221, 644-647; 2) J.W. Head et al. (1983) Characterization of the banded terrain in Akna and Freyja Montes, Venus: Lunar Planet. Sci. Conf. XIV, 293-294; 3) S.C. Solomon and J.W. Head (1984) Venus banded terrain: Tectonic models for band formation and their relationship to lithospheric thermal structure: J. Geophys. Res., 89, 6885-6897: 4) D.B. Campbell and B.A. Burns (1983) Earth-based radar imagery of Venus: J. Geophys. Res., 85, 8271-8281; 5) D.B. Campbell et al. (1982) Venus radar images: Lunar Planet. Sci. Conf. XIII, 83; 6) D. Cummings (1976) Theory of plasticity applied to faulting, Mojave Desert, southern Calif.: GSA Bull., 87, 720-724; 7) P. Mann and K. Burke (1984) Neotectonics of the Caribbean: Rev. Geophys. Sp. Phy., 22, 309-362; 8) K. Burke et al. (1984) Maxwell Montes in Ishtar - A collisional plateau on Venus: Lunar Planet. Sci. Conf. XV, 104; 9) P. Tapponnier et al. (1982) Propagating extrusion tectonics in Asia: New insights from simple experiments with plasticine: Geology, 10, 611-616; 10) Le Dain et al. (1984) Active faulting and tectonics of Burma and surrounding regions: J. Geophys. Res., 89, 453-472; 11) M.P. Coward and R.W.H. Butler (1985) Thrust tectonics and the deep structure of the Pakistan Himalaya: Geology, 13, 417-420.

Figure 1: Arecibo radar image of northwestern Ishtar Terra.
Figure 2: Tectonic sketch map of area of Fig. 1. Long axes of crosses show direction of interpreted maximum principal stress orientation, short axis, strike of bands. Teeth point toward sole of thrust faults: arrows indicate interpreted direction of movement on strike slip faults; closed circles are impact craters.

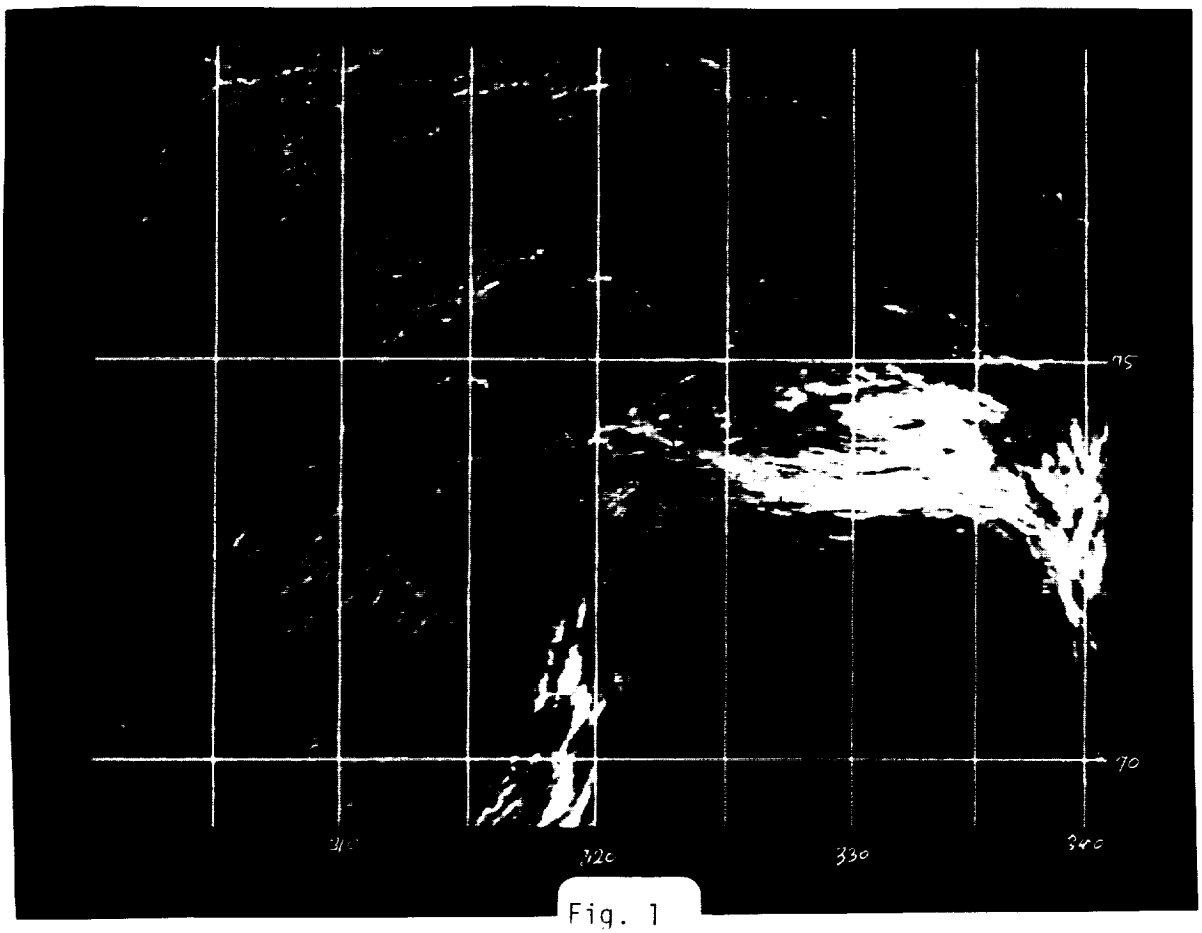
75
70
320
330
340

Fig. 1

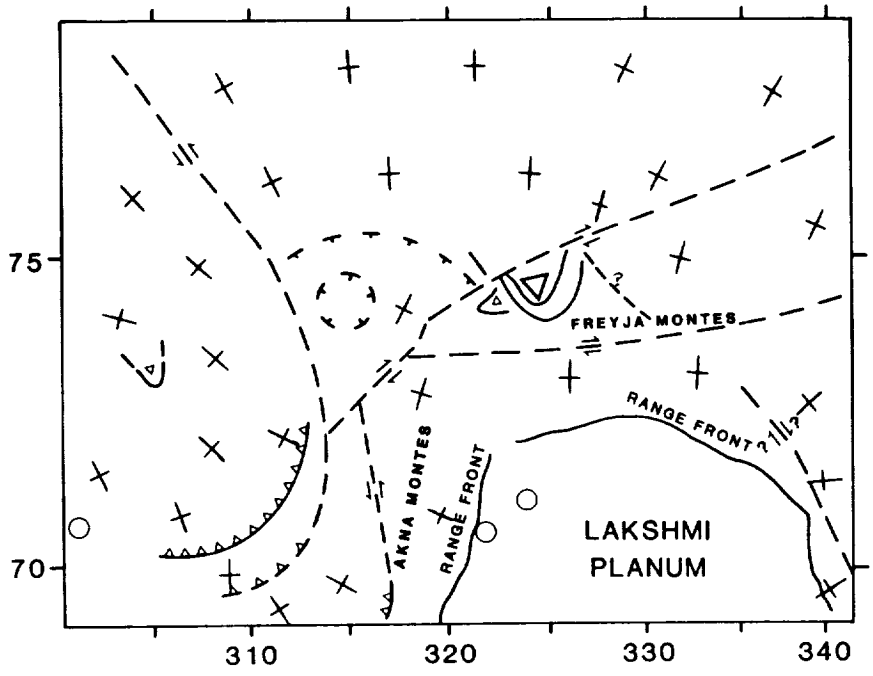
75
70
310
320
330
340
FREYJA MONTES
RANGE FRONT
AKNA MONTES
RANGE FRONT
LAKSHMI
PLANUM

Fig. 2

ANCIENT FRACTURES IN THE THARSIS REGION

Robert A. Francis, Department of Geology and Geography
University of Massachusetts, Amherst, MA 01003

The events that led to the formation of the Tharsis region of Mars continue to generate debate. Three general scenarios for the formation of Tharsis have arisen from this debate. To generalize, these are: the volcanic construct model (Solomon and Head, 1982; Willemann and Turcotte, 1982), the isostatic compensation model (Sleep and Phillips, 1979; Banerdt et al., 1982), and the lithospheric uplift model (Banerdt et al., 1982).

Sleep and Phillips (1982) developed stress history models for both volcanic construction and isostatic compensation. How well these models fit the strain tracers observed in the Tharsis region depends on the relative ages of the radial fractures. If the outer radial fractures surrounding the Tharsis region are older than the fractures found in the central Tharsis region, then the isostatic compensation model gives the best fit to the observed conditions. Conversely, if a subset of the outer radial fractures is younger than the central fractures, then the volcanic construct model gives the best fit.

This use of the outer radial fractures may introduce some error into the degree of fit of these models. Young radial grabens may reflect late stage events that are not necessarily associated with the formation of the Tharsis region. Many of the young radial grabens to the south and west of Tharsis extend from young plains material into old cratered units, where they parallel older radial grabens. Some of these late stage grabens may derive from stresses unrelated to the formation of Tharsis, and owe their apparent radial orientations to pre-existing zones of weakness. Young radial grabens found on recent volcanics might not accurately reflect crustal stresses at depth, or they could reflect events which have no direct correlation with the crustal stresses present as the Tharsis region began to form. Old features, found in the ancient cratered terrains surrounding the Tharsis region, would provide data concerning events that took place during the early growth of Tharsis.

The ancient cratered terrain to the west, south, and east of the Tharsis region includes several different indicators of crustal stress. Figure One indicates the area of study, chosen to exclude the youngest volcanics of central Tharsis. It also includes the locations, orientations (in cartoon form), and descriptions of the observed fracture sets. To date, I have found two types of large scale features that are roughly concentric to the Tharsis region. These are the rotated blocks and the grabens with listric normal faults referred to in Figure One. There are also grabens present with similar concentric orientations. The presence of old, concentric fractures conforms with the isostatic compensation model put forth in Sleep and Phillips (1982);

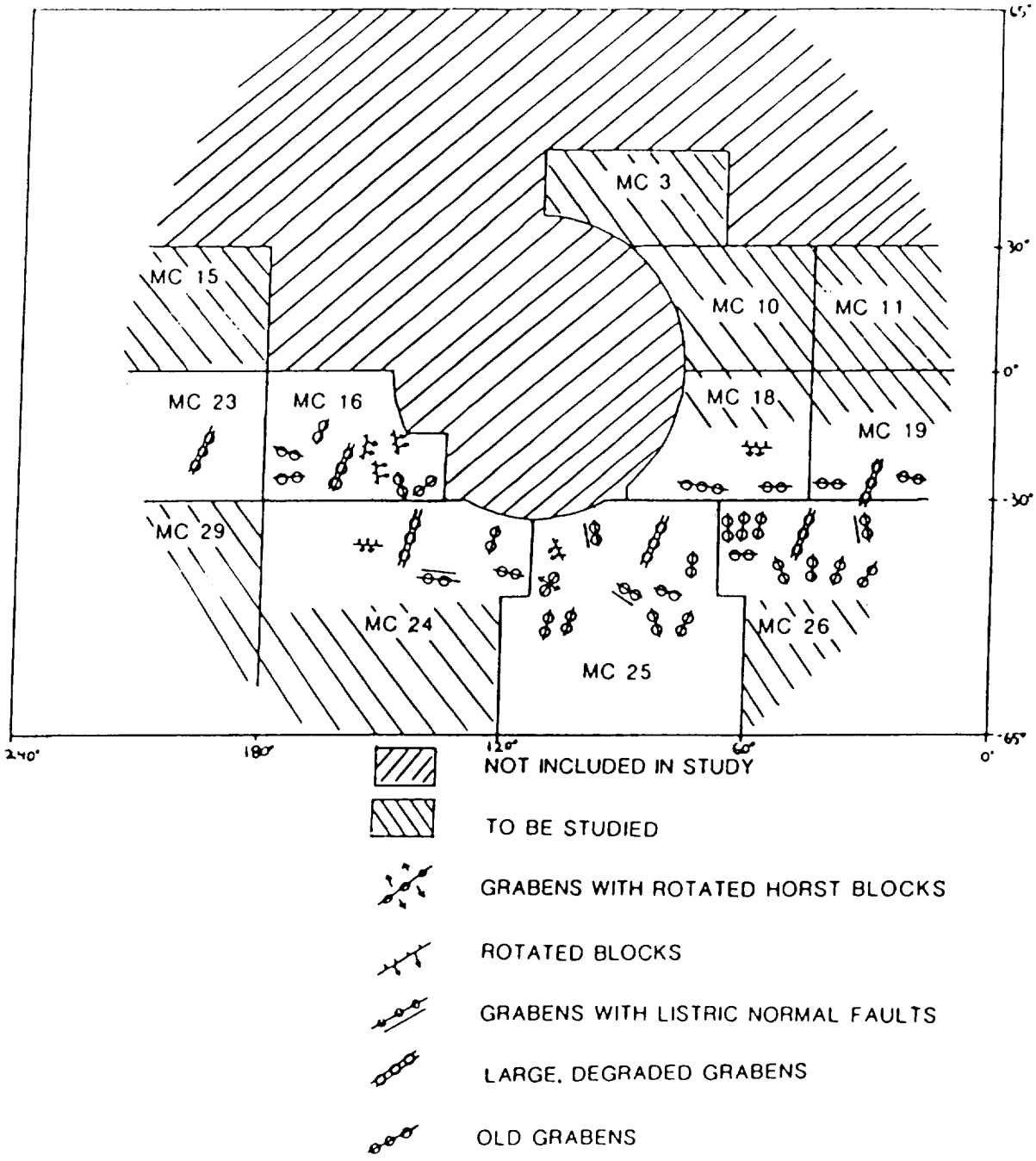

Figure One: Sketch map showing study area, features of interest, and location of features found to date.

hence, the tentative conclusion is that this is the preferred model. When this study is complete, early stress orientations and stress history of the entire Tharsis region will be available for a more complete comparison with the various models proposed.

References cited

Banerdt, W.B., R.J. Phillips, N.H. Sleep, and R.S. Saunders, Thick shell tectonics on one-plate planets: Applications to Mars, J. Geophys. Res., 87, 9723-9733, 1982.

Sleep, N.H., and R.J. Phillips, Gravity and lithospheric stress on the terrestrial planets with reference to the Tharsis region of Mars, J. Geophys. Res., 87, 4469-4489, 1985.

Solomon, S.C., and J.W. Head, Evolution of the Tharsis province of Mars: The importance of heterogeneous lithospheric thickness and volcanic construction, J. Geophys. Res., 87, 9755-9774, 1982.

Willemann, R.J., and D.L. Turcotte, The role of lithospheric stress in the support of the Tharsis rise, J. Geophys. Res., 87, 9793-9801, 1982.

TECTONIC TESTS OF PROPOSED POLAR WANDER PATHS FOR MARS AND THE MOON
Robert E. Grimm and Sean C. Solomon (Dept. of Earth, Atmospheric, and Planetary Sciences, Massachusetts Institute of Technology, Cambridge, MA 02139)

Introduction. Changes in the inertia tensor of a solid planet due to mass redistribution can lead to a reorientation of the planet with respect to its spin axis [1]. Stresses induced by the consequent repositioning of the rotational bulge may fracture the lithosphere. For planets with significant flattening and substantial excursions of the pole, the predicted lithospheric stresses are large enough to yield global faulting in a pattern diagnostic of the polar wander path [2]. The key interpretative element in this pattern is the formation of a province of N-S striking normal faults in the vicinity of the former pole. This region has a radius of roughly 30° of arc and is centered somewhat equatorward of the paleo-pole. Since rocks are generally weakest under extension, the identification of N-S normal faults near the positions of the former rotation poles is a minimum tectonic signature to be expected for significant planetary reorientation. We use this criterion to test recent suggestions that significant polar wander may have occurred on Mars [3-5] and the Moon [6-7].

Mars. Schultz and Lutz-Garihan [3-5] have constructed an approximate Martian polar wander path, based on the identification of regions of mantled and layered terrain that resemble present polar deposits and on the apparent age dependence of the inferred directions of approach of grazing impacts on the Martian surface. We tested the predictions only of the most recent segment of that path, a reorientation of the pole from 15°N, 150°W (in Amazonis Planitia) to its present position. The timing of this proposed reorientation is uncertain, at least partly because various measures of the age of this paleopole [3-5] range between the time of emplacement of Lunae Planum volcanic units and the final stages of construction of Olympus Mons. This wide range in time spans a number of significant volcanic and tectonic episodes in the history of the Tharsis province [8,9], a potential source of the reorientation of principal moments of inertia of the planet [2-5].

For this reorientation, the predicted provinces of N-S normal faulting extend approximately from 30°S to 40°N and from 120° to 180°W for the pole in Amazonis Planitia and from 40°S to 30°N, 300° to 360°W for the opposite pole near Sinus Sabaeus. Predicted shear stresses exceed 2 kbar in these regions. The preserved tectonic features, however, do not match these predictions. N-S normal faults occur in Tharsis, but are too distant to match the reorientation theory and are more probably related to the response of the Martian lithosphere to the development of the Tharsis rise [10,11]. Moreover, the diagnostic features are completely lacking near Sinus Sabaeus.

Stresses induced by polar wander may have been superposed on a pre-existing stress field produced by other processes, particularly the loading of the Martian lithosphere by the Tharsis rise [10,11]. We have superposed the stresses predicted by polar wander with the stresses predicted by the models of Banerdt et al. [10] for Tharsis loading. The

addition of stresses due to their flexural loading model results in only modest changes to the predicted province of N-S normal faulting in Amazonis Planitia and has little effect in the Sinus Sabaeus region. The effects of the alternative isostatic loading model for Tharsis on the reorientation stress field are negligible.

We have also considered the possibility that the duration of reorientation was significantly longer than the time scale for release of accumulated stress by fracturing, in which case the diagnostic tectonic pattern might resemble that of several discrete reorientations of smaller magnitude. The principal tectonic criterion for evidence of polar wander (i.e., regions of normal faults striking roughly N-S along the locus of former rotation poles) would remain valid. Even with the superposition of stresses associated with Tharsis, N-S normal faults would be expected near the paleo-pole at 15°S, 330°W.

Moon. Runcorn [6,7] has suggested that significant polar wander has occurred on the Moon since the formation of the major multi-ring basins. He cites as evidence the clustering of apparent paleomagnetic poles for magnetic anomalies inferred to have similar formation ages, and the tendency for the inferred directions of approach of basin forming impacting bodies to lie in the paleo-equator. We tested the tectonic predictions of the youngest segment of this path, a reorientation of the north rotation pole from 43°N, 170°E to its present position [7].

For the Moon it is necessary to sum the stresses produced by reorienta-tion of both the rotational and tidal figures. Because of the fortuitious position of the postulated paleo-pole near the 0° meridian passing through the greatest and least principal axes of the lunar figure, the stresses due to the rotational and tidal figures interfere constructively, preserving the overall stress pattern including the diagnostic N-S normal fault region. We use the hydrostatic flattenings in both cases; in effect we are assuming that any non-hydrostatic contributions to the lunar figure are simply carried along with the lithosphere during reorientation without causing additional changes in radius of curvature. The predicted stress magnitudes are therefore lower bounds, since rotational and tidal deformation has decreased with the recession of the Moon's orbit [e.g.,12].

The predicted N-S normal fault province for the lunar nearside lies within a region between about 10°N and 50°S, and between 40°W and 20°E. The maximum shear stress in this region for a hydrostatic moon, however, is only 12 bars. No correlation of the predicted stresses with tectonic features is apparent. If reorientation did occur, the most likely explanation is that the magnitude of induced stress was not sufficient to cause failure. Since reorientation stress is proportional to the inverse cube of the Earth-Moon distance, a factor of 10 or more increase in the predicted stress would require the Moon to be within 0.46 of its present distance. However, models of lunar orbital evolution [12] indicate that 98% or more of the total recession time is spent at greater than half the present distance, regardless of absolute time scale. It is therefore likely that the Earth-Moon distance at the time of any reorientation 3.9 b.y. ago was already large enough so that the magnitude of induced stress

was too small to cause lithospheric failure.

Conclusion. While the tectonic test of polar wander for the Moon is inconclusive, the distribution of tectonic features on Mars does not support the proposed polar wander scenario [3-5]. Given that the Tharsis rise is a major contributor to the non-hydrostatic figure [13], it follows either that Tharsis has always been located near the Martian equator or that Tharsis began to dominate the non-hydrostatic figure before the end of heavy bombardment, so that any tectonic signature of reorientation has since been obliterated by cratering. This second alternative is consistent with models calling for the early initiation of volcanic construction and lithospheric deformation in the Tharsis region [14].

References: [1] P. Goldreich and A. Toomre, JGR 74, 2555, 1969; [2] H.J. Melosh, Icarus 44, 745, 1980; [3] P.H. Schultz and A.B. Lutz-Garihan, LPS 12, 946, 1981; [4] P.H Schultz and A.B. Lutz-Garihan, Third Inter. Colloq. Mars, 229, 1981; [5] P.H Schultz and A.B. Lutz-Garihan, PLPSC 13th, JGR 87, A84, 1982; [6] S.K. Runcorn, PEPI 29, 135, 1982; [7] S.K. Runcorn, Nature 304, 5927, 1983; [8] D.H. Scott and K.L. Tanaka, PLPSC 11th, 2403, 1980; [9] J.B. Plescia and R.S. Saunders, JGR 87, 9775, 1982; [10] W.B. Banerdt et al., JGR 87, 9723, 1982; [11] R.J. Willemann and D.L. Turcotte, JGR 87, 9793, 1982; [12] G.J.F. MacDonald, RGSP 2, 467, 1964; [13] W.M. Kaula, GRL 6, 194, 1979; [14] S.C. Solomon and J.W. Head, JGR 87, 9755, 1982.

OLYMPUS MONS AUREOLE: EVIDENCE FOR EXTENSIONAL AND COMPRESSIONAL DEFORMATION ASSOCIATED WITH EMPLACEMENT; James W. Head and Nicholas G. Carras, Dept. Geological Sciences, Brown Univ., Providence, RI 02912.

The distinctive aureole surrounding Olympus Mons has been attributed to a wide range of geologic processes including erosion of a previous volcanic structure (1), subaerial (2) and subglacial (3) lava flows, pyroclastic flows (4), large catastrophic landslides (5), and large-scale thrust sheets (6). Recently, Francis and Wadge (7) have presented new observations of the characteristics of the aureole deposits and have convincingly argued that the aureole lobes could have been formed by gravitational sliding (5,6) away from the scarp surrounding the base of Olympus Mons, rather than by any of the range of other proposed origins. They further outline a gravitational spreading mechanism that involves accumulation of lavas on the ancient flanks of the volcano, spreading of these flank deposits under gravity by decoupling along a basal surface, formation of the peripheral scarp in the proximal areas, and imbricate thrusting in distal regions, analogous with terrestrial thrust sheets (7). They attribute the corrugations in the aureole to erosion along imbricate or listric faults. The purpose of this study is to gain further insight into the mechanisms of emplacement of the aureole deposits by 1) classifying and mapping the structures and textures in the individual aureole lobes, and 2) comparing similarities and differences between lobes. Following the nomenclature of Morris and Dwornik (8), we have mapped the detailed texture and structure of the youngest lobe, au4, and we report our preliminary results here. Aureole lobe au4 extends for a distance of about 600 km NW from the base of the scarp surrounding Olympus Mons and is about 700 km wide at its widest point, forming a crudely circular deposit slightly larger than Olympus Mons itself. The lobe lies along the regional downslope extending away from the Tharsis rise. Although remnants of deposits and structures can be seen over virtually this whole area, the aureole has been modified by subsequent events including eolian and volcanic processes. In particular, large sections of the aureole extending for about 200 km from the base of the Olympus Mons scarp have been covered by volcanic plains. In Fig. 1 we present a preliminary map of the detailed structure and texture of a major portion of the au4 lobe and in our discussion we reference structural orientations to a radial line extending from the summit of Olympus Mons. A major portion of the distal parts of this lobe are made up of a distinctive set of parallel ridges (5-6) which lie approximately normal (transverse) to the radial reference and form a distal band 100-150 km wide. Crest-to-crest distance between ridges averages 4-5 km and average lengths are about 70 km. Individual ridges are usually slightly sinuous. A second patch of this ridged unit approximately 100 km wide lies to the SE of the main deposit. We concur with (7) and interpret these structures as representing topography associated with structural discontinuities, slightly modified by eolian processes. We further interpret these features as representing compressional deformation perhaps including folding, thrusting, and imbricate faulting. Located approximately 350 km from the distal end of the lobe and about 600 km from the crest of Olympus Mons is an apparently elevated rectangular (300 x 150 km) smooth-surfaced region, the SW portion of which can be seen in Fig. 1. The contact with surrounding aureole deposits is very irregular and the eastern boundary is marked by a major linear scarp facing Olympus Mons. A second major feature that characterizes portions of the lobe is a series of flat-floored valleys. The floors of these valleys range from 4.5 - 6.5 km in width and they average about 100 km in length. They have two orientations, generally transverse, and generally radial. On the basis of their linear nature and flat floors, we interpret these to be graben representing extensional deformation. The transverse flat-floored valleys (graben) are widely distributed between the smooth terrain and the transverse ridged terrain. Radially oriented flat-floored valleys are concentrated in two places (see Fig. 1) in this area. A third major structure that characterizes portions of the lobe are narrow linear features without flat floors that extend from 75-240 km in length, and are oriented in a wide range of angles between radial and transverse. At some places these features parallel the edge of an extension of the lobe (type 1), and some evidence is found for small amounts of strike-slip offset (7). In other places, these features are arrayed at a range of angles between radial and transverse (type 2). A wide variety of structural relationships are observed: radial and transverse graben cut transverse ridges, the generally radial linear faults cut transverse ridges and graben, and radial graben appear to cut and be cut by transverse graben. In summary, this portion of aureole lobe au4 can be subdivided on the basis of its structure and texture into a distal region dominated by transverse ridges and compressional deformation, an intermediate region characterized by flat-floored graben and pervasive extensional deformation, and a proximal region characterized by smooth, apparently elevated terrain. It is tempting to speculate that these three units are linked and that this portion of the lobe might be a major detachment fault (8) with the detachment sheet being shed off the smooth high, undergoing thrusting and imbrication in its distal portions, and extension in intermediate areas. In this case, type 1 linear faults might represent the lateral boundaries of the detachment or thrust sheet, and type 2 might represent minor strike-slip faulting patterns occurring at angles to the maximum principle stress axis. We are testing this hypothesis by measuring the relative amounts of deformation in the extensional and compressional regions, establishing the local and regional sequence of deformation, and examining evidence for the scale of lateral movement in various parts of the aureole. In conclusion, our mapping supports the hypothesis of Francis and Wadge (7) that the aureole deposits are tectonic in origin and related to gravitational spreading. We find strong evidence for pervasive tectonic deformation in the region mapped in detail and we

see evidence for a locus of extensional deformation several hundred km from the base of the Olympus Mons scarp. On the basis of these results, we believe that gravitational spreading may be enhanced by topographic variations and stresses produced by lithospheric flexure related to the evolving load of the Olympus Mons volcanic edifice. In particular, models by Comer and others (9) suggest that the eastern part of the map area (Fig. 1) could be characterized by flexural topography and extensional deformation. We are presently examining the role of lithospheric loading in more detail as a potential factor in the formation and evolution of the Olympus Mons aureole deposits.

1) Carr, M.H. et al., Icarus, 78, 4031, 1973.
2) Morris, E.C. and S.E. Dwornik, U.S. Geol. Surv. Map, I-1049, 1978.
3) Hodges, C.A. and H.J. Moore, J. Geophys. Res., 84, 8061, 1980.
4) Morris, E.C., J. Geophys. Res., 87, 1164, 1982.
5) Lopes, R.M.C. et al., J. Geophys. Res., 87, 9917, 1982.
Lopes, R.M.C. et al., Moon Planets, 22, 221, 1980.
6) Harris, S.A., J. Geophys. Res., 82, 3099, 1977.
7) Francis, P.W. and G. Wadge, J. Geophys. Res., 88, 8333, 1983.
8) Frost, E.G., Arizona Geol. Soc. Digest, 13, 25, 1981.
9) Comer, R.P. et al., Rev. Geophys. Sp. Phys., in press, 1985.

Figure 1

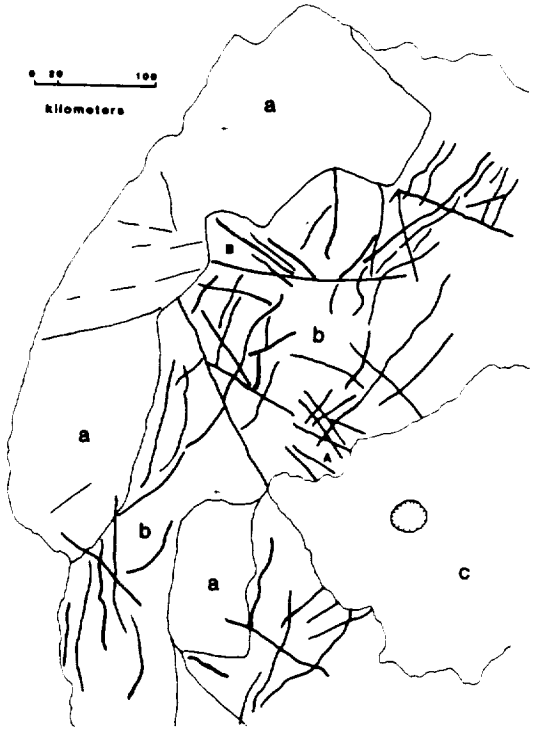

Key

a- distal region, dominated by transverse ridges and compressional deformation.

b- intermediate region, characterized by flat-floored graben and extensional deformation.

c- proximal region, characterized by smooth elevated terrain.

crater

flat-floored valleys (graben).

linear features without flat floors.

A,B- graben with radial orientation.

CREEP OF ICE: FURTHER STUDIES

H. C. Heard[1], W. B. Durham[1], and S. H. Kirby[2]
[1]UCLLNL, Livermore, CA 94550; [2]USGS, Menlo Park, CA 94025

Measurements of the flow of several of the phases of polycrystalline ice as a function of pressure, temperature, stress, and impurity content are needed to constrain evolutionary models of icy bodies in the solar system (in particular Jupiter's large moons Ganymede and Callisto) and to aid in our understanding of surface processes on those bodies[1,2]. The rheology of pure ice I_h is well constrained throughout most of its pressure-temperature stability field[3]. Not well constrained are the rheologies of the higher pressure ice phases nor the rheologies of any ice phase mixed with plausible contaminents in the outer solar system: NH_3, CH_3, and silicate particulates.

In the past year we have completed experimental work in three important areas: 1) Flow and fracture of ices II, III, and V; 2) Frictional strength of ice I_h; and 3) Strength of ice I_h at low strain rate.

1. Flow and fracture of ices II, III, and V. The plastic flow results are summarized in Figure 1. Ice II is the strongest of the three phases, and has roughly the same strength as ice I_h. Ice III is dramatically weaker than any of the other phases. Not shown in the figure are pressure sensitivities. Ice II and ice V strengthen with increasing confining pressure. Over the temperature and strain rate range given in Figure 1, ice II strengthens by roughly 10% per 100 MPa increase confining pressure, ice V by roughly 20%. The pressure effect in ice III is 0% $\pm$ 10% over 100 MPa confining pressure. The ice III data are particularly difficult to resolve because of the very low strength of that phase.

The three phases thus have rather distinct flow laws. This convenient characteristic led us in turn to the discovery that important phase metastabilities exist in pressure-temperature space in ice. The most important of these is the metastability of ice III within the ice II field. It is well known that ice can be supercooled well into the ice II field[4]. What was not known is that such metastable ice III retains its structure even during intense deformation. In repeated tests with ice III at 233 K, we were unable to produce any hint whatsoever of transformation to ice II, even with pressurization to 400 MPa. From all indications, ice III is the preferred phase at T=233 K when the transformation is approached from 233 K or warmer; ice II is the preferred phase at T=233 K (and even cooler, of course) when that temperature is approached from the cooler side. The refractory nature of ice III within ice II is potentially important to Ganymede and Callisto because ice III is so much weaker than ice II and historical temperature (or present) profiles probably passed very close to the II-III phase boundary. The other important metastability we have found, but not investigated deeply, is that ice V seems to retain its structure, even under deformation, well into the ice II field. So far, in fact, we have found that only the III $\rightarrow$ V, and $I_h \rightarrow$ II/III phase boundaries respect, under deformation, the positions reported for them by P. W. Bridgeman[4].

2. Frictional strength of ice I_h. We performed sliding tests on saw cut surfaces last year at T=77 K and a single average slip rate of 3×10^{-3} mm/s. This year we completed that study by performing tests at 90 and 115 K and 3×10^{-3} and 3×10^{-4} mm/s. We found that the shear strength (τ) on prepared ice surfaces varies with the normal stress (σ_n) on the surfaces as $\tau=0.2\sigma_n + 8.5$ MPa and that this relationship is independent of temperature and slip rate over the range studied.

3. Strength of Ice I_h at low strain rate. With some additional hardware in the testing apparatus, we made control of confining pressure partially automatic, sufficiently so that very long runs can be performed with a minimum of effort. We then ran four week-long runs in the ice I_h field at a strain rate ($\dot{\varepsilon}$) of 3.5×10^{7} s^{-1}, at P=50 MPa, covering 140 K<T<223 K. We confirmed the preliminary result reported earlier that flow in the intermediate temperature regime (approximately 195 K<T<243 K) proceeds as predicted by our original flow law. We also found that the low temperature regime extends to at least 140 K, and we have slightly revised the flow law in the low temperature regime. At T=140 K, P=50 MPa, $\dot{\varepsilon}=3.5 \times 10^{-7}$ s^{-1}, ice I_h flows plastically under a differential stress of 110 MPa.

References: [1] G. J. Consolmagno and J. S. Lewis (1976), Structural and thermal models of icy galilean satellites, in Jupiter, T. Gehrels ed., Univ. of Arizona Press, 1035-1051; [2] J. P. Poirier (1982), Rheology of ices: a key to the tectonics of the ice moons of Jupiter and Saturn, Nature, 299, 683-688; [3] W. B. Durham, H. C. Heard, and S. H. Kirby (1983), Experimental deformation of polycrystalline H_2O ice at higher pressure and low temperature: preliminary results J. Geophys. Res., 88, B377-B392; [4] P. W. Bridgeman (1911), Water, in the liquid and five solid forms, under pressure, Proc. Am. Acad. Arts Sci., 47, 347-438.

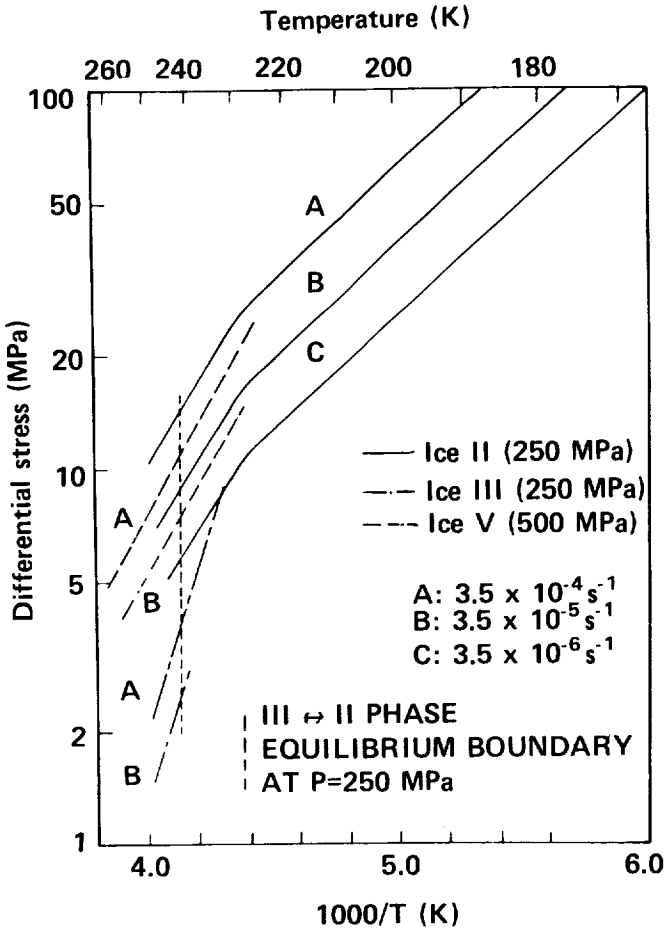

Figure 1. Summary of flow laws determined experimentally for ices II, III, and V. Note that flow for ice V is at P=500 MPa and for ices II and III is at 250 MPa. Points exist outside individual stability fields through a combination of phase metastability and pressure extrapolations.

Pedimentation and Origin of the Basin Beds in Candor Chasma

Peter C. Patton, Department of Earth and Environmental Sciences, Wesleyan University, Middletown, CT 06457

A number of hypotheses have been suggested for the origin of the enigmatic layered deposits in the central chasmata of Valles Marineris (Blasius and others, 1977; McCauley, 1978; Lucchitta 1982, 1985). Given their areal extent, thickness, layering and differing surface texture it is likely that the deposits resulted from various depositional processes as the chasmata enlarged and evolved through scarp retreat. The erosional topography developed on the chasmata filling units is also complex and consists of large, relatively smooth low-gradient plateau surfaces which are separated by major escarpments. The spatial arrangement of these plateau surfaces in Candor Chasma, defined by detailed mapping, suggests one possible mode of origin for these deposits.

In eastern Candor Chasma the basin deposits increase in elevation to the east and south. One large escarpment which forms the northern edge of the basin deposits can be traced the length of the chasma. This large intrabasin escarpment has a complex erosional morphology. The escarpment is dissected by numerous small rills and in places is cut by breaks in slope where the scarp has been reduced to a lower gradient chute. Some of these erosional chutes have depositional lobes at their base and some chutes have streamlined remnants within them. Other less continuous scarps rise to the south of this major escarpment and break the basin deposits up into broad treads. Superimposed on these larger surfaces are second order erosional features which create smaller escarpments. These smaller escarpments trend more north to south and are the major breaks in slope in a west to east direction down the axis of the chasma. On these smaller escarpments the layering of the deposits is etched into relief, the result of differential erosion. In contrast, differential erosion does not appear to be an important process on the larger escarpments, presumably because the steeper gradients allow indiscriminate erosion without regard for minor differences in erodibility. On these larger escarpments the layering of the basin deposits is primarily evident from the albedo contrast.

A high plateau surface is graded to the base of the gullies on the southern escarpment of the chasma. Although this surface is not the highest in the chasma, as several higher surfaces stand above it as isolated mesas, it is the largest. The surface can be traced to the north where it is graded to the chutes cut through the major basin deposit escarpment. Along the southern escarpment of Candor Chasma several of the hollows have debris lobes which extend out onto this surface, but in other hollows the transition appears smooth. In general the deposits from the southern escarpment form an extensive rough-textured debris apron along the chasma

margin which gradually merges with the smoother plain to the north. In contrast, deposits from the northern chasma bounding scarp terminate abruptly on the floor of the chasma.

One process that can explain many of the phenomena associated with the basin deposits is that they are the result of scarp retreat and pedimentation, an idea originally suggested by Sharp (1973), but largely untested by subsequent work. On Earth, pedimentation usually produces erosional surfaces because the transport processes operating on the pediment surface are far more efficient systems than the sediment supply systems on the bounding slopes. A few exceptions occur where plateau-side landslides and associated debris flows cause adjacent pediments to be mantled with relatively thick layers of colluvium (Williams, 1984). On Mars, sediment production on the slopes is likely to be a far more effective process than transport across the pediment surface. In this environment the pediments are likely to be significant sites of sediment deposition. With scarp retreat the pediment surfaces will expand in size, will slope away from the chasma borders and will increase in thickness as sediment accumulates on the margins of the surface. Changes in rates of sediment supply, in transport processes, and in the area of the chasma with scarp retreat may explain the occurrence of surfaces at different elevations. Deposits from other processes will be interbedded with the pediment deposits and tectonic processes may explain the tilting and creation of intrabasin escarpments. Intrabasin escarpments may also mark the position of earlier chasma bounding scarps. A consequence of pedimentation and scarp retreat will be the preservation of spur and gully topography beneath the chasma fill deposits.

References Cited

Blasius, K. R., Cutts, J. A., Guest, J. E., and Masursky, H., 1977, Geology of Valles Marineris: First analysis of imaging from the Viking orbiter primary mission: Jour. of Geophy. Res., v. 82, p. 4067-4091.

Lucchitta, B. K., 1982, Lakes or playas in Valles Marineris: NASA Tech. Memorandum 85127, p. 233-234.

Lucchitta, B. K., 1985, Valles Marineris basin beds; a complex story: NASA Tech. Memorandum 87563, p. 506-508.

McCauley, J. F., 1978, Geologic map of the Coprates quadrangle of Mars: U.S. Geol. Survey Misc. Inv. Ser. Map I-897.

Sharp, R. p., 1973, Mars: troughed terrain: Jour. Geophy. Res., v. 78, p. 4063-4072.

Williams, V. S., 1984, Pedimentation versus debris flow origin of plateau-side desert terraces in southern Utah: Jour. of Geology, v. 92, p. 457-468.

TECTONICS OF THE ELYSIUM REGION, MARS

J. B. Plescia, U.S. Geological Survey, Flagstaff, AZ 86001

The Elysium region is a volcano-tectonic province in the eastern hemisphere of Mars, covering a broad area (2400 x 1700 km) and reaching elevations of 4 km above the surrounding plains. It is characterized by widespread faults and three large volcanoes: Elysium Mons, Hecates Tholus, and Albor Tholus. The tectonic history of the region has not been studied in detail and to this end a tectonic map is being prepared.

Structural features of the region include arcuate and linear grabens, tensional fractures, and wrinkle ridges. Arcuate grabens are generally <3 km wide; they occur on Elysium Mons and the surrounding volcanic plains. Linear grabens are typically 5-10 km wide and occur in what has been termed knobby terrain (Scott and Allingham, 1976; Scott et al., 1978; Elston, 1979). Tensional fractures (e.g., Cerberus Rupes) are a few hundred meters to a kilometer wide and their pattern is typically en echelon. North-south-trending wrinkle ridges cut plains units within the knobby terrain in the northeastern part of Elysium (near lat 20° N., long 180°) and smooth plains units in southwestern Elysium Planitia (near lat 12° N., long 230°). Northwest of Elysium Mons is an extensive series of channels (Elysium Fossae). Although structural control may have localized the channels, their formation has been attributed to various erosive mechanisms (Christiansen and Greeley, 1981; Hall et al., 1983, 1985; Mouginis-Mark et al., 1984).

Arcuate grabens surround Elysium Mons as far out as about 350 km from the caldera. They occur on volcanic plains units of various ages: the "intermediate-stage volcanics" of Mouginis-Mark et al. (1984) exhibit grabens whereas the "flood lavas" do not. Some grabens appear to have been modified by a process that has enlarged them to closed, arcuate depressions. The grabens and arcuate depressions have been interpreted to result from lithospheric loading by Elysium Mons (Hall et al., 1983, 1985; Comer et al., 1985); their spacing and extent indicate a lithospheric thickness of about 56 km when failure occurred.

All observed linear grabens are on the knobby terrain near long 195°, east of the Elysium volcanoes. Structural control, however, may also have influenced the development of the Elysium Fossae channels. Knobby terrain units exhibiting grabens have 5-km crater numbers (the number of craters ≥ 5 km/10^6km^2) of about 700 and are buried by younger plains units (Scott and Allingham, 1976; Elston, 1979) having 5-km crater numbers of 80-120. All of the linear grabens trend N. 65°-80° W. Their consistent orientation, despite their differing locations with respect to the center of the Elysium region, suggests that they reflect a regional stress system other than one centered in Elysium. Modeling of regional lithospheric loading by the Elysium region (Hall et al., 1983, 1985) indicates that the resultant stresses would produce fault trends different from those of the observed grabens. Because of their age, these grabens most likely are associated with radial faults of the "Syria Planum group" in the Tharsis region (Plescia and Saunders, 1982).

The tensional fractures of Cerberus Rupes trend west-northwest and cut volcanic plains of several ages southeast of Elysium Mons. These fractures have been reactivated several times and are probably related to the two "Pavonis fracture groups" in the Tharsis region (Plescia and

Saunders, 1982), as the orientation of Cerberus Rupes is inconsistent with its being the result of Elysium stresses (Hall et al., 1983, 1985). Near lat 10° N., long 190°-205°, plains units having 5-km crater numbers of about 80 are extensively fractured, whereas farther east, plains units having 5-km crater numbers of about 9 are only slightly fractured.

Both the linear grabens and the tensional fractures are interpreted to be the result of stresses associated with the Tharsis region (Banerdt et al., 1982) because: (1) stresses associated with the Elysium region (Hall et al., 1983, 1985) do not have the appropriate orientation to cause the observed fault directions; (2) similar structures are not found north, west, or south of the Elysium region; and (3) stresses due to Tharsis loading do have the appropriate direction and magnitude to cause these features.

Wrinkle ridges occur northeast of the Elysium region between outcrops of knobby terrain material. Their north-south orientation is ambiguous in that it could be circumferential to either the Elysium or Tharsis regions. They are considered to be associated with Tharsis for the same reasons cited above for the tensional fractures and linear grabens, because the ridges appear to have formed contemporaneously with those in Lunae Planum, which are clearly related to Tharsis tectonism, and because they form, together with the ridges in Lunae Planum, a Tharsis-centered symmetric pattern.

The Elysium region, like the Tharsis region, is a broad topographic rise surmounted by large volcanoes. This topography could have resulted from either uplift of the older (prevolcanic) crust or from volcanic construction (cf. Plescia and Saunders, 1982; Solomon and Head, 1982). To determine the thickness of the volcanic units and the origin of the topography, the methods of De Hon (1979) and Plescia and Saunders (1980) were applied: large craters buried to the uppermost parts of their rims were used to determine a local maximum lava thickness. The height of these rims thus provides an estimate of the maximum lava thickness, when the crater-diameter/rim-height relation of Lee (1984) is used. Crater-rim-height data suggest that along the south flank of the Elysium region, the lavas are on the order of 200-400 m thick, indicating that most (perhaps 75%) of the regional topography is the result of uplift of the ancient crust (now exposed as knobby terrain). A thin cover of volcanic material is also consistent with the presence of numerous inselbergs of ancient crust scattered across the Elysium region.

The tectonic history of the Elysium region can be abstracted as follows:

1. Fracturing (linear-graben formation) of the ancient crust (5-km crater numbers of >250) due to stresses associated with the Tharsis region. Uplift of the ancient crust to produce the regional topographic high. Details of the temporal relation between crustal uplift and formation of the linear grabens are uncertain.

2. Formation of plains units (having 5-km crater numbers of 125-250) that display wrinkle ridges.

3. Faulting (graben- and wrinkle-ridge-formation) of plains (5-km crater numbers of about 80) east of the Elysium region by Tharsis-related stresses. Construction of Elysium Mons, Albor Tholus, Hecates Tholus (5-km crater numbers of 53, 199 and 68, respectively) and attendant loading induced failure of the crust surrounding Elysium Mons.

4. Additional plains formation and continued faulting of plains units (5-km crater numbers of <9) due to Tharsis stresses.

In summary, although numerous faults occur within the Elysium region, most were produced by stresses associated with lithosphere deformation by the Tharsis load. Only those grabens circumferential to Elysium Mons reflect local stresses. Such a conclusion is consistent with modeling by Hall et al. (1983, 1985), which suggests that the Elysium load did not produce stresses of sufficient magnitudes to fracture the crust, because of either static support by the lithosphere or isostatic compensation of the load.

REFERENCES

Banerdt, W.B., Phillips, R.J., Sleep, N.H., and Saunders, R.S., 1982, Thick shell tectonics on one-plate planets: Applications to Mars: Journal of Geophysical Research, v. 87, p. 9723-9733.

Christiansen, E.H., and Greeley, R., 1981, Mega-lahars (?) in the Elysium region, Mars: Abstracts Lunar and Planetary Science Conference, 12th, p. 138-140.

Comer, R.P., Solomon, S.C., and Head, J.W., 1985, Mars: Thickness of the lithosphere from the tectonic response of volcanic loads: Journal of Geophysical Research, v. 23, p. 61-92.

De Hon, R.A., 1979, Thickness of the western mare basalts: Proceedings Lunar and Planetary Science Conference, 10th, p. 3635-3650.

Elston, W.E., 1979, Geologic map of the Cebrenia quadrangle of Mars: U.S. Geological Survey Miscellaneous Investigations Series Map I-1140.

Hall, J.L., Solomon, S.C., Head, J.W., and Mouginis-Mark, P.J., 1983, Elysium region, Mars: Characterization of tectonic features: Abstracts Lunar and Planetary Science Conference, 14th, p. 275-276.

Hall, J.L., Solomon, S.C., and Head, J.W., 1985, Elysium region, Mars: Test of lithospheric loading models for the formation of tectonic features: submitted to Journal of Geophysical Research.

Lee, S.W., 1984, Mars: Wind streak production as related to obstacle type and size: Icarus, v. 58, p. 339-357.

Mouginis-Mark, P.J., Wilson, L., Head, J.W., Brown, S.H., Hall, J.L., and Sullivan, K.D., 1984, Elysium Planitia, Mars: Regional geology, volcanology, and evidence for volcano/ground ice interactions: Earth Moon and Planets, v. 30, p. 149-173.

Plescia, J.B., and Saunders, R.S., 1980, Estimation of the thickness of the Tharsis lava flows and implications for the nature of the topography of the Tharsis plateau: Proceedings Lunar and Planetary Science Conference, 11th, p. 2423-2436.

Plescia, J.B., and Saunders, R.S., 1982, Tectonic history of the Tharsis region, Mars: Journal of Geophysical Research, v. 87, p. 9775-9791.

Scott, D.H., and Allingham, J.W., 1976, Geologic map of the Elysium quadrangle of Mars: U.S. Geological Survey Miscellaneous Investigations Series Map I-935.

Scott, D.H., Morris, E.C., and West, M.N., 1978, Geologic map of the Aeolis quadrangle of Mars: U.S. Geological Survey Miscellaneous Investigations Series Map I-1111.

Solomon, S.C., and Head, J.W., 1982, Evolution of the Tharsis province, Mars: The importance of heterogenous lithospheric thickness and volcanic construction: Journal of Geophysical Research, v. 87, p. 9755-9774.

FRAMEWORK OF THARSIS TECTONICS

Jouko T. Raitala and R. Stephen Saunders, Jet Propulsion Laboratory, California Institute of Technology, Pasadena, CA 91109

The tectonic environment of the Tharsis bulge is unique with its numerous well-developed overlapping fossae graben and mare ridge-like dorsa structures. A principal emphasis of our work has dealt with these fossae and dorsa tectonics coupled with the Tharsis bulge and with explanations of how the building of a major huge volcanic complex and the endogeneous forces associated with it may have led to horizontal forces and caused the observed phenomena.

Tensional structures: The crest of the Tharsis bulge displays tensional tectonics especially within the Noctis Labyrinthus area (Ref. 1). Other adjoining tensional tectonic structures associated with the bulge are the numerous radial fossae graben, Valles Marineris valley and other valleys and surface slopes. These structures and the bulge are closely related and the existence of several main radial fossae/valley graben zones is characterist to the Tharsis area (Ref. 2).

The origin of the radial structure system can be traced back to the formatic of the elevated topography associated with Tharsis. The classical concept o triple junctions could be involved although the radial pattern consists rath er of several multiple junctions. The Valles Marineris canyon could easily l interpreted as an aulacogen. Other fossae graben zones resemble linear rift zones extending outwards from the Tharsis bulge.

Although the Valles Marineris canyon and radial fossae graben have been extensively studied, their origin and formation mechanism is still the subject of numerous questions. Rift formation is only one point of view and does not explain all of the rifting processes and the radial pattern of these structures around the Tharsis bulge (Ref. 3). Both active and passive rifting mus be taken into account (Ref. 4). An active mechanism can be invoked in the case of the Tharsis bulge itself, where doming has evidently been associatec with the mantle plume impinging on the lithosphere and causing uplift and ex trusions. The active volcanic doming and complex building has been coupled with the mantle and lower lithosphere swelling, which in the case of the Tharsis bulge has been regional above the deep source of magma generation. Major volcanoes are concentrated within regions of high topographic altitude where the least lithospheric stress has been horizontal. The surrounding fossae and valley structures were caused by more passive crustal rifting due to 1) the tensional failure of the surface layers and opening of these radia faults, 2) adjoining minor doming and rifting along these fault zones, and 3) crustal block formation and minor movements of these blocks.

Block segments: The major crustal and lithosphere blocks of the Tharsis area are indicated by these segments which are cut by rift-like fossae and valley zones radial to the Tharsis bulge swell. The major radial structures do, however, not unambiguously denote the proposed Martian blocks but indicate the importance of Tharsis' activity in block formation. The central parts of the Tharsis bulge are covered by young lavas, which prevent us from observing th true extent of faults and blocks. The surrounding areas are also covered by volcanic materials of different ages which leave defects in direct block recognition. Thus there is a need for further complementing information which could help in locating more exactly the crustal blocks.

Endogeneous doming: The high elevation of the Sinai/Solis Planum segment head near Syria Planum and Noctis Labyrinthus was most evidently caused partly by uplifting and doming of the crust and lithosphere by rising of hot mantle and only partly by lava extrusions.
Syria Planum and Noctis Labyrinthus are located at one of the crests of the proposed impinging mantle and doming lithosphere and they are most extensively faulted. this area has a well developed tensional fracture pattern, possibly developed during the Syria Planum - Tharsis uplifting (Ref. 1). The lithosphere split apart along the crest line of the upward doming area and a spreading center was developed. That this extrusion line is in conjunction with the Vallis Marineris and Claritas Fossae, which are radial to the Tharsis bulge and, it has been proposed, were caused by plume branches secondary to the main Tharsis' plume and extended by the late flexural consequence to the Tharsis load (Ref. 3).
Compressional structures: The compressional fault structures indicated by the main dorsa (Ref. 5) are situated on plateau areas against a terra highland with thick early lithosphere. The compressional body forces generated by gravitational sliding (Ref. 6), volcanic push and mantle traction off the Tharsis swell crest were transmitted through the lithosphere down to those areas where a rigid thick highland lithosphere, mostly unaffected by the mantle impingation, uplift and traction forces, was met with (Refs. 7,8). Within these areas peripheral to the main Tharsis bulge and mantle plume lithosphere was still slightly thinned, thus allowing the crustal shortening and compressional environment to take place.
The locations of dorsa were possibly controlled by the peripheral compression raised by the Tharsis bulge phenomena, but the orientation and arrangement of dorsa ridges were also controlled by other factors. According to Maxwell (Ref. 9) there are conjugate NE-SW and NW-SE oriented main ridge directions within Lunae Planum and Coprates Region and the Tharsis effect has only slightly increased the occurrence of ridges orthogonal to the bulge center. The orientation of dorsa ridges and their occurrence in long linear rows with numerous en echelon structures may indicate the possible importance of the strike-slip component in dorsa ridge formation or, in contrast to Ref. 9, it may indicate the importance of several active centers within the Tharsis bulge (Refs. 6,10,11). Unlike the lunar mare ridges within the Oceanus Procellarum area the importance of crossing conjucate diagonal ridge zones seems to be of minor importance within the Martian areas peripheral to Tharsis bulge. This possibly implies the rather minor significance of the role of the strike-slip stresses in respect to the Tharsis-related compression within these Martian areas as compared to that of Oceanus Procellarum, and pays more attention to the possible existence of several active centers. However, the Martian dorsa ridges may not be solely thrust faults although the compressional component may have been relatively more significant than in the case of lunar mare ridges (Ref. 12).
Discussion: Endogenic block tectonics has provided a framework for understanding many aspects of Tharsis and adjoining structures. The tectonics raised by this wide extrusion and spreading center can be understood qualitatively. The main origin of the volcanism from beneath the Tharsis area is, however, a subject of considerable controversy. When explaining it we must resort to reasons which are coupled with Martian internal structure, energy distribution, magma accumulation and motion below the lithosphere (Ref. 13).
The models of the endogeneous global tectonics (Ref. 14) include thermal con-

vection of the mantle as a necessary consequence and a transient stage of planetary cooling. Thinned Martian lithosphere below the Tharsis and surrounding areas led to regions of elevated topography with tensional stresse These stresses then led to multiple graben systems to form fossae radial to the main bulge. The surrounding surface blocks have concentric compressive dorsa systems consisting of elongated ridges at the margins of the thinner lithosphere against the more resistant thick lithosphere.

References

1) Masson, Ph. (1980). Contribution to the structural interpretation of the Valles Marineris-Noctis Labyrinthus-Claritas Fossae regions of Mars. Moon and Planets 22: 211-219.
2) Raitala, J. (1985). Radial rift and block tectonics around the Tharsis bulge: Introductional postulation. In Papers of the Conference on He and Detachment in Crustal Extension on Continents and Planets, 118-1 Lunar and Planetary Institute, Houston, TX.
3) Banerdt, W.B., Phillips, R.J., Sleep, N.H. and Saunders, R.S. (1982). Thick shell tectonics on one-plate planets: Application to Mars. J. Geophys. Res. 87: 9723-9733.
4) Sengor, A.M. and Burke, K. (1978). Relative timing of rifting and volcanism on Earth and its tectonic implications. Geophys. Res. Lett. 5: 419-421.
5) Chicarro, A.F., Schultz, P.H. and Masson, Ph. (1985). Global and regiona ridge patterns on Mars. Icarus 63: 153-174.
6) Watters, T.R. and Maxwell, T.A. (1985). Orientation, relative age and extent of the Tharsis Plateau ridge system. J. Geophys. Res., in press
7) Raitala, J. (1985). Compressional environmental in the location and orier tation of planetary dorsa and terrestrial earthquake fault structures In Abstracts of the Conference on Terrestrial Planets: Comparative Planetology, 18. CALTECH, Pasadena, CA.
8) Raitala, J. (1985). Implications of Tharsis dorsa on Mars. In Abstract of AGU Fall Meeting, San Francisco, CA.
9) Maxwell, T.A. (1982). Orientation and origin of ridges in the Lunae Palus Coprates region of Mars. J. Geophys. Res. 87: A77-A83.
10) Plescia, J.B. and Saunders, R.S. (1982). Tectocic history of the Tharsis region, Mars. J. Geophys. Res. 87: 9775-9791.
11) Watters, T.R. and Maxwell, T.A. (1983). Crosscutting relations and relative ages of ridges and faults in the Tharsis region of Mars. Icarus 56: 278-298.
12) Raitala, J. (1982). Tectonics of the lunar Oceanus Procellarum area. Act Universitatis Ouluensis Ser. A 135. Oulu, Finland, 41 p.
13) Wise, D.V., Golombek, M.P. and McGill, G.E. (1978). Tectonic evolution o Mars. J. Geophys. Res. 84: 7934-7939.
14) Meissner, R. (1981). Evolution of plate tectonics on terrestrial planets Annales Geophysicae 1: 121-127.

PROCELLARUM BASIN: A MAJOR IMPACT OR THE EFFECT OF IMBRIUM?

P.H. Schultz, Department of Geological Sciences, Brown University, Providence, R.I. 02912, and P.D. Spudis, U.S. Geological Survey, 2255 W. Gemini Dr., Flagstaff, AZ 86001.

INTRODUCTION: Several studies have suggested that the geochemistry, mare-basalt distribution, and structural patterns of ridges on the lunar nearside reflect the existence of a major impact basin 3200 km in diameter (1,2,3,4,5). Whitaker (3) has argued that the distribution of mare shorelines, mare ridges, and isolated scarps delineate a three-ringed Procellarum mega-basin (centered at 23^{o}N, 15^{o}W) with wing diameters of 1700, 2400, and 3200 km. At one time some of these features were ascribed to outer rings of the Imbrium basin centered at 37^{o}N, 18^{o}W (6). Consequently, we have re-examined the pattern of ridges and grabens on the lunar nearside through global projections centered on the proposed mega-basin and the well-known Imbrium basin. In a separate paper (7), the geochemical evidence for such a basin is reviewed and questioned. The present contribution focuses on the geomorphic evidence and offers an alternative explanation.

LUNAR TECTONIC PATTERNS: The primary data set used for this study is derived from references (8) and (9) augmented by additional structural features in the lunar highlands. Figure 1 permits comparison of features centered on the proposed Procellarum basin and Imbrium. The center of Imbrium was chosen principally on the basis of the inner ridge ring in Mare Imbrium, the Alpes-Apennine-Carpatus mountainous arc, and the Harbinger Mountains. Figures 1a and 1b reveal the difficulty in separating tectonic patterns controlled by the proposed mega-basin from those related to the Imbrium basin. The principal landmark used by Whitaker to identify the inner ring of Procellarum basin is a scarp southeast of Imbrium as indicated in Figure 1a. This arc is at least as well matched with an Imbrium-concentric pattern. The second ring is delineated by the northern Mare Frigoris shoreline and wrinkle ridges in Oceanus Procellarum and Tranquillitatis. Although Figure 1a indicates a possible concentric pattern, an equally valid Imbrium-centered pattern can be identified. It is important to point out that wrinkle ridges typically are deflected by local features. On a small scale, this is illustrated by ridge deflections in and around the Flamsteed Ring, Lamont, and Lambert R. On a broader scale, analogous deflections can account for the broad arcs of ridges ascribed by various workers to a mega-basin, particularly north of the Humorum basin. The outermost ring of the proposed nearside mega-basin corrresponds to the western edge of Oceanus Procellarum. Departures from a simple arc, however, are required to the north and to the southeast; the same point could be made for an Imbrium-centered pattern. Figure 1a also shows ridges uniquely concentric to the proposed Procellarum basin and not Imbrium. These residual patterns can be easily explained by altered stress directions by other basins (e.g., Insularum basin). Figure 1b also shows the nearside pattern of grabens and scarps radial to Imbrium (9) and reveals that certain ridge systems may be controlled by this radial pattern as well.

ANOTHER EXPLANATION: The existence of an Imbrium-centered concentric pattern of ridges outside the major basin rim appears contradictory to the often-quoted sequence of basin-interior compression and basin-exterior extension. Wrinkle ridges reflect not only compression by basin-centered basalt loading but also buried features, localized basalt accumulations, and volcanic vents. A broad-scale Imbrium-centered pattern of ridges beyond the Apennines indicates regions of basin-controlled basalt eruptions not subject to subsequent extension. The ponds of basalts encircling the mountain rings of Humorum and Crisium illustrate this process on a smaller scale. The Imbrium impact did not excavate material to these outer structural rings; nevertheless, the lithosphere

responded to this event and subsequent igneous activity. Such an evolution can account for the distribution of basalts and ridges without the need for a mega-basin.

References: (1) Cadogan, P.H. (1974) *Nature 250*, 315-316; (2) Cadogan, P.H. (1975) in *Lunar Science VI*, 123-124; (3) Whitaker, E.A. (1981) in *Multi-ring Basins*, 105-111; (4) Wilhelms, D.E. (1982) NASA TM 85127, 111-113; (5) Wilhelms, D.E. (1983) *Lunar and Planetary Science XIV*, 845-846; (6) Wilhelms, D.E. and McCauley, J.F. (1971) *U.S. Geol. Survey Misc. Geol. Inv. Map I-703;*

(7) Spudis, P.D. and Schultz, P.H. (1985) *Lunar and Planetary Science XVI* (this volume); (8) Guest, J.E. and Murray, J. (1976) *J. Geol. Soc. Lond. 132*, 251-258; (9) Mason, J. *et al.* (1976) *Proc. Geol. Assn. London 87*, 161-168; (10) Schultz, P.H. (1976) *Moon Morphology, U. Texas Press*, 621 p.; (11) Schultz, P.H. (1984) *Lunar and Planetary Science XV*, 728-729.

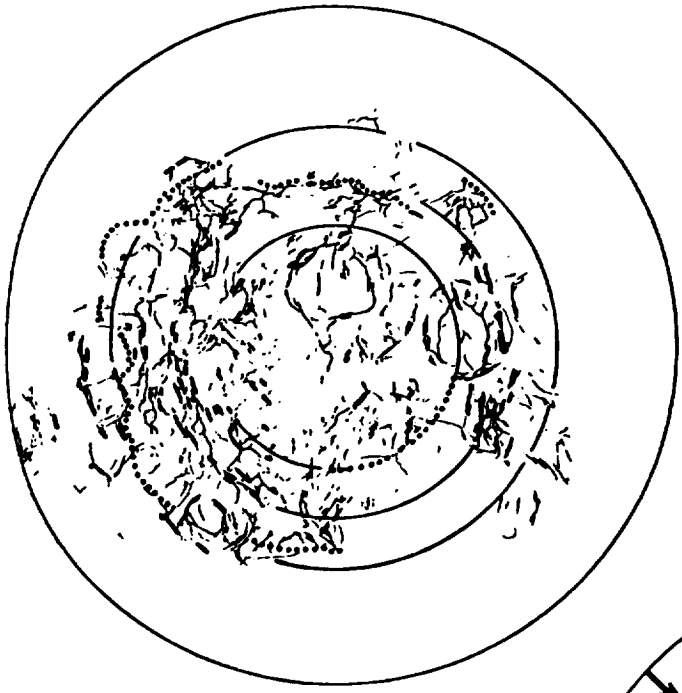

Figure 1a. Tectonic patterns (grabens and rid on the lunar nearside centered on the proposec Procellarum basin (23°N, 15°W). Dotted lines indicate major features used by Whitaker (3) t delineate the basin rings. Emphasized pattern indicate features concentric within + 15° of this basin and not Imbrium.

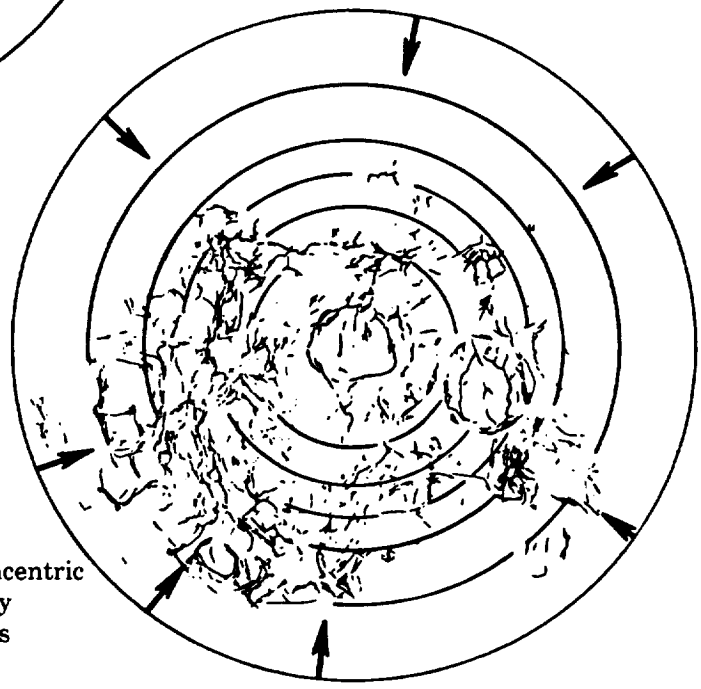

Figure 1b. Tectonic patterns centered on the Imbrium basin (37°N, 18°W). Radial and concentric trends centered on Imbrium provide an equally plausible control over nearside trends. Arrows identify major radial systems of grabens and ridges.

GLOBAL TOPOGRAPHIC AND STRUCTURAL FABRIC ON VENUS

V. L. Sharpton[1] and J. W. Head (Department of Geological Sciences, Brown University, Providence, Rhode Island 02912; [1]present address: Earth Physics Branch, Energy Mines and Resources Canada, Ottawa, Canada K1A 0Y3)

Introduction. Previous analyses of PV altimetry [1] have revealed that Venus is apparently devoid of landforms analogous to the present-day plate boundary features on Earth [2]. The absence of such features does not necessarily rule out a terrestrial style of plate recycling on Venus, however; differences in the surface conditions of the planets could significantly influence the preservation and topographic expression of tectonic and volcanic landforms [3]. The linear extent of the equatorial highlands, elongate planitia and the steep-sided chasmata indicate an underlying tectonic control to these topographic features [4]. Studies of local regions covered by Earth-based radar data have presented evidence for extensional [5] as well as compressional [6] deformation associated with the highland margins and chasmata, but it has remained unclear as to whether or not these zones of deformation are related to global-scale plate recycling. In this study we have used PV topography and regional slope data [7] to examine the distribution and orientation of large-scale topographic features on Venus and explore their structural implications.

Circular features. Circular and elliptical features, detected as discrete variations in large-scale regional slope, are distributed throughout the plains provinces of Venus as shown in Figure 1b. They range in diameter from ~200 km to over 2000 km, and the flanks of these features express a variety of regional slope values, but most typically range between 0.1° and 0.3°. Some circular features correlate with "corona" structures revealed in the Venera 15 and 16 radar data [8] north of Beta Regio. Features with similar radar properties have been detected in Earth-based radar data covering local areas east of Beta Regio [9] and appear to be of internal origin. Several other circular features shown in Figure 1b, such as Hathor Mons, have radar and topographic characteristics which imply a volcanic origin [10]. Many features with similar regional slope characteristics are concentrated within elongate belts of rugged plains; others are associated with the boundaries of the elongate zones of relatively smooth plains discussed below.

Linear variations within the plains. Variations in the distribution of regional slope features are not as dramatic on Venus as on Earth. There are, nonetheless, broad, distinct variations in the concentrations of 0.1 - 0.2° features within the Venus plains associated with systematic linear variations in broad-scale topography. Topographically, these linear trends are most conspicuous when the PV altimetry is averaged over 5 - 10° regions. In some cases these trends are recognizable in PV radar roughness images. Furthermore, the orientation and occurrence of trends east of Beta and Phoebe Regiones coinside with linear variations in radar brightness detected in earth-based data [9]. These trends extend for distances of over 20,000 km and serve to divide the surface of Venus into belt-like zones of relatively smooth or rugged terrain. The more prominent belts are depicted schematically in Figure 1c. The boundaries of these belts are, in places difficult to trace and small irregularities in width and variations in orientation of these belts are noticed; nevertheless, these linear trends in regional slope can be traced for thousands of kilometers with little or no apparent offset. Extensive linear trends within the highlands formed by Aphrodite Terra and Beta Regio have been recognized previously [11] and compelling evidence for these zones being the sites of lithospheric weakness and volcanic activity has been presented by numerous investigators [4, 5, 11]. The variations in regional slope properties and large-scale topography reveal that these NE and NW linear trends are also expressed in the orientation and distribution of topographic features throughout the lowlands and upland rolling plains. These belts and numerous other linear trends aligned with them form a subtle but globally-pervasive fabric to the topography of Venus.

Conclusions. The linear nature and extent of these trends strongly imply an underlying tectonic control to this topography. Furthermore, the topography within central Aphrodite appears to be affected by the intersection with these terrain belts (alignment of steep topography

within Ovda Regio, the northeastward trend of Diana Chasma, the inflections in the highland boundaries near these intersections and the continuation of highland margin trends as linear zones of rugged terrain extending into the plains). The global pervasiveness, consistency in orientation and the lack of apparent offsets in this topographic fabric suggest that deformation on Venus is unlike that associated with the mosaic of laterally moving and recycling plates on Earth. Instead, vertical movement -- perhaps accompanied by limited lateral motion -- along globally extensive zones of weakness may be more characteristic of the Venus lithosphere.

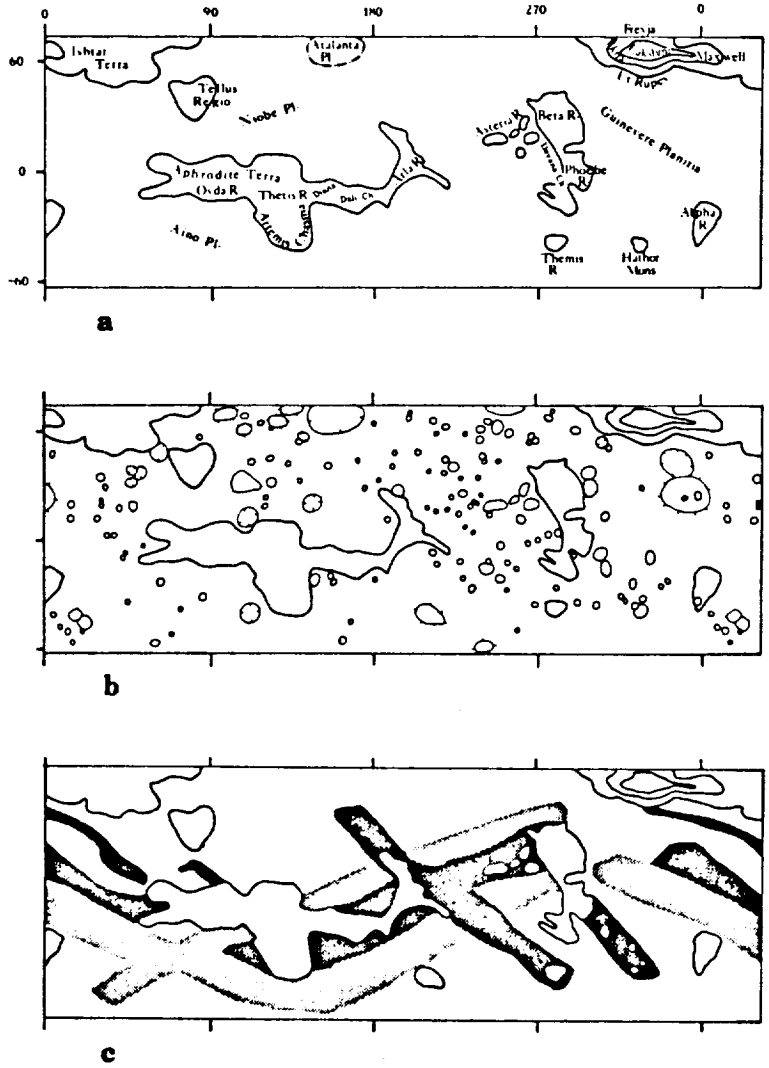

Figure 1. Schematic maps of regional slope variations. Bold lines denote highland margins and interior mountain ranges as labeled. The locations of features discussed in the text are shown in (a). Circular and elliptical features with elevated boundary slopes are shown in (b); the barbs on the larger features indicate direction of regional slope. In (c), the light stippled regions mark the location and the general trend of the more prominent belts of relative smooth, flat surfaces; dark stippled regions are prominent linear zones of relatively rugged terrain within the plains provinces. For details on scale and method of slope calculation see [7].

References. [1] Pettengill, G. H., *et al., J. Geophys. Res., 85,* 1980. [2] Arvidson, R. E., *Lunar Planet. Sci. XII,* 1981. Masursky, H. A., *et al., J. Geophys. Res., 85,* 1980. Phillips, R. J., *et al., Science, 212,* 1981. [3] Head, J. W., *et al., Am. Sci.,69,* 1981; Solomon, S. C., *et al., J. Geophys. Res., 87,* 1982. [4] McGill, G. E., *et al.,* in *Venus,* (Colin *et al.,* Editors), U. A. Press, 1983. [5] Campbell, D. B. *et al., Science, 226,* 1984. [6] Campbell, D. B. *Science, 221, 1983.* [7] Sharpton, V. L. and J. W. Head, *J. Geophys. Res., in press,* 1985. [8] Barsukov, V. L. *et al., Geochimia, 12,* 1984. [9] Stofan, E. R. *et al., Lunar Planet. Sci. Conf XVI, this volume,* 1985. [10] Campbell, D. B. and B. Burns, *J. Geophys. Res., 85,* 1980. [11] Phillips, R. J. *et al., Science, 212,* 1981; Schaber, G. G., *Geophys. Res. Lett., 9,* 1982.

THE ELASTIC LITHOSPHERE: SOME RELATIONSHIPS AMONG FLEXURE, DEPTH OF FAULTING, LITHOSPHERIC THICKNESS, AND THERMAL GRADIENT.

Sean C. Solomon (Dept. of Earth, Atmospheric, and Planetary Sciences, Massachusetts Institute of Technology, Cambridge, MA 02139).

Introduction. The thickness of the elastic lithosphere on a planet is essentially a measure of the reciprocal of the vertical thermal gradient in the lithosphere, i.e., the depth to a temperature at which ductile behavior replaces brittle behavior at typical geological strain rates. Under flexure there is an elastic "core" of the lithosphere occupying the depth interval over which the bending stress is less than an envelope of "strength" versus depth defined by a frictional failure curve at shallow depths and a ductile flow law at greater depth [1,2]. At the shallowest depths, lithospheric bending leads to faulting to a depth that is dependent on the load, the flexural rigidity, and the failure law. The depth of the lower limit to "elastic" behavior is governed primarily by temperature and also by strain rate, composition, and load magnitude. In this paper we apply these concepts to flexural tectonics on the terrestrial planets. Specifically, we relate estimates of elastic lithosphere thickness derived from simple models of flexure to the depth of flexurally induced faulting and to the average vertical thermal gradient in the lithosphere. We illustrate these relationships in detail only for the Moon; some applications to Mars and Venus may be found elsewhere [3,4].

Depth of Faulting. Graben circumferential to mascon mare basins on the Moon are readily explained as the product of lithospheric flexure in response to the mascon load [5,6]. Golombek [7] has measured the widths of a number of these graben and the dip angles of the bounding faults and has argued from graben geometry that faulting does not extend below the projected intersection at depth of the two faults. We propose that this depth marks the intersection of the frictional failure portion of the strength envelope and the curve for the vertical distribution of stress due to lithospheric flexure. This hypothesis, it should be noted, differs fundamentally from the suggestion [7,8] that the faults bounding graben on the Moon intersect at the base of a megaregolith. Following standard practice in terrestrial problems [1,2], we assume that failure at shallow depths is limited by friction on pre-existing faults. This assumption requires the shallow portions of the Moon to be pervasively faulted and cracked at a variety of scales, but this state should be a natural consequence of several processes (impact, differential cooling, tidal and thermal cycling). Byerlee's friction law [2,9] gives an extensional strength of about 200 bars at 5 km depth on the Moon and 400 bars at 10 km depth. Golombek [7] has estimated that the maximum depth of faulting associated with a number of graben peripheral to the mascon maria Humorum and Serenitatis is about 3 km, with an uncertainty (2 - 5 km) dominated by the uncertainty in fault dip.

This value may be compared with the maximum depth of faulting predicted from the intersection of the frictional failure law and the flexure model for stress versus depth due to mascon loading. It should be remembered

that the flexure model is very simple; a variety of potentially important effects (finite strength, additional sources of stress, vertically or laterally heterogeneous elastic properties) are neglected for simplicity. Further, the magnitude of the mascon load at the time of graben formation is not well known, since mare volcanic units postdating graben formation are present in most mascon maria [6]. Simple flexure models for Humorum and Serenitatis at the time of graben formation [6] predict that extensional faulting should extend to 5 and 8 km, respectively, for surface loads equal to the present mascon loads. These values are similar to the estimates of the maximum depth of faulting inferred from graben geometry [7], given the uncertainties in both sets of quantities.

Lithosphere Thickness and Thermal Gradient. The effective thickness of the elastic lithosphere at the time of loading and flexure is controlled by the thermal gradient and by the ductile portion of the strength envelope. We assume that the ductile strength is controlled by the flow law for olivine [10] in the mantle and for anorthosite [11] in the crust. The ductile strength depends further on the strain rate during mascon loading. The maximum extensional strains in the flexural models for mascon maria are typically 10^{-3} to 10^{-4} [6]. We may derive a lower bound on strain rate by assuming that this strain develops uniformly over the $\sim 10^8$ yr time interval between basin formation and graben formation, giving $\varepsilon \sim 10^{-19} s^{-1}$. An upper bound on ε may be obtained by assuming that the mascon basins fill with mare basalt at a rate equal to the maximum inferred eruption rates on the Moon, about $10^{-4} km^3/s$ [12]. The volume of mare basalt in Serenitatis at the time of graben formation has been estimated at $6 \times 10^5 km^3$ [6], implying a minimum time for filling of 10^2-10^3 yr, or a maximum ε of about 10^{-13}. We adopt a value for ε of $10^{-16 \pm 3}$. The effect of the uncertainty in the exponent is not as large as it might seem; the equivalent uncertainty in temperature at a given stress level (e.g., the base of the "elastic" lithosphere) is about 100°C.

With these assumptions, thicknesses of the elastic lithosphere may be converted to mean thermal gradients. For instance, the lithospheric thicknesses of 25 to 50 km inferred for the central and western nearside of the Moon at 3.6-3.8 b.y. ago [6] imply local thermal gradients of 9 to 18°C/km. Such gradients are broadly consistent with global thermal history models [e.g., 6].

It is important to account for the distinct flow laws of crust and mantle material. Because the mantle is "stronger" than the crust, the thickness of the elastic lithosphere will not be a smoothly increasing function of decreasing thermal gradient. Instead, once the elastic lithosphere thickness approaches the thickness of the crust, there will be a discontinuous jump in lithospheric thickness for a small additional decrease in thermal gradient. For a lunar crust 60 km thick, this discontinuity in lithospheric thickness is about 40 km. This effect may account for some of the larger values of lithospheric thickness inferred for the eastern nearside of the Moon [6].

Conclusions. Simple flexural models for lunar mascon maria, when combined with the concept of a strength envelope limited by brittle failure in the upper lithosphere and ductile flow at depth, permit the development

of some approximate relations for the predicted depth of faulting and for the variation of elastic lithospheric thickness with local thermal gradient. These relations are generally consistent with independent estimates of the derived quantities and provide a consistent framework for beginning to understand the evolution of temperature and stress in planetary lithospheres.

References: [1] C. Goetze and B. Evans, GJRAS, 59, 463, 1979; [2] W.F. Brace and D.L. Kohlstedt, JGR, 85, 6248, 1980; [3] J.L. Hall et al., JGR, submitted, 1985; [4] S.C. Solomon and J.W. Head, JGR, 89, 6885, 1984; [5] S.C. Solomon and J.W. Head, JGR, 84, 1667, 1979; [6] S.C. Solomon and J.W. Head, RGSP, 18, 107, 1980; [7] M.P. Golombek, JGR, 84, 4657, 1979; [8] M.P. Golombek and G.E. McGill, JGR, 88, 3563, 1983; [9] J.D. Byerlee, Pure Appl. Geophys., 116, 615, 1978; [10] C. Goetze, Phil. Trans. Roy. Soc., A288, 99, 1978; [11] G. Shelton and J. Tullis, EOS Trans. AGU, 62, 396, 1981; [12] L. Wilson and J.W. Head, Nature, 302, 663, 1983.

LAVA FLOWS: APPLICATION OF PLATE THEORY TO PRESSURE RIDGE FORMATION

E. Theilig and R. Greeley, Department of Geology, Arizona State University, Tempe, Arizona 85287

Pressure ridges, tumuli, and pressure plateaus are characteristic surface features on some lava flows on Earth and Mars. They commonly form on compound pahoehoe lava flows and their formation is an integral part of the flow emplacement mechanism (Theilig, 1984;1985). These flows lack identifiable channels and tubes indicating a different emplacement mechanism and limiting the analysis of such flows since most work on the rheology and movement of lava evolved from the study of channelled flows (Hulme,1974; Moore and Schaber, 1975; Pinkerton and Sparks, 1976; Moore et. al., 1978, Cigolini et. al., 1983; and Borgia et. al., 1984). Understanding the formation of pressure ridges and the factors controlling their morphology will place constraints on the emplacement mechanism and allow the ridges to be used for the interpretation of a different type of lava flow. These features are large enough to be detected on orbital images (Greeley and Theilig, 1985) and may aid in the interpretation of volcanic flows on other terrestrial planets. Plate theory (Timoshenko, 1940) as applied by Pollard and Johnson (1973) can be used as the first step in understanding the relationship between ridge formation and flow emplacement by providing a model of the deformation of the lava flow surface crust. This model allows both the factors controlling the amount of uplift and the stress distribution within the crust to be identified.

Field observations place constraints on the formation of pressure ridges and provide boundary conditions for the model. Tumuli, pressure ridges, and pressure plateaus form a series of features ranging from circular (tumuli) to elongated (pressure ridges). Pressure plateaus are much larger and may be irregular or elongate. These features form as part of individual flow units and represent uplift of the surface crust behind a halted flow front (Theilig, 1984). In cross-section, they vary from domed arches to gable shaped. One of the major characteristics of these features is the presence of medial and/or lateral wedged-shaped cracks. The upper part of the crack walls are typically joint surfaces indicating the presence of a solidified crust prior to uplift and cracking. Lava is commonly extruded from the uplifts, primarily from the base and partly from the cracks.

Plate theory describes the bending of a thin elastic plate by vertical forces. Assumptions used in the model are: 1) elastic behavior of the plate, 2) uniform magma pressure, and 3) maximum plate deflection of 20°. By choosing an elliptical geometry ($x^2/a^2 + y^2/b^2 = 1$) both an elongate and a circular form can be studied by varing the lengths of the axes and therefore is applicable to both tumuli and pressure ridges. The deflection of the plate (w) can be expressed in terms of the driving pressure (p), material properties such as Young's modulus (E) and Poisson's ratio (ν), plate or crustal thickness (t), half length of plate in the x-direction (a), and distance in the x-direction (x). For the two end members, the expressions are:

circular, b=a $$w = \frac{3\ p\ (1-\nu^2)}{16\ E\ t^3}\ (a^4 - 2a^2x^2 + x^4)$$

elongate, b=∞ $$w = \frac{p\ (1-\nu^2)}{2\ E\ t^3}\ (a^4 - 2a^2x^2 + x^4)$$

These equations indicate that the primary factors determining the amount of deflection are: 1) the geometry (elongate ridges are deflected more), 2) lateral dimensions (such that initially wider flow units are deflected more than narrow ones), and 3) plate thickness (thinner crusts will be deflected more). Variations in the pressure driving the crust upward may also be significant. The material properties are less important. Therefore the dimensions of the uplifts are predominantly controlled by the initial extent of the flow units, which in turn may be related to rheology of the lava.

The distribution of longitudinal stress and strain can also be determined from plate theory. Stress (σ_{xx}) in the x-z plane (z being vertical) is given by:

$$\sigma_{xx} = \frac{p\ z}{t^3}\ (6x^2 - 2a^2)$$

where z is the vertical distance from the center of the crust. This predicts tension occurring in the upper part of the crust in the central area of uplift and in the bottom part of the crust at the periphery. Compression dominates in the opposite parts of the crust. Tension in the upper crust is evidenced by the occurrence of medial wedge-shaped cracks. Similar wedge-shaped cracks propagating upward may form in the lower crust around the base of the uplifts, however, no cracks of this type were seen in the field. Their presence would explain the predominant outbreak of lava from the base of pressure ridges since lava would be injected into the opening crack and eventually break through the crust. This secondary material may effectively mask the presence of these cracks. Distribution of strain is similar to that of stress and reaches maximum values at the edges of the uplift.

In addition to plate theory, a simple force balance on the uplifts can be used to obtain an expression of driving pressure as a function of material properties and the dimensions of the uplift. By assuming unit weight and yield strength of the lava and measuring maximum deflection, width, and length of a ridge, the driving pressure can be estimated. It may then be possible to relate driving pressure to the flow of lava.

Plate theory is only the first step in understanding the formation of pressure ridges and their relationship to flow emplacement, however this model does indicate that pressure ridge morphology can be related to the flow units in which they occur. Before these features can be used to interpret lava flows, the factors controlling the extent of the initial flow units need to be identified and the effect of cooling on controlling flow unit length and crustal thickness need to be determined. These aspects are currently being investigated.

REFERENCES

Borgia, A., S. Linneman, D. Spencer, L.D. Morales, and J.B. Andre, 1984, Dynamics of lava flow fronts, Arenal Volcano, Costa Rica. J. Volcanol. Geotherm. Res. 19, 303-329.

Cigolini C., A. Borgia, and L. Cassertano, 1983, Intercraterci activity, aa-block lava, viscosity and flow dynamics: Arenal Volcano, Costa Rica, J. Volcanol. Geotherm. Res.

Greeley, R. and E. Theilig, 1985, Lava flows in southwest Tharsis: Modes of emplacement, Lunar and Planetary Science Conf. 15th, 294.

Hulme, G., 1974, The interpretation of lava flow morphology, Geophys. J. R. Astron. Soc. 39, 361-383.

Moore, H.J., and G.B. Schaber, 1975, An estimate of the yield strength of the Imbrium flows, Proc. 6th Lunar Sci. Conf., 101-118.

Moore, H.J., D.W.G. Arthur, and G.G. Schaber, 1978, Yield strengths of flows on the Earth, Mars, and Moon, Proc. Lunar Planet. Sci. Conf. 9th., 3351-3378.

Pinkerton, H. and R.S.J. Sparks, 1976, The 1975 sub-terminal lavas, Mount Etna: A case history of the formation of a compound lava field, J. Volcanol. Geotherm. Res. 1, 167-182.

Pollard, D.D., and A.M. Johnson, 1973, Mechanics of growth of some laccolithic intrusions in the Henry Mountains, Utah II, Tectonophys. 18, 311-354.

Theilig, E., 1984, Pressure ridges as indicators of flow emplacement, Geol. Soc. Amer. Absts. with Prog. 16, 674.

Theilig, E., 1985, Basaltic pressure ridges: Formation and relationship to flow emplacement (abst.), in Repts. Planet. Geol. Prog. 1984, in press.

Timoshenko, S., 1940, Theory of plates and shells, McGraw-Hill Book Company, Inc., New York, 492 p.

CHANNELS OF MARS' ELYSIUM REGION: EXTENT, SOURCES, AND STRATIGRAPHY

Kenneth L. Tanaka and David H. Scott, U.S. Geological Survey, Flagstaff, Arizona 86001

Ongoing geologic mapping at 1:2,000,000 scale of the Elysium region of Mars has detailed the extent, sources, and relative ages of two major channel systems northwest and southeast of Elysium Mons (Fig. 1). These systems were recognized and studied previously, but new findings are presented here that bear on regional and global geology and climate.

The channels northwest of Elysium Mons, which include Tinjar, Hrad, and Granicus Valles, were mapped initially from Mariner 9 images [1]. The channels extend discontinuously for nearly 2,000 km into Utopia Planitia. Their smooth floors commonly widen at the channel mouths and grade into smooth plains (dotted pattern in Fig. 1). These plains are presumably made up of alluvial deposits, perhaps reworked from the Utopia material (described below) cut by the channels. Channels such as Apsus Valles splay out into complex distributary systems that cut thick, lobate, fan deposits. Teardrop-shaped bars and longitudinal flutes in the channels suggest that they were formed by running water [2]. The channels and their deposits are within a sequence of thick, widespread, rough-textured Utopia flows (unit uf) and thinner, well-preserved Elysium lava flows (unit ef). More recent work [3] based on Viking images identified the sources of these materials as WNW-trending fractures of Elysium Fossae on the northern and western flanks of the Elysium topographic rise. Where the Utopia flows overlie fractured plains material (unit pf) at Adamas Labyrinthus, the flows are themselves fractured and are gradational in appearance with the fractured plains material. Our current work in crater chronology indicates that the fractured plains material is late Hesperian in age. Crater counts of Elysium volcanoes and lava flows and Utopia flows [4, 5] indicate that their age is late Hesperian to early Amazonian.

Some studies [3, 6] have suggested that the Utopia flows are lahars produced by the effusion of melt water from ground ice that contained subsurface materials. Another study [2], however, suggested that, because the Utopia flow deposits and the channels are not everywhere associated, not all Utopia flow deposits are lahars. Further arguments that suggest that the Utopia flows are not lahars include: (1) the plausibility of the inferred process, involving erosion and removal of huge quantities of subsurface material by groundwater flow, has not been demonstrated theoretically; (2) expected collapse features comparable in volume to the proposed removed material are not found; (3) lahars produced by the suggested process are not known on Earth; and (4) other Martian outflow channels do not contain or cut flows of such size and appearance. Perhaps a more likely explanation for the flows is that they are volatile-rich lavas or pyroclastic deposits. Such origins might account for their volume, degradation, and morphology. After emplacement of the flows, volcanic heating may have stimulated melting of ground ice and water runoff. This proposed cycle may have been repeated for particular fissures or fissure sets.

The second channel system, in southeastern Elysium Planitia (Fig. 1), is very different from the first. Near their source areas in the Cerberus

Rupēs, few channels are seen, possibly because they are shallow and image resolution is inadequate for their discrimination. The channels grade into plains formed of smooth, channeled plains material (unit cp). This material has generally low albedo, is marked by light, wispy zones in some areas, and is distinct from surrounding plains units. The wispy zones, also, clearly differ from local wind-streak patterns. These channeled deposits fill a vast basin that extends for about 3,000 km between long 222° and long 168°. Most of the wispy zones and other streamlined albedo features appear to be primary markings that indicate flow direction. South of Cerberus Rupēs, at about long 204°, the channel flow direction is south, dividing to the east and west. To the east, the channeled plains material is as wide as 750 km, but narrows south and east of Orcus Patera. Channel bars and terraces and streamlined albedo patterns occur in the narrow stretch. In its widest part, the channeled plains unit embays remnants of knobby, cratered material (unit kc). Although crater densities of the channeled material near Orcus Patera range from moderate [7] to very low [8], the paucity of craters on the channeled plains to the west suggests that the unit is very young. Furthermore, detailed inspection shows that most craters larger than about 1 km in diameter appear embayed by the deposit, which suggests that it is only tens of meters thick. Except for eolian and polar deposits, where resurfacing is probably still active, this channeled plains material has the youngest surface of regional extent on Mars.

The channels originate from Cerberus Rupēs, a system of thin, en echelon fractures that extends for over 1,000 km through southeastern Elysium Planitia. The fractures also cut channelled plain deposits, and therefore are contemporaneous with or postdate their formation. The fractures follow a much older structural trend observed in local cratered terrain remnants, and thus may simply result from rejuvenation of these older structures.

On the basis of our new studies of the channel systems in the Elysium region, we conclude the following: (1) water runoff was in part stimulated by volcanic activity in the Elysium region, (2) channeling and flooding contributed materially to resurfacing of the northern lowland region of Mars, and (3) the climate on Mars was conducive to fluvial activity during very recent geologic time.

References

[1] Elston, W. E. (1979) U.S.G.S. Misc. Inv. Series Map I-1140.
[2] Mouginis-Mark, P. J. and others (1984) Earth Moon Planets, v. 30, p. 149.
[3] Christiansen, E. H. and Greeley, R. (1981) LPSC (abs.), 12th, p. 138.
[4] Plescia, J. B. and Saunders, R. S. (1979) Proc. LPSC, 10th, p. 2841.
[5] Neukum, G. and Hiller, K. (1981) JGR, v. 86, p. 3097.
[6] Christiansen, E. H. and Ryan, M. P. (1985) NASA TM 87563, p. 239.
[7] Carr, M. H. and Clow, G. D. (1981) Icarus, v. 48, p. 91.
[8] Scott, D. H. and Tanaka, K. L. (1982) JGR, v. 87, p. 1179.

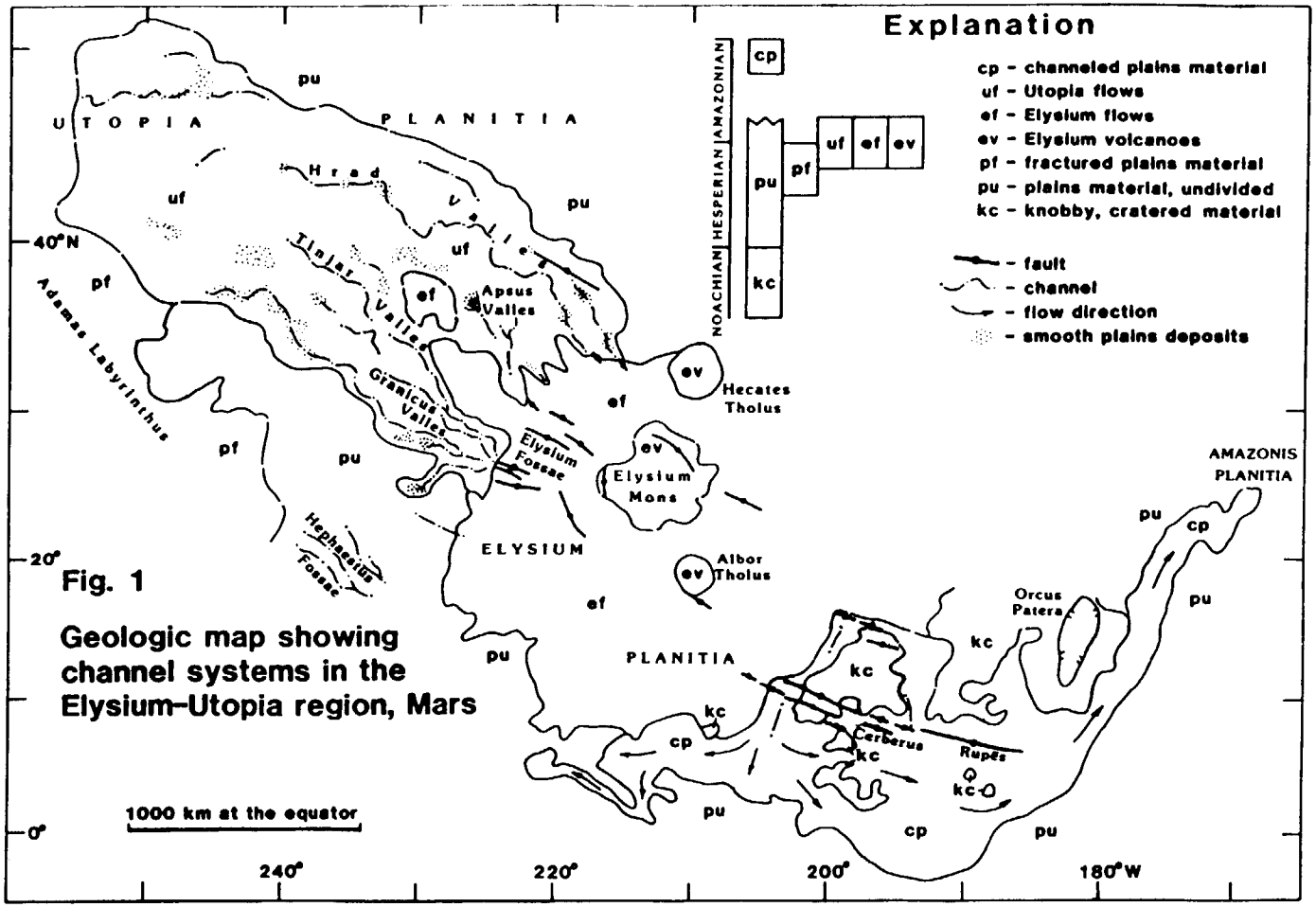

Fig. 1

Geologic map showing channel systems in the Elysium–Utopia region, Mars

THE THARSIS PLATEAU RIDGE SYSTEM: INFERRED AND PREDICTED COMPRESSIVE STRESSES

Thomas R. Watters and Ted A. Maxwell, National Air and Space Museum, Smithsonian Institution, Washington, D.C. 20560

The ridge system of the Tharsis Plateau is approximately circumferential to the regional topographic high in northern Syria Planum and the major Tharsis volcanoes (Watters and Maxwell, 1983). These ridges are interpreted as compressional features that formed in response to a radially oriented stress field with a center near the Pavonis Mons volcano, assuming that the maximum principal compressive stress (σ_1) was perpendicular to the long axes of the ridges (Watters and Maxwell, 1985).

Normals to vector means of ridge orientations were calculated using the over 1850 digitized ridge segments sampled in 10 degree boxes of latitude and longitude (Figure 1) (first reported in Watters and Maxwell, 1984). The ridges were digitized from USGS 1:2,000,000 controlled orthophoto maps. Orientations of individual ridge segments were determined, weighted by length, and mean orientations or vector means were then computed. The magnitude of each resultant vector mean was weighted by the total length of the ridge segments within the given 10 degree box and normals to the vector means were then determined. The resulting vectors are inferred to represent the average regional maximum compressive stress vectors of the stress field that generated the ridges in the Tharsis region. The inferred compressive stress orientations around Tharsis indicate that the ridge system is not concentric to any single point. In order to further evaluate the radial symmetry of the inferred stress field, vector mean orientation were plotted as great circles on the upper hemisphere of a Schmidt equal area stereographic net. Concentrations of 996 intersections of the great circles were determined (using a Kalsbeek counting net) and contoured (Figure 2). Contours represent 1-2-3-4-5% per 1% area (the projection is centered at 0°N, 110°W). This analysis indicates that the inferred stress field is radial to three broad zones centered: 1) southwest of Olympus Mons, 2) north of Lunae Planum, and 3) on Syria Planum. In contrast to the findings of Wise et al. (1979), the greatest concentration of intersections occurs in the Syria Planum region at approximately 17°S, 105°W rather than west of the Tharsis Montes volcanic line. The lack of radial symmetry of the inferred stress field may be explained in two ways: 1) the system formed in two or more distinct events with different stress fields and centers, or 2) a single, radially-oriented stress field was deflected due to locally controlled influences.

If Tharsis evolved from an isostatic state to flexurally supported loads as suggested by Banerdt et al. (1982) and by Sleep and Phillips (1985) (for their model in which the outer radial fractures are older than the central fractures) then the data presented here supports the formation of the ridge system during the period of isostatic uplift. The observed ridge-fault crosscutting may have formed during the transition from a predominantly radially compressive to a dominantly tensile,

circumferentially oriented stress regime. The orthogonal geometry and the relative ages of the ridge-fault crosscuts described by Watters and Maxwell (1983) could be explained by the formation of the radial fault system during and after the waning phase of the compressional ridge formation while maintaining the same general center of tectonic activity.

However, there are several problems with both the models of Banerdt et al. (1982) and Sleep and Phillips (1985). Stress trajectories for both isostatic models predict compression from roughly 40° to 110° (2,400 to 6,600 km) east of their stress centers. Ridges occur from as near as approximately 25° or 1,500 km to only as far as about 70° or about 4,200 km east of their centers. In addition, neither model accounts for the observed differences between the predicted, purely radially-oriented, compressional stress field and the inferred compressive stresses (Figure 1). Finally, the stresses calculated by Banderdt et al. (1982) and Sleep and Phillips (1985) are for the surface of lithosphere and stress must propagate to the free surface of the crust. If ridges are the result of lithospheric and crustal compression (i.e. deformation of the basement as well as the surface units), ridges should be present on the exposed units of basement complex, adjacent to ridged plains, where they have not been observed. Watters and Maxwell (1985) suggest that the ridges formed by thin-skinned deformation of the ridged plains with little influence from the basement. In this model, the ridged plains, under horizontal compression, fold as a result of instability due to the viscosity contrast between the ridged plains units and the regolith substrate. If this is the case, alternative models must be explored to generate compressional stresses that are largely confined to the surface layers.

References

Banerdt, W.B., R.J. Phillips, N.H. Sleep, and R.S. Saunders, Thick shell tectonics on one-plate planets: Applications to Mars, J. Geophys. Res. 87, 9723-9733, 1982.

Sleep, N.H. and R.J. Phillips, Gravity and lithospheric stress on the terrestrial planets with reference to the Tharsis region of Mars. J. Geophys. Res. 90, 4469-4489, 1985.

Watters, T.R. and T.A. Maxwell, Crosscutting relations and relative ages of ridges and faults in the Tharsis region of Mars, Icarus 56, 278=298, 1983.

Watters, T.R. and T.A. Maxwell, Compressional features in the Tharsis Region of Mars: II. Orientations and Timing of Deformation (Abstract), NASA Tech. Mem. 86246, 304-306, 1984.

Watters, T.R. and T.A. Maxwell, Fold model for ridges of the Tharsis region of Mars (Abstract), Lunar and Planetary Science XVI, 987-898, 1985.

Wise, D.U., M.P. Golombek and G.E. McGill, Tharsis province of Mars: Geologic sequence, geometry, and a deformation mechanism, Icarus 38, 458-472, 1979.

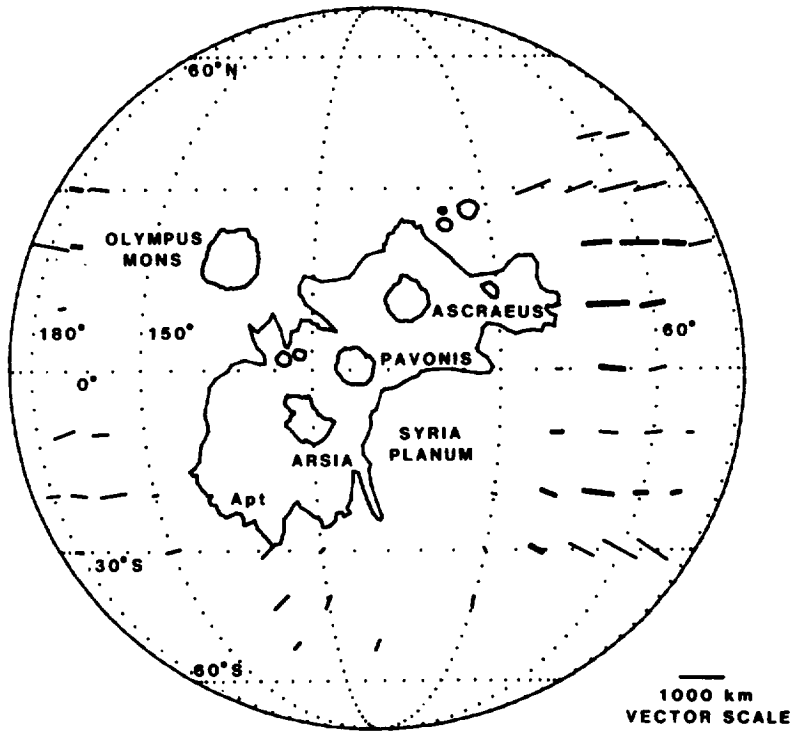
60°N
OLYMPUS MONS
ASCRAEUS
180°
150°
60°
PAVONIS
0°
SYRIA PLANUM
ARSIA
Apt
30°S
60°S
1000 km
VECTOR SCALE

Fig. 1

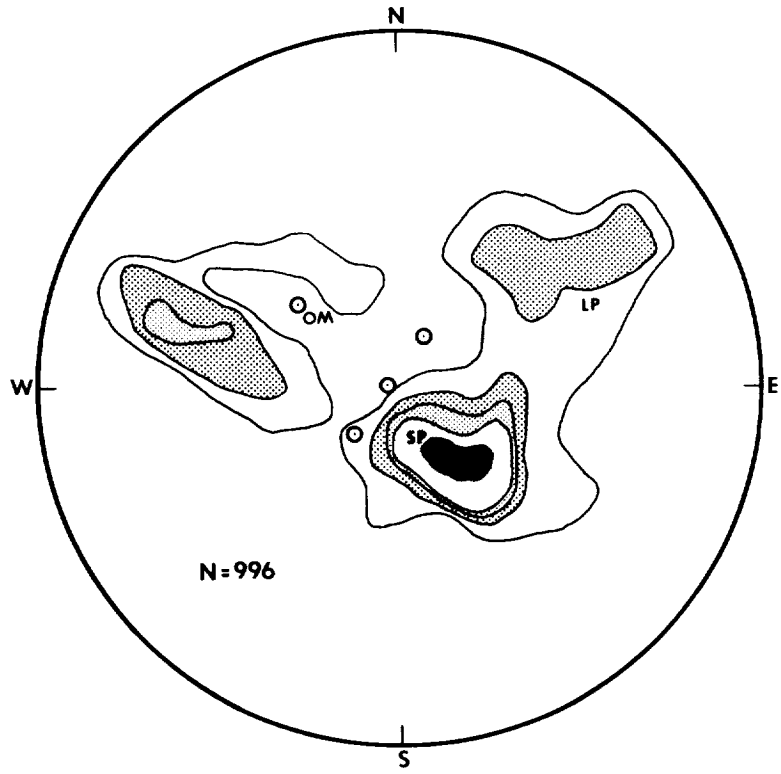
N
W
E
S
OM
LP
SP
N=996

Fig. 2

CHAPTER 11

GEOMORPHOLOGY

GRANICUS VALLES IN ELYSIUM

Duwayne M. Anderson and Gary Brandstrom, Dept. of Geology, Texas A&M University, College Station, TX 77843.

The origin of Granicus Valles has been discussed in five or six recent publications. Two general theories have been developed. One is that the channels were developed on the surface of an extensive sedimentary deposit probably as volcanic debris flows or lahars. The lahars could have involved volcanism by the melting of ground ice and liquifaction of subsurface volcanic ash sediments. This theory is described in papers by Christiansen and Greely (1981), Christiansen (1984), and Christiansen and Ryan (1985).

Another view has been suggested by Mouginis-Mark and Brown (1981), Mouginis-Mark et al. (1984), and Mouginis-Mark (1985). They suggest that some of the channels in this region were created by lava erosion and others by water. One of the criteria for classifying chanels into one or the other of these groups is the observed wavelength to width ratio. However, other channel characteristics also were taken into consideration in suggesting a given channel's origin. The multiple floor levels and streamlined islands in some of these channels were cited as evidence to support a fluvial origin for some. The enlarged source craters and sinuousity of some channels were said to imply a volcanic origin in others.

Most of the channels on Mars have one or more unusual characteristics that set them apart from the typical fluvial channels on Earth. Granicus Valles is one of these. The confined source and distributary pattern of Granicus Valles is more typical of an origin involving debris flows or lava erosion than fluvial erosion. However, many other characteristics of Granicus Valles are consistent with a fluvial origin. The vertical drop over the 1100 km length of the channel system appears to be approximately 3.5 km according to the USGS I-961 topographic map of Mars. This ratio of vertical drop to travel distance is about an order of magnitude lower than similar ratios for terrestrial lahars. Comparing the USGS topography derived from radio occultation data to a radar derived profile from Downs et al. (1982) of a nearby location, one sees that the vertical drop for Granicus valles may be lower (fig 1). However, if the depth of the source crater and canyon is subtracted, the vertical drop of the channel bottom is found to be about 1.7 km less than is characteristic of the region. Considering these facts, a ratio of 0.0008 is a reasonable estimate for Granicus Valles. This is much too low for a lahar or volcanic debris flow (Siebert, 1984); it is sufficient to be consistent with a flood of water.

Shen, Schumm, and Doehring (1979) have illustrated common channel patterns and the nature of the streams that carve them. Most of the Granicus Valles channels are analogous to

types 4 and 5. They are high power, low stability type streams. This is consistent with estimates of flow velocities that may have carved these channels (Table 1). These estimates resulted from calculations following the method described by Komar (1979). The lower gravity on Mars combined with the high discharge of these flows would indicate a capacity for enormous sediment loads. Where stream gradients decrease, one would expect a high aggradation rate together with the resulting morphological features. This seems to be the case in the anastamosing reach where the southern branch of Granicus Valles reaches the lower Elysium Plains. The morphology of anastamosing rivers described by Smith (1983) is very similar in most characteristics to the anastamosing reach of Granicus Valles (Table 2). Some features that both have in common are prominent levees, avulsions, no meander belt, and low sinuousity.

REFERENCES CITED

Christansen, E.H., 1984, Volcanic debris flows in the Elysium region of Mars: Geological Society of America Abstracts with Programs, 97th annual meeting, Reno, Nevada, Nov. 5-8, p.470.

Christiansen, E.H., and Greely, R, 1981, Mega-lahars (?) in the Elysium region, Mars: Lunar and Planetary Science XII, p.138-140.

Christiansen, E.H., and Ryan, M.P., 1985, Volcanic debris flows in the Elysium region of Mars: NASA TM, 87563, p.239-241.

Downs, G.S., Mouginis-Mark, P.J., Zisk, S.H., and Thompson, T.W., 1982, New radar-derived topography for the northern hemisphere of Mars: Journal of Geophysical Research, v.87, p.9747-9754.

Komar, P.D., 1979, Comparisons of the hydraulics of water flows in martian outflow channels with flows of similar scale on earth: Icarus, v.37, p.156-181.

Mouginis-Mark, P.J., 1985, Identification of lava flow- permafrost interactions on Mars: Lunar and Planetary Science Conference, XVI, p.591-592.

Mouginis-Mark, P.J., and Brown, S.H., 1981, Regional volcanic studies in Elysium Planitia, Mars: NASA TM, 82385, p.258-260.

Mouginis-Mark, P.J., Wilson, L., Head, J.W., Brown, S.H., Hall, L.J., and Sullivan, K.D., 1984, Elysium Planitia, Mars: regional geology, volcanology, and evidence for volcano-ground ice interactions: Earth, Moon, and Planets, v.30, p.149-173.

Shen, H.W., Schumm, S.A., and Doehring, D., 1979, Stability of stream channel patterns: Transportation Research Record, 738, Transportation Research Board--Academy of Sciences, p.22-28.

Siebert, L., 1984, Large volcanic debris avalanches: chatacteristics of source areas, deposits, and associated eruptions: Journal of Volcanology and Geothermal Research, v.22, p.163-197.

Smith, D.G., 1983, Anastamosing fluvial deposits: modern examples from Western Canada: in Modern and Ancient Fluvial Systems, Special Publication, 6, International Association of Sedimentologists, p.155-168.

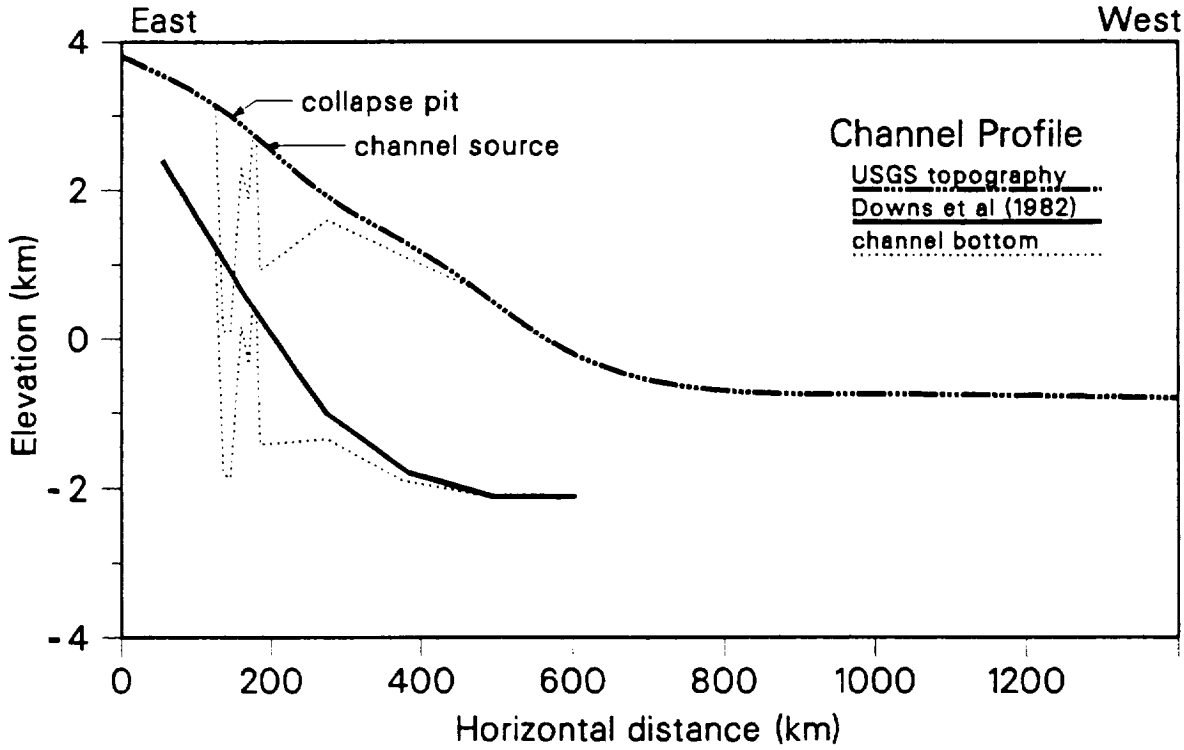

Figure 1. Topographic profile showing the difference between the channel bottom and the unchanneled surface. Solid line shows radar derived topography from Downs et al. (1982) which was measured about 200 km south of the channel source along 22.13 deg N.

Table 1. Hydrologic parameters for two sections of Granicus Valles.

STEEPEST PART						
DIMENSIONLESS DRAG COEFFICIENT Cf	GRAVITY g	SLOPE S	CHANNEL DEPTH m	CHANNEL WIDTH km	VELOCITY IN m/sec	DISCHARGE q
			10	2	7.20	1.44E+05
0.005	3.7	0.007	50	2.5	16.09	2.01E+06
			100	3	22.76	6.83E+06
			300	3	39.42	3.55E+07
BRAIDED PART						
DIMENSIONLESS DRAG COEFFICIENT Cf	GRAVITY g	SLOPE S	CHANNEL DEPTH m	CHANNEL WIDTH km	VELOCITY u	DISCHARGE q
			10	10	4.71	4.71E+05
0.005	3.7	0.003	50	10	10.54	5.27E+06
			10	15	4.71	7.07E+05
			50	15	10.54	7.90E+06
BRAIDED STRETCH	TOTAL IF 10m DEEP			25	4.71	1.18E+06
BRAIDED STRETCH	TOTAL IF 50m DEEP			25	10.54	1.32E+07

Table 2. Geomorphic comparison of the anastamosing section of Granicus Valles with two anastamosed rivers in Canada (Smith, 1983).

Morphology	Lower Saskatchewan	Upper Colombia	Granicus
Gradient	low (12.2 cm/km)	low (9.6 cm/km)	low (<1m/km)
Sinuousity	med 1.4	low 1.16	low 1.1-1.3
Aggradation rate	medium	high	probably high
Levees	prominent	prominent	prominent
Oxbows	rare	absent	absent
Avulsions	few	common	few
Meander belt	confined	absent	absent

EVOLUTION OF VALLEYS DISSECTING VOLCANOES ON MARS AND EARTH

Victor R. Baker, Department of Geosciences and Department of Planetary Sciences, University of Arizona, Tucson, AZ 85721.

Drainage evolution on volcanoes proceeds according to the functional relationship

$$D = f\ (c,\ r,\ p,\ t)\ ,$$

where D is drainage density, c is climate, r is relief, p is rock type, and t is time. Because most volcanic rocks are highly permeable, drainage will not develop until a less permeable ash mantle is emplaced or until weathering reduces infiltration. Examples of both phenomena occur in Hawaii. Kilauea Volcano, youngest of the Hawaiian shields, displays little dissection except where the 1790 Keanakakoi ash was emplaced (1). The older Mauna Loa and Mauna Kea shields display V-shaped ravines where steep slopes on their eastern flanks were mantled by Pahala ash. Dissection is more pronounced on Mauna Kea, which is older than Mauna Loa. Kohala Volcano, dated at 700,000 yrs. B.P., is the oldest shield on the island of Hawaii. Deep weathering of its basalt has reduced infiltration sufficient to promote high-density drainage on its northeastern slopes (Fig. 1).

On volcanic cones, dissection by closely-spaced V-shaped ravines produces a characteristic "parasol ribbing" in which valley sides intersect to form sharp-edged ridges (2). The radial drainage results in a convergence of valley heads toward the volcano summit. Stream abstraction and capture are very common, and may be enhanced by orographic effects on precipitation. The result is greater incision on the upper slopes that may leave the relict surface of the original volcano preserved as triangular facets ("planezes") on the low slopes (2). Continued erosion then reduces the cone to a residual volcano, exposing resistant dikes and vents. Relief inversion may occur where valleys are filled by lava flows that are more resistant than adjacent valley walls.

On shield volcanoes parallel ravine systems incise to expose deeper layers where ground-water activity becomes more important. The deepest incision produces trough-shaped theater-headed valleys (Fig. 2). Once the latter form, they dominate the dissection of the shield. The largest theater-headed valleys probably grow fastest since they tap the largest supplies of ground water. The ground water locally produces spring sapping, but a more general process may be enhanced chemical disintegration of basalt at the water table, which intersects the slope toes at the valley wall/floor junction. This leads to exceptionally steep valley walls (3). On Kohala and the older Hawaiian volcanoes of Maui the characteristic deep valley form is U-shaped in cross section, and valley sides are subject to active soil avalanches, slumps, and other mass movement (4). Continued headward retreat of such valleys isolates uplands drained by V-shaped ravines (Fig. 2) producing hanging valleys. Divides may eventually be reduced to knife-like ridges, as in the pali of northeastern Oahu (5).

Especially large theater-headed valleys occur on Maui, where two such valleys, Kaupo and Keanae, have grown headward into the caldera of Haleakala Volcano. The relationship is remarkably similar to that shown on Tyrrhena Patera of Mars (6). Such large valleys may become conduits for lava flows and lahars, thereby adding to the complexity of their origin.

The climatic factor exerts a strong influence on Hawaiian volcano dissection. The northeastern, windward slopes of Kohala are much more dissected than the southwestern, leeward slopes (Fig. 1). Similar relationships occur on Mauna Kea, where the northeastern Hamakua Coast shows moderate drainage development of long, parallel V-shaped valleys experiencing cross grading by capture. Leeward slopes of Mauna Kea are essentially undissected.

Hawaiian volcano dissection has been suggested as an analog for sapping valleys in the Martian heavily cratered terrains (6,7) and as a model for volcano dissection on Mars (8). Several older shield volcanoes, including Hecates Tholus (Fig. 2), appear to display fluvial dissection. New crater dating studies of these volcanoes suggest that the dissection is coincident with the terminal heavy bombardment on Mars. Thus, the valleys probably formed at the same time as those in the heavily cratered terrains. Both areas of valley formation show two types of valleys: (a) slightly older, more dense networks on higher, probably relict land surfaces, and (b) younger, less dense networks of deeply incised valleys that seem to have grown headward at the expense of type (a) valleys. It is hypothesized that these relationships indicate an evolutionary sequence similar to that observed in the Hawaiian volcanoes. High-density surface-water ravines formed initially because of low-permeability rock types, appropriate climate, adequate relief, or some combination of these factors. With time, some valleys deepened sufficiently to tap ground-water flow in deeper, more permeable rock types. These valleys then enlarged by headward growth at the expense of the older network. The latter was isolated as relict, degraded components of the landscape. The entire system ceased functioning and was "frozen" in its approximate present configuration at the termination of the heavy bombardment on Mars.

REFERENCES

(1) M.C. Malin, D. Dzurisin, and R.P. Sharp, Geol. Soc. America Bull. **94**, 1148-1158 (1983). (2) C.D. Ollier, Volcanoes (MIT Press, Cambridge, Mass., 1970). (3) C.K. Wentworth, Jour. Geology **36**, 385-410 (1928). (4) C.K. Wentworth, Geol. Soc. America Bull. **54**, 53-64 (1943). (5) G.A. Macdonald and A.T. Abbott, Volcanoes in the Sea (Univ. of Hawaii Press, Honolulu, 1970). (6) V.R. Baker, The Channels of Mars (University of Texas Press, Austin, 1982). (7) V.R. Baker, N.A.S.A. Tech. Memo. **81776**, 286-288 (1980). (8) V.R. Baker, N.A.S.A. Tech. Memo. **82385**, 234-235 (1980).

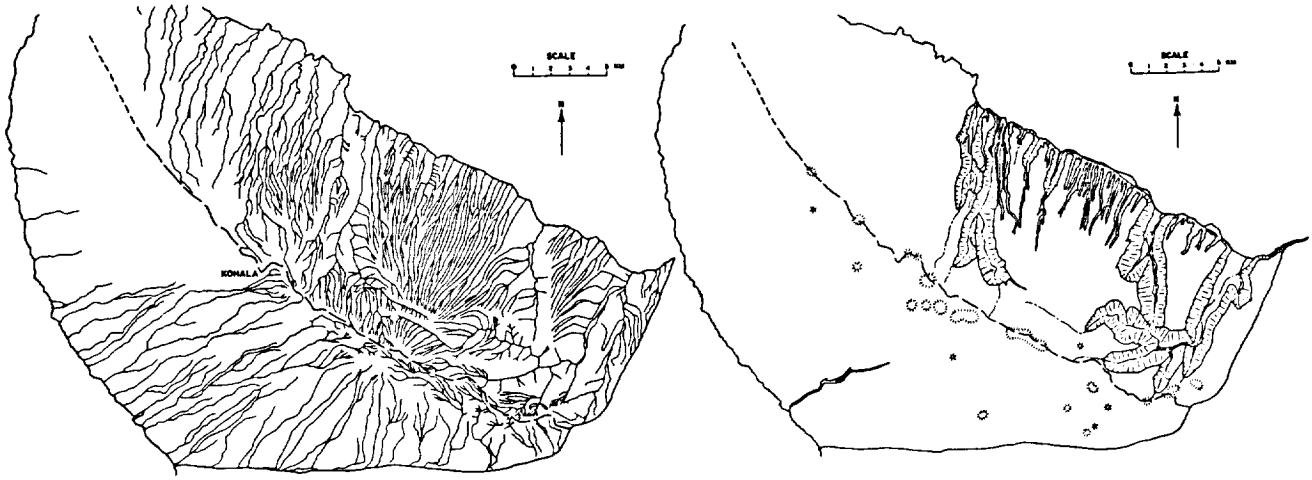

Figure 1. Drainage maps of Kohala Volcano at the northern end of the island of Hawaii. Left map emphasizes V-shaped ravine development; right map emphasizes U-shaped, theater-headed valleys.

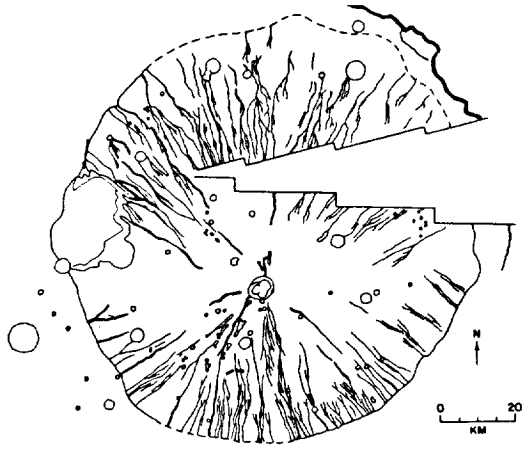

Figure 2. Sketch map of drainage features on Hecates Tholus. Heavy lines indicate relatively deep, U-shaped valleys in contrast to high density ravines.

FLUVIAL DRAINAGE SYSTEMS AND SEDIMENTARY BASINS: MARGARITIFER SINUS, MARS

BOOTHROYD, Jon C., and GRANT, John A., Department of Geology, University of Rhode Island, Kingston, RI 02881

The fluvial drainage basins of the Margaritifer Sinus Quadrangle (MC-19) are dominated by Capri and Eos Chasma and associated chaos on the northwest, by Ladon Basin in the center, and by Noachis Basin (provisional name) to the southeast (Fig. 1). Ladon and Noachis are ancient, multi-ringed impact structures (Schultz et al., 1982).

The Uzboi/Ladon outflow channels are the principal drainage into Ladon Basin, contributing to a major sediment sink on the central Basin plain (18°S,29°W)(Fig. 1). Small valley networks in separate sub-basins drain radially to Ladon Basin plain. The interior plain of the Ladon impact/structural basin could thus be classified as a large sedimentary basin, having received sediment via the meso-scale outflow channels as well as the radial valley networks. Flow out of Ladon Basin to the northeast via Margaritifer Valles (15S,26W)(provisional name) and into a channel and valley distributary area is obscured by Margaritifer Chaos collapse (Fig. 1).

The Osuga Valles outflow system (16S,39W) feeds a small sedimentary basin to the northwest of Ladon (Fig. 1). Osuga Valles upper drainage, and additional small valley networks (12S,37W) flowing into the basin, have been beheaded by the formation of Eos Chasma.

Two major longitudinal valley networks, Samara/Himera to the west and Parana/Loire to the east (Fig. 1), dominate the drainage of eastern Margaritifer Sinus. These networks, through-going to the northwest, cross the outer ring hills of Ladon to debouch into the channel and valley distributary area east of Margaritifer Valles, and near Margaritifer Chaos. Samara Valles heads in northeastern Argyre Quadrangle (35S,9W) and flows northwest to join Himera Vallis. The downstream portion of Himera is part of the Samara system.

The Parana multi-digitate network flows into a small impact basin with a sediment sink characterized by positive relief chaos (22S,12W) (Fig. 1,2). Parana basin serves as an example of a small sedimentary basin, in contrast to the much larger Ladon basin. The positive-relief chaos is interpreted as either pingo-like growth structures in the basin sediment, or as ice-rich erosional remnants left after removal of surrounding sediment by eolian processes.

Loire Vallis heads in Parana basin; thus we treat Parana/Loire as a single system.

Mapping with stereo pairs has allowed not only the delineation of major drainage basins, but also the identification of sub-basins, areas of internal drainage between larger basins, and determination of drainage-basin area. Once the complexity of drainage basins is recognized, the identification of sediment

sinks or sedimentary basins can begin. This ongoing mapping program demonstrates that an integrated series of drainage systems and basins, with a complex fluvial history, encompasses a large part of Margaritifer Sinus.

REFERENCE

Schultz, P.H., Schultz, R.A., and Rodgers, J., 1982, The structure and evolution of ancient impact basins on Mars: Jour. Geophys. Research, v. 87, No. B12, p. 8033-8047.

Figure 1. Western Margaritifer Sinus centered on Ladon Basin. The inner ring of the impact/structural basin is also a large sedimentary basin (sediment sink is inside the solid line). Letter codes identify the following: (LdV) Ladon Valles; (Ldb) Ladon basin; (EC) Eos Chasma; (OB) Osuga basin; (MV) Margaritifer Valles; (MC) Margaritifer Chaos; (LoV) Loire Valles; (HV) Himera Vallis; (SV) Samara Valles; (PB) Parana basin. (Mosaic 211-5821)

Figure 2. Parana Valles and the Parana sedimentary basin. The sedimentary basin (inside the solid line) contains positive relief chaos (Ct_p), interpreted as either pingo-like growth structures, or ice-rich erosional remnants left after stripping of surrounding material by eolian processes. (084A46,47,48, 615A45)

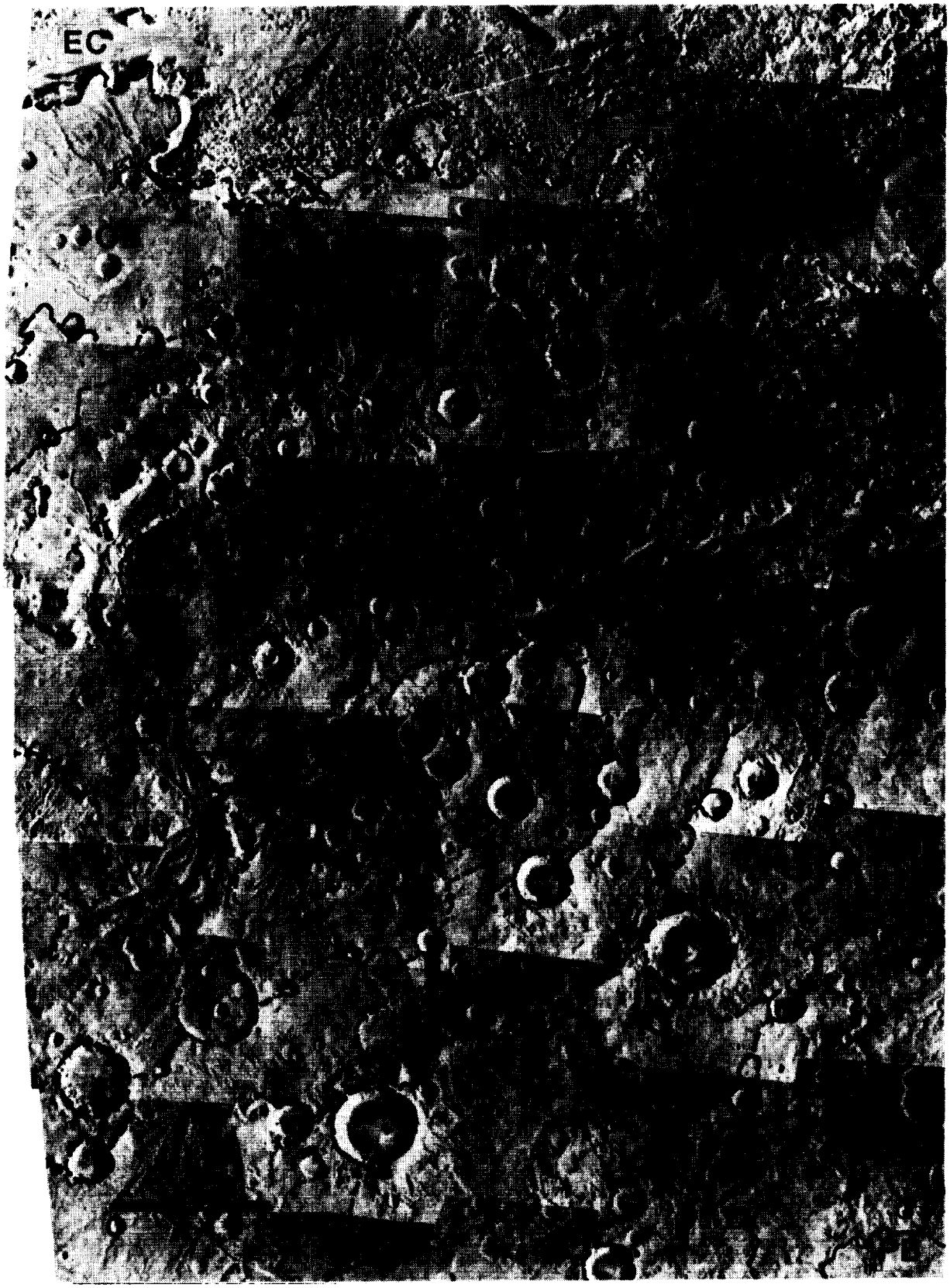

Figure 1

Figure 2

RING FURROWS ON MARTIAN HIGHLANDS: GUIDES TO SURFACE PROCESSES AND STRATIFICATION

R. A. De Hon and E. E. McDaniel, Department of Geosciences, Northeast Lousiana University, Monroe, LA 71209.

Ring furrows (1) are flat-floored trenches, circular in plan-view, forming rings 7 to 50 Km in diameter. Typical ring furrows are about 0.5 Km deep and 5 to 20 Km wide, surrounding a central, flat-topped, circular mesa or plateau. A type example of a ring furrow is defined west of Syrtis Major at 3 N and 308 W (MC 13 SW, Viking Orbiter frame 373S72). This feature is a breeched ring approximately 20 Km inner diameter and 15 Km wide. The ring is open in the northwest to the floor of a flat circular depression. Several other ring furrows are found in the same region.

Viking frames and mosaics were searched for all occurrences of ring furrows on Mars. Ninety-nine rings have been identified (Fig. 1). Almost all ring furrows occur in the cratered highland province of Mars; a few occur on the northern plains; and none occur in the polar regions. They do not occur at either the lowest or highest elevations. In Figure 1, it is apparent that ring furrows are associated with ridged plains (unit prg) and older surfaces. Examination of Viking frames reveals that ring furrows located within hilly and cratered terrain (unit hc) are, in fact, associated with plains and dissected plains surfaces within the hilly terrain (2). All ring furrows tend to be located on channeled, knobby, furrowed, dissected, or otherwise erosionally modified terrain. They are often found on the highland side of a retreating scarp. Ring furrows are usually breeched so that the ring opens to a lower surface or to a channel system. Some rings are defined by circular or arcuate channel segments (3). Often the plain or plateau surface outside the ring, while cut by channel or valley systems, does not show evidence of erosion outside the channels.

Ring furrows are erosional forms produced at the site of partially buried craters. Formation of ring furrows requires that a crater form on a plains surface such as a volcanic plain. Later the crater is partially buried by flows to produce a ring of exposed crater ejecta. Still later, the exposed rim is removed by selective erosion to produce the inverted topography of a ring depression. Erosion is apparently caused by groundwater sapping, and material is removed by overland flow through the adjacent channel systems.

In the process of identifying ring furrows on Mars, several topographic features that appear to be related were found. The interior plateau of normal ring furrows can be observed in several stages of degradation ranging from fractured and dissected plateaus to isolated knobby interiors of rimless circular depressions. Also, the exterior plains of ring furrows are observed in various states of degradation until only the interior plateau remains as an isolated circular mesa or plateau. In similar fashion, isolated plateaus may be degraded to the point that they exist as roughly circular patches of dissected or knobby terrain. Thus a degradational series may be established between ring furrows and isolated knobby terrain, and between ring furrows and shallow dish-shaped craters (patinas).

Ring furrows provide information as to the stucture (stratification in the subsurface), processes shaping the surface, and the geologic history of Mars. Current observations are consistent with the following:

1. A limited thickness (a few hundred meters) of surface plains-forming material
2. The probable presence of a resistant substrate
3. The presence of a buried aquifer
4. A restricted period of ground water release
5. The presence of buried flow material in the northern plains.

REFERENCES

(1.) De Hon, R. A. (1984) NASA Tech. Mem. 86246, 228-229.
(2.) Scott, D. H. and M. H. Carr (1978) U. S. Geol. Surv., Misc. Inv. Map I-1083.
(3.) Baker, V. B. (1982) NASA Tech Mem. 85127, 206-208.

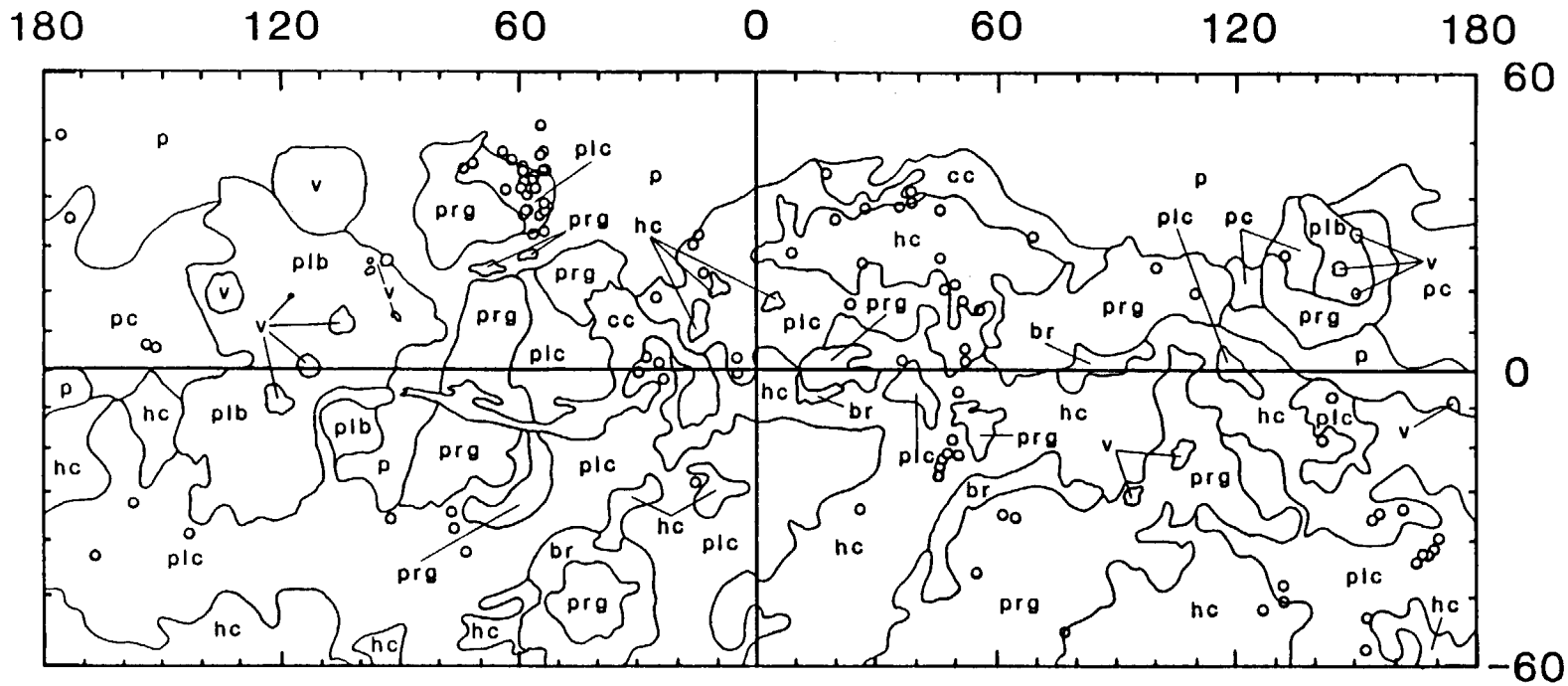

PHYSIOGRAPHIC MAP OF MARS

FIGURE 1. Location of ring furrows on Mars. Physiographic units roughly correspond to geologic units (2). Open circles are ring furrows. Unit cc is canyon, channel, chaos, and furrowed surfaces. Unit prg includes Lunae Planum type surfaces and older ridged plains. Unit plc is cratered plateau terrain. Unit hc is hilly and cratered terrain.

EXTRACTION OF QUANTITATIVE MORPHOLOGY FOR IRREGULAR SURFACE FEATURES ON MARS
Philip A. Davis and Laurence A. Soderblom, U.S. Geological Survey, Flagstaff, Arizona 86001

Mars, like Earth, has a diversity of surface landforms. They represent virtually the entire range of geologic processes that operate on terrestrial planets: lava flows (volcanic), faults (tectonic), channels (fluvial and/or glacial), talus (mass-wasting), dunes (eolian), craters (impact), and polar ice caps (atmospheric condensation-sublimation). These landforms are indicative of the nature, timing, and rate of some geologic processes that have operated on Mars. Thus detailed topographic data for these features will provide important keys to understanding the nature and history of the geologic processes that have operated and may still be operating on Mars.

One critical limitation of previous morphologic studies of Martian landforms has been the lack of quantitative information on the shape of small landforms with low slopes. This lack was the result of: (1) the sparsity and relatively low resolution of available stereogrammetric topographic databases, which typically have 1-km contour intervals; (2) the small amount of high-resolution stereocoverage from Viking Orbiter data; (3) the scarcity of high sun-angle (greater than 75°) images at adequate spatial resolution for detailed shadow-measurement methods; and (4) the inability of either photogrammetric or shadow-measurement methods to obtain slope gradients and heights for features with gentle slopes.

We have developed several photoclinometric techniques to obtain slope profiles for various landforms that overcome many of these limitations. Originally, these techniques were devised for topographic analysis of craters, because craters are important ubiquitous planetary landforms [Davis and Soderblom, 1983]. In addition, craters usually present special circumstances that allow reliable three-dimensional topographic analysis by use of our techniques (i.e., at least two profiles can be selected that differ in illumination geometry but that have similar topography and albedo along their lengths). However, during the development and testing of our crater-profiling methods, we noted that they gave reliable results for many other surface features (e.g., lava-flow fronts, wrinkle ridges, grabens, dune forms, valley scarps, and polar deposits). Therefore, we extended the methods and software to enable extraction of slope data for such topographically "irregular" features [Davis and Soderblom, 1984]. The main purpose of this extension is the decoupling of the two profiles. The technique originally developed for craters requires the two profiles to have a common point, usually the geometric center of the crater. However, our technique for irregular features, which allows the two profiles to be unconnected, is usually necessary for irregular features because their form is such that their surface dip lines (profiles) generally do not converge on a common point. Thus, our techniques now can extract detailed three-dimensional topographic data for a variety of landforms from monoscopic and biscopic (nonstereo) Viking Orbiter images.

The method is as follows. The digital images are first radiometrically calibrated. Individual topographic profiles are then calculated from the image data by using a frame buffer and an interactive display screen connected to a VAX. The primary method uses two profiles that cross the terrain at different azimuths to the Sun; the topography and albedo of the profiles can

be assumed identical. Alternately, the same profile trace can be used across two different images that have different lighting orientations [McEwen, 1985]. The solution decouples surface albedo from topography, accounts for the atmospheric contribution, and iteratively, fully accounts for parallax distortions introduced by nonvertical viewing [detailed in Davis and Soderblom, 1983].

The computer algorithms were recently improved to include estimates of the errors associated with our slope, height, and distance measurements [Davis and McEwen, 1984]. Both the precision and accuracy of these methods are about 2° for slopes, which translates to about 5%-10% for height measurements. Two examples demonstrating the quality of topographic data obtained by these techniques are shown in Figures 1 through 3. In these figures we compare profiles obtained by our technique with profiles obtained by stereophotogrammetry of two canyon scarps located between Ius and Tithonium Chasmata.

The degree of detail in the slope data obtained by these techniques is limited only by the resolution of the image, i.e., the higher the spatial resolution of the image, the greater the amount of detail in slope that can be detected for a particular feature. These techniques can obtain topographic data on features regardless of their slope or the lighting conditions under which the image was acquired. Thus, three-dimensional topographic information can now be derived for Martian landforms that was previously unobtainable, when accurate shadow measurements were prohibited by the low slopes of the features and the requirement of high solar-incidence angles. Given the increased capabilities of photoclinometry, we now plan to investigate several geologic problems on Mars that are associated with volcanic and tectonic features, canyons, and polar landforms.

References:

Davis, P. A., and McEwen, A. S., 1984, Photoclinometry: Analysis of inherent errors and implications for topographic measurements: Lunar Planet. Sci. XV, Lunar and Planetary Institute, Houston, p. 194-195.

Davis, P. A., and Soderblom, L. A., 1983, Rapid extraction of relative topography from Viking Orbiter Images II - Applications to irregular topographic features: Reports of Planetary Geology Programs - 1982, NASA TM 86246, p. 263-265.

Davis, P. A., and Soderblom, L. A., 1984, Modeling crater topography and albedo from monoscopic Viking Orbiter images. 1. Methodology: J. Geophys. Res., v. 89, p. 9449-9457.

McEwen, A. S., 1985, Topography and albedo of Ius Chasma, Mars: Lunar and Planetary Sceince XVI, Lunar and Planetary Institute, Houston, p. 528-529.

Wu, S. S. C., 1979, Photogrammetric portrayal of Mars topography: J. Geophys. Res., v. 84, p. 7955-7959.

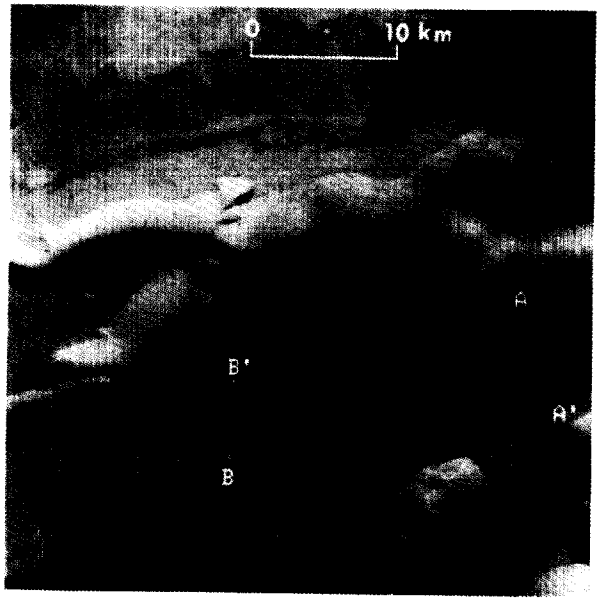

Figure 1. Portion of Viking Orbiter 1 image 64A18, resolution 79 m, showing canyons located between Ius and Tithonium Chasmata, Mars. Lines A-A' and B-B' indicate locations along which topographic profiles were obtained by using the photoclinometric methods of Davis and Soderblom (1983, 1984). North at bottom.

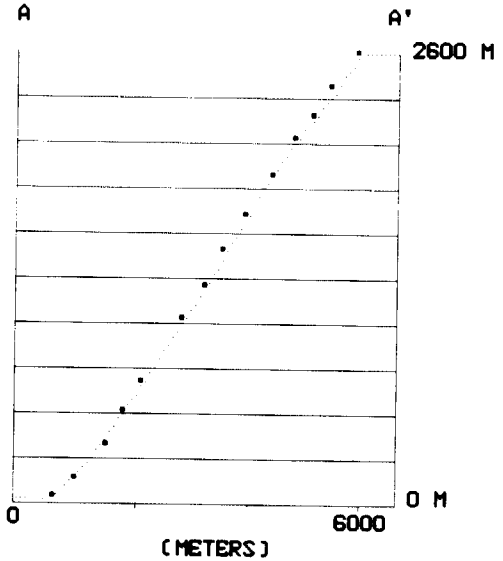

Figure 2. Topographic profile (A-A') across canyon scarp shown on Figure 1. Dots represent photoclinometric data; squares represent stereophotogrammetric data, which are limited by the contour interval (Wu, 1979). The average error along this profile is less than 1 percent.

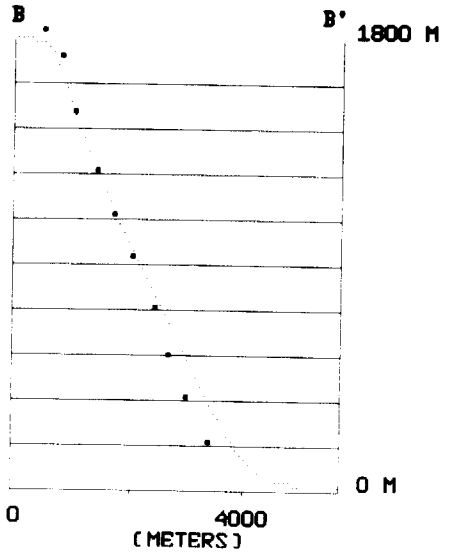

Figure 3. Topographic profile (B-B') across canyon scarp shown on Figure 1. Dots represent photoclinometric data; squares represent stereophotogrammetric data, which are limited by the contour interval (Wu, 1979). The average error along this profile is about 10 percent.

MORPHOLOGY AND RHEOLOGY OF THE ROYAL GARDENS BASALT FLOWS, KILAUEA VOLCANO

Jonathan Fink, Geology Dept., Arizona State University, Tempe, AZ 85287
Jim Zimbelman, Lunar & Planetary Institute, Houston, TX 77058

We have continued our investigation [1-3] into the relevance of several widely used models that relate the post-emplacement morphology of lava flows to their rheologic properties. Our approach involves (1) construction of accurate cross sections and topographic maps for flows whose emplacement has been carefully monitored, (2) measuring various geometric parameters from the cross sections or maps, and (3) calculation of rheologic properties using the measured geometric values. Systematic variations in rheology are then compared with theoretical, laboratory, and field data in order to refine the models. The models are ultimately applied to measurements of extra-terrestrial flows in order to help constrain their compositions.

Ten carefully surveyed topographic profiles across the Phase 5 (July, 1983) Royal Gardens basalt flow from the East Rift of Kilauea Volcano were matched to digitally derived pre-flow profiles in order to construct accurate flow cross sections. Flow margin and levee thicknesses and widths measured on these sections were then used with topographic slope data and observed flow velocities to compute yield strengths and viscosities by means of various rheologic models [4-9]. Calculated yield strengths (1.5-50 x 10^3 Pa) and viscosities (0.2-8.2 x 10^6 Pa-s) are comparable to earlier field estimates [6,10] and slightly higher than laboratory determined values for aa basalt [11].

For any cross section, calculations of rheologic parameters based on flow-margin depths generally gave lower and more consistent values than those based on the dimensions of levees. This relationship may be attributed to the earlier formation and less complex evolution of the margins. The various equations also gave more consistent results for upstream profiles, suggesting that calculations for remotely observed flows should avoid measurements near flow termini, and should use flow margin thicknesses rather than levee heights if available.

Both yield strength and viscosity increased systematically downstream over the 1.8 km distance separating the most distal and proximal profiles (Fig. 1). The maximum temperature drop of 30^{0}C measured by the USGS for these flows is insufficient to account for the 30-fold increase in yield strength [11], but could explain the three-order-of-magnitude increase in viscosity [12]. The downstream yield strength increase is more likely due to increased crystallization and brecciation with time. Upstream extrapolation of the linear yield strength trend suggests that this property should drop to zero about 3 km from the front of the Phase 5 flow. Perhaps coincidentally, this point corresponds to the location of the pahoehoe/aa transition.

Although none of the equations used to calculate rheologic properties include temperature effects directly, longitudinal variations like those observed for the Phase 5 flow may be diagnostic of the crystallization and cooling behavior of specific compositions. In particular, the difference

(Δ T) between liquidus and solidus temperatures may be reflected in the longitudinal rate of viscosity increase. For a given distance, compositions with small values of ΔT (rhyolite) should show less viscosity increase than those with large ΔTs (basalt). Furthermore, owing to their small ΔT values, silicic flows are less able to "drain out" after effusion stops at the vent, so that their final profiles show less well-developed channels than basalts.

In order to characterize these temperature-dependent effects, we have constructed detailed topographic maps of channelized lava flows from the Phase 30 (2/4/85) Royal Gardens basalt flow (Fig.2), an andesite flow from the south side of Mount St. Helens, and the Glass Mountain rhyolite flow in California. We are presently modeling the pre-flow topography in order to construct a series of closely spaced cross sections, from which we will calculate yield strength and viscosity values. We have also compiled other published sets of viscosity versus distance data [10,13]. Future calculations of longitudinal variations in rheology for all these flows may identify composition-specific trends that can be detected using remotely obtained morphologic data for lava flows on Mars, the Moon, and Venus.

References cited

[1] Fink JH, Zimbelman, JR (1985) Field measurements of 1983-84 lava flows at Kilauea and Mauna Loa Volcanoes: Basis for a comparison with Mars. Lun. Plan. Sci. Conf. XVI:238-239.

[2] Zimbelman JR (1985) Estimates of rheologic properties for flows on the martian volcano Ascraeus Mons. Proceedings Lunar Planet. Sci. Conf., 16 (in press).

[3] Fink JH, Zimbelman, JR (1986) Rheology of the 1983 Royal Gardens basalt flows, Kilauea Volcano, Hawaii. Bull. Volc. (in press).

[4] Nichols RL (1939) Viscosity of lava. Jour. Geol. 47:290-302.

[5] Johnson AM (1970) Physical Processes in Geology. Freeman Cooper San Francisco, pp 1-576.

[6] Hulme G (1974) The interpretation of lava flow morphology. Geophys. J. Roy. Astron. Soc., 39:361-383.

[7] Hulme G, Fielder G. (1977) Effusion rates and rheology of lunar lavas. Phil. Trans. R. Soc. Lond. A 285:227-234.

[8] Moore HJ, Arthur DWG, Schaber GG (1978) Yield strengths of flows on the earth, Mars, and Moon. Proc. Lunar Planet. Sci. Conf., 9: 3351-3378.

[9] Wilson L, Head JW (1983) A comparison of volcanic eruption processes on earth, Moon, Mars, Io and Venus. Nature 302:663-669.

[10] Booth B, Self S (1973) Rheological features of the 1971 Mount Etna lavas. Phil. Trans. R. Soc. Lond. A. 274:99-106.

[11] McBirney AR, Murase T (1984) Rheological properties of magmas. Ann. Rev. Earth Planet. Sci. 12:337-357.

[12] Shaw HR (1969) Rheology of basalt in the melting range. Jour. Petrology 10:510-535.

[13] Walker, GPL (1967) Thickness and viscosity of Etnean lavas. Nature 213:484-485.

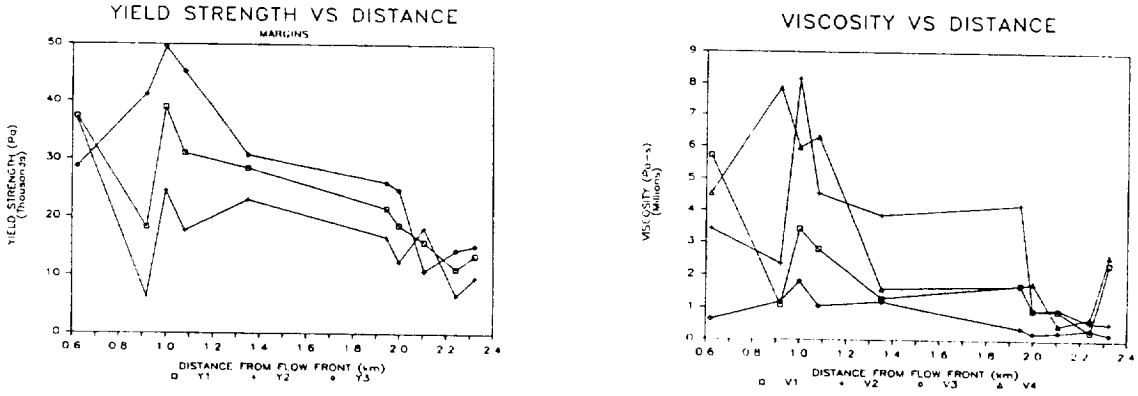

Figure 1. Downstream increases in yield strength (left) and viscosity (right) calculated by several different methods [4-9]. References for equations: Y1 from [5], Y2 [8], Y3 [6], V1 [4], V2-V4 [7,9 with different measures of effusion rate]. Flows moved from right to left.

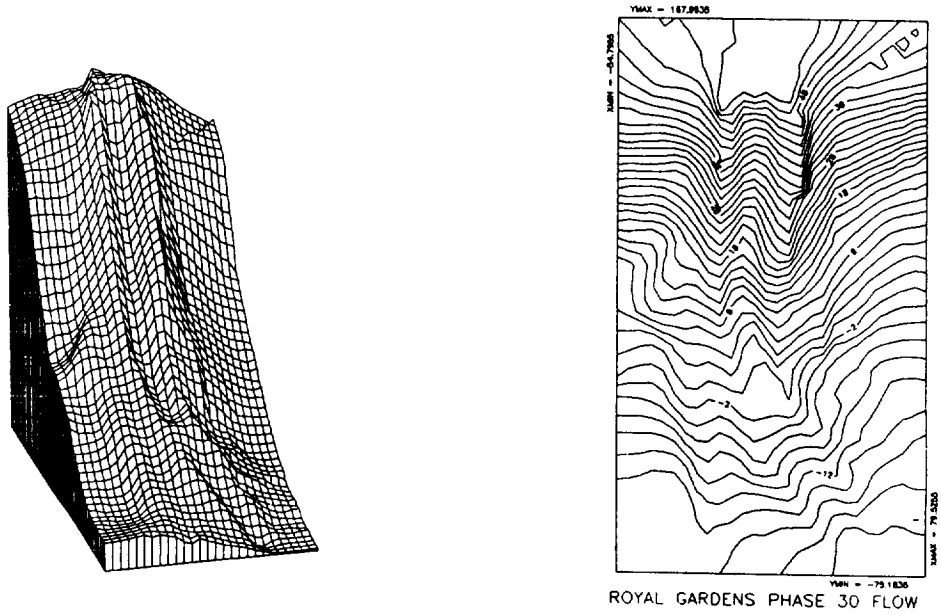

2. Three dimensional surface plot (left) and topographic map (right) of the Phase 30 Royal Gardens basalt flow constructed by surveying 95 points with a GTS-2 Total Station (combined theodolite/EDM). Plots made on a portable microcomputer with commercially available software. Map contour interval is 2 meters. Map width approximately 135 meters. 3-D plot has no vertical exaggeration.

CHARACTERISTIC STRUCTURES OF THE HIGHLAND BOUNDARY ON MARS AND COMPARISON WITH TOPOGRAPHY

Herbert Frey and Ann Marie Semeniuk, Geophysics Branch, Goddard Space Flight Center, Greenbelt, MD 20771

We have assembled a data base for the study of the highland boundary through quantitative geomorphic mapping and crater counts on the 1:2,000,000 controlled photomosaics (Semeniuk and Frey, 1984, 1985; Frey and Semeniuk, 1985). This mapping has been global: features characteristic of the boundary (e.g., detached plateaus, knobby terrain) have been identified wherever they occur between +65 and -45° latitude (the limits of the available controlled photomosaics when this work began). Figure 1 shows a combination map which shows those places on Mars where crater interiors, knobby terrain or detached plateaus exceed 2.5% of the area of each sample box. 2.5% would represent a single 37 km diameter crater at the equator (or a plateau with equivalent area of 1100 km^2). The overlap produced by combinations of these features is especially obvious along the highland boundary in eastern Mars, in the Mareotis-Tempe block and in the knobby terrain in Elysium-Amazonis. Note that other lesser occurrences of knobby terrain, detached plateaus and/or craters occur well north of the present highland boundary, and in Acidalia these form an outer "collar" which partially fills the gap between Deuteronilus and the Mareotis-Tempe block. Likewise the Elysium-Amazonis region seems more connected to the cratered highlands in Memnonia than is generally obvious.

It is interesting to compare these with other data. The left side of figure 2 shows, as a function of latitude, the fractional area of crater interiors, knobby terrain and detached plateaus, for five longitudinal profiles between 280 and 300°W. These cross the boundary in the Nilosyrtis Mensae region. Elevation data from the USGS topographic map of Mars has been superimposed with a freehand connection of the data points. The peak occurrence of detached plateaus corresponds to a rapid decrease in the fractional area of crater interiors in most of the profiles. If the topography is correct, then the transition zone corresponds to a significant change in elevation downward to the north. Note in the 295° and 300°W profiles the detached plateaus dominate in the steeper, upper portions of the transition zone, while knobby terrain occurs mostly in the lower, more gently dipping terrain. Smooth plains to the north, which occur at the lowest elevations, often begin (or the transition zone ends) where the slope again changs to steeper values.

The righthand side of Figure 2 shows additional data for the detached plateaus. The fractional area of all plateaus and the topography are repeated. The actual number of individual detached plateaus and the fractional area of the largest individual plateau have been added. Number and fractional area (of all the detached plateaus) do not always correlate. In the 300°W profile the fractional area decreases northward roughly as does the number of detached plateaus between 32 and 37°N, but from 37 to 47°N there are many small plateaus which add to less than 1% of the sampled area. The fractional area of the largest plateau, the fractional area of all plateaus, and the number of platforms often change where the topography changes. Topography probably plays a significant role in the development of the highland boundary and the transition zone (Semeniuk and Frey, 1984). Unfortunately, it is difficult to establish the exact relationships between

FIGURE 1

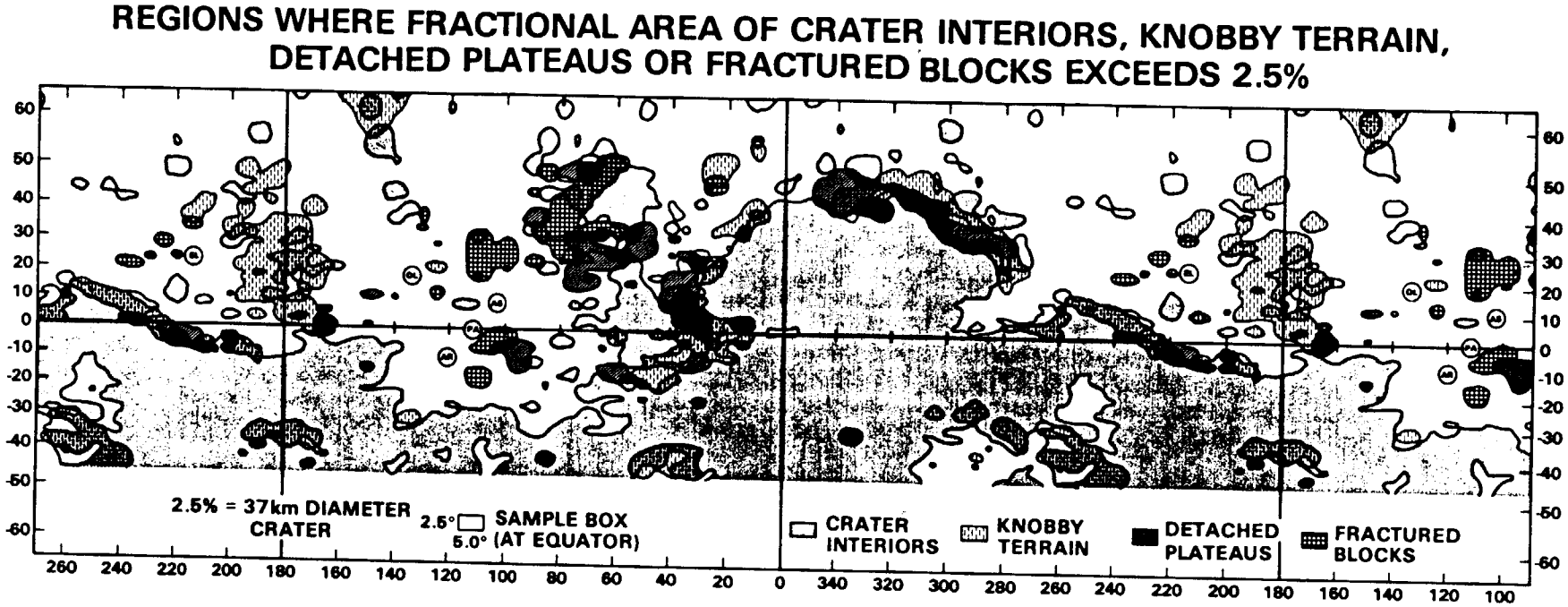
REGIONS WHERE FRACTIONAL AREA OF CRATER INTERIORS, KNOBBY TERRAIN, DETACHED PLATEAUS OR FRACTURED BLOCKS EXCEEDS 2.5%
2.5% = 37km DIAMETER CRATER
2.5°
5.0° (AT EQUATOR)
SAMPLE BOX
CRATER INTERIORS
KNOBBY TERRAIN
DETACHED PLATEAUS
FRACTURED BLOCKS

the transition zone structures and topography because of the curent limitations in the elevation data.

References

Frey, H. and A.M. Semeniuk, The highland boundary on Mars: Distribution of characteristic structures, Lunar Planet. Sci. XVI, 252-253, 1985 (abstract).

Semenik, A.M. and H.V. Frey, Distribution of characteristic features across the boundary scarp in Acidalia and Amazonis-Memnonia, Lunar Planet. Sci. XV 748-749, 1984 (abstract).

Semeniuk, A.M. and H.V. Frey, Mars: Possible relics of the ancient cratere terrain in the northern lowlands, EOS Trans. Am. Geophys. Un. 66, 400, 1985 (abstract).

FIGURE 2

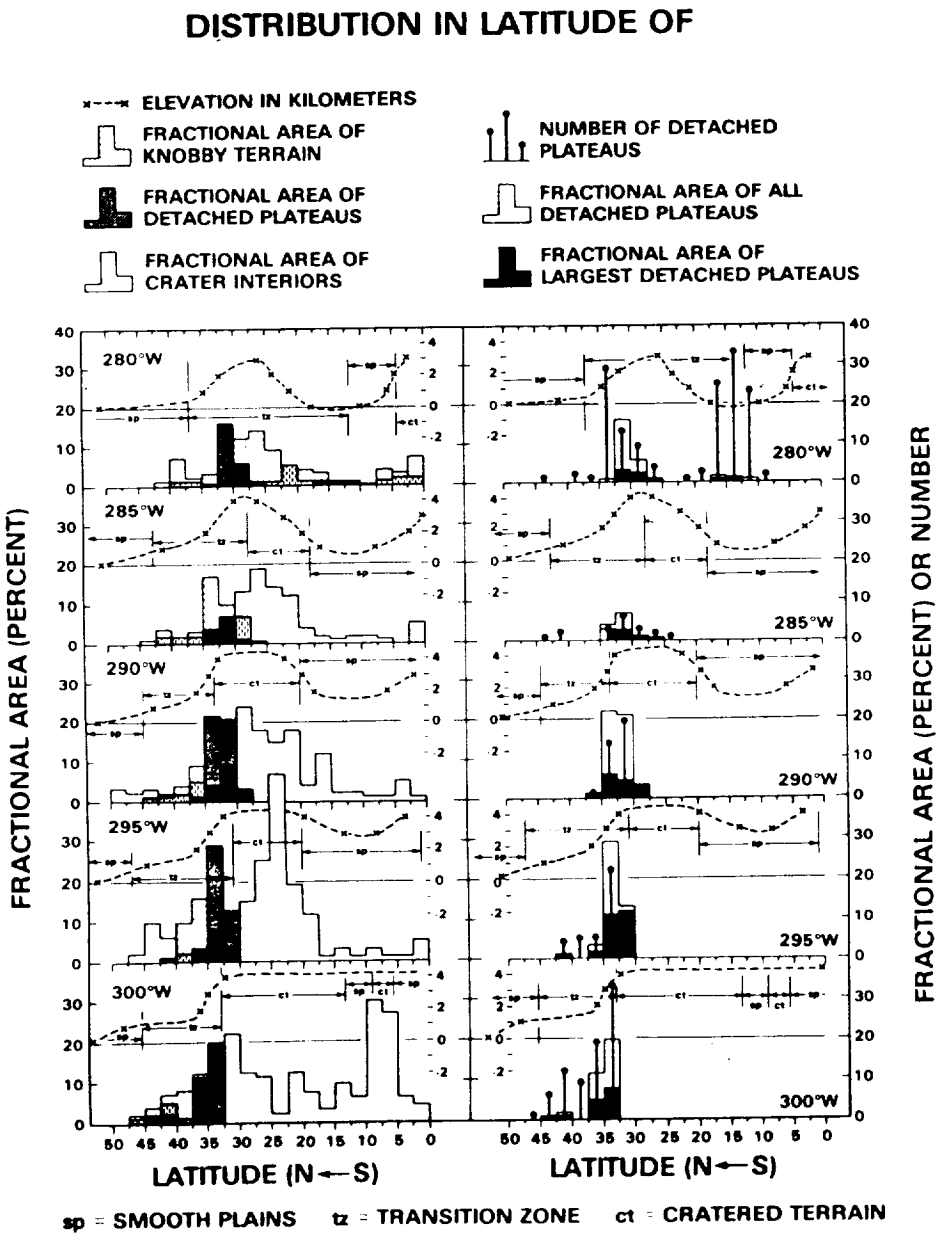

REGIONAL VARIATION IN MORPHOMETRIC PROPERTIES OF LARGE SYMMETRIC KNOBS ON MARS

Herbert Frey, Jennifer Middleton and Ann Marie Semeniuk, Geophysics Branch
Goddard Space Flight Center, Greenbelt, MD 20771

Knobby terrain on Mars may consist of small closely spaced hills, large relatively isolated peaks or mixtures of these. The characteristics of large symmetric knobs between +65 and -45° latitude, as measured on the 1:2,000,000 controlled photomosaics, suggest that two different populations of these features exist.

We determined the distribution of 1634 symmetric knobs larger than 10 km across, subdivided by morphological type (circular, ellipitical, wedgeshaped, others). Many of the large knobs are concentrated along the highland boundary which separates cratered terrain from the northern plains (Frey et al., 1985a). It is interesting that most of these boundary knobs lie within a restricted elevation range of about 2 km (0 to 2 or 1 to 3 km above the reference 6.1 mbar level, as determined from the USGS Topographic Map of Mars). Uncertainties in the current topographic data make this conculsion only tentative. In addition to the highland boundary, large knobs are found in the rims of major impact basins and in the knobby terrain of Elysium-Amazonis. Lesser concentrations also exist in the canyon/chaotic terrain region of Coprates-Margaritifer Sinus. There are also a relative abundance of large knobs east of Hellas, spreading into Eridania but lying south of Hesperia Planum.

We find some variation in the properties of these features which seems to depend on region (Frey et al., 1985b). Figure 1 shows (a) the size-frequency distribution of the knobs and their relative occurrence by morphological type, and (b) the ellipticity of the knobs (87% are elliptical in shape) as given by the ratio of long to short dimension plotted versus diameter. In both (a) and (b) the knobs are grouped by different physiographic/tectonic regions. The upper line shows data for knobs found in volcanic plains, near the outflow channels, and in chaotic terrain or near the large canyons. The lowest line includes regions around the highland boundary, near the rims of major impact basins, and along the edge of the Mareotis-Tempe-Lunae Planum block. The size distribution of knobs in volcanic plains and outflow channels (top line) is generally sharply peaked toward the smallest sizes. By contrast the knobs near basin rims and along the highland boundary in Amenthes-Aeolis have a broader size frequency distribution that extends to larger dimensions. While elliptical knobs dominate in all regions, round or circular knobs are rare in Acidalia (APA) and in the outflow channels (OFC) to the south. This may be related to erosional modification of the knobs, which could also explain their relatively small sizes. In figure 2b there seems to be a relation between increasing ellipticity and increasing diameter which differs for knobs in different areas. Those near basin rims and along the highland boundary range up to 48 km across but rarely exceed a (long to short dimension) ratio of 3.0. By contrast the large knobs in the plains-forming and canyon/chaotic terrain/channel units are generally smaller (see Figure 2a) but become more elliptical more rapidly with increasing diameter, reaching a ratio of 5.0 or more for sizes less than 20 km.

FIGURE 1 a

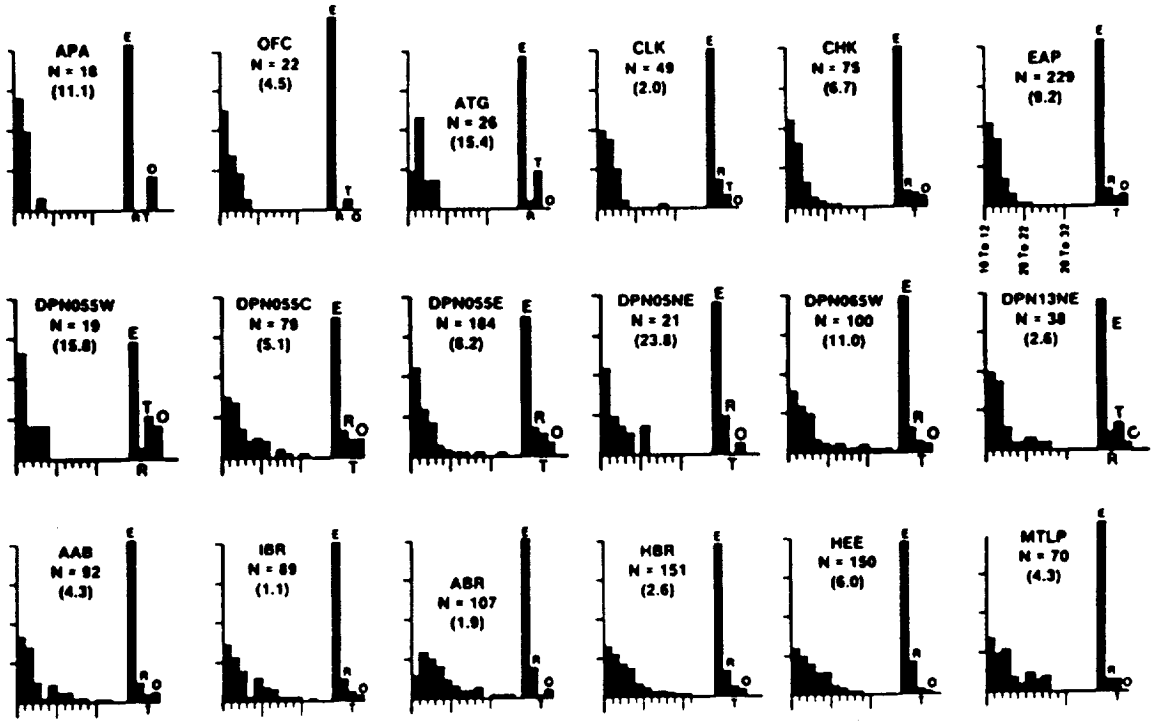

FIGURE 1 b

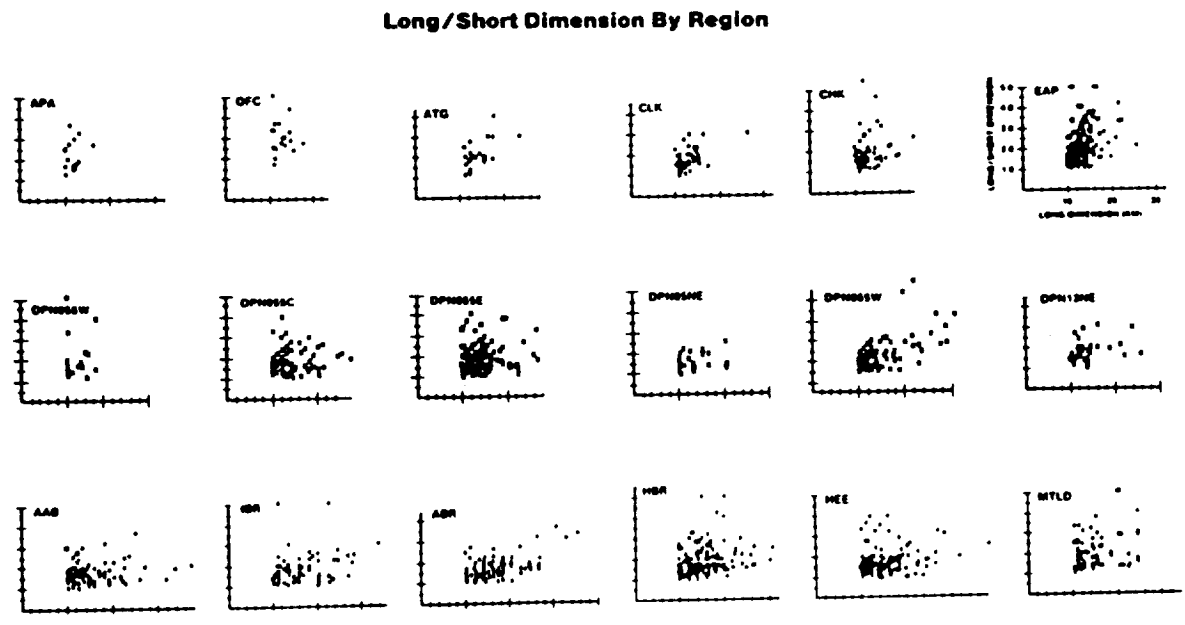

Given the different geologic setting of these groups of knobs, it is possible that two distinct populations exist. If true, it is interesting that the knobs along the highland boundary more closely resemble (in their dimensional characteristics) those near major impact basins than those in volcanic plains. Alternatively it is possible that the current properties of many of the knobs, especially those in southern Acidalia and the outflow channels/chaotic terrain, have resulted from erosional modification of originally larger, perhaps more circular knobs. If this modifcation is related to the formation of the outflow channels, then a similar explanation may not apply to the large population of symmetric knobs in Elysium-Amazonis, unless unrecognized channels exsit there.

References:

Frey, H., J. Middelton and A.M. Semeniuk, Distribution and properties of large symmetric knobs on Mars, NASA Tech. Mem. 87563, p. 355-357, 1985a (abstract).

Frey, H., J. Middelton and A.M. Semeniuk, Properties of large symmetric knobs on Mars, EOS Trans. Am. Geophys. Un. 66, 296, 1985b (abstract).

Figure 1. (a) Size frequency histograms and (b) shape-size diagrams for large symmetric knobs on Mars, arranged by region. Key: APA = Acidalia Planitia Area, OFC = Outflow Channels, ATG = Apollinaris Trough Group, CLK = Canyon Lands Knobs, CHK = Chaotic Terrain Knobs, EAP = Elysium-Amazonis Plains, DPN - Deuteronilus-Protonilus-Nilosyrtis region (graphed by subquadrangle), AAB = Amenthes-Aeolis Boundary, IBR = Isidis Basin Rim, ABR = Argyre Basin Rim, HBR = Hellas Basin Rim, HEE = Hellas East-Eridania, MTLP = Mareotis-Tempe-Lunae Planum area.

CRATER COUNTS IN THE HIGHLAND BOUNDARY TRANSITION ZONE IN EASTERN MARS

Herbert Frey, Ann Marie Semeniuk, Jo Anne Semeniuk and Susan Tokarcik,
Geophysics Branch, Goddard Space Flight Center, Greenbelt, MD 20771

The transition zone which separates the cratered highlands from the northern lowlands in eastern Mars can be subdivided into 4 to 5 subunits based on the varying distribution and character of the detached plateaus, knobby terrain and intervening plains-forming units which characterize this zone. Crater counts in each of these subunits provide evidence for discrete but common episodes of resurfacing, one of which appears to have been synchronous with Lunae Planum volcanics.

Figure 1 shows cumulative frequency curves for the different subunits within the transition zone in eastern Mars. While all have similar character, there are differences in the details of the curves for different subunits. Two of the subunits (B1, B8) occur both east and west of the Isidis Basin. Figure 1b and 1c compare the "eastern" (Amenthes-Aeolis) and "western" (Ismenius-Casius) contributions to the cumulative frequency curves for these common subunits. All of these curves bend over at smaller diameters, suggesting that resurfacing has been important in the development of the transition zone and its subunits. We employ the approach of Neukum and Hiller (1981), breaking the cumulative frequency curves into separate branches where they depart from a "Mars standard production curve" by subtracting the cumulative number at the departure point from the rest of the (smaller diameter) points. The new cumulative frequency values for the smaller diameters are then replotted, resulting in a second branch which follows a younger crater production curve.

Figure 2 shows this process for binned crater counts for the three subunits which make up the transition zone east of the Isidis Basin. The large diameter craters for B0 and B8 lie along a production curve having a crater age (cumulative number with diameter greater than or equal to 1 km per 10^6 km^2) ~90,000, down to a diameter of ~25 km. When subtracted at this point, the smaller craters for B0 and B8 lie on a production curve having crater age ~22,000, which is the production curve for the largest B1 subunit craters (10 to 25 km). This is shown in the middle panel. Note that the B0 and B8 curves bend away from the production curve again at diameters $\lesssim$12 km. Subtracting again produces the result shown in the right hand panel: the small diameter craters representing the uppermost surface for <u>all</u> the subunits (B0, B1, B8) coincide along a production curve with crater age ~4700. The subtraction process always leaves the first few binned values too low (the differences between adjacent cumulative numbers being small), as is obvious from Figure 2. Despite this problem, the data for all three subunits east of the Isidis Basin cluster about three distinct crater ages. This suggests a punctuated or episodic resurfacing history with some episodes common to the different subunits.

Results for all the subunits of the transition zone in eastern Mars are are summarized in Table 1, grouped to show the east-west differences for common subunits. Parentheses indicate crater ages determined from only a few large diameter points. All ages were determined by fitting crater production curves through separate branches, as described above. The +/- values in brackets do not represent error bars, but show a range in crater ages that could be derived from fitting the standard production curves through the data. The clustering of ages which emerges shows remarkable

FIGURE 1

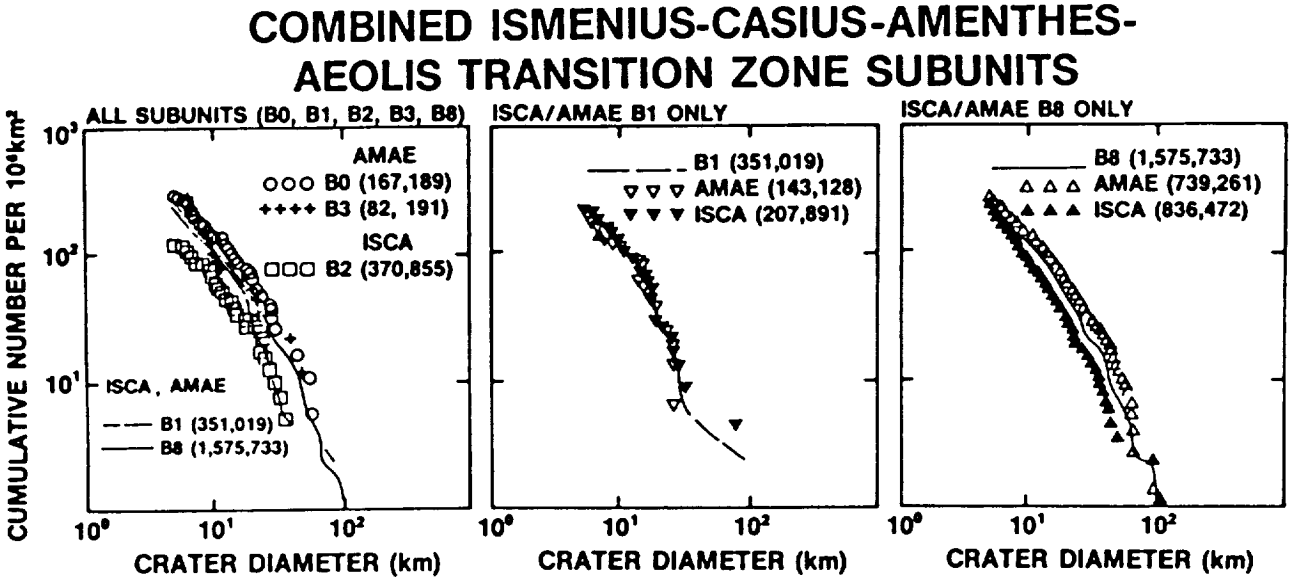

FIGURE 2

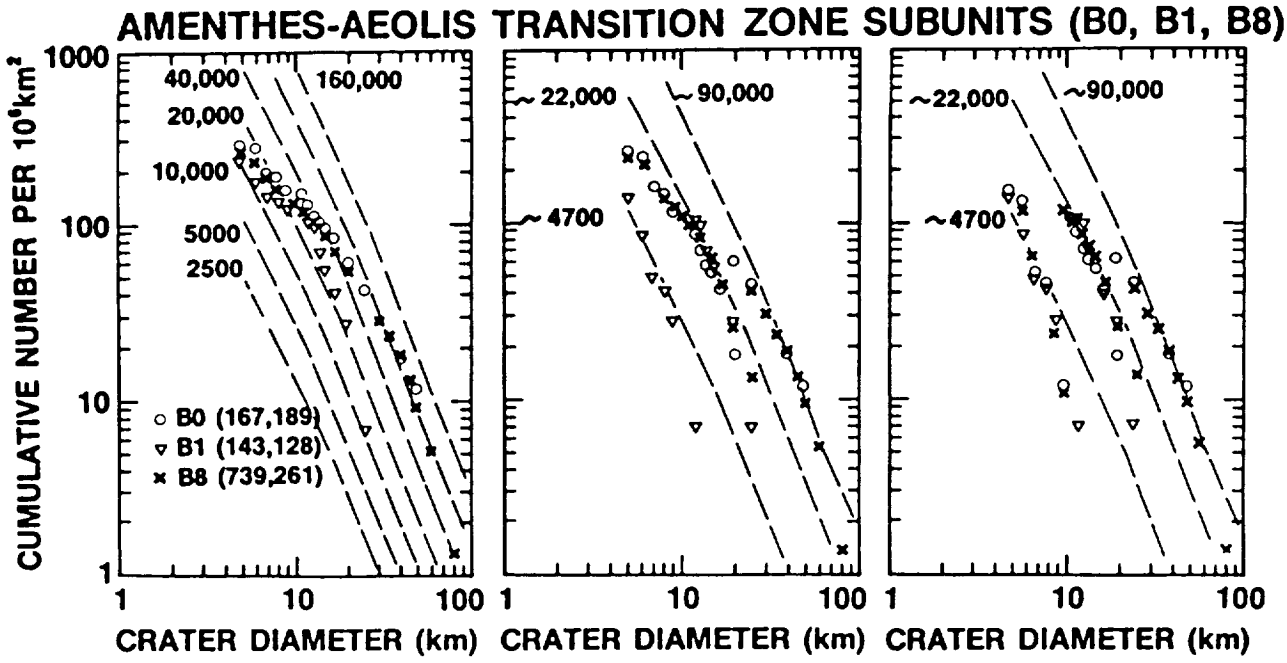

consistency, considering the area and diversity of terrain units from which these ages arise. We interpret these results as follows: there is an old, underlying surface best expressed east of the Isidis Basin with a crater age of ~84,000. Given the "resolution" of this technique, this value could be 75,000 to 100,000. This probably corresponds to the original formation of the transition zone (cf. Wise et al., 1979). There was a major resurfacing common to all the subunits of the transition zone which produced a new underlying surface of intermediate crater age of ~23,000 (18,000 to 25,000?). More recent resurfacing events all have crater ages <10,000, but show some regional variation: in Amenthes-Aeolis the young surface is ~4900, while in Ismenius-Casius the B1 and B2 units have 6600 and the B8 has 9600 crater age for the upper surface.

More exciting than the evidence for discrete, episodic resurfacing events is the common resurfacing event at 23,000. This age is identical (to well within the sensitivity of this technique) to the age of the "old" branch for crater counts in Lunae Planum. As Table 1 shows, our values for Lunae Planum are 20,600 and 6900, essentially identical to the values for subunit B2 in Ismenius Lacus (the fretted terrain). These data strongly suggest that the major resurfacing event in the transition zone in eastern Mars was synchronous with the eruption of Lunae Planum and related volcanics.

References

Neukum, G. and K. Hiller, Martian ages, J. Geophys. Res. 86, 3097-3121, 1981.

Wise, D.U., M.D. Golombek and G.E. McGill, Tectonic evolution of Mars, J. Geophys. Res. 84, 7934-7939, 1979.

TABLE 1

SURFACE AGES [N(1)] FOR TRANSITION ZONE UNITS B0, B1, B2 and B8

UNIT	REGION	OLDEST	MIDDLE	YOUNGEST
B0	AMENTHES-AEOLIS	83,853[+/- 4010]	23,724[+/- 365/439]	4825[+/- 27][a]
B1	AMENTHES-AEOLIS		23,820[+/- 356/646]	4713[+/- 823/616][a]
	ISMENIUS-CASIUS	(100,560??)	23,404[+/- 611/1141]	6394[+/- 592/263][b]
B2	ISMENIUS-CASIUS		20,880[+/- 4124/2158]	6707[+/- 802/939][b]
B8	AMENTHES-AEOLIS	83,699[+/- 340]	25,518[+/- 1984/2714]	5202[+/- 343][a]
	ISMENIUS-CASIUS	(92,109??)	22,329[+/- 2572/2044]	9643[+/- 320/356][c]
		~84,000	~23,000	<10,000 [4900[a],6600[b],9600[c]]
	LUNAE PLANUM		20,581[+/- 469]	6871[+/- 258/208]

THE GEOMORPHIC EVOLUTION OF EASTERN MARGARITIFER SINUS, MARS

GRANT, John A., and BOOTHROYD, Jon C., Dept. of Geology, University of Rhode Island, Kingston, RI 02881

Geomorphic mapping, 102 crater counts performed on selected surfaces, and a detailed study of drainage basins, were used to assign relative ages to selected surfaces in the Margaritifer Sinus Quadrangle. Crater counts were completed using the D.U. Wise method of dating local surfaces. This method utilizes relatively small areas that show a homogeneous distribution of craters in a given size range. All relative ages are given as the cumulative number of craters $\geq$ 1 km$\cdot 10^{6}$ km^{-2}, obtained by projection of the Neukum and Hiller standard curve (1981). A summary of the crater count results is shown in Figure 1.

The oldest features exerting the dominant structural control in MC19 are three multi-ringed impact basins, Ladon (18S, 30W), Holden (26S, 32W), and Noachis (22S, 5W), described by Schultz and Glicken (1979), Saunders (1979), and Schultz et al. (1982). The oldest dated surface covering these basins, the ancient cratered highlands (1,000,000-850,000), evolved during the period of intense bombardment. Since that time four recognized resurfacing events of probable volcanic, eolian or fluvial origin have occurred. The earliest (300,000-100,000), was of wide regional extent and was the first modification of the cratered highlands in the quadrangle. A second event (70,000-40,000), also of regional extent, occurred at the end of the period of intense bombardment and coincided with the crustal destruction of the northern third of Mars. The third event (14,000-8200), the youngest surface dissected by valley networks, occurred near the end of emplacement of the Lunae Planum lava plains. This surface was dated mainly in MC19SE, but undated surfaces with similar crater densities occur elsewhere. The fourth event (6000-2000), also dated mainly in MC19SE, occurs locally, filling basins, and always covers valley networks when they are present. Emplacement of this unit was contemporaneous with the construction of Alba and Uranis Patera and the opening of Valles Marineris.

An extremely active period of channel and valley formation occurred from 10,000-5000, concurrent with peak Tharsis tectonic activity. Events during this period included the formation of the Uzboi/Ladon Valles meso-scale outflow system in MC19SW with deposition in Ladon Basin (11,000-6200), and the formation of Samara and Parana/Loire Valles in MC19SE (8500-4600).

An area of channel and valley distributaries (12S, 22W) formed between 9000-4500 along the axis of the Chryse Lowland Trough at the confluence of Margaritifer Valles (13S, 24W), draining Ladon Basin, and Samara and Parana/Loire Valles. The presence of distributaries associated with lower Margaritifer Valles and the position of flow modified remnants suggests that flow out of Ladon Basin via Margaritifer Valles was largely responsible for the evolution of this area. If ponding in Ladon Basin did not occur, and the Uzboi/Ladon system was simultaneously through flowing out of Ladon Basin, the age of the channel and valley terrain suggests that the formation of the Uzboi/Ladon system

was more concurrent with valley network formation elsewhere in MC19 (between 8500-4600).

Formation of Margaritifer and Iani Chaos (10,000-2300) probably began soon after formation of the nearby channel and valley terrain. The range of dates observed for the chaos may be the result of formation by periodic collapse. Individual periods of collapse may have been associated with: 1) discharge out of Ladon Basin via Margaritifer Valles; 2) discharge out of Samara and Loire Valles; and 3) the extension of Valles Marineris into the quadrangle.

REFERENCES

Neukum, G. and Hiller K., 1981, Martian ages: Jour. Geophys. Research, v. 86, p. 3097-3121.

Saunders, S.R., 1979, Geologic map of the Margaritifer Sinus Quadrangle of Mars: USGS Map I-1144 (MC-19).

Schultz, P.H. and Glicken, H., 1979, Impact crater and basin control of igneous processes on Mars: Jour Geophys. Research, v. 84, No. B14, p. 8033-8047.

Schultz, P.H., Schultz, R.A. and Rogers, J., 1982, The structure and evolution of ancient impact basins on Mars: Jour Geophys. Research, v. 87, No. B12, p. 9803-9820.

Figure 1. Summary of crater count data. Each point plotted represents the relative age of one crater count performed in the terrain indicated. Time intervals of formation of various features and terrain were determined by using the range of relative ages obtained for that feature. Most likely times of resurfacing (dashed vertical lines) were determined by identifying distinct clusters of the relative age values. The period of valley formation (dashed vertical line) was determined by the cross cutting relationships of various dated surfaces incised by, and covering, the valleys.

Figure 1.

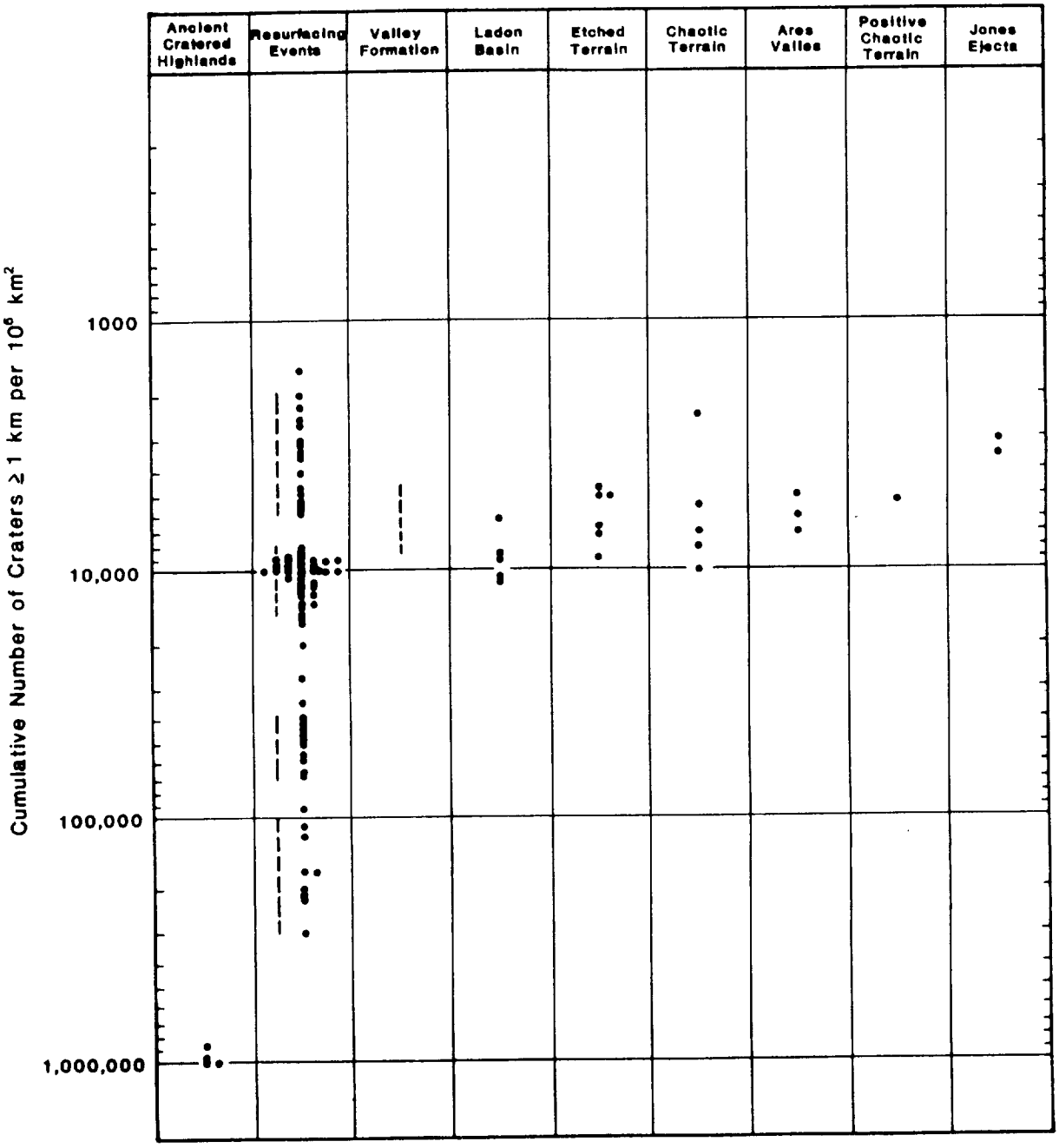
Ancient Cratered Highlands
Resurfacing Events
Valley Formation
Ladon Basin
Etched Terrain
Chaotic Terrain
Ares Vallis
Positive Chaotic Terrain
Jones Ejecta
Cumulative Number of Craters ≥ 1 km per 10^6 km^2
1000
10,000
100,000
1,000,000

DRAINAGE BASIN AREAS AND DENSITIES: SAMARA AND PARANA/LOIRE VALLES, SOUTHEASTERN MARGARITIFER SINUS, MARS

GRANT, John A., and BOOTHROYD, Jon C., Dept. of Geology, University of Rhode Island, Kingston, RI 02881

Drainage densities for the major valley network systems in MC19SE, Samara and Parana/Loire Valles, were calculated using: 1) topographic drainage basin and sub-basin areas, delineated by stereo mapping; and 2) all valley lengths resolvable at a scale of 1:1,000,000 and resolution of 200m/pixel. The complete drainage systems of both Samara and Parana Loire Valles are shown in Figure 1. The locations of the major sub-basins and internal drainage basins of both systems are listed in Table 1 and are also shown in Figure 1.

The combined drainage basins of Samara and Parana/Loire Valles cover an area of 535,550 km^2, equal to 84% of the drainage area of the Colorado River in the southwest USA. Drainage basin areas for the complete systems of Samara and Parana/Loire Valles, individual portions of those sytems, and nearby internal drainage systems are given in Table 2. Overall drainage densities for both systems, portions of the systems, and internal drainage basins are also given in Table 2. Drainage areas and drainage densities for the various sub-basins of Samara and Parana/Loire Valles are shown in Table 3. All densities were calculated first using only those valley segments clearly connected to the trunk valley/tributary (integrated density) and then using all valley segments visible and presumably once connected to the trunk valley/tributary (total density).

Total drainage densities for the two systems are quite similar (Samara= 0.034 $km \cdot km^{-2}$, Parana/Loire= 0.039 $km \cdot km^{-2}$) with the highest values being found along mid portions of both systems and the Parana Valles portion of the Parana/Loire system. The higher values noted along these segments may reflect a slightly higher volatile content in the megaregolith at these locations associated with the ejecta facies of nearby multi-ringed impact basins (Schultz et al. 1982).

The total drainage density values for the sub-basins of Samara and Parana/Loire Valles show more variation than the various trunk portions of the two systems. Samara Valles sub-basin values average 0.039 $km \cdot km_{-2}$ and range from 0.075 $km \cdot km^{-2}$ in sub-basin S8 to 0.013 $km \cdot km^{-2}$ in sub-basin S6. Values for Parana/Loire sub-basins average 0.054 $km \cdot km^{-2}$ and range from 0.107 $km \cdot km^{-2}$ in LP5 to 0.018 $km \cdot km^{-2}$.

The overall similarities in drainage densities may imply that the physical properties of the substrate beneath the two systems are regionally fairly uniform and that roughly equivalent amounts of fluid, whether of meteoric or sub-surface origin, were available to both during formation.

The range of density values observed for the sub-basins of Samara and Parana/Loire Valles may be due to: 1) local variations in the amount of resurfacing that has occurred since valley formation; 2) local variations in the substrate and

regional slope in the area; and 3) local variations in the amount of fluid available during formation.

All drainage density values obtained for these two Martian systems are well below those observed for terrestrial systems formed by overland flow in even the most arid climates (Gregory and Gardiner 1975; Abrahams 1984). However, the presence of through-flowing connections joining tributaries in the sub-basins to the trunk valley, suggests that overland flow was important in at least the early stages of valley formation. Although caution must be exercised when comparing Martian valley networks to terrestrial drainage systems formed by overland flow, the differences in drainage densities and morphology may reflect the immature development of the Martian systems and suggest that some mechanism other than overland flow, such as spring sapping, may have operated during the late stages of evolution of the Martian valley networks.

REFERENCES

Abrahams, A.D., 1984, Channel networks: A geomorphological perspective: Water Res. Research, v. 20, p. 161-188.

Gregory, K.J., and Gardiner, V., 1975, Drainage density and climate: Z. Geomorph. N.F., v. 19, p. 287-298.

Schultz, P.H., Schultz. R.A. and Rogers, J., 1982, The structure and evolution of ancient impact basins on Mars: Jour. Geophys. Research, v. 87, No. B12, p. 9803-9820.

Figure 1. Eastern Margaritifer Sinus, with the drainage basins and sub-basins of Samara and Parana/Loire Valles and their associated internal drainage basins outlined. The locations of the sub-basins and internal basins are given in Table 1. Drainage basin areas and densities are given in Tables 2 and 3 (part of 211-5821).

Table 1.-- SUB-BASINS, names and locations

SAMARA			PARANA/LOIRE			INTERNAL BASINS		
Sub-basin	Location S Lat	W Long	Sub-basin	Location S Lat	W Long	Sub-basin	Location S Lat	W Long
Himera	21	22	Parana	23	9	I1	22	16.5
Oltis	23.5	21	LP1	19.5	16.5	I2	28	12.5
Clota	26.5	21	LP2	21.5	16	I3a	29	12
S1	26.5	19	LP3	26	13	I3b	29	10
S2	28.5-31	18-19.5	LP4	18.5	13.5	I4	26	15
S3	28.5	18	LP5	18	15	I5	26	14
S3a	29.5	17.5	LP6	16	15	I6	26	10
S4	31	16	LP7	17.5	16.5	C1	29	15
S5	31.5	9						
S6	31	11.5						
S7	29	13.5						
S8	28	16						
S9	21	18						

Figure 1

TABLE 2.-- DRAINAGE SYSTEMS, areas and densities

Location (basin)	Area (km)	Integrated Channels (km)	Integrated Density (km/km)	Additional Channels (km)	Total Density (km/km)
COMPLETE DRAINAGE SYSTEMS					
Samara	313,295	8616.7	0.028	2033.1	0.034
Parana/Loire	222,255	7378.1	0.033	1247.0	0.039
Loire	181,835	4547.5	0.025	1247.0	0.032
Parana	40,420	2830.6	0.070	--	0.070
SAMARA TRUNK VALLEY SECTIONS					
Proximal	56,874	834.5	0.015	84.3	0.016
Mid	33,300	2220.0	0.067	--	0.067
Mid/Dist	28,465	948.8	0.033	196.4	0.040
Dist	52,528	509.6	0.010	1002.1	0.028
LOIRE TRUNK VALLEY SECTIONS					
Proximal	22,023	1408.9	0.022	25.9	0.022
Mid	19,255	670.8	0.035	162.4	0.043
Distal	32,898	707.5	0.034	476.3	0.045
INTERNAL DRAINAGE BASINS					
I1	21,966	--	--	596.9	0.027
I2	2,313	--	--	18.4	0.008
I3A	8,081	--	--	57.4	0.007
I3B	11,583	--	--	608.1	0.053
I4	6,529	--	--	41.3	0.006
I5	7,471	--	--	127.1	0.017
I6	5,304	--	--	140.0	0.026
C1	2,136	--	--	95.2	0.045

AVERAGE INTERNAL BASIN DRAINAGE DENSITY = 0.0236

TABLE 3.-- SUB-BASINS, areas and densities

Location (sub-basin)	Area (km)	Integrated Channels (km)	Integrated Density (km/km)	Additional Channels (km)	Total Density (km/km)
SAMARA VALLES SUB-BASINS					
Himera	52,528	509.6	0.010	1002.1	0.028
Oltis	18,090	1149.5	0.064	91.7	0.069
Clota	23,509	631.3	0.027	38.1	0.029
S1	6,794	113.0	0.016	25.1	0.020
S2	28,406	602.6	0.021	147.5	0.026
S3	3,601	--	--	--	--
S3a	3,544	--	--	189.4	0.053
S4	8,320	236.6	0.028	--	0.028
S5	5,578	--	--	--	--
S6	9,009	--	--	118.3	0.013
S7	3,351	242.9	0.073	--	0.073
S8	7,077	533.4	0.075	--	0.075
S9	12,997	379.5	0.029	140.2	0.040
PARANA/LOIRE SUB-BASINS					
Parana	40,420	2830.6	0.070	--	0.070
LP1	7,686	136.5	0.018	--	0.018
LP2	5,225	191.1	0.037	--	0.037
LP3	27,696	71.2	0.003	526.0	0.022
LP4	9,910	396.4	0.040	--	0.040
LP5	3,690	338.9	0.092	56.4	0.107
LP6	12,589	335.0	0.027	--	0.027
LP6a	2,708	212.8	0.079	--	0.079
LP7	2,620	21.9	0.083	--	0.083

Average Samara Sub-Basin Drainage Density = 0.0386
Average Parana/Loire Sub-Basin Drainage Density = 0.0537
Average Internal Basin Drainage Density = 0.0236

EFFECTS OF ELEVATION AND PLAINS THICKNESSES ON MARTIAN CRATER EJECTA MORPHOLOGIES ON THE RIDGED PLAINS

V.M. Horner and R. Greeley, Department of Geology, Arizona State University, Tempe, Arizona 85287

The effects of elevation and ridged plains thicknesses on martian crater ejecta morphologies have been investigated as part of a study of the relationship between crater ejecta characteristics and properties of planetary surfaces. This study incorporates several new supporting data sets: the 1:2M Viking photomosaics, Earth-based radar altimetry for the martian equatorial regions (1) and preliminary Viking-based regional geologic maps (2,3). These revised data sets can be used to constrain the dependencies of martian crater ejecta characteristics on various planetary parameters. Early work involving a limited number of Viking frames indicated a decrease in ejecta extent and a shift towards lunar-like ejecta morphologies with increasing elevation (4). A later study, which used the revised elevation data (5), found no correlation between ejecta extent and elevation within the ridged plains, but made no distinctions among various ejecta morphologies.

Over 360 craters on the ridged plains unit (identified from (2) and (3)), with uneroded ejecta termini were measured and classified from individual Viking images used for the 1:2M photomosaics (resolution ~130 m/pxl to ~280 m/pxl). For each crater, its position, diameter, ejecta diameter and morphology, occurrence of terraces or central features, terrain unit, elevation, solar incidence angle, and image resolution were recorded. Data were entered into a digital data base, so that statistical analyses of the parameters could be performed. In general, Mouginis-Mark's and Blasius and Cutts' ejecta classes were used to identify ejecta morphologies (4,6). An additional morphology was identified in this study: ejecta with one complete lobe around the crater, and a partial outer lobe was designated as type SD (see fig. 1).

Geologic unit, crater size, and latitude were controlled in this study so that correlations between ejecta morphology and elevation could be more easily detected. The ridged plains unit was chosen because it is found over a wide range of elevations. Craters 5-10 km and 10-40 km in diameter were considered separately because ejecta morphologies and extents show some dependence on crater size (7). Data were obtained within 25° of the equator, as ejecta morphology is a function of latitude (6,8), and because this represents the areal coverage of the elevation data set (1). Three elevation ranges were used to investigate a possible relationship between elevation and ejecta morphology: -2.5 to 0 km, 0 to 3 km, and 3 to 6 km.

There appears to be a slight correlation of ejecta morphologies with elevation. For crater diameters = 5-10 km, the single-lobed rampart type (SR) predominates at all elevations, but the percentage of the partial outer-lobed (SD) and double-lobed (D) morphologies increase at high elevations. The occurrence of type SD ejecta is greater than that of type D at high elevations. For crater diameters = 10-40 km, the only statistically significant change in ejecta morphologies with elevation is in the relative occurrence of ejecta types SD and D. At low elevations, type SD is found more often, yet at high elevations, type D predominates. Regional studies within Lunae Planum show that the onset diameter for both

ejecta types decrease with increasing elevation, and that within a given elevation range, the diameters of craters with SD ejecta is almost always less than or equal to the diameters of craters with type D ejecta.

The change in ejecta morphologies with elevation appears to be best explained by a decrease in the thickness of the ridged plains unit with increasing elevation. For a given impact energy, increasingly complex ejecta morphologies would result from increasing atmospheric density (9). If differences in ejecta morphologies with elevation result mainly from changes in the degree of atmospheric drag effects, atmospheric density would have to increase with elevation to explain the current observations. It has also been suggested that double-lobed ejecta forms from an impact into a layered target with a volatile-rich lower layer (10). To explain our observations, the depth to this lower layer would have to decrease with elevation, and there is no a priori reason why this should occur at a given latitude (11). A third possibility is that the thickness of the ridged plains unit decreases with elevation, which is supported by a plot of our data with respect to thickness variations within Lunae Planum (12) and Hesperia Planum (13).

Figure 1 shows the relationship between ejecta morphology and ridged plains thicknesses. For three crater diameter intervals, ejecta morphologies become increasingly simpler as plains thickness increases. Simple ejecta morphologies dominate for large plains thickness and small crater sizes. For intermediate thicknesses and crater sizes, ejecta type SD predominates, progressing to types D and finally MR with increasing crater size and/or decreasing plains thicknesses. (The occurrence of type SS is mainly a function of latitude). Factors which may affect the observed relationship include estimated errors in thickness contours of ±100M (12,13), and the small number of usable rim heights in the study (12,13), so that local ponding or thinning of ridged plains material in some areas would be undetected. Despite these caveats, the degree of correlation between ejecta morphology and ridged plains thickness is quite good.

It is also possible that changes in ejecta morphology with ridged plains thickness may represent changes in the abundance of subsurface volatiles. Different geologic units have different capacities for volatile storage, so that changes in the depth of the contact between the ridged plains and lower units could also represent changes in the depth to a transition in subsurface volatile content.

REFERENCES

(1) Downs, G.S. et al., 1982, (abs.) Lunar Planet Sci. Conf. XIII, 182-183.
(2) Scott, D. and K. Tanaka, 1985, 1:15M Geologic Map of the Western Region of Mars, USGS, in press.
(3) Greeley, R. and J.E. Guest, 1:15M Geologic Map of the Eastern Region of Mars, USGS, in prep.
(4) Mouginis-Mark, P.J., 1979, J. Geophys. Res. 84, 8011-8022.
(5) Mouginis-Mark, P.J. and E.A. Cloutis, 1983, (abs.) Lunar Planet. Sci. Conf. XIV, 532-533.

(6) Blasius, K.R. and J.A. Cutts, 1981, Planet. Geol. Std. Qtr. Rpt.
(7) Mouginis-Mark, P.J., 1978, Nature 272, 691-694.
(8) Johansen, L.A., 1978, Proc. Colloq. On Planet. Water and Polar Proc., 109-110.
(9) Schultz, P.H. and D.E. Gault, 1979, J. Geophys. Res. 84, 7669-7687.
(10) Mouginis-Mark, P.J., 1981, Icarus 45, 60-76.
(11) B. Jakosky, 1985, pers. comm.
(12) De Hon, R.A., 1985, (abs.) Lunar Planet. Sci. Conf. XVI, 171-172.
(13) De Hon, R.A., 1985, (abs.) Lunar Planet. Sci. Conf. XVI, 173-174.

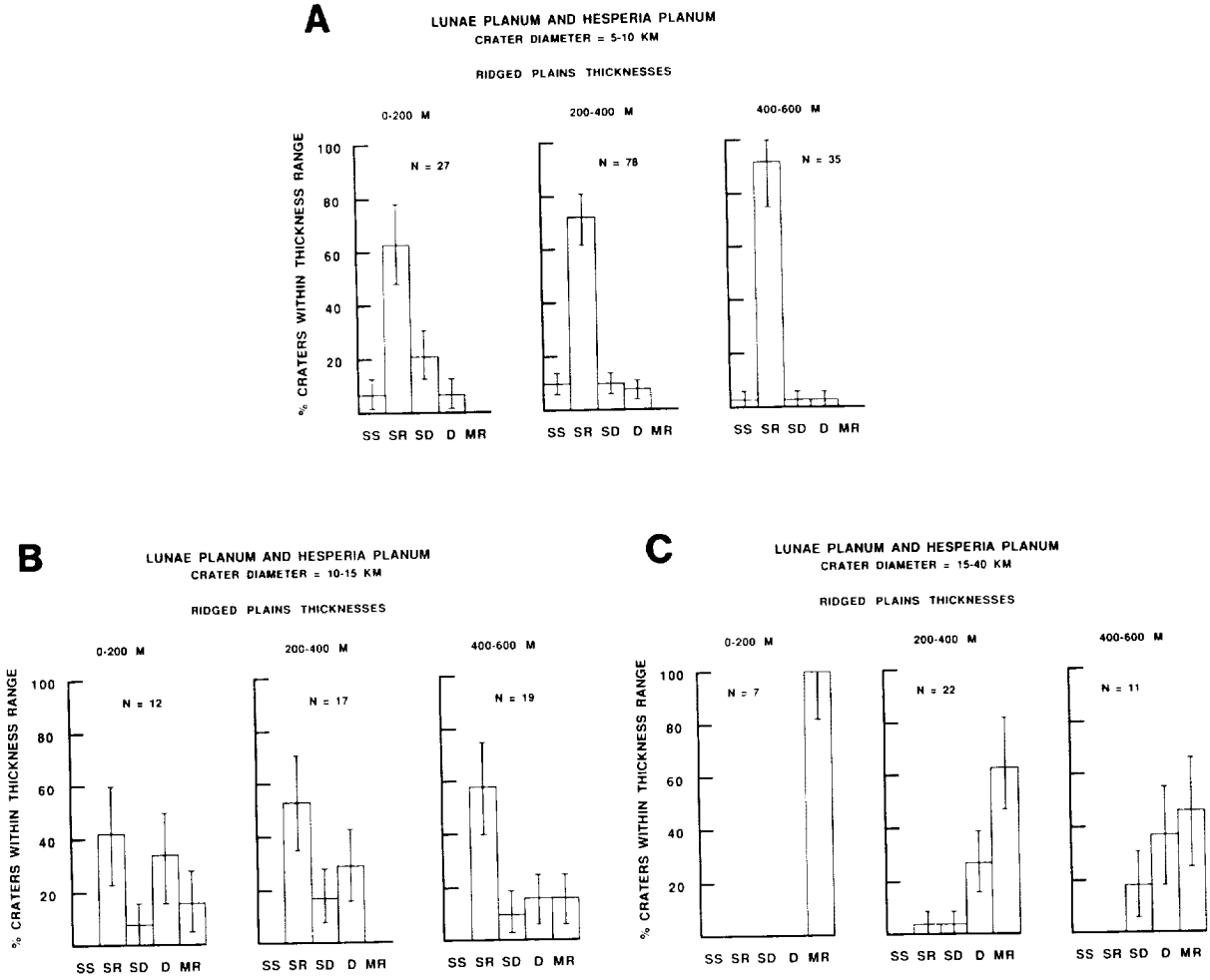

Figure 1 -The relationship between ejecta morphology and ridged plains thicknesses for Lunae Planum and Hesperia Planum, for A) D_c = 5-10 km, B) D_c = 10-15 km, C) D_c = 150-km. SS = single-lobed, scarped terminus, SR = single-lobe, rampart terminus, SD = full inner lobe, partial outer lobe, D = two complete lobes, MR = multilobate. Thicknesses taken from 12,13.

Planetary Geomorphology Field Studies at Mount St. Helens

David R. Janke and Michael C. Malin, Department of Geology, Arizona State University, Tempe, AZ 85287

Working in close collaboration with personnel of the U. S. Geological Survey's Water Resources Division, three months were spent this past summer studying fluvial processes at Mount St. Helens. Particular emphasis was placed on drainage systematics, both in plan view and in longitudinal and transverse section. The evolution of drainages at Mount St. Helens is particularly informative, owing to the excellent exposures and developmental setting, and to the high quality of past monitoring observations. Specific basins were selected that covered a range in slope (1° to 25°), gradient (10:1 to 40:1), stream magnitude (up to 50th order streams), and materials (pyroclastic flows, ash and blast deposit, debris avalanche).

The nature of junction angle evolution was one of several topics explored. Junction angle evolution is an important tenet of models of martian valley network analysis. It was found that junctions at Mount St. Helens evolve through three processes: 1) the introduction of new low order links; 2) lateral channel migration; and 3) stream piracy. Junction angles were measured to be systematically smaller for basins on steeper topography, and the junctions between low order tributaries systematically increased with time. For the most part, observations tend not to support the model of Pieri (1983). However, his model was developed for mature drainages, and he proposed that systems evolved towards random, space-filling patterns. The Mount St. Helens drainages **do** appear to be evolving in the manner predicted by Pieri (1983); analysis of 5 years worth of pattern evolution is now under way to see if a model for youthful drainage pattern evolution can be made consistent with that for mature drainages. Martian valley networks are considered by many investigators to be immature drainage systems. This new model should thus be directly applicable to testing various fluvial hypotheses for the origin of these valleys.

An additional observation of interest is the time evolution of the longitudinal profile of the Mount St. Helens drainages. Some of the profiles evolved under conditions of high and constant discharge for several hundred days, during the pumping to lower the level of Spirit Lake. Observations of many transverse sections permit quantification of the response of the stream to this discharge. The channel height above sea level shows a form that resembles an exponentially damped harmonic function. The channel eventually reached grade through a series of oscillatory erosional and depositional events, dictated by geometric and hydraulic relationships. The model developed at Mount St. Helens from these observations will be used to evaluate the flood of the Jökulá á Fjöllum (Iceland), where observations of sediment transport and other erosional phenomena can be used to test the validity of the model. The same geometric relationships can be measured for some martian valleys and channels, and should provide strong constraints on the evolution of these martian fluvial systems.

AN ANCIENT OCEAN ON MARS?

Baerbel K. Lucchitta, Holly M. Ferguson, and Cathy Summers,
U.S. Geological Survey, 2255 N. Gemini Dr., Flagstaff, AZ 86001

Most of the large outflow channels on Mars debouch into the northern plains. Despite deliberate searches, however, deltaic or sedimentary deposits have eluded detection. Recently, however, McGill (1985 a,b) has proposed that a sedimentary layer may indeed exist in the northern plains of Mars; he suggested that such a layer may be composed of material transported into the northern plains by channels. He inferred that the polygonal fracture pattern observed in the northern plains was superposed on the sedimentary layer. The influence of subsurface craters on this fracture pattern suggests that the proposed layer buried subjacent topography and is relatively thin. McGill further suggested that the fracture pattern is due to tensional stresses that followed bending and contraction of compacted sediments over subjacent topography. Because most craters are superposed on the fractures, fracturing probably occurred soon after emplacement of the deposits. Crater counts suggest that the deposit is similar in age to the outflow channels (McGill, 1985a).

The following observations support McGill's hypothesis. Furthermore, we propose that the sediments were deposited in a body of water frozen over at the surface in the manner of Antarctic ice shelves (Lucchitta, 1985). Our observations are: (1) fractured and chaotic materials appear to have developed preferentially in low areas on Mars, (2) the polygonally fractured ground in the northern plains also occurs in low areas, (3) channels debouch into the areas of polygonally fractured ground, (4) the ages of channels and polygonally fractured ground are similar, and (5) sinuous ridges in front (north) of the northern highland scarp resemble ridges on ice shelves bordering the Antarctic continent.

Fractured ground and associated landscapes of disintegration (chaotic and hummocky terrains) are common in low areas on Mars. A low area in the center of Candor Chasma (lat -7°, long 73°) received outwash from several landslide lobes. This area is occupied by flat-lying deposits that embay the surrounding terrain and have a surface texture of plateaus and hummocks traversed by numerous cracks. Two other smaller low spots in east Candor Chasma show a similar surface texture. These cracked surfaces appear to have been developed in sedimentary deposits composed of outwash from landslides that were soaked with water or charged with water and ice (Lucchitta, 1984); the cracks may have developed when the deposits froze. If the deposits had a large content of ice, its disintegration may explain the later chaotic collapse of some of these deposits (Lucchitta and Ferguson, 1983).

Depressions containing fractured and chaotic materials are also seen elsewhere on Mars. Three large arcuate depressions in Terra Sirenum (lat -35°, long 170°) contain such materials. Paraná Vallis (lat -22°, long 13°) drains into a regional low that contains chaotic

deposits. The major area of chaotic terrain in Margaritifer Sinus (lat 0°, long 20°) also occupies a regional depression between the Tharsis bulge to the west and cratered highlands to the east. This low area received ancient drainages that preceded the outflow channels in the region (Boothroyd, 1982; Boothroyd and Grant, 1985; Grant and Boothroyd, 1985). The ancient drainages may have left water-rich alluvial deposits that fractured upon freezing. The occurrence of fractured terrains in low areas that have apparently received influx of liquid materials supports the contention that cracked terrain preferentially developed on sedimentary deposits that may have contained water or ice.

The polygonally fractured ground in the northern plains occurs in low reentrants of the northern plains projecting into the southern highlands (fig. 1). Three such reentrants are conspicuous on the 1:15 million-scale topographic map of Mars (U.S. Geological Survey, unpub. data). One reentrant is located in Amazonis Planitia, but it is covered by young volcanic deposits (Scott and Tanaka, 1984; in press) that obliterate the record. The other two reentrants are in Acidalia Planitia (fig. 1, hachured area west of long 355°) and Utopia and Elysium Planitiae (fig. 1, hachured areas east of long 275°). These two reentrants contain polygonally fractured deposits that drape over as much as 4 km of relief and only locally occupy the lowest areas of the northern plains. The coincidence of low reentrants and polygonally fractured deposits is consistent with the hypothesis that the deposits are sediments transported into the reentrants from the adjoining highlands. However, it is more difficult to explain why the fractured deposits drape over a surface of considerable relief and are not everywhere deposited in the lowest areas of the northern plains. Either the surface was later warped, or the sediments were deposited from higher levels. Such deposition could have taken place in a standing body of water. Most likely is a combination of the two explanations; later warping would eliminate the need to invoke a body of water as deep as 4 km. That postchannel warping may indeed have occurred on Mars is suggested in the Chryse region, where channels at lat +15°, long 35° cross a 2- to 3-km-deep depression (U.S. Geological Survey, 1:15 million-scale topographic map, unpub. data).

Channels debouch into the reentrants that contain polygonally fractured ground (fig. 1). The reentrant in Acidalia Planitia is surrounded on the south by the mouths of the Chryse channels--Kasei, Maja, Tiu, Simud, Ares, and Mawrth Valles. The Elysium channels--Hebrus, Granicus, Tinja, and Hjard Valles--debouch into the reentrant in Utopia and Elysium Planitiae. Several grabens that show evidence of modification by water also trend toward Utopia Planitia.

Channels and polygonally fractured deposits are of similar ages. The new geologic maps of Mars by Scott and Tanaka (1984; in press) and Greeley and Guest (unpub. data) place the polygonally fractured deposits of Acidalia and Utopia Planitiae in the middle to late Hesperian period of the Martian time scale. The Chryse outflow channels, which debouch into Acidalia Planitia, are given identical ages. The Elysium channels,

which debouch into Utopia and Elysium Planitiae, have the same ages as the Utopia and Elysium deposits (Tanaka, unpub. data), although Christiansen (1985) proposed in a detailed study of the area that Hebrus Valles and Hephaestus Fossae are slightly younger than the polygonally fractured deposits at their mouths. The overall coincidence of the ages of channels and of deposits near their mouths strongly suggests a genetic link.

Sinuous ridges within elongate depressions are abundant near the mouths of the Chryse channels in Acidalia Planitia and in front of the highland scarp in western Utopia Planitia (fig. 1). The ridges (0.5 to 1 km wide) are similar in size and form to ridges at the mouths of ice streams and ice shelves in Antarctica. Sinuous ridges at the mouth of Ares Vallis (Scott, 1982) resemble ridges on the Rutford Ice Stream in Antarctica, where the floating ice stream is diverted by shoals (fig. 2) (Swithinbank and Lucchitta, in press). Along the English Coast in Antarctica, ice moving off the continent is compressed and is diverted by shoals to form narrow ridges in linear depressions. Similar ridges in depressions are found where floating ice streams converge. The striking similarity between these Antarctic ridges and those on Mars suggests that material transported through the mouths of Martian outflow channels had characteristics similar to those of floating Antarctic ice streams; the reduced energy regime at the mouth of Martian channels may have permitted their partial freezing. The location of the ridges in front of the Martian highland scarp is similar to the location of the ridges in front of the Antarctic continent, where the bordering ice-shelf ocean is shallow and shoaly. The similarity suggests that the Martian highlands too were locally bordered by ice shelves.

Under present Martian conditions, water in the northern plains would be frozen solid. Yet, it must once have been liquid beneath the ice to flow like ice shelves and to deposit sediments from outflow channels. Two conditions would have permitted the occurrence of liquid water in the northern plains: (1) Mars was warmer until late Hesperian time, or (2) the water was extraordinarily briny. Brass (1980) suggested likely brines for Mars and gave their freezing temperatures. Alkali-chloride brines would freeze at 250 K, $MgCl_2$-alkali-chloride brines would freeze at 218 K, and $CaCl_2$-$MgCl_2$-alkali-chloride brines would freeze at 215 K. Lucchitta (1982) calculated that at lat + 30° these three brines would produce, respectively, an ice cap 3 km thick, an ice cap 300 m thick, and no ice cap at all.

In summary, several lines of evidence converge to support the hypothesis that the polygonally fractured ground in the northern plains of Mars developed on sediments derived from the Martian channels. Characteristics of the deposits and similarities to Antarctic ice shelves suggest that deposition was in a standing body of water. Perhaps an ancient ocean did once exist on Mars.

References

Brass, G W., 1980, Stability of brines on Mars: Icarus, v. 42, p. 20-28.

Boothroyd, J.C., 1982, Ancient fluvial drainage systems: Margaritifer Sinus Area, Mars: Reports of Planetary Geology Program-1982, NASA TM 85127, p. 209-212.

Boothroyd, J.C. and Grant, J.A., 1985, Fluvial drainage basins, outflow channels and valley networks: Margaritifer Sinus, Mars: Geol. Soc. America, Abstracts with Programs, v. 17, no. 7, p. 528.

Christiansen, E.H., 1985, Geology of Hebrus Valles and Hephaestus Fossae, Mars: Evidence for basement control of fluvial patterns: Geol. Soc. America, Abstracts with Programs, v. 17, no. 7, p. 545.

Grant, J.A. and Boothroyd, J.C., 1985, The geologic evolution of drainage basins: Margaritifer Sinus Quadrangle, Mars: Geol. Soc. America, Abstracts with Programs, v. 17, no. 7, p. 596.

Lucchitta, B.K., 1982, Ice sculpture in the martian outflow channels: Journal Geophysical Research, v. 87, no. B12, p. 9951-9973.

Lucchitta, B.K., 1984, Groundwater in the equatorial region of Mars: evidence from landslides, in Workshop on Water on Mars, LPI Tech. Rept. 85-03, The Lunar and Planetary Institute, Houston, p. 53-55.

Lucchitta, B.K., 1985, Ice-laden debris in outflow channels and northern lowland plains, Mars: Geol. Soc. America, Abstracts with Programs, v. 17, no. 7, p. 647.

Lucchitta, B.K. and Ferguson, H.M., 1983, Chryse Basin channels: low gradients and ponded flows: Proceedings Thirteenth Lunar and Planetary Science Conference, Part 2: Journal Geophysical Research, v. 88, Supplement, p. A553-A568.

McGill, G.E., 1985a, Age and origin of large martian polygons: Lunar and Planetary Science XVI, The Lunar and Planetary Science Institute, Houston, p. 534-535.

McGill, G.E., 1985b, Age of deposition and fracturing, Elysium/Utopia Region, Northern Martian Plains: Geol. Soc. America, Abstracts with Programs, v. 17, no. 7, p. 659.

Scott, D.H., 1982, Meander relics: Evidence of extensive flooding on Mars: Reports of Planetary Geology Program-1982, NASA TM 85127, p. 216-218.

Scott, D.H., and Tanaka, K.L., 1984, Preliminary geologic map of the western equatorial region of Mars, Part A: U.S. Geological Survey Open-file Report 84-659-A, scale 1:15,000,000.

Scott, D.H. and Tanaka, K.L., Geologic map of the western equatorial region of Mars: U.S. Geological Survey Misc. Inv. Series Map I-1802A, scale 1:15,000,000, in press.

Swithinbank, C. and Lucchitta, B.K., Multispectral digital mapping of Antarctic ice streams: Annals of Glaciology, in press.

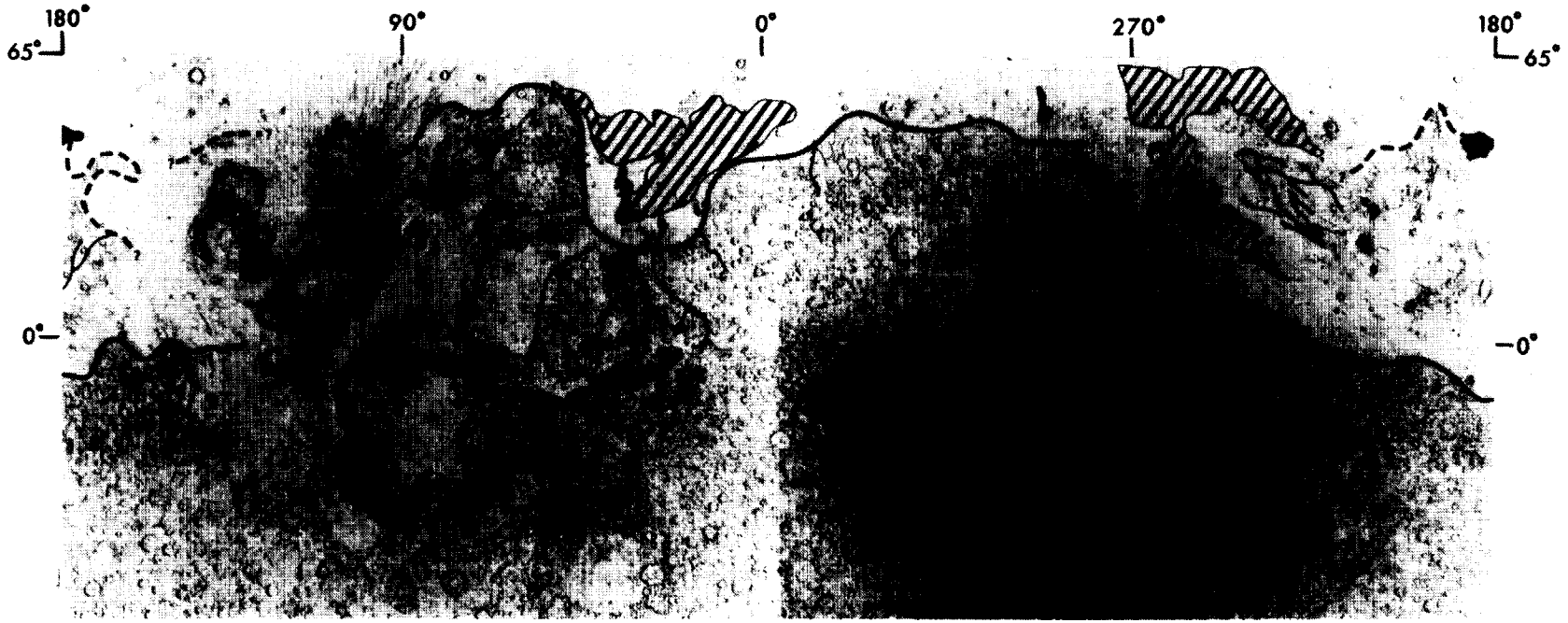

Figure 1

Location of polygonally fractured ground (hachures), channels (arrowed lines), and sinuous ridges (black areas). Highland boundary shown as solid black line. Alternative boundary delimiting outliers of cratered highlands shown as dashed line. Base is shaded-relief map of Mars.

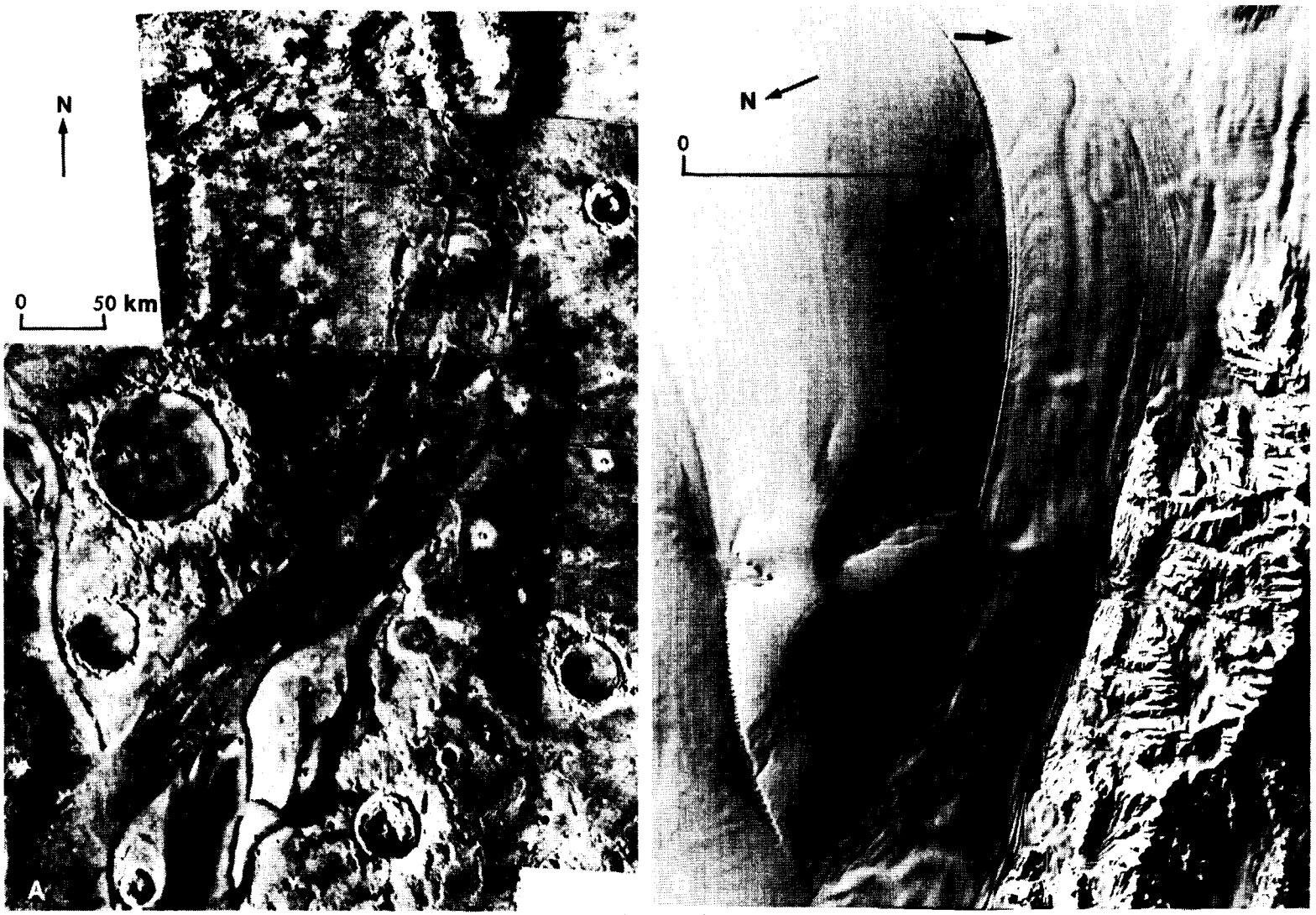

Figure 2

Comparison of Ares Vallis, Mars (A), and Rutford Ice Stream, Antarctica (B). Flow is toward top. Note similarity in size, curvature, and morphology of islands where flows split at bottom of pictures. Also note similarity of sinuous ridge patterns (arrows). (A) is mosaic of Viking Orbiter images 827A21, 864A02 and 04, 524A30. (B) is Landsat image 1560-11492.

Planetary Geomorphology Field Studies in Iceland and Antarctica

Michael C. Malin, Department of Geology, Arizona State University, Tempe, AZ 85287

Iceland

This year marked the end of an extended research activity in Iceland. The goal of the research was to better understand eolian processes in cold, basaltic deserts, and to study the details of geomorphic processes associated with catastrophic floods (*jökulhlaups*). A three week field trip was completed in late August, 1985. Some of the preliminary findings are discussed below.

The "long duration" abrasion experiment, in which basalt, welded and non-welded volcanic tuff specimens were left exposed in several diverse environments in 1981 was completed with the collection of the samples almost exactly 4 years later. These abrasion targets, along with wind-blown material collected by sand samplers at various heights above the surface and facing various directions, are presently under analysis, following procedures developed during study of the "short duration" samples in 1981 and from extensive studies of Antarctic materials. Four-year average abrasion rates as high as 2 mm/yr for non-welded volcanic tuff and 50-70 μm/yr for basalt were observed.

The extended field observations confirmed earlier results that indicated that supply of abrading material was most important in determining the effectiveness of abrasion, followed by the wind speed/frequency relationships and the hardness of the materials. An important factor in controlling the flux of sand and its influence on targets was the effect of surface roughness elements in determining the height of saltating sand and its interaction with surface stones. Areas of continuous sand supply did not necessarily display the greatest abrasion, as saltation did not extend high enough into the wind stream to accelerate the particles to sufficient velocity and high energy. Also, burial was more common in such environments. Rather, maximum abrasion occured in settings where a "Chepil Equilibrium" between immobile surface stones and intervening areas of sediment had been established. This setting permited the maximum transportation of debris and occured when the saltation curtain was at its maximum sustainable height (greatest particle velocity and energy). A quantitative model of the effectiveness of eolian processes, developed to accommodate these results, is presently being used to evaluate eolian processes at the Viking Lander sites on Mars, and the Venera Lander sites on Venus.

Field mapping of the extent and effects of a large, 2500 year old flood in north central Iceland (along the Jökulá á Fjöllum) was completed. The flood covered an area of nearly 2000 km^2, had a peak discharge of about 400,000 m^3/s, a duration of 80 to 120 hours, and a total volume of about 50 to 70 km^3. Surprisingly, it rarely reached a depth in excess of 15 m, and was usually less. Using sediment load and caliber, a map of flow velocities at peak discharge has been constructed, and numerical modelling is underway to evaluate the flow field with respect to hydraulic properties. This research suggests that high resolution photography of martian channels should allow considerable insight into the properties of the fluid flows that created them.

Antarctica

Under National Science Foundation support, field work in Antarctica continued during a 2 month season from mid-December until mid-February. The primary goal of this study is to quantify the rate of physical and chemical weathering in cold, dry conditions, and to develop techniques for using weathering phenomena as a means of age dating. In addition to the obvious application of the results of this study to the surface of Mars, two additional study activities bear more directly on planetary geomorphology: the mixing of dark silicate materials with ice and snow and subsequent controls on ablation, and the organized movement of coarse debris (up to 10 cm diameter) in the form of bedforms.

The chance observation of a 2 km long plume of basaltic ash interbedded with seasonal snow and ice on the Ross Ice Shelf south of Mason Spur (Mt. Discovery) was investigated in order to gain insight into the role and effects of dark material on sublimation phenomena. The plume, created by 150 to 200 km/hr winds in the area during the winter, consisted of sand-sized and smaller ash from a nearby eroded cider cone. The snow was partly crystalized, for the most part having the physical properties of firn. Variations in the accumulated thickness of the plume deposit created a mesa-and-butte topography with relief of several meters, with enhanced sublimation in areas where an ablation-derived mantle was thickest. In areas where the ash particles were not sufficiently abundant to completely cover the surface, the effects of individual grains could be observed. Typically, each grain sat in a small cup formed by preferential sublimation around the grain. Partly on the basis of these field observations, a paper was written with James Zimbleman (Lunar and Planetary Institute) describing these features, providing a numerical simulation of the effects responsible for the observed landforms, and discussing the potential application of the model and field observations to cometary nuclei (Malin and Zimbleman, 1985; see also abstract in this volume).

Numerous large ($\lambda > 2$ m, $A \geq 10$ cm) waveforms are seen throughout the Trans-Antarctic Mountains. These waveforms have been used to infer the direction of movement of major ice sheets believed to have overridden the mountains during the Tertiary (Denton *et al.*, 1984). Field investigation showed several different processes may have acted to create the "bedforms" seen today, some of which may be operable on Mars and Venus. Katabatic winds, where dense (in Antarctica, cold) air moves downslope from the polar domes and off of the Polar Plateau through valleys within the Trans-Antarctic Mountains, appear responsible for modification of many of the "ripples", and in fact may have formed some of them. In some areas, the regularity of the forms resemble the regular dunes seen in the highest resolution Viking Orbiter images. IRTM observations of coarse eolian deposits (e.g., Christensen, 1983) suggest that these Antarctic features may be excellent analogs to forms created by ephemeral, high velocity winds on Mars. Some interpretations of Venus radar images (both earth-based and Venera) suggest that eolian sediments may be scarce (e.g., Head *et al.*, 1985), but areas of high reflectivity may also imply large bedforms of coarse material. The forms seen in Antarctica may also be analogous to venusian eolian forms.

References

Christensen, P. R. (1983) *Icarus* **56**, 496-518.
Denton, G., Prentice, M., Kellogg, D., and Kellogg, T. (1984) *Geology* **12**, 263-267.
Head, J., Peterfreund, A., Garvin, J., and Zisk, S. (1985) *J. Geophys. Res.* **90**, 6873-6886.
Malin, M. and Zimbleman, J. (1985) *Nature*, (submitted).

Photogeological Studies of Mars: Polar Deposits and Small Dunes

Michael C. Malin, Department of Geology, Arizona State University, Tempe, AZ 85287

Photogeological studies of Mars addressed correlation of earlier observations with geophysical phenomena, and new observations made using the highest resolution Viking Orbiter images. Two aspects of this research are summarized here: 1) attempts to constrain the composition of the martian polar deposits (both the layered deposits and the circum-polar debris mantles) using topography and mass calculations (derived from gravity observations); and 2) observations of bedforms in high resolution Viking Orbiter images, in order to develop criteria for landform and wind speed measurements using a possible high resolution/low resolution camera system for the Mars Observer.

The martian polar layered deposits have a mass reliably estimated at about 2×10^{21} gm (Sjogren and Mottinger, 1982), and a volume poorly estimated to be about 2×10^{21} cm^3 (based on topography compiled by Dzurisin and Blasius, 1975). This leads directly to an estimate of density of order unity (Malin, 1985). The circum-polar debris mantle in the northern hemisphere exhibits a gravity anomaly of 3 mgal, and a thickness of about 100 to 300 m. These values also lead to a density estimate of about 1 gm/cm^3. Void space is the principal factor governing the density of a sedimentary deposit. Many granular deposits on Earth have porosities of 20 to 60% and densities of 1 to 2.5 gm/cm^3. Extremely rare deposits of silt and clay have porosities as high as 70% and densities as low as 0.75 gm/cm^3. It is most likely that the north polar debris mantle consists of uncompacted sedimentarty deposits with considerable, unfilled void space. The layered deposits, owing to compaction resulting from their greater thickness, will be less porous. In addition, the layered deposits display morphologies, and occur in areas, that seem to require the incorporation of volatile ices. On Earth, the incorporation of water into a sediment initially increases its density as the water fills the void space without increasing the volume. Only after the volume of water exceeds the void space does the density begin to decrease. The influence of ice is analogous. In both cases, once the water or ice volume exceeds the porosity, the physical properties of the material no longer resemble those of the sediment, but are dominated by the physical properties of the water or ice. This is likely the case for the layered deposits. The results of this analysis indicate that the layered deposits are possibly as much as 95% ice.

Inspection of the highest resolution Viking Orbiter images (resolutions ~ 8 to 20 m/pixel) reveals many more bedforms than previously seen at lower resolution. Given the sampling by the Viking mission, it seems likely that much of the martian surface displays evidence of eolian deposition from saltation (i.e., of sand-sized particles). The portion of any given area covered by these sediments may be relatively small (10 to 30%), but they can be used to evaluate many aspects of short term environmental effects. The uniformity of spacing, the refraction patterns around obstacles, and the local topographic setting of one set of dune forms has been studied to infer several properties of the fluid flow behavior of the wind in the area, including an upper limit to macroscopic turbulance induced by topography, an upper limit to the velocity gradient within the lower portion of the atmospheric boundary layer, and an estimate of the sustained wind speeds responsible for the migration of the dunes.

References

Dzurisin, D. and K. Blasius (1975) *J. Geophys. Res.* **80**, 3286-3306.
Malin, M. (1985) *Geophys. Res. Lett.*, (submitted).
Sjogren, W. and N. A. Mottinger (1982) *Trans. Am. Geophys. Un. (EOS)* **63**, 1021.

EPISODIC CHANNELING PUNCTUATED BY VOLCANIC FLOWS IN MANGALA VALLES REGION, MARS

Masursky Harold, Chapman M.G., Dial A.L., JR., and Strobell, M.E.;
U.S. Geological Survey, 2255 North Gemini Drive, Flagstaff, AZ 86001

At least three episodes of channeling are indicated by detailed geologic mapping of the Mangala region, based on new (1:500,000) photomosaics, topographic profiles derived by photoclinometry, and crater statistics. The ages of these three episodes are early Hesperian, Amazonian-Hesperian, and Amazonian.

Early Hesperian channels form degraded valley networks on intercrater plains west of Mangala Valles (about 100 km west of Labou Vallis, Fig. 1); their age is determined by their degradation and superposition by Hesperian ridged plains deposits.

Examples of Amazonian-Hesperian and Amazonian channels are shown in Figure 2. Amazonian-Hesperian channel-floor material (unit AHch) fills one channel in the western part of Isara Valles and a second in Munda Vallis. Most Amazonian-Hesperian channels are strongly influenced by older faults. These channels are relatively stubby, steep-walled canyons, with theater heads, and thus may have been formed by commonly invoked sapping processes. Alternatively, these channels may be remnants of initial stream cuts formed by overland flow, with concurrent lowering of base level by faulting.

Younger, Amazonian channels are more extensive, narrow, and have dendritic patterns with more tributaries. Some channels are incised into the Amazonian-Hesperian channel floors and extend to the south beyond the theater heads of the older channels, where they cut Amazonian smooth plains deposits. Tapping of several sources and overland flow exclude catastrophic flooding or sapping as the dominant mechanism of origin. At Isara and Munda Valles (Fig. 2), mouths of the broad Amazonian-Hesperian channels are buried by Amazonian-Hesperian lobate plains material (unit AHpl); Amazonian channel-floor material (unit Ach) overlies this lobate material and is buried, in turn, by younger Amazonian lobate plains material (unit Apl).

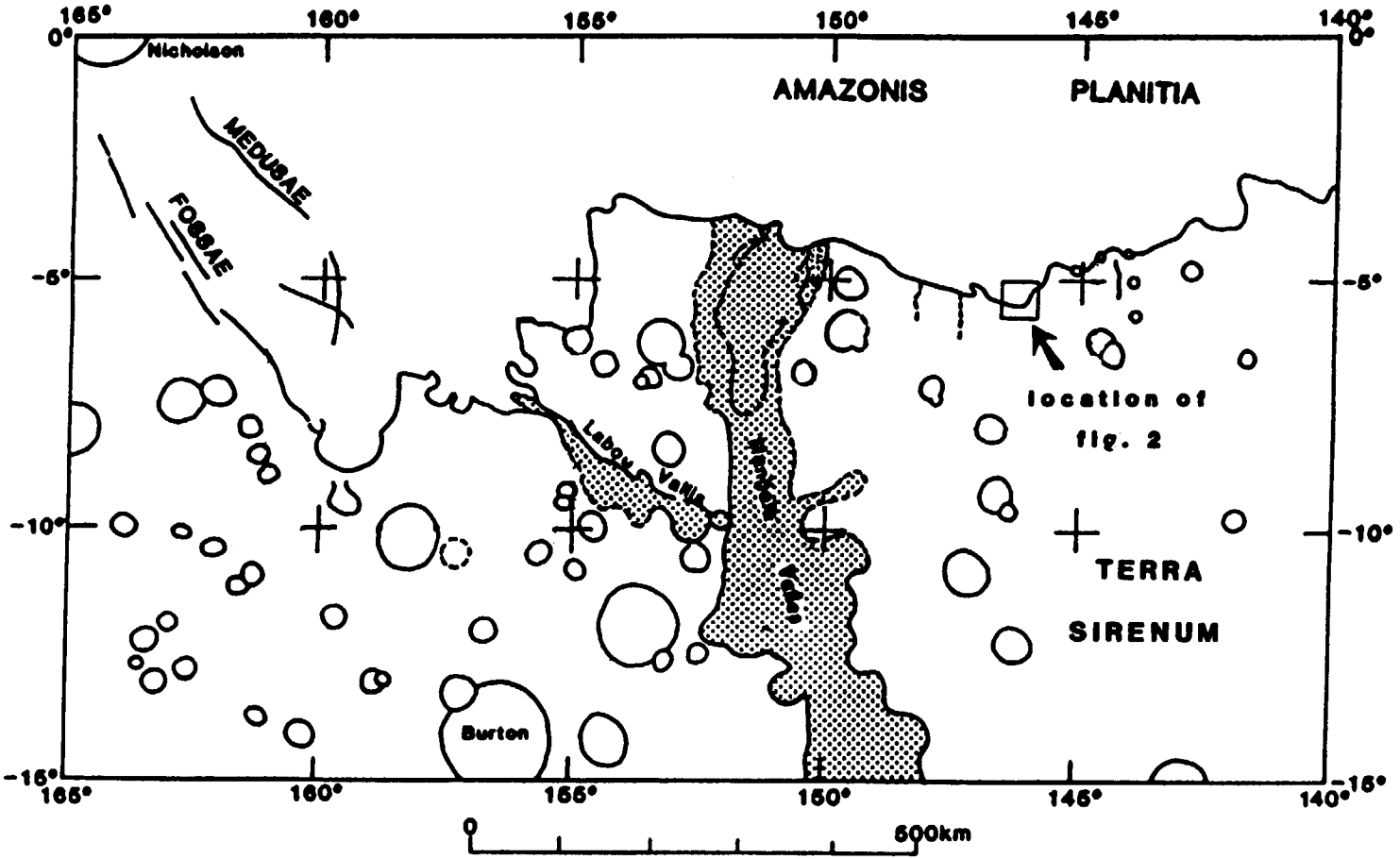

FIG. 1.--INDEX MAP OF THE MANGALA VALLES REGION, MARS. Principal valles shown by stipple. Craters shown by circular outlines. Dashes indicate approximate locations.

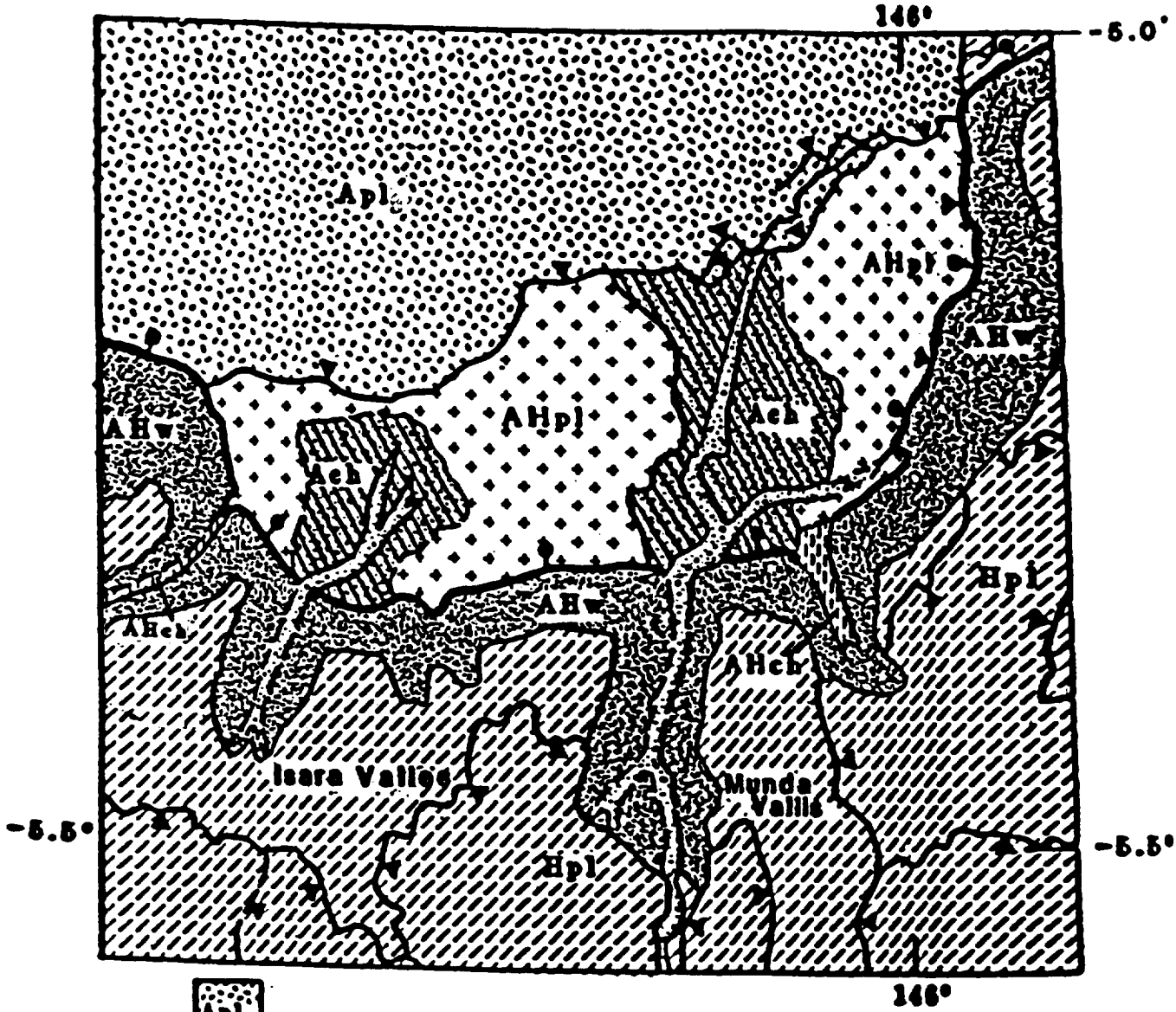

Apl — Amazonian lobate plains material

Ach — Amazonian channel-floor material--Diagonal pattern indicates material interpreted as alluvial fan deposits

AHpl — Amazonian-Hesperian lobate plains material

AHch — Amazonian-Hesperian channel-floor material

AHw — Amazonian-Hesperian wall unit--Interpreted as talus deposits covering scarps and canyon walls

Hpl — **Hesperian lobate plains material**

Volcanic flow front--Barb points in flow direction

Fault--Bar and ball on downthrown side

FIG. 2.--GEOLOGIC MAP OF THE ISARA AND MUNDA VALLES AREA IN THE EASTERN PART OF THE MANGALA VALLES REGION.

STRATIGRAPHIC RELATIONSHIPS IN THE UTOPIA REGION, MARS

George E. McGill, Department of Geology and Geography,
University of Massachusetts, Amherst, MA 01003

The fundamental problem of martian crustal history is the dichotomy between ancient cratered highlands in the south and younger lowland plains in the north. This dichotomy formed very early (Wise et al., 1979). Genetic models include subcrustal erosion (Wise et al., 1979) and a very large impact (Wilhelms and Squires, 1984). The dichotomy boundary may have migrated several hundred km southward as a result of significant erosion (Hiller and Neukum, 1978; Maxwell, et al., 1984); evidence for this consists of isolated knobs, mesas and buttes ("knobs") north of the highland-plains boundary that are interpreted to be erosional remnants of highland terrane projecting through the younger plains. North of the last occurrence of these presumed inliers, there is no direct evidence for the existence of a buried ancient surface. This abstract describes some indirect evidence suggesting that it is present farther north.

The surface units in the Utopia region include various smooth and hummocky plains, "hilly" terranes, and the enigmatic "polygonal" terrane (fractured plains of Scott, 1979). Polygonal terrane appears to grade into hummocky plains and hilly terranes, suggesting roughly similar ages. This is verified by crater counts (Fig. 1). Smooth plains appear to be superposed on all the other terranes, but the age differences are not large enough to be resolved by crater counts (Fig. 1). Fracturing of the polygonal terrane is believed due to shrinking plus compaction over buried topography during or immediately following deposition (McGill, 1985).

The distributions and ages of knobs, well defined buried craters, and ring grabens north of the dichotomy boundary (Fig. 2) provide information about topography buried beneath the northern plains. Locally, knobs are abundant enough to retain "ghosts" of old craters as patterns in knob distribution. A crater count at one such place (20° north, 265° east) yields a highland age (Fig. 1), in agreement with Hiller and Neukum (1978). Generally, however, knobs are more dispersed, and their ancient heritage can be inferred only from morphologic similarity to demonstrably old knobs close to the dichotomy boundary. The relief of knobs above the surrounding plains decreases northward very gradually. I interpret this to mean that the northward slope of the buried old surface is only slightly greater than the slope of the present surface, and that the increasing separation (and eventual disappearance) of knobs is due more to northward increase in structural disruption of the ancient highlands than it is to deep burial.

Craters superposed on faults along the dichotomy boundary provide a young age limit for the faulting and for any post-faulting but pre-northern plains resurfacing. Counts of these craters suggest that faulting occurred at a time that agrees with the estimated crater age of the dichotomy boundary (Wise et al., 1979), but that resurfacing came to an end much later; at a time corresponding roughly with the age of Lunae Planum (Fig. 1). North of the dichotomy boundary, there is a zone where

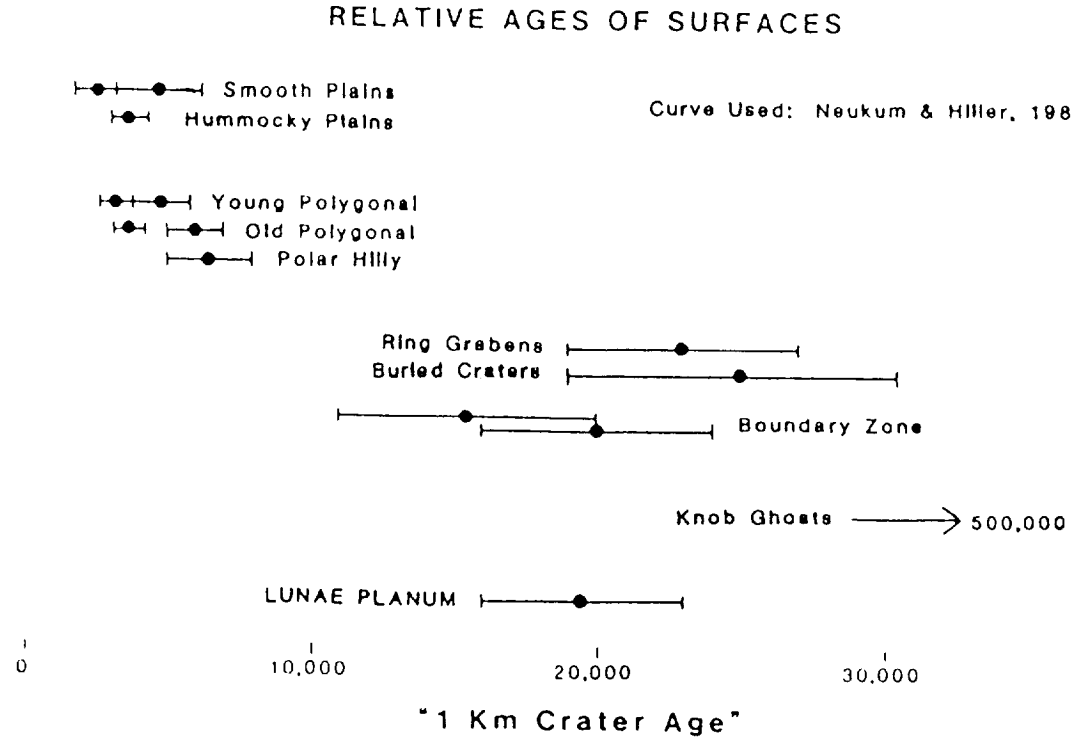

Fig. 1. Crater ages of surface materials and of buried surfaces, northern plains (Lunae Planum for comparison). Ages of polygonal terranes correspond with ages of outflow channel activity and of Elysium volcanism, determined with the same production curve (Neukum and Hiller, 1981).

---

these post-faulting and resurfacing but pre-plains craters are only partially buried by plains (Fig. 2). A count of these yields a Lunae Planum Age (Fig. 1). Finally, north of the last visible buried craters is an area characterized by numerous ring grabens (Fig. 2), structures that almost certainly result from fracturing controlled by buried crater rims. A diameter-frequency plot of ring grabens (Fig. 1) also yields a Lunae Planum age.

Crater ages of the polygonal terranes correspond with ages of outflow channel activity and Elysium volcanism (Fig. 1); hence there are ready sources of compactible wet clay or pyroclastics to deposit over older topography. The observations described here suggest that the surface unconformably beneath polygonal terrane is ancient cratered terrane severely disrupted by faulting and variably resurfaced before Lunae Planum time. The rough, faulted surface plus the post-Lunae Planum craters provided the topography that controlled the pattern and scale of polygonal fracturing. The distributions of buried craters, ring grabens, and knobs indicate that this modified ancient surface becomes gradually

more deeply buried northward. The lack of fracturing farther north could be due to excessive burial, to the absence of suitable buried topography, or to a northward pinchout of surface materials with mechanical properties conducive to fracturing by compaction and shrinkage. This uncertainty remains to be resolved by further work.

References

Hiller, K, and Neukum, G. NASA Tech. Mem. 79729, 91-93, 1978.
Maxwell, T.A., Frey, H., and Semeniuk, A.M. Geol. Soc. America, Abs. with Programs, 16, 586, 1984.
McGill, G.E. Lunar Planet. Sci. XVI, 534-535, 1985.
Neukum, G. and Hiller, K. Jour. Geophys. Res., 86, 3097-3121, 1981.
Scott, D.H. Proc. Lunar Planet. Sci. Conf. 10th., 3039-3054, 1979.
Wilhelms, D.E., and Squyres, S.W. Nature, 309, 138-140, 1984.
Wise, D.U., Golombek, M.P., and McGill, G.E. Icarus, 38, 456-472, 1979.

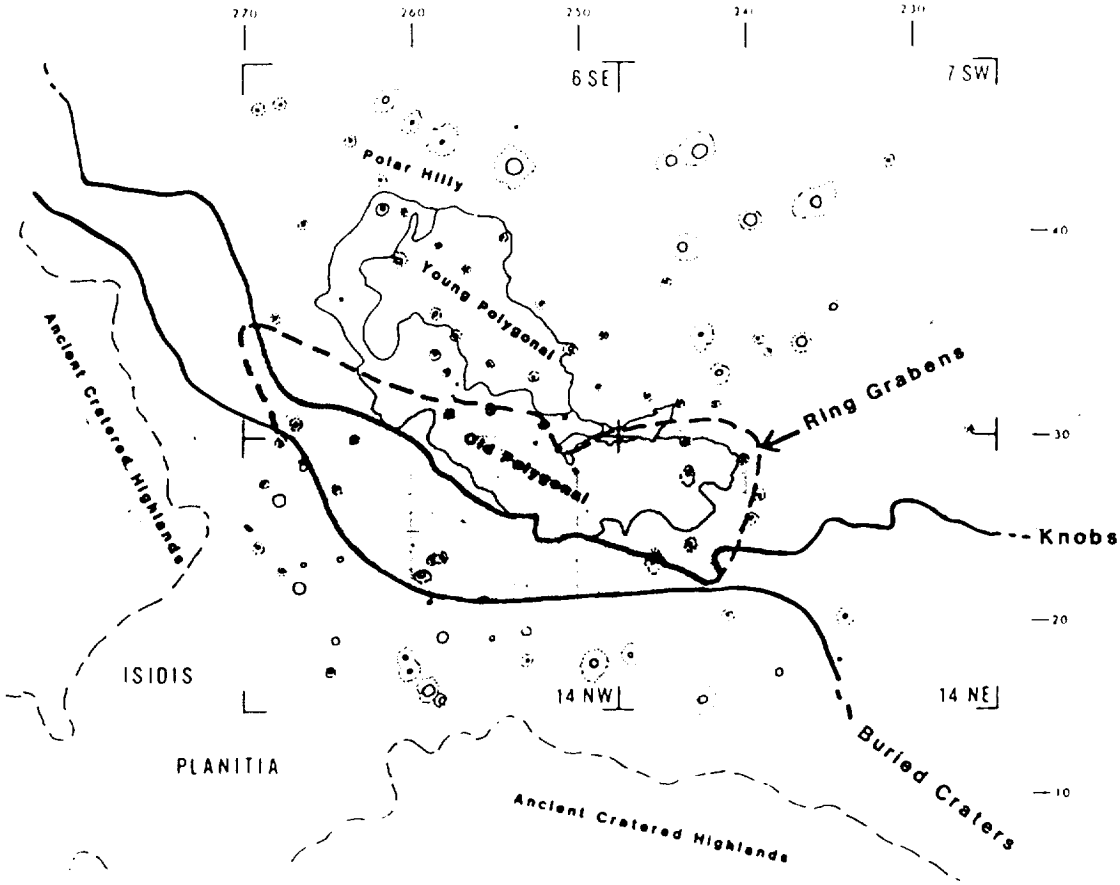

Fig. 2. Distribution of terranes and landforms. Solid heavy lines are northern limits of buried craters and "knobs"; shaded area contains ring grabens; light solid lines are terrane contacts.

LONGITUDINAL DEPTH PROFILE FOR NIRGAL VALLIS

Timothy J. Parker[1,2] and Dale M. Schneeberger[1]
[1]Jet Propulsion Laboratory, Pasadena, California
[2]Department of Geology, California State University, Los Angeles

Nirgal Vallis is located in the southwest Margaritifer Sinus sub quadrangle at -27^0 to -30^0 latitude, 37^0 to 45^0 longitude. It lies on the west side of the broad, northward-dipping Chryse Trough. Its mouth lies on the west wall of Uzboi Vallis, from which it is thought to have developed by headward sapping of a water or ice rich layer exposed in Uzboi Vallis (Sharp and Malin, 1975; Pieri, 1980; Baker, 1982).

Nirgal developed within the Smooth Plains and Channel Modified materials of Parker and Pieri (1984) west of Uzboi Vallis. Its total length (distance from mouth to headward terminus along the valley floor) is about 685 kilometers. The width of the valley (across the entire system) averages 5 kilometers for the eastern (lower) half with a maximum width of 20 kilometers occurring at a point 65 kilometers from the mouth. The average width of the western (headward) half of the valley is 3 kilometers. The average width of the valley across the valley floor is 3 kilometers for the lower third and about 1.5 kilometers for the remaining 2 thirds.

A longitudinal profile for the valley and 26 of its tributaries was obtained by taking 73 shadow measurements of the valley itself and a total of 106 for the tributaries (Figure 1). The surface of the Smooth Plains material and Channel Modified material of Parker and Pieri (1984) was used as a datum. The maximum depth for the entire valley is 2 kilometers at a point 65 kilometers from the mouth. From here to a point 10 kilometers from the mouth the depth decreases to 500 meters. This decrease in the valley's depth is more probably due to a slope in the Smooth Plains and Channel Modified material's surface than to debris choking the valley floor. The minimum depth of the valley is 200 meters at its headward termination.

The slope of the valley floor (relative to the Smooth Plains datum) from 480 kilometers from the mouth of the valley to its headward termination was determined as 1.04 meters per kilometer. From 480 kilometers to 460 kilometers from the valley mouth it increases to 5 meters per kilometer. This increase in slope relative to the datum does not correspond to any visible change in the surface, so it probably reflects an actual change in the slope of the valley floor. From 150 kilometers to 460 kilometers from the valley mouth the slope is 1.19 meters per kilometer. From 65 kilometers to 150 kilometers from the valley mouth, the data points show considerable scatter. The slope value here may be as low as 5 meters per kilometer or as much as 13 meters per kilometer. This may be due to uncertainties in the depth measurements introduced by the increasing width of the valley floor resulting in an increasing separation of the data points from the thalweg (not positively identified). Or it might be due to an increase in the roughness of the valley floor in the lower reaches caused by wall collapse. Another, though probably less likely, possibility is that it might be due to a greater topographic variability in the Smooth Plains surface. From 10 kilometers from the valley mouth to 40 kilometers from the valley mouth, where the depth progressively decreases, the slope is -24.67 meters per kilometer. The data points within this range show very little scatter. The influence on the valley profile by Uzboi Vallis' wall from 0 to 10 kilometers from Nirgal's mouth is undetermined, as no reliable shadows were found.

Most of the tributaries from the main valley mouth to about 550 kilometers from the valley mouth appear to have U-shaped cross-sections in their median and headward reaches and V-shaped cross-sections where they meet the main valley. Also, most of the 26 tributaries on which depth measurements were made have longitudinal profiles which display a flattening of slope around 200 meters below the Smooth Plains datum. Finally, all the tributaries measured from the valley mouth to 520 kilometers from the valley mouth were found to have steeply sloping longitudinal profiles where they meet the main valley.

That the headward reaches of Nirgal Vallis are at approximately the same depth below the Smooth Plains surface as the heads of the tributaries is strongly suggestive of groundwater sapping above a permeability boundary about 200 meters below the surface. This is similar (though the scale may be greater) to sapping channels observed by Laity and Malin (1985) in the Colorado Plateau. Further, the steepening of the tributaries where they join the main valley might indicate they were abandoned as the main valley developed headward. The relatively smooth, uniform longitudinal slope of the valley floor, and its much greater depth toward the mouth beyond the apparent 200 meter depth of the permeability boundary, is suggestive of liquid water flow and transport of material out of the valley.

REFERENCES

Baker, V. R., 1982, The Channels of Mars: University of Texas Press, 198 p.

Laity, J. E., and Malin, M. C., 1985, Sapping processes and the development of theater-headed valley networks on the Colorado Plateau: Geol. Soc. America Bull., V 96, p. 203-217.

Parker, T. J., and Pieri, D. C., 1984, Geomorphology and geoloy of the southwestern Margaritifer Sinus and Argyre regions of Mars - I: Geological and geomorphological overview: Rept. Planet. Geol. Prog. - 1984, p. 361-363.

Pieri, D. C., 1980, Geomorphology of martian valleys: NASA TM 81979, p. 1-160.

Sharp, R. P., and Malin, M. C., 1975, Channels on Mars: Geol. Soc. America Bull., V. 86, p. 331-342.

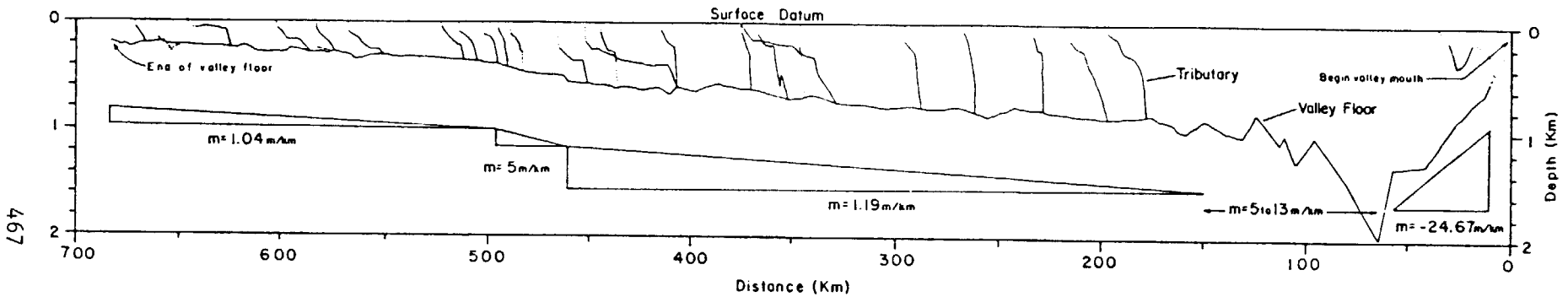

467

Figure 1: Longitudinal profile for Nirgal Vallis and its tributaries. Smooth Plains material and Channel Modified material was used as a datum.

MORPHOLOGY AND DISTRIBUTION OF SINUOUS RIDGES IN CENTRAL AND SOUTHERN ARGYRE

Timothy J. Parker, David C. Pieri, and R. Stephen Saunders, Jet Propulsion Laboratory, Pasadena, California.

The sinuous ridges on the interior floor of Argyre (figure 1) are unusual features that have had little attention in the literature to date. Carr (1984) considered the ridges of southern Argyre as possibly being resistant dikes which were left standing when an intervening material was removed. Howard (1981) described similar features of Dorsa Argentea as Braided Ridges and considered them most likely to be eskers formed by basal melting of an earlier, more extensive south polar cap.

We are studying the ridges in southern Argyre in an effort to better understand and characterize the morphology and relationships to other features and terrain types. Viking Orbiter images used in this study include images from orbits 567B through 569B, which provide good stereo coverage at 40 to 60 m/pixel of central and southern Argyre.

The Argyre ridges occur in association with finely layered, deflated material on the basin's floor. These deposits appear to be well-developed, regularly spaced alternate light and dark layers exposed in wind-deflated areas and hollows. The remaining unmodified surface appears flat to slightly hummocky. These deposits cover most of the interior floor of Argyre and appear also to occur in many of the reentrants of the interior into the circumbasin mountains on the basin's north and west sides.

The ridges appear curvilinear to sinusoidal in plan and range from a few tens of kilometers up to 200 kilometers long and average about a kilometer in width. They typically have a single, smoothly curving crest that occurs along or near the center of the ridge, although double, parallel ridge crests can occaisionally be found where two single-crested ridges join at a low angle. For mapping purposes, the ridges were classified by their degree of preservation. Well defined ridges are those with sharp, distinct outlines and crests which have apparently undergone little or no eolian modification. Moderately defined ridges are those with rounded or indistinct crests and that have partially deflated or otherwise indistinct outlines. These may also occur as topographically inverted features (deflated) grading into positive relief ridges. Where they have been deflated, these ridges may display layering similar to or even continuous with that of the surrounding plains (notably at -54^0 latitude, 42^0 longitude and at -56^0 latitude, 46^0 longitude), suggesting that they are intimately related genetically. Poorly defined ridges are those with very indistinct outlines and typically low profiles and indistinct crests. They are often superposed by moderately or well defined ridges. They may occur as topographically inverted, deflated features within deflated layered terrain (making their identification as separate features difficult at times).

The distribution of these ridges within Argyre does not suggest any apparent relationship to regional or basin-related structural trends. They seem to occur in 2 basic sets. The first set appears to radiate from an area along the southern limit of Argyre's interior floor centered a few tens of kilometers east of the mouth of an unnamed valley at -57^0 latitude, 46^0 longitude. They form a fan-shaped swath of more than 120^0 across the basin floor. Those ridges of this set which occur on the southern, clockwise limit of this swath appear to follow the margin of the basin floor and are deflected around massifs and into reentrants. The second set consists of ridges which tend to sub-parallel one another (trending northwest) and cross the ridges of the first set. Nearly all of the ridges of the second set lie to the north and north-northwest of Charitum Tholus (north of -55^0 latitude).

All the well defined ridges are members of the first set of ridges that lie between the basin's southern interior margin and Charitum Tholus and to the east of Charitum Tholus. The surface of the layered plains here also appears relatively undisturbed by eolian activity. This suggests that the extreme southern plains have been somewhat sheltered from strong winds relative to those of the basin center. Ridges toward the interior of the basin, to the north and west of Charitum Tholus, are increasingly more modified by eolian deflation. This deflation, however, does not preferentially remove layered plains before ridges or vice versa. Positive relief ridges can be found associated with heavily deflated layered

plains material (though they usually have undergone some modification themselves) or deflated, inverted "ridges" can be found within relatively unmodified layered plains. This suggests that both the ridges and layered plains have similarly low resistances to eolian erosion with slight local variations.

By what mechanism did the ridges evolve? Ridge forms can develop by many different geological processes. Tectonic processes are almost certainly responsible for wrinkle ridges on Mars, but these bear little resemblance to the sinuous ridges described above. Volcanic dikes intruding into fractures might be left behind as ridges if the material into which they intruded were somehow removed (Carr, 1984). The distribution of such ridges should reflect local structural trends, however, which the Argyre ridges do not. It is also highly unlikely that dikes would display layering, particularly layering continuous with surrounding plains. Eolian ridges of somewhat similar morphology are common in the vast desert regions of Australia and Africa as longitudinal dunes, but these tend to occur as long, straight, parallel ridges which are much more closely spaced than are those of Argyre. Such features would exhibit layering, however, and could conceivably develop contemporaneously with layered plains sediments. Glacial ridge forms include eskers and moraines which could develop contemporaneously with layered polar deposits. This might be an attractive hypothesis for the ridges of Mare Australe, but it doesn't adequately explain their occurrences elsewhere. In addition, even in Dorsa Argentea, their is a distinct lack of other, corroborative glacial forms, a problem which Howard (1981) recognized. Schultz (1984) suggested that polar wandering through martian history might be responsible for the present global distributions of layered terrain. In Argyre, however, the fortuitous preservation of apparently thick polar dust/ice deposits on the central floor of the basin but a relative lack of such deposits within the mountains of Nereidum and Charitum Montes, where they would be better protected from solar insolation, does not seem very likely. Lacustrine processes can produce concomitant layered ridge and plains deposits, and might provide an explanation for the Argyre forms. The Argyre ridges in this case would represent very long spits or bars, constructed of channel sediments deposited by wave-generated drift currents in a large, shallow lake. This concept may explain the basin floor-only distribution of the ridges and layered deposits and the occurrence of the first set of ridges sub-radial from east of the mouth of the westernmost valley entering Argyre from the south. Terrestrial spits and bars associated with a single river mouth, however, are much shorter than are the Argyre ridges. This scale difference might be partly due to the lower martian gravity. Pieri, (1980) demonstrated that a terrestrial river on Mars would be muddier, due to the lower settling velocities for the suspended load, and that sediment deposits at its mouth may have lower slopes and be spread over larger areas than would be the case on earth.

The sinuous ridges of southern Argyre are the best imaged examples of similar features found elsewhere on Mars. We are presently working on classification schemes and more quantitative methods to assess their morphologies and modes of formation.

REFERENCES

Carr, Michael H., Mars, in The Geology of the Terrestrial Planets, NASA SP-469, 317 p.

Howard, Alan D., 1981, Etched plains and braided ridges of the south polar region of Mars: Features produced by basal melting of ground ice? Repts. Planet. Geol. Program - 1981, NASA TM 84211, p. 286-288.

Pieri, David C., 1980, Geomorphology of martian valleys, PhD dissertation, in Advances in Planetary Geology - 1980, NASA TM 81979, p. 1-160.

Schultz, Peter H., 1984, Polar wandering on Mars and the distribution of water-ice through time, abstract presented to the Workshop on Water on Mars, Nov. 1984, Sponsored by the Lunar and Planetary Institute, p. 71-73.

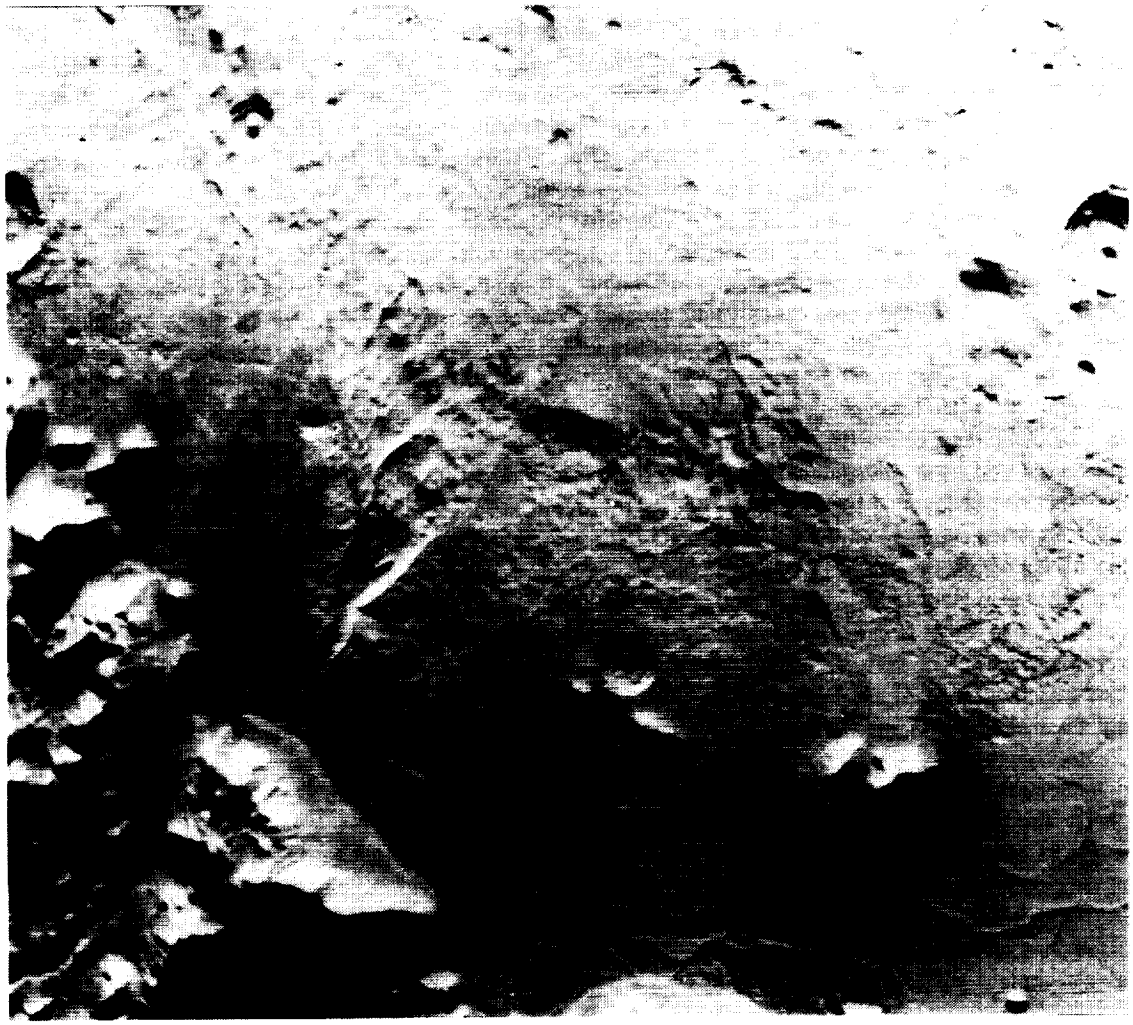

Figure 1: Sinuous ridges on the floor of southern Argyre. Image centered at -50° latitude, 59° longitude. Picture width is 360 kilometers. North is toward upper right. V. O. #352S36.

VOLCANO/GROUND ICE INTERACTIONS AND THE ORIGIN OF FRACTURED TERRAIN ON MARS

Susan Postawko and Peter Mouginis-Mark, Planetary Geosciences Division, Hawaii Institute Geophysics, Univ. Hawaii, Honolulu, HI 96822.

Recent geomorphic mapping (1, 2) has identified the extensive nature of the lobate deposits to the west of Elysium Planitia, and the possible association between these deposits and volcano/ground ice interactions within Elysium. As part of an effort to further understand the geologic history of this volcanic region, our attention has focused on the possible mode(s) of formation of this fractured terrain.

Polygonally fractured terrain is found in three northern plains regions of Mars (SW Acidalia, NW Elysium Planitia, and Utopia Planitia). The individual troughs in these areas are typically 200 - 800 meters wide, 20 - 120 meters deep, and 5 - 10 km apart (although they can be up to 20 km apart; ref. 3). Several hypotheses for the origin of large-scale polygonal troughs on Mars have been proposed. These include contraction cracking in cooling lava (4), cracking due to desiccation of sediment (4), cracking due to thermal contraction and expansion of permafrost (5); tectonic cracking (3); and cracking due to differential compaction of wet sediments overlying an older, cratered surface (6).

A major hurdle in any hypothesis of the formation of the martian northern plains polygons is in explaining their size. These polygons are approximately two orders of magnitude larger than similar features seen on Earth (smaller scale polygons are seen elsewhere on Mars, and may be formed by a very different mechanism; ref. 7). Theory (8) and experience with terrestrial features (8-10) indicate that in order to create 10 - 20 km diameter polygons on Mars, stresses are needed at depths of 500 - 1000 meters. Pechmann (3) has shown that their formation solely by cooling lava, desiccation, or thermal expansion and contraction, is probably mechanically impossible at the scale necessary to explain the features on Mars. Thus Pechmann was left to conclude that only tectonism could provide stress at the necessary depths, although no known tectonic structure (of any scale) on Earth is similar in morphology to the martian systems. Further studies of the polygons on Mars (e.g., 6 and 7) neither substantiate nor disprove Pechmann's tectonic hypothesis.

While tectonism cannot be ruled out as a possible mechanism for the formation of the martian polygons, the correspondence of areas of polygonal ground to regions where deposition of wet sediments by large outflow channels has apparently occurred suggests that there may be a cause/effect relationship between them. McGill (6) proposed that compaction of a thick deposit of either water-saturated clays or ignimbrites over a previously cratered terrain may form fractured ground. McGill maintained that the large size of the polygons resulted from the scale of the buried topography.

Our hypothesis of polygon formation also involves deposition of sediments from the outflow channels. A synopsis of our model is as follows: Sediments and water, derived from interactions between igneous activity and ground ice, carved the observed channels and were subsequently emplaced in low-lying areas. Because the preexisting ground was most likely frozen (unless climatic conditions were very different from those which exist at the present time), little if any of the water could escape into the ground, therefore ponding would occur. The sediments settled out of the water, creating a sediment layer at the bottom of the liquid water column. The water and the sediments then froze. Because the sediments were deposited with a fluid they would freeze in hydrostatic equilibrium with the fluid. Under present conditions on Mars, surface ice is unstable with respect to the atmosphere and will sublimate. Sublimation of the ice above the frozen sediment layer would put the sediments in a tensional stress situation, and fracturing might occur.

Our model assumes that enough sediment might have been entrained within the meltwater to form a sediment layer at least 500 meters thick. We also assume that sufficient ice existed on top of this sediment layer to create a pressure equal to the tensile strength of the sediments at the top of the sediment layer. For a mineral soil with a tensile strength of 2×10^7 dynes/cm^2, an ice thickness of approximately 600 meters would be required. Aspects of this hypothesis which are now being investigated include:

1) How quickly would the sediments settle out of the water? If all the particles were very small, and the water froze before those particles settled out, then a duricrust may have formed after only a small amount of ice had sublimated, preventing the bulk of the ice from being removed.

2) How quickly would the ice be sublimated? If this process is slow compared to the time it took for the stress on the ice to dissipate, fracturing would not have occurred.

The advantage of our hypothesis for the formation of large-scale martian polygons over a formation by tectonics is that there is supporting geomorphic evidence (in the form of the presumed mudflow deposits) for this kind of material existing in these localities. In addition, this hypothesis offers an explanation as to why these polygons are found in some regions of Mars (where the appropriate combination of channels, low-lying plains, and cold temperatures occur), and not in other areas such as Arcadia Planitia. Our current efforts are being devoted to further numerical modelling of the depositional environment under which the fractures may have evolved, and the volcano/ground ice interactions that were responsible for the generation of the melt water.

REFERENCES: 1) P. Mouginis-Mark et al. (1984) Earth, Moon, and Planets 30, pp. 149-173. 2) P. Mouginis-Mark (1985) "Volcano/Ground Ice Interactions in Elysium Planitia, Mars", Icarus, in press. 3) J. C. Pechmann (1980) Icarus 42, pp 185-210. 4) E. C. Morris and J. R Underwood (1978). Rpts. Plan. Geol. Prog. 1977, NASA TM-79729, pp. 97-99. 5) M.H. Carr and G. Schaber (1977) J. Geophys. Res. 82, p. 4039-4054. 6) G. E. McGill (1985) Lunar Plan. Sci. XVI, pp. 534-535. 7) B. K. Lucchitta (1983) Permafost: Fourth Int. Conf., pp. 744-749. 8) A. H. Lachenbruch (1962) GSA Sp. Paper No. 70. 9) J. T. Neal et al. (1968) Geol. Soc. Amer. Bull., 79, pp. 69-90. 10) R.F. Black (1978) 2nd Coll. Planet Water & Polar Proc., pp. 127-130.

EXPERIMENTAL FRACTURE PATTERNS: APPLICATION TO MARTIAN CHANNELS

Pranger, Harold, Department of Earth Resources, Colorado State University, Fort Collins, Colorado 80523

This study compares experimentally generated tension fractures with fluvial features, as some martian channels may be predominantly structural rather than fluvial features. Recent success applying small-scale fracture mechanics principles to large-scale geologic fractures (Rudnicki, 1980, Scheideggar, 1982, Bahat, 1982) suggests that all scales of fractures may be morphologically quite similar. Previous experimental fracture analysis has led to a broader understanding of the causes, processes, and geometry of large-scale faulting (Bain and Beebe, 1954, Cloos, 1955, 1968, Sanford, 1959, Emmons, 1969, Oertel, 1969, and Courtillot, et al. 1974).

Brittle layers of a 90% very fine sand, 10% silt matrix were fractured by Mode I tension (Tada, et al. 1983) in three ways. In the first set of experiments, brittle layers coating a 1.3 x 2.6 m sheet of plywood were upwarped, uniaxially fracturing the surface material. The results show that the mean sinuosity of 25 cm fracture sections initially increases with material thickness from 1.5 to 2.0 cm but then decreases with increasing thickness up to 3.5 cm. Sinuousities for 150 fractures range from 1.03 to 1.22. Fracture density also decreased with increasing material thickness, a result also noted by Pechman (1980). In the second set of experiments, the same apparatus was used to fracture the brittle material by biaxial tension. The average fracture sinuosity was less than that for the uniaxial experiments. Also, fracture branching is common; and the main trunk fractures are much wider than their branches.

A doming apparatus was used with the same experimental material in the third set of experiments. A 1.2 m diameter rubber sheet attached to a rigid steel floor was inflated to fracture the brittle surface. Fractures formed this way appear similar to the previous experiments and are aligned normal to the surface slope. Fracture density is linearly related to average surface deformation.

Understanding the causes and morphology of fracture sinuousity is vital to distinguish curved fractures from curved fluvial patterns. The experimental fractures do not recurve upon themselves, another feature which may help identify fluvial from non-fluvial channels. Explanations for curved cracks include randomly distributed zones of weakness (Neal, 1966), non-aligned microfractures (Scholz, 1970), a tangential stress parallel to the propagating crack (Cotterel and Rice, 1980, and Viola and Piva, 1984), as well as material heterogeneity (Ewalds and Wanhill, 1984). Another mechanism noted in the experiments was sliding of the material along shears perpendicular to the crack propagation direction. The angularity of some fractures is yet another feature that distinguishes fractures from fluvial channel patterns.

Fracture branching is a common feature of the experiments. The narrower branch and wider trunk fractures are qualitatively similar to wider main streams with relatively narrow tributaries above their confluence.

This study has exposed the striking similarity of tension fracture patterns and many fluvial patterns, both qualitatively, and, to some degree, quantitatively. Surface flow of liquids and fracturing, both separately and in combination, may have contributed to the development of martian channels. The first step has been taken towards quantifying the shapes of fractures so they can be compared directly to the martian channels.

References

Bahat, D., 1982. Extensional Aspects of Earthquake Induced Ruptures Determined by an Analysis of Fracture Bifurcation. Tectonophysics, v. 83, 163-183.

Bain, G.W., and Beebe, J.H., 1954. Scale Model Reproduction of Tension Faults: Am. J. Sci., v. 252, 745-754.

Courtillot, V., Tapponnier, P., and Varet, J., 1974. Surface Features Associated With Transform Faults: A Comparison Between Observed Examples and an Experimental Model: Tectonophysics, v. 24, 317-329.

Cloos, E., 1955. Experimental Analysis of Fracture Patterns. Bull. Geol. Soc. Am., v. 66, 241-256.

Cloos, E., 1968. Experimental Analysis of Gulf Coast Fracture Patterns. Am. Assoc. Pet. Geol. Bull., v. 52(3), 420-444.

Cotterell, B., and Rice, J.R., 1980. Slightly Curved or Kinked Cracks: Int. J. Fract., v. 16, 155-169.

Emmons, R.C., 1969. Strike-Slip Rupture Patterns in Sand Models: Tectonophysics, v. 7, 71-87.

Neal, J.T., 1966. Polygonal Sandstone Features in Boundary Butte Anticline Area, San Juan County, Utah: Discussion. Geol. Soc. Am. Bull., v. 77, 1327-1330.

Oertel, G., 1965. The Mechanism of Faulting in Clay Experiments: Tectonophysics, v. 2, 343-393.

Pechman, J.C., 1980. The Origin of Polygonal Troughs on the Northern Plains of Mars: Icarus, v. 42, 185-210.

Rudnicki, J.W., 1980. Fracture Mechanics Applied to the Earth's Crust: Ann. Rev. Earth Planet. Sci., v. 8, 489-525.

Sanford, A.R., 1959. Analytical and Experimental Study of Simple Geologic Structures: Bull. Geol. Soc. Am., v. 70, 19-52.

Scheideggar, A.E., 1982. Principles of Geodynamics. Springer-Verlag, Berlin: 395 pp.

Scholz, C., 1970. The Role of Microfracturing in Rock Deformation: 2nd Intern. Congress of Rock Mechanics, Belgrade: 1-5.

Tada, H., Paris, P.C., and Irwin, G.R., 1973. The Stress Analysis of Cracks Handbook: Del Research Corporation, Hellertown, PA. 313 pp.

Viola, E., and Piva, A., 1984. Crack Paths in Sheets of Brittle Material: Engineering Fract. Mech., v. 19, 1069-1084.

EJECTA FROM THE GLOVER BLUFF CRATER, OR OTHER CRATERS OF THE SAME AGE

W. F. Read, Dept. of Geology, Lawrence University, Appleton, WI 54912

Chert-like nodules, believed to be impact bombs, have been found near the base of the St. Peter formation (Middle Ordovician) in southeastern Wisconsin (Read, 1985). Similar nodules have since been found in rocks of the same age in northern Illinois. Here the bombs are associated with fragments of rock containing great numbers of siliceous spherules, which are probably also of impact origin. They compare favorably with probable impact spherules ("terrestrial chondrules") found by Lowe (1985) in Archean strata of Australia and Africa.

Though exposures are limited, Middle Ordovician rocks are widely distributed in the subsurface of northern Illinois. Drill cuttings of rocks of this age have been obtained from the Illinois Geological Survey and will be studied in thin section during the coming winter. It is expected that a better idea of the true (southward) extent of the stratum containing bombs and spherules can be obtained in this way. Its present known extent in a north-south direction is 350 km.

Middle Orodvician exposures in western Wisconsin, northeastern Iowa, southeastern Minnesota, and eastern Missouri have been briefly visited, but no impact ejecta have yet been found in these areas.

It seems unlikely that all these Middle Ordovician ejecta can have come from one crater, specifically the one at Glover Bluff, which is believed to be of Middle Ordovician age. More likely, they came from a family of craters formed at the same time. The Rock Elm structure in west central Wisconsin, recently described by Cordua (1985), is probably a member of this family (Read, 1986). Other members, if they exist, have yet to be found.

Quite recently, another layer of what are probably impact bombs has been found in Lower Ordovician rocks of southeastern Wisconsin.

Cordua, W.S., (1985), Rock Elm structure, Pierce County, Wisconsin: a possible cryptoexplosion structure. Geology, v. 13, p. 372-374.

Lowe, D.R., and G.R. Byerly, (1985), Chondrule-like particles provide evidence of early Archaen meteorite impacts, South Africe and West Australia. Abstracts, 16th Lunar and Planetary Science Conference, p. 501-502.

Read, W.F., (1985), Impact bombs in Middle Ordovician marine sediments of southeastern Wisconsin. Abstracts, 16th Lunar and Planetary Science Conference, p. 687-688.

Read, W.F., (1986), Comment on Cordua's paper on the Rock Elm structure, Geology, in press.

SIZE AND RANDOMNESS OF GROUND PATTERNS FOR EARTH AND MARS: IMPLICATIONS FOR ORIGIN AND MODIFICATION

Lisa A. Rossbacher, Geological Sciences Department,
California State Polytechnic University, POmona, CA 91768

Polygonal ground patterns can be described by nearest-neighbor analysis; the R-statistic describes the degree to which a pattern deviates from an expected random pattern. All Martian patterns and most terrestrial ones studied to date are statistically more regular than random, with the R-statistic between 1.0 and 2.14, the random and hexagonal nodes (Rossbacher, 1985).

Because the R-statistic is scale independent, the Martian patterns can be compared with terrestrial ones that are an order of magnitude or more smaller. The size of the patterns cannot be ignored, however. Preliminary data suggest that, for both Earth and Mars, larger polygons are more random in pattern than the more regular, smaller polygons (Fig. 1).

This observation about the relationship between size and randomness suggests that the polygons may begin as small, relatively regular polygons (R-statistic in the more-regular-than-random range) and are enlarged by a variety of modifying processes to become larger, less regular polygons (R statistic approaching 1.0, the random node). Processes that modify terrestrial polygons include wind (Davies, 1961; Seppälä, 1982), flowing water (Elton, 1927; Rapp and Annersten, 1969; Svensson, 1982), and vegetation (Elton, 1927; Åkerman, 1983). Certainly the first 2 of these processes could have also been effective on Mars. Wind, for example, would tend to excavate troughs parallel to the dominant wind direction and fill in the depressions perpendicular to it. This evolutionary hypothesis is consistent with the proposal by Helfenstein and Mouginis-Mark (1980) that Martian polygonal ground may begin as small forms that coalesce or enlarge by modifying processes. They cited desiccation as the modifying agent, but wind or water could also be responsible.

Further study of the relationship between the R-statistic and the size of both terrestrial and Martian polygons should help to identify the correlations between size and randomness, the mechanism of formation, and perhaps the agents of modification. Correlation with dominant wind directions, to establish the possible role of modification by aeolian activity, is already underway. The similar relationship between size and pattern on Earth and Mars, despite the different absolute sizes of the polygons, suggests an underlying similarity in the pattern evolution or in the relationship among size, pattern randomness, and the mode of origin.

Relationship between R statistic and polygon diameter

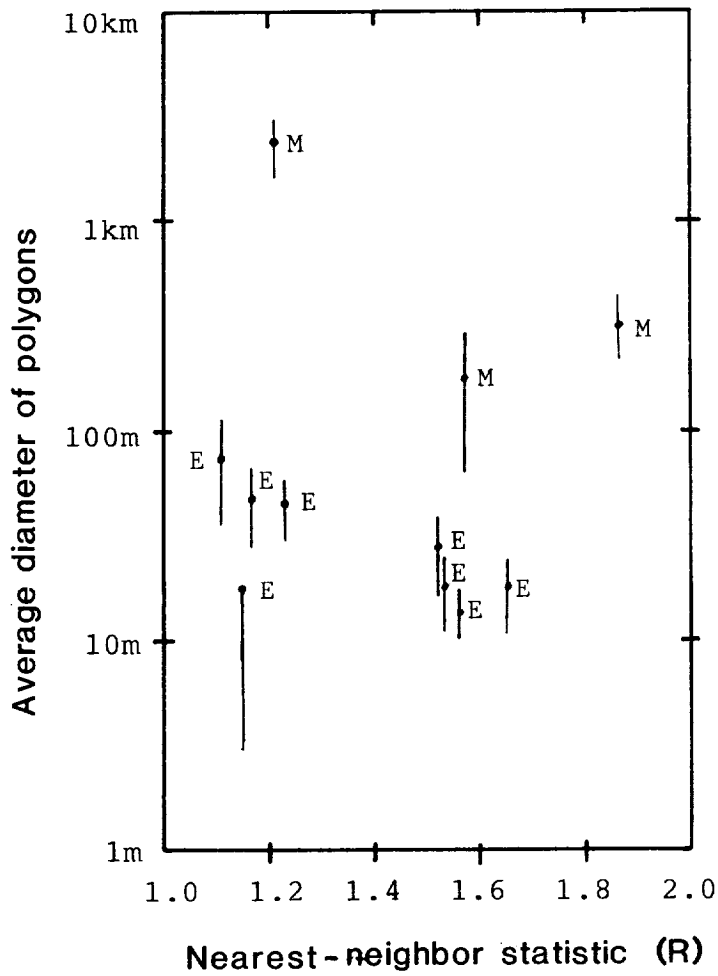

Fig. 1. Polygonal ground patterns on both Earth and Mars are generally less regular with increasing diameter. The nearest-neighbor statistic (R) is a measure of the departure from a random pattern (Rossbacher, 1985). Although R can range between 0.0 (maximum clustering) to 2.14 (hexagonal lattice), only the random (R=1.0) to regular (R=2.0) section is shown here. Error bars represent 1 standard deviation for polygon diameter. (From data presented in Rossbacher, in review; data for Mars and Earth are labeled M and E, respectively.)

REFERENCES CITED

Åkerman, J., 1983, Notes concerning the vegetation on deflation surfaces, Kapp Linné, Spitsbergen: Polar Research, v. 1 n.s., p. 161-169.

Davies, W.E., 1961, Surface features of permafrost in arid areas: Folia Geographica Danica, v. 9, p. 48-56.

Elton, C.S., 1927, The nature and origin of soil-polygons in Spitsbergen: Geological Society of London Quarterly Journal, v. 83, p. 163-194.

Helfenstein, P., and P. Mouginis-Mark, 1980, Morphology and distribution of fractured terrain on Mars: Lunar and Planetary Science XI (Houston, TX), p. 429-431.

Rapp, A., and L. Annersten, 1969, Permafrost and tundra polygons in northern Sweden, in T.L. Péwé, ed., The Periglacial Environment: McGill-Queen's University Press (Montreal), p. 65-91.

Rossbacher, L.A., 1985, Quantitative analysis of Martian polygonal ground: Lunar and Planetary Science XVI (Lunar and Planetary Institute, Houston, TX), p. 710-711.

Rossbacher, L.A., in review, Nearest-neighbor analysis of ground patterns: Geografiska Annaler.

Svensson, H., 1982, Valley formation initiated by ice wedge polygonal nets in terrace surfaces: Biuletyn Peryglacjalny, no. 29, p. 139-142.

This research is supported by NASA's Planetary Geology and Geophysics Program, under Grant NAGW-715.

HIERARCHICAL PATTERNED GROUND ON EARTH AND MARS

Lisa A. Rossbacher, Geological Sciences Department,
California State Polytechnic University, Pomona CA 91768

A continual problem in explaining the origin of polygonally patterned ground on Mars is the size difference between Martian forms and their terrestrial analogs. On Mars, polygons range up to 20 km or more in diameter. In contrast, the largest reported terrestrial polygons are desiccation patterns on playas that can be as much as 500 m wide (Fife, 1980). Polygons that form in cold climates are usually much smaller.

Patterned ground having a range of sizes within a given area, or hierarchies, has been reported from many cold or arid regions on Earth. Curiously, published reports seldom discuss and almost never cross-reference these hierarchies of patterned ground. The terminology usually refers to the order of polygon formation; primary polygons develop first, followed by secondary and tertiary networks. Primary patterns have been reported developing by ice wedging, frost cracking, bedrock weathering, and local or regional desiccation. Secondary polygons form through frost action or desiccation. Almost all reported examples of tertiary polygons were created by desiccation. All of these various sizes were created by one or more of these mechanisms; they were not modified by surficial processes like wind or water. The effects of such modification of polygonal patterns are described elsewhere (Rossbacher, 1985b).

At least 2 scales of patterned ground occur on Mars, although these have not been observed in the same areas. Small polygons, less than 1 km in diameter, occur in the northern plains of Lunae Planum (Evans and Rossbacher, 1980), Chryse Planitia (Brook, 1982), and Dueteronilus Mensae (Lucchitta, 1983). Larger ones, with diameters ranging up to 20 km or more, have been observed on Acidalia, Utopia, and Elysium Planitia (Pechmann, 1980; Rossbacher and Judson, 1981).

Nearly all of the hierarchies of polygonal ground on Earth reported in the literature refer to the large polygons as primary and smaller ones as secondary; this assumes the larger patterns develop first and then are subdivided by further cracking. The major exception to this sequence is polygon development associated with a warming climate (Dostovalov and Popov, 1966) or regional desiccation (Neal and Motts, 1967). The sequence for Martian polygon development is still unknown.

The terrestrial examples of hierarchical patterned ground suggest that the different sizes of polygon on Mars may be created by different mechanisms. In addition to documenting the multigenetic evolution of many ground patterns on Earth,

these analogs provide clues to the possible origin of Martian polygons. The observations of terrestrial analogs are consistent with the proposal that smaller, primary polygons, below the resolution of Viking orbiter images, exist within the larger-scale secondary patterns (Rossbacher, 1985a). Detailed efforts are still needed to correlate different sizes of Martian polygons and their relative ages, to establish the relationship between primary and secondary forms on that planet.

REFERENCES CITED

Brook, G.A., 1982, Ice-wedge polygons, baydjarakhs, and alases in Lunae Planum and Chryse Planitia: Reports of Planetary Geology - 1982, NASA Technical Memorandum 85127, p. 265-267.

Dostovalov, B.N., and A.I. Popov, 1966, Polygonal systems of ice wedges and conditions of their development, in Proceedings, First International Permafrost Conference: National Academy of Sciences (Washington, D.C.), p. 102-105.

Evans, N., and L.A. Rossbacher, 1980, The last picture show: Small-scale patterned ground in Lunae Planum: Reports of Planetary Geology Program - 1980, NASA Technical Memorandum 82385, p. 376-378.

Fife, D.L., 1980, Giant desiccation polygons and playa fissures, in D.L. Fife and A.R. Brown, eds., Geology and mineral wealth of the California desert: South Coast Geological Survey (Santa Ana, CA), p. 414-429.

Lucchitta, B.K., 1983, Permafrost on Mars: Polygonally fractured ground, in Proceedings, Fourth International Permafrost Conference: National Academy Press (Washington, D.C.), p. 744-749.

Neal, J.T., and W.S. Motts, 1967, Recent geomorphic changes in playas of western United States: Journal of Geology, v. 75, p. 511-525.

Pechmann. J.C., 1980, The origin of polygonal troughs on the Northern Plains of Mars: Icarus, v. 42, p. 185-210.

Rossbacher, L.A., 1985a, The role of scale in planetary geomorphology, in R.S. Hayden, ed., Mega-geomorphology: NASA Conference Publication 2312, p. 76-78.

Rossbacher, L.A., 1985b, Size and randomness of ground patterns on Earth and Mars: Implications for origin and modification: This volume.

Rossbacher, L.A., and S. Judson, 1981, Ground ice on Mars: Inventory, distribution, and resulting landforms: Icarus, v. 45, p. 39-59.

This research is supported by NASA's Planetary Geology and Geophysics Program, under Grant NAGW-715.

IMPACT STRUCTURES OF WESTERN AUSTRALIA

E. M. Shoemaker, U.S. Geological Survey, Flagstaff, Arizona 86001
C. S. Shoemaker, Arizona Research and Technology, Inc., P.O. Box 1125, Flagstaff, Arizona 86002

Ten structures of known, probable, or possible impact origin have been identified in Western Australia. They include three proven meteorite craters, two large craters of probable impact origin, three deeply eroded structures of probable impact origin, and two very large possible impact structures.

The three proven impact craters with associated meteorites are the well-known Wolf Creek crater (diameter = 900 m), Dalgaranga crater (diameter = 25 m), and Veevers crater (diameter ≈ 80 m). Veevers was recently discovered on the boundary between the Gibson and Great Sandy Deserts (Yeates et al., 1976); we found iron meteorite fragments here in the summer of 1984. The Veevers discovery increases to 15 the number of craters worldwide with which meteorites are known to be associated.

On the basis of our detailed mapping, the Wolf Creek Crater can be interpreted to have been produced by oblique impact from the northeast. Beds are uplifted and strongly upturned at a deeper level along the southwest crater wall than elsewhere, and the bedrock of the southwest rim is displaced outward along a small reverse fault. In the down-range direction, we discovered impactites associated with meteorite fragments about 3.5 km from the crater.

The large craters that are of probable impact origin are Goat Paddock (diameter = 5 km), of probable early Eocene age, on the Kimberley Plateau (Harms et al., 1980); and Connolly Basin (diameter = 9 km), of Cretaceous or Tertiary age, in the northern Gibson Desert. Our attention was drawn to the Connolly Basin by a circular line on the Morris 1:250,000-scale geologic map (Crowe, 1979) that was thought to outline a possible subsurface salt diapir. The present basin is very shallow and is largely mantled by laterite of possible early or mid-Tertiary age. Our field studies revealed an exposed central peak of strongly deformed sandstone. A seismic reflection profile shows strong reflectors disrupted to depths of about 0.7 sec beneath the central peak and nearly flat-lying reflectors beneath the disturbed region.

Of the three deeply eroded probable impact structures, the Piccaninny structure (diameter = 7 km) and the Spider structure (diameter = 13 km), both in the Kimberley district, are almost completely exposed. The Piccaninny structure, discovered by G. M. Beere (1983), is developed in Devonian sandstone exposed in the Bungle Bungle Range. On the basis of detailed mapping carried out jointly with G. M. Beere and A. Wilson of the Geological Survey of Western Australia, the structure appears to be eroded to depths of about 1 to 2 km beneath the original impact crater. A very subdued central peak is present in which the beds are deformed in series of radial folds.

The Spider structure, discovered by J. E. Harms (Harms et al., 1980), is developed in sandstone and subordinate finer grained clastic rocks of the Early Proterozoic Kimberley Group in the central Kimberley Plateau. This structure also appears to be deeply eroded; regional denudation may have exceeded 1 km since the crater was formed. Our detailed mapping at Spider shows that beds surrounding the central uplift are deformed in a series of small thrust sheets that are consistently displaced to the south-southeast. A structurally low region surrounding the central uplift is distinctly ellipitical in plan; its long axis trends NE-SW. This structure probably was formed by low-angle oblique impact in Early Proterozoic time.

The third deeply eroded probable impact structure is the Lake Teague ring structure (diameter = 30 km), at the southern edge of the Nabberu Basin (Butler, 1974; Bunting et al., 1980; Bunting et al., 1982). This structure is developed in sandstone and siltstone of the Early Proterozoic Earaheedy Group and Late Archean plutonic rocks. It was also probably produced by impact in Proterozoic time.

The two possible impact structures are Dampier (diameter ≈ 100 km?) and Pippingara (diameter ≈ 50 to 100 km). Both are circular or possibly circular features in the Pilbara Block and are recognizable on Landsat images and regional geologic maps. The Dampier structure occurs on the coast, and the degree of its circularity is unknown: only a segment is exposed on the mainland and in the Dampier Archipelago; the remainder is concealed beneath the Indian Ocean. The most striking component of this structure is the Gidley Granophyre (de Laeter and Trendall, 1971), exposed in an arcuate belt. The granophyre forms a crudely stratiform sheet that rests on Archean granite and dips toward the apparent center of the structure. Local concentrations of sheared Archean granite blocks that we observed near the base of the granophyre suggest that it might be a crystallized impact-melt pool. Isotopic data indicate that the granophyre may be Late Archean or very Early Proterozoic in age. The Pippingara structure, 400 km east of Dampier, is underlain chiefly by Archean granite and is partly bounded by Archean metasediments and mafic to ultramafic crystalline rocks. Extensive brecciation of the granite, which we noted during reconnaissance examination, and a pronounced gravity low centered over the structure (Hickman and Gibson, 1982) suggest it may have been deformed and brecciated by impact.

References

Beere, G. M., 1983. West. Australia Geol. Survey Record, 1983/6, 8 p.

Bunting, J. S., J. R. De Laeter, and W. G. Libby, 1980. West. Australia Geol. Survey Ann. Rept., 1979, 125-129.

Bunting, J. A., A. T. Brakel, and D. P. Commander, 1982. West. Australia Geol. Survey 1:250,000 Geol. Ser. Explan. Notes, Nabberu, W. A., 27 p.

Butler, Hadyn, 1974. Search, 5, 534-536.

Crowe, R. W. A., 1979. Bur. Mineral Resources and West. Australia Geol. Survey 1:250,000 Geol. Ser. Explan. Notes, Morris, W. A., 12 p.

de Laeter, J. R., and A. F. Trendall, 1971. West. Australia Geol. Survey Ann. Rept., 1970, 62-67.

Harms, J. E., D. J. Milton, John Ferguson, D. J. Gilbert, W. K. Harris, and Bruce Goleby, 1980. Science, 286, 704-706.

Hickman, A. H., and D. L. Gibson, 1982. Bur. Mineral Resources and West. Australia Geol. Survey 1:250,000 Geol. Ser. Explan. Notes, Port Hedland - Bedout Island, W. A., 28 p.

Yeates, A. N., R. W. A. Crowe, and R. R. Towner, 1976. Bur. Mineral Resources, Jour. Australian Geol. Geophys., 1, 77-78.

MORPHOLOGY OF MARTIAN CENTRAL-FEATURE CRATERS WITH SOME IMPLICATIONS FOR GENESIS MODELS

Susan J. Steenstrup, Department of Geology and Geography
University of Massachusetts, Amherst, MA 01003

In previous studies, central features in martian craters have been classified into only 3 categories: unpitted peaks, pitted peaks, and pits. In general, these studies were based on data from relatively small, localized regions (1, 2, 3, 4). Numerous models have been proposed for the genesis of central features, but few of these have been tested against thorough morphologic studies. The main purposes of this study are: 1) to examine central-feature craters on a large fraction of the planet, 2) to better characterize the wide range of morphologies by increasing the number of classification categories, and 3) to critically examine existing genesis models using these new data.

A total of 3995 central-feature craters were examined using 1:2M U.S. Geologicl Survey photomosaics of the region between 65°N and 65°S latitudes. The area covered includes approximately 50% of the surface of Mars. The central-feature classification developed during this study includes 39 specific types divided into 4 classes and 8 subclasses. In addition to central-feature type, the location, map unit, ejecta type, degree of modification, feature location relative to crater center, and inferred impact angle were noted for each crater. For selected craters, additional characteristics noted were: 1) feature diameter and crater diameter, 2) number of features per crater, and 3) azimuths of lineation, breaching, and elongation.

The more important results include:

1) Craters with unpitted peaks comprise 73%, craters with pitted peaks 22%, and craters with pits 5% of the total study population. All three of these classes of central features occur in craters with a wide range of diameters. Craters with closely packed, irregular clusters of jagged peaks typical of lunar craters are rare (4%). Craters with more than one central feature comprise 47% of the study population. Central features that are round in plan occur in only 27% of the population; the rest are asymmetrical to distinctly elongate.

2) Several new morphologic types of central features have been described. Many craters contain groups of central features whose members vary considerably in height, shape, distribution, and surface texture. The maximum number of members found in a single crater is 29. Some peaks contain multiple pits, some of which are elongate or intersecting. Both floor and summit pits may contain small peaks (up to 6 per pit), and some summit pits are breached or notched. In a few craters, central features seem to have formed long after impact.

3) Central-feature craters seem to be regionally rather than latitudinally distributed; that is, very large variations exist in

the number of central-feature craters per unit area for the same map unit at the same latitude but a different longitudes, and dense clusters of similar craters span several map units.

4) Approximately 63% of all central-feature craters have uncentered features, but single features are more likely to be centered than multiple features. Of the craters with uncentered features, only 2% seem due to low-angle impact.

5) More craters with ballistically emplaced ejecta contain pitted peaks and pits (50%) than do craters with ejecta emplaced by fluidized flow (32%).

6) Peak diameter/crater diameter (Y/X) ratios for all single peaks (pitted or unpitted) can be estimated with the same regression equation: $Y = 0.14X + 0.053$ (for 222 craters, $r = +.80$). Pit diameter/crater diameter ratios for both summit and floor pits can be estimated using: $Y = 0.32X - 0.50$ (for 403 craters, $r = -0.91$). Neither map unit nor crater modification seems to affect these ratios. The large standard errors of estimate (4.08 for peaks and 4.03 for pits at the 99.7% confidence limit) indicate a moderate degree of scatter. For the majority of craters containing multiple central features, these ratios plot within the confidence limits for the single structures, regardless of how many peaks or pits are present.

7) Craters containing one or more rows of features (hereafter referred to as "lineated") or containing elongated features comprise 45% of the study population, but only 3.5% of these occur in craters probably due to low-angle impact. Moreover, lineation or elongation azimuths of central features in low-angle impact craters parallel the elongation of the crater in only 54% of the cases observed.

8) Pitted peaks with breached summit pits occur in 5% of the study population. Because 80% of these craters are fresh, it seems unlikely that breaching results from a lengthy post-impact erosion process. About 7% of breached summit pits show two or more distinct directions of breaching.

9) Craters with breached, lineated, or elongated structures tend to be clustered, and in many regions their lineation, breaching, and elongation azimuths are parallel to each other and to nearby faults and mare ridges. Although there is a significant association between craters with linear central features and faults, there are faulted regions without such craters; also clusters of craters with linear central features occur in regions that are not highly faulted.

Many of these results are not consistent with predictions derived from the published models for central-feature genesis. The elastic-rebound model (5) predicts the existence of only single, centered features, and constant density of craters containing these features

on a single map unit. If multiple features result from rebound following interaction between shock waves and older faults (6), multiple features should progressively diminish in size with distance from the crater center because of declining intensity of rebound, and craters with many central features should contain significantly smaller features than similar craters with few central features because of the need to conserve rebound volume. Asymmetric elastic rebound during low-angle impact (7) is also unlikely because peaks generated by this mechanism should be considerably smaller than peaks in craters resulting from high-angle impacts, and multiple peaks should be present only for low-angle impacts. The data do not support any of these predictions.

If peaks and pits result from viscous oscillations of the crater floor (8), one would expect the ratios of pit diameter and peak diameter to crater diameter to be the same, and also would expect the numbers of craters with either single peaks or single pits to be similar. The data contradict these expectations. Furthermore, this model cannot easily account for multiple structures.

Formation of pits by volatilization of permafrost (3) implies strong latitudinal variations in the abundance of central pits, and also a correlation with fluidized ejecta. Neither is observed.

It is likely that more than one process was involved in the genesis of central features in martian craters. Many of these central features are morphologically similar to volcanoes; hence impact-triggered volcanism is a plausible mechanism for a significant fraction of them. This study clearly highlights the need to describe many craters from a large geographic area in order to evaluate the role of latitude and target materials on morphology. My results indicate that all models predicting significant differences in abundance or type of central-feature craters due to latitude or target are suspect, and also that the uncritical use of central features to map target layering and depths to permafrost is unwise.

References cited

1) Hodges, C.A. (1978) NASA TM-79729, 169-171.
2) Wood, C.A., et al. (1978) Proc. Lunar Planet. Sci. Conf. 9, 3691-3709.
3) Hodges, C.A., et al. (1980) Lunar Planet. Sci XI, 450-452.
4) Hale, W.S., and Head, J.W. (1981) 3rd. Int. Colloq. Mars, 104-106.
5) Baldwin, R.B. (1949) The face of the moon, 239 p.
6) Hale, W.S. (1980) Proc. Conf. Lunar Highland Crust, 197-209.
7) Murray, J.B. (1980) Moon and Planets, 22, 269-291.
8) Greeley, R., et al. (1980) Proc. Lunar Planet. Sci. Conf. 11, 2075-2097.

POLYGONAL GROUND IN THE NORTHERN HEMISPHERE OF MARS

Cathy A. Summers, Planetary Geology Undergraduate Research Program, NASA, and
B.K. Lucchitta, U.S. Geological Survey, Flagstaff, AZ 86001

The origin of polygonally fractured ground, which occurs mostly in the northern hemisphere of Mars, is still poorly understood. Hypotheses on origin have largely centered on thermal-contraction cracking in ground ice (Black, 1978; Coradini and Flamini, 1979; Helfenstein, 1980; Helfenstein and Mouginis-Mark, 1980). However, Pechmann (1980) showed that origin by thermal contraction is unlikely on theoretical grounds, and proposed a structural origin instead. McGill (1985) has proposed that polygons formed when a debris blanket cracked because of tensile stresses upon settling and compacting over buried topography. The present study classifies polygonally fractured ground and attempts to clarify some regional relations.

We first located polygonally fractured ground on 1:2,000,000-scale controlled photomosaics of Mars' northern hemisphere. We also studied Viking Orbiter photographs to verify these occurrences and to determine their characteristics. The results were plotted on 1:15,000,000-scale shaded relief maps.

The inventory revealed two major types of fractured ground, provisionally called rectilinear and curvilinear polygonal ground. Rectilinear polygonal ground occurs dominantly along the boundary scarp between the northern plains and southern highlands. Curvilinear polygonal ground is largely restricted to the northern plains.

Rectilinear polygonal ground occurs in patches and areas whose extent is 100 to more than 500,000 km^2 (fig. 1). It is outlined by fractures that are straight to slightly arcuate, shallow or deep, flat-floored or V-shaped. Conspicuous are many intersections of fractures at or near right angles. Polygons may have a dominant fracture direction with subordinate, usually shorter fractures orthogonal to the major fractures and to one another. This configuration forms a rectangular boxwork pattern; examples are seen in Kasei Vallis (fig. 1, largest black area). Polygons range in size from less than 1 km to about 30 km in diameter and, generally, the lengths of fractures and diameters of polygons are directly proportional to the width and depth of the fractures.

Type and thickness of surficial layers apparently locally influenced the size and shape of the fractures and polygons. In the Kasei Vallis area, the uppermost layer on a plateau is thick and is cut by wide, deep, widely spaced fractures; a thinner, lower layer exposed on an eroded channel floor has narrow, shallow closely spaced fractures.

Rectilinear polygonal ground is most commonly associated with the boundary scarp between the northern plains and the southern highlands. Isolated occurrences are associated with graben systems of the Tharsis and Elysium regions and the volcanoes Olympus Mons and Albor Tholus.

Regional structural patterns appear to control the location and trend of rectilinear polygonal ground. This conclusion is supported by the observations that the fractures are associated with grabens, that many fractures are oriented parallel to the boundary scarp (Maxwell, in press), and that they locally coincide with tectonically disrupted areas around volcanoes. Rectilinear polygonal ground in places appears to be the precursor of fretted terrain (Sharp, 1973).

Curvilinear polygonal ground is formed by fractures that are V-shaped or flat-floored, wide or narrow, which may change abruptly in depth. Many of their edges are rounded. Individual fractures curve broadly, change direction over short distances, and partly or fully enclose roughly polygonal areas that range in size from a few kilometers to about 20 km in diameter (Morris and Underwood, 1978). Some fully closed fractures form well-defined single or double concentric rings.

Two major areas of curvilinear polygonal ground cover millions of square kilometers in Acidalia Planitia (fig. 1, west of long 355°) and in much of Utopia and Elysium Planitiae (fig. 1, east of long 275°). These areas are located in southward-projecting, low reentrants of the northern plains into the southern highlands. Knobby hills, thought to reflect outliers of highlands in the northern plains (Maxwell, in press), and polygonal ground are mutually exclusive.

The layer of material that contains the fractures is known to be relatively thin, as it reflects underlying topography. Especially obvious are buried craters, whose surface expressions are fracture rings (Helfenstein and Mouginis-Mark, 1980; McGill, 1985). In places double rings are stepped down toward the center of the rings; apparently the superposed material collapsed into an underlying crater cavity. The influence of underlying topography on the fractured layer suggests that the fracturing is restricted to that layer. The curvilinear fractures, in contrast to the rectilinear fractures, appear to be a surficial phenomenon that is restricted in depth; apparently curvilinear fractures do not reflect deep-seated structures.

Our observations support McGill's (1985) hypothesis that the curvilinear fractures formed by compaction and fracturing of sediments over buried topography. The association of curvilinear fractured ground with low reentrants of the northern plains that project southward into the highlands supports McGill's contention that curvilinear polygonal ground may have formed in areas where slurries from the outflow channels came to rest.

References

Black, R.F., 1978, Comparison of some permafrost features on earth and Mars: some cautions and restrictions: Proceedings Second Colloquium on Planetary Water and Polar Process, Hanover, New Hampshire, 16-18 Oct., 1978, U.S. Army Cold Regions Research Engineering Laboratory, Hanover, New Hampshire, p. 127-130.

Coradini, M., and Flamini, E., 1979, A thermodynamic study of the martian permafrost: Journal of Geophysical Research, v. 84, no. 14, p. 8115-8130; Helfenstein, P., 1980, Martian fractured terrain: possible consequences of ice-heaving [abs.]: Reports of Planetary Geology - 1980, NASA Technical Memorandum 82385, p. 373-375.

Helfenstein, P., and Mouginis-Mark, P.J., 1980, Morphology and distribution of fractured terrain on Mars [abs.]: Lunar and Planetary Science XI, Lunar and Planetary Institute, Houston, p. 429-431.

Maxwell, T.A., Evolution of the cratered terrain-smooth plains boundary in the Amenthes Region of Mars: Journal of Geophysical Research, Supplement, in press; McGill, G.E., 1985, Age and origin of large martian polygons [abs.]: Lunar and Planetary Science XIV, Lunar and Planetary Institute, Houston, p. 534-535.

Morris, E.C., and Underwood, J.R., 1978, Polygonal fractures of the martian plains [abs.]: Reports of Planetary Geology Program, NASA Technical Memorandum 79729, p. 97-99.

Pechmann, J.C., 1980, The origin of polygonal troughs on the northern plains of Mars: Icarus, v. 42, p. 185-210.

Sharp, R.P., 1973, Mars: Fretted and chaotic terrains: Journal of Geophysical Research, v. 78, p. 4073-4083.

Figure 1

Polygonally fractured ground in the northern hemisphere of Mars. Rectilinear polygonal ground (solid black); curvilinear polygonal ground (hachures).

LAVA-ICE INTERACTIONS ON MARS

D. E. Wilhelms, U.S. Geological Survey (MS-946), Menlo Park, CA 94025

Diverse phenomena that I attribute to the interaction of basaltic lava with ice-rich sediment characterize ten geologic provinces in a large area of Mars between lat 30° N.-30° S. and long 115°-225° W.

Aeolis province (MC-15 SW, MC-23 NW):--An intricately textured deposit near Aeolis Mensae has provided some of the most definitive clues to lava-ice interaction [1]. Narrow ridges are probably moberg dikes formed by intrusion of basalt sills into ice-rich ground and subsequently exhumed by erosion. Volcanic debris created during the interaction has been mobilized by meltwater and flowed as lahars.

Elysium-Hecates province (MC-7 SW, SC; MC-15 NW):--Channeled, thick, irregularly textured deposits originating near Elysium Mons and Hecates Tholus are probably megalahars created by the intrusion of lava into an ice-rich substrate [2]. Several moberg tablemountains and ridges [3] were formed by intrusions into the lahars, showing that the lahars retained interstitial ice for some time after deposition. The exhumation of the resistant tablemountains and a distinctive etched texture of the lahars shows that the lahars, unlike martian lavas, were subject to erosion. Fluid lahars (jökulhlaups) were generated by lava flowing over ice-rich ground [4]. These flows have eroded exposed parts of the thicker lahars.

Phlegra-Orcus province (MC-15 NE):--The thick, distinctively etched, viscous lahars and the smoother, fluid, erosive flows are also evident near Phlegra Montes, Orcus Patera, and other dense concentrations of knobby terrain. Lavas apparently dominate other parts of northern Elysium Planitia. These spatial associations indicate that the knobby terrain was the source of the meltwater in the lahars and jökulhlaups.

Apollinaris (MC-8 SW, MC-15 SE, MC-16 NW, MC-23 NE):--Much of the upland-lowland front (ULF) is characterized by soft-textured, easily erodable deposits called the Medusae Fossae Formation (MFF) [5] and interpreted as silicic ignimbrite [5,6], stranded former polar deposits [7], aeolian deposits [8], or palagonitic mudflows (lahars) [9]. Concentration of thick beds of the MFF near the evident volcano Apollinaris Patera suggests that the MFF is volcanic in origin, although partly eroded and redistributed by the wind. Partly degraded and partly resistant materials like those of the Elysium-Hecates lahars form the contact between the soft material and the Elysium plains, and also form islands in the plains. Thus I suggest that basaltic lavas from Apollinaris interacted with ice-rich material along the ULF, forming the lahars and also creating abundant palagonitic tuff that constitutes the soft material of the MFF. Fluid jökulhlaups mobilized by meltwater from these interactions swept over southern Elysium Planitia, eroding the lahars and crater rims and depositing extensive though thin sediments very recently in martian history.

Amazonis Planitia (MC-8 NW, NE, SW):--Some of the jökulhlaups that originated near Apollinaris and elsewhere flowed NW along a broad braided channel into Amazonis Planitia [10], where they deposited sediment over a large area. This sediment is eroded into distinctive, irregular, cell-like textures whose hollows probably represent concentrations of less resistant debris than that which forms the "cell walls" and plateaus.

Nicholson province (MC-8 SW, MC-16 NW):--The soft MFF terrain is replaced along the ULF between the crater Nicholson (0°, 164° W.) and long. 172° W. by dark and light stratified mesas surrounding knobby terrain. The overall map pattern of degraded terrain and resistant mesas, many of which are sinuous, is like that of the Elysium-Hecates lahars except that more material has been removed here. Very small pedistal craters with extensive but partly eroded ejecta blankets show that the wind has removed some of the MFF. More severely eroded pedistal craters occupy broad valleys whose geometry suggest fluid-flow origin. Erosive jökulhlaups originating from the lahars or the original zones of lava-ice interaction probably formed these valleys and removed most of the MFF. The redeposited MFF sediment merges with the cell-textured sediments of northern Amazonis.

Medusae Fossae-Gordii Dorsum province (MC-8 SW, SE; MC-16 NW, NE):--This most complex and also best photographed province has provided good insights into the process of lava-ice interaction. It contains thick, extensive, stratified deposits of the soft facies of the MFF, which I interpret as palagonitic tuff. The MFF has been eroded into yardangs [9], whose orientations differ in the various layers, and has been redistributed locally as eolian dune fields. Windows eroded in these soft deposits reveal lahars, probable lava sills, fluid-flow lineations emanating from beneath the sills, channels eroded by fluid flow, sediments deposited from the flows, probable moberg dike complexes, and tablemountains.

Mangala Valles (MC-16 NE):--Based on the relations reported above, I interpret the complex, braided, outflow channel system Mangala Valles [11] as another product of lava-ice interaction. Dark, coherent, plains that are probably lava occupy the floors of many craters, a large trough between massifs of the >2,000-km-diameter "Daedalia" basin, and belts of upland parallel to Mangala and the Daedalia rings. The same material also forms a sinuous intrachannel ridge (7.5° S., 151.5° W.), which apparently formed by flow of lava in an earlier, smaller channel and was exhumed by erosion of weaker material of its former banks. I suggest that episodic lava intrusions melted ice contained in the upland deposits, and the meltwater cut the channel system.

Fluid flows emanating from the mouth of Mangala (4° S., 150.5° W.) and from parallel channels have eroded a broad path through the MFF and crater ejecta as far as 9° N., 153.5° W. This erosion is like that of the Nicholson province, and its sediment adds to the Amazonis deposit.

Olympus-Biblis province (MC-8 NE, SE; MC-9 NW, SW):--Lahars like those of the Elysium-Hecates province occur NE of Olympus Mons. My work further supports the general conclusion of [12] that the much-studied, controver-

sial Olympus Mons aureole is another manifestation of lava-ice interaction. Part of the northern Medusae Fossae-Gordii province displays the same short, irregular ridges that characterize the aureole. The ridges of the NW-most aureole lobe have a gridlike pattern lacking evident pull-apart gaps, suggesting that this lobe formed nearly in place. Most of the aureole, however is partly allochthonous, having slid outward along decollement surfaces from an origin closer to the mountain [13,14]. This relation is particularly evident where the SE aureole lobe has overthrust older terrain NW of Biblis Patera. I suggest that meltwater from the lava-ice interaction lubricated the flow. Furthermore, flow patterns of some of the weblike sediments of Amazonis suggest sources in the aureole.

Uplands (MC-16; MC-23):--I believe that a global layer of ice-rich upland material was the ultimate source of the ice whose meltwater converted basalt into the palagonitic material that now constitutes much of the lowland provinces. Loss of some of this ice converted the upland deposit into knobby terrain along much of the ULF and in northern-plains outcrops such as those of the Phlegra-Orcus and Nicholson provinces. However, sufficient ice remained to interact with the lava to form lahars and the MFF, and the uplands retained still more of the ice in more cohesive deposits.

Much of the evolution of the landscape of Mars has resulted from this process, highly diverse in detail but basically originating from the inevitable interaction of two of the most common martian geologic materials, ice and basalt.

---

[1] Squyres S.W., Wilhelms D.E., & Mossman A.C. (submitted to Icarus)
[2] Christiansen E.H. & Greeley R. (1981) Lunar Planet. Sci. XII, 138-140.
[3] Allen C.C. (1980) Jour. Geol. 88, 108-117.
[4] Mouginis-Mark P.H. (submitted to Icarus)
[5] Scott D.H. & Tanaka K.L. (USGS I-Map in press)
[6] Scott D.L. & Tanaka K.L. (1982) Jour. Geophys. Res. 87, 1179-1190.
[7] Schultz P.H. (submitted to Icarus).
[8] Carr M.H. (1981) The Surface of Mars: Yale Univ., 232 p.
[9] Ward A.W. (1979) Jour. Geophys. Res. 84, 8147-8166.
[10] Moore H.J. (1982) NASA TM 85127, 213-215.
[11] Baker V.R. (1982) The Channels of Mars: Univ. Texas, 198 p.
[12] Hodges C.A. & Moore H.J. (1979) Jour. Geophys. Res. 84, 8061-8074.
[13] Lopes R., Guest J.E., Hiller K., & Neukum G. (1982) Jour. Geophys. Res. 87, 9917-9928.
[14] Tanaka K.L. (1985) Icarus 62, 191-206.

RELATION BETWEEN THICKNESS AND DEGRADATION OF MARTIAN UPLAND DEPOSITS
D. E. Wilhelms, R. J. Baldwin, and C. J. Hayden, U.S. Geological Survey (MS-946), Menlo Park, CA 94025

Degradation-prone deposits apparently are superposed on much of the ancient cratered basement of Mars. Their many styles of breakup (chaos, knobs, frets, channels, gullies, etc.) suggest that they are or were ice-rich. We have begun to study their poorly known lithologies, thickness, and spatial and stratigraphic variability. Here we report an attempt to determine the relation between their thickness and degradational style by measuring the areas of geologic units in 6 regions and determining the effects of degradation on craters in 2 of these regions (Figs. 1-3).

The three most extensive and distinctive types of unit are (a) dark, smooth plains that retain sharp-rimmed impact craters and that we interpret as basalt; (b) light-colored, ridged plains commonly also assumed to be volcanic because they are wrinkled like the lunar maria; and (c) gullied terrain ("valley networks"), alteratively thought to have an atmospheric or an endogenic cause [1-4]. "Other" terrain consists mostly of basin massifs (common in eastern third of Fig. 1), extensive ungullied crater deposits, and crater interiors unoccupied by dark plains or ridged plains.

The areal proportions between the possible volcanic materials and the gullied terrain were measured (Fig. 2) to test the hypothesis that internal heating caused the gullying by melting ice contained in the deposits. The areas of dark plains (mostly within craters) and gullied terrain do correlate positively, but probably not strongly enough to demonstrate a genetic relation. Nevertheless, the very great lateral differences in the gullied-terrain areas suggest a nonatmospheric origin. Ridged plains (abundant outside as well as inside craters) show no areal correlation with either

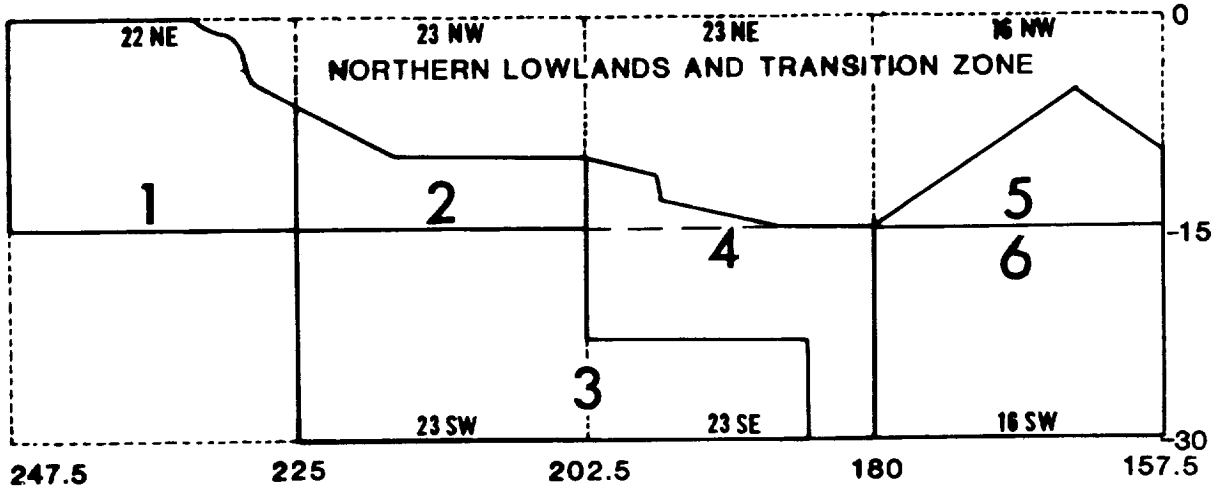

Fig. 1. Study area, divided into 6 regions in parts of 7 1:2M-scale Mars Chart photomosaics (MC). Northern lowlands and transition zone were excluded from study. MC-23 SE was divided into two geologically dissimilar parts, which were combined with geologically similar adjacent regions.

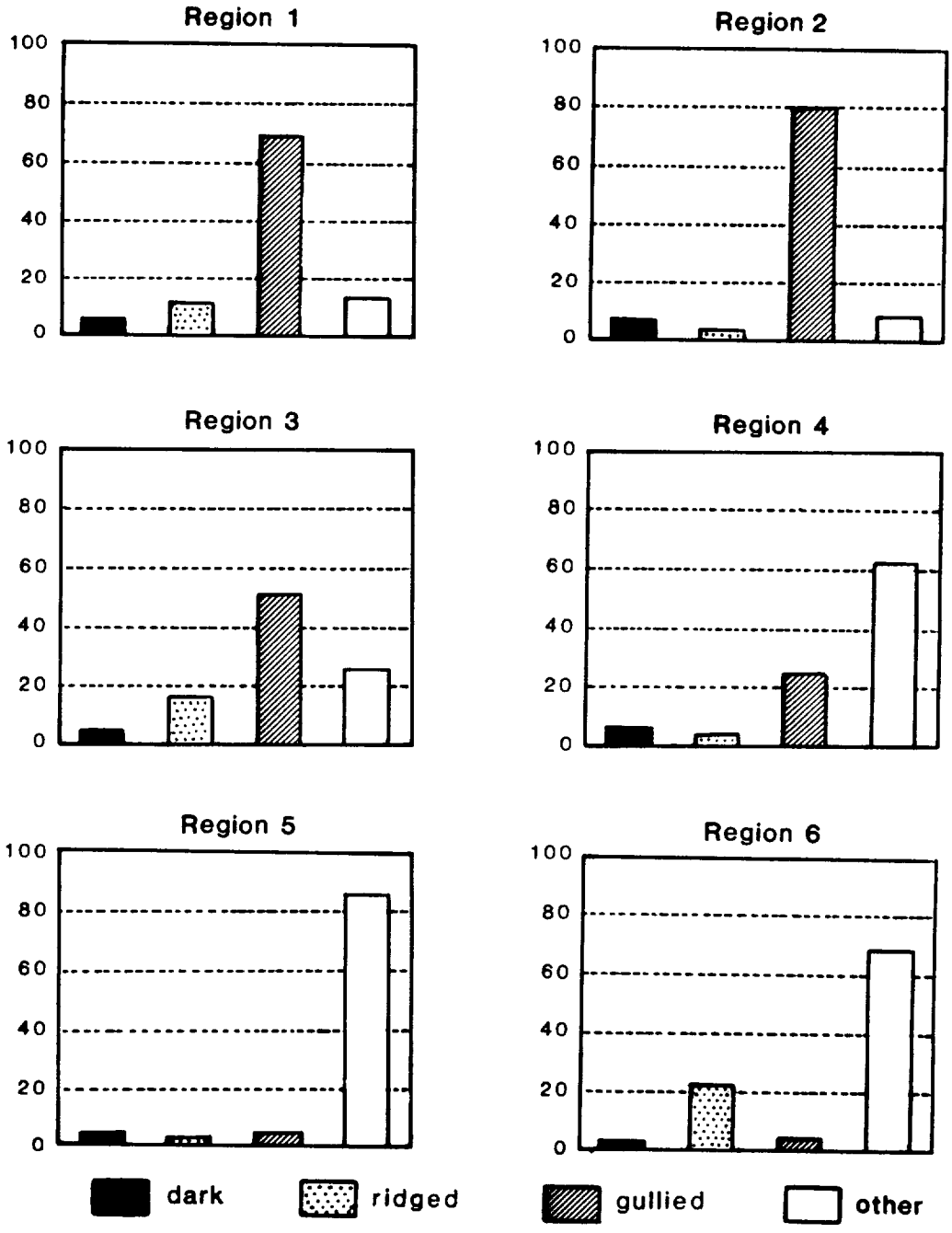

Fig. 2. Areas of four types of geologic unit. Scale, percentage of area.

the dark plains or the gullies, and we consider the origin of the ridged plains to be unknown.

Crater degradation was determined in two large areas that have distinct geologic styles (Fig. 3). For convenience, 3 degradational classes of craters are referred to by age terms. "Young" craters are far more numerous, and "intermediate" craters (especially small ones) somewhat less numerous, in the nearly ungullied reg. 6 than in the densely gullied reg. 1. This indicates that reg. 6 has suffered less degradation of all kinds than reg. 1. The fact that reg. 6 also has more total craters than reg. 1 probably means that deposits capable of burying craters are thinner in reg. 6. Thus, gullying seems to require the presence of a thick upland deposit.

[1] Pieri D.C. (1980) Science, v. 210, p. 895-897. [2] Carr M.H. (1981) The surface of Mars: Yale Univ. Press, p. 136-139. [3] Baker V.R. (1982) The channels of Mars: Univ. Texas Press, p. 41, 56-64. [4] Clow G.D. (submitted to Icarus).

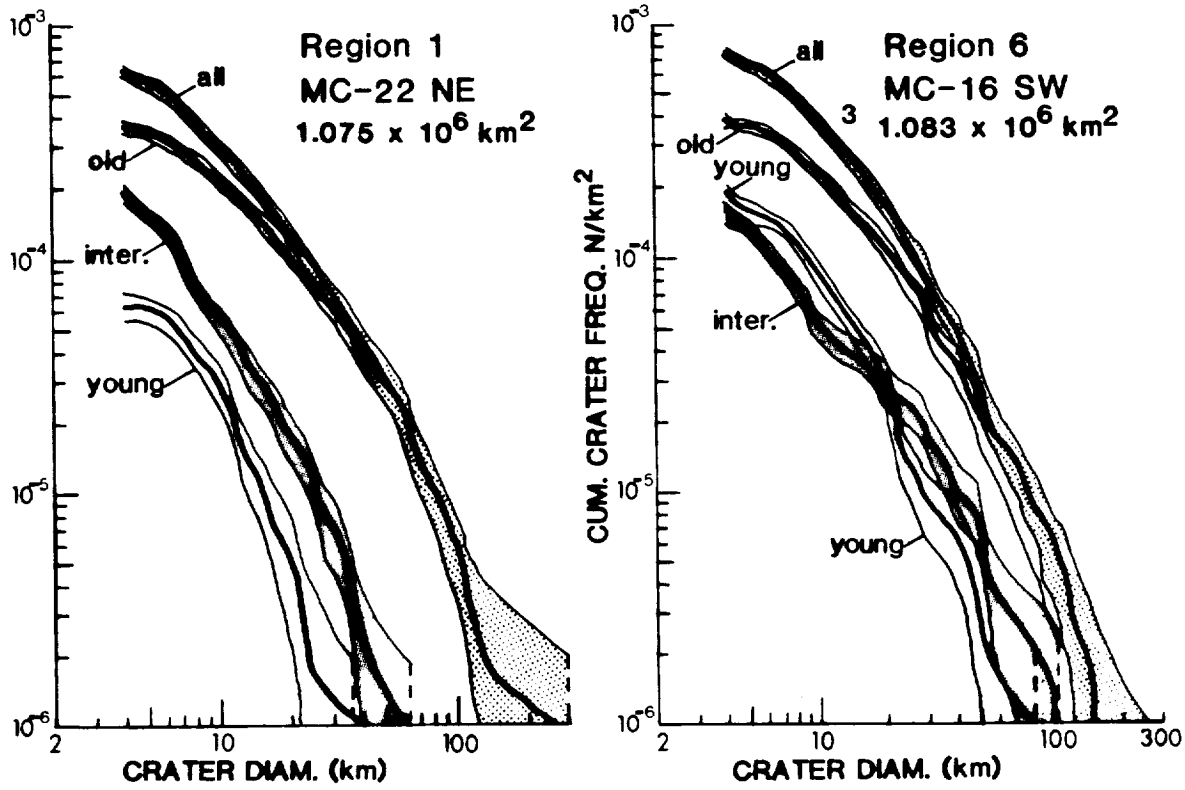

Fig. 3. Cumulative size-frequency distributions of three degradational classes of craters ≥4 km in diameter. "Young" = ejecta and secondary craters appear unmodified at the scale of the photos in the mosaics. "Inter." (intermediate) = ejecta visible but gullied or otherwise modified. "Old" = no visible ejecta except immediate rimflank. Solid lines connect data points; envelopes connect end points of 1-sigma error bars.

CHAPTER 12

REMOTE SENSING AND REGOLITH STUDIES

VEGA LANDING SITES: VENERA 15/16 GEOLOGIC UNIT ANALOGS FROM PIONEER/VENUS REFLECTIVITY AND RMS SLOPE

D.L. Bindschadler[1], J.W. Head[1], and J.B. Garvin[1]; 1) Dept. Geological Sciences, Brown Univ., Providence, RI 02912; 2) NASA Goddard, Greenbelt, MD 20771.

The Vega 1 and Vega 2 spacecraft landed on Venus in June of 1985. Information from the landers on the physical and geochemical properties of the surface may provide important constraints on models of the formation and evolution of the surface of Venus. Although the Vega landing sites are located to the south of the portion of Venus imaged by the Venera 15 and 16 radar mapping orbiters, it would be useful to know how the regions surrounding the landing sites compare to the geologic units mapped on the basis of Venera images (1). The Vega landing sites are located in Rusalka Planitia, on the northern flank of Aphrodite Terra. Vega 1 landed at 7.2°N, 177.8°E, approximately 0.4 km above the planetary datum of 6051.0 km, and Vega 2 landed at 6.45°S, 181.1°E, at an elevation of 1.7 km (2).

A region 2° square centered on each of the two Vega landing sites has been analyzed for rms slope and reflectivity properties using the Pioneer Venus (PV) radar data (2,3). Vega 1 landed in a region with a mean rms slope of 1.8° and a standard deviation of ±0.4°. The region centered on the Vega 2 landing site is somewhat smoother, with a mean and standard deviation in roughness of 1.1° ±0.3°. Both regions lie within the low (smooth) range (<2.5°) of rms slopes (4). Reflectivity measurements at the two sites are 0.12 ± 0.02 percent for Vega 1 and 0.15 ± 0.03 percent for Vega 2, within the moderate range (predominantly rocky) for reflectivity data (0.1 to 0.2 percent) (4). Such values of reflectivity and roughness have been interpreted to indicate that the surface is relatively smooth on the scale of meters to tens of meters and that it is dominated by low porosity rock surfaces (with a minor soil component) probably composed of silicates with little or no enrichment of metals (4).

Digital images of the Pioneer Venus data and the Venera 15/16 unit map have been placed in the same map projection (5) and the location of regions with rms slopes and reflectivities similar to the Vega landing site regions have been noted. To find the Venera unit most analogous in roughness and reflectivity to the Vega 1 or 2 landing site, the percent area covered by best matching regions in each unit was measured. Since the images are in an equal-area projection, the number of matching picture elements (pixels) within a given unit is directly proportional to the area covered by such pixels. Thus, dividing the area covered with matching pixels within a given unit by the total area of that unit will yield the percent coverage of a unit by landing site equivalent regions. The percent coverage of landing site roughness and reflectivity equivalents is shown in Table 1 along with a residual percentage. Because of the large difference in absolute area covered by the Vega 1 and Vega 2 site equivalents, this residual was calculated to allow a comparison between the set of numbers for each landing site. It is calculated by taking the difference between the percent Vega 1 or 2 equivalents for a given unit and the percent that would be expected if the site equivalents were randomly distributed over the surface and normalizing the difference to that random distribution percentage.

For the Vega 1 landing site, all the plains units possess positive residuals. The highland smooth plains and the band and ring plains (Table 1) are most similar to Vega 1 in terms of reflectivity and rms slope, with residuals of +0.63 and +0.46, respectively. Of the remaining units, only the volcanoes unit residual is non-negative and this positive residual appears to

be largely due to the concentration of Vega 1 equivalents in Lakshmi Planum, near and within the calderae Colette and Sacajawea. A striking anticorrelation is seen in the banded and parquet terrain. Only a few regions within these two terrains possess the same reflectivity and rms slope properties as the Vega 1 site. The combined Pioneer Venus data and Venera 15/16 map suggest that the Vega 1 landing site is most like Lakshmi Planum in terms of reflectivity and rms slope. The Vega 2 landing site lies at a somewhat higher altitude than the Vega 1 site, has slightly lower rms slope properties, and slightly higher reflectivity. For these values of reflectivity and roughness there are only approximately one-fifth the number of Vega 2 equivalents as there are for Vega 1. The ridge and band plains have the highest percentage of their area containing Vega 2 equivalents and also display a highly positive residual (+3.39). The Vega 2 equivalent values show two distinct areal groupings, one in central and western Atalanta Planitia, and one in Mnemosyne Regio. Both areas contain broad regions of ridge and band plains. While the band and ring plains show a more strongly positive residual for the Vega 2 site than did the highland smooth plains for the Vega 1 site (+0.87 vs. +0.63), this residual is much smaller than the value for the ridge and band plains. Most of the other units show relatively weak residuals, implying that the presence of Vega 2 equivalent regions within the terrains is due to random statistical fluctuations. Again, however, the banded terrain and parquet terrain are very poorly correlated with the Vega landing sites. The present data suggest that the ridge and band plains are the closest analog to the Vega 2 landing site in terms of reflectivity and rms slope.

In conclusion, we find that in terms of roughness and reflectivity characteristics, the Vega 1 and 2 sites are most similar to plains units in the Venera 15/16 area and differ substantially from other types of units (parquet, banded, etc.). Vega 1 equivalents are widespread, covering over 12% of the mapped area, while Vega 2 equivalents cover less than 3% of the mapped area.

1. Barsukov, V.L. et al., The geology and geomorphology of the Venus surface as revealed by the radar images obtained by Veneras 15 and 16, J. Geophys. Res., in press, 1985.
2. Barsukov, V.L., Presentation to the International Astronautical Federation Stockholm, Sweden, October, 1985; Head, J.W. et al., Vega landing sites: Geological characteristics of the surrounding region, Rusalka Planitia, Venus, (abstract) to be submitted to Lunar and Planet. Sci. Conf. XVII, 1986.
3. Garvin, J.B. et al., Lunar and Planet. Sci. Conf. XV, 292-293, 1984.
4. Head, J.W. et al., J. Geophys. Res., 90, B8, 6873-6885, 1985; Garvin, J. B. et al., J. Geophys. Res., 90, B8, 6859-6871, 1985.
5. Bindschadler, D.L. and Head, J.W., The characterization of Venera 15/16 geologic units using Pioneer/Venus roughness and reflectivity data, in preparation, 1985.

Table 1

Similarity of Venera Units to Vega Landing Sites

Unit[3]		Vega 1		Vega 2	
		% Area[1]	Residual[2]	% Area[1]	Residual[2]
Ps	smooth plains	15.0	+0.18	1.6	-0.30
Phs	highland smooth plains	20.7	+0.63	2.2	-0.04
Ppr	patchy rolling plains	16.1	+0.27	3.3	+0.43
Pdb	dome and butte plains	13.1	+0.03	1.6	-0.30
Pbr	band and ring plains	18.5	+0.46	4.3	+0.87
Prb	ridge and band plains	13.7	+0.08	10.1	+3.39
vol	volcanoes	16.2	+0.28	1.8	-0.22
du	domelike uplifts	4.2	-0.67	2.2	-0.04
ov	ovoids	9.7	-0.24	2.2	-0.04
bt	banded terrain	1.3	-0.90	0.1	-0.96
rb	ridge belts	9.5	-0.25	2.1	-0.09
fb	furrow belts	4.3	-0.66	4.0	+0.74
pq	parquet terrain	4.6	-0.64	0.7	-0.70
Total map		12.7%		2.3%	

[1] Percent area of a given unit covered by Vega 1 or 2 reflectivity and rms slope equivalents.

[2] Percent area covered by Vega 1 or 2 equivalents minus percent areal coverage of that unit, normalized to the total percentage covered by Vega 1 or 2 equivalents.

[3] Unit names based on ref. (1).

IDENTIFICATION OF GEOLOGICAL UNITS REPRESENTING THE SPECTRA OBTAINED BY THE SHUTTLE MULTISPECTRAL INFRARED RADIOMETER FOR A PORTION OF THE TRANS PECOS, TEXAS.

H. Grady Blount II[1] and James L. Whitford-Stark[2]. (1) Department of Geological Sciences, University of Texas at El Paso, El Paso, TX 79968. (2) Department of Geology, Sul Ross State University, Alpine, TX 79832.

Shuttle Multispectral Infrared Radiometer (SMIRR) data for a portion of the Trans Pecos, Texas was obtained in November of 1981. Analysis has been made (Blount, 1985) of an area that is 100 km long and 100 m wide, extending from the Rio Grande near the town of Candelaria to SW of Fort Stockton (see Blount and Whitford-Stark, 1985). The database comprises 1,800 records, with ten wavelengths being recorded within each record.

The study area was divided into three primary geologic regimes: 1) The Sierra Vieja mountains, composing the first 13.5 km of the groundtrack. This is a rugged terrain, composed primarily of tuffs, rhyolites, ignimbrites, and shales. The region is terminated by the Candelaria Rim, an escarpment rising some 400 m above the level of the Rio Grande floodplain. 2) The Marfa Plain region continues for the next 37.5 km and, with the exception of Capote Peak and Ryan's slot, is characterized by gently rolling desert grasslands. Capote Peak is composed of tuffs and welded tuffs. Ryan's Slot consists of detritus derived from adjacent ledges of sandstone, tuffaceous sandstone, and conglomerates. The groundtrack also crosses the Petan Basalt before reaching the Quaternary alluvial plains which make up the majority of this section. 3) The Davis Mountains form the last 50 km of the study area. Hilltop exposures consist of ash flows, trachyte, sandy tuffs, and intrusions of rhyolitic composition. Valley fills are composed of detritus from the hilltops. All three regimes share the common characteristics of low vegetation cover, low mean rainfall, high ground exposure, low population density, and very little chemical weathering or manmade disturbance of the terrain.

A sample of alluvium was obtained from a flay-lying and uniformly illuminated area to the northeast of Capote Peak. This sample, which was used as a normalization standard was sent to Barringer Research, Toronto where laboratory reflectance measurements were performed, these being relative to Kodak BASO 4 standard. Spectra were then produced for twenty three-geologic units (see figs). Unique and consistent spectral signatures were found for the rhyolitic and trachytic units. Likewise unique but isolated spectral signatures were found for a shale, vitrophyre, basalt, ignimbrite, and sandstone. No consistent pattern existed for the six tuff units that were examined. Current research is investigating the reasons for this variability.

Acknowledgement: H.G.B. ackowledges financial support from the Chihuahua Desert Research Fund.

References: Blount, H.G. 1985 An interpretation of Shuttle Multispectral Infrared Radiometer Data for a portion of the Trans -Pecos Texas. MS Thesis, Sul Ross State University. 128pp. Blount, H.G. and Whitford-Stark, J.L. NASA TM-87563 p432-433.

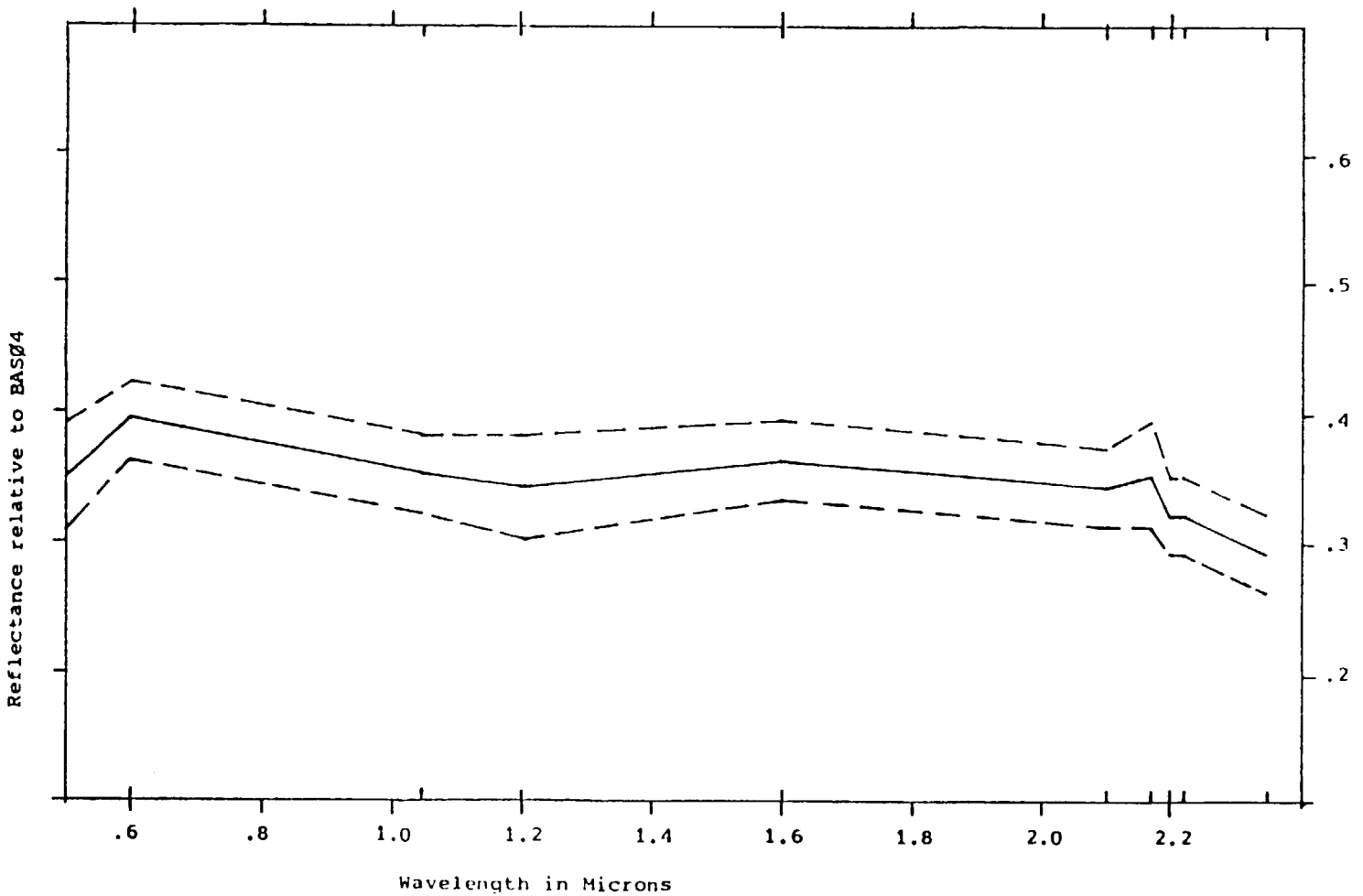

Brack's Rhyolite (Oligocene) Records 316-325 atop the Candelaria Rim. Dark brown to dark reddish brown rhyolite

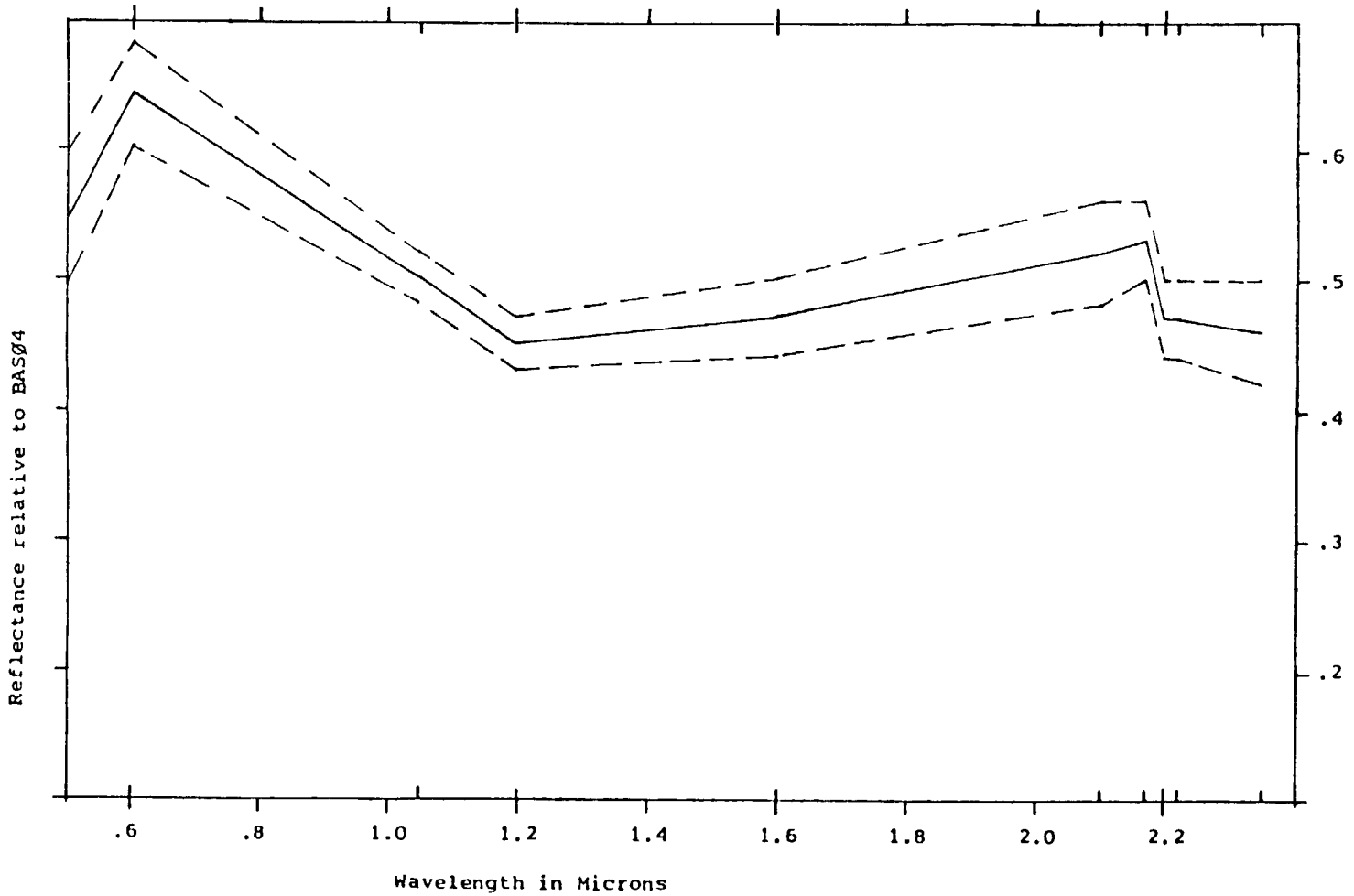

Ojinaga Formation (Upper Cretaceous) Records 277-286
Bright greenish yellow silty shale with abundant gypsum

Reflectance Measurements of Planetary Surface Materials at Small Phase Angles

B.J. Buratti, W.D. Smythe, R.M. Nelson, V. Gharakhani (JPL/Caltech), B. Hapke (U. of Pittsburgh)

It is well known that the surfaces of airless bodies exhibit an anomalous increase in brightness as their faces become fully illuminated to the observer. This "opposition effect" is generally explained as the disappearance of mutual shadowing among the particles of the optically active portion of the regolith. Theoretical models suggest that the regolith's porosity and albedo are the primary factors which determine the effect's amplitude and angular dependence. Very porous, fluffy surfaces should have the most pronounced opposition surges whereas high albedo surfaces should have small surges because multiple scattering illuminates shadows cast by the particles. Other determining factors include particle size and shape and the packing state of the regolith as a function of distance from the surface.

As yet, laboratory measurements of samples of controlled porosity and albedo have been difficult to obtain. We have constructed a goniometer which uses collimated laser light at 0.62 microns as a light source and diverts the light beam with a quartz beam splitter. Measurements below a phase angle of one degree are attainable on this apparatus (Figure 1).

The results of our first measurements show that dark, porous surfaces are not the only ones to exhibit large opposition surges. For example, a compacted sample of basalt with a measured normal reflectance of 0.26 and about 35% void space exhibits an increase in brightness of nearly 20% between phase angles of 3 and 1 degrees. This sample has the same reflectivity as Europa in the near UV and is similarly compact. However, remote sensing observations of Europa suggest that it has little or no opposition effect. This discrepancy should be resolved with the acquisition of additional UV data of Europa at small phase angles. Preliminary measurements from the IUE spacecraft (R. M. Nelson, personal communication) suggest that Europa does indeed have an opposition effect below one degree.

Figure 2 shows the results of our measurements for a fluffy (88% void) sample of the same basalt. It is compared to IUE measurements from Nelson et al. (B.A.A.S. 16, 684, 1984) and Voyager measurements (Simonelli and Veverka, Icarus, in press) for Io, which is believed to have a similarly fluffy surface based on eclipse measurements and cold-trapping models (Matson and Nash, J.G.R. 88, 4771, 1983). In this case agreement between the remote sensing data and laboratory measurements is good.

Figure 2 also shows that fits of our measurements to a computer program based on Irvine's shadowing model (J.G.R. 71, 2931, 1966) are in good agreement for porous surfaces. In the case of compacted surfaces, the model's predictions are good between 3 and 10 degrees, but at smaller phase angles, it underpredicts the size of the increase.

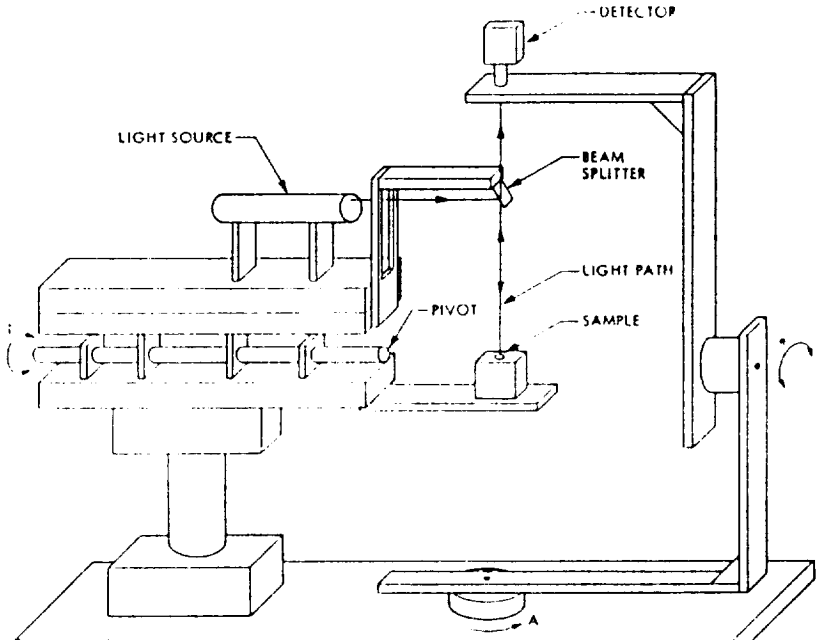

Figure 1. A schematic diagram of the goniometer. The light source is a He/Ne laser with an output at 0.62 microns. The incident (i), emission (e), and azimuthal (A) angles can be varied to achieve a full range in viewing geometries.

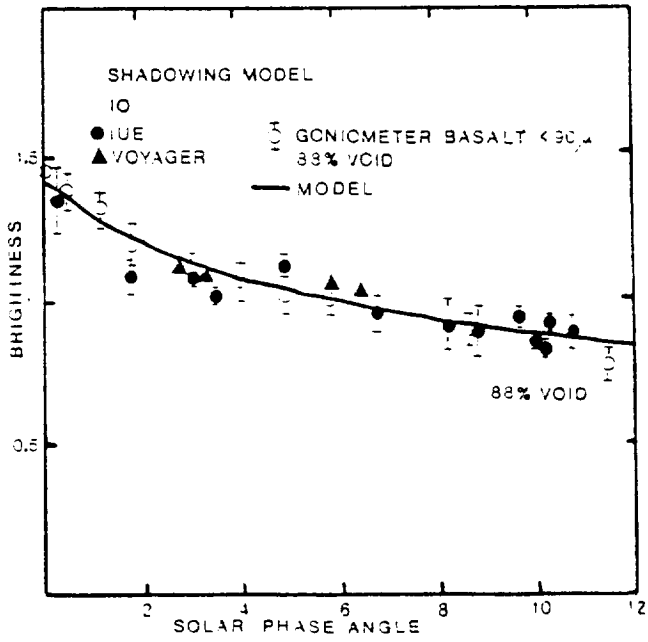

Figure 2. A comparison of our measurements of a fluffy sample of basalt with remote sensing observations of the solar phase curve of Io (Nelson et al., B.A.A.S. 16, 684, 1984; and Simonelli and Veverka, Icarus, in press). Also shown is a comparison of theoretical results of the Irvine shadowing model for the same porosity. All results are normalized to unity at 6 degrees.

CRYSTAL CHEMISTRY AND ORIGIN OF BLUE COLOR IN METEORITIC HIBONITES: EVIDENCE FROM MOSSBAUER SPECTRA OF IRON-57 DOPED ANALOGUES

Roger G. Burns, M. Darby Dyar, Virginia L. Ryan and Teresa C. Solberg, Department of Earth, Atmospheric and Planetary Sciences, Massachusetts Institute of Technology, Cambridge, Massachusetts 02139.

Introduction. Hibonite (ideally $CaAl_{12}O_{19}$), a significant constituent of refractory inclusions in carbonaceous chondrites, usually contains high concentrations of Mg and Ti, minor Si, and variable amounts of V, Cr, and Fe [1-3], any of which could be responsible for the characteristic blue color of this mineral [4]. Visible region spectra of blue hibonites [5] show absorption bands near 400 nm and 700 nm, with minimum absorption around 500 nm producing blue transmitted light. Several assignments have been proposed for the 400 nm and 700 nm bands [4,5] invoking different cation assemblages distributed over distinctive coordination sites in the complex crystal structure. A primary candidate is titanium which, as Ti^{3+} in five-coordinated trigonal bipyramidal Al(5) sites or coupled as Ti^{4+}-Fe^{2+} pairs in face-shared octahedral Al(3) sites, may participate in Ti^{3+} crystal field (CF) or $Fe^{2+} \rightarrow Ti^{4+}$ charge transfer (CT) transitions [4]. However, the presence of Ti^{3+} ions has been questioned on the basis of similar Mg and Ti cation proportions in meteoritic hibonites and the coupled substitution of $Mg^{2+} + Ti^{4+}$ for $2(Al^{3+} + V^{3+} + Cr^{3+})$ [1-3]. We report here the results of Mossbauer spectral measurements of ^{57}Fe-doped synthetic hibonites, equilibrated at ambient and low oxygen fugacities, which provide information on transition metal cation valencies and site occupancies in hibonite. We conclude that Ti^{3+} ions in five-fold coordination sites are responsible for hibonite's blue color.

Experimental Details. Hibonites were synthesized having compositions resembling the Murchison Blue Angel (#1, #2) [2] and other refractory inclusions (#3, #4) [3], Allende Ca-Al-rich inclusion (#5, #6) [1], and terrestrial Madagascar marble (#7) [6] assemblages [4]. Their compositions are listed in Table 1. Specimens #8 and #9 were chosen to exclude Fe and Mg, respectively. Note that specimens #1 and #2 contain no Si. Powders made from reagent-grade oxides, $CaCO_3$, and 95%-enriched $^{57}Fe_2O_3$ (#2, #4, #6, #7, and #9) were homogenized by mixing under methyl alcohol, stirring frequently, and drying in an oven, the process being repeated 3 times for each composition. The specimens were pelletized in a 5/16" steel die with no binder, and then suspended in a vertical quench furnace at 1430°C for 18 hours. Oxygen fugacities of 10^{-5} and 10^{-10} were obtained using H_2-CO_2 gas mixtures. Samples were quenched into a brine/ice bath (-21°C), found previously to be the most efficient practical quenching medium [7]. Hibonite integrities were checked by x-ray diffraction measurements, and Mossbauer spectra were recorded following standard procedures [8].

Results. Representative Mossbauer spectra of a synthetic ^{57}Fe-doped hibonite (specimen #2) are illustrated in Figure 1. The profiles clearly demonstrate that Fe^{3+} ions present in air-grown hibonites are absent in specimens equilibrated at $P_{O_2} = 10^{-10}$ atmos. The Mossbauer parameters obtained from computer-fitted spectra of the Blue Angel analogue (#2) show the predominance of five-coordinated Fe^{2+} ions (δ=0.92 mm.sec.$^{-1}$; Δ=0.45 mm.sec.$^{-1}$), and the presence of five coordinated Fe^{3+} (δ=0.26; Δ=2.57) and tetrahedral Fe^{3+} (δ=0.17; Δ=0.51) ions in the air-grown sample. The spectrum of the terrestrial Madagascar hibonite analogue, however, indicates the presence of some octahedral Fe^{2+} ions having parameters similar to ilmenite (δ=1.01; Δ=0.73).

Discussion. The small amounts of Si present in most meteoritic hibonites probably occupy tetrahedral Al(2) sites and are charge-balanced by Mg^{2+} ions entering nearby octahedral Al(1) and Al(4) sites [4]. Most titanium present as Ti^{4+} ions may be accommodated in face-shared Al(3) octahedra with local charge balance being maintained by the remainder of the Mg^{2+} ions occupying adjacent Al(3) sites, by analogy with geikielite ($MgTiO_3$) which possesses the ilmenite structure. However, surplus Ti could exist as Ti^{3+} ions in those hibonites in which Ti + Si > Mg (+ Fe^{2+}), particularly in specimens equilibrated at low oxygen fugacities. Cation ionic radius and crystal field stabilization energy criteria [4] suggest that such Ti^{3+} ions are enriched in the relatively large five-ccordinate Al(5) trigonal bipyramidal sites of hibonite, by analogy with Fe^{2+} ions shown by Mossbauer spectroscopy here to be concentrated in the five-coordinate sites. The color data summarized in Table 1 also correlate with the suggestion that surplus Ti^{3+} ions occupying Al(5) sites are responsible for blue colors of hibonites. However, Si appears to be necessary to enhance the blue coloration [9].

References. [1] Allen et al., Proc. 9th LPSC, 1209 (1978); Geochim. Cosmochim. Acta, 44, 685 (1980). [2] Armstrong et al., Geochim. Cosmochim. Acta, 46, 575 (1982). [3] Bar-Matthews et al., Geochim. Cosmochim. Acta, 46, 31 (1982). [4] Burns and Burns, J.G.R., 89 (suppl.), C313 (1984). [5] Stolper and Ihinger, Lunar Planet. Sci., XIV, 749 (1983). [6] Maaskant et al., Mineral. Mag., 43, 995 (1980). [7] Dyar and Birnie, J. Non-Cryst. Sol., 67, 397 (1984). [8] Dyar, Amer. Mineral., 69, 1127 (1984).
[9] Research supported by NASA grant no. NSG-7604.

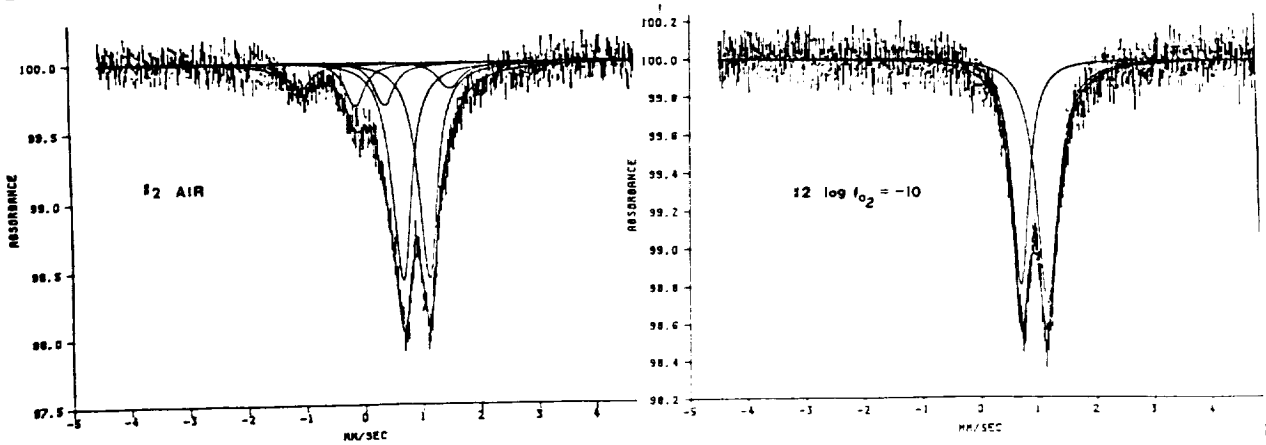

Table 1. Compositions and Colors of Synthetic Hibonites (Compositions expressed as cations per 19 oxygens in ideal formula $CaAl_{12}O_{19}$)

Specimen	#1	#2	#3	#4	#5	#6	#7	#8	#9
Ca	1.02	1.02	1.02	1.02	1.04	1.04	1.00	1.00	0.99
Al	11.68	11.68	11.16	11.16	10.61	10.61	10.45	11.10	10.96
V	-	-	0.12	0.11	-	-	-	-	-
Ti	0.17	0.17	0.35	0.35	0.65	0.65	0.49	0.44	-
Mg	0.11	0.11	0.34	0.34	0.65	0.65	0.49	0.44	-
Fe	-	0.01	-	0.01	-	0.01	0.40	-	0.44
Si	-	-	0.02	0.02	0.04	0.04	0.05	0.05	0.05
air	white	white	white	white	white	white	green	white	yellow
$P_{O_2}=10^{-5}$	white	white	pink	tan	white	white	green	white	yellow
$P_{O_2}=10^{-10}$	white	white	pink	blue/ green	blue	blue/ white	green/ blue	blue/ white	blue/ green

THE COMPOSITION OF THE MARTIAN SURFACE: DETERMINATION BY THERMAL INFRARED SPECTRAL OBSERVATIONS

P.R. Christensen, Department of Geology, Arizona State University, Tempe, Arizona 85287

The potential for compositional mapping of planetary surfaces by remote thermal infrared sensing has long been recognized (e.g. Lyon, 1962; Logan et al., 1975; Kahle and Goetz, 1983). This technique has been applied successfully to the study of several solar system objects: silicate reststrahlen features observed by the IRIS experiment on Nimbus 4 have been used to study the composition of deserts on Earth (Prabhakara and Dalu, 1977); thermal-IR spectral features have been observed in the lunar surface (Potter and Morgan, 1981); and strong spectral features are present in the 15-50 μm spectrum of Io (Pearl, 1983).

The fields of visible and infrared spectroscopy are based on the principle that atoms and molecules within a solid produce absorption bands whose wavelengths and strengths are characteristic of the composition and structure of the material observed. Visible and near-infrared reflectance spectra have been used to discriminate some geologic materials, in particular Fe, CO_3, H_2O and OH bearing clays and other weathering products (McCord et al., 1982a,b; Singer, 1982; Singer 1982; Goetz et al., 1982). However, many geologically important elements, including Si, Al, O, and Ca, do not produce absorption bands in the visible or near-infrared. Therefore, the presence of these elements can only be inferred indirectly from the changes they produce in observed absorption bands (Hunt and Salisbury, 1970), and their abundances cannot be determined.

In contrast, nearly all silicates, carbonates, sulfates, phosphates, oxides and hydroxides have mid-IR spectral features associated with the fundamental vibrational motions of the major elements (Fig. 1; e.g. Lyon, 1962; Hunt and Salisbury, 1974, 1975, 1976; Farmer, 1974). The vibrational energy, and therefore the wavelength, of these bands is diagnostic of both the anion composition and the crystal lattice structure. Thus, mid-IR spectra provide a direct means for identifying the composition of many silicates and other common materials and for interpreting the crystal structure, and therefore the mineralogy, of these materials. Used together, the mid-and near-IR spectral observations provide unique and complementary mineral identification and improved determinations of rock compositions.

The occurrence and spatial variability of strong absorption bands within the thermal-IR was observed in martian materials by the Viking Infrared Thermal Mapper (IRTM) experiment. With spatial resolution typically 30 km, variations of spectral emissivity, attributed to the surface, on the order of 0.1 were observed. The IRTM, however, was a broadband radiometer bandwidth 200 to 400 cm^{-1}) with bands centered at 1400, 1200, 900, and 500 cm^{-1} while the widths of individual thermal-IR spectral features found in most minerals range from 20 to 200 cm^{-1}. Therefore, the IRTM data lack the spectral resolution necessary to

distinguish between a number of reasonable geologic materials. For example, the emissivity variations observed by the IRTM could be produced by silicate rocks varying in composition from peridotite (ultramafic) to diorite (acidic), by hematite (iron oxide) or by kaolinite (hydroxide).

High spectral resolution (2.5 cm^{-1}) thermal-IR observations of Mars were made by the Mariner 9 Infrared Interferometer Spectrometer (IRIS) (Hanel et al., 1972). The IRIS spatial resolution, however, was 125 km at best, thus integrating large regions of differing composition. In addition, the IRIS investigation was designed for atmospheric study and most of the observations were made during an extensive dust storm; thus most analyses have emphasized atmospheric or dust properties (Conrath et al., 1973; Curran et al., 1973). Only a few spectral features have previously been attributed to the surface materials. Lacking analysis of emission angle dependence or day-night spectral contrast reversal during relatively clear conditions, an appreicable (possibly large) fraction of the spectral contrast attributed to atmospheric dust in the late Mariner 9 mission could, however, have been due to the surface.

Nearly 21,000 spectral were acquired by IRIS. Unfortunately, most of these cannot be used to derive surface composition because of the high atmospheric dust opacity during much of the Mariner 9 mission. The 23 available with suitable surface temperature and low atmospheric dust content do, however, show clear differences that vary systematically with surface albedo and thermal inertia. In particular, one set of 5 spectra taken within 12 days of each other show significant variation in the depth of the 9 and 7 μm band, the slope in the 20 to 30 μm region, and in the offset across the 15 μm CO_2 band (Fig. 3). As seen in the IRTM data, the strongest absorption occurs in regions of lowest albedo. In addition, a second set of spectra taken of six areas across a large region of uniform thermal inertia, but with increasing emission angle, show increasingly strong absorptions due to the presence of atmospheric dust. Extrapolation of the spectra on the basis of the secant of the zenith angle to zero air-mass indicates that, when the atmospheric component is removed, there is still an appreciable, and different, surface spectral signature.

The results from the IRTM and IRIS experiments demonstrate that thermal-IR spectral features exist in martian materials. These features vary across the surface and correlate in a systematic way with other surface properties. Variations in the thermal-IR spectral signature indicate differences in composition, although observations of Mars with both the necessary spatial and spectral resolution to uniquely identify rock compositions have not yet been made. The existing observations, together with our improving understanding of the spectral properties of rocks and minerals indicate that thermal-infrared spectral observations, with combined spatial and spectral resolution, would provide a powerful means for mapping the composition of the martian surface and atmospheric components.

REFERENCES

Conrath, B. et al., 1973, Atmospheric and surface properties of Mars obtain by infrared spectroscopy on Mariner 9, J. Geophys. Res., 78, 4267-4278

Curran, R.J. et al., 1973, Mars: Mariner 9 spectroscopic evidence for H_2O clouds, Science, 182, 381-383.

Farmer, V.C. (edt.), 1974, The Infrared Spectra of Minerals, Mineralogical Society, London, 539 pp.

Goetz, A.F.H., et al., 1982, Mineral identification from orbit: Initial resuls from the Shuttle Multispectral Infrared Radiometer, Science, 21 1020-1024.

Hanel, R. et al. 1972, Investigation of the martian environment by infrared spectroscopy on Mariner 9, Icarus, 17, 423-442.

Hunt, G.R., and J.W. Salisbury, 1970, Visible and near-infrared spectra of minerals and rocks. 1:Silicate minerals, Mod. Geology, 1, 282-300.

Hunt, G.R., and J.W. Salisbury, 1974, Mid-infrared spectral behavior of igneous rocks, Environ. Res. Paper 496-AFCRL-TR-74-0625, 142 pp.

Hunt, G.R., and J.W. Salisbury, 1975, Mid-infrared spectral behavior of sedimentary rocks, Environ. Res. Paper 510-AFCRL-TR-75-0256, 49 pp.

Hunt, G.R., and J.W. Salisbury, 1976, Mid-infrared spectral behavior of metamorphic rocks, Environ. Res. Paper 543-AFCRL-TR-76-0003, 67 pp.

Kahle, A.B., and A.F.H. Goetz, 1983, Mineralogic information from a new airborne thermal infrared multispectral scanner, Science, 222, 24-27.

Logan, L.M. et al, 1975, The use of mid-infrared spectroscopy in remote sensing of space targets, in Infrared and Raman Spectroscopy of Lunar and Terrestrial Minerals, C. Karr, (ed.), Academic Press.

Lyon, R.J.P., 1962, Evaluation of infrared spectroscopy for compositional analysis of lunar and planetary soils, Stanford Research Inst. Final Report Contract NASA 49(04).

McCord, T.B. et al., 1982a, Mars: Near-infrared reflectance spectra of surface regions and compositional implications, J. Geophys. Res., 87, 3021-3032.

McCord, T.B. et al., 1982b, Mars: Definition and characterization of global surface units with emphasis on composition, J. Geophys. Res., 87, 10129-10148.

Pearl, J.C., Spatial variation in the surface composition of Io based on Voyager infrared data, Bull. Am. Astro. Soc., 16, 654.

Potter, A.E., and T.H. Morgan, 1981, Observations of silicate reststrahlen bands in lunar infrared spectra, Proc. Lunar Planet. Sci. 703-713.

Prabhakara, C., and G. Dalu, 1976, Remote sensing of the surface emissivity at 9 μm over the globe, J. Geophys. Res., 81, 3719-3724.

Singer, R.B., 1982, Spectra evidence for the mineralogy of high-albedo soils and dust on Mars, J. Geophys. Res., 87, 10159-10168.

MARS WATER-ICE CLOUDS

[1]P.R. Christensen, [2]R.W. Zurek, and [1]R. Greeley, [1]Department of Geology, Arizona State University, Tempe, Arizona, 85287, [2]Jet Propulsion Laboratory, California Institute of Technology

The distribution of water in the martian atmosphere plays an important role in the present meteorology of Mars. It also provides a key to understanding the past climate and climatic changes because direct observations of water and other volatiles provide a means for testing models of volatile transport between the regolith and atmosphere, for determining sources and sinks of volatiles, and for determining the time scales for volatile migration (e.g. 1,2,3).

Many recent studies have addressed the questions of atmospheric water vapor distribution and possible sources and sinks of water on the surface using earth-based observations of water vapor abundances and observations obtained by the Viking Mars Atmospheric Water Detector (MAWD) (e.g. 4,5,6, 7, and many others). In addition to water vapor, however, condensed water in water-ice hazes and clouds plays an important role in the understanding of the processes controlling the distribution and history of water on Mars and must be included with water vapor in order to assess the total atmospheric water abundance. Furthermore, the presence of water-ice clouds provides direct evidence for the occurrence of saturation conditions within the atmosphere. Finally, the seasonal, diurnal, and spatial distribution of water clouds provides information about the variability of atmosphere water on these time scales and about the surface and atmospheric properties which influence cloud formation.

We have used Infrared Thermal Mapper (IRTM) mid-IR spectral observations to locate water-ice clouds using the infrared absorption properties of water-ice. The IRTM instrument obtained data in five thermal bands centered at 7, 9, 11, 15 and 20 μm, and one solar reflectance band between 0.3 and 3 μm (8). The thermal data are used to determine brightness temperatures, referenced to the band for which they were determined (i.e., T_7) that can be used to measure spectral variations in the martian surface and atmosphere due to non-uniform surface properties and atmospheric aerosols (9). In particular, the 11 μm band IRTM is located within a broad 10 to 18 μm absorption feature characteristic of water ice, and is therefore sensitive to the presence of water ice. The 20 μm band only partially overlaps this feature and the 7 and 9 μm bands are nearly transparent to water-ice. Thus, spectral observations can detect water-ice using differences between these brightness temperatures, provided there is sufficient contrast between the ground and atmospheric temperature (10).

Using this technique clouds and hazes have been detected and characterized on Mars through two years of observations. They are consistently observed in four northern hemisphere regions centered over Tharsis (-10°S to 50°N, 60° to 160°W), Arabia (0° to 20°N, 300° to 360°W), Elysium (20° to 40°N, 190° to 220°W), and along the boundary between the

cratered uplands and the northern plains (-10°S to 10° N, 210° to 270°W). Clouds in those regions were observed at all seasons when the atmosphere had a low enough dust content to permit the spectral signature of water-ice to be observed; during the global dust storm period (L_s 200° to 300°) clouds are difficult to distinguish from dust.

During the northern spring and summer (L_s 0° to 180°) when the atmosphere is relatively free of dust, there is a distinct difference between the cloud abundance in the northern and southern hemispheres, with clouds and hazes being rare in the south. There are several possible explanations for this difference. First, clouds will be less likely to form in the south due to low, wintertime atmospheric temperatures and high atmospheric stability (11). A second possibility involves the importance of orographic control for cloud formation, resulting in more clouds centered over topographic highs that are preferentially located in the north. Finally, northern hemisphere clouds appear to occur preferentially over low thermal inertia regions which are primarily located in the northern hemisphere. If seasonal rather than surface, control is the dominant effect then the observed cloud pattern should reverse during southern spring and summer. However, clouds are difficult to detect during southern summer due to the presence of atmospheric dust. Clouds are much less commonly observed in both the north and the south during this season, but their presence within or beneath the dust haze cannot be ruled out on observational grounds.

A second important class of water-ice clouds are those observed along the boundary of the retreating north polar cap between L_s 340° and 65° (10). These clouds occur at all longitudes around the cap and are generally confined to within ±5° of the cap boundary. After L_s 65° polar water-ice clouds are no longer observed. Similar clouds are not observed along the southern cap during retreat, although observations are again impaired by the presence of atmospheric dust during this season.

The cloud opacities can be estimated using a δ-Eddington radiative transfer model (10) which incorporates Mie scattering and the electrical properties of water-ice. Assuming realistic, but non-unique, values for the ice particle size and cloud temperature, the derived opacities range from near-zero to 1.

In summary, IRTM observations provide a direct means of identifying water-ice clouds on Mars. These observations have sufficient spatial resolution, and spatial and temporal coverage to permit a detailed investigation of the important parameters governing their formation. They are consistently observed in four major northern hemisphere locations and along the edge of the retreating north polar cap. The IRTM data are currently being assembled into an "atlas" to permit further studies of their diurnal and seasonal behavior.

REFERENCES

(1) Leovy, C.B., 1973, Exchange of water vapor between the atmosphere an surface of Mars, Icarus, 18, 120-125.
(2) Fanale, F.P., J.R. Salvail, W.B. Banerdt, and R.S. Saunders, 1982, Mars: The regolith-atmosphere-cap system and climate change, Icarus, 50, 381-407.
(3) Pollack, J.B. and O.B. Toon, 1982, Quasi-periodic climate changes on Mars: A review, Icarus, 50, 259-287.
(4) Barker, E.S., R.A. Schorn, A. Woszczyk, R.G. Tull, and S.J. Little, 1970, Mars: Detection of atmospheric water vapor during the southern hemisphere spring and summer season, Science, 170, 1308-1310.
(5) Farmer, C.B., D.W. Davies, H.L. Holland, D.D. LaPorte, and P.E. Doms, 1977, Mars: water vapor observations from the Viking orbiters, J. Geophys. Res., 82, 4225-4248.
(6) Davies, D.W., 1981, The Mars water cycle, Icarus, 45, 398-414.
(7) Jakosky, B.M. and C.B. Farmer, 1982, The seasonal and global behavior of water vapor in the Mars atmosphere: Complete global results of the Viking atmospheric water detector experiment, J. Geophys. Res., 87, 2999-3019.
(8) Kieffer, H.H., T.Z. Martin, A.R. Peterfreund, B.M. Jakosky, E.D. Miner, and F.D. Palluconi, 1977, Thermal and albedo mapping of Mars during the Viking primary mission, J. Geophys. Res., 82, 4249-4292.
(9) Christensen, P.R., 1982, Martian dust mantling and surface composition: Interpretation of thermophysical properties, J. Geophys. Res., 87, 9985-9998.
(10) Christensen, P.R. and R.W. Zurek, 1984, Martian north polar hazes and surface ice: Results from the Viking Survey/Completion mission, J. Geophys. Res., 89, 4587-4596.
(11) Kahn, R., 1983, Some observational constraints on the global scale wind systems on Mars, J. Geophys. Res., 88, 10189-10209.

MARTIAN DURICRUSTS: INTERPRETATION OF THERMAL, RADIO, AND RADAR DATA

P. R. Christensen[1] and B. Jakosky[2]. [1] Department of Geology, Arizona State University, Tempe, Arizona 85287; [2] Laboratory for Atmospheric and Space Physics, University of Colorado, Boulder, CO 80309

Introduction

The small-scale structure of Mars has been observed directly only at the two Viking Lander sites. Elsewhere, it is only through the use of remote-sensing data that the nature of the surface can be infered. Two of the most widely-used techniques, thermal infrared emission, and radar reflection, both measure properties that are dependent on the presence of surface crusts and rocks on the surface. Duricrusts are known to be present on the Mars surface, as evidenced by their presence at the Viking landing sites (Binder et al., 1977; Mutch et al., 1977) and by analysis of thermal infrared remote sensing data (Kieffer, 1976; Jakosky and Christensen, 1985). Important questions remain, however, such as: 1) are ubiquitously present; and 2) what processes lead to their formation. The duricrust seen at the lander sites is characterized by a cohesion greater than that expected for loose particulate fine material (Binder et al., 1977; Mutch et al., 1977) a salt concentration greater than that of neighboring unbonded material (Clark et al., 1982, Clark and van Hart, 1981) and an inferred presence either at or very near the surface everywhere at the Viking landing sites (Binder et al., 1977; Mutch et al., 1977). The global existence and distribution of this duricrust will be an important factor in understanding the nature and evolution of the near-surface layer.

Thermal data

Thermal infrared data can be interpreted in terms of the effective particle size of the surface (Kieffer et al., 1973). For the landing sites, the derived thermal inertia for the fines (after removing the effects of the observed rocks) is greater than that expected on the basis of the particle sizes observed (Kieffer, 1976; Jakosky, 1979); this difference has been attributed to the presence of a duricrust-type material, with bonding together of individual grains increasing the thermal conductivity, and hence the thermal inertia, of the fines (Kieffer, 1976). The observed diurnal temperature variations indicate that the fraction of the surface covered by rocks is relatively constant over the surface, and that variations in thermal inertia are controlled by variations in the thermal inertia of the fines (Christensen, 1982; 1985a). This observation suggests that it is the degree of formation of a duricrust which resulted in the observed distinction between the high and low thermal inertia regions.

Comparison with other remote-sensing data sets

The relatively low rock abundances found by Christensen (1982; 1985a) contrast with the larger abundances obtained by Jakosky and Muhleman (1981)

based on the observed correlation of thermal inertia and radar cross-section. In this latter model, the radar and thermal observations were explained by the presence of rocks controlling the observed thermal inertia. The discrepancy between the models was tentatively attributed to the choice of rock size in the diurnal thermal model. Alternatively, the presence of a global, ubiquitous duricrust of varying degree of formation can reconcile the radar and thermal observations. To produce the correlation of radar cross-section and thermal inertia requires that an increased thermal conductivity be associated with an increased bulk density; this occurs in a duricrust because the increased grain thermal contacts are produced by a deposition of salts or other mobile species by water, simultaneously filling the pores near the surface and increasing the density. The radar observations at 70 cm and at 12.5 cm indicate that scattering by surface and subsurface rocks plays a minor role in the correlations (Jakosky and Muhleman, 1981). These results are consistent with Earth-based 2.8 cm radio observations of Mars (Jakosky and Muhleman, 1980; 1981) and required no spatial variation of rock abundance. They are consistent with the 3.5 mm measurements reported by Epstein et al., (1983) if the high-inertia regions have a higher microwave emissivity at 3.5 mm than at 2.8 cm; that is, the density is greater and the duricrust is better formed some several centimeters below the surface than right at the surface.

Formation of duricrust

On Earth, duricrusts often result from a rising and falling water table (Fuller and Hargraves, 1978), although they may also form from salts deposited by small amounts of adsorbed water (Ugolini and Anderson, 1973; Clark, 1978). Their variable nature on Mars, correlated with the thermal inertia, must be consistent with the depositional formation (Zimbelman and Kieffer, 1979; Christensen, 1982) and current expansion (Christensen, 1985b) of the low-inertia regions and with the paucity of subsurface water (Jakosky, 1983). The duricrust may form from the movement of water in and out of the regolith on the 10^5-year timescale (Fanale and Jakosky, 1982), with the movement tending to concentrate salts near the surface because that is where the water would be the most mobile. This mechanism is consistent with a steady deposition of dust onto the low-inertia regions over this same period, with insufficient time having elapsed for a duricrust to form. In this model, dust accumulates in regions of active deposition more rapidly than the duricrust can form, creating the loose, unbonded deposits seen in low-inertia regions today. In regions where dust is not accumulating, and during periods of relative quiessence, duricrusts are formed at or near the surface. When water moves through the regolith, crusts form over the entire surface, these crusts may be subsequently eroded and the loose material redeposited to form new regions of low inertia. The location of the low-inertia regions is thereby postulated to be controlled by surface and atmospheric properties (Christensen, 1985b), and these may vary from cycle to cycle. The timescale for this process would be $>10^5$ years, and is consistent with global deposition and erosion

rates (Palluconi and Kieffer 1981; Greeley et al., 1982; Christensen, 1985b).

REFERENCES

Binder, A.B. et al., 1977, J. Geophys. Res. 82, 4439-4451.
Christensen, P.R., 1982, J. Geophys. Res. 87, 9985-9998.
Christensen, P.R., 1985b, J. Geophys. Res, in press.
Clark, B.C. et al, 1982, J. Geophys. Res. 87, 10059-10067.
Clark, B.C. and D.C. van Hart, _____, 1981, Icarus 45, 370-378.
Clark, R., 1978, Icarus 34, 645.
Ditteon, R., 1982, J. Geophys. Res. 87, 10197-10214.
Epstein, S. et al., 1983, Icarus 56, 465-475.
Fanale, F. and B. Jakosky, 1982, Planet. Space Sci. 30, 819-831.
Fuller, A.O., and R.B. Hargraves, 1978, Icarus, 34, 614-621.
Greeley, R., et al., 1982, J. Geophys. Res. 87, 10009-10024.
Jakosky, B.M., 1979, J. Geophys. Res. 84, 8252-8262.
Jakosky, B.M., 1983, Icarus, 55, 1-18.
Jakosky, B.M. and D.O. Muhleman, 1980, Astrophys. J. 239, 403-409.
Jakosky, B.M. and D.O. Muhleman, 1981, Icarus, 45, 25-38.
Jakosky, B.M. and P.R. Christensen, 1985, J. Geophys. Res, in press.
Kieffer, H.H. et al., 1973, J. Geophys. Res. 78, 4291-4312.
Kieffer, H.H., 1976, Science 194, 1344-1346.
Mutch T.A. et al., 1977, J. Geophys. Res. 82, 4452-4467.
Palluconi, F.D. and H.H. Kieffer, 1981, Icarus 45, 415-426.
Ugolini, F.C., and D.M. Anderson, 1973, Soil Sci. 115, 461-470.
Zimbelman, J. and H. Kieffer, 1979, J. Geophys. Res. 84, 8239-8251.

PETROLOGIC PROVINCE MAPS OF THE LUNAR HIGHLANDS DERIVED FROM ORBITAL GEOCHEMICAL DATA. P. A. Davis and P. D. Spudis, Branch of Astrogeology, U.S. Geological Survey, Flagstaff, Arizona 86001

Introduction. The lunar highlands consist of rocks and soils that are complex mixtures of pristine rocks (ferroan anorthosite, some KREEP basalts, and the Mg suite that includes troctolite, norite, dunite, and lherzolite) and of mare basalts. Most geochemical studies of the highlands [1-7] have concentrated on lunar sample data because they provide the basis for the determination of the existence, exact chemistries, and origins of pristine rock types. However, the global coverage provided by the Apollo 15 and 16 orbital geochemical data allows geologic inferences to be made for a large portion of the lunar equatorial region, despite the artificial mixing of mare and highland rock types that results from the poor resolution of these data (15 km for the X-ray data; 100 km for the gamma-ray data). Consequently, the orbital data have been used to infer the regional distribution of highland rock types, the relative proportions of pristine rocks in highland soils, and the role of pristine rocks in the origin of the lunar highlands [8-12]. In the present study, we have used all existing orbital geochemical data simultaneously to define more accurately and completely the distribution of distinct petrologic provinces in the lunar highlands. Our methods are similar to those used on sample geochemical data.

Methods. Longhi and Boudreau [3] and Norman and Ryder [6] showed that a plot of Sm/Ti and Mg^* (=100 Mg/Mg+Fe) for pristine lunar rocks separates most of these rock types into distinct fields. In our study, we examined two possibilities: (1) the attaining of a similar degree of separation between rock types by replacing Sm with Th in the Sm/Ti ratio, because of similar geochemical incompatibility of these two large-ion-lithophile elements in minerals that have commonly been involved in lunar igneous processes; and (2) the application of the observed rock-sample relations to the orbital geochemical data. We generated a digital image of both the Th/Ti and Mg^* ratios, using the Fe and Ti [13], Th [14], and Mg [9] orbital data. The resultant Th/Ti values were plotted against the Mg^* values for each pixel (picture element) in the databases. This plot was also generated from lunar sample data, from both pristine rocks [15-17] and mixed rock and soil [18,19]. The Th/Ti ratio used in this study is normalized to C1 chondritic Th and Ti values [20,21], so that a ratio value of 1.0 signifies chondrite abundances. In addition, plots of pixel and sample $(Th/Ti)_C$ versus Fe (wt %) values and $Mg^*/(Th/Ti)_C$ versus Al (wt %) were constructed to determine the usefulness of these plots in unambiguously defining known petrologic regions within the highlands. The former plot was constructed because the lesser coverage of the X-ray data limits the applicability of the $(Th/Ti)_C$-Mg^* relation to the lunar eastern hemisphere; the latter plot provides better discrimination between the Mg-suite rock types than does the $(Th/Ti)_C$-Mg^* ratio plot. Each pair of sample- and orbital-data plots was examined to determine their degree of similarity. In addition, within each of the three orbital-data plots, petrologic fields were defined on the basis of their respective sample-data plots and obvious mixing trends of the rock types. The spatial distribution of each plot's petrologic provinces on the Moon was determined by assigning a distinct color to representative pixels in Lunar Consortium image format. The three resulting classification maps were then examined to determine the distribution of predefined petrologic units or regions in the highlands and the geologic significance of the observed

distributions of petrologic units in terms of highland crustal genesis.

Results. The distributions of sample and orbital data on the three plots are very similar, especially with respect to the soil-sample data. However, the majority of orbital points fall between rock-sample fields. This distribution is related both to a real component (mechanical mixing of rock types) and to an artificial component (the geochemical detectors' rather large field of view). Overall, the $Mg^*/(Th/Ti)_c$-Al plot best discriminates between KREEP and the Mg suite, and among the Mg-suite rocks. Both this plot and the $(Th/Ti)_c$-Fe plot easily discriminate ferroan anorthosites from other rock types, whereas the $(Th/Ti)_c$-Mg^* plot shows considerable overlap between ferroan anorthosites and mare basalts. Even though it is difficult to discriminate between norites and KREEP on the $(Th/Ti)_c$-Fe plot, this plot has an advantage over the other two in that it provides circumequatorial coverage.

Discussed below are two lunar problems that can be addressed from our preliminary analysis of the $(Th/Ti)_c$-Fe and $Mg^*/(Th/Ti)_c$-Al classification maps: (1) the average composition of the lunar crust, and (2) the origin and implications of mare basalt mixed into the terra crust.

Average Composition of Lunar Highland Crust. We used the Th/Ti-Fe data to determine the average composition of the lunar crust because (1) they cover more of the Moon (over 4.5 million km^2) and the area represented on the $Mg^*/(Th/Ti)_c$-Al map, and (2) a substantial fraction of the $Mg^*/(Th/Ti)_c$-Al data is from the Imbrium/Serenitatis highlands, which have been shown previously to be anomalous or atypical of the average lunar crust [12]. These data indicate that the average compositional values for the highlands are Fe (wt%) = 4.9±2.3 and Th/Ti = 1.77±5.49. These values can be modeled by a mixture of about 65% ferroan anorthosite, 25% mare basalt, and 10% KREEP/Mg-suite rock types. The average composition of the total highland surface under the Apollo 15 and 16 groundtracks thus approximates that of an "anorthositic gabbro" (Al_2O_3 approximately equal to 27 wt%). This estimate of Al is 2 wt% higher than that proposed by Taylor [18] for the bulk lunar crust. However, we do not suggest that our composition represents the entire crustal column; in fact, evidence from the composition of multiring basin ejecta suggests a more mafic composition ("noritic") for the lower crust [22].

The key unresolved factors in determining the bulk composition of the lunar crust are the composition of the lower crust and the average depth of impact mixing. Solution of these problems lies beyond the scope of this study. However, our results do imply a lunar crust significantly more feldspathic than that proposed by [7]. As we suggested elsewhere [23], this observation may preclude a pure "serial magmatism" model for the origin of the lunar crust. The results of our study suggest that large-scale plagioclase fractionation occurred early in lunar history, either as a result of a "magma ocean" [24] or as a variant of it [25].

Mare Basalt in the Highland Crust. One of the petrologic units in both the $(Th/Ti)_c$-Fe and the $Mg^*/(Th/Ti)_c$-Al maps has $(Th/Ti)_c$ and $Mg^*/(Th/Ti)_c$ ratios similar to that of lunar ferroan anorthosites, but its Fe and Al values trend toward mare basalt compositions. Thus this unit is not composed of pure anorthosite. The important issue is the identity of the mafic end member(s) with a chondritic Th/Ti ratio. Two such rock types are recognized in the lunar samples: highland "gabbro" and mare basalt. The former rock type is

extremely rare in the Apollo collections and there is no reason to suppose that it is more abundant elsewhere than in samples from the Apollo and Luna landing sites. If gabbro were present in this unit, the consequences of large percentages (greater than 65%) of gabbro in these crustal regions are even more astounding than the remaining possibility.

If the above possibility is untenable, then large regions of the highland crust apparently contain up to 30% mare basalt. Numerous studies of photogeology [26], of sample data [27-29], and of remote-sensing geochemical data [30,31] have marshalled evidence for mare volcanism that predates the final lunar heavy bombardment. An analysis of Fe distribution in the highlands crust [32] suggested that mare-extrusion rates before the end of the heavy bombardment could have been as much as a factor of 10 higher than the rates after the Imbrium and Orientale impacts. The results of our study suggest that these rates may be underestimated. Because the total volume of visible maria constitutes less than 1% of the highland crust [33], the composition of this unit suggests that the pre-Imbrium lava-extrusion rate in the regions of this unit may have been about 30 times the post-Imbrium value. These rates indicate intensely active volcanism on the early Moon, of which only the final phases of mare volcanism have been preserved. Such a scenario for the early Moon has many implications for planetary thermal and geologic evolution, a detailed discussion of which must be deferred.

References: [1] Duncan, A.R., et al. (1976) PLSC 7, 1659; [2] McKay, G.A., et al. (1978) PLPSC 9, 661; [3] Longhi, J., and Boudreau, A.E. (1979) PLPSC 10, 2085; [4] Norman, M.D., and Ryder, G. (1979) PLPSC 10, 531; [5] Ryder, G. (1979) PLPSC 10, 561; [6] Norman, M.D., and Ryder, G. (1980) PLPSC 11, 317; [7] Walker, D. (1983) JGR 88, B17; [8] Hawke, B.R., and Spudis, P.D. (1980) Proc. Conf. Lunar Highlands Crust, 467; [9] Clark, P.E., and Hawke, B.R. (1981) PLPS 12B, 727; [10] Haskin, L.A., and Korotev, R.L. (1981) PLPS 12B, 791; [11] Spudis, P.D., and Hawke, B.R. (1981) PLPS 12B, 781; [12] Spudis, P.D., and Davis, P.A. (1983) Workshop Pristine Rocks, LPI Tech. Rpt. 83-02, 69; [13] Davis, P.A. (1980) JGR 85, 3209; [14] Metzger, A.E., et al. (1977) PLSC 8, 949; [15] Ryder, G., and Norman, M.D. (1978) Catalog Pristine Rocks, NASA JSC-14565 and -14603; [16] Warren, P., and Wasson, J. (1979) PLPSC 11, 431; [17] Warren, P., et al. (1981) PLPSC 12B, 21; (1983) JGR 88, A615; (1983) JGR 88, B151; [18] Taylor, S.R. (1982) Planetary Science, LPI Press, 481 p; [19] Papike, J.J., et al. (1982) RGSP 20, 761; [20] Morgan, J.W. (1971) Handbook of Elemental Abundances in Meteorites, 517; [21] Mason, B. (1971) Handbook of Elemental Abundances in Meteorites, 181; [22] Ryder, G., and Wood, J.A. (1977) PLSC 8, 655; [23] Spudis, P.D., and Davis, P.A. (1985) LPS XVI, 807; [24] Wood, J.A., et al. (1970) Proc. Apollo 11 Lunar Sci. Conf., 965; [25] Shirley, D.N. (1983) JGR 88, A519; [26] Schultz, P.H., and Spudis, P.D. (1983) PLPSC 10, 2899; (1983) Nature, 233; [27] Ryder, G., and Taylor, G.J. (1976) PLSC 7, 1741; [28] Ryder, G., and Spudis, P.D. (1980) Proc. Conf. Lunar Highlands Crust, 353; [29] Taylor, L.A., et al. (1983) EPSL 66, 33; [30] Hawke, B.R., and Spudis, P.D. (1980) Proc. Conf. Lunar Highlands Crust, 467; [31] Hawke, B.R., and Bell, J.F. (1981) PLPSC 12B, 665; [32] Spudis, P.D., and Schultz, P.H. (1983) LPS XIV, 737; [33] Head, J.W. (1976) RGSP 14, 265.

SULFUR DEPOSITION ON SILICATES: EFFECTS ON BAND STRENGTHS

Jonathan Gradie, Planetary Geosciences Division, HIG, 2525 Correa Road, Honolulu, HI 96822

Sulfur is ubiquitous in the inner solar system. The source of the sulfur is the Jovian satellite Io. This fact, in combination with the peculiar spectral properties of the satellite, argues for a sulfur-rich Ionaian surface. However, the form that this sulfur takes on the surface, pure sulfur, sulfur/silicate mixtures or sulfur compounds has not been determined. Furthermore, it is not clear which surface morphological units, i.e., flow-like features can be ascribed to silicate or sulfur volcanism. On the basis of comparisons with the spectral properties of cooled sulfur and the morphology expected for sulfur flows Pieri, at al. (1985) argue for the presence of pure sulfur flows particularly near Ra Patera. Others argue on the basis of morphology and the physical strengths of rock and sulfur that many of morphological features can be explained only by silicate volcanism hence the flow-like features must be silicates.

One of the few methods available for resolving this controversy is the spectral reflectance properties of the flow like features. It has been suggested that the spectral reflectance (λ = 0.4 to 5.0μm) may be able to resolve the issue since sulfur is relatively features at wavelengths greater than 0.5μm whereas most mafic silicates have charge transfer absorptions between 1 and 5μm. Also, silicate flows tend to be much darker (r_N < 0.1) at wavelengths >0.5μm than sulfur or most sulfur compounds. It seems reasonable that silicate flows could be identified by either low reflectance or silicate absorptions. The spectral properties (λ = 0.4 to 0.7μm) of mixtures of silicates and sulfur have been investigated by Gradie and Moses (1985). These studies have shown that under certain conditions of thermal history and silicate to sulfur ratios that the spectral properties of some regions on Io can be matched with the results of Voyager imaging.

An important problem that must be addressed is the effect that the predicted, relatively large resurfacing rate (0.1 to 10 cm/yr) will have on the spectral properties of basalt and sulfur since blanketing by pyroclastics from local vents may be a very effective method of masking or modifying the spectral characteristics while maintaining the morphological identity of the surface. If sulfur is ejected from vents and fumaroles, then sulfur could cover and mask the spectral properties of a basalt flow. Likewise, silicate ash ejected from silicate volcanism can cover and spectrally mask sulfur deposits or flows. This situation is analogous in many respects to the problem of contrast reversal on the Martian surface caused by windblown dust (Wells, et al., 1984).

One measure of the effectiveness of blanketing by sulfur dust is the degree to which a layer (gm/cm^2) can degrade the spectral contrast in mineral absorption bands. We have begun a series of laboratory measurements that examine in detail the issue of how much sulfur dust does it take to mask the spectral properties of a substrate. In our particular experiments we use Hawaiian basalts and the spectrally pure mafic mineral members olivine and pyroxene observed over the wavelength range 0.7 to 2.5μm covered with layers of sulfur (particle size < 10μm) of varying thickness. In Figure 1 below we illustrate the results of one such experiment for olivine. In this case a sulfur surface layer of only 200 milligrams/cm2 is

sufficient to mask completely the spectral contrast in the 1 = 1μm band [spectral contrast defined as r(λ = 1.8μm) / r(λ = 1.1μm)]. From this experiment and other experiments on pure basalts it is apparent that for the apparent resurfacing rates and an upper regolith density of 0.3 gm/cm^3 (Nash, et al., 1985), a silicate surface can be spectrally masked in as little as 30 days. The actual amount of time needed to spectrally mask the surface will depend upon the proximitry and activity of the vent or fumarole. Given the ubiquitous and constant nature of Ionian volcanism it seems unlikely that a silicate spectral signature will be seen on Io except in the freshest, most active flows.

References:

Gradie, J. and J. Moses (1985) Spectral reflectance properties of sulfur/basalt mixtures. Icarus, submitted.

Nash, D.B., M.H. Carr, J. Gradie, D.M. Hunter and C.F. Yoder (1985) Io, in Natural Satellites (D. Morrison and J. Burns, eds.), in press.

Pieri, D., S.M. Baloga, R.M. Nelson and C. Sagan (1984) The sulfur flows of Ra Patera, Io. Icarus, 60, 685-700.

Wells, E.N., J. Veverka, P. Thomas (1984) Mars: Experimental study of albedo changes caused by dust fallout. Icarus, 58, 331-338.

Figure 1:
The spectral reflectance (λ =0.7 to 2.5μm) of olivine (particle size ~1 mm) for several coatings of sulfur dust of different thicknesses. The lower curve is the pure olivine (washed Green Sand Beach, Hawaii), the upper curve is pure sulfur dust.

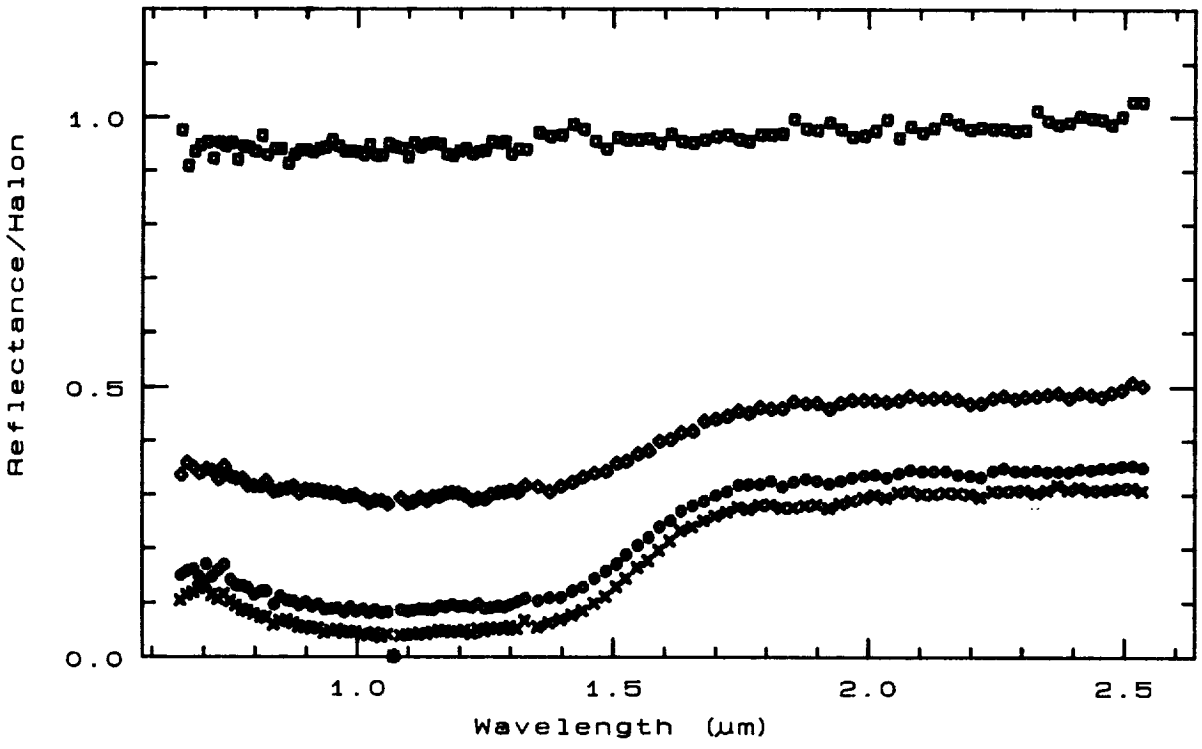

SPECTRAL REFLECTANCE STUDY OF THE HADLEY-APENNINE (APOLLO 15) REGION.
B.R. Hawke and P.G. Lucey, Plan. Geosci. Div., Hi. Inst. of Geophys., Univ. of Hawaii, Honolulu, HI 96822.

Introduction: Detailed information concerning the composition of surface material in the Hadley-Apennine region is necessary in order to understand the nature and origin of Imbrium basin-related units. Even though progress has been made in recent remote sensing studies (e.g., 1-6), many unanswered questions still remain. These include the compositions of Imbrium ejecta and pre-Imbrian material exposed both on the Imbrium backslope and in the Apennine Mts. (Apennine front), the variation in Imbrium ejecta composition as a function of distance from, and position around, the basin, and the nature of the material responsible for the thorium anomaly associated with the region. The purpose of this paper is to present results of an analysis of near-infrared spectral obtained for surface units in the Hadley-Apennine region.

Method: Twenty-three near-infrared spectra were recently obtained at the Mauna Kea Observatory 2.2-m telescope using the Planetary Geosciences Division indium antimonide spectrometer. Spectra were obtained for six relatively fresh surfaces in the Apennine Mts. (front), for five fresh crater deposits on the Imbrium backslope, and for a variety of highland units within the Apennine ring (Imbrium interior). The latter includes the following: 1) two fresh, small (D < 5 km) craters on the Apennine Bench and 2) the eastern wall deposits of Archimedes, Aristillus, Autolycus, and Timocharis craters. Four spectral parameters were derived from each spectrum after the methods of Lucey et al. (1985): the 1 micron band depth, width, and center and the infrared continuum slope.

Result: Examination of scatter diagrams which plot the six combinations of the four spectral parameters reveals the presence of two major spectral classes. Figure 1 shows a plot of band depth versus band width and illustrates the separation between the two classes on the basis of these parameters. Class 1, in the upper left, is characterized by a large band depth (9-15%), and bands narrow with respect to the rest of the region (.15-.24$\Delta\lambda$). The spectra of Class 1 appear to be those of a mixture of low Ca pyroxene and feldspar. The plagioclase to pyroxene ratio of the areas determined from the spectra indicate these locations are anorthositic norite to norite. Class 2 is in the lower right of Figure 1. On the plot of band width vs band center (Figure 2), Class 2 members form a linear trend rather than a cluster. The trend is not consistent with maturing of an end member. Plots of the parameters sensitive to maturity, band depth and continuum slope, show that the trend does not exhibit an increase in continuum slope with decrease in band depth, systematics typical of the maturing process. The trend displayed by spectral Class 2 shows a correlation with location. Areas interior to the Apennine ring have both a longer band center and wider bands than those points on or beyond the Apennine front. The spectra of locations on the Apennine Bench Formation seem to represent a spectral end-member with the widest bands and longest band centers. Spectra of the walls of large craters interior to the Apennine ring show values intermediate between those of the Apennine Bench and Apennine exterior locations.

The Class 2 spectra and trend may be interpreted in several ways. One interpretation is that the spectra represent mixtures of low Ca pyroxene and olivine (with unknown amounts of feldspar) and the trend is caused by a decrease in olivine content with distance from the basin center. These spectra are consistent with mixtures of olivine and pyroxene where the ol:pxn ratio varies from about 40:60 to 70:30 (Singer, 1981). However, two of the Class 2 spectra were collected for small craters (D=2 and 3 km) on the Apennine Bench. This mafic mineralogy is not consistent with the KREEP basalt composition of the Apennine Bench Formation as determined by the orbital geochemistry experiments (Spudis and Hawke, 1985; Clark and Hawke, 1981). Two alternatives present themselves. The small craters in the Apennine Bench Formation for which spectra have been obtained penetrated a thin (<200m) layer of KREEP basalt to excavate sub-Bench material which is more mafic than KREEP basalt. Alternatively, the spectral characteristics of the trend may be caused by variation in the amount of a glass which has a broad Fe^{2+} absorption feature, centered at 1.00μm.

Conclusions: 1) Spectra for features in the Hadley-Apennine region can be placed in two general classes. 2) Class 1 spectra are for some of the craters and massifs in the Apennine Mountains and backslope. Analyses of these spectra indicate that these terrains are composed of feldspar-rich rocks dominated by low-Ca orthopyroxene. Norites and anorthositic norites are suggested. 3) Class 2 spectra were collected for highlands features inside the Apennine ring (Imbrium interior) and for locations on the Apennine ring and on the Apennine backslope. These spectra have shallower, wider bands centered at longer wavelengths than those of Class 1. Class 2 spectra are consistent with the presence of relatively large amounts of olivine in the locations observed. However, at least two of the spectra are for units thought to contain abundant impact or volcanic glass. In addition, the orbital geochemistry data constrains the amount of mafic material in the region. Additional work is necessary to satisfactorily interpret the Class 2 spectra. 4) The material exposed in the Apennine Mts. and backslope should be dominated by Imbrium ejecta derived from several kilometers to tens of kilometers beneath the surface. The presence of two spectral classes in this region suggests that at least two distinct compositions were excavated by Imbrium basin. 5) Class 2 spectra show a compositional trend from interior to exterior of Imbrium which may be the result of decreasing abundance of olivine with distance from the basin center. The trend may be a reflection of a change in composition with depth in the Imbrium target site. 6) The spectrum of one crater on the backslope (Marco Polo F, D = 4 km) appears to be dominated by an olivine absorption.

References:

1)P. Spudis (1978) PLPSC 9 , 3379. 2) B.R. Hawke (1978) PLPSC 9 , 3285. 3) B.R. Hawke, et al. (1979) PLPSC 10, 2995. 4) A. Metzger, et al. (1979) PLPSC 10, 1701. 5) P.E. Clark and B.R. Hawke (1981) PLPSC 12B, 727. 6) M. Etchegaray-Ramirez, et al. (1983) PLPSC 13, 529. 7)P.D. Spudis and B.R. Hawke, this volume. 8) P. Lucey, et al. (1985) PLPSC 16 submitted. 8) R. B. Singer, (1981) JGR, 86, 7967.

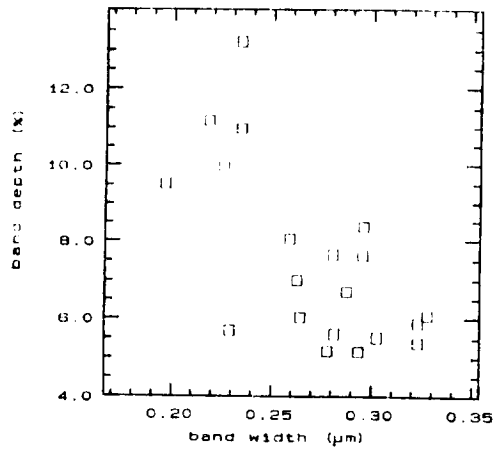

Figure 1. Scatter diagram plotting 1 μm band width versus percent band depth for spectra of Imbrium interior and exterior including the Apennine Bench Formation. Note the seperation of two spectral types. The group in the upper left of the plot is referred to as Class 1. The group in the lower right is referred to as Class 2. Class 1 occurs on the Apennine front and on the Apennine backslope. Class 2 occurs in the interior, on the front, and on the backslope.

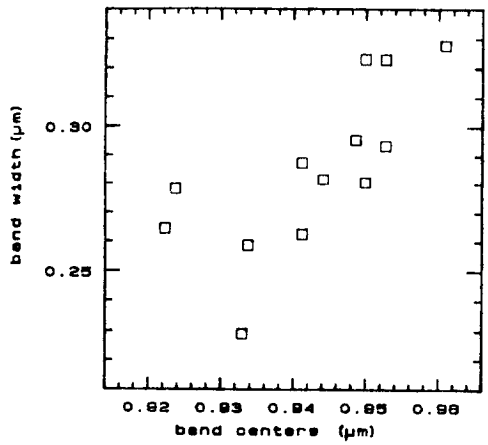

Figure 2. Scatter diagram of 1 μm band centers versus band width for Class 2 spectra. The linear trend shows a correlation with location as discussed in the text.

REMOTE SENSING STUDIES OF THE NECTARIS HIGHLANDS

B.R. Hawke, C.R. Coombs, P.G. Lucey, J.F. Bell, and P.D. Owensby, Planetary Geosciences Div., Hawaii Inst. of Geophys., Univ. of Hawaii, Honolulu, HI 96822; P.D. Spudis and P.A. Davis, U.S. Geological Survey, Flagstaff, AZ 86001.

INTRODUCTION: Studies of materials exposed by the lunar impact basins can provide valuable insight concerning lateral and vertical changes in the composition of the lunar crust. These impacts have excavated materials from a variety of depths and deposited this ejecta in a systematic manner. We have recently presented the results of remote sensing studies[1-3] of the interior and exterior deposits of Imbrium and Orientale basins. The purpose of this paper is to present the preliminary results of spectral studies of the highlands units associated with Nectaris basin. To understand the pre-impact stratigraphy of the Nectaris target site is the primary purpose of this study, while other objectives include: 1) to investigate the nature of geochemical and spectral anomalies in the Nectaris region, 2) to determine the provenance of the Apollo 16 samples, 3) to search for evidence of both pre- and post-basin volcanism in the highlands of the region, and 4) to better understand the composition and origin of the geologic units in the vicinity of the Apollo 16 site.

METHOD: Forty five near-infrared spectra (0.6-2.5μm) were recently (September 1984 and October 1985) obtained at the Mauna Kea Observatory 2.24 m telescope using the Planetary Geosciences Division indium antimonide spectrometer. Extinction corrections were made using the techniques described by McCord and Clark[4]. Analyses of absorption bands and continuum slopes were made using the methods presented by McCord et al.[5]

RESULTS AND DISCUSSION: A preliminary survey of the spectra obtained for fresh craters, massifs, and mature surfaces in the highlands around Nectaris suggests that the bulk of the material is not radically different from that exposed in the vicinity of the Apollo 16 site. Spectrally, the highland rocks are composed of Fe-bearing plagioclase feldspar and Ca-poor pyroxene. In general, anorthositic norites and noritic anorthosites appear to dominate the region. Unusual compositions have been identified, however. Anorthosite exists on the east wall of Kant crater (D=33 km). Kant (10.6°S, 20.1°E) is located on the main Nectaris ring, on the eastern portion of the Kant plateau. A spectrum of the east wall exhibits a shallow orthophyroxene absorption feature centered at 0.87μm and a well-defined feldspar band centered at 1.27μm. We estimate that the pyroxene abundance is between 2 and 4% for this area based on the laboratory spectra for various pyroxene-plagioclase mixtures presented by Nash and Conel[7].

We conclude that the anorthosite deposit was exposed by the Kant impact event. Bohnenberger F, a fresh 10 km impact crater (14.7°S, 39.6°E), also appears to have exposed a deposit of nearly pure anorthosite. The crater is located on an elongated highland massif (Bohnenberger eta) inside the Montes Pyrenaeus ring of the Nectaris basin. The spectrum of Bohnenberger F exhibits no well-defined "1μm" absorption feature as do other fresh highlands craters which expose pyroxene-bearing material[7]. Continuum removal and band analysis, however, reveal the presence of a shallow (3%) band centered at approximately 1.2μm. We attribute this band to plagioclase feldspar. Pyroxene may be present at Bohnenberger F in amounts less than 4%.

Analysis of spectra obtained for Cyrillus A, Neander V, and Bohnenberger E suggest that anorthosite may have also been exposed by these craters. However, the quality of these spectra was not high and repeat observations will have to be made. The presence of shocked anorthosite in the central peaks of Piccolomini and Theophilus has recently been reported[7]. Apparently, anorthosites are not as rare in the Nectaris region as had previously been thought. We have previously reported the occurrence of shocked anorthosites in the inner Rook ring of the Orientale basin on the western limb of the Moon[1].

A mafic geochemical anomaly in the terra north of Nectaris was recently identified by Andre and Strain[8]. The Mg/Al concentration ratios are only 21% less than those determined for mare soil samples in central Fecunditatis. These anomalous values are generally associated with a hummocky unit interpreted as Nectaris basin ejecta or Imbrium secondary ejecta by Wilhelms[9]. Andre and Strain[8], however, have attributed the geochemical anomaly to volcanic resurfacing of the hummocky material. To further investigate this problem, three spectra were obtained for the region. One spectrum was collected for the approximate location of a local Mg/Al high west of Gutenberg eta. Two spectra were obtained for dark portions of the hummocky unit just north of the Apollo 16 groundtrack. While the three spectra are somewhat different from those of the Apollo 16 site, preliminary analyses indicate that all three have similar spectral parameters and represent highlands material. All exhibit 4-5% pyroxene bands centered at 0.92-0.93μm and continuum slopes of about 0.7. There is no evidence for the presence of any mare basalt or pyroclastic glass, rather, a mature noritic highlands composition is indicated. These preliminary results support the basin ejecta interpretation of Wilhelms[9]. More spectra are needed for the immediate area of the geochemical anomaly in order to fully resolve this question.

REFERENCES: 1) P. Spudis et al. (1984), PLPSC 15, C197; 2) B. Hawke et al. (1984), LPS XV, 350; 3) B. Hawke and P. Lucey (1984), LPS XV, 352; 4) T. McCord and R. Clark (1979), Pub. Astron. Soc. Pac. 91, 571; 5) T. McCord et al. (1981), JGR 86, 10883; 6) D. Nash and J. Conel (1974), JGR 76, 1615; 7) C. Pieters (1983), LPS XIV, 608; 8) C. Andre and P. Strain (1983), PLPSC 13, A544; 9) D. Wilhelms (1980), U.S.G.S. Prof. Pap. 1046-A.

MARS: IMPLICATIONS OF DETECTED IGNEOUS PHASES, R.L. Huguenin, R. Carter, and S. Anderson, UMassachusetts, Amherst, MA 01003

Reflectance spectra of twelve surface areas (~1000km diameter) have been analyzed using a new intelligent absorption band detection algorithm (Huguenin and Jones, 1985). The analysis permitted suites of absorption bands to be detected for the first time in Mars spectra and accuracies of detected band positions revealed the apparent identity of exposed igneous minerals (Huguenin and Anderson, 1985). The findings provided significant constraints on models of planetary composition, oxidation state, and volatile content.

One of the significant findings was that minerals in the broadly distributed areas were similar. Six of the twelve areas had bands that could be attributed to olivine of composition $Fo_{65\pm15}$. Four areas had bands consistent with the presence of fayalite (iron-rich olivine). Six of the twelve spectra had bands that were attributed to low-iron enstatite. All twelve areas had bands that could be attributed to high-calcium pyroxene, with the pyroxenes in eleven of the twelve areas being high-iron varieties. The pyroxenes were all oxidized with $Fe_2O_3/FeO \simeq 0.3\text{-}3.0\%$.

The second finding was that the detected minerals were similar to the normative minerals derived from Viking compositional analyses of martian fines with modified Mg (Huguenin and Anderson, 1985). It has been argued that the relative metal abundances of martian fines may represent a globally averaged composition of crustal rocks that have been exposed at the surface over geologic time (Huguenin, 1982). Huguenin et al (1985) modified this proposal with the suggestion that Mg may be preferentially depleted from the fines due to reaction of fines with aerosol sulphate and chlorides derived from brine evaporation. It was argued that aerosols would react principally with Mg^{2+} as a result of incipient removal of Fe^{2+} from ferromagnesian minerals to form iron oxide, resulting in enhanced susceptibility of Mg^{2+} to subsequent reaction. It was argued that the resultant Mg salts would be highly soluble and be dispersed into the planetary hydrosphere, depleting Mg by a factor of 1-10 (Huguenin et al, 1985). Enhancements of Mg in the Viking fines analyses by factors of 2-5 yielded normative mineralogies that were consistent with the detected phases (Huguenin and Anderson, 1985). Results yielded 22-76% normative olivine of composition Fo_{61}-Fo_{80}, compared to detected $Fo_{65\pm15}$. Normative high calcium pyroxene abundances ranged from 13%-7% by weight with compositions of Wo_{50}, En_{30}, Fs_{20} to Wo_{50}, En_{40}, Fs_{10}, compared to detected pyroxene compositions of $Wo_{40\text{-}51}$, $En_{22\text{-}44}$, $Fs_{6\text{-}27}$. Normative low-calcium, low-iron pyroxene ranged from 34-0% of Fs_{39}-Fs_0, compared to detected pyroxene of composition near Fs_{10}. Minor normative orthoclase (1.7-0%), nepheline (0-3.1%), and magnetite (4.4-2.5%) would not have been detectable. Derived normative plagioclase (An_{65}-An_{84}) had sufficient abundance (25-10%) to be detected, but absorption by other phases prevented detection (Huguenin and Anderson, 1985). The similarity of detected and normative phases supported the possibility that the detected phases in the 12 analyzed areas may have been representative of crustal minerals over much of the planet. This possible mineralogic uniformity and possible peridotitic composition suggests that the magmas may have been minimally-evolved near-primitive melts (Huguenin and Anderson, 1985).

This possibility is further supported by the comparison shown in Table I. The column on the left shows the average crustal composition that was derived by Huguenin and Anderson (1985). The column in the middle is the mantle and

crust composition that was predicted from the equilibrium condensation and homogeneous accretion model proposed by J.S. Lewis and coworkers (Basaltic Volcanism Study Project, 1981, p.642). The column on the right is the composition for the mantle plus crust derived by Wanke and Dreibus (1984). The three compositions are very similar. The agreement between the first and third columns is expected, since both are based on measured analyses of surface samples from Mars. The similarity of the middle column to the outer two columns is striking, however, since the middle column represents a first-principles modeling of mantle and crust compositions resulting from equilibrium condensation and homogeneous accretion of the planet from the primitive solar nebula. It was based on no prior knowledge of Mars composition. Earlier support for the model was provided by the excellent agreement of predicted and measured geophysical properties (Basaltic Volcanism Study Project, 1981, p.688). Derived planetary mass (6.31-6.32 x 10^{26}y) in the Lewis-Weidenschilling model differed from actual mass (6.41 x 10^{26}y) by only 1.45-1.73%). Derived $1/MR^2$ (0.3684-0.3682) deviated by less than 1% from the actual value (0.3650).

The agreement of the derived average crustal composition with the two mantle and crust compositional models suggests the possibility that the exposed surface rocks may have virtually indistinguishable composition from the crust plus mantle as a whole. While differentiation may have resulted in core formation, it may not have produced a compositionally segregated crust and mantle. If true, this would be consistent with cold accretion models in which core formation can occur but segregation of a crust by crystal-liquid fractionation would not (Basaltic Volcanism Study Project), 1981, pp.1201-1202).

The agreement further provides a well-supported basis for estimating the abundance of accreted H_2O. From Table I the Lewis-Weidenschilling model predicts that H_2O comprised 0.44-0.47 weight percent of the mantle plus crust. Their model predicts that the mantle plus crust is 71-74% of the total planetary mass, yielding a predicted mass for accreted H_2O of 2.0-2.2 x 10^{24}g. Wanke and Dreibus predicted that accreted H_2O comprised 2.1% of the planet by mass, or 13 x 10^{24}g. If all the H_2O were released from the interior and spread uniformly over the surface of the planet (1.4 x 10^8km^2 surface area), the Lewis-Weidenschilling mass would be equivalent to a 14-16km thick surface layer of ice. The Wanke-Dreibus mass would be equivalent to a 93km thick layer of ice.

The implications that the mantle plus crust may be compositionally uniform, i.e., that crystal-liquid fractionation and crustal segregation may not have occurred, suggests that the H_2O source minerals may have been relatively uniformly accreted throughout the mantle and crust. The Lewis-Weidenschilling model predicts that the primary H_2O source phases would be talc- and tremolite-family silicates. If the low temperature accretion model is correct, such phases could be stable against dehydration to a depth of 300km, except where volcanism and impact produce locally high P-T conditions (Merrill, 1978). The upper 300km of the planet corresponds to ~1/3 of the mantle and crust volume, and it is possible that only ~2/3 of the accreted H_2O may have been lost from the planet during its early history. The H_2O in the upper 300km could have been largely retained and it may have had significant influence on crustal properties and processes.

The presence of talc- and tremolite-family phases in the upper ~300km could produce density contrasts that could possibly explain the partial to

complete isostatic compensation of surface topography. Densities (uncompressed) of the dehydrated phases would be near 3.5g cm^{-3}, while the densities of tremolite- and talc-family phases would be closer to 2.8-3.2g cm^{-3}. Lateral density variations within the upper few hundred kilometers have been proposed as possibly accounting for the observed isostatic compensation (Basaltic Volcanism Study Project, 1981, p.1199). It is thus possible that the principal compositional difference between the crust and mantle is the presence and absence of water of hydration.

Dehydration by impact and volcanism during the late-stage accretion and post-accretionary periods could have released substantial H_2O. Consider a 1 x $10^6 km^3$ volcanic event, such as Arsia Mons or events in the Olympus-Tharsis Province discussed by Scott (1982). Scott estimated the volume of the Olympus-Tharsis Province to be 25 x $10^6 km^3$ in more than 15 eruptive episodes, amounting to ~1.7 x $10^6 km^3$/event. Using the Lewis-Weidenschilling estimate of the H_2O content of the source rocks (0.44-0.47% by weight), a 1 x $10^6 km^3$ volcanic event would release 1.3-1.6 x $10^4 km^3$ H_2O. If all of the H_2O were deposited at the poles (1000km diameter area in the north and 350km diameter area in the south), a 1 x $10^6 km^3$ event could deposit 15-18m layers of ice at each pole. Release of H_2O by volcanism and impact from the upper 1km of regolith over time could result in the deposition of 2.1-2.4km thick layers of H_2O at the two poles, enough to comprise 37-67% of the present cap volumes (4-6km thick at the north and 1-2km thick at the south assumed). Dehydration that accompanied development of an equivalent ~1km thick layer of flood basalts, volcanic shields, and impact material could thus possibly have released enough H_2O to account for the estimated volumes of H_2O in the two caps. Dehydration of another ~10% of the upper 300km could have released enough H_2O to develop a 1-2km-thick global permafrost layer, assuming saturated 25-50% pore spaces. Much of the H_2O (~90%) in the upper few hundred kilometers may remain as water of hydration.

If the upper few hundred kilometers is largely hydrated, volcanism may have occurred in the presence of excess H_2O throughout Martian history. This raises the possibility that melting points may have been depressed by several hundred degrees (Merrill, 1978). Viscosities could have been low, and oxygen fugacities could have been high. Using the Lewis-Weidenschilling estimates of H_2O content, the amount of H_2O released during a melting event would be the equivalent of 1.3-1.6% by volume (1g cm^{-3} assumed density for H_2O) and significant local groundwater and ice production could have potentially resulted during eruptions.

The volumes of H_2O produced according to the Wanke and Dreibus model (Table I, column 3) could possibly have been a factor of 6 higher than the Lewis-Weidenschilling model. Wanke and Dreibus proposed, however, that the H_2O would have essentially all reacted with metallic iron in the interior of the planet, followed by escape of H_2. A resultant depletion factor for H_2O of 5.5 x 10^{-4} was proposed, yielding a total of only 11.5ppm H_2O.

The argument by Wanke and Dreibus (1985) that H_2O would react with metallic Fe in the interior is inconsistent with the equilibrium condensation model as proposed by Lewis and coworkers. The latter model argues that accreted solids would have been in equilibrium prior to and during accretion, with iron accreting primarily as Fe^{2+} in silicates and in FeS. Negligible Fe metal would have accreted. Reaction of H_2O with Fe metal to oxidize iron would have occurred in the nebula prior to accretion, not in the interior

after accretion. Both models produce similar bulk compositions for the mantle and crust, and both predict large initial accreted abundances of H_2O. The principal difference lies in the argument for accretion of equilibrium or disequilibrium phases.

The evidence for high oxygen fugacity inferred from the detected presence of Fe^{3+} in surface pyroxenes and from the analyses of SNC meteorites (Huguenin and Anderson, 1985) is more consistent with the equilibrium condensation model of Lewis and coworkers than with the disequilibrium model proposed by Wanke and Dreibus.

References. Basaltic Volcanism Study Project, Basaltic Volcanism on the Terrestrial Planets, Pergamon, New York, 1286pp, 1981; Huguenin, R.L., J. Geophys. Res. 87, 10069, 1982; Huguenin, R.L., Harris. S., and Carter, R., Injection of Dust into the Martian Atmosphere: Evidence from the Viking Gase Exchange Experiment, sub. to Icarus, 1985; Huguenin, R.L. and Anderson, S., Detection of Igneous Minerals on Mars, sub. to Icarus, 1985; Huguenin, R.L. and Jones, J., Intelligent Information Extraction from Reflectance Spectra: Absorption Band Positions, J. Geophys. Res., in press, 1985; Merrill, R., in LPI Workshop on Mars Petrology, LPI Publ., p.71, 1978; Scott, D.H., J. Geophys. Res. 87, 9839, 1982; Wanke, H. and Dreibus, G., MECA Workshop on Water on Mars, Lunar and Planetary Institute, Houston, 1984.

TABLE I: Mars Composition

	Crust	Mantle and Crust	Mantle and Crust
	Huguenin and Anderson	Lewis-Weidenschilling	Wanke and Dreibus
SiO_2	44.0% (weight)	43.6-43.9%	44.4%
TiO_2	0.62	0.16	0.14
Al_2O_3	7.3	3.1-3.2	3.0
Cr_2O_3	-	-	0.76
MgO	12.0-30.0	31.0-31.2	30.2
FeO	14.5	16.7-17.2	17.9
MnO	-	-	0.46
CaO	5.7	2.9-3.0	2.45
Na_2O	1.5	1.4	0.50
H_2O	-	0.44-0.47	*2.7

* Initial estimated accreted H_2O abundance 2.1% of planet and mantle plus crust comprises 78.3% of planet. All H_2O assumed to be accreted within mantle and crust.

IRTM OBSERVATIONS OF SYRTIS MAJOR: AN ACTIVE AEOLIAN ENVIRONMENT

S.W. Lee, Department of Geology, Arizona State University, Tempe, Arizona 85287

Historically, Syrtis Major is one of the most distinct classical dark albedo features on Mars; seasonal variations in its size and albedo have long been noted by terrestrial observers, with the eastern boundary displaying large changes in albedo and position, while the western boundary remains relatively stable [1]. Spacecraft observations have shown the feature to be composed of numerous westward-trending bright and dark wind streaks [2] and dune fields [3] lying on the generally low-albedo slopes of a volcanic shield [4]. Several radar studies (summarized in [4]) have shown the shield to rise ~6 km above Isidis Planitia (~600 km to the east); the surface appears to be relatively smooth and homogeneous at radar wavelengths [3].

A study of albedo variations in Syrtis Major spanning more than one martian year has been carried out using data from the Viking Orbiter Infrared Thermal Mapper (IRTM) experiments. Contour maps of Lambert albedo [5] and single-point thermal inertia [6] have been constructed from observations obtained at ~30° L_s time intervals (sample thermal inertia and albedo maps are shown in Figs 1 and 2). Coupled with Orbiter images of the regional wind pattern (inferred from wind streak orientations), the noted albedo variations can be related to aeolian transport of bright dust into and out of the area [7,8].

During the Viking missions, the maximum observed extent of Syrtis Major was from about -5° to 25° lat. and 275° to 300° lon.; the region was generally darker than ~0.2 in albedo (Fig.2), the minimum albedo (~0.10) being closely associated with the area of dunes located on the crest of the shield (between about 0°-10° lat. and 290°-295° lon.) noted in [3]. A general increase in albedo following the global dust storms and a steady darkening of Syrtis Major throughout the balance of the year is apparent, as is the relative constancy of the western border and the greater variability of the eastern portion of the feature. Syrtis Major exhibits a relatively uniform thermal inertia of ~8 x 10^{-3} cal/cm^2/sec$^{1/2}$/°K (Fig.1), while the surroundings have thermal inertias of from ~12 in Isidis Planitia (to the east) to ~3 in Arabia (to the west) and albedos between ~0.2 and 0.3.

These observations reveal a very active aeolian enviornment to be the source of the dramatic variability of the Syrtis Major feature. The observed trend of the bright and dark wind streaks (Fig.3) is indicative of dust transport in response to winds directed generally upslope and westward. The regional slopes of 0.8° or less [3,4] are too shallow to produce the more vigorous nighttime downslope winds [9] found to be effective agents of aeolian dust transport in Tharsis [7]. However, daytime heating of the low-albedo slopes of Syrtis Major, coupled with the westward Hadley circulation expected throughout the year at these latitudes [10], could result in the observed circulation pattern. The presence of

dunes, numerous dark intracrater splotches (many with associated deflational wind streaks oriented upslope), and the thermal inertia of the region are all consistent with a surface covered with sand-sized particles. If driven to saltation, this sandy surface will readily eject into suspension whatever bright dust has been deposited from the atmospheric dust load, leading to net removal of dust from the region. When this relatively mobile surface is coupled with the actions of effective daily winds, dust transport upslope and out of Syrtis Major should result throughout the year. Such activity is consistent with elevated dust opacity over Syrtis Major and enhanced deposition in neighboring Arabia (as suggested in [11]), and may also produce significant surface abrasion or mantling, in accord with the region's smooth appearance to radar [3].

REFERENCES: [1] Slipher, E.C., A Photographic History of Mars, 1905-1961, Northland Press, Flagstaff, AZ, 1962. [2] Sagan, C. et al., J. Geophys. Res. 78, 4163-4196, 1973. [3] Simpson, R.A. et al., Icarus 49, 258-283, 1982. [4] Schaber, G.G., J. Geophys. Res. 87, 9852-9866, 1982. [5] Kieffer, H.H. et al., J. Geophys. Res. 82, 4249-4295, 1977. [6] Christensen, P.R., Icarus 56, 496-518, 1983. [7] Lee, S.W. et al., J. Geophys. Res. 87, 10025-10041, 1982. [8] Lee, S.W., Submitted to Icarus, 1985. [9] Magalhaes, J. and P. Gierasch, J. Geophys. Res. 87, 9975-9984, 1982. [10] Kahn, R., J. Geophys. Res. 88, 10189-10209, 1983. [11] Christensen, P.R., J. Geophys. Res. 87, 9985-9998, 1982.

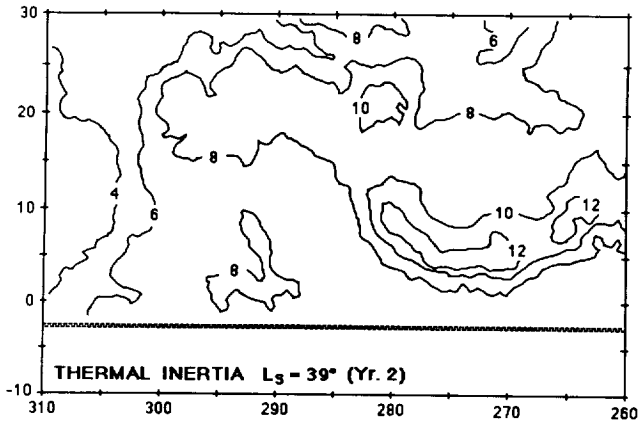

Figure 1: Contour map of thermal inertia in Syrtis Major. No data were obtained below the dotted boundary.

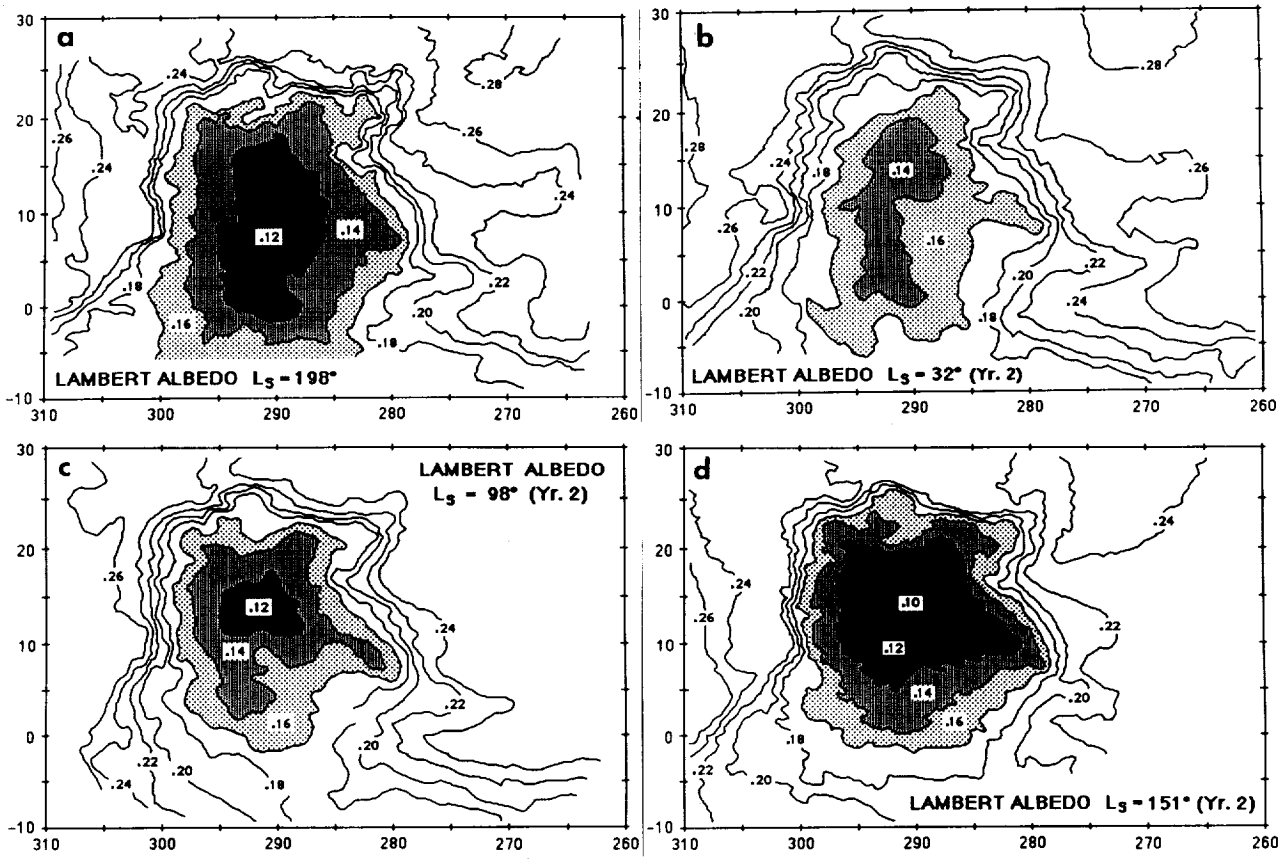

Figure 2: Contour maps of Lambert albedo in Syrtis Major spanning one martian year. Areas darker than 0.16 in albedo have been shaded. a) Early northern fall (Year 1); b) early northern spring (Year 2); c) early northern summer (Year 2); d) late northern spring (Year 2).

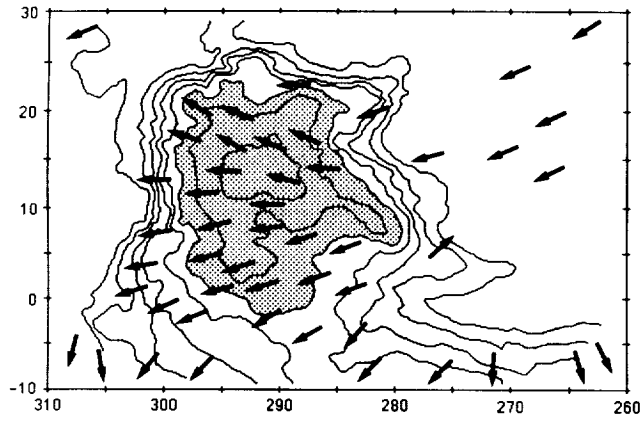

Figure 3: Map of effective surface wind directions inferred from observations of bright and dark wind streaks. Individual arrows are representative of the general wind directions, and do not correspond to individual streaks. The base map is from Fig. 2c.

The Reflectance Properties of the Surface of Venus from Venera Lander Color Panoramas

A Joint Study between Brown University Planetary Geology and the V. I. Vernadsky Institute, ASUSSR. Presented by C. M. Pieters (Brown University, Providence, RI 02912)

Two types of spectrophotometric data are available for the surface of Venus: 1) multispectral images obtained for three channels in the visible by the Venera 13 and 14 landers (Selivanov et al.,1983, *Kosm. Issled.,21,* p176), and 2) wide-angle photometer measurements for five channels in the visible to about 0.9 μm by Venera 9 and 10 (Ekonomov et al., 1980, *Icarus*, p65). We have processed Venera 13 and 14 digital images to remove the effects of the strongly colored incident diffuse radiation. In the visible the two-color reflectance of the Venera 13 site is in general agreement with the reflectance spectra obtained for Venera 9 and 10 sites: the rocks and soil are dark, with very little coloration, suggesting the iron is in the ferrous state. We have recently made laboratory measurements of the reflectance properties of basaltic minerals and rocks from room temperature up to 500°C. These spectra show that the absorption edge of ferric oxides moves significantly toward the near-infrared for the temperature of the surface of Venus; hematite becomes essentially black throughout the visible. Thus, the reflectance spectra of both unoxidized as well as highly oxidized basaltic material is consistent with the Venera 13 multispectral results. Our laboratory measurements suggest the reflectance properties of the surface of Venus in the near-infrared may be used to further constrain the oxidation state of iron.

REMOTE SENSING INFORMATION APPLIED TO GEOLOGICAL STUDIES OF PLANETS

Carle M. Pieters, Associate Professor, Brown University, Dept. of Geological Sciences, Box 1846, Providence, RI 02912

a) Objective: This research program concerns visible and near-infrared reflectance spectroscopy and geochemical remote sensing of planetary surfaces, with primary emphasis on the Moon, Mars, and asteroids. Many of the anticipated results address fundamental requirements for geochemical exploration of the Solar System with Observer and Mariner II class missions. Telescopic reflectance data for small lunar regions are obtained and analyzed to solve problems in lunar geology/geochemistry. The reflectance experiment laboratory (RELAB) is used to spectroscopically measure the nature of light interaction with geologic materials (under conditions comparable to remote measurements). Analytical and modeling techniques are utilized to extract geochemical information from the observational data and controlled laboratory experiments. When applicable, topics are studied in a consortium or coordinated research mode.

b) Progress: A major review and analysis of lunar highland crater spectra and how they relate to the composition of the lunar crust is submitted for publication. Major highland rock types are spectroscopically identified (norites, gabbros, anorthosites, troctolites); their distribution indicates that the composition of the highland crust is relatively homogeneous for the upper 1-2km, but is distinctly heterogeneous and *not* well mixed to a depth of 10 km. Manuscript concerning the nature of crater rays is in press; extensive rays do contain a measureable component of material from the primary crater. Another manuscript is in press that discusses the composition of impact melts for large lunar craters (pyroxene, feldspar (recrystalized), glass) as detected from telescopic spectra. Preliminary laboratory spectroscopic studies concerning plagioclase mineral mixing experiments and regolith formation processes are progressing well.

c) Proposed: Three interrelated approaches are essential: acquisition and processing of planetary reflectance data, acquisition and utilization of supportative laboratory laboratory data for compositional interpretations, and development and application of data analysis tools to extract desired information. New telescopic reflectance spectra will be obtained for high-priority targets on the lunar near-side: small fresh craters in the highlands and mare, high resolution areas in and around large craters with central peaks, etc. A major science goal is to characterize compositional variations of the lunar crust with depth. Data analysis efforts include quantifying the properties of existing data bases of telescopic and laboratory lunar spectra and developing analytical techniques for identifying major and minor rock types. We will also investigate the Apollo 12 site (and samples) to better identify material from Copernicus. Integrated laboratory bi-directional reflectance studies include mineral mixing experiments to quantify features from Fe-bearing plagioclase and determination of spectroscopic effects of (asteroid) regolith formation. Additional new efforts include: a major program of lunar sample studies to develop the data base necessary for detailed exploration of the Moon and high temperature spectral measurements of basaltic materials to constrain the composition of the surface of Venus.

Summary Bibliography: (1985)

C.M. Pieters (1985) Composition of the Lunar Crust from Reflection Spectroscopy, submitted to *Reviews of Geophysics*.

Joint Brown/Vernadsky study (1985) The Reflectance Properties of the Surface of Venus from Venera Lander Color Panoramas, abstract submitted to DPS/AAS annual meeting.

D.A. Crown and C.M. Pieters (1985) spectral Properties of Plagioclase and Pyroxene Mixtures, *Lunar and Planet. Sci. XVI*, p. 158-159.

C.M. Pieters and F. Horz (1985) Spectral Characteristics of Experimental Regoliths, *Lunar and Planet. Sci. XVI* p. 661-662.

L.A. McFadden, C.M. Pieters, R.L. Huguenin, R.L. Hawke, T.V.V. King, and M.J. Gaffey (1985) Reflectance Spectroscopy of Lunar Meteorite Y791197, Relation to Remote Sensing Data Bases of the Moon, submitted to Nat. Inst. Polar. Res. special issue on Y791197.

S. Smrekar and C.M. Pieters (1985) Near-Infrared Spectroscopy of Probable Impact Melt from Three Large Lunar Highland Craters, *Icarus*, in press.

C.M. Pieters, J.B. Adams, P. Mouginis-Mark, S.H. Zisk, J.W. Head, T.B. McCord and M. Smith (1985) The Nature of Crater Rays: The Copernicus Example, *JGR*, in press.

L. Gaddis, C.M. Pieters and B.R. Hawke (1985) Remote Sensing of Lunar Pyroclastic Mantling Deposits, *Icarus, 61*, 416-189.

The Mid-Infrared (2.3-5.4μm) Spectral Reflectance of Mafic and Phyllosilicates

Ted L. Roush and Robert B. Singer, Planetary Geosciences, Hawaii Institute of Geophysics, University of Hawaii, 2525 Correa Rd., Honolulu, HI 96822

In order to aid the interpretation of Galileo NIMS and Mars Orbiter mapping spectrometer data we have undertaken a laboratory study of the bidirectional spectral reflectance properties of particulate mafic and phyllosilicate minerals in the 2.5-5.0μm wavelength region. The spectra were obtained using a cooled circular variable filter (CVF) spectrometer with an indium antimonide detector. The CVF consisted of two segments, the first has a wavelength range of 2.37-4.52μm with $\Delta\lambda/\lambda\sim0.01$. The second has a wavelength range of 3.9-7.7μm with $\Delta\lambda/\lambda\sim0.025$. Data were collected for all samples at room temperature and compared to a powdered sublimed sulfur standard which was measured just prior and subsequent to each sample measurement.

The spectra of all samples, measured under ambient conditions, are dominated by a strong broad absorption centered near 3.0μm due to the presence of adsorbed water, interlayer water, and/or structural OH (Figures 1-4). We now review the variety of vibrational fundamentals which occur in this region. The metal-OH stretching fundamental occurs from 2.7 to 2.8μm depending on site location and ion coordination (Hunt, 1977). There are two liquid water fundamentals which occur in this region. The asymmetric OH stretch at 2.9μm and the symmetric OH stretch at 3.1μm (Bayly et al., 1963). Additionally, there is the second order overtone of the H-O-H bending fundamental which can occur at 3.0μm (Bayly et al., 1963).

In the case of the mafic silicates (eg. the olivine of Figure 1), which contain no interlayer water or structural OH, we believe the broad absorption seen in the 3-4μm region is due solely to the presence of adsorbed water on the surface of the samples. Decreasing the particle size of the mafic silicates increases the 3-4μm band depth (Figure 1). We believe this is due to an increase of surface area available for adsorption of atmospheric water.

Spectral comparison of three montmorillonites, with different reported amounts of adsorbed and/or interlayer water content, show there is a correlation in the increase of the 3-4μm band depth with increasing amount of adsorbed and/or interlayer water content. No such correlation exists when comparing 3-4μm band depths to reported amounts of structural OH. Decreasing the particle size of hydrous silicates decreases the 3-4μm band depth (eg. the montmorillonite of Figure 2). We believe this is due to the fact that the band is nearly saturated for the larger grain size (due to the presence of abundant adsorbed and/or interlayer water) and reducing the grain size increases the amount of photon scattering within the surface more than the amount of water which can be adsorbed onto the surface due to the increase of surface area. The increase in scattering acts to reduce the mean optical path length within the 3-4μm band and results in the band becoming less saturated. It is clear that all samples will have to be placed in a dessicating environment in order to investigate the spectral behavior of the minerals themselves.

We also had the opportunity to measure the reflectance of a reagent grade calcite (Figure 3) and a smectite which has approximately 17 weight percent calcite as a contaminate (Figure 4). The absorption seen at about 4μm in the reagent grade calcite is easily identified in the spectra of two different grain sizes of the smectite. The presence or absence of carbonates on Mars has important implications concerning the atmospheric history and evolution of the planet. Since the ~4μm absorption is located in atmospheric windows of both the martian and terrestrial atmospheres, it appears that the identification of proposed carbonates on the surface of mars could be

accomplished from earth-based telescopic studies and/or the mapping spectrometers proposed for Mars Orbiter, at least at the 17 weight percent level.

REFERENCES

Bayly, J.G., V.B. Kartha, and W.H. Stevens, The absorption spectra of liquid phase H_2O, HDO, and D_2O from 0.7μm to 10μm, *Infrared Physics*, *3*, 211-223, 1963.

Hunt, G.R., Spectral signatures of particulate minerals in the visible and near-IR, *Geophysics*, *42*, 501-513, 1977.

This research was supported by NASA grants NSG 7312 and NSG 7590.

Figure 1

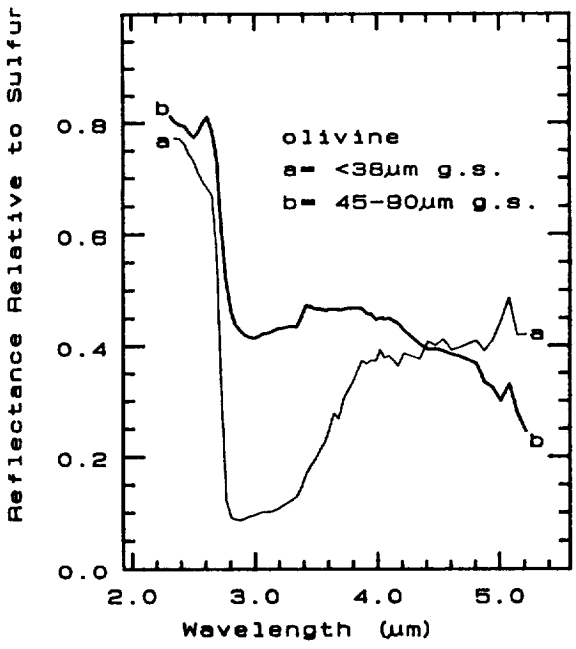

Figure 2

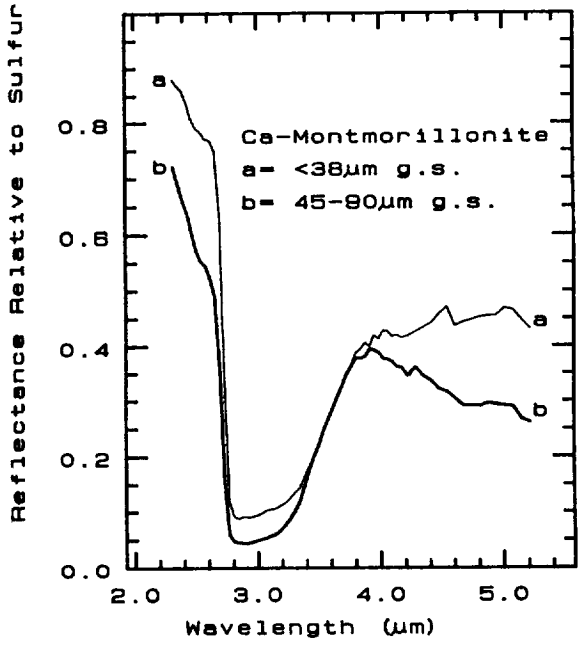

Figure 3

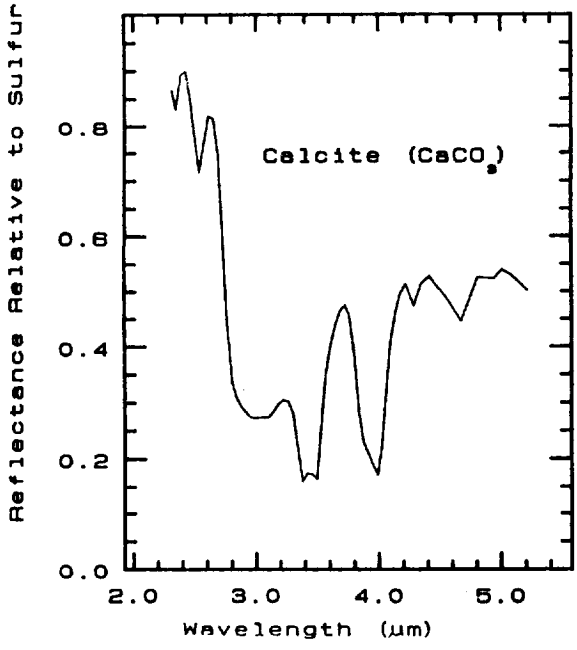

Figure 4

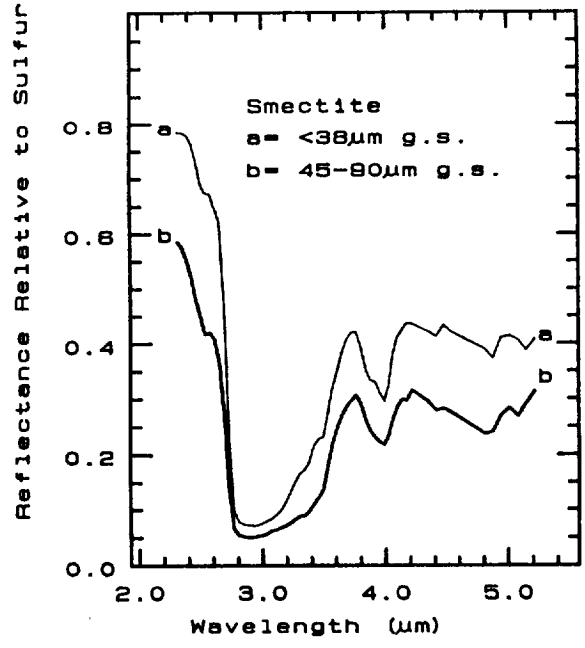

Contrast Reversal in Reflectance Spectroscopy

Williams, Audrey and Hapke, Bruce (Dept. of Geology and Planetary Science, University of Pittsburgh, Pittsburgh, PA 15260)

In reflectance spectroscopy the phenomenon of contrast reversal is often encountered, in which a powder of small particles is brighter than a powder of large particles when the absorption coefficient is small, but the relative brightnesses are reversed in a strong band. We studied this phenomenon experimentally in hematite, which has a very strong band at 450 nm. The experiments showed that contrast reversal apparently occurs because the particle angular scattering function changes from back-scattering outside the band to forward-scattering in the band, reflecting the change from volume-scattering to surface-scattering dominating the reflectance in the band.

A surprising finding was that the effective particle angular scattering function is affected by packing when the powder contains a large number of particles which are of the order of the wavelength in size. In 200 nm sifted hematite powder the particles were back-scatterers, but when compressed they behaved as forward-scatterers. Probably this occurs because the effective particles were clumps of many individual particles and the nature of the clumps changed with packing. At large phase angles this caused the brightnesses of sifted and compressed powders to differ by a factor of nearly ten. These factors must be taken into account in the interpretation of remotely-sensed spectra.

LUNAR SCIENCE FROM LUNAR LASER RANGING

J. G. Williams
X X Newhall
J. O. Dickey
C. F. Yoder

Jet Propulsion Laboratory,
California Institute of Technology

There have been frequent changes in the sources and accuracy of the available lunar range data during the past year. Most important to the lunar science is ranges to different reflectors on the moon at adjacent times on the same night. From the beginning of 1982 until the fall of 1984 there was a paucity of multiple reflector data (prior to 1982 the coverage was good). In the fall of 1984 the CERGA station, operating with 16 cm accuracy, started ranging the four reflectors frequently. The efforts at the other stations were concentrated on upgrading the accuracy of the ranging systems and sub-decimeter accuracies started at the Haleakala site in January 1985 and at McDonald Observatory in March 1985. The Apollo 15 reflector (Hadley) has the largest area and is the reflector of choice for testing out new ranging systems and making measurements for geophysical purposes. Multiple reflector coverage has recently started at Haleakala and is scheduled at McDonald Observatory. The new McDonald ranges have a scatter of about 4-5 cm and the best of the Haleakala data shows a 2 cm scatter. The true accuracies may exceed the scatter. With these improvements of at least a factor of three the accuracy of the lunar science will benefit proportionately.

Lunar science can be extracted from the lunar laser ranging (LLR) data. The standard lunar parameters in the solutions are the selenocentric reflector coordinates, the moment of inertia combinations (C-A)/B and (B-A)/C (where A<B<C), the third degree gravitational harmonics, the potential Love number, and the rotational energy dissipation. Several analytical partial derivatives permit solving for nonstandard terms that might arise from lunar structure not accounted for in the deformable solid body model used when numerically integrating the lunar physical librations (three dimensional rotation). The six initial conditions of the libration integration are also solved for.

The adequacy of the libration model and fit can be tested by examining the difference in post-fit residuals between different reflectors ranged in succession on the same night as common systematic errors, such as polar motion error, cancel. The CERGA data gave the first opportunity to make this important test in nearly three years. Systematic libration signatures are suspected during some days. Solutions with our full set of standard and nonstandard libration parameters did not significantly change this impression. We must be cautious in claiming a real effect because the above solutions do not use differenced data and corruption,

particularly by the noise from the older values of polar motion, is possible. Nevertheless, the evidence seemed strong enough to consider several effects not included in our models.

The physical libration model does not include torques on the moon from the planets. An analytical study supported this approximation. Torques at ordinary periods were much too small and even near resonances seemed inadequate to be observable. The indirect effect of planets perturbing the orbits of the earth and moon which in turn influence the librations is much more important and has long been included in our model.

More rewarding, but still too small for the observed effect, was an analytical calculation of the relativity effect called the geodesic precession. Larger than the usual relativity terms this relativistic precession amounts to 0.0195 arcseconds / year. This causes a shift in the lunar obliquity, already an implicit solution parameter, of 0.002 arcseconds which is equal to 1.7 cm at the lunar surface. This is big enough that it should be included in our model at some future time for thoroughness, but it is unobservable. The geodesic precession has been embedded in our orbit integrations for a long time.

Solid body tides on the moon are included in the libration calculations, where they give the sensitivity to the potential Love number k, but they are not accounted for in the displacement of the individual reflectors when calculating the range. The tidal variations on the moon are of decimeter size. But the larger terms have signatures which mimic those of the solution parameters for eccentricity and reflector coordinates. The unabsorbed signatures are estimated to be a few centimeters so with the improved data accuracies it is timely to add this modeling in the near future though the size is smaller than the suspected signatures.

From previous studies we also know that the interior structure of the moon may give rise to signatures of a few centimeters. Such possible signatures are the reason for the nonstandard parameters mentioned above. The nature of structure such as a liquid core is little enough known that possible models are not well constrained. Some of the possibilities permitted by the lunar laser range analyses were discussed by C. F. Yoder at the October 1984 meeting on the Origin of the Moon (C. F. Yoder, J. G. Williams, J. O. Dickey, and X X Newhall, Tidal Dissipation in the Earth and Moon from Lunar Laser Ranging).

This is an unfinished story. The new more accurate data will determine whether the suspected signatures are really there. The capability to analyze differenced reflector data is under development. New modeling will incorporate some centimeter sized effects that the older data accuracies did not demand. Then we shall be able to study the behavior of the moon's dynamics at the few centimeter level.

CHAPTER 13

RADAR APPLICATIONS

THE SURFACE OF MERCURY: GEOLOGICAL ANALYSIS AND INTERPRETATION OF RADAR OBSERVATIONS

P. E. Clark, R. F. Jurgens, M. Kobrick, NASA/JPL

Detailed study has been done of available topographic profiles and scattering parameters derived from available ground-based S- and X-band radar observations (1,2,3,4) to determine a) the relationship between topography and visual features on Mercury, and b) the character, distribution, and origin of terranes and structures typical of that planet. Although the Mercurian landscape is dominated by impact craters and thus is superficially similar to the lunar landscape, the terrane distribution and tectonic features on the two planets are actually strikingly different (5,6,7).

Radar data included in the study are topographic profiles derived from earth-based radar observations taken at Goldstone (1,2,3) and Arecibo (4) radar facilities during the 1970's; Hagfors scattering parameters derived from the Goldstone S-band observations (1,8); and relative scattering indices derived from the Haystack X-band observations (9). Resolution of this data is 12 to 20 km in the longitudinal direction and 50 to 100 km in the latitudinal direction. Height error may be as much as 150 m. The area of coverage for the radar data set includes the equatorial region, a band extending approximately 15 degrees above and below the equator and encircling the globe. Topographic profiles, with ephemeris-derived coordinates shifted by as much as 0.5 degrees in longitude because of a slight difference between the IAU ephemeris (10) and the USGS reference coordinate system (11), were plotted on USGS maps (12) derived from Mariner 10 visual data. In this way, radar-derived parameters could be directly compared to structural and textural features of the visual data. Radar data combined with visually-derived information in this manner are considered by many planetary geologists to be a most valuable tool for determining the structure of planetary terrains. This is especially true for Mercury, where photographic coverage is incomplete and often of poor quality (13).

First of all, a systematic study was done to determine whether typical visually observable structures have distinctive morphologies (14). The most typical features in the area of overlapping coverage (equatorial region of the eastern hemisphere) were considered. Major types of structures, including craters, scarps, valleys, ridges and troughs, were found to have distinctive morphologies. Where profiles cross the floors of craters (for example, Titian, Homer, Mozart, Chiakovskij, Handel, Rudaki, Lysippus), apparent depth-to-diameter ratios range from 1:75 to 1:90. This typical ratio indicates that Mercurian craters are considerably shallower

than their lunar counterparts. Typical scarp systems, such as Santa Maria Rupes, have characteristic asymmetrical profiles and often consist of two adjacent scarps of different relative sizes. Such evidence supports the contention that scarps are expressions of en echelon overthrust faults that formed during the period of global compression. There are indications that characteristic ridge and trough terrane, as described below, is associated with bright rays. Valleys, such as Goldstone Vallis, appear to have characteristic V-shaped profiles.

A systematic correlation of radar and visually-derived features was done in areas of overlapping coverage (15). Topographic highs account for over 90% of the radar-derived features, which are generally correlated with either single or a series of closely spaced or crossing curvilinear visual features. Over half of these features are albedo bright and ray-like in form. Most of the larger positive relief features have larger positive relief features have distinctively scarp-like signatures, although bright rays range from ridge-like to scarp-like in form. These topographically-correlated bright rays seem also to occur exclusively in heavily cratered or intercrater plains terranes, although some selection effect may be operating here because of the nature of available visual observations. (Observations are generally at low sun angle, and thus albedo differences are emphasized.) Some of the major concentrations of elevated rays are associated with a) Sobkou Planitia, b) Budh Planitia, c) an area that appears to consist of intercrater plains centered at 20 degrees latitude and 75 degrees longitude, d) Goldstone Vallis, and e) Haystack Vallis. These bright linear features, unlike their proposed lunar counterparts, crater rays, often do not have distinctive crater sources but seem to occur near plains boundaries and to be predominantly N- and NE-trending features. Perhaps these linears are remnants of the proposed global lineament system, reactivated by later episodes of crustal expansion of crater formation. The negative relief features are apparently correlated with mapped valleys or extensions of these valleys, including Haystack and Goldstone Valles. All observed valleys occur in heavily cratered or intercrater plains terranes. Some valleys, which are elevated and appear to consist of bright ray doublets with a drop of half a km or greater between them, seem rift-like in form.

In addition, a study was undertaken to determine the relationship between roughness on the meter (rms slope) and kilometer (topography) scales for the major terranes of the equatorial region, and to determine the harmonic distribution of topography in there (16,17). Topography has a unimodel distribution, which apparently results from the lack of dichotomy in plains terranes. The histogram does have a high elevation tail, however, which apparently corresponds to rugged

terrane. There is an asymmetry in the distribution of topography, with topographic highs distributed antipodally. Mercurian topography is considerably subdued, typically ranging one kilometer or less from the mean radius. Such smoothness may be an indication of extensive plastic deformation because it cannot be accounted for on the basis of gravity scaling alone. There are systematic differences in roughness and average elevation for plains and rugged terranes. Both smooth and intercrater plains are relatively low in elevation and smooth, but greater variation occurs in intercrater plains.

These observations tend to support the following model for the history of Mercury (13, 18, 19, 20, 21). Proposed tidal despinning was accompanied in its later stages by incipient core formation and crustal expansion. Such a sequence of events resulted in the production of a global lineament system, accompanied by formation of ridges, which occurred preferentially along existing lineaments, as observed. This was followed by crustal contraction and scarp formation, and scarps also formed preferentially along existing lineaments. The similarity in properties of all plains terranes, combined with the correlation between roughness parameters on the planet, tends to support the contention that there has been systematic resurfacing or degradation of the surface which occurred continuously throughout the period of plains formation. Smooth plains may thus be the final result of an extensive period of volcanic activity, which began with intercrater plains formation.

REFERENCES: (1) S. Zohar, R. Goldstein, 1974, ASTRO J 79, 85-91; (2) S. Zohar, 1974, unpublished report; (3) P. Clark, R. Jurgens, 1984, AMER ASTRO SOC 16, 668; (4) J. Harmon, D. Campbell, D. Bindschadler, J. Head, I. Shapiro, 1985, NAIC Report 204; (5) P. Clark, 1983, LUN PLAN SCI XIV, 119; (6) M. Strobell, P. Clark, G. Schaber, R. Jurgens, G. Downs, 1983, GSA 15, 700; (7) P. Clark, G. Schaber, M. Strobell, R. Jurgens, G. Downs, 1983, AMER ASTRO SOC 15, 838; (8) R. Jurgens, 1974, unpublished report; (9) R. Ingalls, L. Rainville, 1972, ASTRO J 77, 185-190; (10) E. Standish, M. Keesley, X. Newhall, 1976, JPL DEV EPHEMERIS 96, JPL TR 32-1603; (11) M. Davies, 1976, RAND R-1914-NASA, 1-20; (12) M. Davies, S. Dwornik, D. Gault, R. Strom, 1976, NASA Atlas of Mercury; (13) P. Clark, 1985, in PHYSICS OF THE PLANETS, in publication; (14) P. Clark, M. Strobell, G. Schaber, R. Jurgens, 1985, in preparation; (15) P. Clark, R. Jurgens, 1985, LUN PLAN SCI XVI, 139-140; (16) P. Clark, M. Kobrick, R. Jurgens, 1985, IEEE TRANS, IGARSS; (17) P. Clark, R. Jurgens, M. Kobrick, 1985, AMER ASTRO SOC 17, 712 (18) J. Pechman, H. Melosh, 1979, ICARUS 38, 243-250; (19) R. Strom, 1984, NASA SP-469, 13-56; (20) G. Schaber, J. Boyce, N. Trask, 1977, EARTH PLAN INTERIORS 15, 189-201; (21) D. Wilhelms, 1976, ICARUS 28, 551-563;

MERCURY RADAR ALTIMETRY: NEW RESULTS, J. K. Harmon[1], D. B. Campbell[1], D. L. Bindschadler[2], J. W. Head[2], and I. I. Shapiro[3]. (1) Nat'l Astronomy and Ionosphere Center, Arecibo, PR 00613; (2) Dept. of Geological Sciences, Brown Univ., Providence, RI 02912; (3) Harvard-Smithsonian Center for Astrophysics, Cambridge, MA 02138.

Radar altimetry measurements of Mercury have been made at Arecibo Observatory during 1978-84. The measurement techniques and preliminary results were reported by Harmon et al. (1984). Since then, additional data reduction and geological analyses have been completed, some results of which are reported here.

A major step has been the reduction of all data through 1982 to absolute altitudes (Fig. 1). The altitudes show a total variation of 6 km, although long-wavelength topography has an amplitude of about 3.5 km. The topography is dominated by two large bulges centered roughly at 10°W and 190°W longitude, with a third, smaller highlands region appearing in the unimaged hemisphere at 305°W (Figs. 1, 4). Fig. 1 indicates that Mercury's equatorial topographic figure is roughly aligned with its dynamical figure as inferred from the 3:2 spin-orbit resonance. The western edge of one of the large bulges is very sharp, dropping by 3 km at 37°W, near crater Handel (Fig. 2). This drop coincides with an extensive N-S-trending fault system seen in images. Another dramatic drop has been seen across crater Zeami which may be a signature of the fault system seen NE of Tolstoj basin.

Two smooth, bowl-shaped depressions centered on Tir Planitia (Fig. 3) and at 210°W in the unimaged hemisphere (Fig. 1) provide support for the existence of an annulus of circum-Caloris smooth plains. The observed downwarping is suggestive of subsidence under volcanic load, while adjacent topographic highs may be an uplift response to this subsidence. The Arecibo data indicate that the circum-Caloris region possesses the largest expanse of smooth plains in the equatorial zone of Mercury, although less extensive "smooth" regions can be seen in profiles from both the imaged and unimaged (Fig. 4) hemispheres.

Three features identified as scarps from images (Santa Maria Rupes, a second scarp just east of Santa Maria, and a third scarp east of crater Asvaghosa) were found to exhibit radar altimetric signatures (Fig. 2). Each is approximately 70 km across and 750 m high. In at least one case (the feature east of Asvaghosa) the radar profile is sufficiently symmetrical to establish it as being closer to a ridge than a scarp in appearance.

Large Mercury craters (diameter $\geq$ 40 km) average 2.3 km in depth as estimated from radar profiles. Some large and/or fresh craters yield radar depths of 3 km or more. These depths are consistent with shadow-derived values from Mariner 10 imagery. The one very large basin observed with the radar (centered at 130°W, 2°N) is shallower than some smaller basins and craters, consistent with degradation or isostatic relaxation, but does exhibit some distinctive topographic features.

The unmapped hemisphere (Fig. 4) shows a number of large craters as well as topographically smooth areas indicative of smooth or intercrater plains. No marked topographic differences are found between this and the imaged hemisphere nor is there evidence for another feature on the scale of Caloris.

Reference: J. K. Harmon, D. B. Campbell, J. W. Head, D. L. Bindschadler, and I. I. Shapiro (1984). Lunar Planet. Sci. XV, 343.

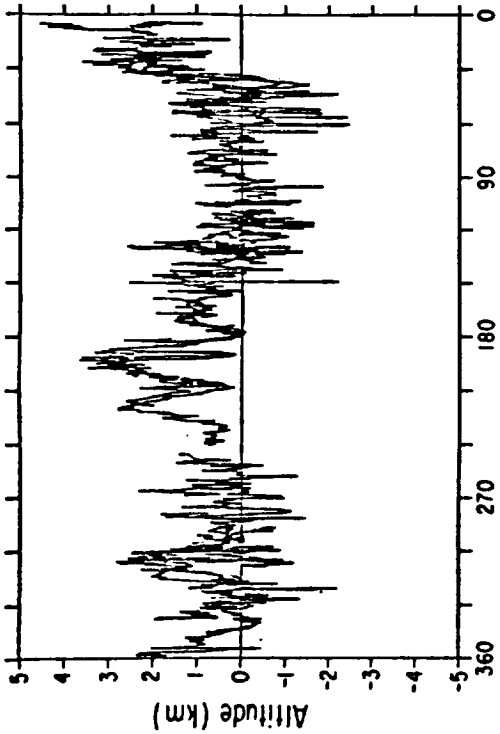

Fig. 1. Mercury altitude profiles from 1976-82 on absolute altitude scale. The zero-altitude datum corresponds to a 2439.0-km-radius reference sphere.

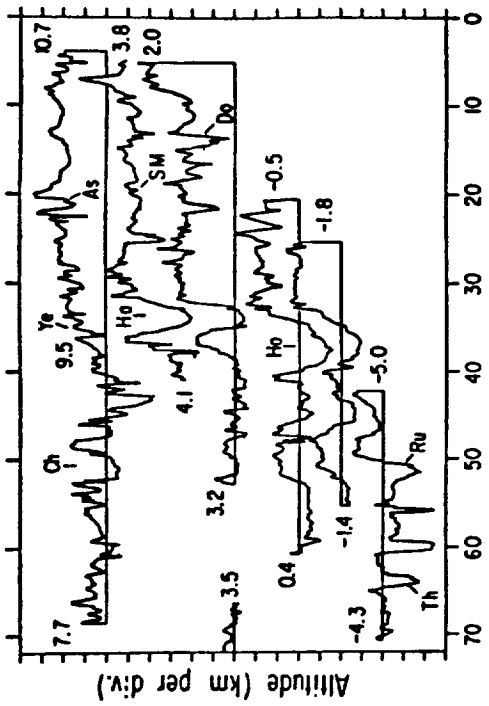

Fig. 2. Altitude profiles for the H-6 quadrangle. Numbers denote latitude. Horizontal lines give datum level. As=Asvaghosa, Ye=Yeats, Ha=Handel, Ho=Homer, SM=Santa Maria scarp.

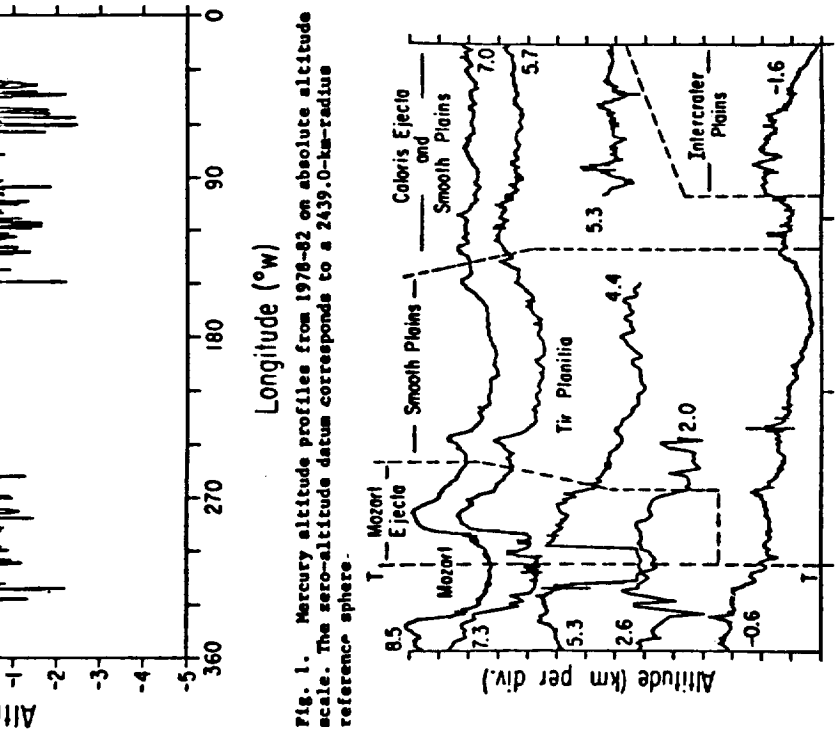

Fig. 3. Altitude profiles in the vicinity of the circum-Caloris smooth plains (Tir Planitia) and crater Mozart. Numbers are latitudes. Dotted lines separate major geologic units. The line T-T shows the Mariner 10 terminator.

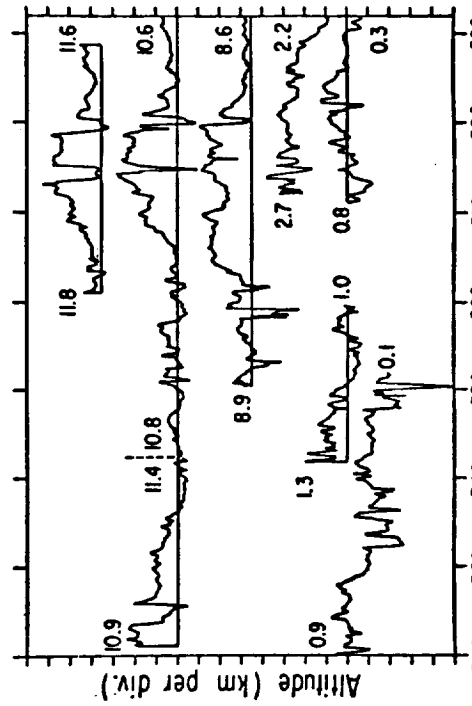

Fig. 4. Altitude profiles for the H-10 quadrangle. Numbers give latitude. Horizontal lines give datum level. This quadrangle was not imaged by Mariner 10.

LUNAR RADAR IMAGES - LANDFORM IDENTIFICATION

Henry J. Moore, U.S. Geological Survey, Menlo Park, CA 94025
T. W. Thompson, Jet Propulsion Laboratory, Pasadena, CA 91109

Three sets of polarized radar-echo images of the Moon are being examined to establish the relation between radar resolution and landform-identification resolution [1,2]. The wavelengths, radar resolutions (cell sizes), and approximate number of real or apparent landforms for the sets are as follows:

Set #	Wavelength	Cell sizes	Number of landforms
1	3.8 cm [3]	1-2 km	602
2	70 cm [4] (high resolution)	2.5-5 km	695
3	70 cm [5] (low resolution)	10-20 km	424

The results of the study should be valuable to those planning to acquire or interpreting radar images of the Earth or other planetary bodies.

After comparison with lunar maps and photographs, real and apparent landforms on the radar images are grouped into one of seven classes [1,2]: (1) resolved and clearly identified; (2) resolved and would probably be correctly identified; (3) resolved, but interpretation is uncertain; (4) detected, but elements are not resolved; (5) not detected; (6) array of landforms is resolved, but interpretation of the array is uncertain; and (7) radar portrays a fictitious landform.

Data recorded for each real or apparent landform for each set of images includes: (1) a name, (2) selenographic coordinates, (3) diameter and relief obtained from lunar maps and photographs, (4) the class, (5) diameter measured on the radar image, (6) background terrain, (7) geologic age, and (8) the Lunar Aeronautical Chart number. A computer program sorts and orders the data by diameter or relief, computes the percent of each class in frequency bins of 100, and computes the geometric mean of the landform diameter or relief for each frequency bin. Calculations are made in frequency steps of 10.

Current results show strong relations between radar resolution and diameter or relief of landforms that are clearly identified and those that would probably be correctly identified (class 1 + class 2), as shown in table 1 and in figure 1.

Landforms are not detected (class 5) at all diameters and

reliefs, but the percentage of undetected landforms decreases with increasing mean diameter in all cases and increasing mean relief (except the low-resolution 70-cm data). Landforms are simply detected (class 4) at all mean diameters and reliefs. Ambiguous arrays (class 6) portrayed by the radar constitute up to about 10 percent of the landforms at various diameters and relief values. As much as 6 percent of the landforms portrayed by the radar images at various diameters and relief values are fictitious (class 7).

When enough data have been acquired, they will be analyzed as functions of angle of incidence (lunar-scattering function) [6], background terrain, and geologic age [7].

Table 1. Percentage of resolved and identified landforms portrayed in lunar radar images.

Percentage of class 1+2 landforms	Mean diameters of landforms (km) corresponding to the indicated percentage.		
	3.8 cm	70 cm high	70 cm low
3	4	9-10	34
9	5	12	42
46	10	41	--
88	28	--	--

Percentage of class 1+2 landforms	Mean relief of landforms (km) corresponding to the indicated percentage.		
	3.8 cm	70 cm high	70 cm low
6	0.3	0.5-1.3	2.8
36	0.9	2.9	--
77	2.7	--	--

References

[1] Thompson, T. W. and Moore, H. J., 1984, Landform Identification in Radar Images: Lunar and Planet. Science XVI, p. 860-861.

[2] Moore, H. J., and Thompson, T.W, 1985, Landform Identification on Radar Images: Repts. Planet. Geol. and Geophys. Prog.--1984, NASA TM 87563, p. 458-460.

[3] Zisk, S. H., Pettengill, G. W., and Catuna, G. W., 1974, High-resolution radar maps of the lunar surface at 3.8-cm wavelength: The Moon, v.10, p. 17-50.

[4] Thompson, T. W., unpublished data.

[5] Thompson, T. W., 1974, Atlas of lunar radar maps at 70 cm wavelength: The Moon, v.10, p. 51-85.

[6] Hagfors, T., 1970, Remote probing of the Moon by infrared and microwave emissions and by radar: Radio Science, v. 5, p. 189-227.

[7] Wilhelms, D. E., 1980, Stratigraphgy of part of the lunar near side, U. S. Geol. Survey Prof. Paper 1046-A, 71p.

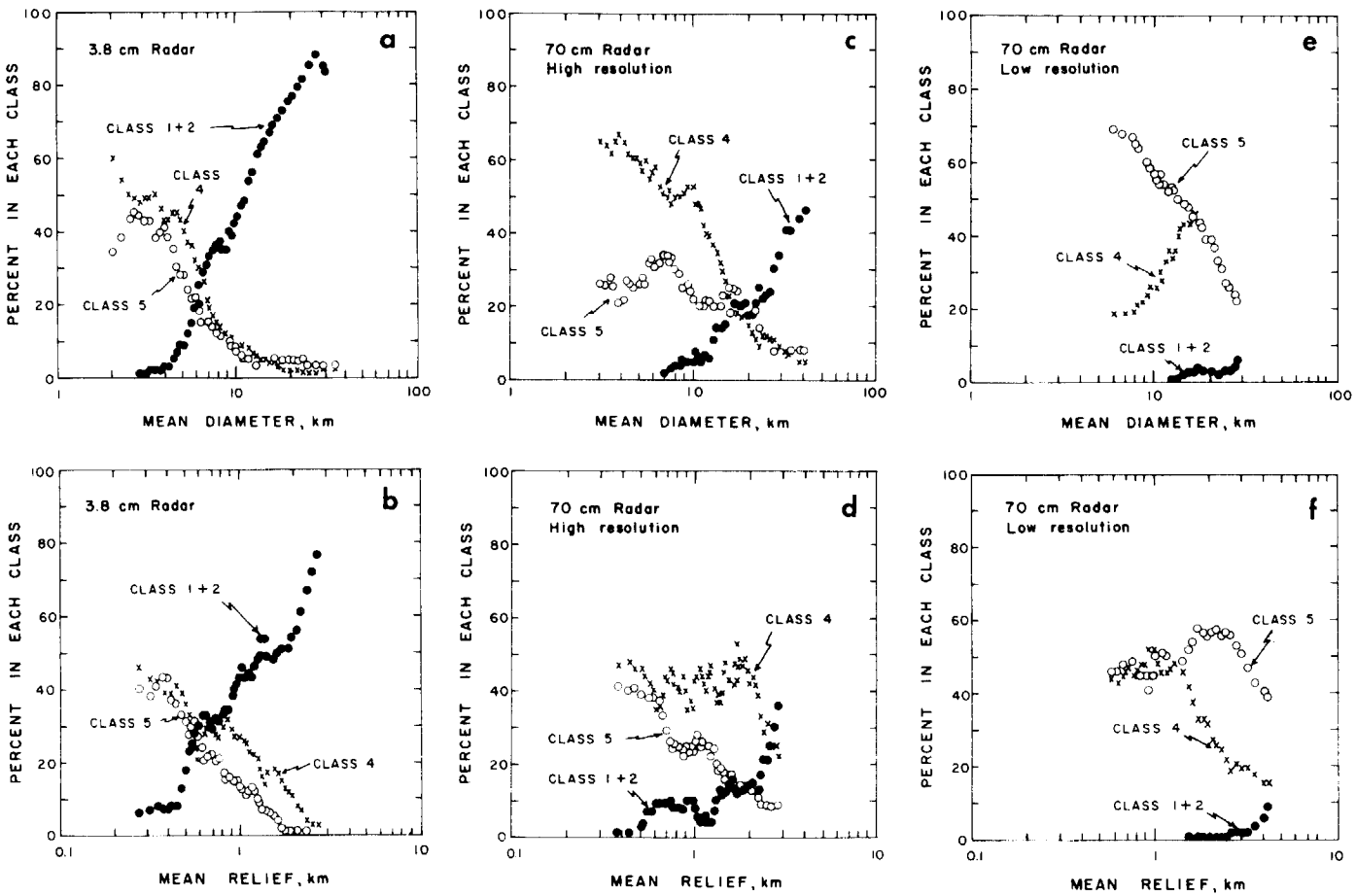

Figure 1. Percent of resolved, identified plus probably correctly identified (class 1 + class 2), unresolved but detected (class 4), and undetected (class 5) landforms portrayed and not portrayed by radar images of the Moon as a function of diameter and relief: (a & b) 3.8 cm radar, (c & d) high resolution 70 cm radar, and (e & f) low resolution 70 cm radar.

VENUS SURFACE COMPOSITION FROM RADIO/RADAR MEASUREMENTS

Gordon H. Pettengill, Peter G. Ford, and Bruce D. Chapman
Center for Space Research
Massachusetts Institute of Technology

In our quest to understand relationships between the composition of a planetary surface and its various electromagnetic signatures, with primary application to Venus, we have during the last year undertaken observations of several targets in the solar system using the Very Large Array (VLA). As discussed in last year's abstract under this program, there are three quite different approaches possible in applying electromagnetic waves to the measurement of surface dielectric properties:

1) Measure the coherent radar reflectivity of a resolved element of the surface and, from the Fresnel equations, derive the corresponding dielectric constant;

2) Measure the thermal radiation emitted by a planetary surface (stated as a brightness temperature) and from this measurement, together with a knowledge of the corresponding physical temperature, derive the surface emissivity and thus the surface dielectric constant;

3) Observe the degree of linear polarization associated with thermal emission from a spatially resolved element of planetary surface as a function of angle to the surface normal. From these measurements derive the surface dielectric constant from the Fresnel equations.

As also stated last year, the first two of these methods have led to results in good agreement with each other, but the last has tended to yield substantially lower estimates of dielectric constant [1]. To help understand the apparent failure of the polarization approach to yield accurate results, we have made observations of the polarized emission from both the Moon and the planet Mercury using the VLA during the last year. The lunar data have proven refractory to analysis, because of the large angular size of the Moon relative to the VLA's antenna pattern. Results for Mercury are interesting, however, as shown in the attached figures.

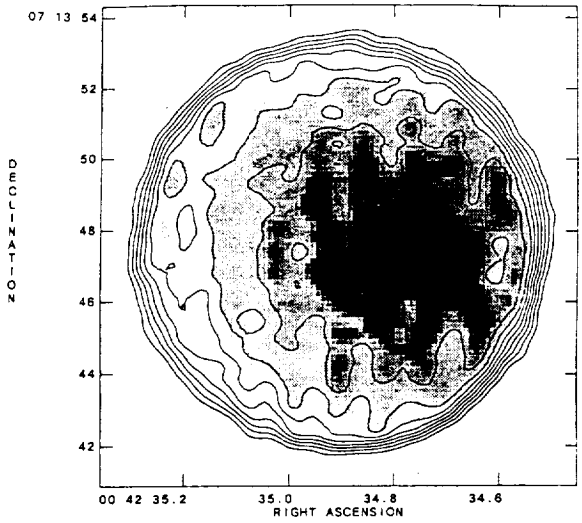

Fig. 1. Thermal brightness of Mercury at a wavelength of 6 cm as observed at the VLA near inferior conjunction on 5 April, 1985. The solar phase angle was 172°, and the disk radius 5.7" arc. Contours at 45K intervals.

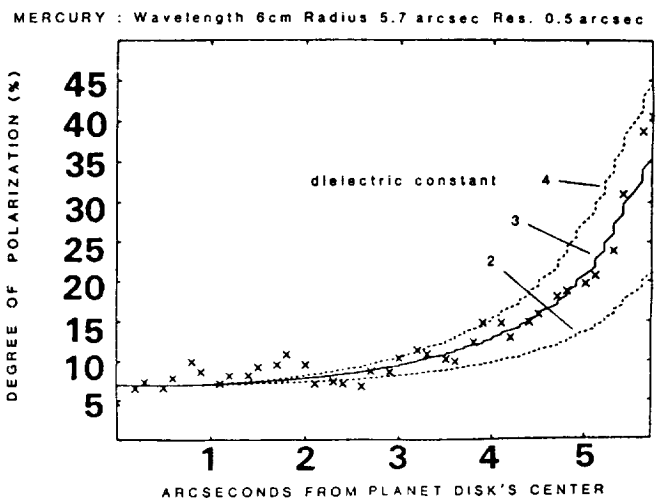

Fig. 2. Degree of Polarization (m) of the emitted thermal radiation as a function of position on the disk of Mercury; obtained from the same data as shown in Fig. 1. Measured data shown as x. Theoretical curves for the behavior of polarization at various values of dielectric constant are based on calculation from Fresnel relations.

Figure 2 shows the degree of linear polarization: $m=\sqrt{(Q^2+U^2)}/I$, where Q and U are the linear components and I is the total intensity component of the Stokes' vector. At each angular offset from the center of the disk, the maximum value of m was plotted in Fig. 2. Also shown are three curves showing the theoretical behavior for dielectric constants of 2, 3 and 4. The agreement of the measurements with a dielectric constant of 2.7, the value implied by the measured radar reflectivity of 0.06 (ref. 2), is excellent.

REFERENCES

(1) B. D. Chapman and G. H. Pettengill, "Venus Radio Emission: Ground-Based Observations", Presented at the 16th Annual DPS Meeting, Kona HI; *Bull. A.A.S.*, **16** 693, (1984).

(2) G. H. Pettengill, "Physical Properties of the Planets and Satellites from Radar Observations", *Ann. Rev. Astron. Astrophys.*, **16** 269, (1978).

VIKING RADIO SCIENCE DATA ANALYSIS AND SYNTHESIS

Robert D. Reasenberg, Smithsonian Astrophysical Observatory

During the past year, we made progress toward our primary objectives: (a) an investigation of the rotational motion of Mars and its geophysical ramifications, and (b) the study of solar-system dynamics and the laws of gravitation. We obtained a new bound on the rate of change of the rotation period of Mars, $|\dot{P}/P| < 7 \times 10^{-11}$ per year, and obtained estimates of the seasonal changes in the spin rate. These results were presented at the October 1985 meeting of the AAS, Division for Planetary Science (DPS).

Below we consider the recent technical progress which made possible our new results and which will be the basis of additional scientific results in the near future. This discussion is divided into three parts: A. Solar System Model; B. Rotation of Mars; and C. Solar System Constants. The second part includes the results that were presented at the DPS Meeting.

SOLAR SYSTEM MODEL. The central element in our data analysis is the Planetary Ephemeris Program (PEP) which embodies our mathematical models of the solar system and observables. It functions as a weighted-least-squares fitting (and Kalman filtering) facility for observations related to the positions, velocities, rotations, etc. of solar-system bodies, natural and manmade. PEP contains approximately 10^5 lines of code, which is written mostly in Fortran with a small part in assembly language. Over the past few years, PEP has been systematically upgraded to take advantage of changes in computing and software-development techniques.

During the past year, we examined the relativistic terms included in our numerically integrated equations of motion. We included some additional terms because it appeared that they could change the best of the observables by the order of their nominal uncertainty. Using the enhanced code, we recalculated the prefit residuals and formed new normal equations. In a series of solutions of these normal equations, we found that none of the scientifically interesting parameters changed by as much as 50% of their formal uncertainty; most changes were closer to 10%. For these parameters, the realistic estimate of the uncertainty ranges from 2 to 10 times the formal estimate. Other parameters (e.g., initial orbital elements of inner planets) changed by as much as their formal uncertainty, but these changes have no scientific consequences.

We have been collaborating with our JPL colleagues to uncover and correct defects in PEP and the corresponding JPL software. This is a valuable activity since the codes are large and were independently developed. In particular, we have been making comparisons between intermediate numerical products of their software and ours. We have found small discrepancies which have been traced to model errors in both sets of software. However, since none of the corrections has thus far had a significant effect on the observables or our parameter estimates, the net effect has been to increase the confidence with which both groups can rely on the software.

ROTATION OF MARS. In addition to precession and nutation [Reasenberg and King, 1979], our model of the rotation of Mars includes a secular rate of change of the period and both annual and semiannual variations in the phase of rotation [Williams, 1977, private communication; Philip, 1979; Reasenberg and King, 1979]. Our preliminary investigation with a 400-day set of Lander delay data provided a marginal detection of the semiannual terms [Reasenberg et al., 1979] and showed that these could not be clearly distinguished from the annual terms with such a small span of data.

After obtaining the above preliminary result, we modified our model of the rotation of Mars so that, before adding the above perturbations, the spin rate is constant in Mars proper time, and therefore varies by about $\pm 10^{-9}$ in ephemeris time. The associated rotational phase shift is of the same order and phase as the predicted annual effect of the atmospheric condensation at the poles. The new relativistic correction is thus critical for the accurate determination of the amplitudes and phases of the proposed meteorological effects.

At the October 1985 meeting of the DPS, Chandler [Chandler, et al., 1985] presented some of our recent results. The semiannual terms are found to be small and only moderately correlated in the estimator with the annual terms. The annual terms have an amplitude (expressed as an equatorial surface displacement) and a phase (9.3 ±1.2 m, 257° ±10°) consistent with the result expected on the basis of Viking pressure data (11.1 m, 242°), but the semiannual terms (1.5 ±1.2 m, 108° ±50°) are not so consistent with the expected result (4.7 m, 168°). These results are summarized in Figure 1.

The published measurements of atmospheric pressure [Hess et al., 1980] cover a time span of only about one Mars year. However, the results of an analysis of a much longer span of Lander pressure measurements have been supplied to us by James Tillman who is preparing this material for publication [private communication, 1983, 1984] and distribution through the NSSDC. These data show that the general features of the annual and semiannual pressure fluctuations at the Landers repeat from year to year. The use of the Viking data to determine the amplitude and phase of the annual and semiannual terms in the rotation of Mars provides one of the few independent constraints on global models of the circulation and condensation of the atmosphere of Mars. (See, for example, Shimazaki and Shimizu [1979] and references therein.)

SOLAR SYSTEM CONSTANTS. Recently, as a result of several small improvements, we have obtained a new estimate of the Earth-Moon mass ratio: $81.300589 \pm 1.5 \times 10^{-5}$. This is in very good agreement with the independently derived estimate of 81.300588 which is given in the Astron. Almanac [1984].

REFERENCES

Cazenave, A. and G. Balmino, "Meteorological Effects on the Seasonal Variations of the Rotation of Mars," Geophys. Res. Letters, 8, 245-248, 1981.

Chandler, J. F., R. W. Babcock, R. D. Reasenberg, and I. I. Shapiro, "The Rotation of Mars," BAAS, 17(3), 1985.

Hess, S. L., J. A. Ryan, J. E. Tillman, R. M. Henry, and C. B. Leovy, "The Annual Cycle of Pressure on Mars Measured by Viking Landers 1 and 2," Geophys. Res. Letters, 87, 197-200, 1980.

Philip, J. R., "Angular Momentum of Seasonally Condensing Atmosphere, with Special Reference to Mars," Geophys. Res. Letters, 6, 727-730, 1979.

Reasenberg, R. D. and R. W. King, "The Rotation of Mars," J. Geophys. Res., 84, 6231-6240, 1979.

Reasenberg, R. D., R. B. Goldstein, P. E. MacNeil, and I. I. Shapiro, "Mars Rotation: Bound on Seasonal Variation," Bull. Am. Astron. Soc., 11, 571, 1979.

Shimazaki, T. and M. Shimizu, "The Seasonal Variation of Ozone Density in the Martian Atmosphere," J. Geophys. Res., 84, 1269-1276, 1979.

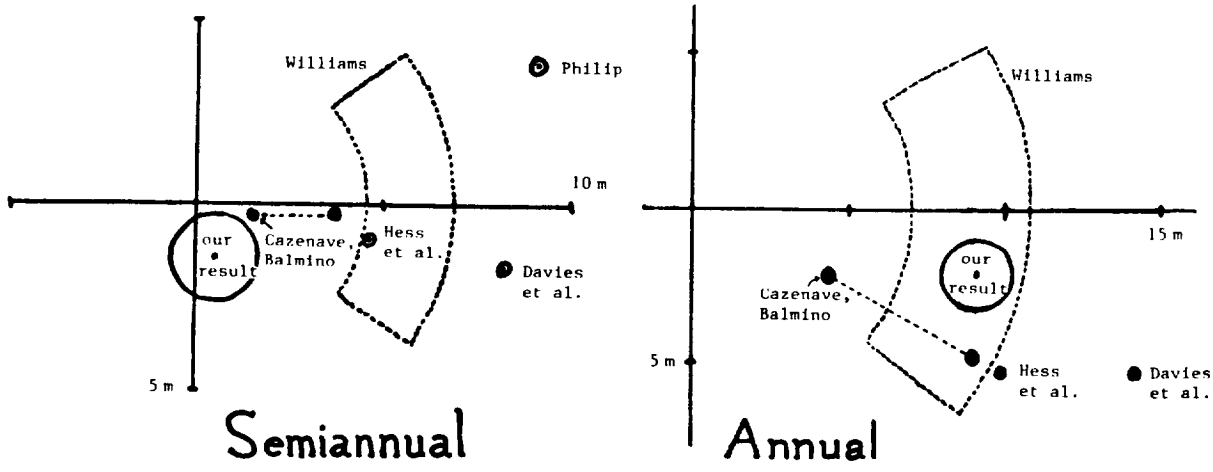

Figure 1. Seasonal variation of the spin rate of Mars determined by the analysis of the tracking data from the Viking Landers. The figure comprises two VuGraphs presented to the DPS [Chandler et al., 1985]. The Cartesian coordinates represent the quadrature components of the seasonal term; the amplitude is thus represented by the distance from the origin. In addition to the experimental result, several theoretical predictions are shown.

MARS: SEASONALLY VARIABLE RADAR REFLECTIVITY

L. E. Roth and R. S. Saunders, Jet Propulsion Laboratory, California Institute of Technology, Pasadena, California, 91109

In the course of the favorable 1971/1973 oppositions the Goldstone radar scanned Mars along constant-latitude tracks within the -14^{o} to -22^{o} latitude band, producing topographic and surface scattering information along 68 such tracks (1). The 1971 Goldstone experiment commenced 20 Jun 71 and terminated 4 Oct 71. Over the duration of the experiment Mars progressed from the position corresponding to the areocentric solar longitude $L_s=200.94^{o}$ to $L_s=267.13^{o}$. The 1973 experiment commenced 24 Jul 73 and terminated 24 Nov 73. Mars progressed from $L_s=249.39^{o}$ to $L_s=324.12^{o}$. Since the vernal equinox, summer solstice, and the autumnal equinox in the Southern hemisphere are associated with $L_s=180^{o}$, $L_s=270^{o}$, and $L_s=360^{o}$, respectively, the subequatorial areas observed by radar passed, ignoring the lapse of one Martian year, from the early spring to the late summer. Previous investigation (2) of the Goldstone Mars data set demonstrated an apparent link, mostly within the longitude interval from 80^{o} to 100^{o}, between the radar reflectivity and the seasons of the Martian year (the 'Solis Lacus radar anomaly' (2)). We extended the analysis to cover all longitudes.

The logical first step when examining a data set of the size of the Goldstone Mars set (13,400 reflectivity-roughness pairs) is to look for the gross, zeroth-order trends. Searching for such trends, we computed the mean reflectivity for each individual scan and correlated the coputed means with L_s, i.e., with the season of the year. An overall trend toward higher reflectivities deeper into the Southern hemisphere summer was seen to emerge (3). In the next step we identified the coincident segments of those scans that differ in latitude by less than $.7^{o}$, i.e., by less than one-half of the N-S extent of the radar resolution cell. The coincident segments consist of concatenations of coincident points. Two points of identical longitudes are defined as coincident if the full scattering-law solution is available for both. For each pair of coincident scans we formed a ratio of the mean reflectivity of the scan at the higher L_s (later in the season) to the mean reflectivity of the track at the lower L_s (earlier in the season). For targets whose reflectivities are not a function of time these ratios should always equal unity. Most of the mean reflectivity ratios in the Goldstone Mars data are found to lie in the range from 1.0 to 1.4. The ratios for scans whose separation in time corresponds to less than $\Delta L_s=10^{o}$ tend to cluster around unity. The ratios for scans taken at intervals $\Delta L_s>10^{o}$ tend toward values larger than unity. This trend is characteristic of the planet as a whole (Figs. 1a through 1d); the Sinai Planum/Solis Lacus area is not exceptional in this respect. We conclude that the mean reflectivities in the entire Goldstone 1971/1973 data set do not remain constant throughout the cycle of the Martian seasons. Generally, they are lower in the Southern hemisphere spring, higher in the Southern hemisphere summer. Applying identical procedures to the analysis of the roughness parameter C, the other free variable in the Hagfors law, we found that roughness also does not remain constant throughout the Martian year; the trends are not clear, however.

The reflectivity and roughness variations noted in the Goldstone data are suggestive of, but they do not prove, the seasonal presence of liquid water below the Martian surface. A number of unanswered questions that still reamin are being addressed presently. Among those: (1) Some investigators have expressed doubts about the integrity of the Goldstone Mars data set. The goal of the validation effort, currently under way, is to determine the reality of the observed phenomena. (2) In forming the reflectivity ratios discussed above no distinction was made between the 1971 data and the 1973 data. Preliminary investigation of each subset separately indicates that the trends toward higher reflectivities deeper into the season are not uniform in both subsets and differ from those in the combined set. (3) Presence or absence of correlation between the reflectivity variations and the local/regional geology might provide additional clues to the reality of the phenomena. These correlations are being investigated for each pair of coincident scans.

References: (1) Downs, G. S., Reichley, P. E., and Green, R. R. (1975) Icarus 26, 273. (2) Zisk, S. H. and Mouginis-Mark, P. J. (1980) Nature 288, 735. (3) Roth, L. E., Saunders, R. S., and Schubert, G. (1985) Lunar and Planet. Sci., XVI, 712.

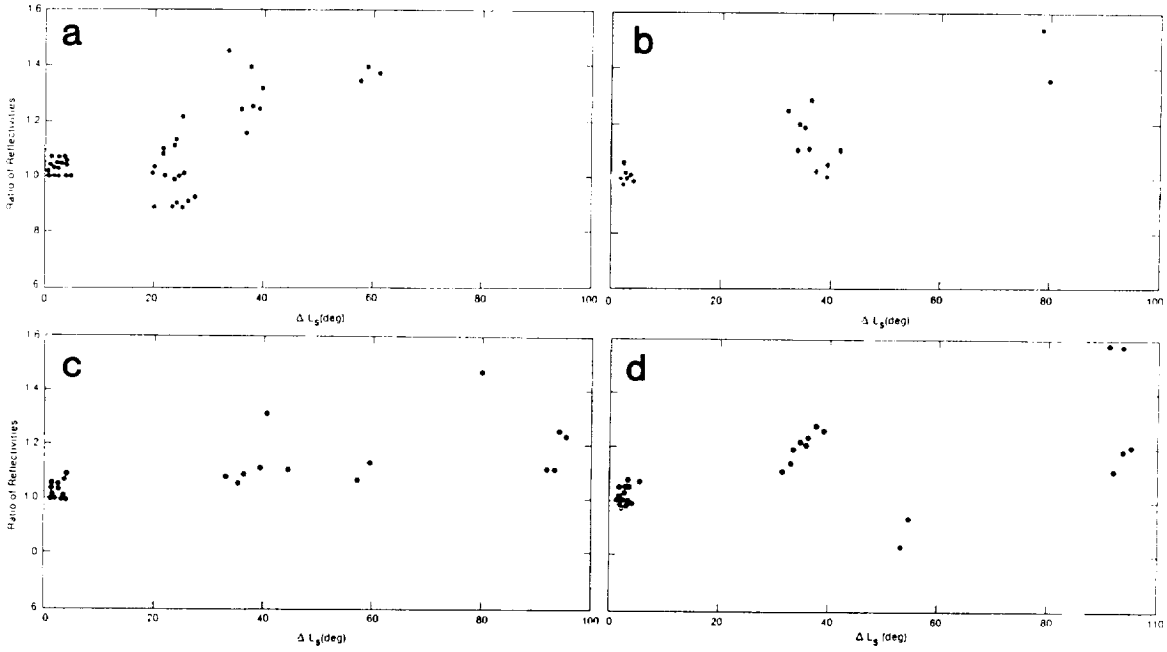

Fig. 1. Reflectivity ratios for the coincident segments of the Goldstone Mars radar tracks vs. the increments in the solar longitude, ΔL_s, for the following quadrangles: (a) Memnonia (MC-16); (b) Margaritifer Sinus (MC-19); (c) Sinus Sabaeus (MC-20); (d) Iapygia (MC-21).

RADAR SIGNAL ATTENUATION, "SKIN DEPTH", AND "RADAR IMAGING DEPTH"
(modified from [1])

Schaber, G. G., U.S. Geological Survey, Flagstaff, Arizona

Factors Contributing to Signal Attenuation

The principal factor that limits depth of microwave penetration is attenuation of the electromagnetic wave in the material. Attenuation can result from the conversion of electromagnetic energy to thermal energy through losses by electrical conduction or by dielectric relaxation. Conduction losses occur primarily through movement of ions and electrons; relaxation losses, commonly severe, occur mostly through induced oscillations of the dipolar water molecule. Additional attenuation can result from scattering of the electromagnetic energy in unwanted directions by material inhomogeneities. Scattering may dominate the attenuation process if the scale of inhomogeneities such as rocks or carbonate nodules is similar to the wavelength of the probing signal.

Roth and Elachi [2] reported a parametric analysis of the coherent electromagnetic losses due to scattering from volume inhomogeneities. They calculated scattering losses as a function of relative size of scatterers, contrast in dielectric constant, and radar wavelength. Scattering losses were found to dominate; they are considerable for grain sizes larger than one-fifth the wavelength. Roth and Elachi [2] found that although signal losses do not prohibit subsurface imaging where grain sizes are smaller than about one-tenth wavelength, only a few embedded scatterers that exceed this size strongly inhibit subsurface imaging. They concluded that even very weak inhomogeneities can result in appreciable loss in a resonance region and thus play a more dominant role than conductivity losses.

The presence of clays with diffusion-limited colloidal dielectric-relaxation processes increases losses dramatically and severely limits penetration. For example, an almost complete absence of clays in the Selima Sand Sheet, southern Egypt, is clearly a significant factor in the exceptional degree of SIR-A signal penetration in this region.

Radar "skin depth" and "radar imaging depth"

Given a knowledge of the stratigraphy, mineralogy, particle-size distribution, and electromagnetic properties of a material, we can estimate the depth of radar-signal penetration by using the radar equation and selected radar-system parameters [3]. For all practical purposes, radar signals of centimeter to decimeter wavelength are usually not expected to penetrate to a depth of more than about one wavelength in most soils of normal moisture and clay content in temperate to semiarid climates. Penetration depth can be estimated by the following formula [4]:

$$P = P_0 e^{-2\alpha d} \qquad (1)$$

where P is the power at depth d and P_0 is the power at the surface, and

$$\alpha = 2\pi/\lambda \sqrt{|E|} \cdot \frac{\sin \delta}{2} \qquad (2)$$

where λ is the wavelength used; $|E|$ is the resultant dielectric constant ($|E| = \sqrt{\varepsilon'^2 - \varepsilon''^2}$) where ε' and ε'' are the real and imaginary parts, respectively, of the dielectric constant; and δ is the loss angle ($\tan \delta = \varepsilon''/\varepsilon'$), a measure of energy loss (the reciprocal of the electromagnetic Q, analogous to seismic Q). The penetration depth is thus defined by $2\alpha D = 1$, the depth at which the power is attenuated to 1/e (37 percent), called the "skin depth". Thus

$$D = \frac{1}{2\alpha} = \frac{\lambda}{4\pi \sqrt{|E|} \cdot \frac{\sin \delta}{2}} \qquad (3)$$

As DeLoor [4] points out, even for the driest materials in semiarid or arid environments (e.g., dry sand), $\sqrt{|E|} > 1.5$, $\frac{\sin \delta}{2}$ must be smaller than $1/6\pi$ or 0.053, and thus $\tan \delta$ must be less than 0.106 to make D larger than λ (the wavelength used).

The term "penetration depth" as used above is misleading, however, when applied to radar-image data such as that of SIR-A. The two-way signal path (into and back out of a low-loss medium) has been shown to reduce the effective subsurface mapping capability to a maximum of half the theoretical skin depth. We proposed in [1] the term "Radar Imaging Depth" (RID) and the symbol D_i, and defined it as the maximum depth to which a radar signal can penetrate unconsolidated material and return a backscattered signal through the medium to the antenna. From our field studies of natural materials in the Nubian Desert (S. Egypt-N. Sudan), it appears that those materials with the lowest loss result in a maximum D_i of one-half D ("skin depth") or

$$D_i \simeq \frac{D}{2} = \frac{\lambda}{8\pi \sqrt{|E|} \cdot \frac{\sin \delta}{2}} \qquad (4)$$

References

[1] Schaber, G. G., McCauley, J. F., Breed, C. S., and Olhoeft, G. R., Space Shuttle Imaging Radar: Physical controls on signal penetration and subsurface scattering in the Eastern Sahara: IEEE Transactions on Geoscience and Remote Sensing, in press.

[2] Roth, L. E., and Elachi, Charles, 1975, Coherent electromagnetic losses by scattering from volume inhomogeneities: IEEE Transactions on Antennas and Propagation, v. 23, p. 674-675.

[3] Ulaby, F. T., Moore, R. K., and Fung, A. K., 1982, Microwave remote sensing: active and passive, chapt. 2, in Radar remote sensing and surface scattering and emission theory: Reading, Penna., Addison-Wesley, p. 816-846.

[4] DeLoor, G. P., 1983, The dielectric properties of wet materials: IEEE Transactions on Geoscience and Remote Sensing, v. GE-21, p. 364-369.

RADAR BACKSCATTER FROM A SUBSURFACE INTERFACE FOLLOWING PENETRATION OF A LOW-LOSS MEDIUM (modified from [1])

Schaber, G. G. and Kozak, R. C., U.S. Geological Survey, Flagstaff, Arizona

When microwave penetration and refraction take place in a low electrical-loss material such as dry sand, theoretical modeling of simple refraction and subsurface scatter can be accomplished with some degree of confidence. Elachi, Roth, and Schaber [2] on the basis of SIR-A results described by McCauley et al. [3], described spaceborne radar subsurface imaging in hyperarid regions. These authors, using a simple two-layer backscatter model with no volume-scattering components, showed that the presence of a low-loss, thin sand layer can actually enhance the capability to image a discrete subsurface interface, particularly at the large incidence angles and HH polarization used on the SIR-A sensor. Such enhancement occurs when permittivity contrast between the sand and a subsurface interface is substantial, and is due to refraction of the SIR-A wavefront at the air-sand interface. This refraction results in a smaller "effective" incidence angle and a stronger backscatter, which can compensate for both the losses due to both absorption in the sand layer and the specular reflection (away from the SIR-A receiver) occurring at the air-sand interface.

The "apparent" wavelength of the refracted wave in the ground is given by

$$\lambda = c/(f\sqrt{\varepsilon_r}) \tag{1}$$

where λ is the wavelength in meters, c is the speed of light in free space in meters per second, f is the frequency in Hertz, and ε_r is the ratio of the permittivity (dielectric constant) of the ground to that of free space (relative permittivity) [4]. From Figure 1 one can see the relation between the angle of incidence at the air-surface interface Θ and the refracted angle of incidence (Θ') after penetration of the SIR-A signal into a sand mantle with resultant dielectric permittivity of 3.3.

The backscatter cross section for a slightly rough surface is given by Valenzuela [5,6] as:

$$\sigma_s = f_i\ (\varepsilon_1, \lambda, \Theta)\ \omega\ (2k \sin\theta) \tag{2}$$

where ε_1 is the real part of the dielectric constant of the medium, λ is the wavelength of the incident wave, θ is the incidence angle, $k = 2\pi/\lambda$ is the wave number of the incident wave, $\omega(k)$ is the surface roughness spectrum, and f_i is a function given by:

$$f_H = 4\ \pi\ k^4\ \cos^4\ \Theta\ \left[\frac{\varepsilon_1 - 1}{(\cos\Theta + \sqrt{\varepsilon_1 - \sin^2\Theta})^2}\right]^2 \tag{3}$$

for horizontal polarization used on the SIR-A mission. Elachi, Roth, and Schaber [2] showed that in the presence of a sand layer of thickness L, dielectric constant ε_2, and skin depth D, the backscatter cross section becomes

$$\sigma_{ss} = T_i^2\ (\Theta)\ e^{-2L/D\ \cos\ \Theta'}\ f_i\ \left(\frac{\varepsilon_1}{\varepsilon_2}, \frac{\lambda}{\sqrt{\varepsilon_2}}, \Theta'\right)\ \omega(2k\sqrt{\varepsilon_2}.\sin\Theta') \tag{4}$$

where $T(\theta)$ is the transmissivity (not the transmission coefficient, as stated in [3]) at the surface [7], and $\sin\theta = \sqrt{\varepsilon_2}\cdot\sin\theta'$. Equation 4 shows that the roughness term ω is identical in the expressions for both σ_s and σ_{ss}. Thus the effect of the layer can be characterized by the ratio R:

$$R = \frac{\sigma_{ss}}{\sigma_s} = T_i^2(\theta)\, e^{-2L/D\cos\theta'} \frac{f_i\left(\frac{\varepsilon_1}{\varepsilon_2}, \frac{\lambda}{\sqrt{\varepsilon_2}}, \theta'\right)}{f_i(\varepsilon, \lambda, \theta)} \qquad (5)$$

The behavior of R as a function of L/D, θ, and ε is shown in Figures 2-4 for HH, HV, and VV polarization, respectively, given the SIR-A wavelength of 23.5 cm. Values for R above 1.0 indicate a positive enhancement effect due to beneficial levels of refraction of the signal in the sand layer. Values below 1.0 indicate a negative effect; that is, the signal losses (absorption) in the sand layer would not be compensated for by the increased power resulting from signal refraction to higher incidence angle. The sand layer is taken to have $\varepsilon_2 = 3.3$, which is the average of all eolian sands and sandy alluvial materials collected from the Nubian Desert and measured in the laboratory.

The subsurface dielectric constant is taken as $\varepsilon_1 = 6$, a value within the range of dielectric constants for low-porosity quartzitic sandstones. From equation (1) above, the "effective" wavelength of the 23.5-cm signal would be 12.9 cm following refraction in the sand layer.

Figure 2 shows that the presence of a sand layer as thick as 40 percent of the skin depth will in effect enhance the capability to image the subsurface interface with HH polarization and a 50° incidence angle such as was used on SIR-A. At depths as great as the maximum SIR-A skin depth of 6 m measured for dune sand in the Nubian Desert, this favorable effect will occur for layers as thick as 2.5 m, given loose, dry sand with no cementing agents to increase density. Similarly, in Figure 2 we can see that for 30° and 40° incidence angles, the positive effect of the sand layer is limited to 20 and 30 percent of the skin depth, respectively. Figure 3 shows that for HV polarization, the enhancement effect due to the sand layer is positive only for a 60° incidence angle and sand-layer thickness less than 10 percent of the skin depth. For VV polarization, the enhancement is negative for incidence angles of less than 60° (Fig. 4).

REFERENCES

[1] Schaber, G. G., McCauley, J. F., Breed, C. S., and Olhoeft, G. R., Space Shuttle Imaging Radar: Physical controls on signal penetration and subsurface scattering in the Eastern Sahara: IEEE Transactions on Geoscience and Remote Sensing, in press.

[2] Elachi, Charles, Roth, L. E., and Schaber, G. G., 1984, Spaceborne radar subsurface imaging in hyperarid regions: IEEE Transactions on Geoscience and Remote Sensing, v. GE-22, p. 383-388.

[3] McCauley, J. F., Schaber, G. G., Breed, C. S., Grolier, M. J., Haynes, C.V., Issawi, B., Elachi, Charles, and Blom, Ronald, 1982, Subsurface valleys and geoarcheology of the eastern Sahara revealed by shuttle radar: Science, v. 218, p. 1004-1020.

[4] Wright, D. L., Olhoeft, G. R., and Watts, R. D., 1984, Ground-penetrating radar studies on Cape Cod: NWWA/EPA Conf. on Surface and Borehole Geophysical Methods in Ground Water Investigations, San Antonio, Texas, Feb. 7-9, 1984, p. 666-680.

[5] Valenzuela, G. R., 1967, Depolarization of EM waves by slightly rough surfaces: IEEE Transactions on Antennas and Propagation, v. AP-15, p. 552-557.

[6] Valenzuela, G. R., 1968, Scattering of electromagnetic waves from tilted slightly rough surfaces: Radio Science, v. 3, p. 1057-1066.

[7] Born, M., and Wolfe, E., 1980, Principals of optics: Pergamon Press, New York, 808 p.

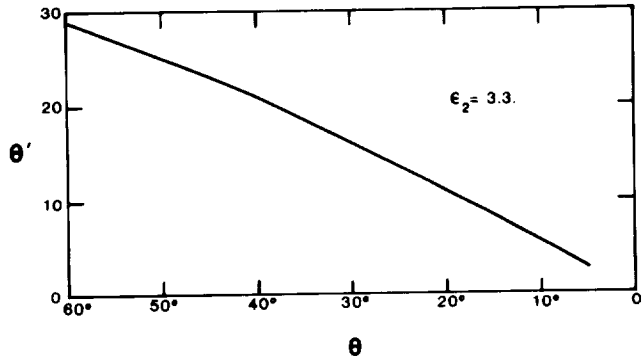

Fig.1

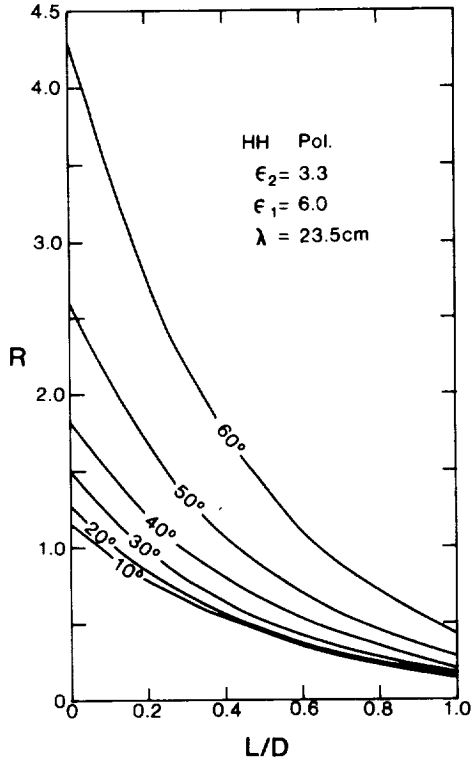

Fig.2

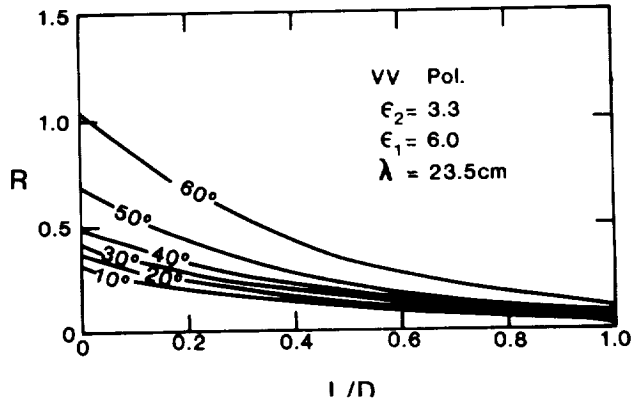

Fig.3

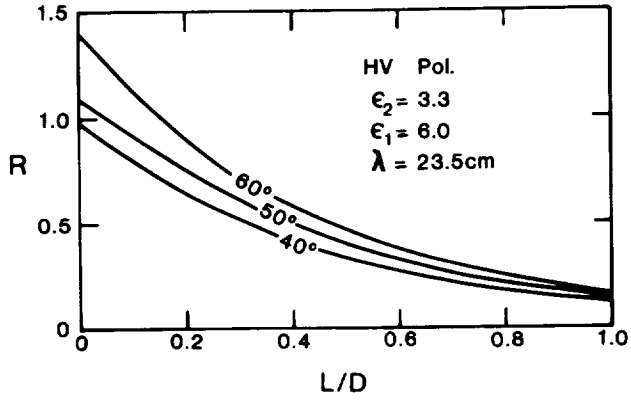

Fig.4

SOUTHERN ISHTAR TERRA AND GUINEVERE/SEDNA PLANITIA: NEW OBSERVATIONS FROM EARTH-BASED RADAR E.R. Stofan[1], D.B. Campbell[2], J.W. Head[1], and A.A. Hine[2] (1)Dept. of Geological Sciences,Brown Univ.,Prov.,R.I. 02912 (2)National Astronomy and Ionosphere Center, Arecibo, PR 00612

The southern Ishtar Terra region is one of the more complex areas on Venus. Significant volcanic and tectonic activity in the region have been identified, including possible calderas and folded or faulted terrain (1-3). High resolution (1-3 km) images of the southern Ishtar region were collected by the 12.6 cm radar at Arecibo in the summer of 1983. The area of study has been divided into four provinces, defined by topographic and radar characteristics (Figure 1). We review these characteristics, and suggest some preliminary inter- and intra-province age relationships.

Province I is a predominantly radar-dark, generally featureless region known as Lakshmi Planum. It is a high plateau, rising over 3 km above the mean planetary radius, with distinct, steeply-sloped boundaries. Two major circular depressions, Colette and Sacajawea, lie in the plateau, and are believed to be volcanic calderas (3). Colette has a dark circular center (2-5 km diameter) surrounded by a quasi-circular bright area (approximately 55 km wide). Sacajawea is less distinct in radar images, appearing as arcuate bright segments defining a quasi-circular area. The other major features of the plateau are small groups of bright lines, occurring near the eastern and western margins. The lines occur in closely spaced groups that appear to be embayed in places by the dark plains material. An exception to this is the set of lines that lie near the easternmost extent of the plateau. This set of lines is more widely spaced and distinct, and does not appear embayed. A few small (< 10 km) bright circular features of possible impact origin can be seen in Province I, although distinctive structure cannot be resolved.

Province II is characterized by highly lineated terrain bordering Lakshmi Planum. The brightest areas include the southern Akna Montes and the mountainous region above Vesta Rupes. Vesta and Ut Rupes appear as darker regions bounded by bright linear features. The linear features may be classified as bands (2) and lines (4). Bands are long, very bright, lie in parallel groups, and occur in topographically high terrain. On the border of Lakshmi, the banded region ranges from 2.5-6 km above mpr. The bands first appear in the east as a narrow bright set that defines two oval, depressed areas. The bands widen, then die out, then reappear as a wider group (> 40 km wide) that rim the plateau. To the west, the bands become discontinuous lines that trend to the northwest for over 400 km before dying out. The bands reappear in a northeast-trending coherent group that corresponds to the southern portion of Akna Montes. The majority of Province II is dominated by lines, which are less bright, narrower, and shorter than bands (4). The lines have a dominant trend to the west-northwest, apparently cutting a set in the western region that trend to the northeast. The lines are more widespread than the bands, corresponding to gentler slopes lying between 2.5 km and the mean planetary radius. Several probable impact craters (over 30 km in diameter) can be seen in the zone comprised primarily of lines. A few large circular structures, possibly coronas (3), are also present in the western region, with diameters of over 100 km.

Province III is composed of flow-like units, interpreted as volcanic plains (4). The flows range from low to high backscatter return, and frequently have a lobate appearance. Some flows appear to be over 100 km long. The area is topographically low; its boundaries generally following the topography. A large depression, approximately 140 km across, lies in the western half of the province. The flows appear to originate from two types of vents. Type I is a bright spot surrounded by radar-dark material. Type II has a dark circular center with wide bright surrounds, resembling the feature Colette. One probable impact crater is located near the eastern margin of the province. The boundaries with Province II are quite distinct, while the boundaries with Province IV are transitional.

Province IV, characterized by plains, is generally radar-dark like the plateau, but has more abundant bright lines. Bright lines occur in a variety of orientations and types. 1) Single, often arcuate lines- occur predominantly in the western region. Near the

southwestern margin, the arcuate lines are associated with extension at the northern end of Beta and Devana Chasma. 2) Paired lines- occur in both IVa and IVb. Paired lines are generally closely spaced and range from straight to arcuate. 3)Arcuate groups- majority in IVb. Two or more parallel arcuate segments occur in groups that usually approximately define a circular area. We interpret the lines to be of tectonic origin, most likely representing faults. The province is also characterized by coronas that range in diameter from 60-300 km. They occur in IVa as isolated, generally circular features, elongate structures as in the center of the plains, and in clusters. In general, they are relatively high topographically. The rims of coronas in IVa range from distinct, bright and continuous to discontinuous and faint, probably representing varying states of degradation and/or flooding. The arcuate segment groups in IVb are interpreted as portions of coronas that have been more thoroughly flooded. Most of the coronas have multiple, concentric rings. In addition, IVa and IVb have areas of anomalous brightness. This corresponds to high, probably rough topography in IVb. In the western region, no topographic correlation is seen, indicating isolated areas of high roughness. Both IVa and IVb have scattered probable impact craters, with a somewhat higher density in IVb. The majority of the craters are <10 km in diameter.

Analysis suggests that volcanism and tectonism are significant in the geological evolution of the region. On the basis of cross-cutting, superposition, and embayment relationships, multiple volcanic and tectonic events have occurred in each province. The style and proportion of volcanic and tectonic activity (e.g. coronas, bands, flows) is significant in defining each province. We do not feel that these provinces represent distinctly sequentially formed geologic units, but rather we suggest that different styles of tectonic and volcanic activity have occurred in different provinces. However, some relative age relationships can be determined. Stratigraphic relationships suggest that the deformation associated with the west-northwest trending lines in Province II postdates the deformation associated with Akna Montes, and that the volcanic plains in Province III postdate the major deformation surrounding Ishtar Terra (Province II). Volcanic flooding has locally postdated corona formation, particularly in IVb. Some of the lines of Province II are superposed over a corona in IVa. The relatively small number of impact craters seen throughout the area (3,5) suggest that most of the observed geologic activity has taken place in the last one-third of solar system history.

References 1)Masursky,H. *et al.* (1980) *JGR, 85,* 8232-8260. 2)Campbell,D.B. *et al.* (1983) *Science,221,* 644-647. 3)Barsukov,V.L. *et al.* (1984) *Geochimia,12.* 4)Head,J.W. *et al.* (1985)Lunar Planet. Sci. Conf. XVI,this volume. 5)Campbell,D.B. and Burns,B.A.(1980) *JGR,85,* 8271-8281.

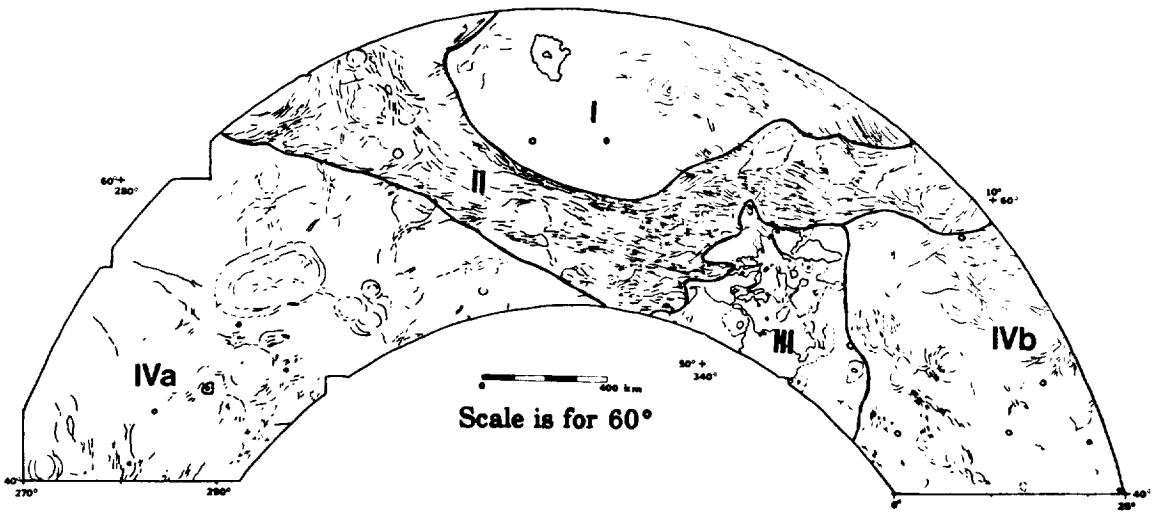

Figure 1. Sketch map of the southern Ishtar region from high resolution Arecibo images.

MULTIPLE RING FEATURES IN THEMIS REGIO: EVIDENCE FOR ENDOGENIC ORIGIN E.R. Stofan[1], J.W. Head[1], and D.B. Campbell[2] (1)Dept. of Geological Sciences,Brown Univ.,Prov.,R.I. 02912 (2)National Astronomy and Ionosphere Center, Arecibo, PR 00612

Previous studies (1-3) have described and classified circular features on Venus. However, unanswered questions remain concerning the modes of origin (e.g. impact, volcanic, tectonic) of various classes of circular features. Stofan *et al.* (1984) developed a classification scheme for circular features seen in radar images of Venus, including a class that has a probable volcanic mode of origin (4). In this study, we review some Class IV, or multiple ring, features in an attempt to understand their formational processes.

High resolution (1-3 km) radar images from Arecibo, obtained in the summer of 1983, reveal the presence of two types of multiple ring features in the southern hemisphere. Type I has at least two distinct, fairly continuous rings that are isolated from other ring structures. Examples of this are found at 56°S, 321° (Lise Meitner, diameter 81 km) and at 63°S, 322° (diameter about 220 km). Type II ringed features have discontinuous, sometimes merged rings of varying brightness that are associated with other ringed and bright linear features. The group of features in Themis Regio (Figures 1,2), which fall under Type II, is used to investigate potential modes of origin of these type of multiple ring features.

Themis Regio, centered at approximately 40°S, 280°, has been described as part of a northwest trending linear zone that extends for over 14,000 km from east of Themis to the northwest border of Atla Regio (5). Figure 2 illustrates that the linked ring structures are in an elevated region, that rises in places to over 3 km above the mean planetary radius. The linked ring structures appear bead-like in the northwest, in places connected by short paired lines. The beads are about 200 km in diameter, and have at least one concentric interior ring. In the central and eastern region, the ring structures appear to be merged as opposed to beaded, and are cut by bright lines that trend dominantly to the northwest, parallel to the topographic axis. The merged rings are larger than the beaded features, with diameters generally >300 km. The line segments frequently occur in pairs, spaced over 60 km apart. The lines link, cut, and/or radiate from the rings. The rings in the central and eastern area are quasi-circular, often polygonal, with some discontinuous, arcuate, concentric segments.

Several possibilities exist for the origin of these features. The high topography could be a relict highland region that has been heavily cratered. However, two observations seem to argue against an impact origin. In the northwest, the bead-like sequence of features seem unlikely to be produced by random impacts. Secondly, in the central region of Themis the linked rings appear to be merged rather than a distinctly superposed or cross-cutting sequence expected from cumulative impacts. The dominant presence of the linear features that parallel the topographic axis, and the high topography related to the regional structure (5), suggest that the features are endogenic in origin, and related to tectonic activity. The features also may be related to the features identified as coronas in the northern hemisphere (6). Major linear trends on Venus, that can be detected in several data sets (7), appear to be defined, as at Themis Regio, by significant tectonic and/or volcanic activity. It is evident that while some Class IV or multiple ring structures on Venus (Type I features) may resemble multiring impact basins on other planets, many (particularly Type II) are of internal origin, such as those in the Themis region.

References 1)Campbell,D.B. and Burns,B.A.(1980) *JGR,85,* 8271-8281. 2)Burns,B.A.(1982) PhD. Thesis, Cornell Univ.,602 pp. 3)Stofan,E.R. *et al.* (1984) Lunar Plan. Sci. Conf. XV,824-825. 4)Stofan,E.R. *et al., in preparation* 5)Schaber,G.G.(1982) *GRL,9,* 499-502. 6)Barsukov,V.L. *et al.* (1984) *Geochimia, 12.* *7)Sharpton,V.L. and Head,J.W. (1985) Lunar Planet.* Sci. Conf. XVI, this volume.

Figure 1: High resolution (1-3 km) Arecibo image of Themis Regio.

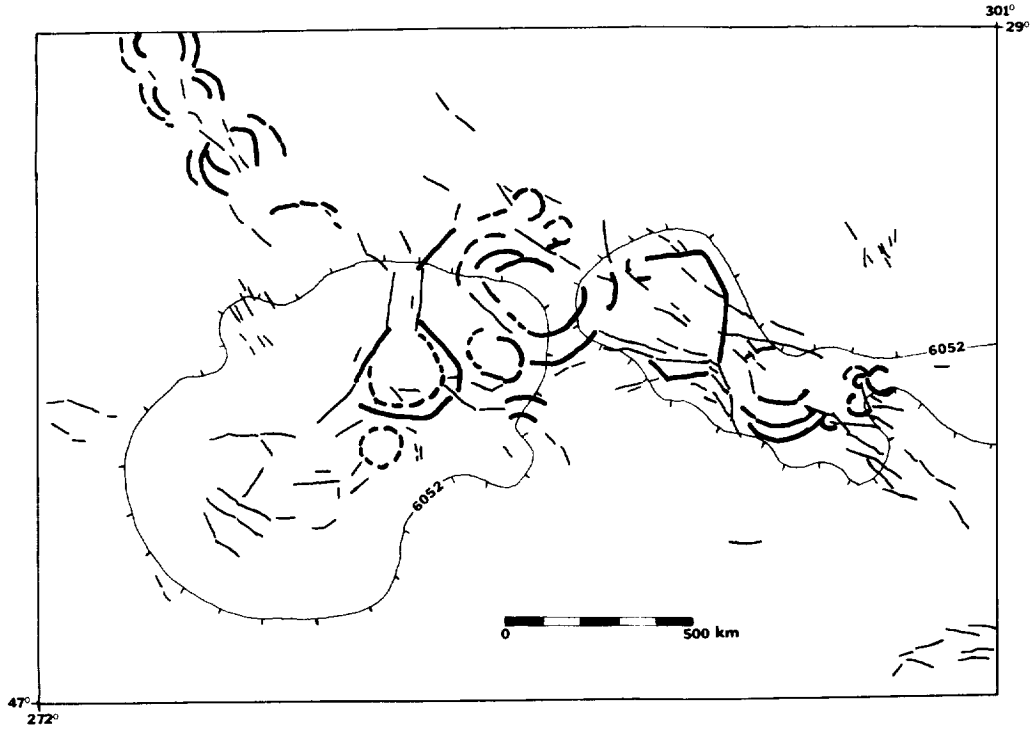

Figure 2: Sketchmap of Themis Regio with Pioneer-Venus topography.

APPLICATION OF NUMERICAL METHODS TO PLANETARY RADAR SCATTERING

G. Leonard Tyler and Richard A. Simpson
Center for Radar Astronomy
Stanford University, Stanford, CA 94305

Radio wave scattering is an effective method -- in some cases, one of the only methods -- for remote study of planetary surface structure. It is particularly appropriate when information on surface texture at scales of centimeters to meters is desired or when surfaces (such as those of Venus and Titan) are shrouded by optically opaque atmospheres.

Despite use of radio wave scattering for a period now approaching four decades, theoretical interpretation of experimental observations is inadequate. Theoreticians reached a bottleneck in the mid 1960's when no mathematical techniques could be found to handle scattering by surface structures having dimensions on the order of the radio wavelength. This is a particularly important regime since polarization and wavelength-dependent phenomena are believed to be strongly connected with wavelength-sized structure.

Numerical techniques provide one possible route through this barrier. Relatively simple algorithms, albeit ones which demand considerable computational power, now permit simulation of some electromagnetic problems. Wires, and grids of wires, are the most easily simulated geometries -- and the most readily checked -- but numerical codes now exist also for surfaces made from elemental, flat "facets."

We are in the process of collecting a set of such computer programs. In the longer term our expectation is that we can apply numerical techniques to geologically meaningful computer representations of stochastic surfaces and, eventually, to the interpretation of planetary radar data. Our present efforts focus on adapting existing codes to our operating system, experimenting with input parameters, and testing their power for both two- and three-dimensional simulations.

RADARGRAMMETRY FOR THE VENUS RADAR MAPPER MISSION

Sherman S. C. Wu, Francis J. Schafer and Annie-Elpis Howington,
U.S. Geological Survey, Flagstaff, AZ 86001

Venus Radar Mapper (VRM) radargrammetry represents the development of techniques for the extraction of topographic information related to features on Venus by using stereoradar images obtained from the Venus Radar Mapper Mission. Photogrammetric measurements from radar imagery can be made with techniques and orientation procedures similar to those used for conventional photogrammetry. The mensuration principle, however, is different: a camera records angles, and radar measures distances. In other words, normal photographic imagery has a point-perspective geometry, whereas radar imagery has a range and time geometry. The process of taking photographs enforces the collinearity of the camera-lens center, image point, and ground point. Recovery of three-dimensional information about a ground point is made by locating conjugate image points on a pair of stereophotographs. Radar, however, forms an image of a ground point through the use of range and squint angle (azimuth), and is therefore analogous to an imaging vector defined by the collinearity condition in the photographic system. The radar-projection lines are circles that are concentric with respect to the flight path. A ground point in object space can be located by the intersection of the two circular loci from images of two flight paths. In order to relate image space to ground-object space, radargrammetry is based on the two conditions of range and squint (azimuth) (Blackwell, 1981). If D is the distance from the instantaneous spacecraft position to the directly measured ground point, and D' is the same distance deduced from biscopic image measurements, then $F=D'-D=0$ is the range-condition equation that enforces the condition that the slant range from an instantaneous spacecraft position to the ground point is identical, whether deduced from image measurements or from the displacement vector between the spacecraft and the ground point. If ϕ is the angle between the spacecraft velocity vector and the range vector to the ground point (nominally 90°), and ϕ' is the squint angle derived from the Doppler equation with the component of radar-image coordinates, then $G = \cos \phi - \cos \phi' = 0$ is the squint (azimuth) condition equation that enforces the condition that the angle between the instantaneous spacecraft velocity vector and the image ray is identical, whether radargrammetrically inferred or derived from the Doppler equation (Jackson, 1985). The reduction of the condition equations involves solving for the vehicle velocity vector, range bias, range scale, Doppler rate of change, and height.

On the basis of these two condition equations and the associated geometric theory, compilation software for synthetic aperture radar imagery has been developed on the AS-11AM analytical stereoplotter. This is a joint effort with the Defense Mapping Agency. SeaSat stereoradar images have been used in tests for the compilation of both planimetric maps (Fig. 1) and contour maps (Fig. 2) from stereomodels set up on the analytical stereoplotter at the Branch of Astrogeology, Flagstaff, Arizona. Error analysis has not been made. Continuing development on VRM radargrammetry will emphasize the improvement of the accuracy of compilation based on stereoradar imagery.

References

Blackwall, B. H., 1981, Realtime math model for SAR imagery: Final Tech. Report, RADC-TR-301, 70 p.
Jackson, Michael, 1985, SAR compilation, Final Tech. Report: RADC-TR-85-82, 57 p.

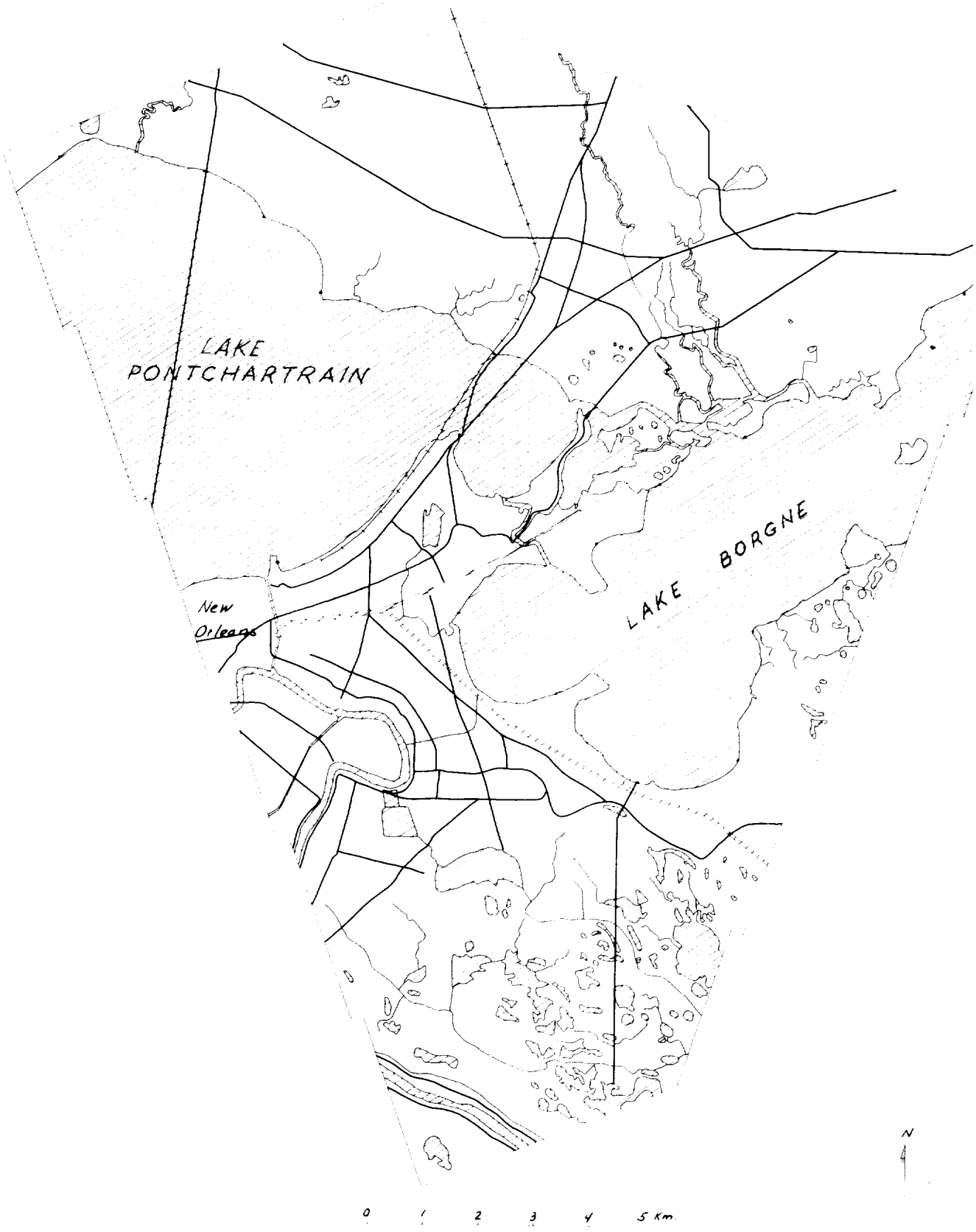

Figure 1. Planimetric map of New Orleans area compiled on the AS-11AM analytical stereoplotter by using SeaSat radar images. Diagonal lines indicate water. Map scale is 1:500,000.

Figure 2. Contour map of Los Angeles area compiled on the AS-11AM analytical stereoplotter by using SeaSat radar images. Map scale is 1:200,000. Contour interval is 10 m.

CHAPTER 14

GEOLOGIC MAPPING, CARTOGRAPHY AND GEODESY

A DIGITAL IMAGE MODEL OF MARS

R. M. Batson, U.S. Geological Survey, Flagstaff, AZ 86001

A mosaic of approximately 4700 Viking Orbiter images covering all of Mars, at resolutions of about 200 meters per pixel, is being compiled. This Digital Image Model (DIM) will contain radiometrically corrected, photometrically modeled images and mosaics displaying accurate reflectance properties of Mars at uniform resolution, geometrically tied to the best available control. The model will provide a planimetric control base to which future Mars data can be registered. The database is being encoded in a single, unzoned, Sinusoidal Equal-Area projection, because in this configuration the location of each pixel is specified by a latitude/longitude (rather than rectangular) coordinate, precluding the mathematically complex inverse projection computations that are normally required to change data from one map projection to another. The projection allows contiguous presentation of an entire globe on a single, unzoned image. Each image line is a parallel of latitude. Images near the central meridian appear nearly orthographic, but are increasingly foreshortened toward the edge. Meridians can be easily repositioned, however, simply by sliding image lines with respect to one another. For example, the central meridian in figure 1 is 180° west of the 0° meridian; it is at 0° in figure 2 and 180° east of 0° in figure 3. Each of these three images contains 360° of longitude and extends from pole to pole. The resolution of the database in the figures is 1/16° (~3700 meters) per pixel, whereas the resolution of the planned image model is 1/256° (~230 meters) per pixel.

Until now, most Viking images have been used primarily as black-and white photographs in systematic investigations made to define geologic relations and structures on Mars. These investigations are relatively complete for resolutions lower than about 300 meters. The fact is, however, that the Viking images are more than photographs; each is a complex array of digital data with a scope and dynamic range far beyond the capability of film to display. Not only is it becoming difficult to pursue major research areas on Mars because of the unwieldiness of the Viking dataset, but the usefulness of data returned by future missions, such as Mars Observer, will be jeopardized unless they can be registered digitally with Viking. Three examples are:

(1) Geologic regimes distinct from any studied to date can be examined systematically on images with resolutions as high as 20 to 30 meters. Geologic conditions observable at these resolutions must be understood, not only to relate them to their regional context, but to insure effective planning and operation of future Mars Rover and sample-return missions. High-resolution image data must be efficiently registered with lower resolution base materials to establish the regional context of these studies.

(2) Some aspects of the composition and minerology of Mars can be deciphered and mapped with multispectral reflectance information contained in the Viking database [1]. Viking multispectral data must be related to spectroscopic data from Mars Observer if the latter is to be exploited effectively.

(3) The relations of new structural, geological, geochemical, and geophysical interpretations must be accurately placed in their global contexts (both planimetric and topographic) before they can be evaluated realistically [2].

The Viking Orbiter image dataset contains a tremendous amount of imbedded geometric and photometric data, the extraction of which requires complex photogrammetric and radiometric investigation and processing. Techniques to do this work have been developed. At the present time, however, any attempt to register one image to another, or some dataset to an image, and to utilize the full dynamic range of each, tends to become a research project unto itself, entailing considerable manpower and computer resources. An entirely new capability has been developed at the USGS Flagstaff Image Processing Facility that makes extensive use of new computer-processing techniques to calibrate, organize, store, manage, manipulate, and display the data.

Stages consist of the following.

1. Application of newly developed radiometric calibration data (L. A. Soderblom and E. M. Eliason (unpub. data, 1985) to all frames in the DIM.

2. Application of geometric correction to each of the frames to produce a set of projected image files (Frame DIM, or FDIM). The full resolution of each frame will be preserved by oversampling in the output array. This database will thus consist of a collection of map fragments at resolutions commensurate with those of the original spacecraft images.

3. Application of photometric corrections throughout each frame, based on known illuminations, viewing geometry, and reflectance properties.

4. Production of a controlled digital mosaic model (MDIM) of the entire planet, formatted for convenient digital storage and access and use on small interactive image-processing work stations.

A parallel effort by S.S.C. Wu and his colleagues is the compilation of a geometrically compatible Digital Terrain Model, or DTM, based on topographic information currently being derived [3,4]. This model will consist of rasters of elevation, as opposed to brightness values, in registration with the DIM's.

REFERENCES

[1] Soderblom, L. A., Edwards, Kathleen, Eliason, E. M., Sanchez, E. M., and Charette, M. P., 1978, Global color variations on the Martian surface: Icarus, v. 34, p. 446-464.

[2] Kieffer, H. H., Davis, P. A., and Soderblom, L. A., 1981, Mars' global properties: Maps and applications: Proceedings of the 12th Lunar and Planetary Science Conference, Houston, Texas, March 16-20, 1981, p. 1395-1417.

[3] Wu, S. S. C., Jordan, Raymond, and Schafer, F. J., 1985, Compilation of the Mars 1:2,000,000-scale topographic map series: Reports of the Planetary Geology and Geophysics Program--1984, National Aeronautics and Space Administration Technical Memorandum 87563, p. 612.

[4] Wu, S.S.C., and Howington, Annie-Elpis, 1985, Digital data base and its application to Mars topography: Reports of the Planetary Geology and Geophysics Program--1985, National Aeronautics and Space Administration Technical Memorandum (this issue).

Figure 1. Simusoidal Equal-Area image of a mars synoptic Digital Image Model (DIM), with central meridian at long 180°.

Figure 2. Mars synoptic DIM with central meridian at long 0°.

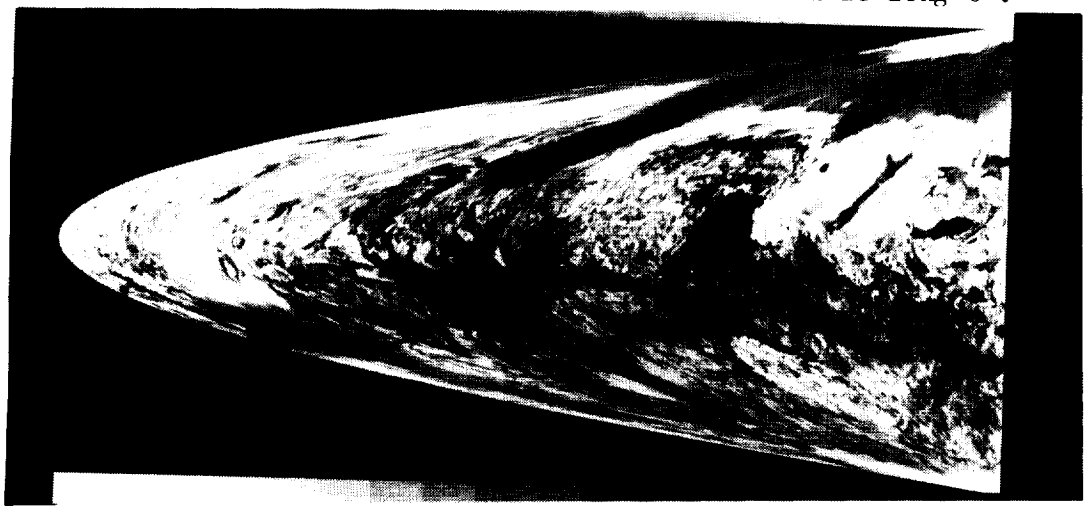

Figure 3. Mars synoptic DIM with Central meridian at long 270°.

MARS PLANIMETRIC MAPPING

R. M. Batson, P.M. Bridges, and J. L. Inge, U.S. Geological Survey, Flagstaff, AZ 86001

Controlled Photomosaics: Controlled photomosaics of areas of special scientific interest on Mars are being compiled from high-resolution Viking Orbiter pictures at a scale of 1:500,000 [1]. The mosaicking is done manually, but new techniques developed for compilation of a Mars Digital Image Model [2] will be used when the new systems become fully operational.

Revisions of 1:5,000,000-scale shaded relief maps: The 1:5,000,000-scale shaded relief maps of Mars originally compiled from Mariner 9 pictures are being upgraded by adding details visible on Viking Orbiter images [3]. Revised versions of MC2, 3, 4, 5, 6, 7, 10, 11, 12, 16, 18, 19, 20, and 23 have been published and MC13 is in press.

Mars color albedo mapping: Visual albedo maps of Mars are being compiled that are based on Viking Orbiter pictures taken from near apoapsis with small phase angles. A preliminary map compiled by airbrush methods is in press [4]. Further compilations, consisting of computer mosaics, depend heavily on methods developed for compiling the Mars Digital Image Model. These compilations have therefore been temporarily suspended.

Status of all production mapping is reported quarterly to Planetary Geology Principal Investigators [5].

REFERENCES

[1] Batson, R.M., and Inge, J.L., 1984, Controlled photomosaics of Viking Orbiter images of Mars: Reports of the Planetary Geology Program--1984, NASA TM 87563, p. 550-551.

[2] Batson, R.M., 1985, A digital image model of Mars: Reports of the Planetary Geology Program--1985, NASA TM (this issue).

[3] Batson, R.M., Bridges, P.M., and Lee, E.M., 1984, Mars planimetric mapping: Reports of the Planetary Geology Program--1984, NASA TM 87563, p. 548-549.

[4] U.S.G.S., Shaded relief and surface markings of Mars, western region (sheet 1) and eastern region (sheet 2), U.S. Geol. Survey Misc. Inv. Ser. Map I-1535, in press.

[5] Batson, R.M., and Wu, S.S.C., 1985, Progress in planetary mapping for the fourth quarter of FY 1985: U.S.G.S., Flagstaff, Arizona, 18 p.

VOYAGER CARTOGRAPHY

R. M. Batson, P. M. Bridges, and K. F. Mullins, U.S. Geological Survey, Flagstaff, AZ 86001

The Jovian and Saturnian satellites are being mapped at several scales from Voyager 1 and 2 data [1,2,3]. The maps are specially formatted color mosaics [4], controlled photomosaics, and airbrush maps.

Special techniques for producing hybrid photomosaic/airbrush maps of Callisto have been developed (figures 1 and 2). The techniques involve making controlled computer mosaics of highest resolution superimposed on lowest resolution images. Special processing is used to subdue the effects of the terminator. The mosaics are then improved by airbrushing, which removes seams and artifacts and enhances image details that had been lost by saturation in some images. These methods are being used for Callisto rather than the traditional airbrush techniques employed for Ganymede and other planetary bodies because the repetitious, high-frequency landforms that characterize the surface of Callisto can be accurately portrayed without airbrush treatment.

A controlled mosaic of Rhea is being compiled by digital methods. This mosaic was made previously with inadequate control, and is now being revised to fit a new net.

Status of the various map series is reported quarterly to Planetary Geology Principal Investigators [5].

REFERENCES

[1] Batson, R.M., Bridges, P.M., Inge, J.L., Isbell, C.E., Masursky, Harold, Strobell, M.E., and Tyner, R.L., 1980, Mapping the Galilean satellites of Jupiter with Voyager data: Photogrammetric Engineering and Remote Sensing, 46, 10, 1303-1312.

[2] Batson, R.M., Bridges, P.M., and Mullins, K.F., 1981, Voyager cartography: in Reports of the Planetary Geology Program, NASA TM 84211, 484-485.

[3] Batson, R.M., Bridges, P.M., Inge, J.L., Lee, E.M., Masursky, Harold, Mullins, K.F., Skiff, B.A., and Strobell, M.E., 1984, Voyager 1 and 2 atlas of six Saturnian satellites: NASA Spec. Pub. SP 474.

[4] McEwen, A.F., and Soderblom, L.A., 1984, High-resolution color images of Io: in Reports of the Planetary Geology Program, NASA TM 86246, 38.

[5] Batson, R.M., and Wu, S.S.C., 1985, Progress in planetary mapping for the fourth quarter of FY 1985: U.S.G.S., Flagstaff, Arizona, 18 p.

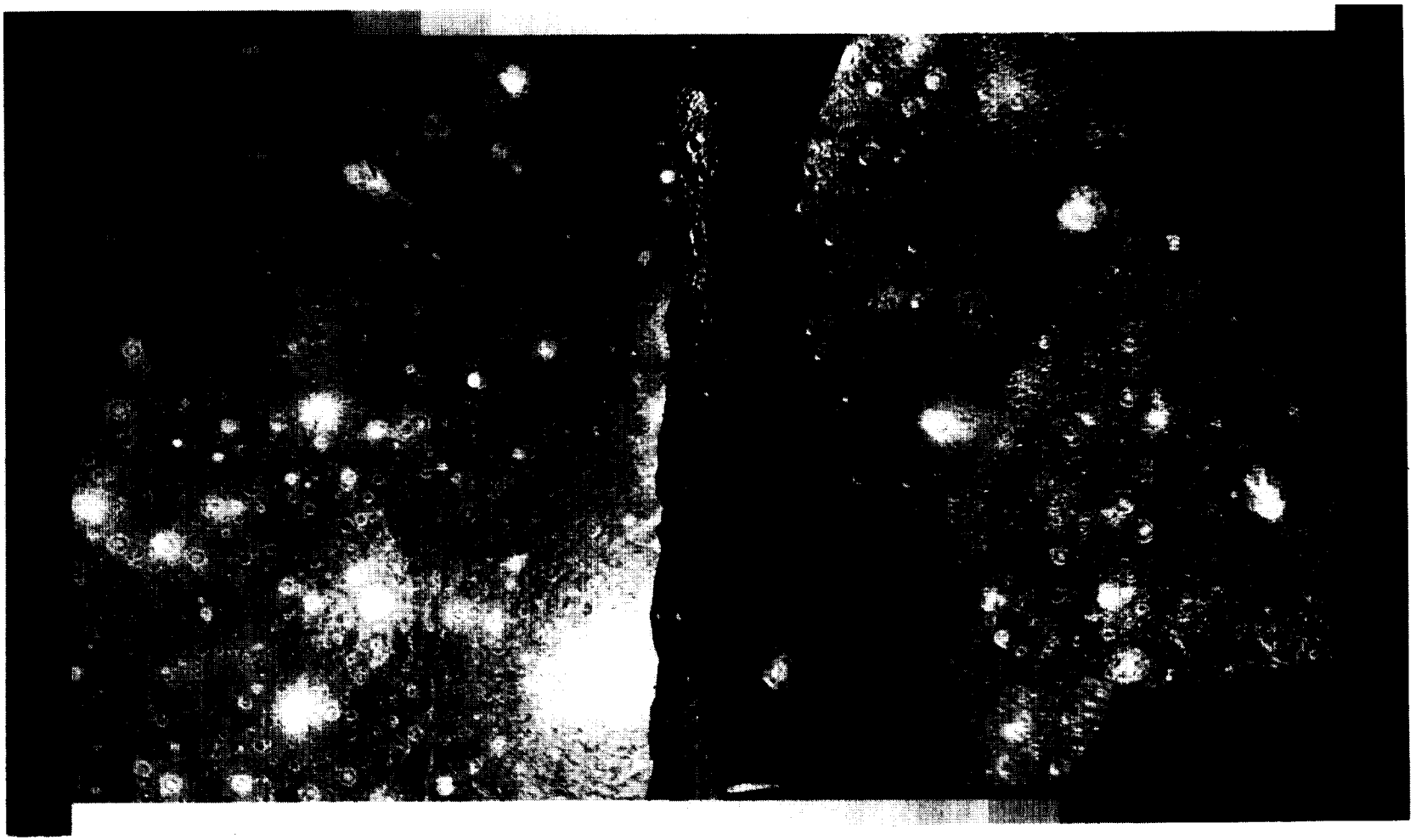

Figure 1. Computer mosaic of Jc3, on Callisto. The utility of this version is reduced because of many image artifacts, including shadows near the terminator on the high-resolution image.

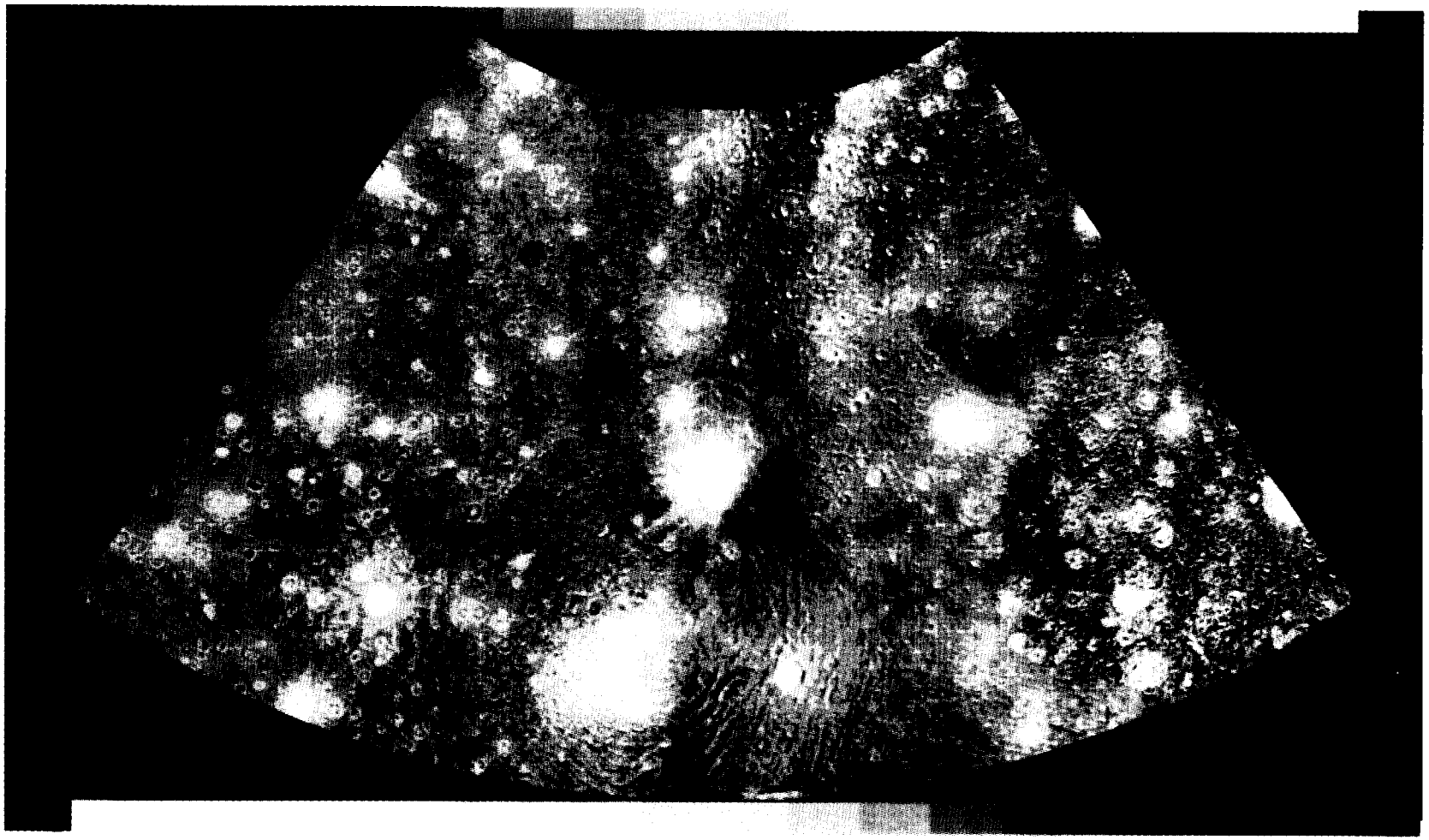

Figure 2. Computer mosaic of figure 1 with cartographic enhancements. Areas outside the quadrangle are masked.

PLANIMETRIC MAPPING WITH RADAR IMAGES

R. M. Batson, S. L. Davis, and H. F. Morgan, U.S. Geological Survey, Flagstaff, AZ 86001

Techniques are being developed for representing planetary surface forms on planimetric maps by using images from synthetic aperture radar. Data used for this effort include radar images of Venus provided by the USSR and side-scan sonar images provided by a separately funded sea-floor mapping project.

Photographic images taken by Venera 15 and 16 (figure 1) were treated by airbrush retouching (figure 2) and by recompilation with the airbrush (figure 3). Airbrush retouching is an economical aid to preliminary mapping because it can be done quickly. When cross-track shading variations and registration discrepancies are large, however, excessive redrawing is required both to retain the level of detail present in the original images and to reconcile image-placement discrepancies. Complete redrawing with the airbrush produces excellent results, but is likely to be too labor intensive for mapping at other than reconnaissance scales (generally 1:5,000,000 and 1:25,000,000).

Continued development will emphasize digital processing techniques, both radiometric and geometric, for producing acceptable maps. A by-product of this development work is expected to be a reconnaissance map of Venus based on Venera 15 and 16 data. Present experience indicates that some mixture of digital image-processing methods, airbrush retouching, and airbrush compilation will be required for effective planetary mapping with radar images.

Figure 1. Radar image-mosaic of the surface of Venus west of Ishtar Terra. The images were taken by the Soviet Venera 15 and 16 spacecraft. North is at the top. Scale is approximately 1:25,000,000.

Figure 2. Retouched radar image-mosaic of the area shown in figure 1.

Figure 3. Airbrush drawing of the area shown in figure 1 (rendition by Susan L. Davis and Patricia G. Hagerty).

CARTOGRAPHY OF NONSPHERICAL SATELLITES AND ASTEROIDS

R. M. Batson, Kathleen Edwards, and C. E. Isbell, U.S. Geological Survey, Flagstaff, AZ 86001

Irregularly shaped satellites such as Phobos and Amalthea do not lend themselves to mapping by conventional methods, because mathematical projections of such surfaces fail to convey an accurate visual impression of landforms and because large and irregular scale changes make features on maps difficult to measure. A system of digital mapping is therefore being developed in which digital files can be used to make measurements and to produce specially designed image-map formats economically, either for analysis on display devices or for photographic or lithographic reproduction.

Digital files of this kind must incorporate the three-dimensional form of the body. Existing stereoscopic-image coverage is inadequate for this purpose, although it is sufficient for triangulating latitudes, longitudes, and radii for a collection of control points. Measurements can be made indirectly, however, from a sculptured model. The sculpturing is performed through successive comparisons of illuminated models and similarly illuminated spacecraft images. Turner made a plaster model of Phobos with Mariner 9 images [1], but techniques are now available for doing the work digitally.

We are compiling a contour map of radii of Phobos on a spherical (simple cylindrical) array of latitudes and longitudes, based on the data of [1] and of Duxbury [2,3]. When the contour map is complete, a "digital radius model" will be made with interpolation algorithms now used to make digital terrain models from topographic contour maps. The model will be converted from the spherical system (latitude, longitude, and radius) to a rectangular system (X, Y, and Z) by elementary analytical geometry. Digital shaded relief images will be made by shading [4] and viewing the resulting model from a variety of orientations for comparison with spacecraft images. We expect to produce an accurate geometric model of Phobos by iteration of this process. We will then attempt to compile a three-dimensional mosaic of spacecraft images by techniques already available [5].

REFERENCES

[1] Turner, R. J., 1978, A model of Phobos: Icarus, v. 33, p. 116-140.

[2] Duxbury, T. C., 1974, Phobos: control network analysis: Icarus, v. 23, p. 290-299.

[3] Duxbury, T. C., Callahan, J. D., and Ocampo, A. C., 1984, Phobos: close encounter imaging from the Viking Orbiters: NASA Reference Publication 1109, 51 p.

[4] Batson, R. M., Edwards, Kathleen, and Eliason, E. M., 1975, Computer-generated shaded-relief images: Jour. Research U.S. Geol. Survey, v. 3, no. 4, p. 401-408.

[5] Batson, R. M., Edwards, Kathleen, and Skiff, B. A., 1981, Orthophoto mosaics and three-dimensional transformations of Viking Orbiter pictures: Reports of the Planetary Geology Program--1981, NASA TM 84211, p. 493-495.

Geology of the Amenthes (MC-14) Northeast Quadrangle, Mars, and the Fluvial Development of Hebrus Valles and Hephaestus Fossae

Eric H. Christiansen and Jennifer Hopler
Department of Geology, University of Iowa, Iowa City, Iowa 52242

Hebrus Valles and Hephaestus Fossae are valley systems located southwest of the volcano Elysium Mons in the low northern plains of Mars. The distribution of surface geologic units and tectonic features in this region (the northeast quarter of the Amenthes Quadrangle) as determined by photo-geological mapping is shown in Figure 1. Both Hebrus Valles and Hephaestus Fossae originate in a broad expanse of knobby plains (Pk) that bury older fractured polygonal plains of Adamus Labyrinthus (Ppf; McGill 1985). The knobby plains grade southward into a terrane of isolated to interconnected erosional valleys or troughs. Layered materials are exposed in the ragged margins of plateaus (Ple). The mounds and mesas of the knobby plains appear to be erosional remnants of this unit.

The northwest-trending **Hebrus Valles** system is 250 km long and begins in an elongate depression with narrow finger-like projections. The source depression is about 10 km across in maximum dimension. Individual channels are broadly sinuous and less than 1 km wide; an anastomose reach of the channel is about 10 km wide. Streamlined islands or channel bars are abundant in the middle reaches of the system. The channels are diverted around the mounds of the knobby plains. Hebrus Valles terminate as a series of narrow distributaries. These channels become narrower and eventually disappear. To quantify the stream pattern, junction angles between converging and diverging channels were measured in a down-stream direction. Angles scatter broadly with no well-defined mode ($54^{o} \pm 17^{o}$ at 1 SD). The extreme northwestern end of the Hebrus channels create a polygonal pattern by their mutual intersections. In contrast to the Granicus channels that trend northwest down the flanks of the Elysium dome (Christiansen and Ryan, 1985), no sedimentary deposits or contemporaneous volcanic activity are obviously related to the development of the channel.

Hebrus Valles share many of their characteristics with other martian outflow channels which are widely interpreted as having formed by catastrophic flooding. We suggest that Hebrus Valles developed as the result of the outbreak of a confined aquifer (Carr, 1979) within the materials of the knobby plains.

Hephaestus Fossae are a connected series of linear valley segments which branch in the same direction as the Hebrus channels suggesting that the regional slope was important in their generation. The entire valley system is about 600 km long. Hephaestus Fossae originate from a depression in the knobby plains that is similar in size and shape to that from which Hebrus Valles start. However, Hephaestus Fossae valley segments are decidedly linear and have high junction angles. The troughs outline polygonal blocks on the uplands surface. Hephaestus Fossae valleys are about the same width as the channels of Hebrus Valles but they are considerably deeper (300 m vs 100 m as derived from shadow measurements of the deeper parts of both systems). In the distal part of the system, valley segments become discontinuous and in places appear beaded, as if

they formed by coalescence of small pits. This suggests that excavation occurred beneath the surface and led to collapse. To the northwest, Hephaestus Fossae terminate near the gradational boundary between the younger knobby plains (Pk) and polygonally fractured terrain (Ppf) of Utopia Planitia.

The linearity of the channel segments and their striking patterns have led some investigators to suggest that Hephaestus Fossae are tectonic features. However, based on comparisons of the two valley systems described here, it is suggested that like Hebrus Valles, Hephaestus Fossae are also of fluvial-outflow origin. This conclusion is drawn from the following observations: 1) the depression from which Hephaestus Fossae arise is similar to that from which the clearly fluvial Hebrus Valles originate; 2) at least two broadly sinuous, apparently fluvial channels arise from the same depression which defines the upslope termination of Hephaestus Fossae (Fig. 1); 3) the two valley systems are parallel and both branch in the direction of the regional slope; and 4) Hephaestus valleys branch from a single source unlike most graben systems.

Hephaestus Fossae channels developed on a relatively smooth-surfaced deposit (Pk) that appears to overlie a fractured terrain like that exposed in the Adamus Labyrinthus region (Ppf). Downcutting to, or subsurface flow at, this pre-existing surface helped produce a channel pattern that was strongly controlled by the polygonal troughs buried beneath the younger knobby plains materials. These troughs probably controlled the direction of fluid flow. To further test this hypothesis, valley junction angles of Hephaestus channels and troughs in the fractured polygonal plains of Adamus Labyrinthus (immediately northwest of the end of the Hephaestus Fossae) were measured. Both sets of data appear to come from very similar populations that are strongly unimodal (Hephaestus Fossae $91^{o} \pm 21^{o}$ and Adamus Labyrinthus $93^{o} \pm 25^{o}$). This result is consistent with basement control of the fluvial pattern. Although Hebrus Valles channels developed in the same area, they did not excavate or cut through the knobby plains unit and hence show features more typical of a small outflow channel.

References

Carr, M. H. (1979) Journal of Geophysical Research, v. 84, p. 2995-3007.

Christiansen, E. H., and Ryan, M. P. (1985) NASA Technical Memorandum 87563, p. 239-241.

McGill, G. E. (1985) Geological Society of America Abstracts with Programs, v. 17, p. 659.

Figure 1. Geologic map of the Amenthes (MC-14) Northeast quadrangle. Key (youngest to oldest): **Lc** - channeled lahar (margin stipled); **Ps** - smooth plains; **Lp** - lava plains; **Pr** - ridged plains; **Ppk** - patterned knobby plains (crater ejecta stipled); **Ple** - layered etched plains; **Pg** - faulted plains; **Ppf** - fractured polygonal plains. Symbols: **channels** are shown as solid lines; **graben or fractures** as line with ball symbol; **mare-type ridges** as lines with bar; **buried craters** as dotted circles; and **impact crater rims** as circles with two tic-marks (ejecta unlabeled).

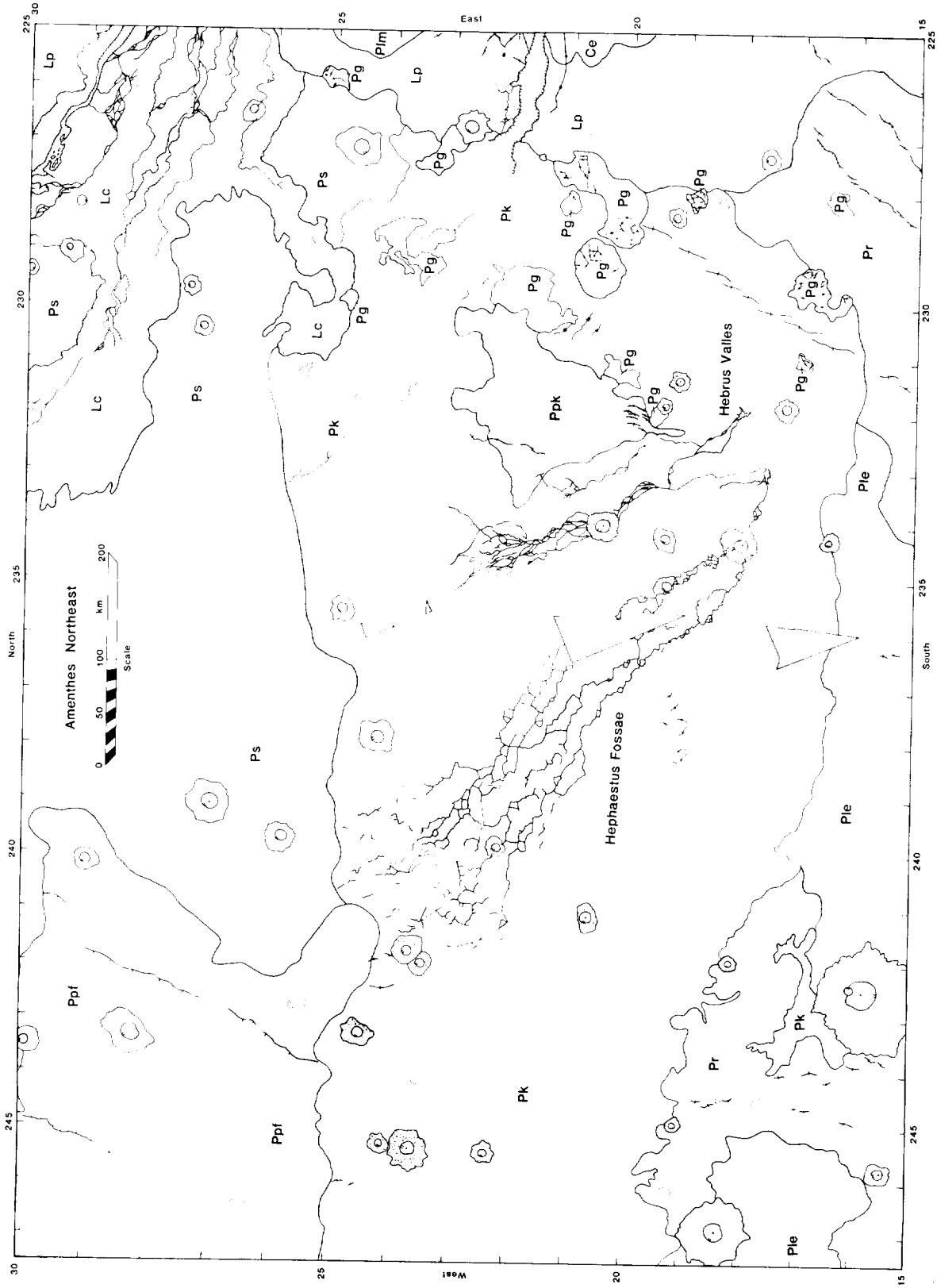
Amenthes Northeast
Scale
0
50
100
200
km
Hephaestus Fossae
Hebrus Valles
Lp
Lc
Ps
Pg
Plm
Ce
Pk
Ppk
Pr
Ple
Ppf
North
South
East
West

THE CONTROL NETWORKS OF THE SATELLITES OF JUPITER AND SATURN

Merton E. Davies, The Rand Corporation, Santa Monica, California 90406

Geodetic control networks are being computed photogrammetrically for the large satellites of Jupiter and many of the satellites of Saturn using pictures from the Voyager 1 and 2 encounters. Control points have been identified on the satellites and their coordinates computed by single-block analytical triangulations. Currently, these data sets are being converted from B1950 to J2000 coordinates. All of the Saturnian are completed, as well as Europa and Callisto. Ganymede is not yet finished.

STATUS OF J2000 CONTROL NETWORKS

	Europa	Ganymede	Callisto
Points	179	1079	818
Pictures, V1	53	145	190
V2	67	144	96
Measurements	3847	16426	15436
Normal Equations	718	3025	2494
Overdetermination	5.36	5.43	6.19
Standard Error, μm	10.50	9.46	11.57

	Mimas	Enceladus	Tethys
Points	110	71	110
Pictures, V1	32	22	6
V2	0	0	21
Measurements	1080	1052	924
Normal Equations	316	208	301
Overdetermination	3.42	5.06	3.07
Standard Error, μm	12.57	10.59	11.73

	Dione	Rhea	Iapetus
Points	126	331	62
Pictures, V1	27	82	14
V2	1	3	66
Measurements	1322	4902	1872
Normal Equations	336	917	364
Overdetermination	3.93	5.35	5.14
Standard Error, μm	12.44	12.27	11.87

The control network of Io is still in B1950 coordinates. It contains 644 points with 11,100 measurements of these points on 205 Voyager 1 and 43 Voyager 2 pictures. This system contains 2,032 normal equations with 5.46 overdetermination. When completed, it is estimated that the Ganymede control network will contain 1,888 points measured on 300 pictures.

THE CONTROL NETWORK OF MARS: OCTOBER 1985

Merton E. Davies, The Rand Corporation, Santa Monica, California 90406

Strips of Viking mapping pictures are being added to the planetwide control network of Mars. These high resolution strips run from the Viking 1 lander site east to Airy-0, north along the 0° meridian to 60° latitude, southwest through the Viking 1 lander site to the equator, and along the equator encircling the planet. Everywhere along these strips, old points are incorporated in the measurements, thus assuring that the strips and planetwide net make a single large data set. The control points are much denser in the areas covered by the strips than in those regions not covered by strips and as they are usually associated with smaller craters their coordinates will be more accurate. Within the strips the standard error of the coordinates of the control points is estimated to be less than 3 km and the error in longitude of a few points near Airy-0 is less than 40 m.

The horizontal coordinates of the control points on Mars have been updated with a single-block planetwide analytical triangulation computed in September 1982 (Davies and Katayama, 1983). The computation contained 47,524 measurements of 6,853 points on 1811 pictures. These comprised 1054 Mariner 9 and 757 Viking frames. The overdetermination factor was 2.48 and 19,139 normal equations were solved. The standard error of measurement was 18.06 μm. The longitude of the Viking 1 lander site was $47^{\circ}.962$ and the latitude $22^{\circ}.480$. The latitude of Airy-0 was $-5^{\circ}.152$.

The Mars data set now contains 7,764 points, 52,856 measurements on 1054 Mariner 9 and 994 Viking Orbiter pictures, 21,672 normal equations, and a 2.44 overdetermination factor.

References

Davies, M. E., and F. Y. Katayama, "The 1982 Control Network of Mars," J. Geophys. Res., Vol. 88, No. 89, September 10, 1983, pp. 7503-7504.

A UNIFIED LUNAR CONTROL NETWORK

Merton E. Davies and Tim R. Colvin, The Rand Corporation, Santa Monica, CA 9040
Donald L. Meyer, Defense Mapping Agency, Aerospace Center, St. Louis AFS, MO 63

At this time, control on the Moon is composed of a number of independent regional networks. These networks frequently have different origins but never have common ties, even in overlapping areas. The objective of the unified network program is to tie the regional networks into a single consistent planetwide control network. The plan is to start with the best defined regions, create common ties with neighboring data sets, and then expand into poorly defined regions.

The most accurately defined points on the Moon are locations of the laser ranging retroreflectors (Ferrari et al., 1980) and the VLBI measurements of the locations of the Apollo 15, 16, and 17 ALSEP stations (King et al., 1976). The accuracy of these locations is about 30 m and their locations are used to define the center-of-mass and, hence, the origin of the unified lunar coordinate system. The coordinates of the retroreflectors are given in both principal axis and mean Earth/Polar axis Systems. Mean Earth/Polar axis coordinates have been recommended by the IAU (Davies et al., 1980) for the Moon. The difference in the coordinates is important, more than 600 m in latitude and longitude.

The Apollo 15, 16 and 17 ALSEP stations have been identified on Apollo panoramic photography and their locations transferred to Apollo mapping frames. Thus, their coordinates are available in the control network computations.

Three control networks have been computed based on the Apollo mapping pictures. They are the DMA/A15 system (Schimerman, 1976), the NOS/USGS system (Doyle et al., 1977), and the DMA/603 system (DMAC Contract Report, 1981). The DMA/A15 system contained 1284 pictures and 9940 points, the NOS/USGS system contained 1244 pictures and 5324 points, and the DMA/603 system contained 603 pictures and 5346 points. The coordinates of points in one system can be transferred to another system by interpolation between nearby common points. Thus the coordinates of the three ALSEP stations which are available in DMA/A15 coordinates, are transferred to NOS/USGS and DAM/603 coordinates. The coordinates are based on picture measurements and the photogrammetic solutions and can then be compared to the coordinates derived by King et al., 1976 and Ferrari et al., 1980.

In order for the control network to have the same origin and mean Earth/Polar axis coordinate system defined by Ferrari et al., 1980, the coordinates of the ALSEP stations should be identical. The RMS of the true distance between corresponding ALSEP points is 334 m for DMA/A15, 2115 m for NOS/USGS, and 319 m for DMA/603. Transformations permitting translation, rotation, and scale (7 parameters) have been computed for each control system to minimize the distances between these corresponding points. The RMS of the residuals after the transformations is 73 m for DMA/A15, 76 m for NOS/USGS, and 58 m for DMA/603.

With respect to the entire Apollo network, the three ALSEP appear close together so it is not reasonable to base the desired transformation on just these points. Four distant points (E6847, lat. 29°.8, long. -56°.6; R6445, lat. -11°.1, long. -28°.; G1243, lat. 6°.5, long. 152°.5; TO849, lat. -15°.9, long. 174°.4) were selected and a transformation computed that minimized the distances between the corresponding ALSEP coordinates and minimized the shift in coordinates of these four points. The DMA/603 network was selected to minimize the required shift and the resulting network called DMA/603MOD. The RMS of the residuals of the transformation is 97 m. The RMS of the shift of the seven points is 209 m and of all 5346 of the DMA/603 points is 265 m.

Many control networks have been computed based on pictures of the Moon taken through telescopes; these cover the Earth-facing region. Probably the most carefully prepared network is that published by Meyer, 1980. This is the one incorporated into the present program. 130 points common to Meyer's and the Apollo networks were selected and transformation parameters computed to shift Meyer's coordinates to the DMA/603MOD network. The RMS of the residuals of this transformation is 808 m. The RMS of the true distances between corresponding points before and after transformation is 1503 m. The RMS of the true distance between all 1088 Meyer coordinates and DMA/603 MOD coordinates is 1610 m.

The DMA/603MOD is believed to be an improved Apollo control network, and all of Meyer's telescopic network coordinates have been transferred to the DMA/603MOD center-of-mass mean Earth/Polar axis coordinate system.

References

Doyle, Frederick J., Atef A. Elassal, and James R. Lucas, "Selenocentric Geodetic Reference System," National Oceanic and Atmospheric Administration, Technical Report NOS70NGS5, February 1977.

Ferrari, A. J., W. S. Sinclair, W. L. Jjogren, J. G. Williams, and C. F. Yoder, "Geophysical Parameters of the Earth-Moon System," J. Geophys. Res., Vol. 85, No. B7, July 10, 1980, pp. 3939-3951.

King, R. W., C. C. Counselman III, I. I. Shapiro, "Lunar Dynamics and Selenodesy: Results from Analysis of VLBI and Laser Data," J. Geophys. Res., Vol. 81, No. 35, December 10, 1976, pp. 6251-6256.

Meyer, Donald L., Selenocentric Control System (1979), Defense Mapping Agency, DMA TR 80-001, April 1980.

Schimerman, Lawrence A., The Expanding Apollo Control System, Defense Mapping Agency Aerospace Center, August 1976.

Report on Lunar Control under Contract No. W-14, 453, Defense Mapping Agency Aerospace Center, St. Louis AFS, MO 63118, October 1981.

Davies, M. E. et al., "Report of the IAU Working Group on Cartographic Coordinates and Rotational Elements of the Planets and Satellites," Celestial Mechanics, Vol. 22, January 1980, pp. 205-230.

THE GALILEAN SATELLITE GEOLOGICAL MAPPING PROGRAM, 1985

B.K. Lucchitta, U.S. Geological Survey, Flagstaff, AZ 86001

The Galilean Satellite Geological Mapping Program was established to illuminate detailed geologic relations on the four large satellites of Jupiter. The program involves more than 40 investigators from various universities, research institutes, and government offices in the United States, England, Germany, and Italy. A total of 24 researchers were assigned to map 10 quadrangles on Ganymede, 15 to map 6 quadrangles on Io, and 3 to map 2 quadrangles on Europa. No assignments have yet been made for Callisto. All maps are at a scale of 1:5 million except for three on Io that cover selected areas where high-resolution pictures permit compilation at 1:2 and 1:1 million scales.

During 1985, preliminary base materials were sent to mappers of Ganymede quadrangles Jg1 and Jg6. Preliminary airbrushing is completed for Jg2, Jg5, and Jg13. Final airbrush base materials were distributed to mappers of Jg4 and Jg12. First drafts of geologic maps were received from mappers of Jg3 and Jg8 and of Io quadrangles Ji2, Ji4, Ji2a, and Ji2c. Of these maps, Ji2 is undergoing the first technical review, Jg8 and Ji4 have received one review, Ji2a has undergone two reviews, and Ji2c has received editorial review. A meeting was convened in March, 1985, in Houston, Texas, to discuss geological results and changes to the previously established guidelines. A report detailing the changes was sent to the mappers in April.

Preliminary results and new discoveries are as follows:

Io

Major units on Io are patera (vent) materials including those of floors, flows, and shields. Other flow materials are from fissures and unidentified sources. Additional units are plains, plateau, and mountain materials (Schaber, Scott, and Greeley, mapping in progress of the Ruwa Patera quadrangle). High-resolution maps show that the interrelations between flow units and eroded or faulted scarps are more complex than previously thought (Moore, H. G., mapping in progress of the Maasaw Patera region). Flow units apparently abut or overlap scarps in places. Elsewhere, flow units show "breakout" tongues, suggesting remobilization of previously solidified sulfur flows (Greeley, Spudis, and Guest, mapping in progress of the Ra Patera region). Some mountain materials of high relief have associated craters and are sources of distinct flows that overlap other units. These observations suggest that some mountains are composed of silicate volcanic materials of high yield strength and are relatively young (Whitford-Stark, 1982; Whitford-Stark, Mouginis-Mark, and Head, mapping in progress of the Lerna quadrangle).

Europa

Europa's surface consists of two basic units: light plains materials and dark materials. The subdivision of light plains units may have to be based on different structural styles or density of fracture patterns (Pieri and Hiller, 1984). Dark materials occur mostly as patches, as central swaths in linear structures, or as crater ejecta (Lucchitta and Soderblom, 1981). The subdivision of dark materials may be possible only if subtle color differences can be verified by detailed measurements of spectral values.

Ganymede

Major units on Ganymede are dark and light terrain materials. Dark materials tend to be older than light materials, which developed at the expense of the dark units (Shoemaker et al., 1982). Dark materials have irregularly textured surfaces and are in places smoothed by other superposed dark material (Casacchia and Strom, 1984). Dark materials in slivers and wedges are ridged or lineated, suggesting that they were structurally disrupted (Glotfelty and Barnes, 1984; Lucchitta, 1985). Furrows with raised rims are common in the dark units. In some places, they are widely spaced individual features; in other places they are so densely spaced that the entire unit acquires a lineated aspect (Guest, Bianchi, and Greeley, mapping in progress of the Uruk Sulcus quadrangle). An arcuate furrow set and two linear sets have been recognized in the dark material of Galileo Regio (Casacchia and Strom, 1984). Each set is parallel to one of three linear boundaries of the region, implying structural control of the boundaries (Murchie and Head, 1985a). High-resolution pictures in the Memphis Facula quadrangle (Lucchitta, 1985) show that the rim materials of furrows have a somewhat higher albedo than the dark materials on which they are superposed; the rim materials apparently have either a different chemistry or, more likely, a different structure (Lucchitta, Barnes, and Glotfelty, work in progress). Some furrows, traced into structurally disrupted slivers of dark material in the transition zone between dark and light terrains, have been slightly rotated, suggesting lateral motion. In general, however, boundary relations between dark and light materials suggest that the transformation from dark to light took place *in situ*.

Light terrain materials are subdivided into smooth and grooved materials. Smooth units appear to have locally different origins and ages. Smooth material has generally embayed other units, implying that it was emplaced in a liquid state (Murchie and Head, 1985a). Grooved materials are classified into groove lanes and groove polygons. Intersecting groove lanes or throughgoing grooves generally outline groove polygons. Groove sets within the polygons commonly terminate abruptly against groove lanes (Murchie and Head, 1985b). Overall, groove trends follow local zones of weakness predetermined by furrow location. Bianchi et al. (1984) found two dominant groove trends in Uruk Sulcus; the groove orientations appear orthogonal and parallel to arcuate furrows in Galileo Regio. On the basis of a global study of groove trends, Bianchi et al. (1985) considered the trends to be controlled by tectonic regimes rather than by local stresses.

Most impact craters and palimpsests (ancient crater scars) postdate the furrows in dark materials (Casacchia and Strom, 1984). Some palimpsests have conspicuous ring structures and secondary craters, and they postdate emplacement of the light materials (Guest, Bianchi, and Greeley, mapping in progress of the Uruk Sulcus quadrangle). The transition from flat-floored craters to those with peaks and pits takes place at larger crater diameters in the light terrain than in the dark terrain (Lucchitta, 1985), implying that the two terrains have different crustal properties. Some craters have ejecta with indistinct flow lobes at their margins similar to craters on Mars (Horner and Greeley, 1982), suggesting that the target material liquefied. Other craters have central domes or platforms surrounded by conspicuous depressions. These "moat" craters appear to be abundant on the icy satellites of Jupiter. They are found in all stages of degradation, but are most common

as transitional forms between craters and palimpsests. They appear to be associated with impacts into ice, but their precise origin is not fully understood.

REFERENCES

Bianchi, R. et al., 1984, Tectonics of the grooved terrain, Ganymede (abs.), in Lunar and Planetary Science XV, The Lunar and Planetary Institute, Houston, p. 54-55.

Bianchi, R. et al., 1985, Azimuthal distribution of the grooves on Ganymede (abs.), in Lunar and Planetary Science XVI, The Lunar and Planetary Institute, Houston, p. 53-54.

Casacchia, R. and Strom, R. G., 1984, Geologic evolution of Galileo Regio, Ganymede: Proceedings 14th Lunar and Planetary Conference, Journal Geophysical Research 89, Supplement, p. B419-B428.

Glotfelty, M. F. and Barnes, C. W., 1984, Relationships and tectonics of the Jg7 quadrangle of Ganymede (abs.), in Reports of Planetary Geology Program - 1983, NASA TM-86246, p. 314-315.

Horner, V. M. and Greeley, R., 1982, Pedestal craters on Ganymede: Icarus, v. 51, p. 549-562.

Lucchitta, B. K., 1985, Geology of the Jg7 quadrangle of Ganymede (abs.), in Reports of Planetary Geology Program - 1984, NASA TM 87563, p. 546-547.

Lucchitta, B. K. and Soderblom, L. A., 1981, Geology of Europa, in Morrison D., ed., Satellites of Jupiter, University of Arizona Press, Tucson, p. 521-555.

Murchie, S. L. and Head, J. W., 1985a, Tectonic features in the Jg-4 quadrangle of Ganymede (abs.), in Lunar and Planetary Science XVI, The Lunar and Planetary Science Institute, Houston, p. 601-602.

Murchie, S. L. and Head, J. W., 1985b, Global tectonic mapping of Ganymede: a preliminary report (abs.), in Lunar and Planetary Science XVI, The Lunar and Planetary Institute, Houston, p. 599-600.

Pieri, D. and Hiller, K., 1984, Je3 quadrangle, Europa: Preliminary geologic designations (abs.), in Reports of Planetary Geology Program - 1983, NASA TM 86246, p. 318-319.

Shoemaker, E. M. et al., 1982, The geology of Ganymede, in Morrison, D., ed., Satellites of Jupiter, University of Arizona Press, Tucson, p. 435-520.

Whitford-Stark, J. L., 1982, The mountains of Io (abs.), in Lunar and Planetary Science XIII, The Lunar and Planetary Science Institute, Houston, p. 859-860.

GEOLOGY OF THE RUWA PATERA QUADRANGLE OF IO

Gerald G. Schaber[1] David H. Scott[1] and Ronald Greeley[2]; U.S. Geological Survey, Flagstaff, AZ 86001[1], Arizona State University, Tempe, Arizona 85287[2]

Geologic mapping of the Ruwa Patera quadrangle (Ji2) of Io at 1:5,000,000 scale has been completed (unpub. data, 1985). The quadrangle, lying between lat ±50° and long 90° and 270° (centered at long 360°), covers half of the volcanically active trailing hemisphere that faces Jupiter. Image resolution of the quadrangle's east and south quadrants is high (0.5 to 2 km/line pair), but it is significantly lower (2 to 20 km/line pair) for the west and north quadrants. The westernmost third of the quadrangle has not been mapped geologically owing to insufficient image resolution. The surface of Io within the quadrangle can be divided into four basic physiographic terranes: (1) volcanic centers (paterae and tholi), including the vents and their associated deposits, (2) interpatera plains, (3) plains, and (4) rugged mountain massifs. Relief within the quadrangle is poorly known, but intervent walls of paterae, as well as erosional or tectonic scarps associated with interpatera plains and plateau materials, are estimated to exceed 2 km in height at places. (In other regions of Io, heights of mountain massifs have been estimated [1] to reach 9 km.)

To map the quadrangle, conventional planetary photogeologic techniques described by Wilhelms [2] were combined with techniques developed for mapping terrestrial volcanic deposits, but the absence of reliable topographic information significantly hindered interpretation of volcanic features and geologic history. Another complication, common to all Io quadrangles, is the coalescing of flows from adjacent vents and anastomosing of flows from single vents. The question of relative ages of flow sequences from individual vents has been addressed by Greeley and others (mapping in progress, 1985) for the Ra Patera (Ji2a) quadrangle (1:2,000,000 scale), which is included in the Ruwa Patera quadrangle. In places, mapping of geologic units was further complicated by near-surface [3] and airborne gases and ash that partly obscure large areas of the surface (extending possibly as far as 500 km from active vents), especially in the vicinity of Loki Patera (+12°, 309°) and Pele Patera (-18°, 255°).

Nineteen geologic units have been mapped, including materials of the following major categories and their subdivisions: patera floors, patera and patera shield flows, fissure flows, patera cones, tholi, plateaus, plains, mountains, dark mantles, and miscellaneous other flow materials. The virtual absence of recognized impact craters in the quadrangle precludes the development of a stratigraphy based on crater counts. Materials of volcanoes, lava flows, plateaus, and plains have overlapping boundaries and may range widely in age. Older geologic units are, in order of decreasing age, the mountain units, plateau materials, and much of the interpatera plains materials. Youngest mapped units are dark patera and patera shield flows, dark mantle

material, and high-albedo material interpreted to be sulfur dioxide sublimate deposits. The various units associated with pateras are generally superposed on the interpatera plains, but are overlapped locally by younger plains, dark mantle, and bright sublimate deposits. The areal distribution of central vents (mapped as patera floor deposits) is uniform, averaging about one vent per 5 X 10^4 km^2 [1]. Mantling materials of very low albedo (0.05) [4] occur dominantly around Babbar Patera (-40°, 272°), a major hot spot on Io, and are attributed [4] to cooling pyroclastic material.

Tectonic activity within the Ruwa Patera quadrangle is expressed by scarps, linear and arcuate depressions, and grabens and ridges. Most of these features are <200 km long; some transect only a single material unit and therefore, may be only near-surface phenomena. The most conspicuous grabens and scarps extend east from Galai Patera (-11°, 288°) and occur on the southern flanks of Babbar Patera (-44°, 273°). Some scarps within plains materials and some that bound plateau material may result from thermal erosion and/or SO_2 sapping [5]. Mountain materials are most disrupted by tectonic processes, followed, in decreasing order of disruption as well as age, by plateau material and interpatera plains materials. Thus, at least in these units, intensity of tectonic activity and relative age are parallel. Mountain materials are concentrated in the extreme southern and eastern parts of the quadrangle and are assumed to represent islands of the oldest exposed silicate crust, perhaps underlain or dynamically supported by a silicate crust that is substantially thicker than the average Ionian crust.

Nine volcanic plumes were active during the Voyager 1 encounter, and eight during the Voyager 2 encounter [6,7,8]. Three of these plumes were within the Ruwa Patera quadrangle, centered in the western and eastern parts of Loki Patera (+13°, 309° and +18°, 303°, respectively) and in Masubi Patera (-45°, 55°). Two additional plumes within the quadrangle were identified by McEwen and Soderblom [8] as having been initiated between the Voyager 1 and 2 encounters, one centered at Surt (+45°, 338°), and the other at Aten Patera (-45°, 310°). McEwen and Soderblom [8] described two distinct classes of plumes that they referred to as Pele type and Prometheus type. The driving volatile for the larger Pele type is sulfur heated by hot silicates in a lower crustal zone. The Pele type plumes occur in an historically redder region within the Ruwa Patera quadrangle centered at 300°, where sulfur-rich debris layers overlying the hot silicate lithosphere may be thinner than elsewhere.

That the trailing, Jupiter-facing hemisphere, part of which is covered by the Ruwa Patera quadrangle, is geologically different from the opposite hemisphere is supported by several lines of evidence, including a markedly higher heat flow [9] and the absence of widespread SO_2 frost in the trailing hemisphere. Thermal (5-um) enhancements ("hot spots") have been observed in this "active sector" [10] where over 90 percent of the global hot-spot heat flow of 1 to 2 W m^2 [11] originates. Of the seven major hot spots identified on Io [11], five

are within the Ruwa Patera quadrangle: Loki Patera (+12°, 309°), Babbar Patera (-40°, 272°), Ulgen Patera (-38°, 294°), Svarog Patera (-48°, 268°) and Amaterasu Patera (+38°, 307°). According to McEwen and others [4], these five features may contribute up to 30 percent of the total hot-spot power emitted by Io. Pele Patera (-18°, 255°), lying immediately to the east of the Ruwa Patera quadrangle, contributes up to an additional 3 percent.

REFERENCES

[1] Schaber, G. G., 1982, The geology of Io, in Satellites of Jupiter (D. Morrison, ed.), University Arizona Press, p. 556-597.

[2] Wilhelms, D. E., 1972, Geologic mapping of the second planet: U.S. Geological Survey Interagency Report, Astrogeology, v. 55, 36 p.

[3] Lee, S. W., and Thomas, P. C., 1980, Near-surface flow of volcanic gases on Io: Icarus, v. 44, p. 280-290.

[4] McEwen, A. S., Matson, D. L., Johnson, T. V., and Soderblom, L. A., Volcanic hot spots on Io: correlation with low-albedo calderas: Journal Geophysical Research, in press.

[5] McCauley, J. F., Smith, B. A., and Soderblom, L. A., 1979, Erosional scarps on Io: Nature, v. 280, p. 736-738.

[6] Strom, R. G., Terrile, R. J., Masursky, H., and Hansen, C., 1979, Volcanic eruption plumes on Io: Nature, v. 280, p. 733-736.

[7] Strom, R. G., and Schneider, N. M., 1982, Volcanic eruption plumes on Io, in Satellites of Jupiter (D. Morrison, ed.), University Arizona Press, p. 498-633.

[8] McEwen, A. S., and Soderblom, L. A., 1983, Two classes of volcanic plumes on Io: Icarus, v. 55, p. 191-217.

[9] Johnson, T. V., Morrison, D., Matson, D. L., Veeder, G., Brown, R. H., and Nelson, R. M., 1984, Volcanic hot spots on Io: Stability and longitudinal distribution: Science, v. 226, p. 134-137.

[10] Sinton, W. M., 1983, Io, the near-infrared monitoring program, 1979-1981: Icarus, v. 54, p. 133-157.

[11] Pearl, J. C., and Sinton, W. M., 1982, Hot spots of Io, in Satellites of Jupiter (D. Morrison, ed.), University Arizona Press, p. 724-755.

NEW GEOLOGIC MAP OF MARS

Kenneth L. Tanaka[1], Ronald Greeley[2], David H. Scott[1], and John E. Guest[3]; [1]U.S. Geological Survey, Flagstaff, Arizona, 86001; [2]Arizona State University, Tempe, Arizona, 85287; [3]University of London Observatory, London, England, NW74SD

The new 1:15,000,000-scale geologic map of Mars is in final stages of preparation. The map is in three parts: the western equatorial region (long 0° to 180°; Scott and Tanaka), eastern equatorial region (long 180° to 360°; Greeley and Guest), and polar regions (lat >±55°; Tanaka and Scott). The map is slated for publication in the U.S. Geological Survey Miscellaneous Investigations Series. It incorporates new geologic and stratigraphic data [1-6] and includes an up-to-date bibliography of significant research developments in Martian geology. Major improvements in the geologic mapping were possible because it is based on Viking images, whose quality and resolution are much better than those of the Mariner 9 images from which the previous geologic map of Mars [7] was produced. Relative ages of the map units, based on stratigraphic relations and crater counts, enable their correlation over the entire Martian surface. Because stratigraphy and all map units and contacts are consistent, the geologic data can be digitized in a global format.

In Table 1, the number of map units and symbols shown on the new 1:15,000,000-scale map can be compared with those on the 1:25,000,000-scale map based on Mariner 9 images. The new mapping not only distinguishes many more geologic units, but it also locates contacts with much greater precision. Further, some of the new map symbols are more informative. For example, craters are distinguished on the basis of superposition relations and are shown as superposed on or partly buried by the surrounding map unit(s).

Martian chronostratigraphy is also being reanalyzed [K. L. Tanaka, work in progress]. Previously, three systems--the Noachian, Hesperian, and Amazonian--broadly portrayed the time-stratigraphy of Mars. These systems are widely recognized and are still fairly accurate in representing major episodes of Martian geologic activity. The new mapping, however, shows that subdivision of the systems is possible and useful. Therefore, a more detailed stratigraphy of Mars is being developed that defines eight new chronostratigraphic series--the lower, middle, and upper Noachian; lower and upper Hesperian; and lower, middle, and upper Amazonian.

Many of the developments in the mapping materialized through communication among authors. Of particular benefit were careful reviews by Michael Carr, Donald Wilhelms, and Henry Moore. Their expertise in Martian geology and planetary mapping aided in the development of the format of the maps and accompanying texts.

References
[1] Greeley, R. (1982) NASA TM 85127, p. 353.
[2] Scott, D. H. (1982) NASA TM 85127, p. 304.
[3] Scott, D. H. (1984) NASA TM 86246, p. 321.
[4] Scott, D. H. and Tanaka, K. L. (1984) U.S.G.S. Open-File Rept. 84-659A.
[5] Scott, D. H. and Tanaka, K. L. (1985) NASA TM 87563, p. 541.
[6] Tanaka, K. L. and others (1985) NASA TM 86346, p. 321.
[7] Scott, D. H. and Carr, M. H. (1978) U.S.G.S. Misc. Inv. Series Map I-1083, scale 1:25,000,000.

Table 1.
Number of Map Units and Symbols Portrayed on New Geologic Map of Mars

Region	Map units	Symbols
Western equatorial	54 (20)	13+ (8)
Eastern equatorial	47 (18)	11+ (7)
Polar	32 (15)	10+ (8)
Global	87 (24)	15+ (9)

Note: Numbers in parentheses are on previous 1:25,000,000-scale map [7] based on Mariner 9 data.

GRAVITY-PROFILE ANALYSIS OVER CENTRAL VALLES MARINERIS, MARS

Kenneth L. Tanaka, Nanci E. Witbeck, and David H. Scott, U.S. Geological Survey, Flagstaff, Arizona 86001

As part of a detailed mapping project of the Valles Marineris-Noctis Labyrinthus region of Mars (1:2,000,000 scale), Viking gravity profiles over the chasmata are being studied. This work involves (1) selection of favorable profiles, (2) simulation of topographic effects (Bouguer correction), and (3) modeling of subsurface mass anomalies. These procedures and our preliminary results are reported here.

Five gravity profiles were obtained by Viking Orbiter 2 [1] over the deepest Valles Marineris canyons, between longitudes 50° and 90°. Of these, profiles of revs 487, 489, 528, and 641 are dominated by regional, high-amplitude anomalies or complicated by local anomalies north and south of the canyons. Because of these complexities, those profiles were not studied. However, the profile of rev 488, which passes over the center of Valles Marineris (Melas, Candor, and Ophir Chasmata), is dominated by a gravity low centered over the canyons (Fig. 1). This profile, therefore, is suitable for a simplistic gravity analysis of the canyons.

The gravity effect of topography is accounted for on a new topographic map of Mars [2]. This map, showing 1-km contours superposed on the 4th-order spherical harmonic geoid of Mars [3], was converted into a terrain model for the area between lat 40° S. and 20° N. and long 40° and 90°. In the canyon region, where relief is high and slopes are steep, 1° by 1° latitude-longitude bins were used; in the surrounding plateau regions, 2° by 2° bins suffice. Theoretical line-of-sight gravity profiles were then determined by using the orbital simulation program of the Geophysical Data Facility at the Lunar and Planetary Institute in Houston.

The range in profile relief resulting from this simulation was too great to match that of the observed gravity profile. Thus, a subsurface correction was introduced that represents a compensation mass at depth. This mass was opposite in sign to the anomalous mass produced by the topography. Of the various simulations of depths of compensation, 50- to 75-km depths produced optimal simulation of the regional effects, particularly of the southern limb of the profile (Fig. 1). These depths, although somewhat lower than estimates for the old cratered terrain [4, 5], are in the range of values estimated for the large shield volcanoes of Tharsis Montes and Elysium Mons [6].

The theoretical anomaly over the canyons, however, remained too high. Again, it can be attributed to a subsurface anomaly. If the canyons are relatively young features to which the subsurface mass distribution has not responded, then a different subsurface geophysical model is required. Valles Marineris dissects the high-elevation area of the Lunae-Sinai Plana. If the subsurface has been compensated according to the pre-Valles Marineris topography, then a large compensating mass for the presently missing material in Valles Marineris should be introduced into the model. When we respond by placing negative masses at compensation depth below the central canyons and below Hebes Chasma, we approach a reasonable fit for the observed gravity profiles within

geologic constraints (Fig. 1). The north limb of the profile, however, is not closely simulated. This offset may be caused by unknown subsurface mass deficiencies or overestimation of surface elevations.

A possible tectonic history for Valles Marineris, in accord with this preliminary gravity study and our detailed mapping and stratigraphic work, is as follows:

(1) An elongate thermal anomaly developed under the Valles Marineris region where the lithosphere was originally about 100 km thick.

(2) The thermal anomaly eroded the lithosphere, converting it to asthenosphere and thinning it to 50 to 75 km. Concomitantly, the region was uplifted because of the volume increase produced by melting at the base of the lithosphere.

(3) Effusion of magma and removal of ground ice and canyon material by erosion resulted in continued rifting and expansion of canyons. These processes caused a mass imbalance that for the most part is not isostatically adjusted, but is withheld by the flexural strength of the lithosphere.

[1] Sjogren, W. L. (1979) Science, v. 203, p. 1006.
[2] Wu, S. S. C. and others (1986) this volume.
[3] Jordan, J. F. and Lorell, J. (1975) Icarus, v. 25, p. 146.
[4] Sjogren, W. L. and Wimberley, R. N. (1981) Icarus, v. 45, p.331.
[5] Sjogren, W. L. and Ritke, S. J. (1982) GRL, v. 9, p. 739.
[6] Comer, R. P. and others (1985) Rev. Geophys., v. 23, p. 61.

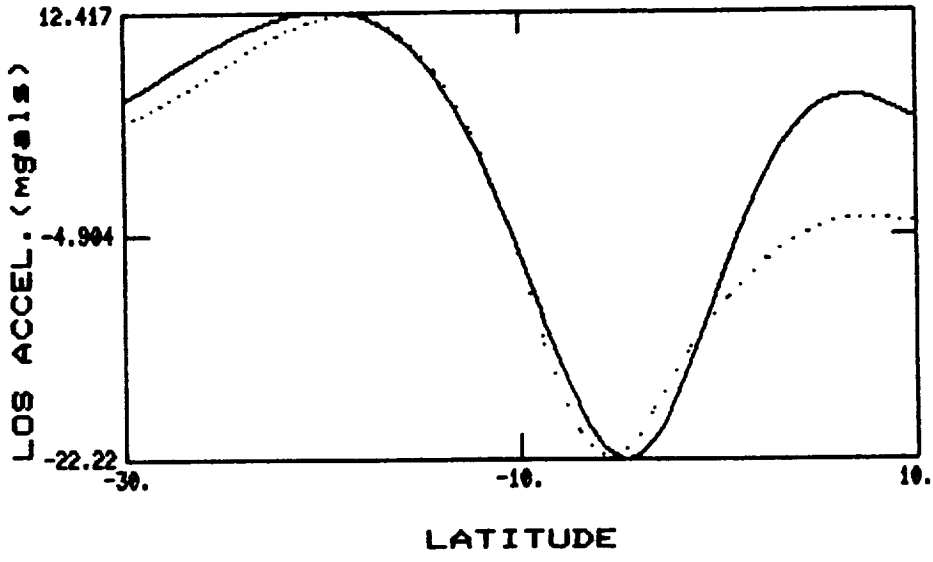

Figure 1. Rev 488 gravity data over central Valles Marineris. Line-of-sight accelerations (dots) and simulated accelerations (solid line) produced by topographic-geophysical model (see text).

PLANETARY RADARCLINOMETRY IN 1985

Robert L. Wildey, U.S. Geological Survey, Flagstaff, AZ 86001

Radarclinometry is defined as the production of a topographic map or its equivalent, with or without the metric precision normally associated with stereophotogrammetry, from monoscopic radar images through the dependence of the look-averaged pixel signal strength on the local orientation of the surface. Pixel signal, as a single parameter, is uniquely dependent on the two parameters that characterize surface orientation. The inverse dependence of surface orientation on pixel signal is not uniquely defined when applicable knowledge is limited to the radiometric transfer characteristic of the look-averaged pixel and the radar-reflectance function for the surface under investigation (in themselves, somewhat elusive). Therefore, in terms of strict mathematical determinism, radarclinometry is impossible. My investigation continues under the assumption that an adequately benign heuristic hypothesis concerning the curvature properties of the surface of terrain can be found that renders the height function in terms of uniquely defined line integrals [1]. The goal of metrically precise topography may prove elusive, but the threshold of precision adequate to enhance morphometry in the geologic interpretation of terrain has already been surpassed [2]. Justification of this work requires only the improvement of performance in the latter category.

I previously reported an expansion of options in the selection of local curvature assumptions [3]. I have since extended this aspect of the investigation to include global-curvature hypotheses. Such hypotheses as the minimization of the total surface area, subject to radarclinometry as a nonholonomic constraint, and the maximization of the frame-average dot product between the local normal and the local vertical, have been incorporated. The global hypotheses can be localized by using the calculus of variations. To date, the minimization of surface area appears superior by a narrow margin to all other local and global hypotheses that have been incorporated.

I have also previously indicated my apprehension concerning the coarseness of mesh of the numerical integration when taken as the pixel separation, especially when the line integral is directed in an azimuthal rather than a ground-range direction, inasmuch as the pixel signal depends on slope components in the azimuthal direction only to second order and higher. I have also investigated this aspect of the problem. Although the equations of radarclinometry are partial differential equations, the mathematics can be made to mimic a system of two ordinary differential equations, when the line integral formulation is uniquely directed. The systems are different for azimuthal and ground-range directions. The algorithm developed by Hindmarsch [4] based on the Gear technique for the numerical integration of systems of stiffly stable equations was adapted. The driving function represented by the pixel distribution of an image was rendered continuous by using a two-dimensional Lagrange interpolation formula for a local 3x3 patch of pixels. The range of integration in each instance of application was one pixel separation. This approach caused very little change in the ground-range profile, but the change in the cross-tying azimuthal profile at the ground-range threshold was profound.

I have previously demonstrated the crucial role played by the accuracies of the transfer characteristic for pixel signal and the reflectance function

for the surface, in the derivation of topographic maps, if the distortion bands parallel to ground-range are to be avoided [1]. In order to evaluate radarclinometry in the absence of radiometrically calibrated radar, I have developed an algorithm that performs radarclinometry in reverse. That is, a radar image is produced from a topographic map through a hypothetically uniform and linear radar system, based on an assumed reflectance function. This reflectance function is then adopted in the attempt to rederive the topographic map from the synthesized radar image. The result is a test of the fundamental limitations of the curvature hypotheses, arithmetic precision, and the mesh-fineness of integration, to the virtual exclusion of other possible sources of error that would be inherent in real data. These tests have provided the basis for the comparisons reported above.

Not only was the azimuthal integration profoundly altered by the Gear integration technique, but the revision was not beneficial. The conclusion must be reached that radarclinometric integration in azimuth is not possible for a pixel-signal dependence on the azimuthal component of slope that is as weak as the one utilized. As a matter of fact, the reflectance function used was sufficiently gentle as to make this dependence considerably weaker than what would be found in nature in most cases. I plan to redo the test with a more strongly sloped reflectance function. Nevertheless, there is a strong possibility that the conclusion militating against azimuthal integration will be strengthened by the new tests.

The loss of a cross-tie integration in azimuth has not precluded the improvement of the morphometric capabilities of radarclinometry. Topographic maps have been produced by least-squaring the mean height of each profile in ground-range in a minimization of the sum of squares of its residuals, with the preceding adjacent profile as a model. Of course, an initial strike-line orientation is needed for each integration in ground-range. For the first ten lines this is accomplished by a relaxation into self-consistency. Thereafter, the strike-line orientation is evaluated as that of a plane that has been least-square fitted to a 6x6 patch of topography abutting the ground-range threshold in the preceding six lines. The resulting topography shows no banding distortion perceptible to the eye and appears equivalent to the original given topography in all but the few very lowest spatial frequencies of the topographic block.

The ubiquitousness of radiometrically calibrated radar, which appeared imminent when this research was begun, has since proved to be elusive. The ability to assume an applicable reflectance function with adequate precision is also open to question. In any event, these problems will not be solved in time for application to the nominal mission of the Venus Radar Mapper. With justification in terms of a morphometric rather than a geodetic goal, my research in the immediate future will be directed toward the circumvention of these problems.

For a given radar transfer characteristic and reflectance function there is a unique correspondence between the slope-frequency distribution corresponding to an image and the frequency distribution of pixel signal strengths. I plan to assume an isotropic gaussian slope-frequency distribution with a dispersion parameter as given. A likely source for this parameter will be radar-altimetry profiles, augmented by interpretation of the range-width of the profile elements. The coefficients of both a transfer

characteristic and a reflectance function will be determined by least-squares in fitting the predicted frequency distribution of the pixel signal strength to the histogram of pixel-DN values of a candidate image.

In 1985 the radarclinometric processing time for a 600x600 $(\text{pixel})^2$ image was additionally cut in half to 2 hours.

References:

[1] Wildey, R.L., 1985, manuscript submitted to Journal of Geophysical Research.
[2] Wildey, R.L., 1984, Science, 224, 153-156.
[3] Wildey, R.L., 1985, NASA Technical Memorandum No. 87563, 445-447.
[4] Hindmarsch, A.C., 1974, Lawrence Livermore Laboratory VCID-30001, 1-70.

A MARS DIGITAL TERRAIN MODEL AND SAMPLE CORRELATION WITH A MARS DIGITAL IMAGE MODEL

Sherman S. C. Wu and Annie-Elpis Howington
U. S. Geological Survey, Flagstaff, AZ 86001

A Digital Terrain Model (DTM) is being derived as a byproduct of the topographic mapping of Mars described by Wu et al. (1985). The DTM is a raster of elevation values compatible with the raster of brightness values of the Digital Image Model (DIM) described by Batson (1985). Like the DIM, it is encoded in the Sinusoidal Equal-Area projection, with elevation values at 1/256-degree increments. It is also geometrically compatible with the geological, geophysical, and geochemical databases described by Kieffer et al. (1981).

The interpretive use of DTM/DIM combinations can be illustrated with three-dimensional transformations described by Batson et al. (1981) and exemplified in Figures 1-3. The digital file, from which Figure 1 was converted to raster format, was made into a digital shaded relief image (Fig. 2). The DTM was also used as control to rotate a DIM that contains four Viking Orbiter frames to a new perspective view (Fig. 3).

Planetwide coverage by geometrically compatible elevation and image models should allow production of images like Figure 3 on a routine basis.

References

Batson, R. M., 1985, A digital image model of Mars: NASA Tech. Memo. (this issue).

Batson, R. M., Edwards, Kathleen, and Skiff, B. A., 1981, Orthophoto mosaics and three-dimensional transformations of Viking Orbiter pictures: NASA Tech. Memo. 84211, p. 493-495.

Kieffer, H. H., Davis, P. A., and Soderblom, L. A., 1981, Mars' global properties: Maps and applications: Proceedings of the Twelfth Lunar and Planetary Science Conference, Houston, Texas, March 16-20, 1981, p. 1395-1417.

Wu, S. S. C., Jordan, Raymond, and Schafer, F. J., 1985, Compilation of the Mars 1:2,000,000-scale topographic map series: NASA Tech. Memo. 87563, p. 612-613.

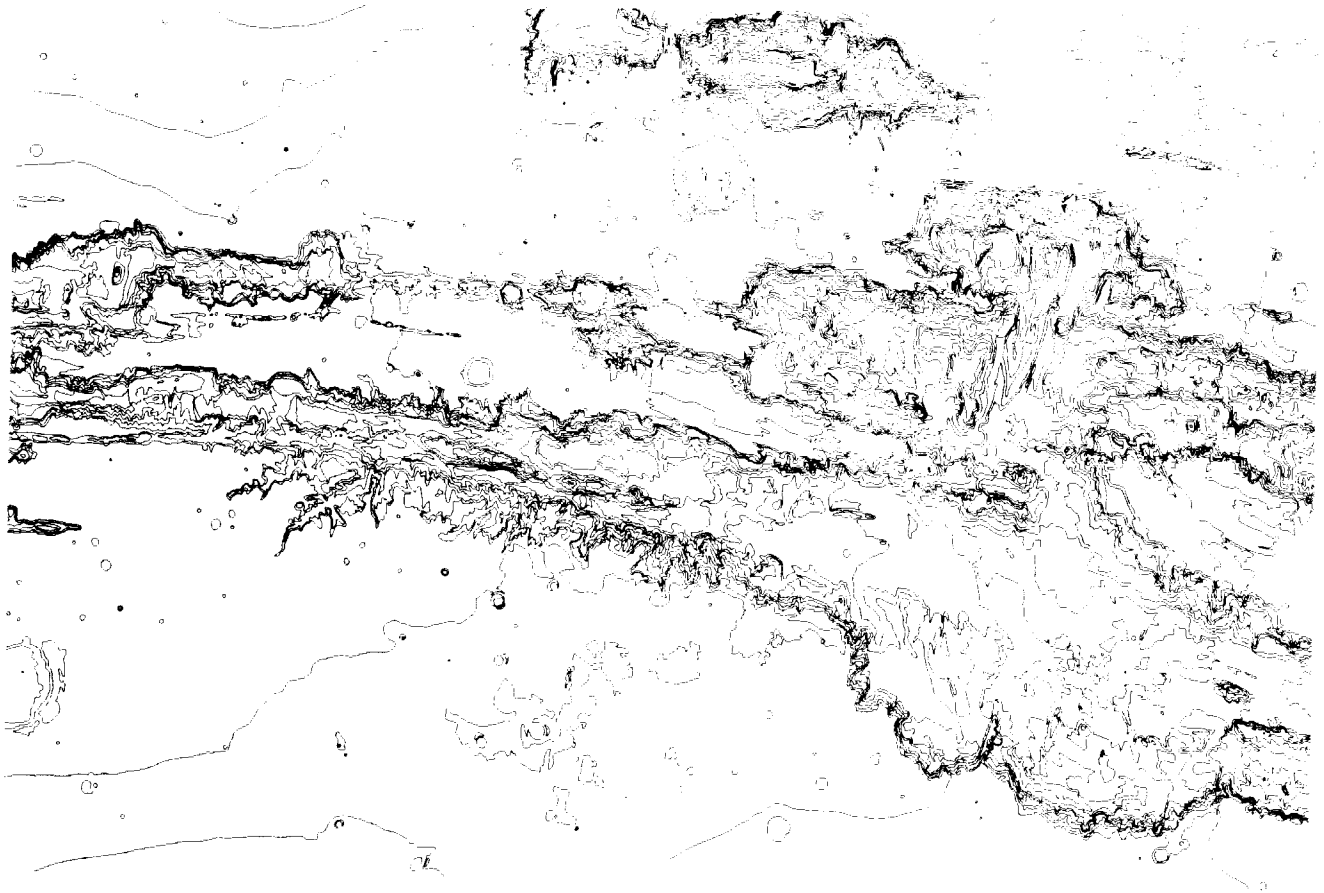

Figure 1. Reduction of a digitized contour map of the Coprates (MC-18) NW quadrangle of Mars. Contour interval 1 km. Original map compiled at 1:2,000,000 scale.

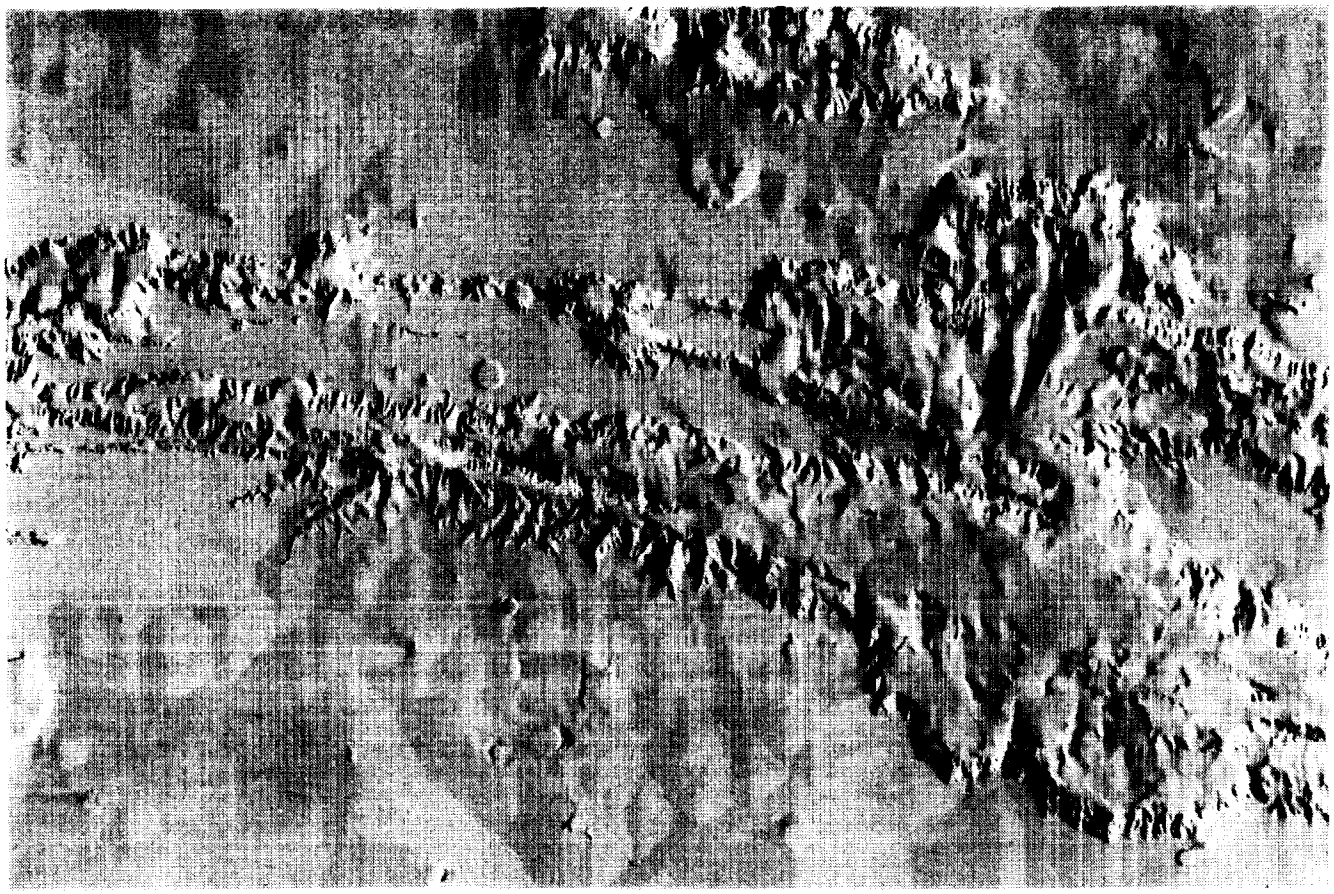

Figure 2. Shaded relief map of the area shown in Figure 1, generated by computer image-processing techniques using digital elevation data.

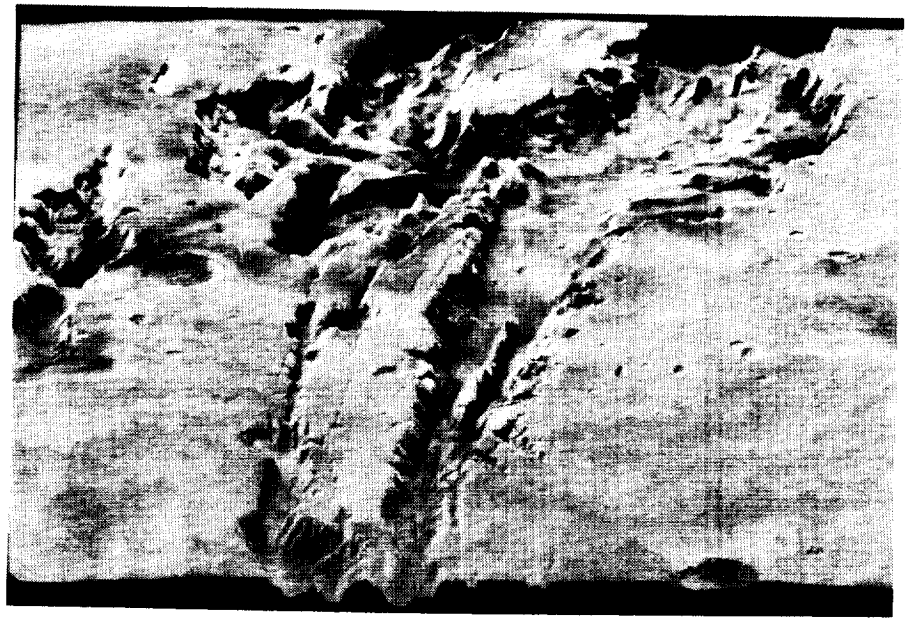

Figure 3. Perspective view of a small part of the Mars canyonland shown in Figures 1 and 2, made with Viking Orbiter pictures 663A44, 663A42, and 613A61. Projection is controlled by digital elevation data collected from the map shown in Figure 1. View is toward due east at an angle of 25^{0} from the horizon. Vertical exaggeration, 5 times.

ON-LINE DISTORTION CORRECTIONS FOR VIKING ORBITER IMAGES

Sherman S. C. Wu, Annie-Elpis Howington, and Francis J. Schafer
U. S. Geological Survey, Flagstaff, AZ 86001

Viking Orbiter pictures must be corrected for camera distortions if they are to be useful for photogrammetry. In the past these corrections were made off-line, by digital image-processing techniques. On-line distortion correction, in the computer of an analytical stereoplotter, should greatly improve stereoplotting efficiency and accuracy.

Development requires modification of plotter software so that image distortions are corrected in real time with reference to calibration data and reseau marks. Polynomials used are:

$$\Delta X = X_c - X = a_1 + a_2 X^2 + a_3 X + a_4 X Y + a_5 Y + a_6 Y^2$$

$$\Delta Y = Y_c - Y = b_1 + b_2 X^2 + b_3 X + b_4 X Y + b_5 Y + b_6 Y^2$$

where (X_c, Y_c) and (X, Y) are, respectively, calibrated and measured coordinates of reseau marks. Coordinates of a minimum of 12 reseau points must be determined, although all 103 reseau marks are usually measured on each picture in order to generate coefficients of the two polynomials by applying least-squares adjustment. Computations are based on the original image geometry by comparing measured distances to calibrated distances between all measured reseau marks and the reseau mark at the center of the picture.

Once coefficients are calculated, coordinates of any image point are corrected on line in real time by applying $X_c = X + \Delta X$, $Y_c = Y + \Delta Y$, where ΔX and ΔY are calculated from the polynomials with established coefficients.

This is the program used for correcting photocoordinates in the Mars control network. Measurements were made on the Mann comparator for pictures that have already been decalibrated by digital image processing.

The software of the AS-11AM analytical stereoplotter has been augmented with this algorithm, so that map compilation can proceed by using raw (uncalibrated) pictures from Viking Orbiter. Distortions can be corrected in real time and on line by the plotter. The augmented plotter software allows the use of polynomial coefficients from previous measurements, if available, so that it is not necessary to measure reseau marks on each picture.

Tests are being conducted by comparing results from three sets of stereomodels. Model 1 uses the pair of pictures that have been decalibrated (distortion corrected) through off-line digital image processing; models 2 and 3 use the same pair but the pictures are uncalibrated (raw). Model 2 applies the on-line distortion correction (real time) and model 3 applies no correction. Results from these three models will be documented when final tests are completed.

MARS GLOBAL TOPOGRAPHIC MAP: 1:15,000,000 SCALE

Sherman S. C. Wu, Raymond Jordan, and Francis J. Schafer
U. S. Geological Survey, Flagstaff, AZ 86001

A new global topographic map of Mars has been compiled at a scale of 1:15 million and a contour interval of 1 km. This map was produced by the synthesis of data acquired from various scientific experiments of both the Mariner 9 and Viking missions, including S-band radio-occultation, the ultraviolet spectrometer, the infrared interferometer spectrometer, and Earth-based radar data collected at Goldstone and Haystack Observatories. Contour lines of the map are referred to the Mars topographic datum (Wu, 1981); elevation precision is within 1 km. The newly completed planetwide control net of Mars was used for control (Wu and Schafer, 1984). The new map replaces the 1:25 million-scale global topographic map compiled from Mariner 9 data (Wu, 1975, 1978).

The map consists of three sheets: (1) the western hemisphere from long 0° to 180° (Fig. 1), (2) the eastern hemisphere from long 180° to 360° (Fig. 2), and (3) the two polar regions above lat ± 55°. Contour lines between lat ±30° and long 60° and 180° (Fig. 1) are much denser than other areas. These contour lines were produced by photogrammetric compilation from stereomodels by using Viking pictures on analytical stereoplotters; they were reduced from the 1:2 million-scale topographic maps. As the compilation of these larger scale maps progresses, they will be used to update the global map.

References

Wu, S. S. C., 1975, Topographic mapping of Mars: U. S. Geological Survey Interagency Report: Astrogeology 63, 193 p.

Wu, S. S. C., 1978, Mars synthetic topographic mapping: Icarus, 33, 3, 417-440.

Wu, S. S. C., 1981, A method of defining topographic datums of planetary bodies: Annales de Géophysique, Centre National de la Recherche Scientifique, Numero 1, Tome 37, 147-160.

Wu, S. S. C. and Schafer, F. J., 1984, Mars control network: American Society of Photogrammetry, in Technical Papers of 50th annual meeting of Am. Soc. of Photogrammetry, v. 2, 456-463.

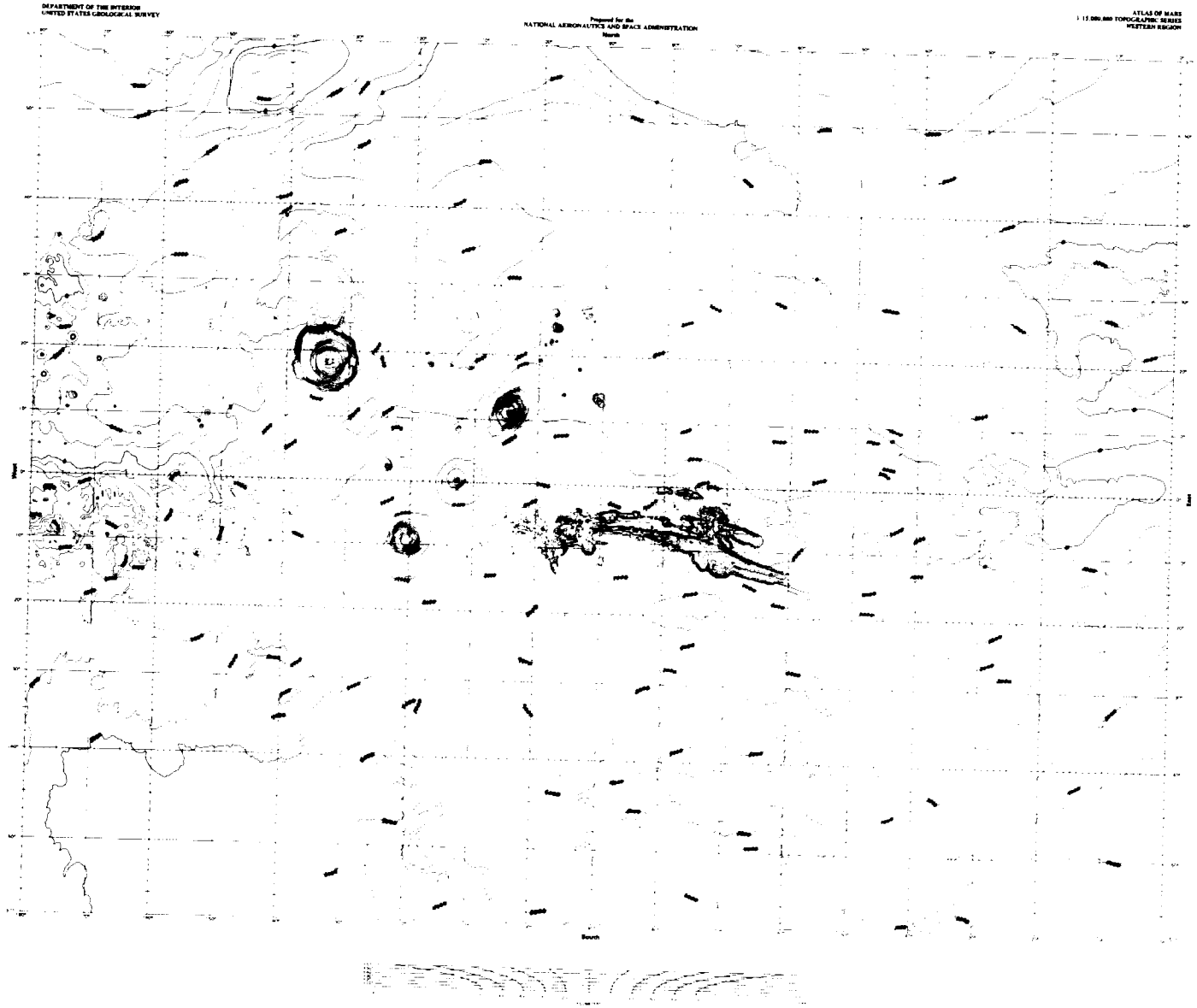

Figure 1. Global topographic map of Mars at reduced scale (western hemisphere). Contour interval 1 km.

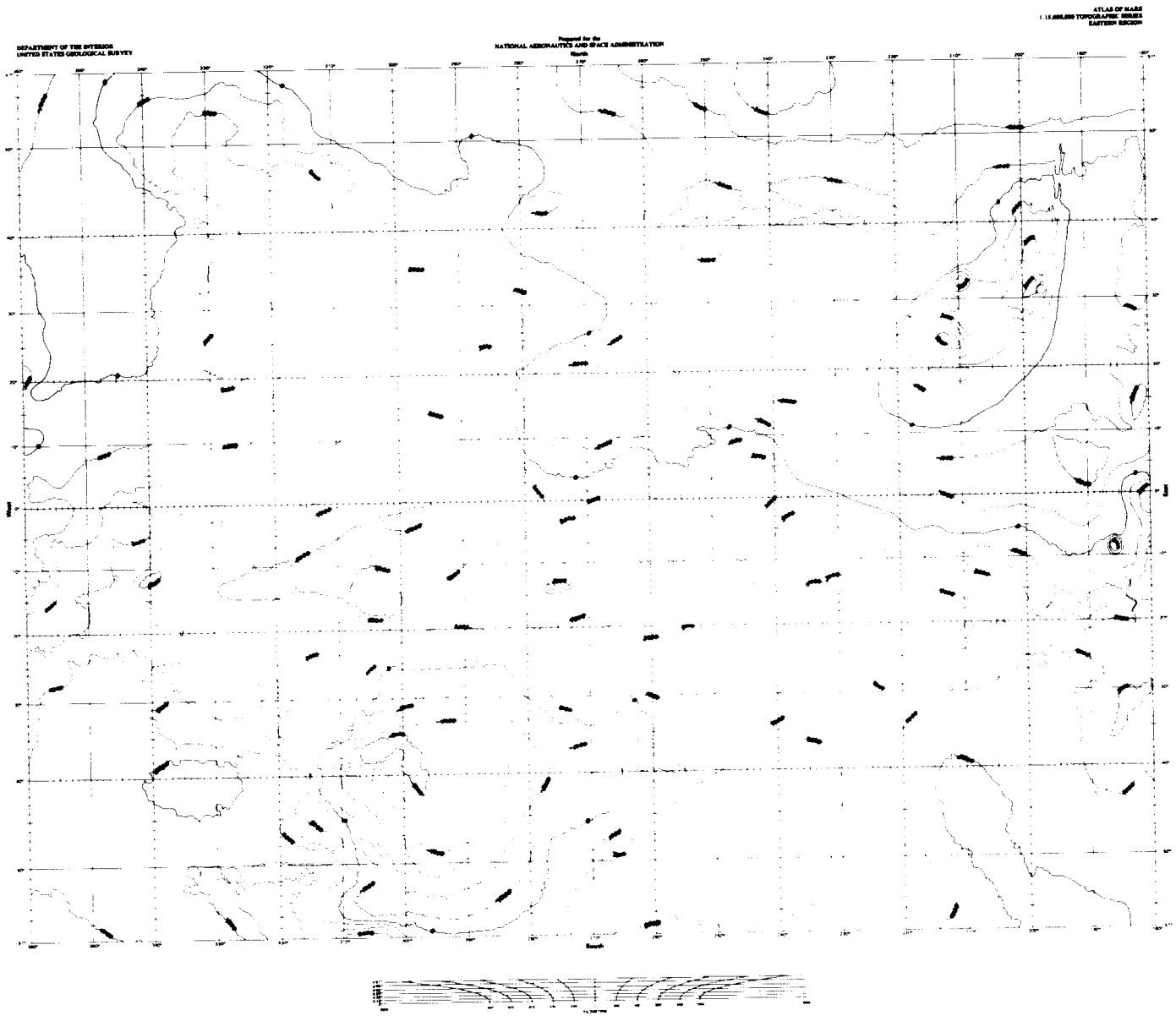

Figure 2. Global topographic map of Mars at reduced scale (eastern hemisphere).
Contour interval 1 km

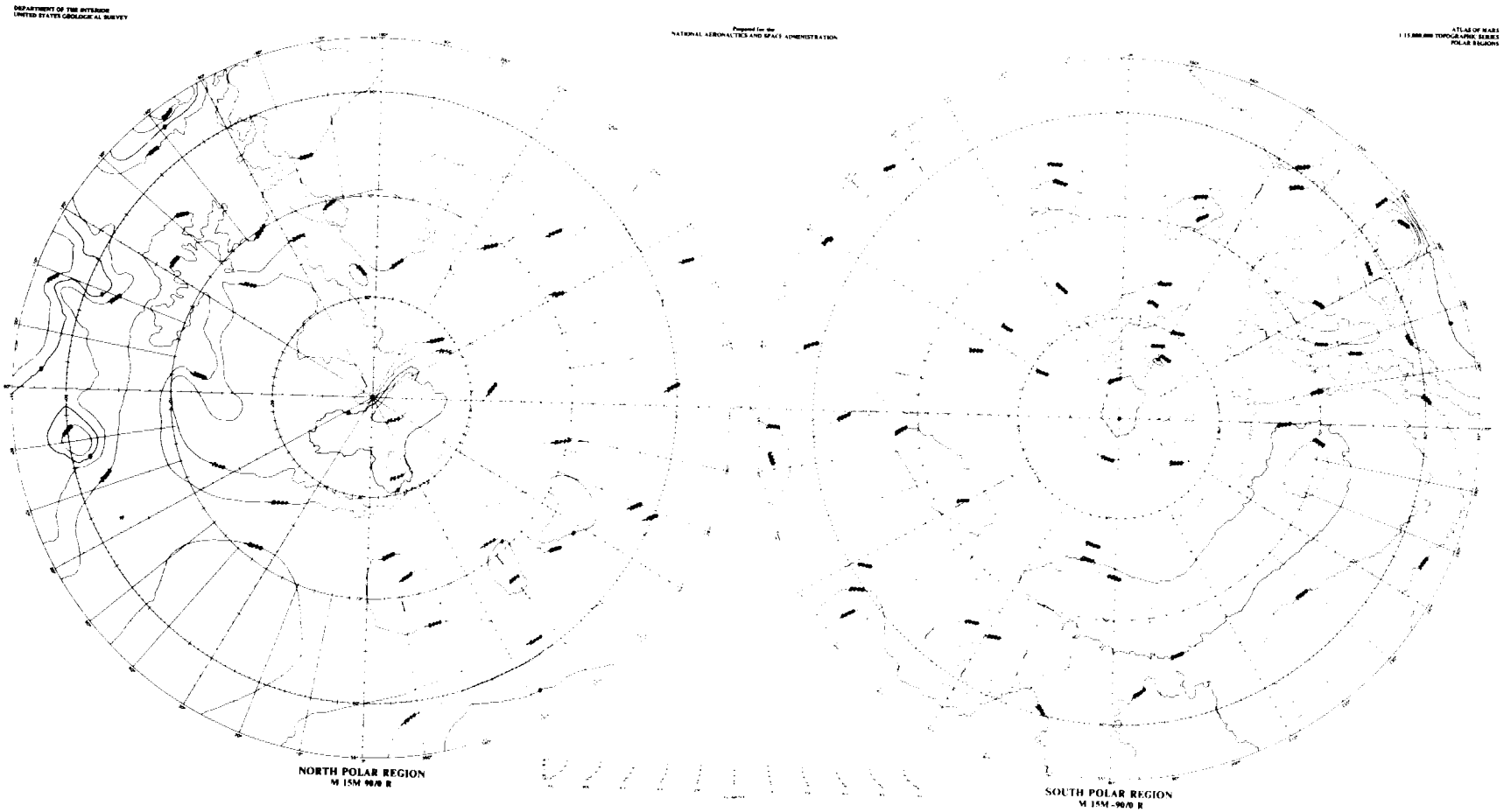

Figure 3. Global topographic map of Mars at reduced scale (northern and southern polar regions). Contour interval 1 km.

STATUS OF COMPILATION OF THE MARS 1:2,000,000-SCALE TOPOGRAPHIC MAP SERIES

Sherman S. C. Wu, Raymond Jordan, and Francis J. Schafer
U. S. Geological Survey, Flagstaff, AZ 86001

The development of special photogrammetric techniques (Wu et al., 1982) and the completion of the Mars planetwide control network (Wu and Schafer, 1984) have enabled the systematic mapping of Mars; topography at a scale of 1:2,000,000, based on high-altitude Viking Orbiter pictures. In addition to the 17 quadrangles previously completed, 19 quadrangles have been compiled during fiscal year 1985. All of the contour maps of the equatorial belt (between lat ±30°) of the western hemisphere (between long 0° and 180°) have now been compiled. They include four subquadrangles each of MC-8, MC-9, MC-10, MC-11, MC-16, MC-17, MC-18, and MC-19. Two subquadrangles each of the two polar regions (MC-1A, -B, MC-30A, -B) have also been compiled.

Elevations of all topographic maps are referred to the Mars topographic datum (Wu, 1981). The maps have a contour interval of 1 km and a precision of ±1 km. The equatorial-belt maps are Mercator projections with true scales at lat ±27.476°. An example of these maps is shown in Figure 1, the topographic map of the Margaritifer Sinus Northwest quadrangle (MC-19NW).

We anticipate that all 140 quadrangles will be completed by the end of fiscal year 1989. These maps will provide more precise knowledge of Martian topography and will help in understanding the geologic processes that have shaped the Martian surface.

References

Wu, S. S. C., 1981, A method of defining topographic datums of planetary bodies: Annales de Géophysique, AGEPA 7, Tome 37, fasc. 1, 147-160.

Wu, S. S. C., Elassal, A. A., Jordan, Raymond, and Schafer, F. J., 1982, Photogrammetric application of Viking orbital photography, Planetary and Space Science, vol. 30, no. 1, p. 45-55.

Wu, S. S. C. and Schafer, F. J., 1984, Mars control network: Tech. Papers of the 50th Annual Meeting, American Society of Photogrammetry and Remote Sensing, 2, 456-463.

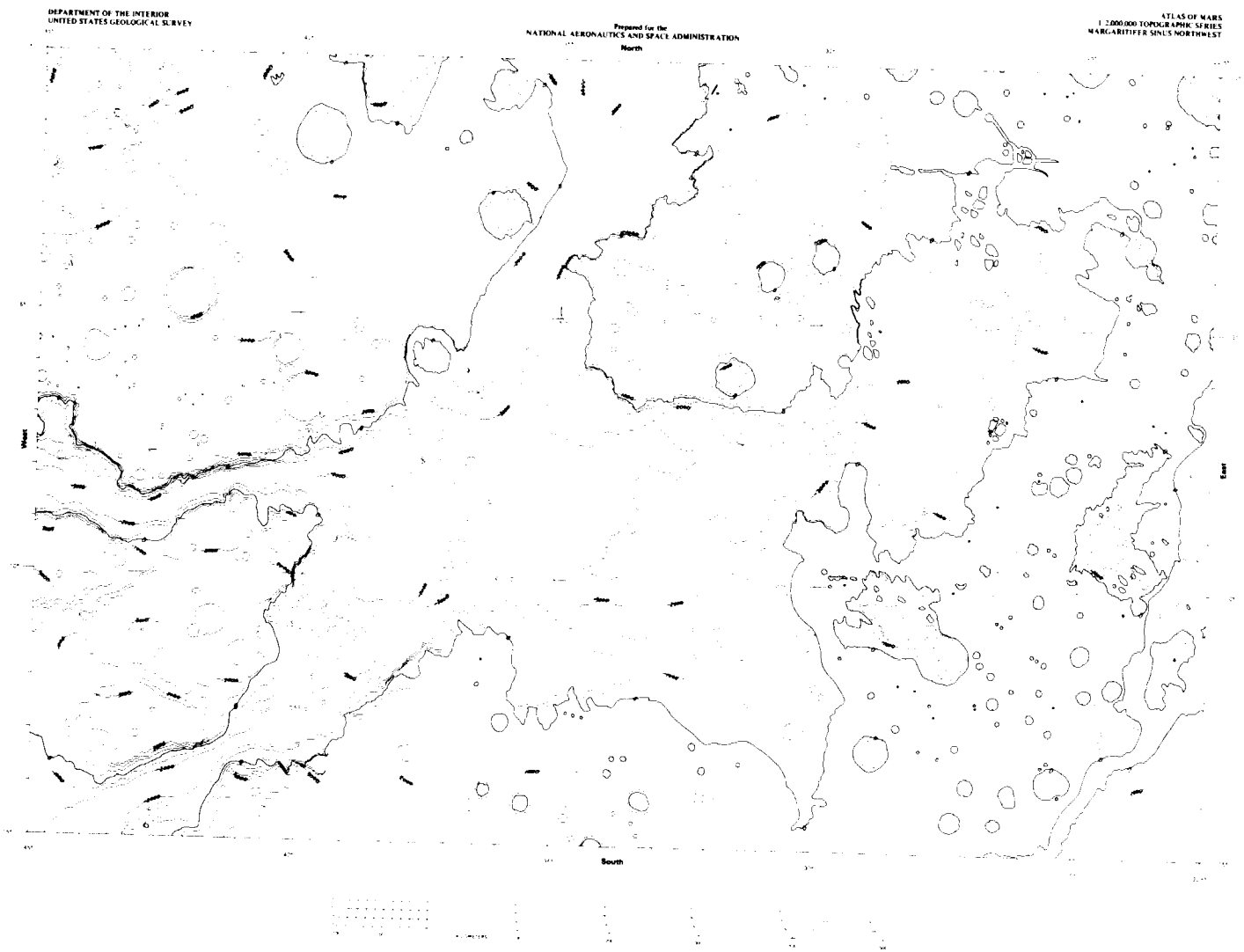

Figure 1. Topographic map of the Margaritifer Sinus Northwest quadrangle (MC-19NW) at reduced scale. Contour interval 1 km.

CHAPTER 15

SPECIAL PROGRAMS

PLANETARY GEOLOGY SPEAKERS BUREAU AND SHORT COURSE

R. Greeley, Department of Geology, Arizona State University, Tempe, Arizona 85287

The Planetary Geology Speakers Bureau is a national lecture program coordinated by Arizona State University to provide the opportunity for colleges, universities, and other institutions to invite planetary geologists to give presentations on various aspects of planetary geosciences. Present speakers include Raymond Arvidson, Joseph Boyce, Farouk El-Baz, James Head, Elbert King, Hal Masursky, George McGill, Steve Saunders, Peter Schultz, Dave Scott, Sean Solomon, David Stevenson, Joe Veverka, and John Wood. A brochure describing the program and the speakers is sent twice a year to all geoscience departments listed in the American Geological Institute directory. On average, each speaker visits 2-3 institutions each year. Typically, a general lecture is given (open to the public) and a more specialized presentation is given on current research topics as a departmental seminar.

In addition to the Speakers Bureau, a short course was held in association with the annual meeting of the Geological Society of America in Orlando. The 34 participants attending the course included geology faculty, high school earth science teachers, and students. During the intensive two-day course, instruction was given by A. Albee, R. Arvidson, J. Head, R. Greeley, K. Sullivan and P. Schultz on various aspects of planetary geology through lectures, demonstrations, and "hands-on" activities.

Activities such as the Speakers Bureau and the Short Course provide means for disseminating the results from solar system exploration to the general scientific community.

PLANETOLOGY EXPERIMENTS ON SPACE STATION: WORKSHOP RESULTS

R. Greeley, Department of Geology, Arizona State University, Tempe, Arizona 85287

A NASA-sponsored workshop involving about 45 planetary scientists was held in June to discuss potential experiments that could be conducted in the unique environment afforded by the Space Station proposed for the 1990s. Following the initiative to establish a permanently manned Space Station in Earth orbit, numerous studies have been undertaken to identify the potential science activities that could be conducted on board. Activities related to planetary science include using the station: (1) as a platform for planetary observations, (2) as a staging base for lunar and planetary missions, (3) to collect extraterrestrial "dust", and (4) as an environment for carrying out planetary-related experiments. The latter topic was the basis for the workshop held June, 1985 at the U.S. Geological Survey, Center for Astrogeology, in Flagstaff, Arizona. The workshop provided a forum for discussing possible experiments, the science rationale, and the requirements on the Space Station, should such experiments eventually be flown.

The primary consideration at the workshop was the low gravity environment (10^{-5} g) that might be provided for long periods by the Space Station. Many planetary environments involve gravitational accelerations less than Earth. The Space Station could enable experiments to be conducted in which gravity a critical term in certain planetary processes, especially for planetary experiments appropriate for extremely low gravity is environments such as comets and asteroids. In other experiments, "g" may not be a critical term for study, but its near-absence may enable experiments to be conducted which cannot be done on Earth. Some of the general experiment areas that have be suggested include impact cratering, experimental petrology, the formation and interaction of small particles, and aeolian processes.

The impact process is ubiquitous in the Solar System affecting planetary surfaces from the microscale (regolith evolution) to the megascale planetary disruption). Over the last two decades research has focused on processes in which gravity plays a key role, whether in returning ejecta to the surface of the target body or in limiting crater growth. As earth-based observations and missions return new data about small bodies, the understanding of impact cratering under very low-gravity conditions is severely limited because of difficulty in removing this variable in 1 g experiments. A Space Station Impact Facility would provide the unique opportunity to reproduce impact conditions unachievable on Earth and to explore parameteres "masked" by the gravity term.

A wide variety of experiments can be conducted on the Space Station that involve the physics of small particles (μm to cm in size). Processes include nucleation and condensation of particles from a gas, aggregation of small particles into larger ones, and low velocity collisions. The microgravity environment of the Space Station would be necessary to perform many experiments regarding these processes, as they generally require that particles be suspended for periods substantially longer than are practical at 1 g.

PLANETOLOGY EXPERIMENTS...Greeley

A report including summaries of each subsection, abstracts of contributed papers, and a list of participants is currently in press on a NASA Contractor Report.

Space Station Planning in the Solar System Exploration Division

Joseph A. Nuth, Chemistry Department, University of Maryland

The Solar System Exploration Division has begun serious consideration of support for a Space Station based, experimental effort. The effort will be geared toward a series of planetology related experiments at IOC (the 1993-94 time frame) and to build on this knowledge base during the Growth Phase of the Space Station era (post 1994) in order to deploy a Planetology Research Module. This module would provide a shirtsleeve environment in which to carry out a series of experiments related to aeolian phenomena, low gravity cratering dynamics, refractory particle nucleation and coagulation phenomena as well as several microgravity and ultrahigh vacuum petrology investigations (to name just a few). The module would house the control racks for the Astrometric Telescope and for various Cosmic Dust Collection experiments as well as the control and data acquisition racks for several proposed attached payloads. Candidate attached payloads include several artificial comet experiments, a planetary plasma sheath investigation and a slitless ultraviolet spectrometer to monitor the elemental abundances in meteors.

The Solar System Exploration Division has begun putting into place the bureaucratic structure to accommodate the development of flight qualified candidate experiments by IOC. It is expected that flight experiments for IOC will be selected by the conventional AO process. The development program will be funded by PIDDP under the direction of individual PI/Co-I teams with the intention that the resulting experimental systems will be facility instruments available for use by the entire community. The development effort will be monitored by a Headquarters Committee to include Bill Quaide, Joe Boyce, Henry Brinton, Roger Bourke, Bud Powell, Roger Crouch, and Joe Nuth and will be advised by a panel of outside experts who have no direct interest in the experimental program. The Headquarters Committee will also receive input from an Advocacy Group consisting of the PI's of the funded development efforts and possibly other members of the community.

The Division is currently investigating the possibility of funding the development of cosmic dust collection experiments by this same mechanism. A workshop is planned for mid-December at which the participants will attempt to formulate a comprehensive plan leading to IOC dust collection experiments (including preliminary studies on LDEF and Shuttle) and the logical evolution of these collection efforts during the post-IOC phase. Preliminary experiment development efforts might appropriately be funded under PIDDP; funding decisions will be in response to specific proposals from the community.

It should be noted that the Microgravity Sciences Division will co-fund some of the laboratory development projects while the Exobiology Program will support part of the dust related efforts. Close cooperation with these and other NASA programs will be maintained for our mutual benefit whenever possible.

18/4

REFLECTANCE EXPERIMENT LABORATORY (RELAB)

Carle M. Pieters, Associate Professor, Brown University, Dept. of Geological Sciences, Box 1846, Providence, RI 02912

a) Objectives: The Reflectance Experiment Laboratory (RELAB) is a visible and near-infrared swinging arm spectrometer/gonimeter designed to accurately measure the reflectance properties of materials under the same optical and geometric conditions as remote measurements of planetary surfaces using satellites or earth-based telescopes. The high precision (< 1/2%) and broad spectral coverage (0.35 to 2.6 μ m; 1 nm sampling resolution) capabilities of the RELAB make it ideally suited for laboratory studies needed for current and future programs of exploration involving remote sensing of surface composition. Such reflectance data have applications for the Moon, Mars, asteroids and the Earth.

b) Progress: The RELAB started operation at Brown University in 1984. A full-time technical assistant was hired to run, maintain, and upgrade the system. Much of the orginial hardware and software required adjustment or replacements. A new PMT and cooling housing has been implemented and the entire spectrometer calibrated. The old LSI 1103 control system has been patched innumerable times, and we eagerly await the arrival of its replacement, a Micro VAX II. Software was developed to manage the increasing data base of spectra and samples. A new high resolution viewing optics system (1mm to 6mm fov) has been designed and parts ordered. Use of the facility has included mineral mixing experiments, experimental regoliths, meteorites, shocked feldspar, Mars and Venus analogues, and samples from a kimberlite dike (southern Utah). RELAB now produces bidirectional reflectance data of *exceptional* quality. A manual has been prepared to familarize potential users with the RELAB current capabilities.

c) Proposed: The RELAB is run as a facility for NASA sponsored research. Work with mineral mixtures, experimental regoliths, meteorites and terrestrial material will continue. Significantly expanded programs with lunar samples and Mars and Venusian analogues are expected. The computer control will be upgraded when the Micro VAX arrives early Fall, although the full transfer of operations will take longer. Data management and processing capabilities will be expanded. The new optics should be implemented by winter. Additional planned upgrades include extension of the wavelength range further into the near-infrared and design of an environmental chamber.

Bibliography:

Reflectance Experimental Laboratory Description and Users Manual (1985) 13 pp, available on request

C.M. Pieters and F. Horz (1985) Lunar and Planet. Sci. XVI, p 661-662

D.A. Crown and C.M. Pieters (1985) Lunar and Planet Sci. XVI, p 158-159, L.A. McFadden *et al.* Nat. Inst. Polar Res. special issue on Y791197.

DEBRIS-CLOUD COLLISIONS: ACCRETION STUDIES IN THE SPACE STATION

P.H. Schultz, Department of Geological Sciences, Brown University, Box 1846, Providence, RI 02912. D.E. Gault, Murphys Center of Planetology, Murphys, CA

BACKGOUND: The growth of planetesimals in the Solar System reflects the success of collisional aggregation over disruption. It is widely assumed that aggregation must represent relatively low encounter velocities between two particles in order to avoid both disruption and high-ejecta velocities (1,2). Such an assumption is supported by impact experiments (3) and theory (4). Experiments involving particle-particle impacts, however, may be pertinent to only one type of collisional process in the early Solar System. Most models envision a complex protoplanetary nebular setting involving gas and dust. Consequently, collisions between clouds of dust or solids and dust may be a more realistic picture of protoplanetary accretion. Recent experiments performed at the NASA-Ames Vertical Gun Range (5) have produced debris clouds impacting particulate targets with velocities ranging from 100 m/s to 6 k/s. The experiments produced several intriguing results that not only warrant further study but also may encourage experiments with the unique impact conditions permitted in a microgravity environment.

COLLISIONS BETWEEN DEBRIS-CLOUDS AND PARTICULATE SURFACES: Impact experiments at the NASA-Ames Vertical Gun Range have assessed differences between clustered and single-body impacts on particulate surfaces. The primary goal was to examine the effects of atmospheric entry on cratering and possible implications for secondary cratering processes (5). Impacting debris clouds were produced during passage of a brittle pyrex projectile through a thin sheet of paper or aluminum foil. At hypervelocities ($v > 5$ km/s), a 2.5 mil sheet of paper was sufficient; at supersonic velocities ($v \approx 2$ km/s), a 1 mil aluminum foil was used. Because the launch tubes are rifled in order to induce separation between the projectile and sabot, the effective dispersion of the debris cloud could be varied by changing the distance between the target surface and paper or foil. High-frame rate photographs recorded the resulting dispersion in the impacting debris cloud and thus the effective density at impact.

The experiments revealed a factor of 5 decrease in predicted cratering efficiency for an impact by a solid projectile of the same mass (m) and velocity (v). If the energy density of the impacting cloud is included (6) by using a dimensionless expression of cloud radius (r) divided by v^2, then cratering efficiency is only slightly decreased. As might be expected, the crater aspect ratio and morphology were significantly altered (5). As typical for laboratory experiments, however, several unexpected phenomena also occurred. First, the high frame-rate photographic record revealed an intensely luminous cloud immediately after impact (7). The early stages of ejecta-plume growth were characterized by an amorphous cloud rather than the systematic expansion of a funnel-shaped curtain typical for single-body impact. Second, unusually large (1-5 cm across) fairy-castle aggregates were produced. Many of these aggregates had low-ejection velocities. An impact by a 0.2 g/cm^3 cloud at 4.1 km/s produced an unusually large aggregate extending from the floor to above the crater rim. The exact nature of such aggregates is not yet known; they appear to be melt-welded target material. We also do not yet know for certain if melt production increased relative to a single-body impactor. The early-time film record showing a bright luminous cloud and the slight decrease in cratering efficiency, however, may be indicating greater partitioning into internal energy losses. These preliminary results would indicate that collisions between two debris clouds might produce aggregates, thereby increasing particle sizes, whereas a single particle impacting a particle results in disruption and comminution. Such an experiment could provide new insight for early planetary growth processes and for interpreting the record of this stage (e.g., 8,9).

POSSIBLE SPACE STATION EXPERIMENTS: The microgravity environment of a Space Station would allow detailed studies of the competing processes of aggregation and disruption using conditions more appropriate (or at least scalable) for an evolving protoplanet. A cloud of impactor fragments can be readily produced in a manner already performed on Earth, but of different density, composition, and initial size distribution. Of specific interest would be the change in size distribution, shock state, velocity distribution, mixing, and the possible production of chondrite breccias (10). The formation of chondrules is more equivocal (10) but objections could reflect an incomplete experimental simulation. Collisional velocities would range from values expected for collisions in a nebular disk (< 100 m/s) to values possible from the early stages of planetesimal growth (< 6 km/s). Perhaps the most intriguing aspect is the capability of repetitive collisions and more unusual conditions, e.g., passage of a large projectile through a suspended debris cloud. The latter experiment could be performed over long path lengths by tubular extensions from the proposed impact facility.

References: (1) Greenberg, R., Hartmann, W.K., Chapman, C.R., and Wacker, J.F., (1978) in *Protostars and Planets* (T. Gehrels, ed.), 599-622. (2) Hartmann, W.K. (1978) in *Protostars and Planets* (T. Gehrels, ed.), 58-73. (3) Gault, D. and Heitowit, E.D. (1963) *Proc. Sixth Hyper. Impact Symp. 2*, 419-456. (4) Goldreich, L.E. and Ward, W.R. (1973) *Astrophys. J. 183*, 1051-1061. (5) Schultz, P.H. and Gault, D.E. (1985) *J. Geophys. Res. 90*, 3701-3732. (6) Holsapple, K.A. and Schmidt, R.M. (1982) *J. Geophys. Res. 87*, 1949-1970. (7) Schultz, P.H. and Gault, D.E. (1983) *Lunar Planet. Sci. Conf. 14*, 674-675. (8) Weidenschilling, S. J. (1980) *Icarus 44*, 172-189. (9) Wieneke, B. and Clayton, D.D. (1983) in *Chondrules and their Origins* (E. King, ed.) 284-295. (10) Taylor, G.J., Scott, E.R.D., and Keil, K. (1983) in *Chondrules and their Origins (E. King, ed.), 262-278.*

IMPACTS OF FREE-FLOATING OBJECTS: UNIQUE SPACE STATION EXPERIMENTS

P.H. Schultz, Department of Geological Sciences, Brown University, Box 1846, Providence, RI 02912. D.E. Gault, Murphys Center of Planetology, Murphys, CA

The transfer of momentum and kinetic energy between planetary bodies forms the basis for wide-ranging problems in planetary science ranging from the collective long-term effects of minor perturbations to the catastrophic singular effect of a major collision. In the former case, we can cite the evolution of asteroid spin rates and orientations (1,2,3,4) and planetary rotation rates (5). In the latter case, we include the catastrophic disruption of asteroids (3,6), sudden but lasting changes in planetary angular moments (7,8), and the near-global disruption of partially molten planets (9,10). Although the collisional transfer of momentum and energy has been discussed over the last two decades, major issues remain that largely reflect current limitations in earth-based experimental conditions and 3-D numerical codes. Two examples with potential applications in a Space Station Laboratory, are presented below.

ASTEROID SPIN RATES AND ORIENTATIONS: Understanding the transfer of impactor translational momentum to target angular momentum is fundamental to understanding the present-day spin rates, orientations, and spin-limited disruption of asteroids (e.g., see 3). The efficiency of angular momentum transfer is typically expressed as a factor (ζ) ranging from 0 for purely elastic collisions to 1 for inelastic collisions with no ejecta loss (3). Although ζ is usually adopted as unity, Harris (4) prefers a value closer to 0.5 corresponding to a moderate forward-scattering of ejecta. Davis *et al.*, (3) suggest that ejecta are uniformly distributed -- even for low-angle impacts; consequently values of ζ closer to 1 might be justified. Such estimates, however, are largely based on intuition. For vertical impacts into basalt, ejecta carry away 4-6 times the original impactor momentum; therefore, the azimuthal distribution of these ejecta is crucial. For very low-angle impacts, the impactor is ricocheted down-range and carries with it considerable momentum (11). These results would indicate a value of ζ significantly less than 1. Even lower values may occur for curved surfaces. Recent experiments in easily volatilized material (12) reveal significant differences in the partition of energy at low-impact angles. Such differences might lead to differences in impact-induced spin rates between comets and asteroids. (13).

Thus a wide range of values in ζ that depend on impact velocity and target composition/strength can be justified. Experiments are needed wherein free-floating non-spinning and spinning objects of varying strength, porosity, volatility, and strength are impacted at varying impact velocities and angles. A Space Station provides a unique and ideal environment for performing such experiments.

PLANETARY DISRUPTION/SPIN-RATES: The existing rotation periods and total angular moments of gravitationally bound planets and planet-satellite systems may provide a fundamental link between the accretion and post-accretion stages of planetary evolution. The Moon and Mercury preserve a record of impacts of sufficient energy to produce possible antipodal disruption of the surface as indicated by observations and simplified calculations (9). More sophisticated 2-D axisymmetric finite-element codes reveal that a molten interior enhances disruption. Taken to extreme, a collision-vaporization model of the Earth-Moon system has been recently revived with vigor and substance (14,15). Although preliminary calculations have been made to describe the impact-induced vaporization of the early terrestrial crust and the transfer of angular momentum (16), such models are limited by necessary simplifying assumptions including 1-D and 2-D descriptions of a 3-D event. It is unlikely (albeit fortunate) that a directly

scaled event will occur. A space station platform, however, provides a unique opportunity to test important facets of such models by allowing freely suspended spherical targets of varying viscosities, internal density gradients, and spin rates. Although a centralized gravity term cannot be introduced or completely simulated, such limitations are far outweighed by variables that can be readily introduced and controlled.

References: (1) McAdoo, D.C. and Burns, J.A. (1973) *Icarus 18*, 285-293. (2) Burns, J.A. and Tedesco, E.F. (1979), in *Asteroids* (T. Gehrels, ed.) 494-527. (3) Davis, D.R., Chapman, C.R., Greenberg, R., and Weidenschilling, S.J. (1979), in *Asteroids* (T. Gehrels, ed.) 528-557. (4) Harris, A.W. (1979) *Icarus 40*, 145-153. (5) Harris, A.W. (1977) *Icarus 40*, 168-174. (6) Hartmann, W.K. (1979), in *Asteroids* (T. Gehrels, ed.), 466-479. (7) Hartmann, W.K. and Davis, D.R. (1975), in *Icarus 24*, 504-515. (8) Cameron, A. and Ward, W. (1978) *Lunar Planet. Sci. IX*, 1205-1207. (9) Schultz, P.H. and Gault, D.E. (1975) *The Moon, 12*, 159-177. (10) Hughes, G.H., App, F.N., McGetchin, T.R. (1977) *Phys. Earth Planet. Inst. 15*, 251-263. (11) Gault, D.E. and Wedekind, J.A. (1978) *Proc. Lunar Planet. Sci. Conf. 9th*, 3843-3875. (12) Schultz, P.H. and Gault, D.E. (1985) *Lunar and Planet. Sci. XVI*, 740-741. (13) Whipple, F. (1982), in *Comets* (L. Wilkening, ed.), 227-250. (14) Stevenson, D.J. (1984), Conference on the Origin of the Moon, 60. (15) Hartmann, W.K. (1984), Conference on the Origin of the Moon, 52. (16) Melosh, H.J. (1985) *Lunar Planet Sci. XVI*, 552-553.

PLANETARY NOMENCLATURE

M. E. Strobell, Harold Masursky, and C. D. Nordquist; U.S. Geological Survey, Flagstaff, AZ

In FY 1985, nomenclature activities reached a new high as the 1:500,000-scale maps of Mars, new outer-planet satellite maps, and the Venera 15 and 16 radar images of Venus became available. Eighty-two new features were named on Mars, mostly on 52 new high-resolution maps. In addition, nomenclature on the 1:15 million-scale planetwide Mars maps was finished and checked against all existing maps of Mars; names on 24 1:2 million-scale maps and 4 1:5 million-scale maps were also checked in proof stage. Publication of the 1:15 million-scale maps of Mars in FY 1986 will mark the first time that a complete set of names for Martian features (other than landing-site names) is available in one map series.

Between early March and mid-September, the Soviets proposed names for 239 features portrayed on mosaics of Venera radar images. We checked each of these proposals for morphological and etymological accuracy and made the extensive changes required by the International Astronomical Union (IAU). The mosaics and updated lists were then sent to members of the IAU committees for their review and approval.

Thirteen names were added to features on three 1:5 million-scale maps of Ganymede.

A report on resolutions and three computer printouts of the names proposed since the 1982 meeting of the General Assembly of the IAU were prepared for adoption at its 1985 triennial meeting in New Delhi. Names approved by the IAU Executive Committee in 1984, names proposed in 1985 for consideration by the Executive Committee, and a combined list of names were presented separately, as required by the IAU.

A new Task Group to name surface features on asteroids and comets was appointed by the IAU Working Group for Planetary System Nomenclature; the chairman will be confirmed by the Executive Committee. Members include:

Dr. David Morrison, USA, chairman pro tempore
Dr. Joseph Veverka, USA
Dr. Andre Brahic, France
Dr. Marcello Fulchignoni, Italy
Dr. Tomas Gombosi, Hungary
Dr. Leonid Kasantfomaliti, USSR
Dr. Yaroslav Yatskiv, USSR
Dr. Y.C. Chang, China
Dr. Syuzo Isobe, Japan

A bank of suitable names for features on preliminary maps of the Uranian satellites has been prepared by the Outer Planets Task Group.

The annual Gazetteer of Planetary Nomenclature has been extensively corrected and its format revised; it has been open filed by the U.S. Geological Survey (OF 84-692) and is expected to be distributed by the end of the calendar year. An illustrated Gazetteer with revised feature coordinates is planned later as a NASA Special Publication.

A preliminary draft of a chapter on planetary nomenclature, to be included in a book on planetary cartography, has been prepared.

Future work includes the following tasks. Names will be added to features on additional 1:500,000-scale maps of Mars and 1:5 million-scale maps of Ganymede and possibly of Callisto. Additional names will be chosen for Venusian features as the Soviet maps become available to the planetary geology community. The final lists of adopted names will be prepared for publication in the Transactions volume of the 1985 IAU meeting in New Delhi. The nomenclature chapter for the book on planetary cartography will be completed.

REGIONAL PLANETARY IMAGE FACILITIES' DATA DIRECTORY

B. Weiss, T. Stein, R. Arvidson, McDonnell Center for the Space Sciences, Department of Earth and Planetary Sciences, Washington University, St. Louis, MO 63130

Although the concept of a global or combined data directory for the RPIFs was originally suggested in 1982, it was not until November 1983 that the RPIF Librarians prepared a document (which was addressed and delivered to the RPIF Directors) pertaining to a "Catalog of RPIF Holdings." The first paragraph in that paper declared:

> The Librarians feel it is critical that all Facility data sets and support materials be fully documented and catalogued in a digital format and be made available on-line, thus providing an automated "card-catalog" for all data products housed by the RPIF system. In order to function as a network of data exchange for investigators it is crucial this information be available.

Time schedules adopted at the November 1983 meeting suggested a useable on-line directory should be initiated within a year. That goal was not attained, although a "mini-catalog" which utilized D-Base II software on an IBM PC was developed at Washington University and demonstrated to the Librarians and Directors in March 1985. At that same meeting the decision was made to proceed with the RPIF Data Directory and to use MicroVAX or VAX hardware as the host at each RPIF.

We began work on the next version of the Directory - this time using VAX Datatrieve software - but it soon became evident that we needed a more powerful software package. We investigated several commercial relational database management systems, and decided in August 1985 to proceed with System 1032, from Software House, Cambridge, Massachusetts. We are now concentrating on a System 1032 prototype of the Directory.

DIRECTORY CONTENTS

The prototype Directory is designed to reflect RPIF holdings which are housed as data sets (e.g., Apollo 17 Hasselblad 70mm prints; Mariner 10 strip contact prints of 1st, 2nd, and 3rd Mercury encounters; Viking Orbiter 1 and 2 orthographic orbital photography prints; etc.) plus indexes, journals, texts, and other related materials. It will not include any listing of products by unique identifiers (i.e., an inventory similar to BIRP or Mark IV SEDR), although this will be added in the future.

GENERAL PHILOSOPHY

1. Main Directory

The Main Directory - to be maintained at a central site - will store ALL data holdings for ALL facilities, excluding Local Notes and Location information. Copies of that Directory will be distributed to RPIFs on a regular basis.

A. The following outputs to be feasible:
   1. on-line monitor display
   2. hardcopy printouts
   3. choice of partial or full output
   4. full printout of every field
   5. option to sort fields in a given order

B. Search/find procedures to use a menu-driven program with varying degrees of user instruction.

C. Main Directory updates will be the responsibility of the Washington University RPIF.

D. Directory to expand eventually to include an inventory which will provide collection access on a picno by picno basis.

2. Local Directories

Individual facility directories will provide users with "Local Notes" and "Location" information for that particular RPIF only. Each RPIF will be responsible for inputting and maintaining its own local information.

GENERAL PROCEDURES

1. Each record will be assigned a unique number as it is entered in the Directory. That number is the "key" for this relational database management system. (See Figure 1)

2. AT THE BEGINNING the Directory will be sent to each RPIF where the Data Manager/Librarian will be responsible for reporting to the Washington University RPIF all Directory record numbers which reflect that RPIF's holdings. This information will be used to update the Holdings field of the Directory.

3. After the initial phase of the project is completed the Data Managers/ Librarians can routinely check the Directory for new record numbers -- and again report their holdings to the Washington University RPIF.

AUTHOR INDEX

A'Hearn, M. F., 14
Adams, J. B., 221, 341
Alfvén, H., 47, 123, 124
Anderson, D. M., 411
Anderson, S., 528
Arvidson, R. E., 233, 234, 245, 344, 347, 353, 358, 634

Baker, V. R., 271, 274, 414
Baldwin, R. J., 494
Baloga, S., 291, 315, 318
Banerdt, W. B., 68, 147, 363
Barlow, N. G., 211
Batson, R. M., 577, 580, 581, 584, 586
Bell, J. F., 3, 526
Bindschadler, D. L., 499, 548
Birnie, D. P., 156
Bjorkman, M. D., 224
Blount, H. G., 502
Bodenheimer, P., 134
Boone, S., 173
Boothroyd, J. C., 417, 439, 442
Boss, A. P., 125
Bougan, S., 257
Bowin, C., 150
Brandstrom, G., 411
Bratt, S. R., 366
Bridges, F., 48
Bridges, P. M., 580, 581
Brown, R. H., 54
Bruckenthal, E. A., 344, 347, 358
Bruegge, R. M. V., 369
Buratti, B. J., 71, 505
Burns, R. G., 153, 507
Bus, S. J., 18
Bush, M. M., 294

Campbell, D. B., 369, 372, 548, 565, 567
Carr, M. H., 51
Carras, N. G., 381
Carter, R., 528
Casacchia, R., 111
Cassen, P., 126
Chapman, B. D., 553
Chapman, C. R., 214
Chapman, M. G., 459
Christensen, P. R., 237, 350, 509, 512, 515
Christiansen, E. H., 587
Clark, P. E., 545
Clark, R. N., 54
Colvin, T. R., 592
Coombs, C. R., 526
Cristofferson, B., 134
Croft, S. K., 57, 193
Crumpler, L. S., 372
Cuzzi, J., 60

Dale-Bannister, M., 344, 347
Davies, M. E., 590, 591, 592
Davis, D. R., 136, 214
Davis, P. A., 196, 424, 518, 526
Davis, S. L., 584
De Hon, R. A., 421
Dehn, J., 321
Dermott, S. F., 63
Dial, A. L., 459
Dickey, J. O., 541
Duncan, C. D., 333
Durham, W. B., 383
Durisen, R., 60
Dyar, M. D., 156, 507

Edwards, K., 586
Ellsworth, K., 184

Fanale, F., 25
Ferguson, H. M., 450
Fillius, W., 89
Fink, J. H., 336, 427
Flammer, K. R., 4
Ford, P. G., 553
Fox, A., 297
Fox, D., 257
Francis, R. A., 375
Frey, H., 430, 433, 436

Gaffey, M. J., 3, 5
Garvin, J. B., 499
Gaskell, R. W., 66
Gault, D. E., 222, 227, 628, 630
Gharakhani, V., 505
Gibson, J., 38
Gibson, E. K., 158
Goertz, C. K., 88

Golombek, M. P., 68, 71, 147, 363
Gooding, J. L., 161, 239
Gradie, J. C., 3, 521
Graham, F., 73
Grant, J. A., 417, 439, 442
Greeley, R., 90, 242, 257, 265, 302, 306, 309, 400, 446, 512, 598, 601, 623, 624
Greenberg, R., 74, 214
Grimm, R. E., 378
Grün, E., 76, 88
Guest, J. E., 601
Guinness, E. A., 245, 344, 347, 353, 358

Hapke, B., 73, 77, 78, 505, 540
Harmon, J. K., 548
Hartmann, W. K., 129, 130, 217
Hawke, B. R., 3, 199, 523, 526
Hayden, C. J., 494
Head, J. W., 92, 94, 221, 331, 366, 369, 372, 381, 395, 499, 548, 565, 567
Heard, H. C., 383
Hill, J. R., 79, 88, 89
Hine, A. A., 565
Holsapple, K. A., 218, 224
Hood, L. L., 164
Hooper, D. M., 131
Hopler, J., 587
Horanyi, M., 8, 9, 10
Horner, V. M., 446
Houpis, H. L. F., 11
Housen, K. R., 224
Howington, A. E., 570, 608, 612
Huguenin, R. L., 528

Inge, J. L., 580
Ip, W. H., 11, 88
Isbell, C. E., 586

Jackson, B., 4
Jakosky, B. M., 350, 515
Janke, D. R., 449
Jeanloz, R., 167
Johnson, M., 173
Johnson, R. E., 80
Jones, J., 164
Jordan, R., 614
Jordan, R., 618
Jurgens, R. F., 545

Kahn, R., 234, 245, 353
Keiffer, H. H., 33
King, J. S., 294, 322
Kirby, S. H., 383
Knittle, E., 167
Kobrick, M., 545
Kochel, R. C., 277, 280
Komar, P. D., 283
Kozak, R. C., 562

Lee, S. W., 248, 251, 532
Lin, D., 48
Lissauer, J., 83
Lucchitta, B. K., 311, 450, 488, 595
Lucey, P. G., 523, 526

MacKinnon, D. J., 254
Malin, M. C., 12, 449, 456, 458
Marouf, E. A., 117
Marshall, J. R., 257
Masursky, H., 459, 632
Maxwell, T. A., 131, 406
McCord, T. B., 3, 221
McDaniel, E. E., 421
McFadden, L., 14
McGill, G. E., 462
McKinnon, W. B., 84, 105
Mendis, D. A., 4, 8, 9, 10, 11, 76, 79, 87, 88, 89
Middleton, J., 433
Mitchell, A. C., 170
Moore, H. J., 355, 550
Moore, J. M., 90
Morfill, G. E., 76
Morgan, H. F., 584
Morris, E. C., 297
Mouginis-Mark, P. J., 221, 328, 471
Muenow, D. W., 161
Mullins, K. F., 581
Murchie, S. L., 92, 94

Naney, M. T., 156
Nash, D., 96
Nellis, W. J., 170
Nelson, R. M., 99, 505
Newhall, X. X., 541
Nicholson, P. D., 101
Nicol, M., 173
Nordquist, C. D., 632
Northrop, T. G., 89

Nuth, J., 626

O'Conner, J. E., 274
Ostro, S. J., 15
Owensby, P. D., 526

Parker, T. J., 260, 465, 468
Patton, P. C., 385
Peale, S. J., 104, 125
Pettingill, G. H., 553
Phillips, L. F., 286
Phillips, R. J., 176
Pieri, D. C., 291, 315, 318, 468
Pieters, C. M., 221, 535, 536, 627
Pisias, N. G., 283
Plaut, J., 245
Plescia, J. B., 387
Podolak, M., 134
Pollack, J. B., 134, 179
Porco, C. C., 101
Postawko, S., 471
Pranger, H., 474

Radousky, H. B., 170
Raitala, J. T., 390
Read, W. F., 476
Reasenberg, R. D., 181, 555
Riedel, J. E., 66
Ross, M. N., 170, 186
Rossbacher, L. A., 477, 480
Roth, L. E., 558
Roush, T. L., 538
Rowland, S. K., 325
Ryan, V. L., 507

Saunders, R. S., 25, 260, 291, 318, 390, 468, 558
Schaber, G. G., 560, 562, 598
Schafer, F. J., 570, 612, 614, 618
Schenk, P. M., 105
Schmidt, R. M., 224
Schneeberger, D. M., 291, 318, 465
Schubert, G., 184, 186
Schultz, P. H., 188, 203, 222, 227, 393, 628, 630
Schumm, S. A., 286
Scott, D. H., 403, 598, 601, 603
Semeniuk, A., 430, 433, 436
Semeniuk, J., 436

Shapiro, I. I., 548
Sharpton, V. L., 395
Sheridan, M. F., 257, 321
Shoemaker, C. S., 482
Shoemaker, E. M., 18, 482
Shu, F., 60
Simmons, A. M., 322
Simmons, D. W., 280
Simonelli, D. P., 108
Simpson, R. A., 569
Singer, R. B., 344, 347, 358, 538
Sjogren, W. L., 190
Smith, M. O., 221, 341
Smoluchowski, R., 22
Smythe, W. D., 99, 505
Soderblom, L. A., 424
Solberg, T. C., 507
Solomon, S. C., 366, 378, 397
Spencer, J. R., 193
Spudis, P. D., 196, 199, 203, 302, 393, 518, 526
Steenstrup, S. J., 485
Stein, T., 634
Stephens, J., 25
Stofan, E. R., 565, 567
Strobell, M. E., 459, 632
Strom, R. G., 28, 211
Summers, C. A., 450, 488
Swanson, S. E., 156
Synnott, S. P., 66

Tanaka, K. L., 403, 601, 603
Teeling, M. J., 111
Theilig, E., 306, 400
Thomas, P., 114, 263
Thompson, T. W., 550
Thurber, C. H., 206
Tokarcik, S., 436
Turcotte, D. L., 207
Tyler, G. L., 117, 569

Underwood, J. R., 111

Veverka, J., 108, 114

Walker, G. P. L., 325
Watters, T. R., 406
Weidenschilling, S. J., 136, 214
Weiss, B., 634
Weissman, P. R., 31, 33
Wetherill, G. W., 139
Whipple, F. L., 35

Whitford-Stark, J. L., 502
Wildey, R. L., 605
Wilhelms, D. E., 491, 494
Williams, A., 540
Williams, J. G., 18, 38, 541
Williams, S. H., 265
Wilson, L., 328, 331
Wisdom, J., 142
Witbeck, N. E., 603
Wolfe, R. F., 18
Wood, C. A., 41, 333
Woronow, A., 111, 229
Wu, S. S. C., 570, 608, 612, 614, 618

Yoder, C. F., 541
Yuan, C., 126

Zebker, H. A., 117
Zimbelman, J. R., 12, 336, 427
Zisk, S. H., 221
Zurek, R. W., 512

1. Report No.	2. Government Accession No.	3. Recipient's Catalog No.
NASA TM-88383		

4. Title and Subtitle	5. Report Date
Reports of Planetary Geology and Geophysics Program - 1985	March 1986
	6. Performing Organization Code: EL

7. Author(s)	8. Performing Organization Report No.
S.J. Bougan,* compiler	
	10. Work Unit No.

9. Performing Organization Name and Address	11. Contract or Grant No.
Planetary Geosciences Program Solar System Exploration Division Office of Space Science and Applications	
	13. Type of Report and Period Covered: Technical Memorandum

12. Sponsoring Agency Name and Address	14. Sponsoring Agency Code
National Aeronautics and Space Administration Washington, DC 20546	

15. Supplementary Notes

*Center for Earth and Planetary Studies, National Air and Space Museum, Smithsonian Institution, Washington, DC 20560

16. Abstract

This is a compilation of abstracts of reports from Principal Investigators of NASA's Planetary Geology and Geophysics Program, Office of Space Science and Applications.

The purpose is to provide a document which succinctly summarizes work conducted in this program (for 1985). Each report reflects significant accomplishments within the area of the author's funded grant or contract.

17. Key Words (Suggested by Author(s))	18. Distribution Statement
Planetary Geology and Geophysics Solar System Evolution Planetary Geologic Processes	Unclassified - Unlimited Subject Category 91

19. Security Classif. (of this report)	20. Security Classif. (of this page)	21. No. of Pages	22. Price
Unclassified	Unclassified	668	A99

For sale by the National Technical Information Service, Springfield, Virginia 22161

NASA-Langley, 1986

National Aeronautics and
Space Administration
Code NIT-4

Washington, D.C.
20546-0001

Official Business
Penalty for Private Use, $300

SPECIAL FOURTH-CLASS RATE
POSTAGE & FEES PAID
NASA
Permit No. G-27

UNIV OF TEXAS
GEOLOGY DEPT
SCIENCES
ATTN: MR WILLIAM MUEHLBERGER
P O BOX 7909
AUSTIN TX 78712

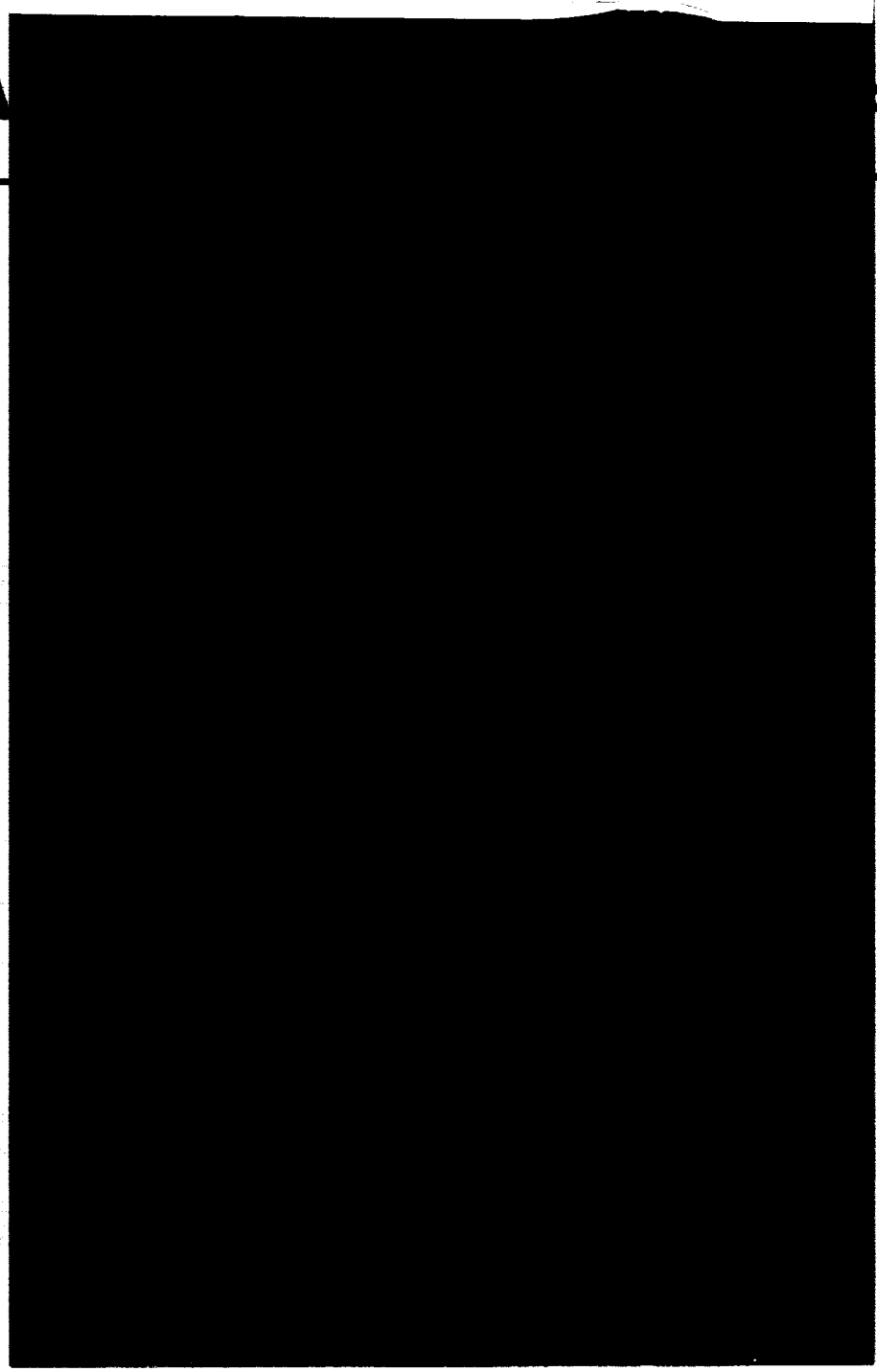

NASA

liverable (Section 158
Manual) Do Not Return